Transactions of the ASME®

Transactions of the ASME, Journal of Turbomachinery (ISSN 0889-504X) is published quarterly (Jan., Apr., July, Oct.) by The American Society of Mechanical Engineers, Three Park Avenue, New York, NY 10016. Periodicals postage paid at New York, NY and additional mailing offices. POSTMASTER: Send address changes to Transactions of the ASME, Journal of Turbomachinery, c/o THE AMERICAN SOCIETY OF MECHANICAL ENGINEERS, 22 Law Drive, Box 2300, Fairfield, NJ 07007-2300.
CHANGES OF ADDRESS must be received at Society headquarters seven weeks before they are to be effective. Please send old label and new address.
STATEMENT from By-Laws. The Society shall not be responsible for statements or opinions advanced in papers or ... printed in its publications (B7.1, Par. 3).

INDEXED by Applied Mechanics Reviews and Engineering Information, Inc. Canadian Goods & Services Tax Registration #126148048

Journal of Turbomachinery

Published Quarterly by The American Society of Mechanical Engineers

VOLUME 123 • NUMBER 2 • APRIL 2001

TECHNICAL PAPERS

(**Contents continued on inside back cover**)

This journal is printed on acid-free paper, which exceeds the ANSI Z39.48-1992 specification for permanence of paper and library materials. ♾™
♻ 85% recycled content, including 10% post-consumer fibers.

ANNOUNCEMENTS

High Lift and Aft-Loaded Profiles for Low-Pressure Turbines

R. J. Howell
O. N. Ramesh
H. P. Hodson

Whittle Laboratory,
University of Cambridge,
Cambridge, United Kingdom

N. W. Harvey
Rolls Royce plc.,
Derby, United Kingdom

V. Schulte
BMW Rolls-Royce, GmbH,
Dahlewitz, Germany

This paper shows how it is possible to reduce the number of blades in LP turbines by approximately 15 percent relative to the first generation of high lift blading employed in the very latest engines. This is achieved through an understanding of the behavior of the boundary layers on high lift and ultra-high lift profiles subjected to incoming wakes. Initial development of the new profiles was carried out by attaching a flap to the trailing edge of one blade in a linear cascade. The test facility allows for the simulation of upstream wakes by using a moving bar system. Hot wire measurements were made to obtain boundary layer losses and surface-mounted hot films were used to observe the changes in boundary layer state. Measurements were taken at a Reynolds number between 100,000 and 210,000. The effect of increased lift above the datum profile was investigated first with steady and then with unsteady inflow (i.e., with wakes present). For the same profile, the losses generated with wakes present were below those generated by the profile with no wakes present. The boundary layer behavior on these very high lift pressure distributions suggested that aft loading the profiles would further reduce the profile loss. Finally, two very highly loaded and aft loaded LP turbine profiles were designed and then tested in cascade. The new profiles produced losses only slightly higher than those for the datum profile with unsteady inflow, but generated 15 percent greater lift. [DOI: 10.1115/1.1350409]

Introduction

The fan of a high bypass ratio turbo fan engine produces up to 80 percent of the total thrust of the engine. It is the low-pressure turbine that drives the fan, and on some engines, the LP turbine drives a number of compressor stages. The efficiency of the LP turbine has a large effect on the specific fuel consumption of an engine, where typically, a 1 percent increase in LP turbine efficiency gives rise to 0.7–0.9 percent increase in engine efficiency [1]. In over 50 years of extensive research, the efficiency of the LP turbine has risen just 10 percentage points. The development of the gas turbine as a whole and the LP turbine in particular has therefore reached a stage where rises in efficiency are increasingly hard to obtain. Manufacturers are therefore looking at other ways to make their products more competitive.

The initial cost of the engine, its weight, fuel consumption, maintenance, and servicing costs all contribute to the total cost of ownership. However, an engine's weight has a bearing on both the manufacturing costs and fuel consumption. If one can reduce the number of components in an engine, then any airplane it powers will be able to carry increased cargo for the same fuel load. Reducing the number of components may also increase reliability, since there are fewer components to fail. The heaviest single component is often the LP turbine. In some engines, it can comprise one third of the total weight. The LP turbine is therefore a prime component for reducing total engine weight.

Profile loss in the boundary layers is the main loss-generating mechanism caused by the blades in an LP turbine. This is because the high aspect ratio (typically 5:1) of these blades means that there is relatively little surface covered by secondary flow. A well-behaved pressure side flow will also contribute little to the total losses generated. Curtis et al. [2] report a loss breakdown for a conventional LP turbine blade. This indicated that up to 60 percent of the losses were generated by the suction surface boundary layers.

The weight and manufacturing cost of the LP turbine can be reduced by reducing the number of blades. It is to this end that the research described in this paper is aimed. In reducing the number of blades in a stage, each blade must carry a greater aerodynamic load. This leads to greater deceleration over the rear of the suction surface. Conventional (i.e., steady) wisdom dictates that this would increase the risk that a separated laminar boundary layer might not reattach. An open separation at the trailing edge would result in an unacceptably high profile loss.

Hourmouziadis [3] introduced the concept of controlled diffusion blading that was designed to keep the suction surface boundary layer attached. Boundary layer separation was allowed, but it was designed to occur soon after peak suction. Because peak suction occurred at midchord, the separated boundary layer could reattach before the trailing edge. These profiles were designed to give low loss coefficients and only steady flow effects were considered.

Schulte and Hodson [4] investigated the effects of moving bars and their wakes on the losses generated by an LP turbine cascade. In some cases and at some Reynolds numbers, the effect of incident wakes resulted in the cascade producing lower losses than it did with steady flow. As wakes shed from upstream blade rows travel over the downstream blade rows, they disturb the boundary layers. As the boundary layers become more receptive to disturbances, the wakes eventually cause the formation of turbulent spots through the mechanism of bypass transition. These spots travel downstream in a characteristic manner [5]. Behind the spot is a calmed region of flow that has a full velocity profile. This profile is very stable and does not separate in adverse pressure gradients as easily as a laminar profile. Schulte and Hodson [4] argued that it was this ability to withstand adverse pressure gradients that allowed the spots to keep a flow from separating. It was also shown that this interaction was responsible for the loss reductions.

The main objective of this research was to improve the understanding of the suction side boundary layers under the influence of wakes with the aim of increasing the lift of the profiles. The datum profile to which all other measurements are compared is the high lift profile *H* as described by Curtis et al. [2].

Experimental Details

Figure 1 shows a schematic diagram of the experimental rig. This consists of the cascade of seven blades and a moving bar

Contributed by the International Gas Turbine Institute and presented at the 45th International Gas Turbine and Aeroengine Congress and Exhibition, Munich, Germany, May 8–11, 2000. Manuscript received by the International Gas Turbine Institute February 2000. Paper No. 2000-GT-261. Review Chair: D. Ballal.

mechanism that allows bars to be traversed upstream of the leading edge of the cascade. The bars are fitted to belts and carried on wheels that are driven by a variable-speed DC motor. The speed of the bars was set to give the required flow coefficient ($\phi = V_x / V_{\text{bar}} = 0.7$). The bar to cascade pitch ratio was set to the same value (1.5) as that of an equivalent LP turbine. The traverse mechanism allows measurements to be performed within the blade passage.

The inlet stagnation temperature was measured using a thermocouple that was placed within the inlet plenum. A Pitot probe placed downstream of the moving bars provided the reference cascade inlet stagnation pressure.

The bar diameter was chosen so that the wakes they produced gave rise to the same losses as those generated by a typical upstream LP turbine blade row. It can be shown that the approximate total pressure loss coefficient for the bars is given by the following expression:

$$Y_p = \frac{C_d D}{S_{\text{bar}} \cos\beta} \tag{1}$$

where C_d is the drag coefficient of the bar at the bar Reynolds number used in the tests and D is the bar diameter. Full details of the simulation capabilities of the moving bar rig can be found in Schulte [6].

The moving bars also accurately simulated the inlet turbulence intensity of an upstream blade row. Measurements showed that the bars produced a variation in inlet turbulence comparable to that at the inlet to a 1.5-stage large-scale turbine with the same profiles [7]. The bars produced a peak turbulence measured at inlet to the cascade of 13 percent, with a velocity defect of approximately 10 percent of the undisturbed free-stream value. The reduced frequency of the bar and cascade system was set to the value (0.78) where minimum losses were measured for the datum profile; see Schulte and Hodson [4].

In one series of experiments, a number of pressure distributions were created by placing a flap below the one instrumented with static pressure tappings (see Fig. 2). These were then tested for their performance with steady and unsteady inflow. As the flap is rotated around the trailing edge of the blade to which it is attached, it alters the effective exit area of the blade row above. Obviously, the cascade is no longer periodic, but if it is only the suction side distribution that is of interest, this does not matter. Details of the analysis of the data obtained from this flap-modified cascade are given in the next section.

In addition to the flap, a number of inserts were placed into the blade passage as shown in the same figure and these were used to alter the position of peak suction on the blade surface. When the flap was at large angles from the vertical, suction was also applied to the flap surface. This was designed to keep the boundary layer attached to the flap, so that very high loadings could be achieved on the test profile.

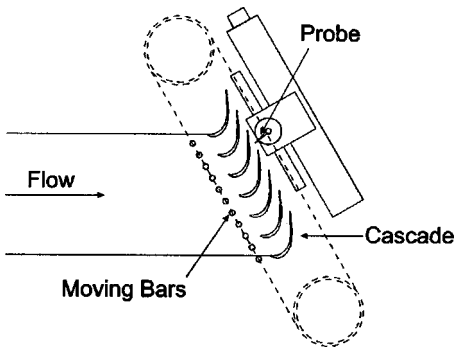

Fig. 1 Schematic of moving bar rig and cascade

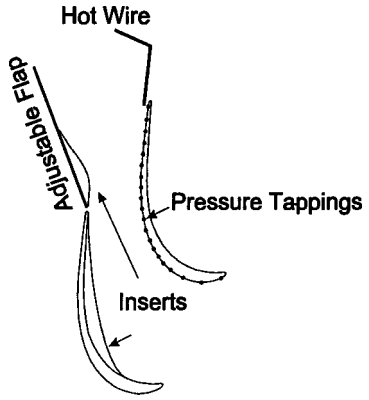

Fig. 2 Schematic of flap and inserts used in the cascade

A single-wire hot wire boundary layer probe was used for boundary layer traverses and was calibrated in a low-turbulence calibration wind tunnel according to a modified form of King's Law. Heat transfer from the hot wire to its surroundings is affected by the presence of walls, and a correction [8] has been applied to the data. The effect due to changes in ambient temperature upon the hot wire calibration were accounted for with the correction of Bearman [9].

The hot wire traverses were made near the blade trailing edge, at 96 percent surface length and in a direction normal to the surface. Up to 30 positions through the boundary layer were measured, depending on the height of the boundary layer for a given blade profile. The use of a single hot wire (at the trailing edge) is perfectly acceptable because any loss data presented is from only turbulent and *attached* boundary layers. The use of a hot wire within a separation bubble is subject to many errors.

Hot film measurements have also been performed to assess the development of the blade surface boundary layers and relate these findings to the losses generated by the profiles. The measurement of wall shear stress using hot films was developed by Bellhouse and Schultz [10] and is now a well-established technique. It is possible to calibrate hot films, but this is a difficult and time-consuming process (see Hodson [11] and Davies and Duffy [12]). In addition, errors of 20 percent or more arise when hot films calibrated in a laminar flow are used to measure a turbulent flow. The hot film sensors used on the aft part of the suction surface were likely to see laminar, turbulent, and separated flow at different positions of the upstream rotor. Their calibration would therefore be extremely difficult and quite probably impossible.

The hot film and hot wire measurements were carried out at midspan of the blade. The spacing between each hot film sensor was approximately 3 percent surface length. Error analysis showed that the total pressure loss error is ± 0.15 percent, the traverse positioning accuracy was ± 0.05 mm, and the momentum thickness repeatability was within 1 percent.

Measurement of Relative Lift and Loss. When the flap is fitted, the cascade is no longer periodic. Therefore, it is not possible to carry out wake traverses to measure profile loss. The measured boundary layer momentum thickness at 96 percent *s* of the blade is used to calculate the loss due to the suction side boundary layer. Denton [13] used a control volume analysis to derive an expression for the loss generated by the suction and pressure side boundary layers, trailing edge, and mixing out of the flow over a turbine blade. The calculation of loss in the current paper only takes into account the suction side boundary layer losses.

The suction side losses are assumed proportional to the momentum thickness at the trailing edge and inversely proportional to the pitch of the blade. The value of loss relative to the datum profile is given by the expression below:

$$Y_{\text{rel}} = \frac{\theta}{\theta_{\text{datum}}} \cdot \frac{S_{\text{datum}}}{S} \tag{2}$$

where θ is the trailing edge momentum thickness, and S is the equivalent pitch of the pressure distribution under investigation. Implicit in these arguments are the assumptions that the shape factor and exit angles remain constant. All the measurements made with wakes present produced an attached turbulent boundary layer at the trailing edge of the blade, resulting in very similar shape factors. When wakes are present, the separation bubble is suppressed and the exit angles are assumed constant.

Increasing the lift of a profile amounts to increasing the pitch of an equivalent cascade, i.e., reducing the number of blades. There are then fewer blades generating losses and this is taken into account in Eq. (2). The expression given above requires a value of equivalent pitch that would result in the profile for which the losses were measured. The circulation related to the pitch by the following expression:

$$\oint V \cdot ds = S\cos\alpha_2(\tan\alpha_1 - \tan\alpha_2)/\rho V_x h \tag{3}$$

The circulation is evaluated from the measured pressure distribution and is used to find the pitch of the equivalent cascade. A constant value of inlet and exit angle was used because the new pressure distributions were for a particular duty. The pressure side pressure distribution from the datum profile (*H*) was used for all calculations.

Curtis et al. [2] assumed constant values for the losses produced by the pressure side, trailing edge, and boundary layer blockage. In the following analysis, rather than assuming that those losses are constant, they have not been included because it is extremely difficult to determine how they change with increasing lift. Including these ''extra'' losses will dilute the effects of the loss reduction that occurs on the suction side due to the presence of wakes.

Results and Discussion

Datum Profile. The suction side pressure distribution of the datum profile (*H*) is shown in Fig. 3. This was measured with steady inflow and at a Reynolds number of 130,000. It is designated profile *H*, by Curtis et al. [2]. However, it should be noted that Curtis et al. conducted their investigations at a Reynolds number of 210,000. The profile is typical of those used in some of the newer turbofan engines currently in service.

The datum profile (*H*) exhibits high leading edge loading with a continual acceleration up to peak suction, which occurs at around 53 percent surface length. The flow then undergoes a large deceleration and consequently (with steady inflow) separates from the blade surface and forms a separation bubble. The bubble undergoes transition at about 95 percent *s* and the flow reattaches before the trailing edge of the blade.

The effect of Reynolds number changes on the losses produced by the datum profile is shown in Fig. 4. The trailing edge momentum thickness is made nondimensional by the momentum thickness measured with *unsteady* inflow at a Reynolds number of 130,000.

The variation of momentum thickness for the datum profile was calculated up to just before separation using Thwaites' expression:

$$\theta_s \sqrt{\frac{0.45v}{V_s^6}} \int_{le}^{te} V^r ds \tag{4}$$

Subtracting the momentum thickness calculated using Eq. (4) from the measured value at 96 percent *s* gives the amount of loss due to the separation, reattachment process, and development of the turbulent boundary layer. On the datum profile, the separation bubble is responsible for producing more than 60 percent of the total boundary layer losses. The development of the very small (less than 2 percent *s*) amount of turbulent boundary layer after reattachment was ignored in this simple calculation.

Figure 4 shows that there is a large loss reduction at low Reynolds numbers due to the effects of the wakes. As the Reynolds number is increased, the loss reduction diminishes to the point where at a value of 2.1×10^5 there is almost no loss reduction. The reduction in the difference in losses with increased Reynolds number is due to the reduction in the size of the separation bubble. If the size and loss generated by a separation bubble are smaller, then so is the possible loss reduction due to the wake effects. This is the situation at the higher Reynolds numbers.

The low Reynolds number condition (1.3×10^5) was selected for the tests presented here since this is where the greatest loss reduction occurred. This Reynolds number is also that found in the last stages of the largest turbofan engines such as the Trent series and it is also that found in the first few stages of smaller engines such as the BR700 series. The datum pressure distribution (profile *H*) shown in Fig. 3 and its measured trailing edge momentum thickness were taken as the datum values for nondimensionalizing the results presented in this paper.

Higher Lift Profiles. Having described the performance of the datum profile, it is now appropriate to look at the performance of more highly loaded profiles, using the attached flap. One way

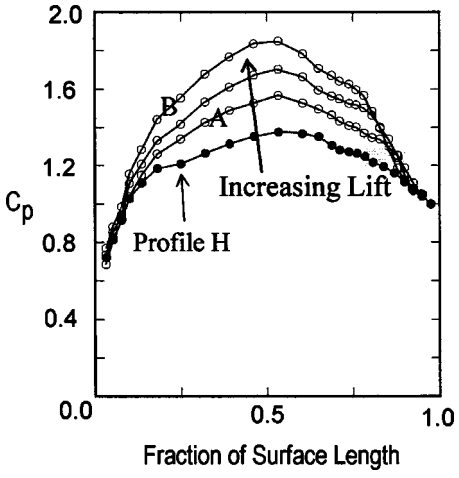

Fig. 3 Pressure distributions of datum profile and others with increased lift measured at a Reynolds number of 130,000, with unsteady airflow

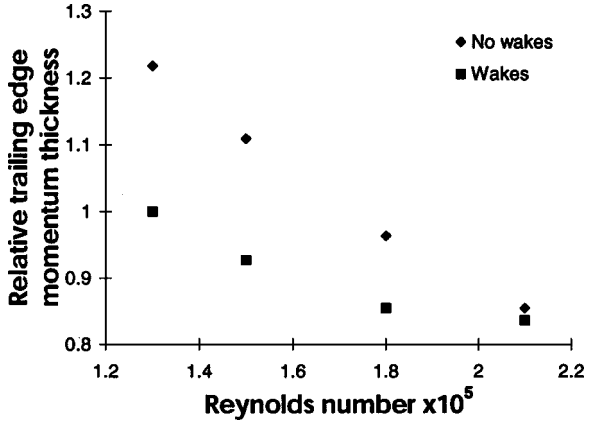

Fig. 4 Relative trailing edge suction side boundary layer momentum thickness variation with Reynolds number for datum profile

of increasing the lift further is to decrease the minimum pressure on the suction side. Unfortunately, this increases the deceleration that the flow must go through. To increase the lift on the instrumented blade, the flap was rotated away from the suction surface of that blade. The pressure ratio driving the flow through the passage is that from the inlet to the cascade, to the exit created between the instrumented blade suction surface and flap. When the outlet area increases, so does the mass flow through the passage. The exit velocity is approximately constant, as is the throat area, so the velocity there must increase resulting in a larger deceleration over the back surface.

Figure 3 shows the effect of increasing the flap angle on the resulting pressure distributions. The geometric position of the throat and therefore the approximate position of peak suction was kept constant in these tests.

Hot film measurements carried out on these profiles indicated that the location of boundary layer separation remained approximately constant (i.e., within the 3 percent *s* resolution of the hot film gages) with steady inflow. The reattachment location of the steady flow separation bubble moved *away* from the trailing edge of the blade with increased loading. Howell [14] showed that the surface length of the bubble reduced with increasing lift, but the surface normal height of the bubble *increased* as did the losses it generated.

Table 1 shows a summary of the measurements and analysis of hot film data taken from the above profiles and profile *C*, which is discussed later. The location of wake-induced transition also remained constant with increases in peak velocity and occurred in all cases just *after* the separation position. The data in Table 1 indicate that the increase in deceleration seems to cause the separation to become more receptive to disturbances and it starts to undergo transition and therefore reattachment earlier. Hot film data confirm this, but it is not shown for brevity. Wake-induced transition only occurs around the separation position. This detail has also been noted in flows over other high lift turbine blade profiles. For example, Howell [14] used hot film gages to measure transition phenomena on a high-speed, full-scale rig of the BRR 715 and 710 LP turbines. These measurements showed that wake-induced transition does not occur until around the region where the boundary layer separates. The value of Re_θ is approximately 250 just before separation (measured 5 percent *s* before the separation location) on both the BMW Rolls-Royce high-speed profiles and the profiles presented in this paper. The details of the pressure distribution will also affect Re_θ. However, calculation of the momentum thickness showed that there was very little variation between profiles. In all cases, the values approached a value of approximately 250 just before separation. Profiles *A* and *H*, for example, give rise to a difference in momentum thickness of only 5 percent. They are, however, radically different pressure distributions. This illustrates that details in the pressure distribution are not particularly important in determining momentum thickness just before separation.

At a Reynolds number of 130,000, the results suggest that a wake produced by a well-behaved LP turbine blade (in this case producing an inlet turbulence intensity of 14 percent, Banieghbal et al. [7]) does not cause transition before separation. This is because there is a continual acceleration up to peak suction, keeping the boundary layer stable. From a practical standpoint, this means that sophisticated transition onset models are not required. Once the position of separation is known, this essentially fixes the wake-induced transition onset location at design conditions. Larger bars producing stronger wakes do, however, cause transition onset before separation, as noted by Schulte [6]. However, these wakes cannot be considered typical of an LP turbine operating at design conditions.

Table 1 Separation and multimode transition locations for a range of profiles taken from hot film measurements and at a Reynolds number of 130,000

Profile	Separation (%s)	Wake Induced Transition (%s)	Separated Flow Transition[1] (%s)
H	74	77	95
A	74	77	92
B	74	77	86
C	80	83	92
U1	74	79	84

At higher Reynolds numbers, the flow is more receptive to disturbances, and one would expect wake-induced transition to occur earlier. However, hot film measurements on the datum profile at a Reynolds number of 210,000 indicate that wake transition still occurred at approximately the separation location.

Figure 5 shows the relative suction side boundary layer loss ratio against lift ratio. The losses are made nondimensional by the loss of the *datum profile (H) with unsteady inflow*. The lift ratio is also made nondimensional by the lift value of the *datum profile with unsteady inflow*. As expected, when the lift is increased above that of the datum profile, the suction surface loss increases. This loss increase under steady flow conditions is partly due to the increased turbulent boundary layer that is allowed to develop because the laminar bubble length has reduced. Figure 5 also shows that only when the loading level reaches 120 percent of the datum profile do the losses produced with wakes present become higher than the losses produced by the datum with steady inflow.

Figure 5 also shows that the potential for obtaining a loss reduction with the use of wakes increases as the loading increases. It may be possible to keep the losses well below the steady flow loss at lift levels higher than were possible with the current experimental rig. One must assume, however, that there will come a loading level where the ability of wakes and calmed regions to suppress separation bubbles may be lost.

Aft-Loaded Profiles. Results have shown that the effect of upstream wakes on the profile loss of a downstream suction surface boundary layer is beneficial, especially at high loadings and low Reynolds numbers. At very high loading, hot film measurements indicated that there was a large amount of surface covered in transitional and turbulent flow after boundary layer reattachment. Reducing this area of turbulent flow will result in a reduction in profile loss. An ST diagram can illustrate the unsteady transition process by placing variations of boundary layer state in time and space on a single diagram; see Fig. 6. The *y* axis shows multiples of wake passings and the *x* axis shows the surface distance. Transitional flows caused by wakes are marked *W*, turbulent flow caused by separated flow transition is marked *T*, and calmed flow is marked *C*. The diagram shows two cases of wake passings at different reduced frequencies. Figure 6(*a*) shows a

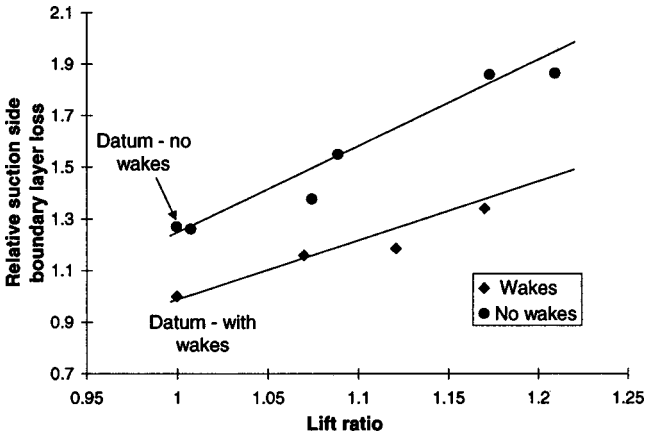

Fig. 5 Variation in loss with increased lift, with and without wakes, at a Reynolds number of 130,000

reduced frequency similar to that for the profile shown here where separated flow transition occurs between wake passings. The region marked *B*, between wakes one and two, shows turbulent flow due to the separation bubble. At this lower reduced frequency, the flow at the trailing edge is turbulent because of the wakes, then calmed and then turbulent again due to the separation bubble transition. However, if the time between wake passings was sufficiently short (i.e., a high reduced frequency), then the separation bubble may never have time to re-establish itself. This is the case in Fig. 6(*b*). In this case, the flow at the trailing edge is fully turbulent because of the wakes alone. Removing some turbulent boundary layer (by pushing the position of peak suction/velocity, and therefore separation) toward the trailing edge would reduce the profile loss. This was carried out by placing inserts into the blade passage as shown in Fig. 2. It should be noted that in all of the experiments presented in this section, the reduced frequency was kept constant.

The datum pressure distribution resulted in a position of peak suction at about 53 percent *s* and boundary layer separation at 74 percent *s*. In the following investigations, the position of peak suction was moved to 60, 65, and 68 percent *s*. For example, the profile with peak suction at 65 percent *s* resulted in separation at 80 percent *s*, a rearward shift of 6 percent *s*. Steady flow hot wire and hot film measurements of the boundary layer at 96 percent *s* showed that sometimes the separation bubble did not reattach before the trailing edge of the blade on some pressure distributions. Open separations result in an unacceptably large profile loss. However, when the same pressure distribution was subjected to incoming wakes, it was found that the boundary layer at 96 percent *s* was *always* attached, no matter what the loading, or position of peak suction. The loss measurements (i.e., of momentum thickness) at 96 percent *s* with unsteady inflow with a hot wire are therefore valid.

Due to the construction of the experimental rig, it was not possible to conduct a well-ordered parametric investigation. This is because accurate control over the details of the pressure distributions was difficult to achieve. An ideal pressure distribution would look like the one for the datum blade but with a higher loading with peak suction nearer the trailing edge. Some pressure distributions produced large decelerations, but little loading over the forward part of the blade. These sorts of pressure distributions resulted in only a small or no increase in lift over the datum profile. Therefore, a wide spread of measurements for various pressure distributions was obtained, but some of which turned out not to be satisfactory.

Figure 7 shows the pressure distribution of the aft-loaded profile C, and also the datum profile measured with wakes present. The results show that the separation bubble, if it exists, has a small effect.

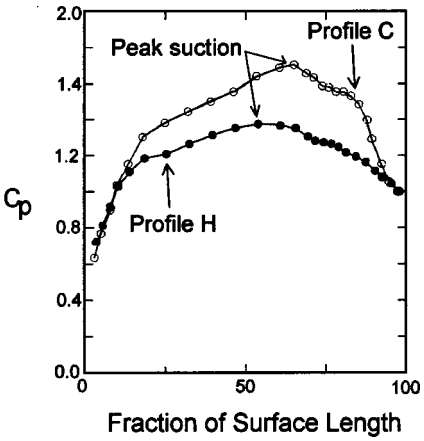

Fig. 7 Aft-loaded and datum pressure distributions; all measurements carried out at Re=130,000 and with wakes present

Figure 8 shows the variation in relative suction side loss versus the position of peak suction for a range of lift coefficients. The losses are made nondimensional by the loss of the datum profile with unsteady inflow. Unless otherwise stated, all measurements were made with wakes present. Figure 8 shows an obvious trend for the profile losses to decrease when the position of peak suction is moved aft. The reduction in loss can be attributed to a reduction in surface covered in turbulent boundary layer and also to the reduction in turbulent boundary layer due to the wakes, as illustrated in Fig. 6. The scatter of the data for each peak suction position is due to the different loadings that the pressure distributions produced. Profile *C* produced 15 percent more lift than the datum profile and a similar level of loss. Table 1 shows details of the transition mechanisms for this profile. The value of Re_θ just before separation is around 250, which is similar to other profiles such as those in the BR700 series of LP turbines as measured by Howell [14].

Hot film measurements from profile *C* also showed that wake-induced transition occurred just after separation; see position *S* in Fig. 9. Figure 9 is an ST diagram of the nondimensional ensemble mean shear stress on profiles *C* and *H*. The locations of the hot film sensors are indicated by black dots at the top of the figure. The shear stress is made nondimensional by the maximum value of shear stress measured by each sensor, i.e., $\tilde{\tau}(s,t)/\tilde{\tau}_{\max}(s)$ is plotted, where *t* is time. This serves to enhance the periodic fluctuations in shear stress, but at the expense of the overall levels of shear stress. In fact, the levels of shear stress at 60 percent *s* are much less than those at 96 percent *s*.

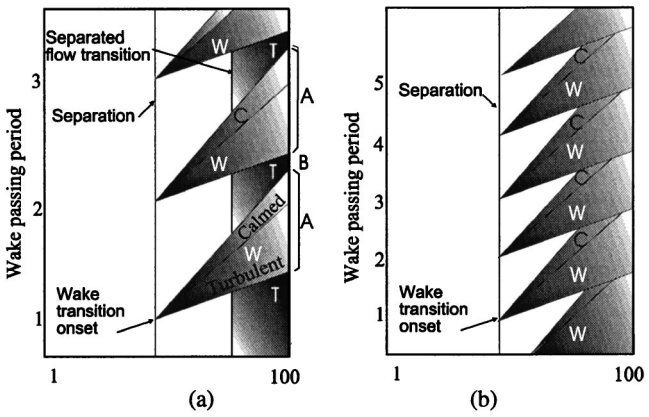

Fig. 6 ST diagram of wake-induced transition showing two different reduced frequencies

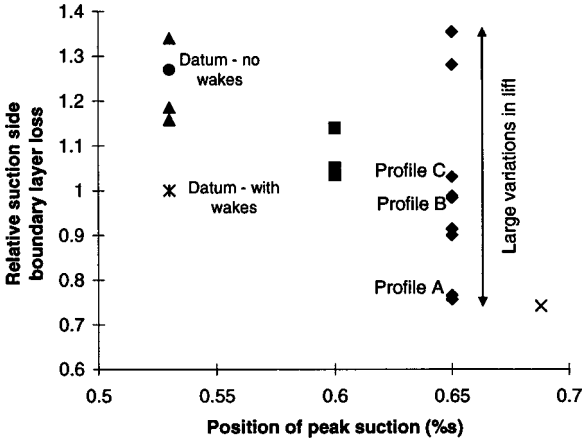

Fig. 8 Variation of losses with position of peak suction

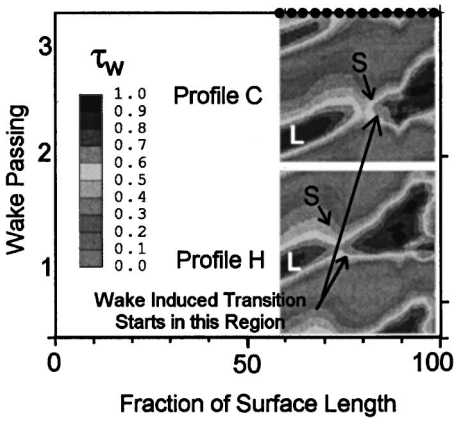

Fig. 9 ST diagram of nondimensional ensemble mean quasi-shear stress data from profiles *H* and *C* at a Reynolds number of 130,000, and flow coefficient of 0.7

Hot film data from profiles *C* and *H* exhibit the same basic structure. Wake-induced transition starts in the regions marked and this coincides with the position of flow separation, marked *S*. The regions of transitional flow are classical in that they are wedge shaped. The wedge is caused by the difference in leading and trailing edge propagation rates of the turbulent spots that are created by the wakes. The regions marked *L* have a lower shear stress level than the wake-induced transition regions downstream. These are caused by the wake's velocity defect on the laminar boundary layer and are not caused by transitional flow.

Figure 10 shows relative suction surface boundary layer loss against relative lift for distributions with peak suction 65 percent *s*, for cases with and without wakes. Again, the losses are made nondimensional by the loss of the datum profile (*H*) with unsteady inflow. The lift ratio is also made nondimensional by the lift value of the datum profile (*H*) with unsteady inflow. This figure does show that aft loading turbine blades are only possible when wakes are present to control the losses generated in the reattaching part of the separation bubble.

Ultra-High Lift Profiles. Having established the boundary layer features that are present on ultra-highly loaded LP turbine blades with incoming wakes, two new *ultra-high lift* profiles were designed and tested in cascade.

Figure 11 shows the new ultra-high lift velocity distributions, *U*1 and *U*2 and the datum profile (*H*) measured with unsteady inflow. The design brief for these profiles was to achieve an increase in lift of approximately 15 percent compared to the datum profile *H*. The inlet and exit angles were the same as the datum cascade and the design Reynolds number was chosen to be 130,000. The best lift–loss pressure distributions, presented earlier, seem to be those that produced peak suction at 65 percent *s* and separation at around 80 percent *s*. The position for laminar separation was therefore designed to occur at approximately 80 percent *s*, and the value of Re_θ was designed to be approximately 250. This ensures that wake-induced transition would be initiated in this region. The presence of the turbulent spots, calmed regions and wake turbulence then controls the separation bubble growth and loss generation.

The velocity distributions in Fig. 11 were made nondimensional by the cascade exit velocity. This is the correct way of presenting cascade data, whereas for the tests using the attached flap, the static pressure at 96 percent *s* was used. Unfortunately, Fig. 11 shows that increasing the lift tends to depress the trailing edge velocity. This occurs because as the lift increases, the amount of uncovered turning on the rear of the suction surface also increases. For example, the geometric throat is at approximately 45 percent *s* for the profile *U*1 and there is approximately 10 deg of inviscid deviation. The uncovered turning is used to maintain the high suction side velocities, downstream of the geometric throat. This large amount of uncovered turning suppresses the velocity at the trailing edge of the aerofoil. This occurs because, for a given mean exit angle, the potential field of each profile increases in strength as the lift increases. Therefore, there is a greater redistribution of the streamlines once the flow passes beyond the trailing edge plane. This means that the velocity at the trailing edge is lower than that at the cascade exit plane.

The deceleration between peak suction (or peak velocity) and the exit plane is what would be expected on a profile without a convex rear suction surface. On these ultra-high lift profiles, the flow must decelerate to a much lower value at the trailing edge. An unfortunate consequence is that as the lift is increased, the amount of suction surface deceleration increases far more than would be expected if only the peak velocity and cascade exit velocity were considered. Ultimately, this will limit the amount of lift that is practicably possible.

The two ultra-high lift profiles (*U*1 and *U*2) both generate the same lift and so must have the same total circulation. However, the ultra-high lift profiles are of two different designs with different circulation distributions. Profile *U*1 resulted in a rather flat-topped velocity distribution. Hot film measurements showed separation was detected at approximately 75 percent *s* and wake-induced transition occurred at 80 percent. The flat top pressure

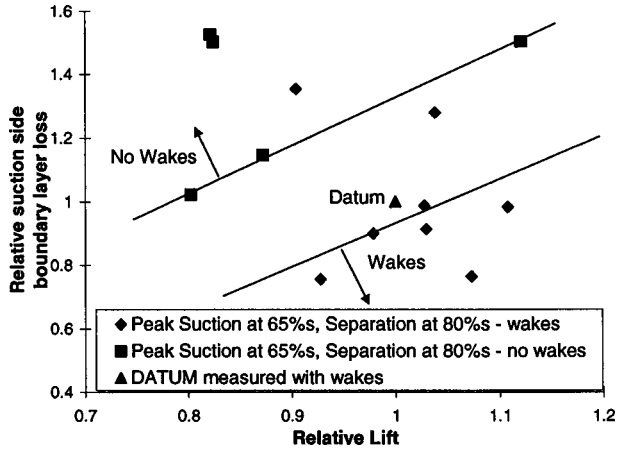

Fig. 10 Relative suction side boundary losses for aft-loaded profiles measured with and without wakes present; Re =130,000

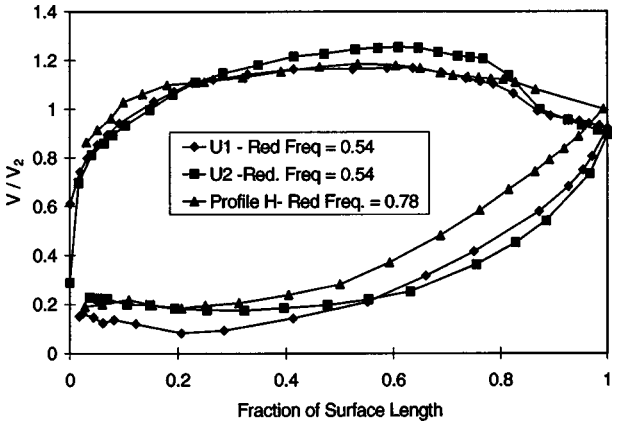

Fig. 11 Velocity distributions for the ultrahigh lift profiles, *U1* and *U2*, and the datum profile *H*; all distributions measured with unsteady inflow; velocities are made nondimensional using the cascade exit velocity; Re=130,000

distribution allowed the boundary layer to grow more quickly than it would if the flow was still accelerating. Unfortunately, this profile has a similar separation location to the datum profile and this, combined with the flat top pressure distribution and increased diffusion, is likely to lead to higher losses.

To avoid the flat top pressure distribution, profile *U*2 has an increased peak velocity to give the continual acceleration and allow proper aft loading of the velocity distribution. However, as discussed above, this led to an even larger back surface diffusion than for profile *U*1 and resulted in much higher losses than expected.

Figure 12 shows the variation of relative total pressure losses from the ultra-high lift profiles (and for the datum profile) for a number of reduced frequencies. All total pressure loss values are made nondimensional by the loss for the datum profile (*H*) at a Reynolds number of 130,000 with wakes present (reduced frequency of 0.78).

The losses generated by profile *U*2 are considerably higher than those for the other profiles, even when wakes are present. To illustrate this, the losses produced with steady inflow on profile *U*2 reached seven times the datum profile losses with unsteady inflow. The losses of profile *U*2 were high, but this was due to the elevated level of deceleration caused by the suppressed trailing edge velocity. Profile *U*1 produces losses that are also very high with steady inflow. However, when wakes are present, the losses reach a level that is more comparable to the datum profile. It should of course be remembered that both profiles *U*1 and *U*2 have 15 percent more lift than profile *H*. As the Reynolds numbers are increased, the performance of the ultra-high lift profiles improves dramatically. This is because the separation bubble losses are being reduced. By a Reynolds number of 170,000, the losses are roughly the same as the datum profile.

Further Discussion. The new ultra-high lift profiles produced greater losses than those for the datum profile at the design Reynolds number, but resulted in a decrease in the number of blades by 15 percent. Laminar separation occurred on profile *U*1 at approximately the same surface position as for the datum profile. Hot film measurements indicated the presence of turbulent boundary layer near the trailing edge. The separation location was moved further aft for profile *U*2, but required an increase in peak velocity to achieve this. The increased deceleration caused by this resulted in higher losses than those for the datum profile.

At very low Reynolds numbers, the greater the reduced frequency, the lower the losses. Howell [14] and Arndt [15] showed that stator 3 of a three-stage LP turbine had wake-induced turbulent regions on the suction surface appearing at twice the frequency of the wake passing of rotor 2. This effectively results in a doubling of the reduced frequency to which stator 3 is subjected. This can be considered beneficial for the current ultra-high lift profiles. This effect should reduce losses if this type of profile was used in an imbedded stage rather than just subjected to the wakes from a single upstream rotor. Higher Reynolds numbers occur in the first stages of the LP turbine while lower Reynolds numbers occur in later stages. This is fortuitous as high reduced frequencies (caused by multistage interactions) occur in later stages in the LP turbine where the larger separations (due to lower Reynolds numbers) are likely to be better controlled. In the first few stages, there are fewer blade row interactions, but as Fig. 12 showed, one does not desire reduced frequency doubling as this increases losses.

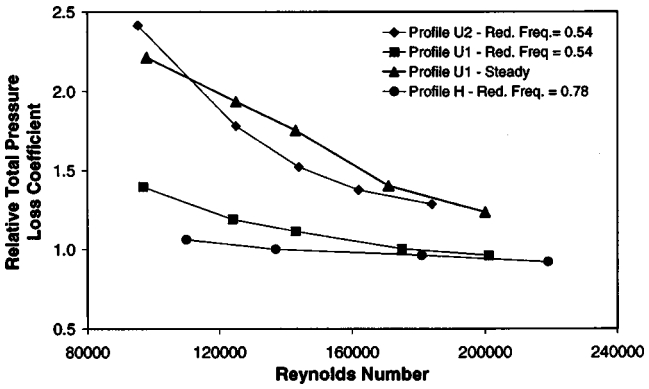

Fig. 12 Nondimensional total pressure loss variation versus Reynolds number for the datum and ultrahigh lift cascades

The measurements presented in this paper were carried out with a free-stream turbulence level of 0.5 percent. This level is lower than that in the engine environment and can be considered a worse case scenario. The size (and losses) of separation bubbles reduce when subjected to elevated levels of free-stream turbulence. With a higher turbulence level, the losses are likely to be further reduced at low Reynolds numbers. Using the ultra-high lift profiles in an engine environment is therefore likely to reduce the losses further.

Conclusions

In low Reynolds number flows (typically 130,000), the presence of wakes on the suction side boundary layer on a highly loaded LP turbine blade has a profound effect on the losses generated.

For a fixed position of peak suction with increased loading, steady flow reattachment of the boundary layer moved farther from the trailing edge. This resulted in a large amount of blade surface covered in turbulent boundary layer. Aft loading the pressure distributions decreased the amount of turbulent boundary flow present and so reduced the losses generated. Aft-loaded profiles are only viable when they are used with incoming wakes.

Two new highly loaded LP turbine profiles were designed using the data presented in this paper. With steady inflow the profiles, as expected, performed poorly. When subjected to unsteady inflow, the profile loss reduced dramatically. The profiles generate 15 percent more lift than the datum. The amount of suction surface deceleration was greater than anticipated due to the large back surface curvature on these profiles used to aft load the profiles. This curvature suppressed the trailing edge velocity, increasing the deceleration required by the flow. This effect limits how high the lift on such profile may be pushed in the future because of the effect on the losses. It may well be that the limit has been reached with these profiles and even the effect of wakes cannot control the large losses generated by the separation bubble.

Controlled diffusion blading takes no account of the effects of upstream wakes. By understanding the unsteady effects of wakes and using them carefully, the current limits placed on the deceleration level, location of peak suction and separation are reduced. Profiles that generate acceptable losses but increased lift will therefore be possible by including the new design ideas.

Acknowledgments

The first author would like to thank the Schiff Foundation for funding most of this work. Some of this work was carried out with the support of Rolls Royce plc and the DERA and DTI CARAD. The authors would like to thank them for granting permission to publish this paper.

Nomenclature

C_p = pressure coefficient $= \sqrt{(P_{01}-p)/(p_{01}-P_{te})}$
C_d = drag coefficient
C = chord
D = bar diameter
$\underline{f}$ = wake passing frequency
$\bar{f}$ = reduced frequency $= fC/V_2$
p = surface pressure
p_{01} = stagnation pressure at inlet

p_2 = pressure on surface at trailing edge
S = pitch, or maximum surface length
s = surface length
v = kinematic viscosity
V = isentropic viscosity on surface
V_2 = isentropic velocity at 96 percent s
Y_p = total pressure loss
Y_{rel} = relative suction side loss
datum = value from the datum profile
le = leading edge
te = trailing edge
x = axial
$\alpha_{1,2}$ = inlet and outlet flow angle, respectively
β = wake relative flow angle
θ = boundary layer momentum thickness
ρ = density
τ = wall shear stress at the wall
∞ = local free stream

References

[1] Wisler, D. C., 1998, ''The Technical and Economic Relevance of Understanding Boundary Layer Transition in Gas Turbine Engines,'' Minnowbrook II, 1998 Workshop on Boundary Layer Transition in Turbomachines, NASA/CP-1998-206958.

[2] Curtis, E. M., Hodson, H. P., Banieghbal, M. R., Denton, J. D., Howell, R. J., and Harvey, N. W., 1997, ''Development of Blade Profiles for Low-Pressure Turbine Applications,'' ASME J. Turbomach., **119**, pp. 531–538.

[3] Hourmouziadis, J., 1989, ''Aerodynamic Design of Low Pressure Turbines,'' AGARD Conf. Proc. LS-167, June.

[4] Schulte, V., and Hodson, H. P., 1998, ''Unsteady Wake-Induced Boundary Layer Transition in Highly Loaded LP Turbines,'' ASME J. Turbomach., **120**, pp. 28–35.

[5] Schubauer, G. B., and Klebanoff, P. S., 1955, ''Contributions on the Mechanism of Boundary-Layer Transition,'' NACA TN 3489.

[6] Schulte, V., 1995, ''Unsteady Wake Boundary Layer Interaction,'' Ph.D. thesis, Cambridge University, England.

[7] Banieghbal, M. R., Curtis, E. M., Denton, J. D., Hodson, H. P., Huntsman, I., Schulte, V. S., and Harvey, N. W., 1995, ''Wake Passing in LP Turbines,'' AGARD Conf. Proc. No. 23.

[8] Hodson, H. P., 1985, ''An Inviscid Blade-to-Blade Prediction of a Wake-Generated Unsteady Flow,'' ASME J. Eng. Gas Turbines Power, **107**, pp. 337–344.

[9] Bearman, P. W., 1971, ''Correction for the Effect of Ambient Temperature Drift on Hot-Wire Measurements in Incompressible Flow,'' DISA Inf. No. 11, pp. 25, 30.

[10] Bellhouse, B. L., and Schultz, D. L., 1966, ''Determination of Mean and Dynamic Skin Friction Separation and Transition in Low-Speed Flow With a Thin-Film Heated Element,'' J. Fluid Mech., **24**, No. 2.

[11] Hodson, H. P., 1984, ''Boundary Layer and Loss Measurements on the Rotor of an Axial-Flow Turbine,'' ASME J. Eng. Gas Turbines Power, **106**, pp. 391–399.

[12] Davies, M. R. D., and Duffy, J. T., 1995, ''A Semi-empirical Theory for Surface Mounted Aerodynamic Wall Shear Stress Gages,'' ASME Paper No. 95-GT-193.

[13] Denton, J. D., 1993, ''Entropy Generation in Turbomachinery Flows,'' 7th Cliff Garrett Turbomachinery Award Lecture, SAE Paper No. 902011.

[14] Howell, R. J., 1999, ''Wake Separation Bubble Interaction on Low Reynolds Number Turbomachinery,'' Ph.D. thesis, Cambridge University, England.

[15] Arndt, N., 1993, ''Blade Row Interaction in a Multistage Low-Pressure Turbine,'' ASME J. Turbomach., **115**, pp. 137–146.

Measurements in Separated and Transitional Boundary Layers Under Low-Pressure Turbine Airfoil Conditions

Ralph J. Volino
United States Naval Academy,
Department of Mechanical Engineering,
Annapolis, MD 21402
e-mail: volino@usna.edu

Lennart S. Hultgren
National Aeronautics and Space Administration,
Glenn Research Center at Lewis Field,
Cleveland, OH 44135
e-mail: hultgren@grc.nasa.gov

Detailed velocity measurements were made along a flat plate subject to the same dimensionless pressure gradient as the suction side of a modern low-pressure turbine airfoil. Reynolds numbers based on wetted plate length and nominal exit velocity were varied from 50,000 to 300,000, covering cruise to takeoff conditions. Low and high inlet free-stream turbulence intensities (0.2 and 7 percent) were set using passive grids. The location of boundary-layer separation does not depend strongly on the free-stream turbulence level or Reynolds number, as long as the boundary layer remains nonturbulent prior to separation. Strong acceleration prevents transition on the upstream part of the plate in all cases. Both free-stream turbulence and Reynolds number have strong effects on transition in the adverse pressure gradient region. Under low free-stream turbulence conditions, transition is induced by instability waves in the shear layer of the separation bubble. Reattachment generally occurs at the transition start. At Re=50,000 the separation bubble does not close before the trailing edge of the modeled airfoil. At higher Re, transition moves upstream, and the boundary layer reattaches. With high free-stream turbulence levels, transition appears to occur in a bypass mode, similar to that in attached boundary layers. Transition moves upstream, resulting in shorter separation regions. At Re above 200,000, transition begins before separation. Mean velocity, turbulence, and intermittency profiles are presented. [DOI: 10.1115/1.1350408]

Introduction

Modern low-pressure turbine airfoils are subject to increasingly stronger pressure gradients as designers impose higher loading in an effort to improve efficiency. The adverse pressure gradients on the suction side of these airfoils can lead to boundary-layer separation, particularly under low Reynolds number conditions. Separation bubbles, particularly those that fail to reattach (referred to as ''burst'' bubbles), can result in a significant loss in lift, and, consequently, can cause a significant degradation of engine efficiency, e.g., Hourmouziadis [1], Mayle [2], and Sharma et al. [3]. A component efficiency drop of the order of 2 percent may occur between takeoff and cruise conditions, due to the lower Reynolds numbers at altitude for large commercial transport engines, and could be as large as 7 percent for small military engines at high altitude. Accurate prediction of separation and reattachment is, therefore, crucial to improved turbine design.

The prediction of boundary-layer separation in the low-pressure turbine is complicated by the fact that a substantial fraction of the boundary layers on the airfoils may be transitional at cruise conditions [2], whereas at takeoff conditions the boundary layers are generally more turbulent. Transition may begin before or after separation, depending on the Reynolds number and other flow conditions, and has a strong influence on subsequent reattachment. Further complicating the problem are the high free-stream turbulence levels in a real engine environment, the strong pressure gradients along the airfoils, the curvature of the airfoils, and the unsteadiness associated with wake passing from upstream stages. Because of the complicated flow situation, transition in these devices can take many paths that can coexist, vary in importance, and possibly also interact, at different locations and instances in time. Mayle [2] classified the major paths of transition in turbomachinery as: ''natural'' transition involving Tollmien–Schlichting waves, normally not considered a dominant feature in a real environment; ''bypass'' transition, caused by high free-stream turbulence levels; ''separated-flow'' transition, occurring in the shear layers of separation bubbles; and ''periodic-unsteady'' transition, such as wake induced bypass transition. The performance degradation noted above indicates that existing engineering models are not quite adequate, particularly in cases of separated flow transition. To design against separation while still pushing toward higher loading, a better understanding of the flow physics clearly is needed.

The literature contains considerable information on boundary layer transition. Since transition may begin either before or after separation on a turbine airfoil, both attached and separated flow studies are pertinent. Most of the earliest work considered attached flow transition under low free-stream turbulence conditions. In this case, the transition sequence generally consists of a region of growth of linear Tollmien–Schlichting waves followed by nonlinear interactions and shortly thereafter breakdown to turbulence. At higher free-stream turbulence levels, the Tollmien–Schlichting waves do not appear to play a significant role and turbulent spots are created directly. This is known as bypass transition [4]. Mayle [2] and Volino and Simon [5] provide reviews of work for low to moderate free-stream turbulence conditions from a turbomachinery point of view.

At free-stream turbulence levels above about 5 percent, transition under zero pressure gradient conditions tends to be rapid, as shown by Kim et al. [6]. With strong acceleration, however, Volino and Simon [7] showed that extended transition zones are still possible, even at free-stream turbulence intensities (TI) as high as 8 percent. At high TI the flow transitions between a highly disturbed nonturbulent state, which is characterized by high-amplitude fluctuations at relatively low frequencies, and a fully turbulent state, which is characterized by fluctuations over a broad

Contributed by the International Gas Turbine Institute and presented at the 45th International Gas Turbine and Aeroengine Congress and Exhibition, Munich, Germany, May 8–11, 2000. Manuscript received by the International Gas Turbine Institute February 2000. Paper No. 2000-GT-260. Review Chair: D. Ballal.

range of both high and low frequencies. The nonturbulent fluctuations are induced directly by the free-stream unsteadiness, while the turbulent fluctuations are due to near-wall production. The transition region is characterized by intermittent switching between the two types of flow. These results are in agreement with the earlier study of Blair [8], which documented bypass transition in accelerating flow with free-stream turbulence levels up to about 5 percent.

Separated flow transition has also been considered. Among recent studies, Malkiel and Mayle [9] documented transition in the shear layer over a separation bubble. They report a transition similar to that in a free shear layer, in which instability waves break down to turbulence. Intermittency grew in a manner similar to that in an attached boundary layer, but with a higher turbulent spot production rate. Hatman and Wang [10] considered cases on a flat plate under low free-stream turbulence conditions and various Reynolds numbers and adverse pressure gradients. They reported cases in which transition began over the separation bubble and cases in which separation occurred after the boundary layer was already transitional.

Documentation at moderate to high free-stream turbulence levels is more limited. Halstead et al. [11] provide a study from a rotating cascade with multiple stages and TI characteristic of an actual low-pressure turbine. The adverse pressure gradients in this study, however, did not induce separation. Qiu and Simon [12] documented separated flow transition at high TI in a study of the flow over a low-pressure turbine airfoil. Experiments were conducted using a single passage cascade utilizing the so-called ''Pak-B'' airfoil shape, which is an industry supplied shape representative of a modern aggressive design. This shape was also used by Murawski et al. [13]. Qiu and Simon [12] considered inlet free-stream turbulence levels of 0.5, 2.5, and 10 percent, and Reynolds numbers (based on nominal exit velocity and suction-surface wetted length) ranging from 50,000 to 300,000. They observed a variety of behaviors, including short separation regions and complete transition at the higher Reynolds numbers and TI levels, and long separation bubbles and incomplete transition at the low Reynolds numbers and low-TI levels. Sohn et al. [14] conducted a similar study in the same wind tunnel as the present experiments. The facility has been altered, however, in both geometry and flow conditions for the present work.

Computational work has followed the experiments, including work by Dorney et al. [15], Chernobrovkin and Lakshminarayana [16], and Huang and Xiong [17]. More experimental work will provide insights for further improvements in computational models and test cases for code validation.

In the present study, the boundary layer on a flat plate is subject to a streamwise pressure gradient corresponding to that on the suction side of the ''Pak-B'' airfoil. Choosing this pressure gradient allows comparison to the Qiu and Simon [12] study, to determine the significance of convex curvature on the boundary layer behavior. Reynolds numbers from 50,000 to 300,000 are considered, spanning the range from cruise to takeoff conditions. Cases with high (nominal 7 percent) and low (0.2 percent) inlet free-stream turbulence are documented. As will be seen later, these inlet TI levels in the present study correspond to about 0.2 and 2.5 percent in the test section when normalized with the exit velocity. Free-stream turbulence levels in low-pressure turbines could be as low as about 3 percent [11] on the suction side of the airfoils. The present high-TI case, therefore, represents a realistic value. Further, a larger quantity of experimental data, with long time records at each measurement location, are acquired to provide more detailed documentation than in previous work.

The focus in this paper is on the mean velocities and turbulence statistics, as measured at stations throughout the boundary layer. From the velocity measurements, quantities such as intermittency, skin friction coefficients, transition start and end locations, and the locations of separation and reattachment are determined.

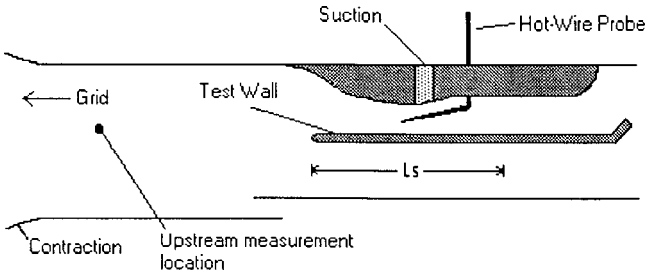

Fig. 1 Schematic of the test section, side view, approximately to scale. L_s=208 mm (wetted length, streamwise length is 206 mm).

Experimental Facility

All experiments were conducted in a low-speed, recirculating wind tunnel. The wind tunnel was used in earlier studies, such as that of Sohn and Reshotko [18]. A blower capable of 4.72 $m^3 s^{-1}$ (10,000 cfm), with an 18.6 kW (25 hp) motor and variable speed controller, supplies air to a rectangular channel of cross section 0.635 m×0.686 m. The channel contains a series of screens and flow straighteners. Turbulence generating grids may be placed at the exit of the channel. In the present study, a coarse grid with 40 percent blockage, constructed with 50 mm wide, 13 mm thick (in the streamwise direction) vertical and horizontal bars, was used for the high-TI case. Grid spacing is 178 mm. For the low-TI case, no grid was used. Just downstream (29 mm) of the grid location is an 0.914 m long, two-dimensional contraction, which reduces the flow area to 0.178 m×0.686 m. The long dimension is horizontal, the shorter is vertical. Following the contraction is an 0.245-m-long straight section, at the end of which is an upstream facing double bleed-scoop, located at the bottom of the channel, that further reduces the vertical dimension to 0.152 m. Following this is a rectangular channel, which serves as the test section. A side view schematic of the test section is shown in Fig. 1.

A 12.7-mm-thick horizontal Plexiglas plate with a 4:1 elliptical leading edge is mounted with its top surface at the vertical center of the channel, spanning the 0.686 m width, and with its leading edge 54 mm downstream of the beginning of the test section. The leading edge is, hence, 0.299 m downstream of the end of the contraction and 1.242 m downstream of the grid location. The upper surface of the plate is the test wall for the experiments. A two-dimensional contoured shape is attached to the wall opposite the test wall to produce the desired pressure gradient along the test wall. The shape of the top wall was determined through experimental trial and error. A contoured shape from a previous study was initially tested and then built up until the pressure profile along the test wall matched the ''Pak-B'' airfoil profile.

In a cascade experiment, favorable pressure gradients prevent separation on the pressure side of the airfoils. In the present situation, however, suction is needed to insure that the flow remains attached on the contoured wall, and separates only on the test wall. Suction was applied through holes along a 30 mm ×0.686 m strip in the contoured wall, just downstream of the throat (position of maximum free-stream velocity). A blower with a 0.75 kW (1 hp) electric motor and variable speed controller was used to produce the suction. The blower speed was adjusted for each Reynolds number considered, to prevent separation (as indicated by tufts attached to the contoured wall) and to produce the desired minimum pressure along the test plate at the throat. In addition, the contoured wall was covered by sandpaper upstream as well as a short distance downstream of the suction slot to promote a turbulent boundary layer on that surface via tripping.

Downstream of the test section, the flow entered a diffuser, then was routed through filters and a heat exchanger (cooler) before returning to the blower. The latter, of course, is needed to keep the wind-tunnel operating temperature from drifting.

Table 1 Station locations

Station	1	2	3	4	5	6	7
s/L_s	0.28	0.33	0.39	0.45	0.51	0.57	0.63
Station	8	9	10	11	12	13	14
s/L_s	0.69	0.75	0.81	0.88	0.94	1.00	1.06

Instrumentation

Streamwise velocity was measured using a single-sensor hot-wire probe with a 5-μm-dia platinum wire. The probe was inserted through a slot in the spanwise center of the top wall of the test section, and could be traversed in the streamwise direction and normal to the test wall. Traversing was accomplished using stepper motors controlled by the same computer used for data acquisition. Velocity profiles were acquired at the 14 streamwise stations listed in Table 1. Each profile consisted of 55–57 points spaced normal to the wall, with finer spacing closer to the wall. Voltage data were acquired from the constant-temperature anemometer using a 16 bit digitizer, controlled through an IEEE 488 interface bus with a computer. At each measurement location, 53 s long time records were acquired consisting of just over 1 million ($1{,}048{,}576 = 2^{20}$) data points collected at a 20 kHz sampling rate using an anti-aliasing 10 kHz low-pass filter before sampling. The uncertainty in mean and fluctuating velocities is 5 percent, which is primarily due to bias error resulting from calibration uncertainty. Bias errors cancel when the velocities are normalized on the free-stream velocity, resulting in 3 percent uncertainty in the normalized quantities.

Upstream velocities were measured just after the contraction, 236 mm upstream of the leading edge of the test wall, using a cross-wire probe inserted in two orientations to obtain all three velocity components.

Results

Experimental data were acquired with inlet TI of 0.2 and 7 percent and Reynolds numbers of 50,000, 100,000, 200,000, and 300,000, for a total of eight cases. The focus in this paper is on the Re=50,000 and 300,000 cases at both high and low TI. Details of all cases are available in Hultgren and Volino [19]. Streamwise pressure profiles for all cases are shown in Fig. 2 along with the expected profile for the suction side of the ''Pak-B'' airfoil. The pressure coefficients, C_p, were computed from free-stream velocity measurements at a fixed height above the test wall. The streamwise distance is normalized on the nominal suction surface length. The section of the test plate representing the airfoil is 208 mm long, while the actual plate is 356 mm long. The last measurement station is downstream of the point that represents the trailing edge of the airfoil. The pressure profiles upstream of the throat are in good agreement with the ''Pak-B'' profile for all cases. Downstream, the agreement is good for the high-Re, high-TI cases. At the lower Reynolds numbers, the C_p values indicate separation. At low-TI and Re=50,000, the boundary layer does not appear to reattach.

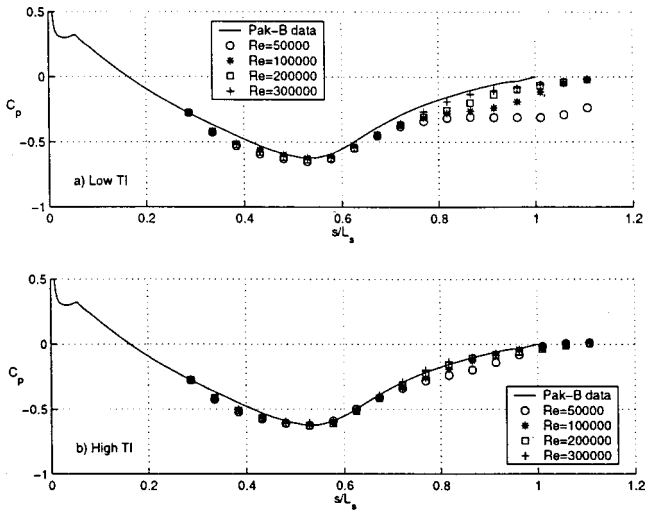

Fig. 2 C_p profiles; (*a*) low TI, (*b*) high TI

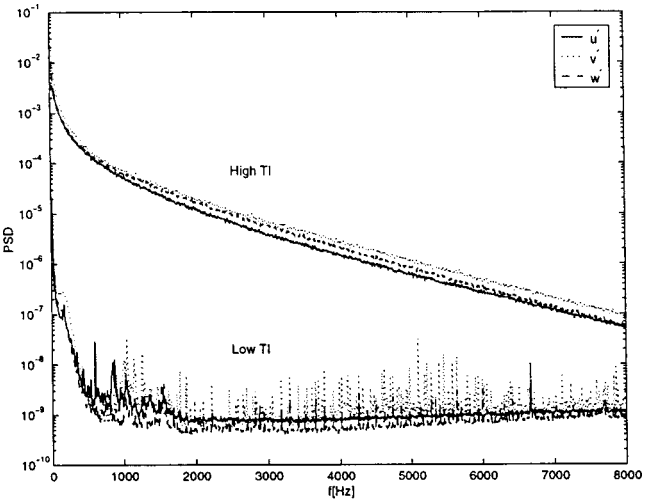

Fig. 3 Free-stream spectra at contraction exit. Re=300.000

Free-stream spectra were computed from the cross-wire measurements at the exit of the contraction. Figure 3 shows the upstream free-stream spectra at Re=300,000 for the high and low-TI cases. At the low-TI, the turbulence intensities in u', v', and w' are 0.3, 0.13, and 0.08 percent, respectively, at all Reynolds numbers. Most of this TI is due to low-frequency streamwise unsteadiness, as opposed to turbulent eddies. Downstream, the TI remains at about 0.2 percent, despite the strong acceleration over the leading section of the test wall. At the high TI, the upstream turbulence intensities for the 50,000 Reynolds number case are 5.0, 7.9, and 6.3 percent in u', v', and w'. These quantities are 5.8, 9.7, and 7.7 percent for the Re=300,000 case. The lower value in u' compared to v' and w' is due to the streamwise straining in the contraction, downstream of the grid. The integral length scales are 20, 40, and 30 mm as determined from the u', v', and w' spectra. The integral scales are comparable to the width of the bars of the grid, and are representative of the large eddies in the free stream. The integral scales did not vary significantly with the Reynolds number. Downstream, over the test wall, the TI drops to about 2.5 percent. This is in part due to decay of the free-stream turbulence, but is mainly due to the increase in mean free-stream velocity as the flow is accelerated. The ratio of the free-stream velocity at the exit of the contraction to the velocity in the throat is 0.45. Qiu and Simon [12] had the same ratio of inlet to throat velocity in their cascade experiment.

Low-TI Cases. The momentum thickness Reynolds number, Re_θ, and the shape factor, H, were computed from the mean velocity profiles and are presented in Fig. 4 for the low-TI cases. At the upstream stations for all cases, Re_θ grows very slowly due to the strong acceleration. The three higher Re cases show a jump at $s/L_s \approx 0.8$, which will be shown below to be indicative of transition and reattachment. The shape factors begin at a laminar value of about 2.3 in all cases and remain near this level until the fifth station, which corresponds to the throat. Downstream of the throat, there is a sharp rise in H for all cases due to a rise in the displacement thickness as the boundary layer separates. The Re

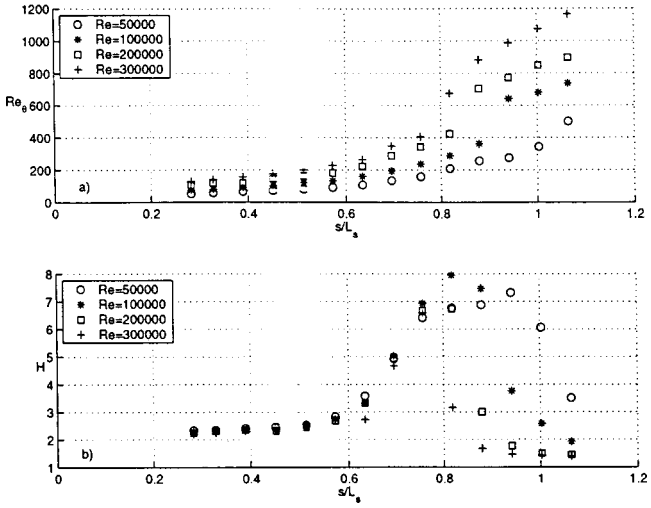

Fig. 4 Momentum thickness Reynolds numbers (*a*): and shape factors (*b*) for low-TI cases

=300,000 case returns to lower H first, as the boundary layer reattaches. A fully turbulent value of $H=1.4$ is achieved by the 12th station. The Re=200,000 case just reaches $H=1.4$ at station 13, which would correspond to the trailing edge of the airfoil. At the lower Re, the turbulent value is never achieved.

The mean streamwise velocity profiles, streamwise fluctuating velocity profiles, and intermittency profiles are presented for all streamwise stations of the low-TI, Re=50,000 case in Fig. 5. The mean velocity profiles (Fig. 5(*a*)) are normalized on the nominal free-stream exit velocity, which would correspond to the free-stream velocity at Station 13 if the boundary layer was attached there. Mean velocity shows the expected laminar boundary layer profile for the first five stations, up to the throat. At station 6, just past the throat, there is a hint of an inflection point near the wall, but the boundary layer may still be attached. At Stations 7–13, the boundary layer is clearly separated and the separation bubble is growing. At Station 14, the low, but nonzero velocity near the wall indicates that the boundary layer is reattaching, although it may be intermittently separated and attached. Since Station 13 represents the end of the airfoil in question, the mean velocity profiles indicate that the boundary layer would not reattach on the airfoil at this Re and TI.

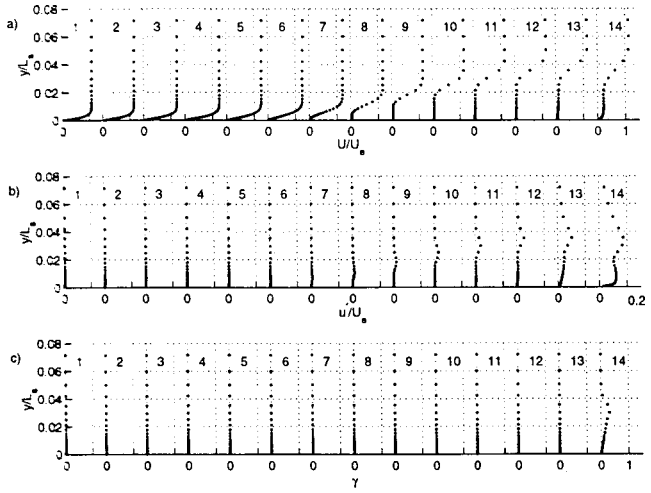

Fig. 5 Profiles for low-TI, Re=50,000 case: (*a*) mean velocity, (*b*) turbulence, (*c*) intermittency

The fluctuating velocity profiles (Fig. 5(*b*)) show very low turbulence at the first six stations, as expected for an accelerated laminar boundary layer subject to very low free-stream turbulence. At Station 7, there is a slight increase in u' just above the separation bubble seen in the mean profile. The u' fluctuations continue to grow in the shear layer over the separation bubble at Stations 8–12. The u' level is still very low inside the bubble, indicating that the flow is largely stagnant in this region. This is expected based on the near-zero mean velocity in the separation bubble. Since the hot wire cannot distinguish flow direction, a reversing or turbulent flow in the separation bubble would have resulted in false positive mean velocity if the magnitude of the fluctuations were significant. At Station 13, u' continues to grow in magnitude, and significant fluctuations also begin to appear near the wall. This may indicate that the boundary layer is starting to reattach. The fluctuations are also extending farther from the wall toward the free stream. By the last station, the u' profile shows a double peak, with a high value near the wall and a second peak in the shear layer. The near-wall peak indicates that an attached turbulent or transitional boundary layer is developing.

Intermittency profiles are shown in Fig. 5(*c*). The intermittency was computed from the digitized instantaneous streamwise velocity signal. Turbulent flow is classified as flow containing fluctuations over a broad band of frequencies, including high frequencies. This choice deliberately includes as turbulent the typical fluctuations associated with a turbulent boundary layer, but excludes the fluctuations associated with free-stream unsteadiness or narrow frequency band unsteadiness in a shear layer. While this definition is used in the present study, it is recognized that other researchers might choose different definitions of ''turbulence.'' The signal was digitally high-pass filtered to eliminate fluctuations associated with the free-stream unsteadiness and any coherent motion (instability waves) in the shear layer of the separation bubble. Both the free-stream-induced fluctuations and the instability waves occur at relatively low frequencies compared to ''true'' turbulence, which occurs over a wide range of scales, resulting in both high and low-frequency fluctuations. The filter frequency was varied linearly with Re, and was set at 750 Hz for the Re =50,000 cases. This filter cuts most of the turbulence, along with the other fluctuations, but passes enough of the high-frequency tail of the turbulence spectrum to allow determination of the intermittency. The first and second time derivatives of the filtered signal are computed and compared to thresholds. When either derivative is above its threshold, the flow is declared turbulent at that particular instant in time. The thresholds are set based on the local velocity at the measurement point and the free-stream velocity at that station. The comparison of time derivatives to thresholds is a standard technique documented in such studies as Hedley and Keffer [20] and Kim et al. [21]. The high-pass filtering is believed to be new, and is needed in the present study to separate the turbulence from other fluctuations in the boundary layer. In a low-TI attached boundary layer such filtering is not needed, as shown in studies such as Kim et al. [21]. Volino [22] computed intermittency for a high-TI attached boundary layer based on the turbulent shear stress, $u'v'$. The shear stress, in that situation, is primarily attributable to turbulent mixing, as opposed to other fluctuations induced in the boundary layer, and therefore serves as a good basis for intermittency determination, without the need for filtering. The present scheme allows intermittency determination from a single velocity component and rejects coherent motions in the shear layers of separation bubbles. The uncertainty in intermittency is 7 percent. Further details are available in Hultgren and Volino [19].

The profiles in Fig. 5(*c*) show a nonturbulent flow for the first 13 stations. The upstream stations are laminar. Over the separation bubble, the fluctuations due to shear layer instability have not resulted in broadband turbulence. Only at the most downstream station, as the boundary layer begins to reattach and fluctuating

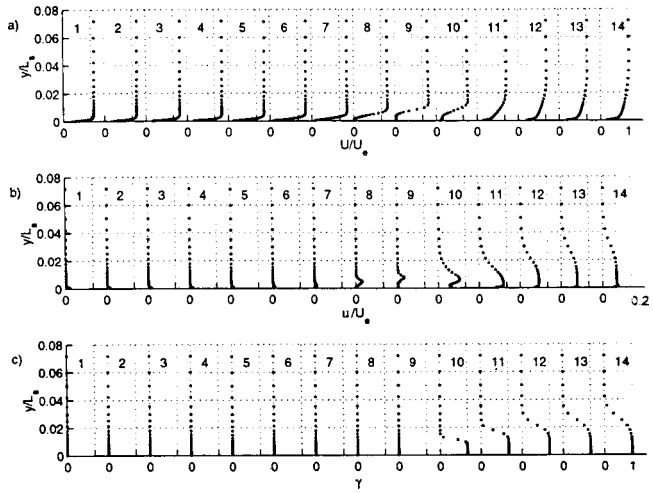

Fig. 6 Profiles for low-TI, Re=300,000 case: (*a*) mean velocity, (*b*) turbulence, (*c*) intermittency

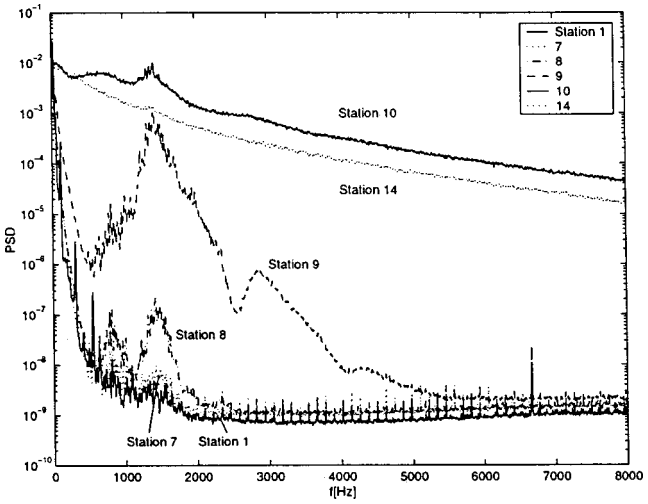

Fig. 7 Boundary layer u' spectra at locations of maximum u', low-TI, Re=300,000 case

velocities become significant near the wall, does transition begin. Peak intermittency is 31 percent at this station, and the peak is away from the wall in the shear layer.

Results for the Re=300,000, low-TI case are shown in Fig. 6, in the same format as Fig. 5. The mean-velocity profiles show an attached laminar boundary layer for the first seven stations. The Re=50,000 case started to show signs of separation already at Station 6, but the higher Re reduces the dimensionless acceleration parameter, K, by a factor of six, making the boundary layer more resistant to separation. At Station 8, the boundary layer is separated and the separation bubble has grown at Station 9. By Station 10, the near-wall velocity has increased, indicating the beginning of reattachment. By Station 11, reattachment appears complete, and the boundary layer recovers over the remaining stations to a fully developed turbulent profile.

The fluctuating velocities are at low, laminar levels over the first seven stations. A very low magnitude near wall peak is present in u', which is typical of a laminar boundary layer under low-TI conditions. At Station 8 there is an increase in u' in the shear layer as the boundary layer begins to separate. These fluctuations are due to a shear layer instability, and were observed in the hot-wire signal to occur at a coherent frequency. They increase in strength at Station 9, and result in the rapid breakdown to turbulence at Station 10, as the boundary layer begins to reattach. Station 10 shows a double peak, with a smaller peak in the near wall region, presumably due to near-wall generated turbulence, and a larger peak away from the wall, caused by the breakdown of the shear layer instability. At the downstream stations, the u' profile adjusts to the expected fully turbulent, attached boundary layer shape. Figure 7 shows boundary layer spectra from the location of maximum u' from several stations. The peak at 1400 Hz that appears at Station 8 is due to the shear layer instability. The frequency agrees with theoretical estimates. The 1400 Hz peak increases in magnitude and two higher harmonics appear at 2800 and 4200 Hz at Station 9. At other frequencies the magnitude is still low, indicating that the boundary layer is not yet turbulent. Between Stations 9 and 10 there is a sudden jump to higher levels at all frequencies, indicating a transition to turbulence. The peak at 1400 Hz is still visible above the turbulence until Station 13. Similar spectral behavior was observed in the lower Re cases.

The intermittency profiles (Fig. 6(*c*)) show nonturbulent flow for the first nine stations, then a sudden appearance of fully turbulent flow at Station 10, as the intermittency jumps to 100 percent. This sudden jump in intermittency was also seen in the Re =100,000 and 200,000 cases at low TI. Transition is clearly induced by the unsteadiness in the shear layer. The results agree with those of Malkiel and Mayle [9], who also reported a rapid rise in intermittency over the shear layer. Presumably, if more measurement stations had been concentrated between the present Stations 9 and 10, the growth of intermittency from 0 to 100 percent could have been documented.

Skin friction coefficients were determined from the mean velocity profiles, and are presented for all the low-TI cases in Fig. 8 as c_f versus Re_θ. Also shown for reference are laminar and turbulent correlations for low-TI, zero pressure gradient boundary layers on at plates. The c_f values for the attached laminar profiles were determined by profile fitting, using the technique of Volino and Simon [23]. This technique accounts for the effect of nonzero pressure gradient on profile shape, and allows a fit of most of the profile, including the near-wall region but not the wake. The same technique was also applied for the downstream stations, where the profile had recovered from separation to a fully developed turbulent shape. In these cases the uncertainty in c_f was 10 percent. Under the separation bubble, c_f was assumed to be zero. Determining c_f was most difficult in the region just downstream of reattachment. Here the boundary layer was believed to be intermittently separated and attached, and the profile included a pronounced defect, which was a remnant of the separation bubble. In

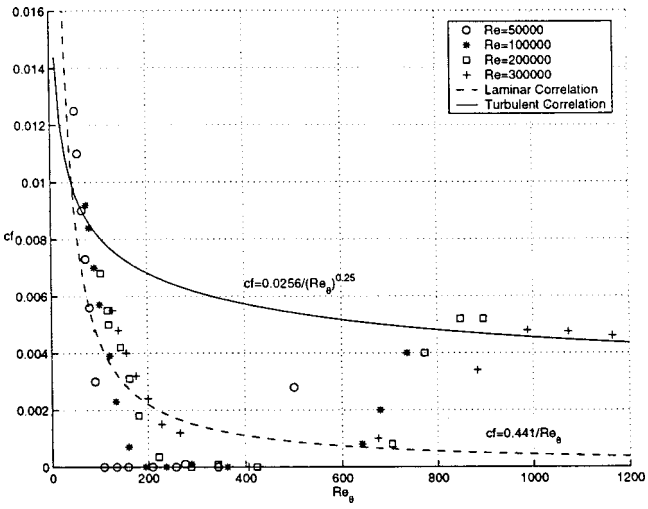

Fig. 8 Skin friction coefficient versus Re_θ for low-TI cases

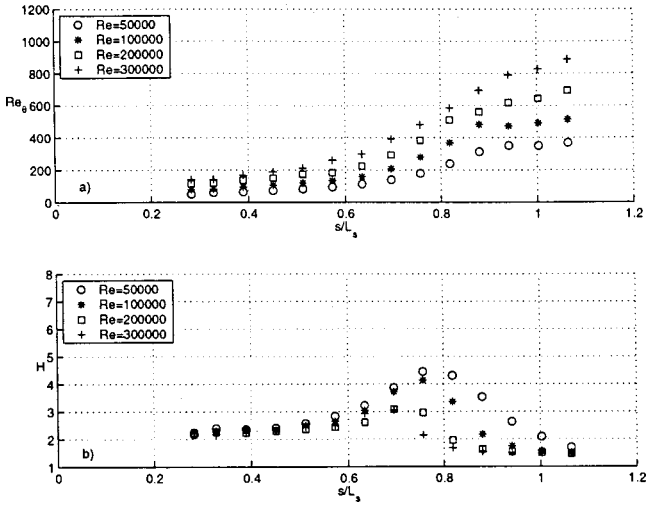

Fig. 9 Momentum thickness Reynolds numbers (*a*); and shape factors (*b*) for high-TI cases

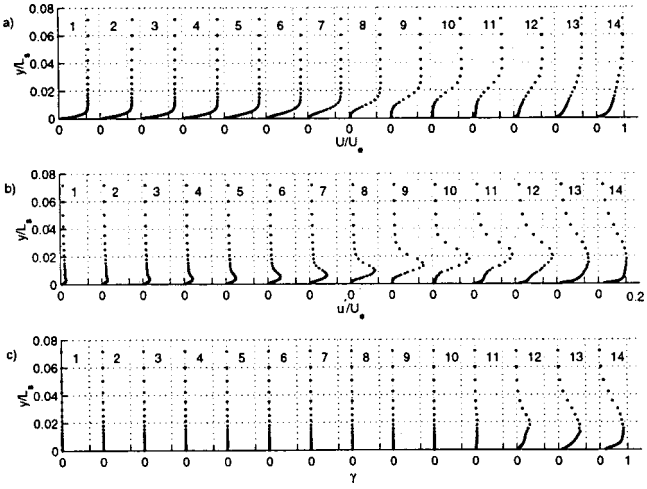

Fig. 10 Profiles for high-TI, Re=50,000 case: (*a*) mean velocity, (*b*) turbulence, (*c*) intermittency

this region c_f was determined by fitting only the very near-wall profile, with an uncertainty of 30 percent. The Re=200,000 and 300,000 cases show good agreement with the zero pressure gradient turbulent correlation by the downstream stations.

High-TI Cases. The Re_θ and H distributions for the high-TI cases are shown in Fig. 9. The momentum thickness grows slowly at the upstream stations and is equal to or just slightly larger than the corresponding cases at low TI (Fig. 4). This is expected; the high TI promotes slightly faster boundary layer growth. The high-TI cases do not show the jump in Re_θ observed in the low-TI cases after reattachment. At the downstream stations, Re_θ are lower for the high-TI case, at about 70 percent of the low-TI values. As will be shown below, the separation bubbles are smaller at the high TI, resulting in thinner boundary layers after reattachment. The shape factors begin at the laminar value of about 2.3, as in the low-TI cases, and rise as the boundary layer separates. The H values do not rise to the high levels of the low-TI case, again because the separation bubbles are not as thick, resulting in considerably lower displacement thicknesses. Fully turbulent attached boundary layer values of about 1.4 are achieved in the three higher Re cases, upstream of the locations for the low-TI case. Even the Re=50,000 case comes close to $H=1.4$ by the last station.

The velocity profiles for the Re=50,000 case are shown in Fig. 10. The mean profiles appear very similar to the Re=50,000, low-TI case (Fig. 5) for the first seven stations. At Station 7, the laminar boundary layer begins to separate. At Stations 8, 9, and 10, the boundary layer is separated, but the thickness of the separation bubble is only about half that of the low-TI case at the same stations. At Station 11, the boundary layer has begun to reattach, and at Stations 12, 13, and 14, the profile shape recovers to that of an attached turbulent boundary layer. In the low-TI case, reattachment did not occur until Station 14.

The u' profiles show a near-wall peak of about 3 percent of the mean free-stream velocity even at the most upstream station. These u' fluctuations in the nonturbulent boundary layer are primarily of low frequency and are induced by the free-stream fluctuations, as described in Blair [8] and Volino [24]. The near-wall peak grows slowly, but steadily through Station 6. At Stations 7–10, the peak moves away from the wall and into the shear layer over the separation bubble. No coherent frequencies were observed in the hot-wire signal in the shear layer. Any instabilities similar to those in the low-TI case appear to be overwhelmed by the free-stream turbulence induced phenomena. At Station 10, the peak u' is 26 percent of the free-stream velocity. At Station 11, the fluctuation levels rise near the wall, as the boundary layer begins to reattach. By Station 14, the u' profile looks like that of an attached turbulent boundary layer, but the peak u' is still higher (at 20 percent of U_e) than for a fully developed turbulent boundary layer. This indicates that the recovery from separation is not yet complete.

The intermittency is zero at the first ten stations in spite of the high TI. At Station 11 transition has begun, corresponding to the beginning of reattachment. The peak intermittency increases from 7 percent at Station 11 to 47 percent at Station 12. The peak is away from the wall, indicating that transition is initiated in the shear layer over the separation bubble. Transition occurs upstream of its location in the Re=50,000, low-TI case. Spectral results, which are qualitatively similar to those shown in Fig. 12 (high-TI, Re=300,000 case) show no amplification of select instabilities as in Fig. 7 (low-TI, Re=300,000 case), but rather a rising energy level across the entire spectrum as transition proceeds. This indicates that transition occurs through a bypass mode, rather than the breakdown of the instability waves seen in the low-TI case. The intermittency reaches 85 percent by the last station.

The high-TI, Re=300,000 profiles are shown in Fig. 11. The profiles show good agreement with the low-TI case (Fig. 6) through Station 7. At Station 8, the high-TI case is on the verge of

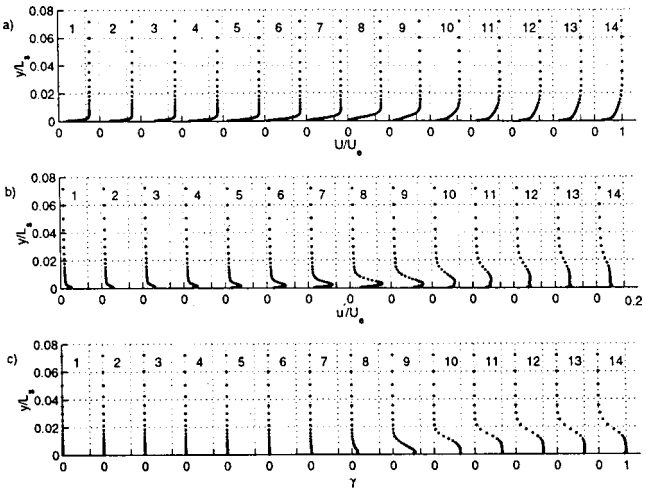

Fig. 11 Profiles for high-TI, Re=300,000 case: (*a*) mean velocity (*b*) turbulence, (*c*) intermittency

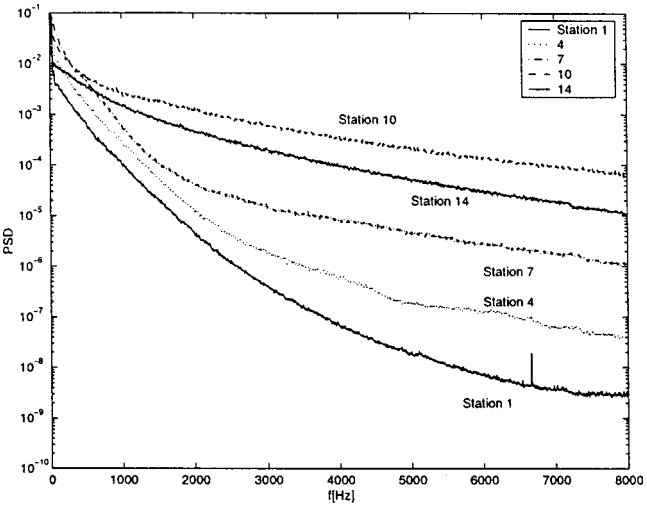

Fig. 12 Boundary layer u' spectra at locations of maximum u'. high-TI, Re=300,000 case

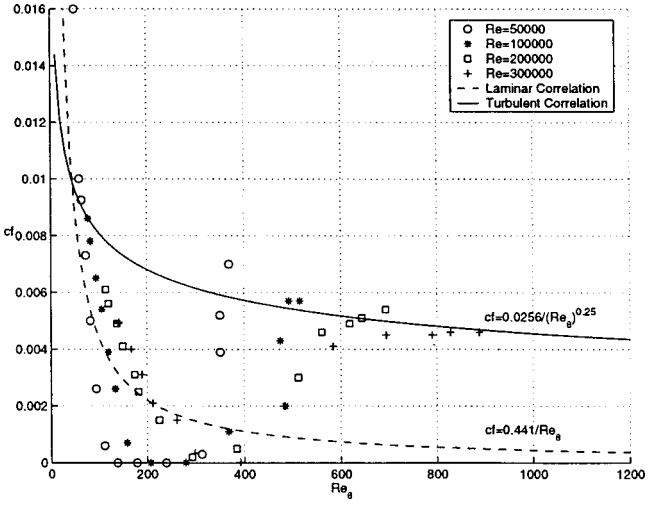

Fig. 13 Skin friction coefficient versus Re_θ for high-TI cases

separation, whereas the low-TI case already showed a small but clear separation bubble. At Station 9, the high-TI boundary layer is clearly attached, and continues to develop as an attached turbulent boundary layer at the further downstream stations. Hence, the combination of high Re and high-TI prevents separation in this case or a least limits it to a very small separation region.

The fluctuating velocity profiles are similar to the Re=50,000, high-TI case for the first six stations, showing significant u' due to the action of the free-stream turbulence on the boundary layer. At Stations 7–9, the u' level increases substantially to a peak value of 23 percent of the mean free-stream velocity. Downstream of this the peak u' drops to 11 percent of the free-stream velocity, and the profile assumes a turbulent shape. The transition process is typical of a high-TI attached boundary layer transition.

The intermittency profiles show nonturbulent flow for the first six stations. Transition has started at Station 7, with a peak intermittency of 5 percent, and continues at Stations 8 and 9. By Station 10 the intermittency is near 100 percent, and by Station 11 transition is complete. Transition begins just downstream of the throat, which is well upstream of the transition start in the low-TI, Re=300,000 case (Fig. 6). If there is a small separation region, it occurs downstream of the onset of transition. Transition end occurs at about the same location in the high and low-TI cases.

Figure 12 shows spectra at the locations of maximum u' in the boundary layer. Comparing to Fig. 7, there is considerably more fluctuation energy in the high-TI case at the upstream stations than in the low-TI case. This energy is induced by the free-stream over all frequencies, with no frequency spikes. However, comparing to Fig. 3, it is clear that the lower frequencies are more successful in penetrating the upstream boundary layer. The energy level rises gradually from Station 1–7, then rises more rapidly as the flow goes through transition. Downstream of transition, the spectra for the low and high-TI cases are essentially the same.

Skin friction coefficients are plotted versus Re_θ in Fig. 13. The upstream stations are very similar to those at low TI (Fig. 8). Downstream there is good agreement with the zero-pressure-gradient turbulent boundary layer correlation.

Transition and Separation Locations. The locations of separation, reattachment, and transition start and end are tabulated in Table 2. Locations are given as distance from the leading edge normalized on L_s and in terms of Re_θ. Separation location is estimated by extrapolating the separation bubble thickness upstream to the point of zero thickness. Reattachment was observed to occur simultaneously with transition onset. Transition occurs abruptly in the low-TI cases, and its location can only be estimated to within the station spacing, so a range is given for the transition start and end locations in Table 2. At high TI there are enough stations within the transition region to extrapolate to the beginning and end of transition using the technique presented by Narasimha [25]. As explained in Volino and Simon [5], the function

$$f(\gamma_{pk})=[-\ln(1-\gamma_{pk})]^{1/2}, \quad \gamma_{pk}=\gamma_{pk}(s) \tag{1}$$

is computed from the peak intermittency at each streamwise station and plotted versus streamwise location. A line is then fit through the points for each case and extrapolated to $f(\gamma_{pk})=0$ to determine the start of transition location, and to $f(\gamma_{pk})=2.146$, which corresponds to $\gamma_{pk}=0.99$, to determine the end of transition location. Intermittency is plotted versus position within the transition zone in Fig. 14 along with a theoretical line from Dhawan and Narasimha [26]. Although the theoretical line is associated with attached flow transition, agreement is still good for the separated flow cases, as expected by Narasimha [27].

Comparison to Correlations. Transition begins in all the high-TI cases at Re_θ between 250 and 350. Correlations by Abu-Ghannam and Shaw [28] and Mayle [2] for attached flow transition predict transition start at about $Re_\theta=250$ for 2.5 percent TI, which is the free-stream turbulence level over the test wall. The agreement with the correlations suggests that the attached flow bypass transition correlations may be useful at high TI, even in

Table 2 Separation and transition locations: s=separation, ts=transition start, r=reattachment, te=transition end

Re	s (s/L_s) / Re_θ	ts and r (s/L_s) / Re_θ	te (s/L_s) / Re_θ
Low TI			
50000	0.63/106	1.0-1.06/344-501	–
100000	0.66/177	0.88-0.94/363-642	0.94-1.0/642-680
200000	0.67/260	0.76-0.82/344-423	0.82-0.88/423-704
300000	0.67/314	0.76-0.82/406-675	0.76-0.82/406-675
High TI			
50000	0.63/111	0.85/271	1.11/383
100000	0.63/158	0.78/230	0.92/477
200000	–	0.72/322	0.85/533
300000	–	0.66/336	0.82/592

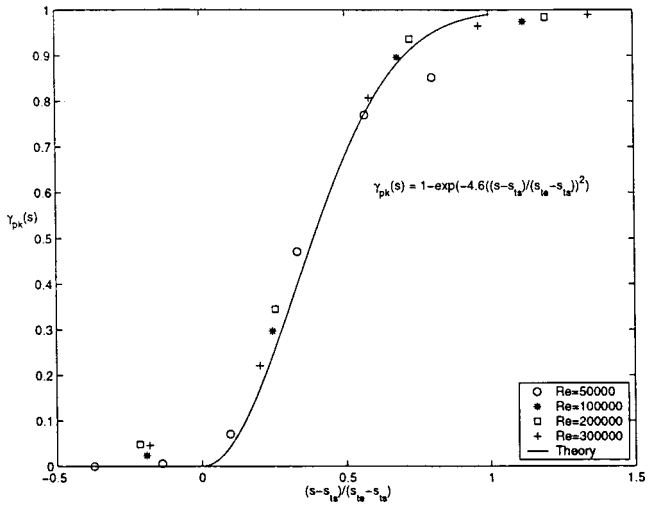

Fig. 14 Peak intermittency distributions for high-TI cases

cases with separation. The correlations predict transition end at Re_θ of about 600, which agrees with the Re=300,000 case. The velocity profiles for this case show that there may be a small separation region, but the flow is essentially behaving as an attached boundary layer. The lower Re cases complete transition at lower Re_θ than the correlations predict.

At low TI, the Abu-Ghannam and Shaw [28] correlation predicts transition start and end at Re_θ of 900 and 2600, respectively, for 0.2 percent TI. Transition occurs at much lower Re_θ in the experiments, showing that the attached flow correlations are not useful for low-TI separated flow transition.

Separation is expected in laminar boundary layers when the pressure gradient parameter $\lambda_\theta = -0.082$, as given by Thwaites [29]. To within the resolution of the station locations in the present experiments, this correlation holds. When separation occurs before the start of transition, Mayle [2] suggests the following correlations for the start of transition:

$$Re_{st} = 300\, Re_{\theta s}^{0.7} \quad \text{(short bubbles)} \tag{2}$$

$$Re_{st} = 1000\, Re_{\theta s}^{0.7} \quad \text{(long bubbles)} \tag{3}$$

The present low-TI cases have Re_{st} between the long bubble and short bubble correlations. The high-TI cases are closer to the short bubble correlation. The Re_{st} values for the Re=50,000 and 100,000 high-TI cases are 30 and 44 percent above Eq. (2). The Re=200,000 and 300,000 high-TI cases begin transition before separation, so the correlations are not applicable.

Mayle [2] also provides the following correlation for the length of the transition region:

$$Re_{LT} = 400\, Re_{\theta s}^{0.7} \tag{4}$$

The present Re=50,000 and 100,000 high-TI cases agree with this correlation to within 20 percent. In the low-TI cases, the resolution of the transition start and end locations is limited by the station spacing, resulting in large uncertainties in Re_{LT}. The upper ends of the uncertainty bands for these cases lie within 25 percent of Eq. (4).

Davis et al. [30] provide the following correlation for Re_{st}, which takes free-stream turbulence effects into account:

$$Re_{st} = 25000 \log[\coth(17.32TI)] \tag{5}$$

where TI is given as a fraction of the local free-stream velocity. Equation (5) predicts Re_{st} of 9800 and 36,000 for the high and low-TI cases, respectively. The low-TI prediction is within about 30 percent of the present experimental results. The high-TI prediction is too low by between 30 and 50 percent of the experimental results.

Comparison to Previous Study. The results presented above are very similar to those presented by Qiu and Simon [12] for boundary layers subject to the same nominal pressure gradient in a single passage cascade. An examination of the shapes of the mean velocity, u_0, and intermittency profiles shows similarity between the studies. There are some differences, however, in the locations of separation and transition. In the present study, separation occurred at s/L_s between 0.63 and 0.67. Qiu and Simon [12] reported locations further upstream, at $s/L_s = 0.54$ for 2.5 and 10 percent TI, and between 0.46 and 0.54 for their 0.5 percent TI case. The $s/L_s = 0.54$ location is immediately downstream of the throat. Some of the differences in separation location between the present study and Qiu and Simon [12] may be due to curvature effects. Since separation depends strongly on the streamwise pressure gradient, it is also possible that these differences might be due to slight differences in the actual streamwise pressure gradients (even though nominally being the same) in the two studies, however.

Qiu and Simon [12] also reported the start of transition further upstream than in the present study. In the present low-TI cases, transition began near $s/L_s = 1.0$ in the Re=50,000 case, and moved upstream with Reynolds number to $s/L_s = 0.8$ when Re =300,000. Qiu and Simon [12] reported locations between $s/L_s = 0.68$ and 0.79, also moving upstream with Re. At high TI, Qiu and Simon [12] reported s/L_s of about 0.6, while in the present study $s/L_s = 0.8$. Transition end behavior was similar, with Qiu and Simon [12] reporting s/L_s values about 0.1 less than the present study. Since separation strongly influences transition, the differences in separation location between the two studies may explain the differences in transition location. Another possible explanation for the differences in transition location is the way in which intermittency was determined. Qiu and Simon [12] did not filter (apart from anti-aliasing low-pass filtering) their hot-wire signal, while in the present study the digitized velocity signal was also high-pass filtered before the intermittency determination, as described above. It is possible that some of what Qiu and Simon [12] considered turbulence was due to free-stream-induced unsteadiness and instability waves. This would have resulted in higher intermittency values at all locations, which would have indicated both transition start and end locations farther upstream than in the present study.

Reattachment occurred in the present study at the same location as the onset of transition, and the locations agree closely with those given by Qiu and Simon [12], to within s/L_s of 0.03 in most cases. The good agreement in reattachment location between the studies contrasts with the differences in transition end location, and supports the conclusion that the apparent differences in transition zone location may be due at least in part to differences in intermittency processing as opposed to physical differences in transition location.

Conclusions

Boundary layer separation, transition, and reattachment have been documented under Reynolds number and pressure gradient conditions typical of low-pressure turbine airfoils. Reynolds number and free-stream turbulence level do not have a significant effect on boundary layer separation unless they are high enough to induce transition upstream of separation. The location and extent of the transition zone, in contrast, depend strongly on Re and TI. The beginning of reattachment occurs simultaneously with the onset of transition. Under low free-stream turbulence conditions, the boundary layer is laminar at separation and then begins to exhibit fluctuations in a finite frequency band in the shear layer over the separation bubble. These fluctuations are due to instability waves. The fluctuations grow in magnitude; higher harmonics are generated, and finally lead to a breakdown to turbulence. Transition begins in the shear layer, but quickly spreads to the near-wall region and causes the boundary layer to reattach. The transition is rapid and the resulting turbulence contains a full range of

high and low frequencies. Under high free-stream turbulence conditions, slow-growing low-frequency fluctuations are induced in the pre-transitional boundary layer by the free-stream, e.g., Dryden [31], Blair [8], and Volino [22]. Separation bubbles are considerably thinner than in the low-TI cases, resulting in thinner boundary layers at the end of the test wall. At Re=50,000 and 100,000, the pre-transitional boundary layer separates at about the same location as in the low-TI cases. Transition occurs through a bypass mode and begins upstream of the locations in the corresponding low-TI cases. The transition proceeds in a manner more similar to an attached boundary layer than in the low-TI cases. Under high TI at Re=200,000 and 300,000, transition begins before separation. The boundary layer may separate, but if it does the separation bubble is very short and does not significantly affect the downstream development of the boundary layer.

The documentation of attached and separated boundary layers should provide good test cases for further model development. Future processing of the data, including detailed spectral analysis will provide further insight into the nature of the boundary-layer behavior in these cases.

Acknowledgments

The first author was supported by the NASA/ASEE Summer Faculty Fellowship program with matching support through a U.S. Naval Academy Recognition Grant. The work was done under the NASA Low Pressure Turbine Flow Physics Program managed by Dr. David Ashpis and the NASA Turbomachinery and Combustion Technology Program managed by Kestutis Civinskas.

Nomenclature

c_f = skin friction coefficient
C_p = pressure coefficient$=1-(U_\infty/U_e)^2$
f = frequency
$f(\gamma_{pk})$ = function of peak intermittency
H = shape factor$=\delta^*/\theta$
K = acceleration parameter$=(\nu/U_\infty{}^2)(dU_\infty/ds)$
L_s = nominal suction surface wetted length
PSD = power spectral density$=u'^2(f)/df$, $v'^2(f)/df$, $w'^2(f)/df$
Re = Reynolds number based on nominal exit velocity and suction-surface wetted length$=U_eL_s/\nu$
Re_{st} = Reynolds number based on nominal exit velocity and distance from separation to transition onset
Re_θ = momentum thickness Reynolds number$=U_\infty\theta/\nu$
$\mathrm{Re}_{\theta s}$ = Re_θ at separation
s = wetted streamwise distance along suction surface
s_{ts} = transition start location
s_{te} = transition end location
TI = free-stream turbulence intensity
U = local mean streamwise velocity
U_e = nominal exit free-stream velocity
U_∞ = local free-stream velocity
u' = rms fluctuating streamwise velocity
v' = rms fluctuating wall normal velocity
w' = rms fluctuating spanwise velocity
y = distance from wall
γ = intermittency
$\gamma_{pk}(s)$ = peak intermittency in profile at location s
δ^* = displacement thickness
λ_θ = pressure gradient parameter$=\mathrm{Re}_\theta{}^2K$
ν = kinematic viscosity
θ = momentum thickness

References

[1] Hourmouziadis, J., 1989, ''Aerodynamic Design of Low Pressure Turbines,'' AGARD Lecture Series 167.
[2] Mayle, R. E., 1991, ''The Role of Laminar–Turbulent Transition in Gas Turbine Engines,'' ASME J. Turbomach., **113**, pp. 509–537.
[3] Sharma, O. P., Ni, R. H., and Tanrikut, S., 1994, ''Unsteady Flow in Turbines,'' AGARD-LS-195, Paper No. 5.
[4] Morkovin, M. V., 1978, ''Instability, Transition to Turbulence and Predictability,'' NATO AGARDograph No. 236.
[5] Volino, R. J., and Simon, T. W., 1995, ''Bypass Transition in Boundary Layers Including Curvature and Favorable Pressure Gradient Effects,'' ASME J. Turbomach., **117**, pp. 166–174.
[6] Kim, J., Simon, T. W., and Russ, S. G., 1992, ''Free-Stream Turbulence and Concave Curvature Effects on Heated Transitional Boundary Layers,'' ASME J. Heat Transfer, **114**, pp. 338–347.
[7] Volino, R. J., and Simon, T. W., 1997, ''Boundary Layer Transition Under High Free-Stream Turbulence and Strong Acceleration Conditions: Part 1: Mean Flow Results; Part 2: Turbulent Transport Results,'' ASME J. Heat Transfer, **119**, pp. 420–432.
[8] Blair, M. F., 1992, ''Boundary-Layer Transition in Accelerating Flow With Intense Freestream Turbulence: Part 1: Disturbances Upstream of Transition Onset,'' ASME J. Fluids Eng., **114**, pp. 313–321.
[9] Malkiel, E., and Mayle, R. E., 1996, ''Transition in a Separation Bubble,'' ASME J. Turbomach., **118**, pp. 752–759.
[10] Hatman, A., and Wang, T., 1999, ''A Prediction Model for Separated-Flow Transition,'' ASME J. Turbomach., **121**, pp. 594–602.
[11] Halstead, D. E., Walker, G. J., Wisler, D. C., Hodson, H. P., Okiishi, T. H., and Shin, H.-W., 1997 ''Boundary Layer Development in Axial Compressors and Turbines: Part 3 of 4—LP Turbines,'' ASME J. Turbomach., **119**, pp. 234–246.
[12] Qiu, S., and Simon, T. W., 1997, ''An Experimental Investigation of Transition as Applied to Low Pressure Turbine Suction Surface Flows,'' ASME Paper No. 97-GT-455.
[13] Murawski, C. G., Sondergaard, R., Rivir, R. B., Simon, T. W., Vafai, K., and Volino, R. J., 1997, ''Experimental Study of the Unsteady Aerodynamics in a Linear Cascade With Low Reynolds Number Low Pressure Turbine Blades,'' ASME Paper No. 97-GT-95.
[14] Sohn, K. H., DeWitt, K. J., and Shyne, R. J., 2000, ''Experimental Investigation of Boundary Layer Behavior in a Simulated Low Pressure Turbine,'' ASME J. Fluids Eng., **122**, pp. 84–89.
[15] Dorney, D. J., Ashpis, D. E., Halstead, D. E., and Wisler, D. C., 1999, ''Study of Boundary Layer Development in a Two-Stage Low-Pressure Turbine,'' AIAA Paper No. 99-0742; also NASA TM-1999-208913.
[16] Chernobrovkin, A., and Lakshminarayana, B., 1999, ''Turbulence Modeling and Computation of Viscous Transitional Flow for Low Pressure Turbines,'' *Proc. 4th International Symposium on Engineering Turbulence Modeling and Measurements*, Corsica, France.
[17] Huang, P. G., and Xiong, G., 1998, ''Transition and Turbulence Modeling of Low Pressure Turbine Flows,'' AIAA Paper No. 98-0039.
[18] Sohn, K. H., and Reshotko, E., 1991, ''Experimental Study of Boundary Layer Transition With Elevated Freestream Turbulence on a Heated Flat Plate,'' NASA CR 187068.
[19] Hultgren, L. S., and Volino, R. J., 2000, ''Measurements in Separated and Transitional Boundary Layers Under Low-Pressure Turbine Airfoil Conditions,'' NASA TM to be published.
[20] Hedley, T. B., and Keffer, J. F., 1974, ''Turbulent/Non-Turbulent Decisions in an Intermittent Flow,'' J. Fluid Mech., **64**, pp. 625–644.
[21] Kim, J., Simon, T. W., and Kestoras, M., 1994, ''Fluid Mechanics and Heat Transfer Measurements in Transitional Boundary Layers Conditionally Sampled on Intermittency,'' ASME J. Turbomach., **116**, pp. 405–416.
[22] Volino, R. J., 1998, ''Wavelet Analysis of Transitional Flow Data Under High Free-Stream Turbulence Conditions,'' ASME Paper No. 98-GT-289.
[23] Volino, R. J., and Simon, T. W., 1997, ''Velocity and Temperature Profiles in Turbulent Boundary Layers Experiencing Streamwise Pressure Gradients,'' ASME J. Heat Transfer, **119**, pp. 433–439.
[24] Volino, R. J., 1998, ''A New Model for Free-Stream Turbulence Effects on Boundary Layers,'' ASME J. Turbomach., **120**, pp. 613–620.
[25] Narasimha, R., 1984, ''Subtransitions in the Transition Zone,'' *Proc. 2nd IUTAM Symposium on Laminar–Turbulent Transition*, Novosibirsk, pp. 141–151.
[26] Dhawan, S., and Narasimha, R., 1958, ''Some Properties of Boundary Layer Flow During the Transition From Laminar to Turbulent Motion,'' J. Fluid Mech., **3**, pp. 418–436.
[27] Narasimha, R., 1998, ''Post-Workshop Summary,'' *Minnowbrook II—1997 Workshop on Boundary Layer Transition in Turbomachines*, LaGraff, J. E., and Ashpis, D. E., eds., NASA CP 1998-206958, pp. 485–495.
[28] Abu-Ghannam, B. J., and Shaw, R., 1980, ''Natural Transition of Boundary Layers—The Effects of Turbulence, Pressure Gradient and Flow History,'' J. Mech. Eng. Sci., **22**, pp. 213–228.
[29] Thwaites, B., 1949, ''Approximate Calculations of the Laminar Boundary Layer,'' Aeronaut. Q., **7**, pp. 245–280.
[30] Davis, R. L., Carter, J. E., and Reshotko, E., 1985, ''Analysis of Transitional Separation Bubbles on Infinite Swept Wings,'' AIAA Paper No. 85-1685.
[31] Dryden, H. L., 1936, ''Air Flow in the Boundary Layer Near a Plate,'' NACA Report 562.

Turbine Separation Control Using Pulsed Vortex Generator Jets

Jeffrey P. Bons
Air Force Insitute of Technology.

Rolf Sondergaard

Richard B. Rivir

Air Force Research Laboratory,
Wright-Patterson AFB, OH 44135

The application of pulsed vortex generator jets to control separation on the suction surface of a low-pressure turbine blade is reported. Blade Reynolds numbers in the experimental, linear turbine cascade match those for high-altitude aircraft engines and aft stages of industrial turbine engines with elevated turbine inlet temperatures. The vortex generator jets have a 30 deg pitch and a 90 deg skew to the free-stream direction. Jet flow oscillations up to 100 Hz are produced using a high-frequency solenoid feed valve. Results are compared to steady blowing at jet blowing ratios less than 4 and at two chordwise positions upstream of the nominal separation zone. Results show that pulsed vortex generator jets produce a bulk flow effect comparable to that of steady jets with an order of magnitude less massflow. Boundary layer traverses and blade static pressure distributions show that separation is almost completely eliminated with the application of unsteady blowing. Reductions of over 50 percent in the wake loss profile of the controlled blade were measured. Experimental evidence suggests that the mechanism for unsteady control lies in the starting and ending transitions of the pulsing cycle rather than the injected jet stream itself. Boundary layer spectra support this conclusion and highlight significant differences between the steady and unsteady control techniques. The pulsed vortex generator jets are effective at both chordwise injection locations tested (45 and 63 percent axial chord) covering a substantial portion of the blade suction surface. This insensitivity to injection location bodes well for practical application of pulsed VGJ control where the separation location may not be accurately known a priori.
[DOI: 10.1115/1.1350410]

Keywords: Separation, Control, VGJ, Turbine

Introduction

During high-altitude cruise, the operating Reynolds number (based on axial chord and inlet velocity) for the low-pressure turbine (LPT) in an aircraft gas turbine engine can drop below 25,000. This low-Reynolds-number condition is particularly acute in the class of small gas turbine engines typically used or planned for use in many high-altitude air vehicles. At these low Reynolds numbers, the boundary layers on the LPT blades are largely laminar, even in the presence of free-stream turbulence, making them susceptible to flow separation near the aft portion of the blade suction surface, with associated loss increase and performance drop. Sharma et al. [1] indicated a nearly 300 percent increase in loss coefficient at Reynolds numbers below 95,000 compared to the loss coefficient at higher Reynolds numbers (Fig. 1). This increase was found to be primarily due to separation occurring over the trailing 50 percent of the suction surface. Matsunuma et al. [2,3] have also reported increased separation and secondary flow losses when operating at turbine inlet Reynolds numbers below 60,000. Although the exact Reynolds number at which separation related losses become significant is machine specific, the increased loss inevitably translates to a significant decrease in turbine efficiency at these operating conditions (measured values have been as much as a six point loss in component efficiency for the AE3007H [4], a small high-altitude engine). Altering the blade shape to avoid this low-Reynolds-number separation problem is not desirable, since such a modification is likely to impair the engine operation at higher (design) Reynolds numbers. As such, flow control techniques that can be practically implemented on a separating turbine blade are of current interest.

Boundary layer separation control in diffusing flows (under pressure conditions similar to the aft portion of a turbine blade) has been studied in the laboratory for many years. Lin et al. [5] presented results from a number of passive and active strategies employed with varying degrees of success to a turbulent boundary layer flowing over a backward-facing, curved ramp. Of the two classes, active techniques have the advantage that they can be shut off when not required for flow control. This is especially desirable for a turbine blade application, since any passive technique that is effective at low Reynolds number would likely increase the blade's drag penalty and surface thermal loading at higher (non-separating) Reynolds numbers. Of the active strategies studied by Lin et al., only vortex generator jets (VGJs) had a significant effect on reducing diffuser separation.

VGJs are typically configured with a low pitch angle (30–45 deg) and aggressive skew angle (45–90 deg) to the near-wall flow direction (see detail in Fig. 3 for the VGJ configuration in this study). Here pitch angle is defined as the angle the jet makes with the local surface and skew angle is defined as the angle of the projection of the jet on the surface relative to the local free-stream direction. In this skew configuration, the VGJ creates a horseshoe vortex pair with one very strong leg accompanied by a weak leg of opposite sign. The result is a single, dominant, slowly decaying streamwise vortex downstream rather than the two relatively weak counterrotating horseshoe vortices generated by a jet with 0 deg skew or a symmetric, passive boundary layer obstruction. It has been shown both experimentally [6] and computationally [7] that this single-sign vortex energizes the separating turbulent boundary layer by effectively bringing high momentum free-stream fluid down near the wall.

Nonsteady pulsing has been combined with jet injection to inhibit separation of wall-bounded flows in a number of applications. Hsiao et al. [8] employed pulsed, normal (90 deg pitch, 0 deg skew) air injection using a loudspeaker to inhibit laminar separation over a cylinder and an airfoil at high angle of attack. In the post-stall airfoil, forcing was most effective when applied at 1 percent chord and at Strouhal numbers ($St = fc/U_\infty$ from 2 to 8. More recent applications of pulsed, normal jet injection include the use of synthetic (zero net mass flux) jets to promote flow reattachment over a thick airfoil [9] and the application of pulsed upper surface blowing to control dynamic stall on a simulated helicopter rotor [10]. Amitay et al. found that effective stall con-

Contributed by the International Gas Turbine Institute and presented at the 45th International Gas Turbine and Aeroengine Congress and Exhibition, Munich, Germany, May 8–11, 2000. Manuscript received by the International Gas Turbine Institute February 2000. Paper No. 2000-GT-262. Review Chair: D. Ballal.

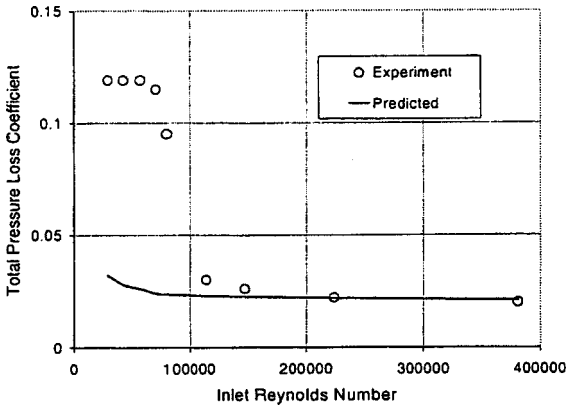

Fig. 1 Pressure loss coefficient versus Reynolds number (from [1])

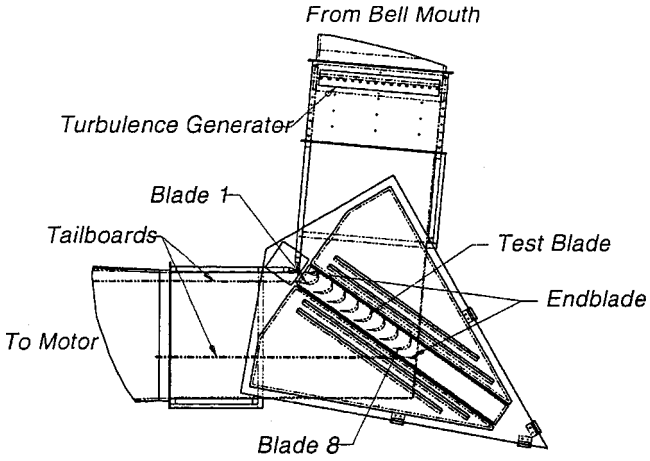

Fig. 2 Low-speed linear cascade test facility

trol required larger amplitude pulsations the further upstream the injection location was moved from the natural separation point. They also investigated the effect of forcing frequency over the range from 1 to 20 times the natural shear layer instability frequency. Pulsing at frequencies near the shear layer instability improved the stalled airfoil's performance but resulted in significant (up to 45 percent) oscillations in the augmented c_L. By contrast, pulsing frequencies an order of magnitude greater than the shear layer instability resulted in an increased but steady c_L. Flowfield measurements in the former case revealed time-periodic shedding of vortex trains from the injection site which corresponded to the fluctuations in c_L. A recent numerical study of pulsed, normal jets by Wu et al. [11] documented the roll-up of the pulsed jets into large vortices. These vortices then entrained higher momentum mainstream fluid and brought it down near the wall, inhibiting separation. In this numerical study, pulsing was effective at or near the blade shedding frequency (1/7th of the shear layer instability).

Pulsed, streamwise (0 deg pitch, 0 deg skew) jet injection (from a backward-facing slot or step) has also been successfully employed by a number of researchers. Seifert et al. [12] produced an increased c_L (and decreased c_D) using slot injection over the adjustable aft flap of an NACA 0015 airfoil. This was obtained with an order of magnitude decrease in the required mass flow compared to steady injection. Kwong and Dowling [13] reported similar gains in two-dimensional and axisymmetric diffusers using streamwise injection from slots and discrete nozzles at the diffuser inlet.

Besides the numerous normal and streamwise pulsed jet injection experiments mentioned above, two additional studies have investigated the combination of unsteady forcing with skewed (VGJ) injection. McManus et al. [14] and Raghunathan et al. [15] have both employed pulsed VGJs to effectively control separation in two-dimensional diffusers. McManus et al. reported comparable separation control effectiveness for massflow reductions up to 1/20th of the required steady massflow at matched maximum blowing ratio over the cycle. A follow-on report by Johari and McManus [16] documented the formation of a strong starting vortex from a pulsed VGJ into a turbulent boundary layer. They noted substantial interaction between this starting vortex and the boundary layer when the vortex dimension (injection hole dimension) was smaller than the local boundary layer thickness. Then, if the blowing ratio was not high enough to cause the jet to enter the free stream, the combination of a tilted initial vortex (caused by skewed injection) and an ambient shear layer generated and intensified streamwise vorticity in the pulsed case relative to the steady blowing case. This finding would imply that pulsed injection at high skew angles (skew $\approx$ 90 deg) may be more effective than normal or streamwise jet injection.

These reports documenting the success of pulsing and VGJs for boundary layer separation control have led to the present investigation into low-pressure turbine separation control at reduced Reynolds numbers. Initially, steady VGJ injection was investigated and shown to be effective over a wide range of operating conditions. The results of this study are reported in Sondergaard et al. [17] and are summarized later in this report. Given the obvious engine cycle costs of implementing VGJs on the LPT, and the promise of comparable effectiveness at greatly reduced required massflow, pulsed VGJs quickly became the subject of a companion study. This report documents the successful implementation of pulsed VGJs at two chordwise stations upstream of the naturally separated zone on the suction surface of a prototypical LPT blade profile. The effects of jet blowing ratio, injection location, and pulsing frequency are also discussed.

Experimental Facility

The linear turbine cascade facility used for this study is described in detail in Sondergaard et al. [17] so only a brief description will be provided here. All modifications made to accommodate the pulsed VGJ research are outlined in detail. The open loop, induction wind tunnel, which houses the cascade, draws air through the bell-mouth inlet equipped with flow straighteners and into the 0.85 m tall $\times$ 1.22 m wide test section at up to 80 m/s (Fig. 2). Flow velocity uniformity across blades 3–7 is within ± 2 percent at 25,000 Reynolds number with less than 1 percent freestream turbulence. This background level of turbulence can be augmented to 4 percent through the use of a turbulence-generating grid located 10 axial chord lengths upstream of the cascade. The linear cascade consists of eight 0.88 m span $\times$ 0.18 m axial chord (C_x) blades fabricated from molded polyurethane resin. The two-dimensional blade shape studied is the Pratt & Whitney ''PakB'' research design, which is a Mach number scaled version of a typical highly loaded LPT blade design. The cascade has a solidity (axial chord to blade spacing) of 1.13, an inlet flow angle of 55 deg (measured from the plane of the cascade), and a design exit angle of 30 deg.

Blades 4 and 6 are each instrumented with 40 static pressure taps around the full blade profile to allow verification of blade c_p profiles. Uncertainties in the pressure measurement translated to an uncertainty of ± 6 percent in the c_p data (at Re=25,000). The active separation control (ASC) blade mounted in position #5 of the cascade was manufactured with a hollow cavity running the span of the blade and covering the region from 40 percent to 90 percent axial chord (Fig. 3). It is instrumented from 48 to 89 percent chord with 19 static pressure taps spaced every 6.4 mm along the suction surface near midspan. Fittings at the lower end of the blade allow for pressurized feed air for the VGJs, cavity

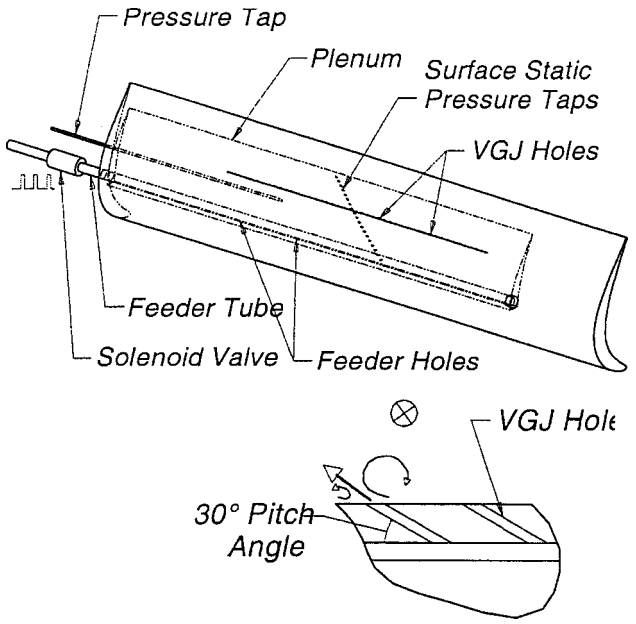

Fig. 3 ASC blade geometry and pulsed valve configuration; inset shows VGJ configuration (free-stream into page)

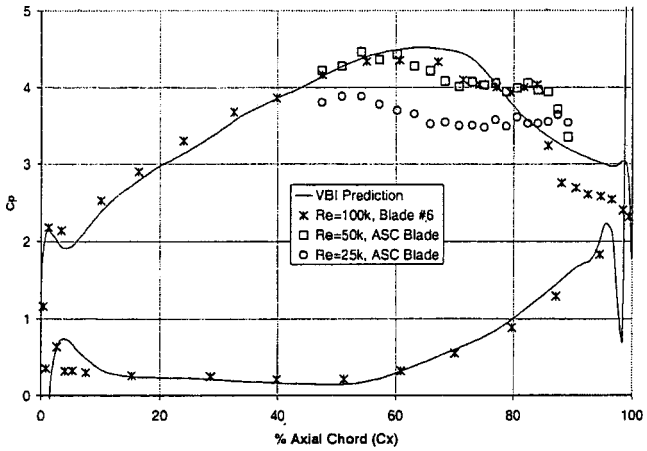

Fig. 4 Pressure coefficient versus axial chord for uncontrolled blade. Re=100k, 50k, and 25k and Tu=1 percent versus VBI prediction. Re=50k and 25k data over limited portion of suction surface only.

static pressure measurement, and pressure tap tubing. A needle-valve located upstream of the feed port allows fine control of the mass flow rate into the blade cavity. A high-speed solenoid valve is located just downstream of this needle valve. The solenoid is controlled by a General Valve Inc. Iota One pulse driver, which has a maximum pulse rate of 250 Hz, with a minimum ''open'' pulse duration of less than 1 ms. Air exhausts from this valve into a copper tube running the span of the blade inside the cavity. Holes spaced every 2.54 cm along the copper tube produce an even distribution of airflow to the VGJs. The 1-mm-dia (d) cylindrical VGJ holes have a 30 deg pitch angle and a 90 deg skew angle. They are spaced every $10d$ along the center 0.46 m of the ASC blade span. For this study, two spanwise rows of VGJ holes were used, at 45 and 63 percent C_x. Given the approximate $2\times$ blade geometric scaling, these 1-mm-dia injection holes would be equivalent to 0.5-mm-dia holes in a real turbine application. This is about a factor of two smaller than current film cooling holes.

To determine the mean jet blowing ratio, the average static pressure of the ASC blade cavity was monitored during tunnel operation. This pressure was then correlated to the average jet exit velocity, which had been measured at the hole exit plane with a sub-miniature hot-film probe prior to blade installation in the cascade. This measurement was made outside the cascade tunnel with the jets injecting into stagnant air. The mean jet blowing ratio (B) was computed as the ratio of the average jet exit velocity to the local free-stream velocity as calculated from the local pressure coefficient. Jet to free-stream density ratios were approximately unity ($\rho_{\text{jet}}/\rho_{\text{local}} \cong 1$).

Bulk flow instrumentation consisted of flow thermocouples for inlet temperature measurement and an upstream pitot-static reference probe. To calculate the blade wake loss coefficient, a Kiel probe was used to measure the total pressure $0.64C_x$ downstream of the trailing edge. A Dantec three-axis traverse located atop the wind tunnel was used to traverse the blade wakes with the probe at midspan. Uncertainties in the pressure measurement translated to an uncertainty of ± 8 percent in the loss coefficient (at Re $=25{,}000$). A small National Aperture micro-traverse system, mounted inside the test section (but outside the outer tailboard), was used to make boundary layer profile measurements at several chordwise locations on the ASC blade. A standard single hot-wire probe was mounted on the micro-traverse to measure mean and fluctuating velocity components. When compared to a collocated pitot-static probe velocity measurement, the velocity error in the hot-wire and hot-film probes was within ± 2 percent at flow rates of interest.

Results and Discussion

The low-Reynolds-number separation characteristics of the PakB blade profile have been documented in previous studies [18]. They are summarized here so that the effectiveness of the pulsed control technique can be fully appreciated. Following this, critical findings of a recent steady blowing study on the same blade configuration [17] are briefly presented. This will allow for a cogent comparison of the steady and unsteady methods of control. Finally, the success of pulsed VGJs is documented in detail and differences between the two mechanisms are highlighted.

Baseline Case ($B=0$). The baseline, unblown blade c_p profile is shown in Fig. 4 for three Reynolds numbers and low (1 percent) free-stream turbulence. Also shown is a Navier–Stokes CFD calculation using the two-dimensional Vane Blade Interaction (VBI) code developed under contract to the US Air Force by Allison Engine Company. The flattened region, or plateau, in the data between 60 and 90 percent axial chord on the suction surface, where the c_p data depart from the calculated profile, delineates the region of boundary layer separation. As shown in the figure, the extent of this region expands with decreasing Reynolds number. To document this region further, boundary layer traverses were made at 68, 73, and 77 percent axial chord for the Re$=25{,}000$ case (Fig. 5). The shape factor of the first profile (at 68 percent) is 2.8, indicating a laminar boundary layer. By 73 percent chord, the profile begins to exhibit a doubly inflected shape in the region y/blade spacing <0.01, denoting a vanishing wall shear. At the final station the profile is obviously separated, with mean velocities in the separated region approaching zero. Since a single hot-wire probe was used, no flow direction information was available, and reverse flow could not be resolved. Smoke flow visualization, however, confirmed that flow reversal was present at the 77 percent measurement station. Power spectral density data from within this separated zone (reported in Sondergaard et al. [17]) revealed a broad energy peak at 100 Hz. This frequency corresponds to the shear layer instability frequency for the separated boundary layer.

By contrast, boundary layer velocity data taken at Re$=100{,}000$ (not shown here) indicated attached laminar or transitional flow over the same region of the blade. This reduction in the separation zone with increasing Reynolds number is also apparent in the

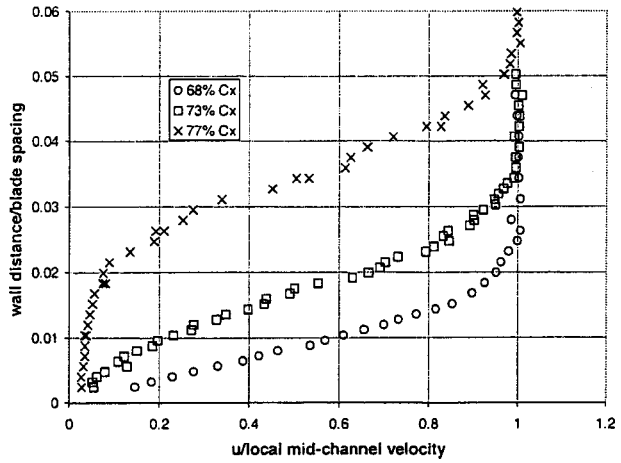

Fig. 5 Boundary layer profiles of streamwise velocity normalized by midchannel velocity at three chordwise stations: 68, 73, and 77 percent axial chord. Re=25k, Tu=1 percent, and $B=0$.

wake loss coefficient (γ) profiles shown in Fig. 6. The Re =100,000 wakes are shallower and narrower than the broad, deep wakes for the lower Reynolds number cases.

Steady Blowing. To briefly summarize results reported in detail elsewhere [17], steady VGJs have the effect of reducing or entirely eliminating the separation zone on the blade suction surface. The success of this control technique is most clearly evident from the measured 60 percent reduction in the integrated wake loss coefficient. The integrated wake loss coefficient, γ_{int}, is the integrated sum of the blade loss measured across its wake at 0.64 axial chord lengths downstream of the trailing edge.

$$\gamma_{\text{int}} = \int_{-wake/2}^{+wake/2} \left(\frac{P_{T,in} - P_{T,ex}}{P_{T,in} - P_{S,in}} \right) dy \tag{1}$$

This is an area-averaged formulation rather than the standard mass-average. As such, the losses are slightly overestimated (up to 10 percent for the uncontrolled case and less than 5 percent for the controlled cases). Since the measured reductions in γ_{int} with control are over 50 percent, this discrepancy does not significantly impact the conclusions of the study.

In addition to a dramatically reduced wake signature, the attached boundary layer also resulted in a higher pressure loading on the blade. This translates into an increase in the available work from a turbine rotor as measured by the blade Zweifel coefficient. The Zweifel coefficient represents the component of the integrated blade c_p distribution contributing to the direction of rotation (for a rotating stage).

$$Z = \int_{\text{full-blade}} \left(\frac{P_{T,in} - P_{S,\text{local}}}{P_{T,in}} \right) \frac{\hat{e}_n \cdot \hat{e}_t}{C_x} ds \tag{2}$$

The Zweifel coefficient defined in this manner is similar to the lift coefficient for external airfoils, which have significantly less camber than turbine airfoils. Increases in this parameter of approximately 6 percent were reported with steady blowing.

The minimum blowing ratio required for effective separation control varied with injection location. The optimum location occurred at 63 percent chord, just upstream of the nominal separation location, where $B_{\min}=1$. Steady blowing was shown to be effective as far upstream as 45 percent chord and as far downstream as 83 percent chord, although at the farthest downstream location $B_{\min}$ increased to nearly 5.

Boundary layer data indicated that steady injection caused early transition on the blade suction surface. This effect is in addition to the stabilizing effect of the streamwise vortices created by the VGJs. The majority of steady VGJ research ([6,5], etc.) has been focused on the effect of the strong streamwise vortices produced by skewed jet injection. This vortical motion has been identified as the mechanism for bringing high-momentum free-stream fluid down near the wall, energizing the otherwise separation-prone boundary layer. However, this research has been conducted almost exclusively with boundary layers that were already turbulent. In the Sondergaard et al. [17] study, this vortex mechanism was accompanied by the presence of transition at or near the injection site. So, while the VGJ jet vortices were coherent beyond $50d$ downstream of the injection station, the laminar boundary layer also transitioned in this same region. Thus, natural separation was inhibited on the full blade span due to both the vortex momentum exchange mechanism and the turbulent nature of the profile. As corroborating evidence of this VGJ influence on transition, spectra taken in the VGJ wake region showed a strong energy peak at approximately 500 Hz. This frequency corresponds to the wake shedding frequency of the free stream around the steady flow being injected from the 1-mm-dia VGJ holes. Sondergaard et al. proposed this shedding instability as a contributing mechanism promoting premature transition (and thus effective separation control).

At higher Reynolds numbers, steady blowing was shown to have more limited beneficial (but no adverse) effects as measured by the integrated wake loss coefficient and the Zweifel coefficient. This is good news for the application of this control strategy by the turbine designer. A turbine with known separation problems at low Reynolds number can be successfully controlled without impairing aerodynamic performance at higher Reynolds number, even if the control jets are left on above the Reynolds number at which separation is a problem. Of course, the jets can also be shut off completely at higher Reynolds numbers, eliminating the potential for adverse effects altogether.

Finally, steady VGJs were effective (though to a lesser degree) in flows with elevated free-stream turbulence. Free-stream turbulence is an important feature of turbomachinery flows, which can cause early transition, thus mitigating the effect of separation on the blade suction surface. This notwithstanding, steady VGJs still produced a reduction in γ_{int} of up to 30 percent for 4 percent free-stream turbulence at Re=25,000.

Unsteady Blowing. In a turbine blade application of active separation control using VGJs, the obvious source of injected air is the compressor. For low-pressure turbine (LPT) control, compressor bleed air can be extracted from stages earlier than that used for film cooling of the high-pressure turbine (HPT) stages. Still, any loss of compressor air represents a penalty to the engine cycle. Consequently, the reported success of steady VGJs leads

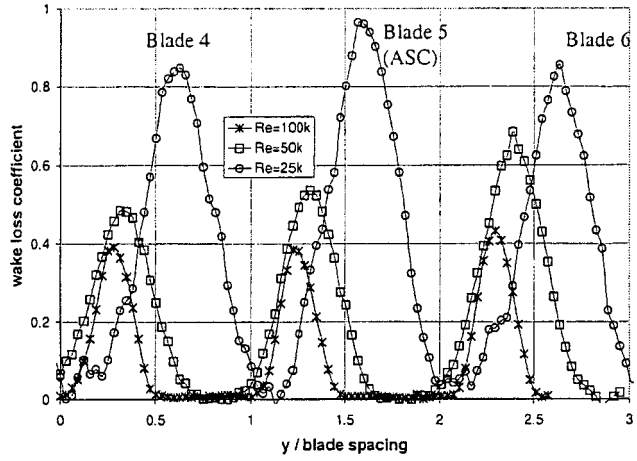

Fig. 6 Wake loss coefficient profiles at 0.64 axial chord lengths downstream of trailing edge. Re=100k, 50k, and 25k and Tu=1 percent, Wakes from blades 4, 5, and 6 with $B=0$.

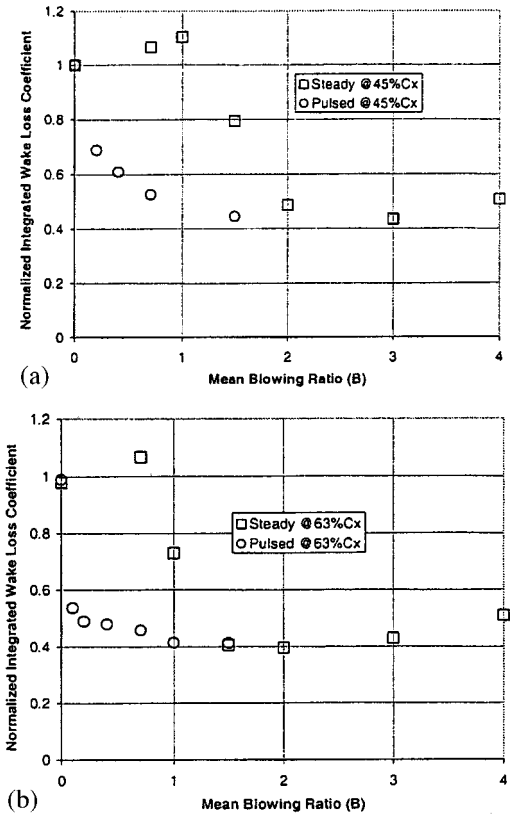

Fig. 7 Integrated wake loss coefficient (γ_{int}) normalized by loss coefficient for $B=0$ versus mean blowing ratio (B). Data for pulsed blowing at 10 Hz and 50 percent duty cycle versus steady blowing at Re=25k.

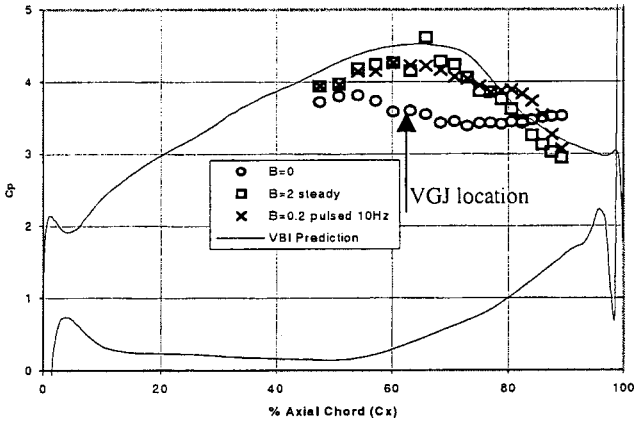

Fig. 8 Pressure coefficient versus axial chord for $B=0$, $B=2$ (steady blowing), and $B=0.2$ (pulsed blowing at 10 Hz and 50 percent duty cycle). VGJs at 63 percent C_x and Re=25k. (VBI prediction also indicated.)

immediately to the search for ways to reduce the minimum injected mass flow required for effective control. One potentially promising candidate is unsteady or pulsed vortex generator jets. As mentioned earlier, pulsed VGJs have been effectively employed by McManus et al. [14] and Raghunathan et al. [15] to control separation in two-dimensional diffusers. By essentially reducing the blowing duty cycle from 100 percent (steady blowing) to 50 percent or lower, they have shown that the average mass flow over a cycle can be reduced significantly while still controlling separation. Results of the application of unsteady blowing to the PakB turbine cascade configuration are presented in what follows. Particular attention is paid to the mechanism responsible for the effectiveness of pulsed blowing and how it differs from steady blowing.

Effect on γ_{int} and Z . The effect on the integrated blade loss coefficient, γ_{int}, of pulsed blowing at 10 Hz with 50 percent duty cycle is shown in Fig. 7. The 10 Hz forcing frequency was selected based on two factors. The reduced frequency of flow over the blade, defined as the average free-stream velocity through the blade passage divided by the suction surface distance from leading to trailing edge, is approximately 13 Hz at Re=25,000. So, the forcing frequency of 10 Hz has a Strouhal number of $0.77 \approx 1$. This is consistent with the finding of numerous studies, which indicate that Strouhal numbers near unity are most effective at preventing separation. Also, 1/7th of the shear layer instability, measured at 100 Hz in the separating boundary layer, is approximately 15 Hz. This is roughly equal to the blade shedding frequency, which was found to be an effective forcing frequency by Wu et al. [11]. So, the 10 Hz pulsing frequency (used almost exclusively in this report) was chosen to be of the same order as these two relevant frequencies. In Fig. 7, γ_{int} is normalized by γ_{int0}, the value obtained without any control. Results are presented for two injection locations: 45 (7(*a*)) and 63 percent (7(*b*)). The abscissa of the plots is the mean blowing ratio over one blowing cycle. The figures also include the same data for steady blowing, taken from Sondergaard et al. [17].

Injection at 45 percent chord shows effective operation below a mean blowing of 0.5 compared to $B_{min}=2$ for steady blowing. Limited effectiveness was measured for blowing ratios down to $B=0.2$, the lowest setting attempted at this location. The improvement from steady to unsteady blowing is even more pronounced when the injection location is just upstream of the natural separation location. Figure 7(*b*) shows a greater than 50 percent reduction in wake loss coefficient at $B=0.2$. This is nearly the same effect as that for steady blowing but with an order of magnitude less mean mass flow. So, whereas steady blowing required an addition of approximately 0.2 percent of the LPT throughflow, pulsed VGJs would require an insignificant 0.02 percent additional massflow. This finding is of the same order as the effectiveness reported in the diffuser study of McManus et al. [14]. Their results were obtained by systematically lowering the pulsing duty cycle at constant frequency and constant maximum jet blowing ratio. The blowing ratios used in the McManus et al. diffuser study were 7.5 and 11. The results shown in Fig. 7 are not for constant maximum B over the cycle. Instead, the duty cycle was held constant at 50 percent and the maximum B was reduced to lower the mean blowing ratio over the cycle. Results using the constant maximum B format with the turbine cascade are presented later.

The effectiveness of pulsed blowing is documented equally well with the c_p distribution over the controlled blade. Figure 8 shows this distribution for no control ($B=0$), steady blowing of $B=2$ at 63 percent chord, and pulsed blowing at 10 Hz, 50 percent duty cycle with a mean blowing of $B=0.2$ (also at 63 percent chord). The integrated Zweifel coefficients for the three cases are respectively: 1.99, 2.12, and 2.13.

Proposed Physical Mechanism for Effectiveness of Pulsed Control. Figure 9 shows mean boundary layer velocity and turbulence profiles at three locations downstream of the injection site for the same pulsed case ($B=0.2$ at 10 Hz and 50 percent duty cycle). The profiles, with shape factors from 2.4 at 68 percent chord to 1.6 at 87 percent chord, are full and stable. Turbulence levels in the boundary layer are elevated and show a strong 10 Hz signature, which is amplified spatially with distance downstream. Figure 10 shows hot-wire traces near the wall and at the boundary layer edge for the 77 percent profile. The 10 Hz pulsing frequency is clearly evident throughout the boundary layer. By comparison, the 10 Hz signature is undetectable at $\delta/2$ for the 68 percent pro-

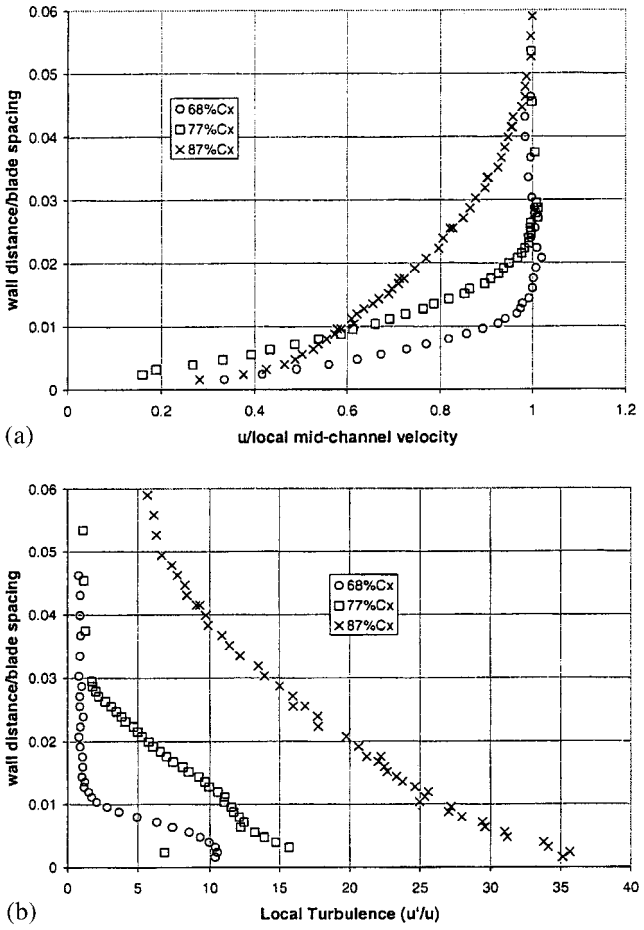

Fig. 9 Boundary layer profiles of *u* normalized by mid-channel velocity and local turbulence level. Profiles at 3 chordwise stations: 68, 77, and 87 percent axial chord. Re=25 k. Pulsed VGJs at 63 percent C_x with $B=0.2$, 10 Hz and 50 percent duty cycle. (*a*) Mean streamwise velocity (u/U_∞) boundary layer profiles. (*b*)Turbulence (u'/u) boundary layer profiles.

file and is visible at 3δ for the 87 percent profile. Evidently, the forcing has a profound effect on the character of the developing boundary layer even at such reduced mean blowing rates.

The finding that unsteady blowing is as effective as steady blowing for a greatly reduced massflow leads to questions regarding the physical mechanism(s) responsible for the bulk effect of separation control. As mentioned earlier, previous findings with steady blowing [17] suggested that boundary layer transition (triggered by instabilities associated with shedding about the injection site) was a contributing factor to the effectiveness of VGJ-induced streamwise vortices. The laminar boundary layer appeared to be sufficiently receptive to this instability, nominally centered around 500 Hz in the energy spectrum. Transition occurred within 25*d* (by 73 percent chord) from the injection site at 63 percent axial chord. The peak at 500 Hz then attenuated rapidly until it was no longer evident in the 77 percent chord spectrum.

Boundary layer data in the pulsed case show a markedly different signature than that for steady jet injection. Spectra for the pulsed case (e.g., Fig. 11) show strong peaks at the pulsing frequency and harmonic multiples. This figure includes spectra for $B=0$, 2 (steady), and 0.2 (unsteady) at midboundary layer on the 68 percent profile. The power spectral density (PSD) computed here is twice the FFT multiplied by its complex conjugate divided by the number of samples squared. Each of these PSD plots is the average of 20 records taken consecutively at 10 k Hz. Individual records consist of 65,536 data points. The uncontrolled spectrum

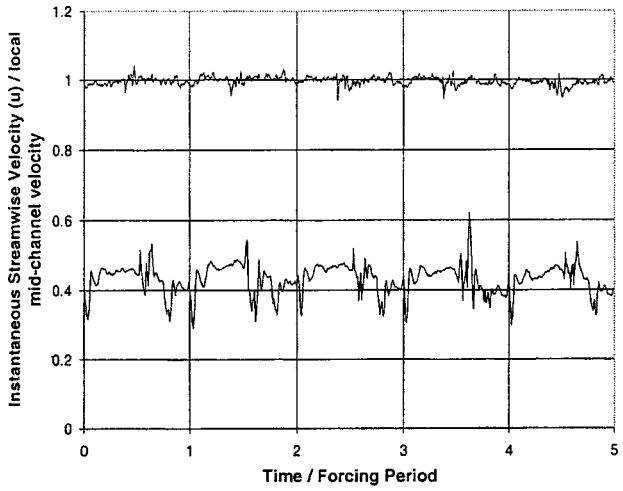

Fig. 10 Instantaneous streamwise velocity measurements near the wall and at boundary layer edge for the 77 percent C_x profile. Pulsed blowing at 63 percent C_x with $B=0.2$ at 10 Hz. five-forcing periods evident. Re=25k.

was taken upstream of the natural separation zone and shows no significant energy peaks over the frequency band. The steady VGJ spectrum shows the strong shedding frequency energy peak (around 500 Hz) mentioned earlier. The pulsed spectrum, however, is dominated by the forcing frequency and its harmonics with no strong 500 Hz peak. Thus, in the pulsed case, the shedding frequency is dominated by the forcing frequency. This same effect was observed at higher pulsing frequencies (e.g., 100 Hz).

From the boundary layer data of Figs. 9 and 10, it is clear that the pulsing frequency is not confined to the wake of the VGJ. It is visible from upstream of the injection location (at 60 percent chord) all the way to the trailing edge. Figure 12 shows the evolution of spectral energy content as the boundary layer moves down the blade from 60 percent to 96 percent chord. The first data point is at $y\cong\delta/2$ for 60 percent chord, the second at $y\cong\delta$ for 81 percent chord, and finally $y\cong2\delta$ for 96 percent chord. The 10 Hz forcing signature appears to have propagated throughout the entire flowfield. Clearly the pulsed blowing affects the bulk flow over the blade and is not simply isolated to the VGJ wake. One mechanism for creating this bulk effect from such a negligible mass injection is through boundary layer transition. In the steady blowing case, shedding frequencies were identified and connected to

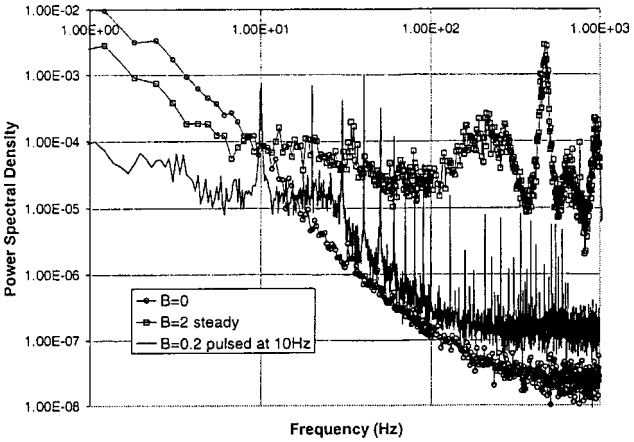

Fig. 11 Power spectral density plots at midboundary layer on the 68 percent C_x profile. Data for $B=0$, $B=2$ (steady blowing), and $B=0.2$ (pulsed blowing at 10 Hz and 50 percent duty cycle). VGJs at 63 percent C_x. Re=25k.

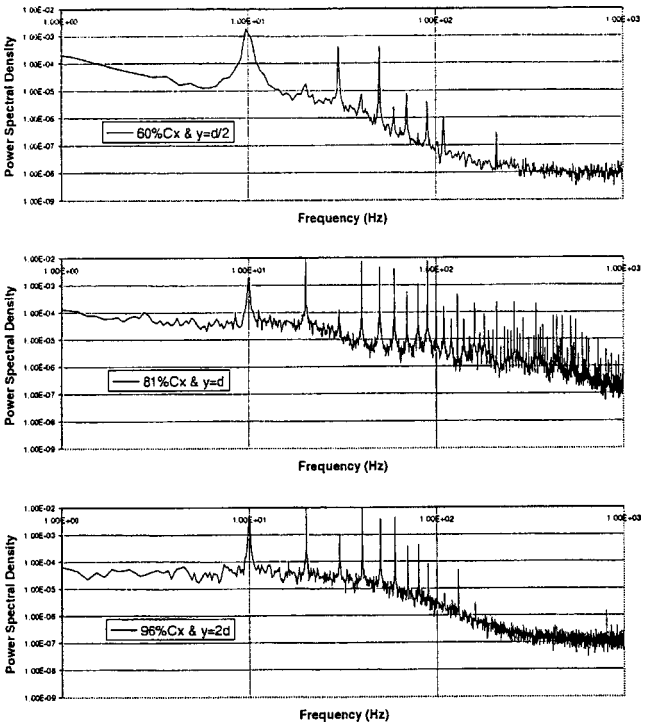

Fig. 12 Power spectral density plots for $B=0.2$ (10 Hz pulsed) with VGJs at 63 percent C_x. Data at $y=\delta/2$ on the 60 percent C_x profile, $y=\delta$ on the 81 percent C_x profile, and $y=2\delta$ on the 96 percent C_x profile. Re=25k [$d\equiv\delta$ in legends].

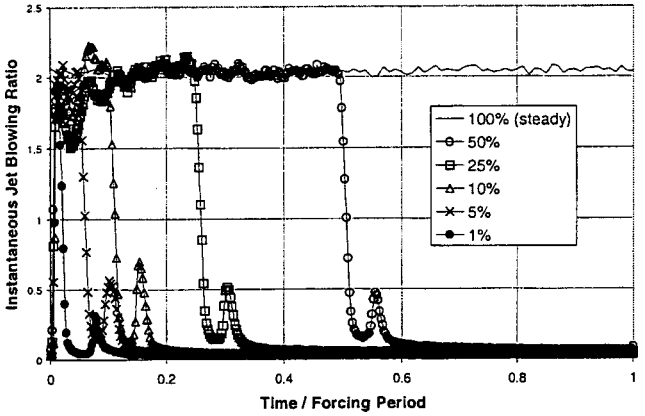

Fig. 13 Instantaneous jet exit blowing ratios for various duty cycles all at 10 Hz. Data taken with subminiature hotfilm probe in VGJ exit at 63 percent C_x. Re=25k.

early boundary layer transition. In the pulsed case, the shedding frequency is not prominent in the energy spectrum, so the pulsing itself must be affecting transition.

From the pulsed spectra in Figs. 11 and 12, it is apparent that the harmonic lines dominate the energy content of the boundary layer. Peaks at 20 and 40 Hz, in particular, are everywhere stronger than the forced frequency, except very near the injection site. Since the pulsed jet is well approximated by a square wave (Fig. 13), the starting and stopping of the jet create two fluid events for each pulse cycle. From the Johari and McManus [16] study it is clear that the formation of a strong starting vortex from a pulsed VGJ can intensify streamwise vorticity relative to the steady blowing case. In the present experiment, the boundary layer thickness at the injection location is 2.5 mm=2.5d and the blowing ratios tested are all near unity. So, the starting vortex should remain intact inside the boundary layer. This is the flow disturbance most likely responsible for the unsteady transition and corresponding bulk flow pulsations in the boundary layer (and beyond).

To validate the hypothesis that the starting and ending events of the pulse are the key to its effect rather than the intervening mass flux, a test was conducted similar to the ''constant maximum B'' format used by McManus et al. and referred to earlier. With the pulsing frequency constant at 10 Hz, the duty cycle was reduced from 100 percent (steady) to 1 percent, maintaining approximately the same maximum B. By 1 percent duty cycle, the pulse is essentially a narrow spike without any steady massflow component (Fig. 13). Figure 14 shows that the integrated wake loss coefficient remained approximately constant from 100 percent (steady blowing at $B=2$) down to the 1 percent duty cycle case. This is an equivalent mean B of approximately 0.05, and remarkably the pulsing is still effective. From this it is clear that the vortices associated with starting (and stopping) the jets are the mechanism that inhibits separation. As with the steady VGJ case, these vortices can influence separation in two distinct ways: by initiating transition or by drawing free-stream momentum down to the wall.

Variations in Pulsed VGJ Effectiveness With Chordwise Location. The interplay between these two different mechanisms is evident when pulsed blowing is implemented at the two injection locations, 45 and 63 percent chord, and at constant $B=0.2$. From the boundary layer plots in Fig. 9, it appears that early boundary layer transition is initiated when pulsed injection occurs very close to the natural separation point. For this case there is no evidence of a coherent jet pattern 12d downstream (68 percent C_x) of the injection location. Figure 15 contains three mean and fluctuating velocity profiles taken 5d apart in the spanwise direction at the 68 percent chord location for pulsed blowing of $B=0.2$ at 63 percent chord. With a hole pitch of 10d, some periodicity would be expected between the three profiles if the jets were coherent structures. Instead the profiles are nearly identical, both in mean velocity and turbulence level. So, in this case the VGJs are affecting separation primarily through early transition versus sustained vorticity-induced momentum exchange with the free stream.

When the jets are pulsed at the same mean blowing ratio but farther upstream, the situation is reversed. Pulsed injection at 45 percent chord successfully reduces separation (Fig 7(a) indicates $\gamma_{int}/\gamma_{int0}\cong 0.68$ for $B=0.2$) but not through transition of the boundary layer. Figure 16 shows boundary layer velocity and turbulence profiles at 77 percent chord for the pulsing at 45 percent chord case. Three profiles are shown: $B=0.2$ (pulsed), $B=2$ (steady), and a case with a 1-mm-dia wire trip at 45 percent chord (and $B=0$). The pulsed boundary layer at 77 percent shows negligible turbulence at the wall with a shape factor of 2.1. This

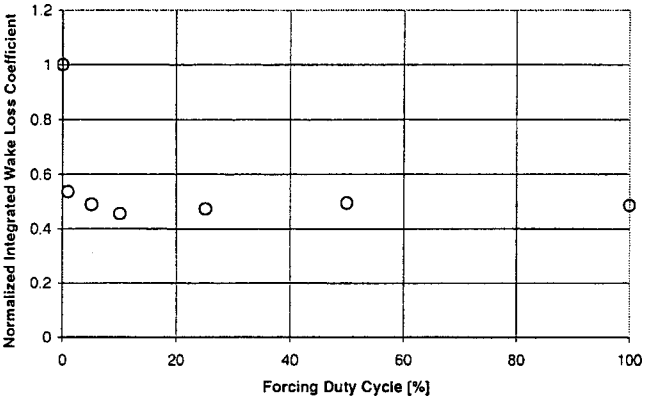

Fig. 14 Normalized integrated wake loss coefficient ($\gamma_{int}/\gamma_{int0}$ versus pulsing duty cycle for constant maximum blowing ratio ($B_{max}=2$, see Fig. 13). Data for pulsed blowing at 10 Hz. Re =25k.

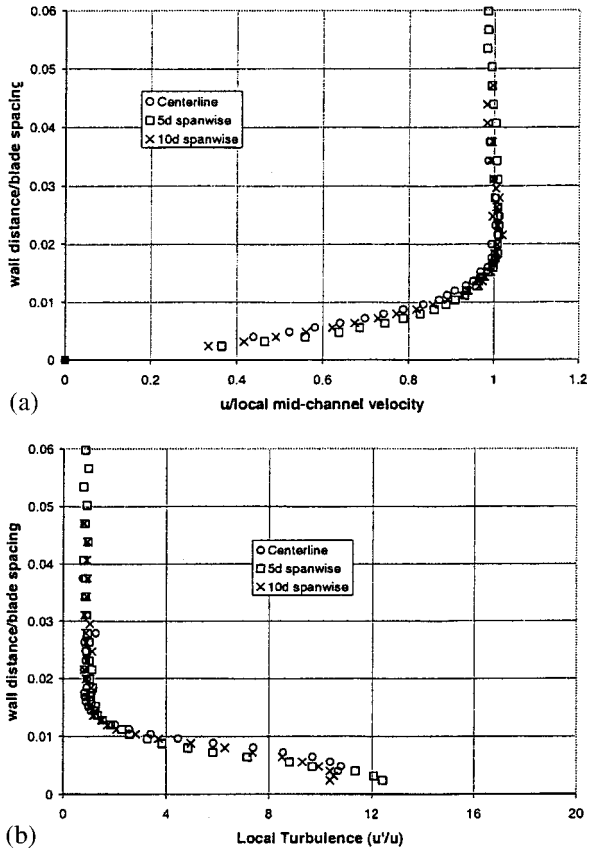

Fig. 15 Boundary layer profiles of u normalized by mid-channel velocity and local turbulence level. Profiles at 68 percent C_x and 3 spanwise stations spaced 5d apart (VGJ spacing is 10d). Re=25k. Pulsed VGJs at 63 percent C_x with $B=0.2$, 10 Hz and 50 percent duty cycle. (*a*) Mean streamwise velocity (u/U_∞) bounday layer profiles. (*b*) Turbulence (u'/u) boundary layer profiles.

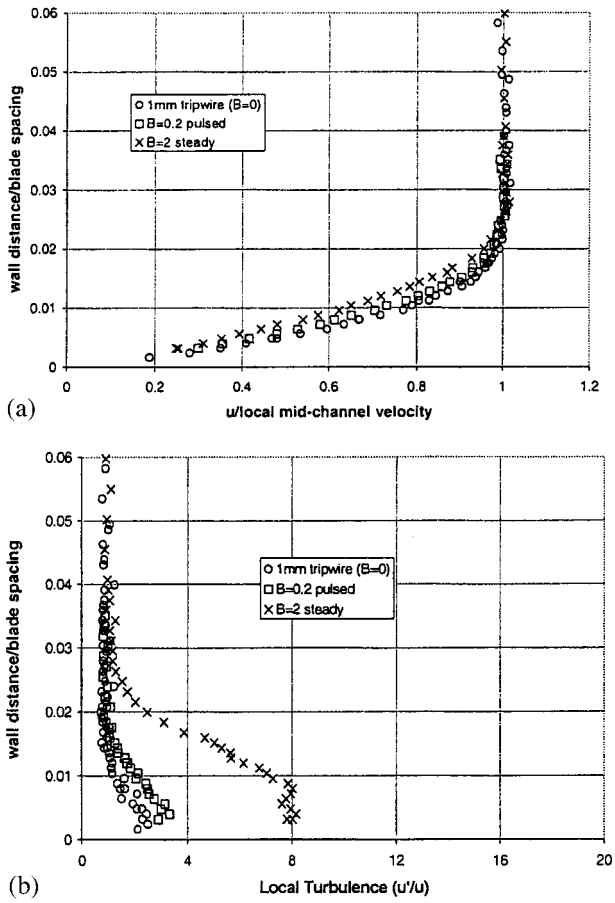

Fig. 16 Boundary layer profiles of u normalized by midchannel velocity and local turbulence level. Profiles at 77 percent C_x for three different cases: pulsed VGJs at $B=0.2$ and 10 Hz (50 percent duty cycle), steady VGJs at $B=2$, and 1-m diam. trip all at 45 percent C_x. Re=25k. (*a*) Mean streamwise velocity (u/U_∞) boundary layer profiles. (*b*) Turbulence (u'/u) boundary layer profiles.

measurement station is approximately 75d from the injection station, the same distance from the 63 percent injection station to the 87 percent profile shown in Fig. 9(*a*), where the shape factor was calculated to be 1.6 with wall turbulence levels greater than 10 percent. Apparently the pulsed vortices play a different role other than producing transition when injected at such an early stage in the boundary layer development. While no hot-wire measurements were taken at 45 percent chord, the boundary layer is certainly thinner and still enjoying a favorable pressure gradient at this point. Perhaps conditions are not conducive to instability growth or the blowing ratio is too low to sustain transition here. And yet, the 77 percent boundary layer is not separated ($\gamma_{\text{int}}/\gamma_{\text{int0}} \cong 0.68 < 1$). So, the pulsed vortices must be playing the more traditional role of momentum transfer between the free stream and the boundary layer. In fact, the pulsed velocity and turbulence profiles in Fig. 16 look very similar to those for a two-dimensional wire trip. The trip at 45 percent chord is placed early enough on the blade that the flow downstream of its wake relaminarizes with a fuller, separation-resistant profile. By comparison, the $B=2$ steady VGJ profile at 77 percent C_x has a maximum wall turbulence of 8 percent and a distinct profile shape. Boundary layer transition has been (or is being) triggered and consequently steady blowing at 45 percent C_x (with $B=2$) is more effective in the separation prevention role, with a $\gamma_{\text{int}}/\gamma_{\text{int0}}$ of less than 0.5 (Fig. 7(*a*)). From the same figure (7(*a*)) it is apparent that as the pulsed blowing ratio is increased to greater than 0.5, $\gamma_{\text{int}}/\gamma_{\text{int0}}$ approaches the value for steady blowing at $B=2$. This may be evidence of some threshold for pulsed blowing to initiate transition. If so, this threshold evidently increases with distance upstream of the natural separation point.

Summary of Unsteady Blowing. To summarize, pulsed VGJs create strong vortices with turbulent energy concentrated at two and four times the forcing frequency. These pulsed vortices initiate early transition if injected near the natural separation point or replenish the laminar boundary layer with free-stream momentum when employed well upstream. By contrast, steady blowing requires significantly more massflow to inhibit separation and appears to affect the boundary layer by a shedding instability and free-stream momentum entrainment. The combined effect is early boundary layer transition and an observed reduction in separation.

Other pulsing frequencies were investigated as well, up to 100 Hz, with similar results. For $B=0.4$ pulsing at 63 percent C_x, $\gamma_{\text{int}}/\gamma_{\text{int0}}$ was 0.48, 0.46, and 0.44 for 10 Hz, 50 Hz, and 100 Hz, respectively (all at 50 percent duty cycle). Above 100 Hz the exit velocity from the VGJ became more sinusoidal rather than the square wave shape shown in Fig. 13 due to the settling chamber inside the blade. Since slowly varying pulse streams generate far weaker vortices than sharp transitions, frequencies up to the valve maximum of 250 Hz were not attempted. It is expected that at pulsing frequencies significantly below 10 Hz ($\leqslant$1 Hz), intermittent separation and reattachment would occur with each pulsing cycle. This is generally the case when the forcing frequency is an order of magnitude lower than the blade reduced frequency (13 Hz at Re=25,000).

Although unsteady testing with the present cascade has yet to be conducted at higher Reynolds numbers or with elevated free-

stream turbulence levels, it is assumed that the effects would be similar to that for steady blowing. Pulsing should have a diminishing effect for increased Re with no anticipated adverse effects at nonseparating Reynolds numbers. With free-stream turbulence (and Re still low enough to see natural separation) pulsing should play a reduced role since the boundary layer may already be turbulent. The pulsed vortices would then be relegated to the role of free-stream momentum entrainment into the turbulent boundary layer.

As for the practical application of pulsed VGJ control in a working LPT, there are as yet many unanswered questions: compressibility effects, upstream wakes, endwall flows, rotational effects, full cascade VGJ implementation, and passage vortices, to name a few. Notwithstanding these potential limitations, the findings of this study show that for a negligible massflow penalty pulsed VGJs can produce considerable reductions in blade wake signature and increase turbine efficiency.

Conclusions

Active boundary layer separation control has been successfully demonstrated on a low-pressure turbine blade using pulsed vortex generator jets (VGJs). The experiments were performed in a low-speed linear cascade using a typical high-performance blade shape with documented separation limitations at low Reynolds numbers. Pulsed injection was employed at two chordwise stations and at frequencies ranging from 10 to 100 Hz. The following conclusions are submitted based on the data presented:

1 Pulsed VGJs drastically reduce suction surface boundary layer separation at low Reynolds numbers. Reductions in wake losses of up to 60 percent were measured in combination with improved blade pressure distributions.

2 Pulsed VGJs produce a comparable improvement to that for steady VGJs but with an order of magnitude less required massflow.

3 The bulk effect on separation appears to be insensitive to frequency over the range of frequencies studied ($1 < \mathrm{St} < 10$).

4 The beginning and end of the jet pulse (and not the injected mass itself) provide the means for influencing the boundary layer. This is done through the mechanisms of early boundary layer transition and vortical entrainment of free-stream fluid. The steady flow mechanism of shedding instability does not appear to be relevant in the pulsed jet case.

5 The distance from the jet injection location to the natural separation point is a critical factor in determining the effectiveness of pulsed blowing. Just upstream of the separation point (63 percent C_x), even a minute level of blowing (B down to 0.05) can substantially reduce separation. This occurs primarily through boundary layer transition. Farther upstream (45 percent C_x), small levels of blowing reduce separation but not through boundary layer transition. Free-stream entrainment appears to be the mechanism which produces a reduction in separation for this case.

These results led the authors to conclude that the application of pulsed VGJs for low-Reynolds-number separation control on LPT blades shows great promise.

Acknowledgments

The authors are indebted to the Air Force Institute of Technology Machine Shop personnel (Russ Hastings, Jan LeValley, and Condie Inman) for the fine craftsmanship they demonstrated in the construction of the modified wind tunnel. Also, this work would not have been possible without the superior technical expertise of AFRL technician Bill Nilson. This work was performed under sponsorship from the Air Force Office of Scientific Research, with Dr. Tom Beutner as contract monitor. The views expressed in this article are those of the authors and do not reflect the official policy or position of the United States Air Force, Department of Defense, or U.S. Government.

Nomenclature

B = jet blowing ratio$=(\rho u)_{\mathrm{jet}}/(\rho u)_{\mathrm{local}}$
C_x = blade axial chord$=0.18$ m
Re = inlet Reynolds number$=\rho_{in} u_{in} C_x/\mu$
St = Strouhal number$=fc/U_\infty$
Z = modified Zweifel coefficient (Eq. (2))
c = airfoil true chord
c_D = airfoil drag coefficient
c_L = airfoil lift coefficient
cp = blade pressure coefficient$=(p_{T,in}-p_{S,local})/(p_{T,in}-p_{S,in})$
d = jet hole diameter = 1 mm
$\hat{e}_n$ = unit vector normal to blade surface
$\hat{e}_t$ = unit vector in rotational direction
f = forcing frequency, Hz
p = pressure, Pa
U, u = streamwise mean velocity, m/s
u' = streamwise rms fluctuating velocity, m/s
γ = wake loss coefficient $=(p_{T,in}-p_{T,ex})/(p_{T,in}-p_{S,in})$
γ_{int} = integrated wake loss coefficient (Eq. (1))
δ = boundary layer thickness
μ = dynamic layer thickness
ρ = density

Subscripts

ex = cascade exit conditions
in = cascade inlet conditions
jet = vortex generator jet conditions
local = local blade conditions
S = static or ambient condition
T = stagnation or total condition
∞ = free-stream conditions

References

[1] Sharma et al., 1998, private communication.
[2] Matsunuma, T., Abe, H., Tsutsui, Y., and Murata, K., 1998, ''Characteristics of an Annular Turbine Cascade at Low Reynolds Numbers,'' ASME Paper No. 98-GT-518.
[3] Matsunuma, T., Abe, H., and Tsutsui, Y., 1999, ''Influence of Turbulence Intensity on Annular Turbine Stator Aerodynamics at Low Reynolds Numbers,''ASME Paper No. 99-GT-151.
[4] Helton, D., 1997, private communication.
[5] Lin, J. C., Howard, F. G., Bushnell, D. M., and Selby, G. V., 1990, ''Investigation of Several Passive and Active Methods of Turbulent Flow Separation Control,'' AIAA Paper No. 90-1598.
[6] Compton, D. A., and Johnston, J. P., 1992, ''Streamwise Vortex Production by Pitched and Skewed Jets in a Turbulent Boundary Layer,'' AIAA J. **30**, No. 3, Mar.
[7] Henry, F. S., and Pearcey, H. H., 1994, ''Numerical Model of Boundary-Layer Control Using Air-Jet Generated Vortices,'' AIAA J. **32**, No. 12, Dec.
[8] Hsiao, F., Liu, C., and Shyu, J., 1990, ''Control of Wall-Separated Flow by Internal Acoustic Excitation,'' AIAA J. **28**, No. 8, pp. 1440–1446.
[9] Amitay, M., Kibens, V., Parekh, D., and Glezer, A., 1999, ''The Dynamics of Flow Reattachment Over a Thick Airfoil Controlled by Synthetic Jet Actuators,'' AIAA Paper No. 99-1001.
[10] Weaver, D., McAlister, K., and Tso, J., 1998, ''Suppression of Dynamic Stall by Steady and Pulsed Upper-Surface Blowing,'' AIAA Paper No. 98-2413.
[11] Wu, J., Lu, X., Denny, A., Fan, M., and Wu, J., 1998, ''Post-stall Flow Control on an Airfoil by Local Unsteady Forcing,'' J. Fluid Mech., **371**, pp. 21–58.
[12] Seifert, A., Bachar, T., Koss, D., Shepshelovich, M., and Wygnanski, I., 1993, ''Oscillatory Blowing: A Tool to Delay Boundary-Layer Separation,'' AIAA J., **31**, No. 11, pp. 2052–2060.
[13] Kwong, A., and Dowling, A., 1994, ''Active Boundary-Layer Control in Diffusers,'' AIAA J. **32**, No. 12, Dec.
[14] McManus, K., Legner, H., and Davis, S., 1994, ''Pulsed Vortex Generator Jets for Active Control of Flow Separation,'' AIAA Paper No. 94-2218.
[15] Raghunathan, S., Watterson, J., Cooper, R., and Lee, S., 1999, ''Short Wide Angle Diffuser With Pulse Jet Control,'' AIAA Paper No. 99-0280.
[16] Johari, H., and McManus, K., 1997, ''Visualization of Pulsed Vortex Generator Jets for Active Control of Boundary Layer Separation,'' AIAA Paper No. 97-2021.
[17] Sondergaard, R., Bons, J., and Rivir, R., 2000, ''Control of Low-Presure Turbine Separation Using Vortex Generator Jets,'' submitted for publication in J. Propul. Power.
[18] Bons, J., Sondergaard, R., and Rivir, R., 1999, ''Control of Low-Pressure Turbine Separation Using Vortex Generator Jets,'' AIAA Paper No. 99-0367.

Reduction of Secondary Flow Losses in Turbine Cascades by Leading Edge Modifications at the Endwall

H. Sauer

R. Müller

K. Vogeler

Dresden University of Technology,
01062 Dresden, Germany

Experimental results are presented which show the influence on the secondary flow and its losses by a profile modification of the leading edge very close to the endwall. The investigation was carried out with a well-known turbine profile that originally was developed for highly loaded low pressure turbines. The tests were done in a low speed cascade wind tunnel. The geometrical modification was achieved by a local thickness increase; a leading edge endwall bulb. It was expected that this would intensify the suction side branch of the horse-shoe (hs-) vortex with a desirable weakening effect on the passage vortex. The investigated configuration shows a reduction of secondary losses by 2.1 percent points that represents approximately 50 percent of these losses compared to the reference profile. Detailed measurements of the total pressure field behind the cascade are presented for both the reference and the modified profile. The influence of the modified hs-vortex on the overall passage vortex can be clearly seen. The results of a numerical analysis are compared with the experimental findings. A numerical analysis shows that the important details of the experimental findings can be reproduced. Quantitative values are locally different. The theoretical approach taken cannot yet be used for an exact prediction of the loss reduction. However, the analysis of the interaction and the resulting tendencies are considered to be valid. Hence, theoretical investigations as a guideline for the design of a leading edge bulb at the endwall are a valuable tool.
[DOI: 10.1115/1.1354142]

Introduction

Secondary losses are a considerable part of the total losses in turbomachines. This holds especially for blades with low aspect ratio. Therefore the understanding and proper consideration of the secondary flow is crucial for the reduction of the overall losses and hence for the optimized efficiency of modern gas and steam turbines.

A typical modern 3D Navier-Stokes analysis is able to predict and to visualize the fluid mechanics of the main flow field and the vortex pattern in a turbine cascade. However, for a new or for an improved design it is required to compare this analysis with experimental results which at the same time are absolutely necessary to improve and to calibrate the available computer codes.

Secondary flow is taken as the general term for the complex 3D flow pattern near the walls of a cascade of turbomachinery profiles. However, it is well known that this pattern is composed from discrete phenomena which eventually can strongly interact with each other. The dominant components of the secondary flow are the passage vortex, the trailing edge vortices, the corner vortex and the hs-vortex (Fig. 1).

Basic investigations have shown that the secondary losses of a turbine cascade could be reduced by modifying the leading edge profile of an inlet stator vane at the transition from the wall into the leading edge [1]. As the results were quite encouraging, a follow-up investigation was initiated with a very well-known, highly deflecting rotor blade to confirm these findings. The tested modification was a bulblike geometry; see Fig. 2*a*,*b*. In contradiction to a standard fillet radius, the transition of the bulb to the endwall is rectangular.

Contributed by the International Gas Turbine Institute and presented at the 45th International Gas Turbine and Aeroengine Congress and Exhibition, Munich, Germany, May 8–11, 2000. Manuscript received by the International Gas Turbine Institute February 2000. Paper No. 2000-GT-473. Review Chair: D. Ballal.

This paper reports the results of that test series and its numerical analysis. The objective of the investigation was to create a strong suction side branch of the hs-vortex by the described geometrical leading edge modification. Then this vortex was expected to interact by its opposite rotational direction with the main passage vortex such that it would move it away from the suction side profile boundary layer. Due to the reduced interaction of the passage vortex with the profile boundary layer it was expected that endwall losses could be considerably reduced. In order to isolate the effect of this loss mechanism, the measured results were reduced by subtracting the known profile losses and the losses due to the incoming wall boundary layer in front of the test section. These components were measured separately. Only these reduced losses are shown in this paper. The comparison with the equivalent losses of the reference blade is a direct measure how effective the modification reduces the secondary losses. A second objective was a comparison of these experimental results with those of a numerical analysis achieved with a commercial code [2].

Test Rig and Profile Selection

The experiments were done in a low speed cascade windtunnel. It can deliver an exit velocity of 70 m/s which translates into $Ma_2=0.2$ at the cascade exit. Air is delivered by a two-stage compressor. It has to pass through a sequence of straighteners and sieves to break down the turbulence to less than 1 percent. In the core of the inlet flow. Then it is accelerated by a nozzle into a $300\times 900\,mm^2$ turnable test section which allows inlet angles between 25 deg and 150 deg. The cascade is built from 12 blades with a blade height of 300 mm and a profile length of $l_p = 100\,mm$. This results in a Reynolds number of $4.5\cdot 10^5$. The chosen aspect ratio of 3 ensures basically a 2D passage flow over a large portion around the 50 percent blade height. The air leaves into the free atmosphere expanding to ambient conditions. Losses measured in a plane behind the cascade would be a direct function

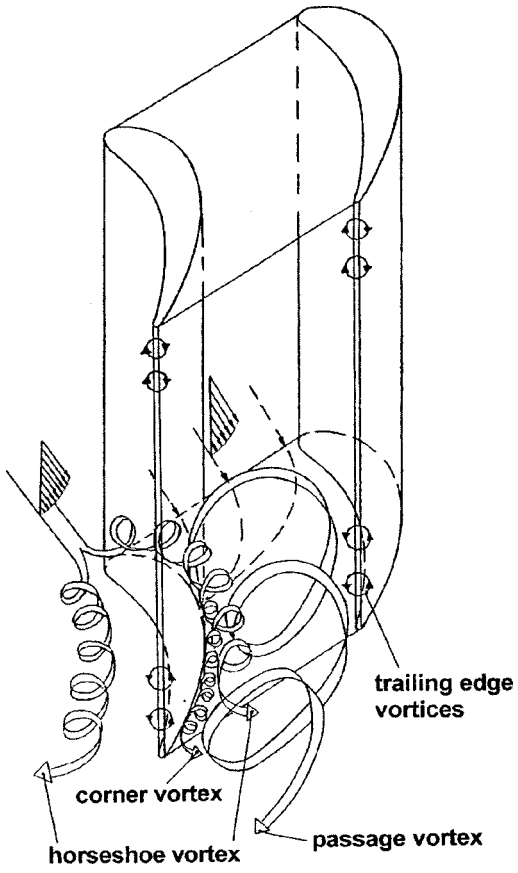

Fig. 1 Secondary flow vortices

of the distance of that plane to the cascade. Hence the results of all tests are compared only for a measuring plane in one defined relative distance behind the cascade: $s_2/l_p=1.0$. Figure 3 shows this dependency for various testcases [3].

The T106 was taken for reference as a well-known profile from literature [4–6]. Figure 3*b* shows the T106 together with a sketch of the investigated leading edge modification. When designing a contour in the endwall region, the idea is to increase the strength of the hs-vortex as it develops near to the stagnation point of the profile. Then the suction side branch of the hs-vortex interacts with the counter-rotating passage vortex, moving that away from the suction side profile boundary layer and hence weakening the interaction with it. Part of the experiment was also to investigate the effect of the hs-vortex pressure side branch on the pressure side profile boundary layer interacting with the co-rotating channel vortex. Directly at the leading edge the bulb increases its radius by a small amount lengthwise it extends for $b_0=5$ mm staying constant. From there it merges within $b=15$ mm into the reference profile. The transition follows a cosine function (Fig. 2*b*).

All total pressures were measured with pneumatic probes. Across the measuring planes in the flow-field a pitot-probe was used behind the cascade. The total pressure distribution across the incoming boundary layer was picked up with a flattened pitot-probe. The exit flow angles were measured with an adjustable pitot-probe. Prerequisite for that was the positioning of the pressure tap of the probe in its axis of rotation. As the flow field shows large gradients in total pressure and flow angles the precision of the measured values was very high. Spatial flow angles were measured using a five-hole probe calibrated for flow angle. These were only used to determine the velocity component c_z. Measurements were taken across the passage along 18 traces which were distributed pitchwise from blade to blade. The losses are mass flow averaged.

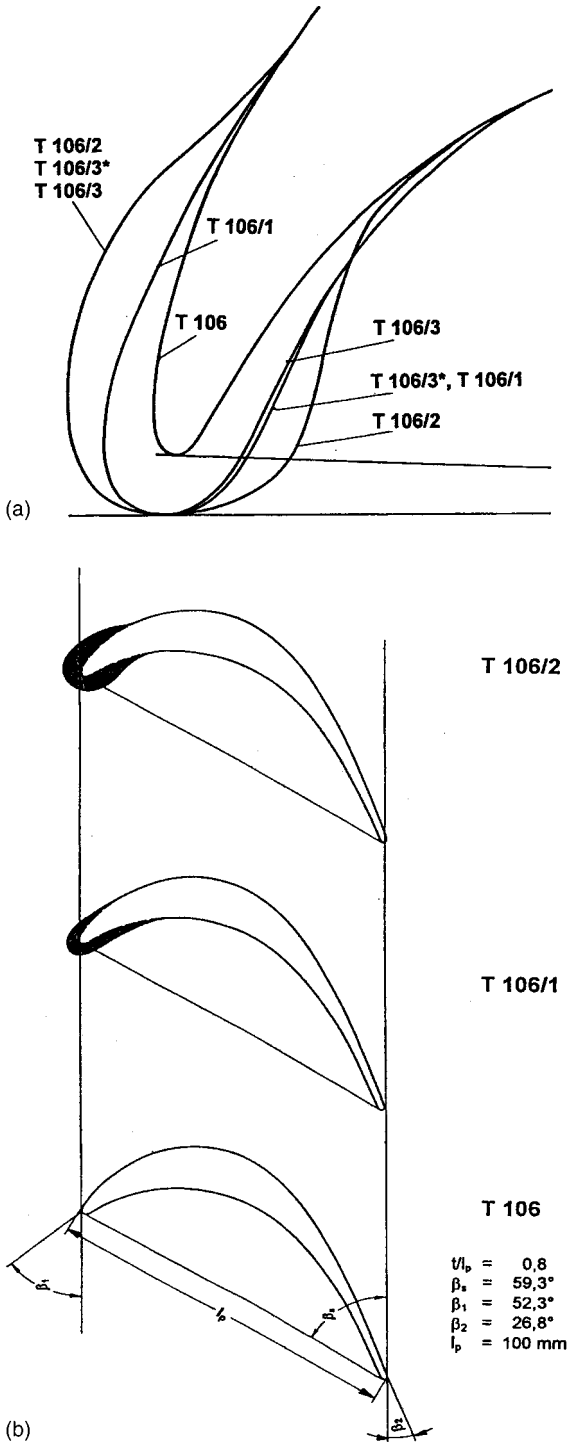

Fig. 2 (*a*) T106 Cascade data (equal blading for each modification) and (*b*) T106 profile and the modification (leading edge endwall bulb)

Using this measuring technique time mean values are acquired. This allows a good representation of vortex structures. Fluctuations cannot be considered. The original measuring result is reduced via subtracting the profile loss, Eq. (1)

$$\zeta_{ew}=\frac{\frac{2}{L}\int_0^{L/2}[\zeta(z)-\zeta_p]\cdot\overline{\rho c_{ax}}(z)dz}{(\overline{\rho c_{ax}})} \tag{1}$$

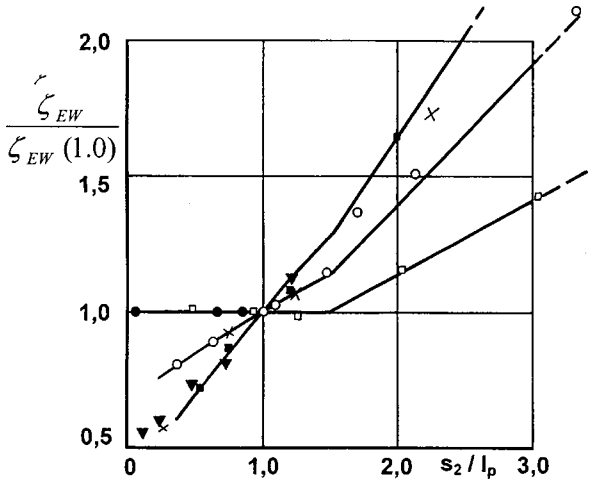

Fig. 3 Increase of the integral endwall loss coefficient downstream of a turbine cascade

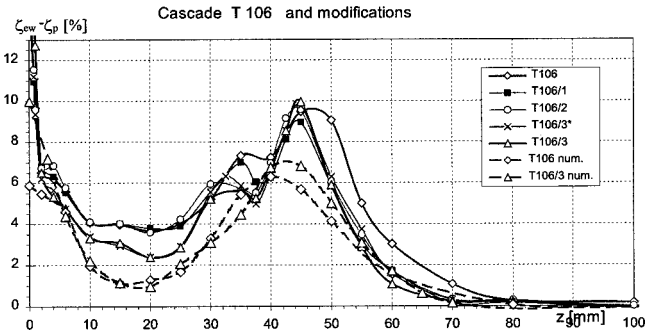

Fig. 4 Spanwise endwall loss distribution/averaged pitch wise

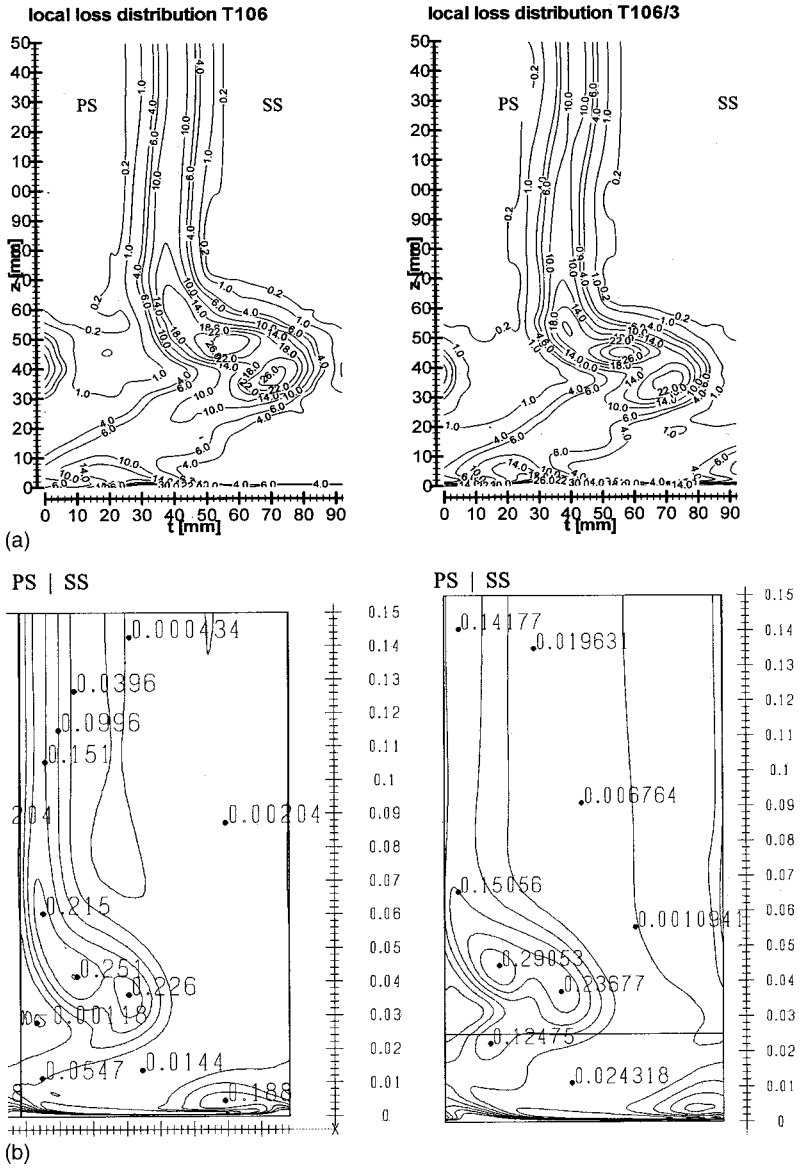

Fig. 5 Local endwall loss distribution/measuring plane behind T106 and T106/3 at $s_2/l_p=1$

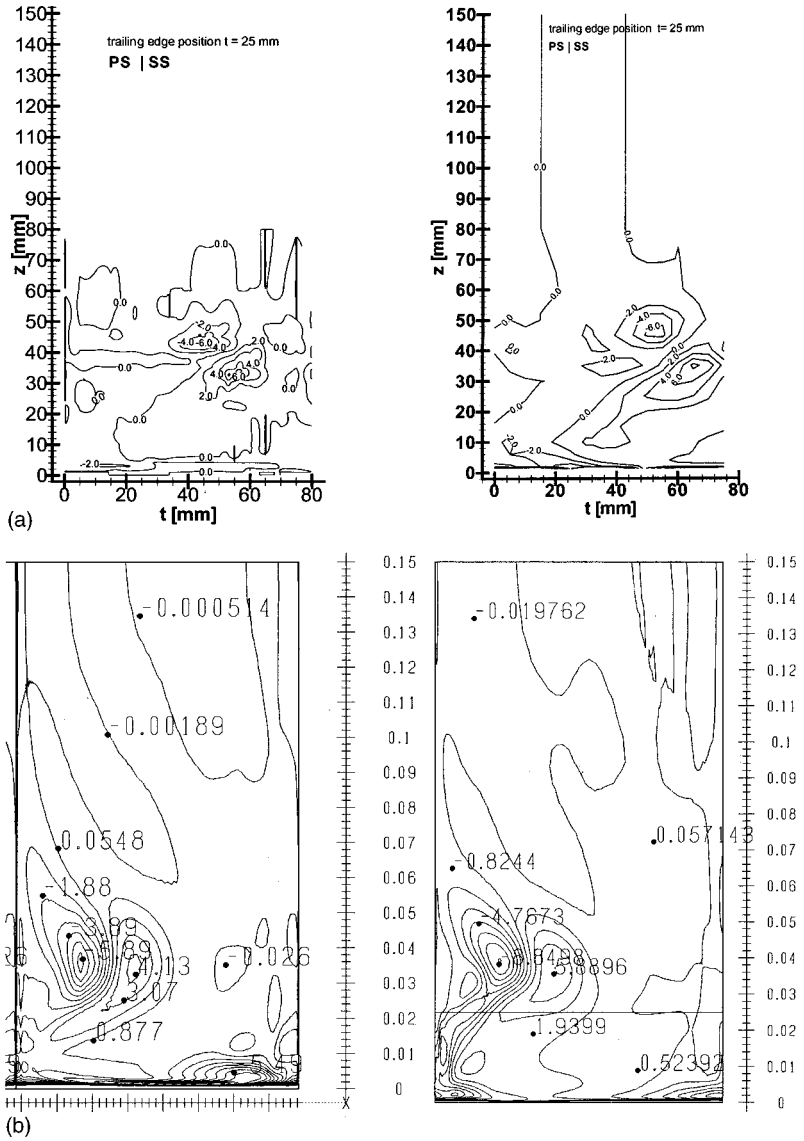

Fig. 6 Streamwise vorticity downstream of T106 and T106/3

Experimental Results/Loss Distribution

$$\zeta(z)=\frac{\frac{1}{t}\int_0^t \zeta_t\cdot\rho_2\cdot c_{2ax}dy}{\overline{\rho c_{ax}}(z)},$$

$$\zeta_l=\frac{c_{2is}^2-c_2^2}{c_{2is}^2},\quad \overline{\rho c_{ax}}(z)=\frac{1}{t}\int_0^t \rho_2\cdot c_{2ax}dy$$

and

$$(\overline{\rho c_{ax}})=\frac{2}{L}\int_0^{L/2}\overline{\rho c_{ax}}(z)dz \tag{2}$$

As long as the endwall loss areas does not merge over the blade this result is independent from the blade length as the profile loss is subtracted. It represents the isolated secondary loss. Hence, it can be expressed with respect to a blade length of $L_0=100$ mm, Eq. (3), normalized endwall loss:

$$\zeta_{ew0}=\zeta_{ew}\cdot\frac{L}{L_0} \tag{3}$$

The massflow averaged loss coefficient of the incoming endwall boundary layer ζ_{ibl} which was normalized with respect to the pressure ratio of the cascade is also expressed with respect to the length $L_0=100$ mm, [Eq. (3)]. Now the net endwall loss can be expressed by Eq. (4)

$$\zeta_{ew0}^n=\zeta_{ew0}-\zeta_{ibl0} \tag{4}$$

The measurement of the profile loss in the middle section in a free jet wind tunnel showed that the transition of the boundary layer does not occur via a seperation bubble. This is different to reported results from literature [4–6], but it could have been expected considering different test conditions. Otherwise the agreement is excellent. The low profile losses from 1.68 percent (blade material: machined perspex) to 1.83 percent (thermoplast) confirm this.

Figure 4 shows the distribution of the reduced and averaged endwall losses in spanwise direction for the unmodified reference and various modified leading edges (T106-T106/1-3). It can clearly be seen that the leading edge bulb results in a considerable decrease of the endwall losses, with T106/3 being the best case tested so far. But it can also be seen that a certain dimension of the bulb is necessary to make the desired interaction of the two

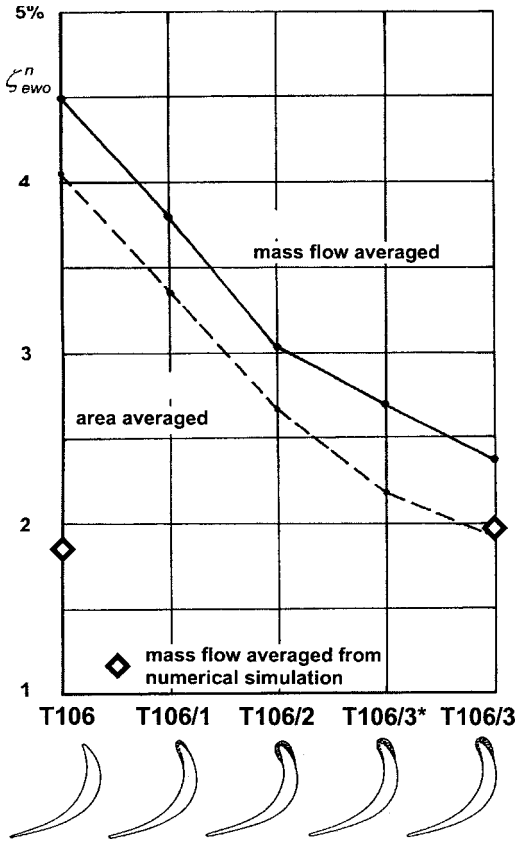

Fig. 7 Net endwall losses for various bulb geometries

vortices effective (T106/1,2). T106/3 and T106/3* have a more pronounced bulb geometry with the suction side being larger than the pressure side. Typically the local loss decrease can be found in two regions. For the investigated cascade it is the spanwise distance from the endwall from 2–30 mm and from 45–80 mm where the vortex interaction is effective. Different bulb geometries show different results. Especially it can be seen that it is advantageous to have a stronger suction side bulb in order to intensify the hs-vortex locally as desired.

T106/3 and T106/3* are geometrically nearly identical. Small differences on the pressure side of the bulb do not show large differences in losses. All measurements were taken independently in two different test runs to ensure reproducibility.

Figure 5*a* shows local endwall loss distribution comparing T106 and T106/3. The expected concentration of boundary layer material on the suction side is clearly visible for both cases approximately 40–50 mm spanwise from the endwall. Maximum values are of the same order of magnitude. However the T106/3 shows this area to be considerably condensed. This results in an overall reduced loss value when averaged over the whole plane.

The pattern of the loss distribution shows the typical ''dog-bone'' geometry of a twin peak for highly loaded turbine cascades. The less pronounced peak positions itself close to core of the channel vortex ($z=35$ mm; $t=70$ mm). The second loss peak ($z=50$ mm; $t=60$ mm) shows larger gradients. This represents the trailing edge vortex which developes as a discrete vortex collecting the low energy material from the boundary layer around its core. These two vortices have opposite rotational directions. Figure 6 shows the normalized streamwise vorticity [5] for T106.

$$\mathrm{SVO}=\frac{\Gamma_s \cdot l}{c_{2is}} \tag{5}$$

with $\Gamma_s=\Gamma_x \cdot \cos\beta_M+\Gamma_y \cdot \sin\beta_M$,

$$\Gamma_x=\frac{\partial c_z}{\partial y}-\frac{\partial c_y}{\partial z} \quad \text{and}$$

$$\Gamma_y=\frac{1}{c_x}\left[\frac{1}{\rho}\frac{\partial p}{\partial z}+\frac{1}{2}\frac{\partial c^2}{\partial z}+\Gamma_x \cdot c_y\right]$$

Although the numerical results show an increase in amplitudes of the SVO, the experimental results do not. There are no significant differences. A summary of the results of the total investigation is given in Fig. 7. The reduced and 2D averaged endwall losses for the various bulb geometries from T106 (reference) to T106/1,2,3* and three are presented. In the presented investigation the endwall loss could be lowered by 47 percent from originally 4.5 percent to 2.39 percent for configuration T106/3.

It becomes clear that the optimal geometry is a nonsymmetric leading edge bulb which should have a pronounced suction side and a less extended pressure side. The measured distribution of the averaged exit flow angle deflection $\Delta\beta_2$ is presented in Fig. 8. It shows the typical pattern for a turbine cascade. Regions of decreased and increased deflection can be observed. They reflect the distortion due to the main channel vortex towards the suction side close to and towards the pressure side far from the endwalls. At a distance <10 mm the influence of the corner vortex is visible which weakens the local deflection enhancement of the channel vortex. A direct effect on this phenomenon from the various leading edge bulb configurations could not be established from these results.

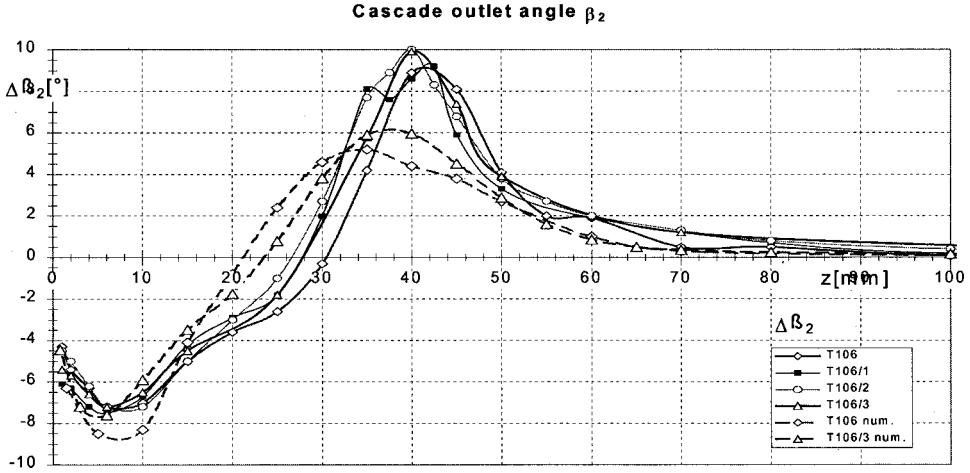

Fig. 8 Averaged exit flow angles vs. span/exp. and analytical results

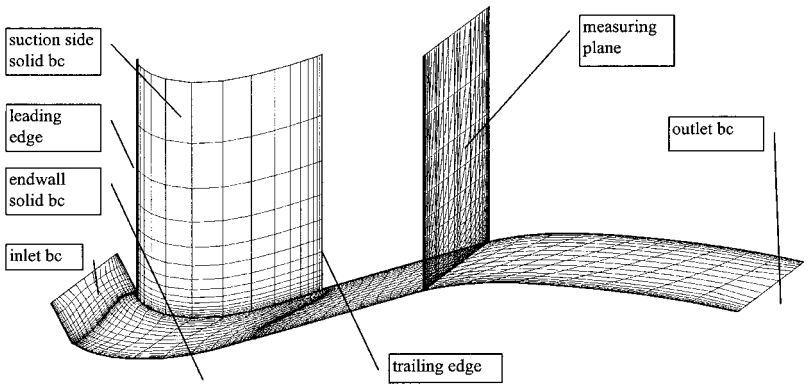

Fig. 9 Numerical domain and mesh geometry for T106 (coarsened)

Numerical Analysis/Set Up

The flowfield through the passage of a turbine cascade with high deflection shows large gradients of its flow properties pressure and velocity. Therefore a high resolution grid has to be taken for the numerical analysis. The numerical domain was built from a single block *H*-type grid with 1.62 million nodes ($257\times97\times65$) for the reference cascade T106 (Fig. 9).

This allows locally a fine resolution of the flowfield for the boundary layers and the trailing edge region with the embedded wake. The mesh was produced using the IGG gridgenerator. The subsequent numerical analysis was done with a commercial flow solver [2]. The Baldwin-Lomax turbulence model was used as it gave the most stable convergence behavior for this problem. The result of the measured total pressure distribution across the incoming boundary layer on the endwall was taken as the inlet-boundary condition (bc) of the numerical domain which was positioned according to that measurement. A further inlet bc was the measured flow angle field at the inlet. The exit plane of the numerical domain was positioned 4.3 x chord behind the cascade in order to develop the wake. A constant static pressure across this plane was taken as exit-bc averaged from the experiment at this position.

For cascade modification T106/3 with the leading edge bulb the grid was split into two blocks, both with an *H*-type mesh. The cylindrical part was enmeshed accordingly to the T106. The leading edge area was set up separately (Fig. 10) and embedded as the second block into the numerical domain.

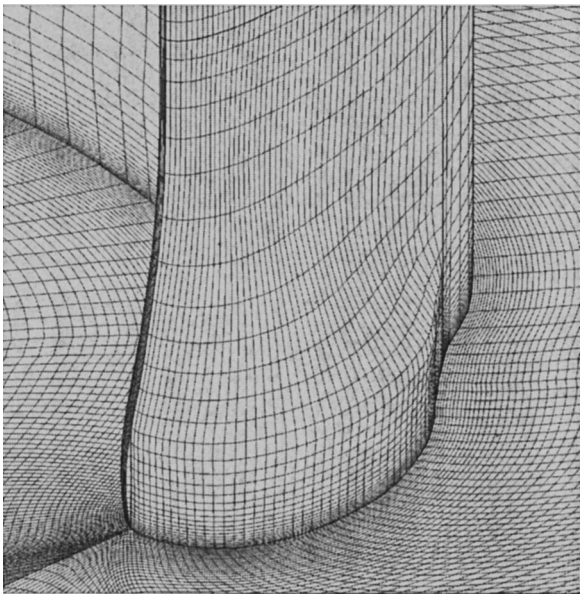

Fig. 10 Mesh geometry for T106/3 at the leading edge endwall

The calculation was considered to be converged sufficiently when inlet and exit massflows differed by less than 0.1 percent and when the RMS values were below 10^{-4}. Both cases converged reliably within approximately 500 steps for the reported conditions.

Numerical Analysis/Results

As a check for consistency the steady pressure distribution was compared with results from literature [5,7–9] for the midsection. The agreement was excellent. A comparison has to be done with identical bc, in physical meaning as well as in numerical meaning. The cfl number, time step algorithm, and other parameters like smoothing factors have to be equal. Nevertheless, a different convergence behavior is to be seen due to a different mesh around the leading edge. The used Baldwin Lomax turbulence model gives an underestimation of the endwall boundary layer growing, which is indeed a turbulent boundary layer. The profile boundary layer cannot be modeled exactly, because the pressure side layer is usually of laminar type as well as a front part of the suction side layer. Thus the profile loss is overestimated by approximately 1 percent. In interaction this lead to a good qualitative match but a slight difference in the absolute values.

All fluid mechanical properties are available after the solver run. The numerical data were now treated in the very same way as the raw experimental data in order to achieve comparable reduced losses. The numerical analysis of the experiment is presented for the reference cascade T106 and its modification T106/3 with the leading edge bulb. The comparison of the resulting distribution for the reduced losses is presented in Fig. 5*b* at a distance of 1 chord length in main flow direction behind the cascade. All results presented are in this measuring plane (Fig. 9). The distribution of losses shows the typical dog-bone pattern as already found in the experiments. Pattern geometry and the position of the loss maxima agree very well with experimental findings. The position of the wake behind the trailing edge and its gradients are in good agreement too.

Comparing the enhanced respectively weaker deflection close to the side walls (Fig. 8) with the experiment shows that position and order of magnitude agree very well. However, the exact value of the measured results are not met. This holds also for the analytical results in Fig. 4. The distribution of the mass-flow averaged endwall losses along the blade height in the representative measuring plane behind the cascade meets the overall pattern very well, but agrees quantitatively only in the order of magnitude with local differences up to 3 percent points. This is also true for the streamwise vorticity field, Fig. 6 [Eq. (5)]. The analytical results

meet the experiments quite well in terms of maxima and minima, Fig. 6*b*, whereas Weiss [5] found lower amplitudes.

The conclusion is that the absolute values of local properties compared to a very carefully designed experiment are not met exactly by analysis due to various possible reasons. However, the dominating physical effects of the secondary flow with a strong 3D component are obviously well presented in the applied procedure. Local improvements are expected with a better adaption and a finer resolution of the mesh in areas with very steep gradients. Eventually these have to be treated by separate blocks and an improved mesh design has to be applied.

Summary

The experiments were carried out with a turbine profile intended for highly loaded low pressure turbines but at low velocities ($Ma_2=0.2$). The suction side branch of the hs-vortex is intensified by a leading edge bulb in the endwall region. As it is counter-rotating to the secondary channel vortex it is able to move it away from the suction side profile boundary layer and to deform it. This mechanism results in a considerable reduction of the endwall losses by approximately 50 percent inspite of having a displacement thickness of 3 mm in the incoming boundary layer. Various modifications resulted in a basic guideline how to design a leading edge bulb to yield optimum results.

A possible reduction of secondary losses in subsonic cascades depends on deflection and velocity ratio. Variations of the inlet boundary layer and the incidence lead to different dimensions of a bulb. The influence of skewed boundary layers and conical endwalls has to be investigated in the future. The behavior of a compressor cascade is under investigation.

With the numerical simulation of the flow through the turbine cascade T106 and its modification T106/3 excellent qualitative and acceptable quantitative results were achieved in comparison with the reported experiments. The strong 3D effects in the flow that result from the leading edge bulb near the endwall can be reproduced.

Acknowledgments

The project underlying to this publication was supported by the German Bundesministerium für Bildung, Wissenschaft, Forschung und Technologie. This work has been carried out within the project group AG Turbo in cooperation with MTU Munich.

Nomenclature

L = blade height [m]
Ma = Mach number [-]
Re = Reynolds number [-]
Tu = degree of turbulence [-]
$a(s)$ = diff. of contour thickn. [m]
b = height of the bulb [m]
c = velocity [m/s]
l_p = profile length [m]
s = length in main flow direction [m]
SVO = streamwise vorticity [-]
t = pitch [m]
v = velocity ratio [-]
x = axial coordinate [m]
y = pitchwise coordinate [m]
z = spanwise coordinate [m]
Δ = difference
Γ = circulation [s^{-1}]
β = flow angle in the passage; stagger [°]
δ = spatial flow angle [°]
δ_1 = displacem. thickn. of b.l. [m]
ρ = density [kg/m^3]
ξ = loss coefficient [-]

Indices

0 = reference value
1 = upstream of cascade
2 = downstream of cascade
ax, x = axial direction
ew = endwall
ibl = incoming boundary layer
is = isentropic
l = local
M = midspan
n = net-value
p = profile
s = streamwise
y = circumferential direction
z = spanwise

References

[1] Sauer, H., and Wolf, H., 1997, ''Influencing the Secondary Flow in Turbine Cascades by the Modification of the Blade Leading Edge,'' 2, *European Conference on Turbomachinery*, Antwerpen.
[2] NUMECA International, 1997, ''Manual FINE/TURBO™, IGG, Euranus, CFView,'' Brussels.
[3] Sauer, H., and Wolf, H., 1993, ''The Influence of the Inlet Boundary Layers on the Secondary Losses of Turbine Stages,'' *AGARD-Conference Proceedings*, 537, Montreal, Canada, Oct.
[4] Römer, N., 1990, ''Untersuchungen zum Umschlagverhalten der Profilgrenzschicht an Verdichter- und Turbinengittern,'' Dissertation Univ. d. Bundeswehr München.
[5] Weiβ, P. A., 1993, ''Der Einfluss der Profilgeometrie auf die Entwicklung der Sekundärströmungen in Turbinengittern,'' Dissertation Univ. d. Bundeswehr München.
[6] Raab, I., Duden, A., and Fottner, L., 1998, ''Controlling the Secondary Flow in a Turbine Cascade by 3D Airfoil Design and Endwall Contouring,'' ASME Paper No. 98-GT-72.
[7] Hildebrandt, T., 1997, Weiterentwicklung von 3D Navier-Stokes-Strömungsrechenverfahran zur Anwendung in hochbelasteten Verdichter- und Turbinengittern, Dissertation Univ. d. Bundeswehr München.
[8] Mobarak, A., 1989, ''Study of Various Factors Affecting Secondary Loss Vortices Downstream a Straight Turbine Cascade,'' ASME Paper No. 89-GT-12.
[9] Gotthardt, H., 1983, ''Theoretische und experimentelle Untersuchungen an ebenen Turbinengittern mit Pfeilung und V-Stellung,'' Dissertation TU Braunschweig.

An Experimental Study of the Effect of Wake Passing on Turbine Blade Film Cooling

James D. Heidmann

Barbara L. Lucci

NASA Glenn Research Center,
Cleveland, OH

Eli Reshotko

Case Western Reserve University,
Department of Mechanical
and Aerospace Engineering,
Cleveland, OH

The effect of wake passing on the showerhead film cooling performance of a turbine blade has been investigated experimentally. The experiments were performed in an annular turbine cascade with an upstream rotating row of cylindrical rods. Nickel thin-film gauges were used to determine local film effectiveness and Nusselt number values for various injectants, blowing ratios, and Strouhal numbers. Results indicated a reduction in film effectiveness with increasing Strouhal number, as well as the expected increase in film effectiveness with blowing ratio. An equation was developed to correlate the span-average film effectiveness data. The primary effect of wake unsteadiness was found to be correlated by a streamwise-constant decrement of 0.094St. Steady computations were found to be in excellent agreement with experimental Nusselt numbers, but to overpredict experimental film effectiveness values. This is likely due to the inability to match actual hole exit velocity profiles and the absence of a credible turbulence model for film cooling.
[DOI: 10.1115/1.1354621]

Introduction

As a result of efforts to improve turbine engine performance, turbine inlet temperatures have increased dramatically over the past 50 years. Current turbine inlet temperatures are approaching 2000 K, while the best available metallic turbine materials can withstand a maximum temperature of only about 1300 K. When internal cooling alone is inadequate, film cooling must be employed. In film cooling, the coolant air is discharged through small holes in the turbine surface to form a protective film between the turbine blade and the hot combustor discharge gas.

The flow in turbomachinery blade rows is inherently unsteady due to the relative motion of adjacent blade rows. Wake passing from upstream blade rows causes periodic fluctuations in the magnitude and relative direction of the flow velocity in downstream blade rows. Precisely modeling a turbomachinery flow field thus requires inclusion of the time-varying quantities. However, due to the complexity of the unsteady flow field, the design of turbine film cooling schemes has tended to rely on steady databases.

Because of its importance in turbine design, there has been much investigation into the behavior of turbine film cooling flows. Goldstein [1] reviewed the early research in the film cooling arena. This review consolidated flat plate experiments of various hole geometries and blowing parameters, and summarized analytical solutions for two-dimensional slot injection. The experimental studies typically had long film holes (L/d greater than 10.0). More recent steady film cooling research is summarized by Heidmann [2] and by Heidmann et al. [3]. The more recent studies generally consider L/d values more typical of turbine blades (between 2.0 and 4.0), shaped holes, compound-angle holes, and actual blade profiles.

Relatively less work has been done on the impact of unsteadiness on film cooling in a turbine blade. Rigby et al. [4] used a rotating wheel wake generator with cylindrical bars to model inlet guide vane wakes and shock waves under transonic flow conditions. The test blade was film cooled on both the suction and pressure sides. The main effect of the wake passing was a reduction in effectiveness caused by enhanced film mixing, and the shock passing effect was found to produce large fluctuations in the heat transfer rate. Ou et al. [5] and Mehendale et al. [6] used an experimental approach similar to Rigby et al. [4], except with a different blade profile, subsonic flow, and including showerhead cooling. Both air and CO_2 injection were employed for different density ratios. Ou et al. [5] found that increasing wake passing frequency increases local Nusselt numbers for all blowing ratios, but this effect is reduced at higher blowing ratios. Mehendale et al. [6] found that an increase in wake passing frequency causes a decrease in film effectiveness over most of the blade surface for all cases considered. Funazaki et al. [7] used a rotating wheel wake generator with cylindrical bars upstream of a showerhead-cooled blunt body. Heated air was used as the injectant. Increasing wake passing frequency was found to reduce film effectiveness, especially at lower blowing ratios where the influence of the wake on the low momentum film is strongest. The wake effect was reduced as free-stream turbulence increased.

Three more recent papers by a group at Texas A&M University have studied the effect of unsteady wake on film cooling performance. Du et al. [8] measured heat transfer and film effectiveness for air and CO_2 injection from pressure-side, suction-side, and showerhead holes with and without bar wakes. It was found that the presence of film injection causes earlier boundary layer transition on the suction surface. Heat transfer coefficients were increased slightly with wake passing, but film effectiveness values were greatly reduced. Du et al. [9] performed a similar experiment with the addition of trailing edge coolant ejection from the wake-producing bars. The addition of wake coolant was found to have a relatively small effect on downstream blade heat transfer coefficient, but to appreciably reduce leading edge film effectiveness below the wake case with no coolant ejection. Teng et al. [10] used transient liquid crystal and cold-wire techniques to measure the film effectiveness and coolant jet temperature profiles downstream of a single row of holes on the suction side of a turbine blade. Wakes were again produced by a spoke-wheel consisting of round bars. The film effectiveness results showed the expected reduction in film effectiveness with wakes. The coolant jet temperature profiles showed the effect of wake passing in enhancing mixing of the jets and thereby elucidated the mechanism of film effectiveness reduction. An additional study by Seo et al. [11] investigated heat transfer and film effectiveness on a film cooled flat plate with bulk flow pulsations such as might be caused by wake passing or potential flow fluctuations. One interesting observation from this study was that the pulsations have a

Contributed by the International Gas Turbine Institute and presented at the 42nd International Gas Turbine and Aeroengine Congress and Exposition, Orlando, Florida, June 2–5, 1997. Manuscript received at ASME Headquarters February 1997. Paper No. 97-GT-255. Associate Editor: H. A. Kidd.

greater effect on film effectiveness for small L/d and low blowing ratio, perhaps due to the greater ability of the pulsations to affect the instantaneous blowing rate for those cases.

Another set of recent studies acknowledges the importance of freestream turbulence on film cooling performance. Ekkad et al. [12], Ames [13,14], and Kohli and Bogard [15] performed film cooling studies with maximum freestream turbulence intensities of 7.1, 12, and 20 percent, respectively. In general, it was found that the effect of elevated freestream turbulence on film cooling performance is similar to that of unsteady wake passing in the time-average: i.e., an appreciable reduction in film effectiveness and a small increase in heat transfer coefficient.

Several studies have investigated film cooling performance on a turbine blade in an actual rotating turbine stage environment. Dring et al. [16] studied film cooling performance on a large scale model of a high pressure turbine first stage. Coolant was injected from a single hole on both the pressure and suction sides of the rotor blade. Density ratios from 1.0 to 4.0 were investigated and flow visualization studies showed radial migration of the coolant, especially on the pressure side. The migration was found to be relatively insensitive to the coolant properties. Film effectiveness profiles were measured downstream of the holes. The suction surface profiles were found to correlate well with flat plate data, while the pressure surface film effectiveness was significantly reduced. Takeishi et al. [17] also measured film cooling effectiveness for a rotating turbine blade. In this case, the blade had a realistic cooling geometry with showerhead, pressure, and suction surface rows of cooling holes. The results of Dring et al. [16] were corroborated, as the pressure surface film effectiveness was found to decrease relative to cascade tests due to the radial flow and concave curvature. The suction surface film effectiveness was in good agreement with the stationary blade tests except far downstream where enhanced mixing reduced the film effectiveness. Abhari and Epstein [18] used a short duration turbine test facility to again study a film-cooled rotating blade in a turbine stage environment. The cooling arrangement consisted of three rows of coolant holes on the pressure surface and two on the suction surface, but no showerhead cooling. Unlike Dring et al. [16] and Takeishi et al. [17], this study considered transonic flow. This introduced unsteady shock passing in addition to wake passing as unsteady effects. For these tests, the suction surface had a 12 percent decrease in heat transfer, while the pressure surface had a 5 percent increase relative to cascade tests. The unsteady effects were attributed to coolant flow rate changes caused primarily by shock passing pressure fluctuations.

Although not directly related to film cooling, many recent studies have investigated the highly complicated effect of unsteady wake passing on boundary layer transition. Funazaki et al. [19,20], Chakka and Schobeiri [21], and Kim and Crawford [22] have studied wake-induced transition on flat and curved walls. Intermittency-type models are used to account for the fraction of time during which the local boundary layer is turbulent. On a film-cooled surface, Ames [13] found that the effect of film injection on a laminar boundary layer is much greater than the additional effect of high freestream turbulence. This indicates that wake-induced boundary layer transition may be a less important consideration for a film-cooled surface.

Unsteady numerical simulations for an entire film-cooled turbine stage are scarce due to the large computational time associated with capturing both the small time scales of blade passing and the small length scales of film cooling and heat transfer. However, Dorney and Davis [23] showed that such a simulation could be achieved using a time-accurate Navier-Stokes solver. The computational constraints limited the simulation to only two grid points per film hole, so local effects due to hole exit profile could not be modeled.

Although recent research has begun to focus on the unsteady flow environment, the majority of research on film coolant flow has considered the turbine free stream flow to be steady. Studies of film cooled turbine stages include unsteadiness, but lack the ability to vary the unsteady parameter. Cylindrical wake experiments solve this problem, but have not sought to resolve spanwise and time variations to isolate the important physical phenomena associated with film coolant flow. The present study aims to investigate the effect of flow unsteadiness on turbine film cooling in a more detailed and fundamental manner. Showerheadcooling is chosen because of the larger temporal fluctuations in static pressure in the leading edge region and the effect of incidence on showerhead cooling behavior.

Experimental Apparatus and Procedure

The experiment was conducted in the NASA Glenn Rotor-Wake Heat Transfer Rig. This annular-flow open-circuit wind tunnel was described in detail by Simoneau et al. [24]. The facility has a rotor upstream of the test section (Fig. 1) which is capable of rotating at speeds up to 7000 rpm. The rotor has 24 equally spaced 3.2 mm diameter cylindrical rods at 15 deg intervals. O'Brien and Capp [25] described the two-component phase-average turbulence statistics downstream of the rods. Cylinder wakes cannot model the boundary layer and loading of an upstream blade. However, the velocity deficit, turbulence production, and rotative speed are all modeled to some degree. Downstream of the rotor is an annular turbine cascade consisting of 23 turbine blades with 67 deg of turning. The blade profile is shown in Fig. 2. Since the nominal inlet flow direction is axial, blades in the cascade have an inlet angle of 0 deg for optimum incidence with the freestream direction. As a result of this, the cylinder wakes strike the blade at an angle to the leading edge, unlike in the engine condition where the wakes are aligned with the freestream direction and strike the blade aligned with the leading edge. However, this effect is considered secondary to the periodic disturbance effect. All tests were conducted at a cascade inlet Mach number of 0.27. This corresponds to a blade Reynolds number of about 4.0×10^5 based on blade chord.

A secondary flow supply system was developed to allow injection of film cooling flow through the test blade. This system was designed to supply both air and CO_2 to the test blade. CO_2 has a molecular weight of 44.01 compared to 28.97 for air, so at the same pressure and temperature, it has a density 1.519 times that of air. This allows more realistic density ratios to be achieved in the

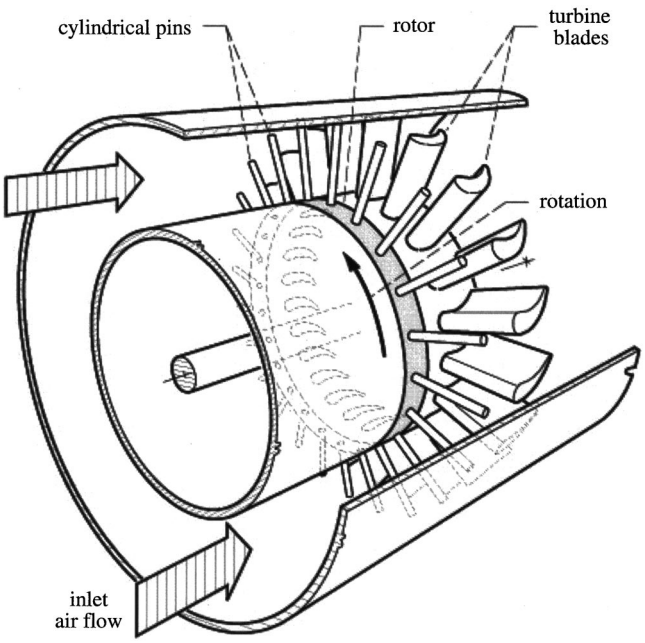

Fig. 1 Rotor-wake facility schematic

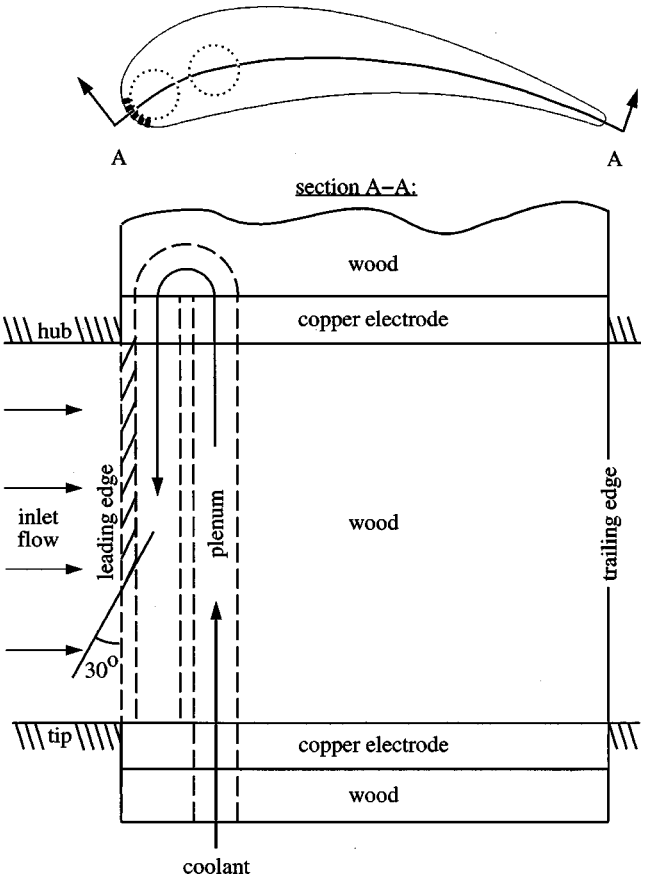

Fig. 2 Blade geometry

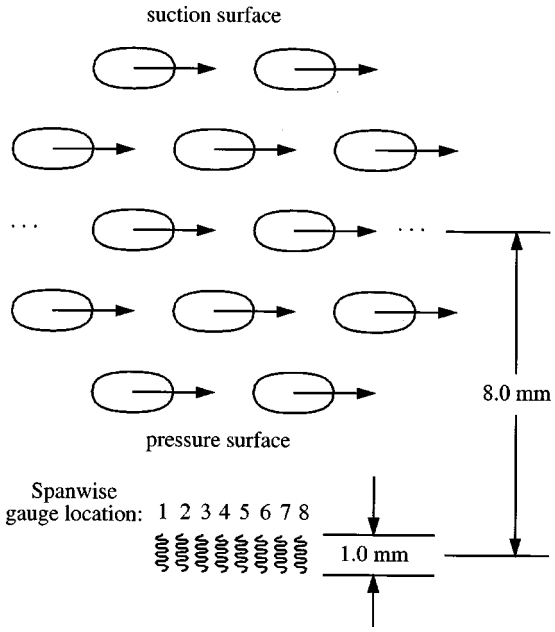

Fig. 3 Film hole and gauge arrangement

experiment. In order to measure thermal film effectiveness values, the secondary flow must be at a different temperature than the free-stream. To heat the secondary flow in the test facility, an electrical resistance heater was employed. For air and CO_2, this heater provided secondary flow temperature rises of about 35 and 30 K, respectively, owing to differences in specific heat for the two gases. A thermocouple and static tap measured the secondary flow temperature and pressure, respectively, centered in an upstream plenum.

The test blade was assembled in several parts, as shown in Fig. 2. The bulk of the blade is wood, which was used because of its low thermal conductivity to reduce thermal conduction in the blade. In order to allow determination of heat transfer coefficients on the blade surface, a heat source is required. A 0.025 mm thick sheet of Inconel foil was used as a resistive heater. A rectangular sheet of the foil was used to cover both the suction and pressure surfaces of the blade, leaving the showerhead region exposed. Two copper electrodes were machined having the same profile as the blade, and a thickness of 6.3 mm. These electrodes were glued into the test blade. The foil was attached to both electrodes using a continuous line of very small spot welds to assure a uniform distribution of heat flux over the blade surface. A circuit current of 36 Amperes was used in the experiment. This current was determined to be sufficient to generate a nominal temperature increase of 10 K on the blade surface under standard flow conditions.

The secondary flow passage as shown in Fig. 2 is a 6.3 mm diameter hole which extends the length of the rig annulus to the inner diameter, makes a 180 deg turn, and extends back toward the outer diameter. The film cooling hole pattern is presented in Fig. 3, and consists of five staggered rows of 1.0 mm diameter showerhead film holes. The holes are angled at 30 deg to the surface in the spanwise direction and are oriented toward the outer diameter. The holes are 3.5 mm long, resulting in a length-to-diameter ratio (L/d) of 3.5. The pitch-to-diameter ratio in both the spanwise and streamwise directions is 4.0. There are 17 holes in rows 1, 3, 5, and 16 holes in rows 2 and 4. In order to establish a more periodic flow in the midspan region of the blade, holes 11 through 17 in all rows were permanently covered with smooth tape. Computations by Heidmann [26] using the viscous flow solver $rvc3d$ (Chima and Yokota [27]) were used to place the holes such that the flow from the center row would evenly split between the suction and pressure sides.

The test blade was instrumented with an array of 72 nickel thin-film gauges. The gauges were manufactured by Tao Systems, Inc., and consist of serpentine nickel sensing elements with copper leads. To allow spanwise resolution of the temperature profile behind the film cooling hole pattern, eight gauges were placed near midspan at each of nine streamwise locations, five on the suction side and four on the pressure side. These eight gauges were situated to completely span one unit cell of the hole pattern as shown in Fig. 3. The streamwise length of each gauge is 1.0 mm. The first row on each surface is 8.0 mm downstream of the center row of film holes, and the subsequent rows are spaced at 13.5 mm intervals. Pressure surface distances are considered positive. The Cortez III Service Corporation calibrated the thin-film gauges. The steady data recording system reads the gauge signals once per second for twenty seconds and records the average value of all data. The amplified AC component of the gauge signals are recorded on the Masscomp data system at a frequency necessary to record about 50 time steps per wake passing. The signals are recorded for a period of about 1200 wake passings. The unsteady data are then phase-averaged.

The experiment was conducted for blowing ratios of 0.5 and 1.0. The definition of blowing ratio used to determine the required injectant velocity is

$$M = \frac{\rho_c V_c}{\rho_\infty V_\infty} \tag{1}$$

where c indicates injectant conditions and ∞ indicates freestream conditions. The ratio of injectant to freestream density for air and CO_2 was 0.90 and 1.38, respectively. The experiment was conducted for Strouhal numbers of 0.167, 0.250, 0.500, and 0.600. The definition of Strouhal number used to determine the required rotor speed is

$$\mathrm{St} = \frac{2\pi NDn}{60V_\infty} \tag{2}$$

where N is the rotor speed in rpm, D is the cylindrical rod diameter, n is the number of rods in the rotor, and $V\infty$ is the cascade inlet axial velocity. Baseline steady cases for comparison to the rotating data were established by two different methods. In the first method, eight test cases were investigated with the rotor fixed in eight equispaced positions relative to the test blade. The results from these cases were averaged for comparison to the rotating cases. An alternative baseline case was established with no upstream rotor.

The definition of film effectiveness for compressible flow is

$$\eta = \frac{T_f - T_r}{T_c - T_r} \tag{3}$$

where T_f is the film temperature, T_r is the recovery temperature, and T_c is the injectant stagnation temperature. Film temperatures were measured in the presence of film injection under an adiabatic wall condition. Recovery temperatures were determined from tests with thin tape over the film holes without heating the blade. Radiation errors were estimated to be approximately offset by backside heating due to the warm plenum. The definition of heat transfer coefficient is

$$h = \frac{q''}{T_w - T_f} \tag{4}$$

where T_f is the film temperature as measured in Eq. (3) and T_w is the wall temperature with film cooling and a local heat flux of q''. The errors in q'' due to radiation and conduction are now complementary, but their magnitudes are small since only differences between the adiabatic wall and heated wall cases are important. The maximum error in q'' due to these effects is approximately 1.0 percent, which is well within the experimental accuracy. The Nusselt number is defined as

$$\mathrm{Nu} = \frac{hc}{k} \tag{5}$$

where c is the blade chord length (63.5 mm), and k is the thermal conductivity of the film. For air injection, a constant thermal conductivity is used. For CO_2 injection, a mixture of gases is present at the wall, and the procedure of Bird et al. [28] is used to estimate the thermal conductivity at the wall.

Experimental Results

Figure 4 shows the steady span-average film-effectiveness versus streamwise distance for the four blowing conditions. The symbols indicate experimental data and the curves represent the correlating equation to be discussed in the following section. The no rotor case is with the rotor removed and no wakes present. The St=0, ave. case is the average of the eight equispaced stationary rotor test cases. Each case has an incrementally varying wake location relative to the blade, spanning one circumferential pitch of the rotor rods. Although the Strouhal number is thus zero for this case, the effect of the wake is apparent as a reduction in film effectiveness relative to the no rotor case. All four plots indicate a general reduction in film effectiveness as the level of unsteadiness increases. This reduction is nearly monotonic with increasing Strouhal number, and may be explained by the increased mixing which dissipates the film layer. The reductions in film effectiveness are most pronounced on the blade suction surface. This phenomenon is explained by the swirl caused by the rotor. For the no rotor and stationary rotor cases, no swirl is imparted to the flow by the rotor, and the flow enters the cascade with zero swirl. This condition establishes a particular attachment line on the blade, and determines the split of coolant between the suction and pressure sides of the blade. As the Strouhal number increases, the wake-producing rods impart swirl to the freestream toward the pressure side of the blade. This moves the attachment line toward the suction side, and skews the coolant flow toward the pressure side of the blade. This in turn increases the film effectiveness on the pressure side compared to the suction side. However, this effect is smaller than the reduction due to increased mixing, so the overall effect of increased Strouhal number is to reduce film effectiveness on both the suction and pressure sides of the blade. For both

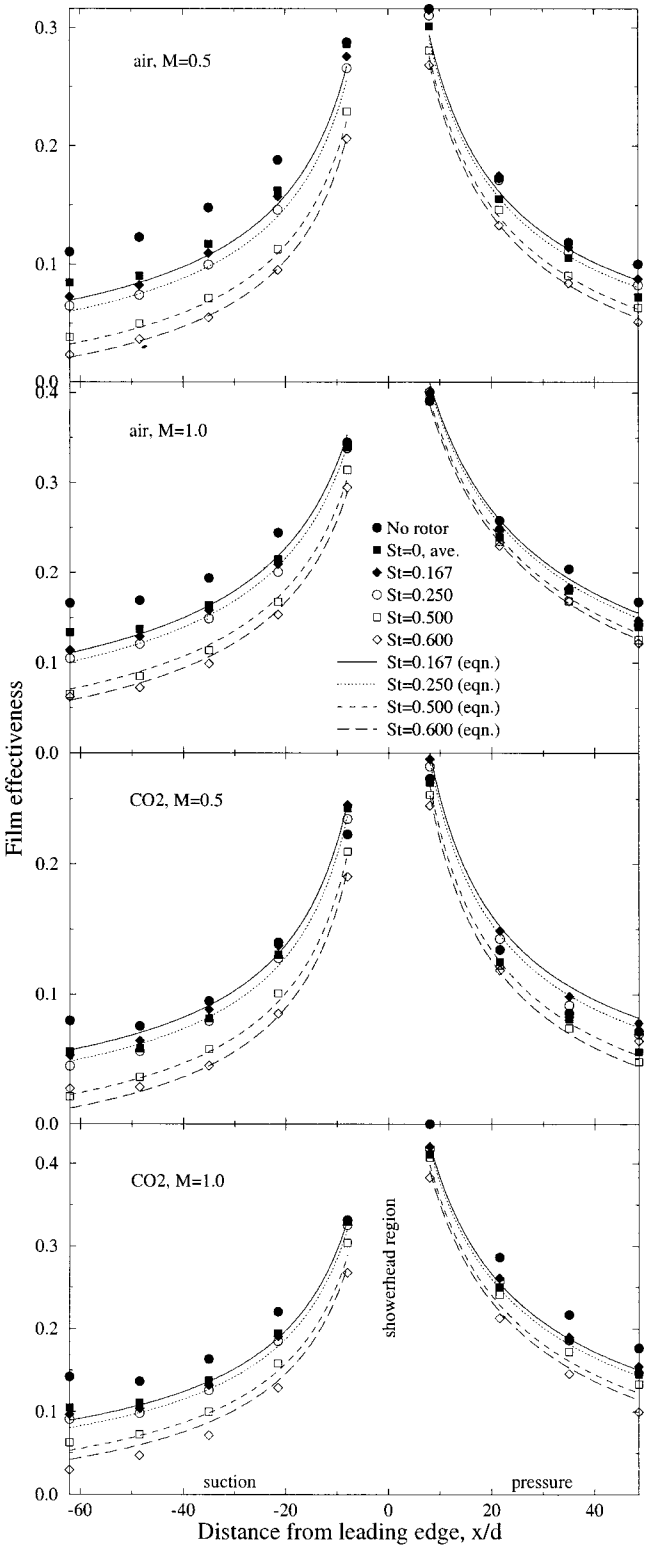

Fig. 4 Time- and span-average film effectiveness

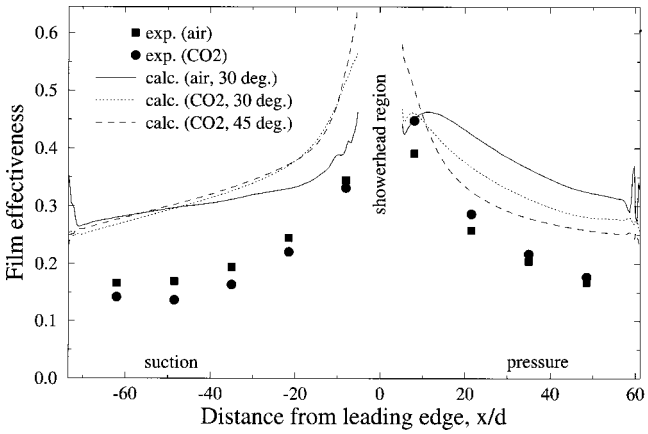

Fig. 5 Steady span-average film effectiveness, $M=1.0$

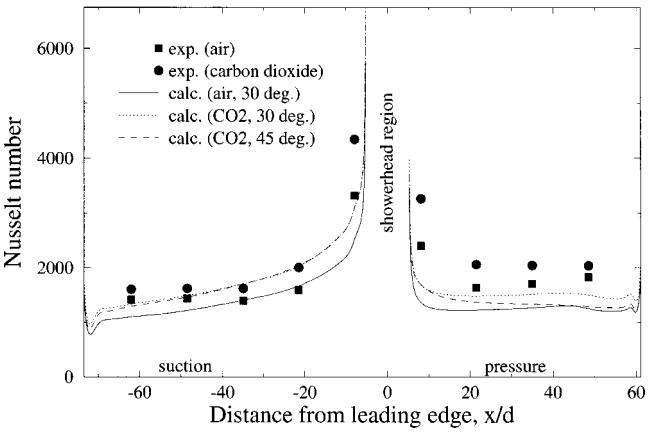

Fig. 6 Steady span-average Nusselt number, $M=1.0$

injectants, the $M=1.0$ case provides higher film effectiveness than the $M=0.5$ case, indicating that the film remains attached to the blade surface at $M=1.0$. This is due to the relatively shallow angle of injection and the very nature of showerhead cooling. The freestream velocity is nearly normal to the blade surface, which tends to force the injectant to remain attached. Nusselt numbers are found to remain nearly constant under changes in Stouhal number.

Figure 5 presents the $M=1.0$ no rotor experimental film effectiveness data in comparison with calculations performed using the viscous flow solver $rvc3d$ with no upstream wake. Heidmann [26] describes the computational method in detail. The present computations were performed using a $305\times90\times20$ grid with a y^+ value of less than 1.0 at the first grid point from the wall and with the Baldwin-Lomax turbulence model. Three different injectant conditions were computed: CO_2 injection at an angle of 30 deg, CO_2 injection at 45 deg, and air injection at 30 deg. All cases are for $M=1.0$. Since the code cannot model multiple species, CO_2 injection was modeled using a reduced injection temperature to match the experimental density ratio. All three computations overpredict the experimental film effectiveness, particularly on the downstream suction surface. Since the blowing ratio and hole area are matched, this must be due to an underprediction of film mixing by the computation. This may result from not resolving the flow inside the film holes as well as the lack of an accurate turbulence model for film cooling. The injectant temperature has a moderate effect on the film effectiveness. Decreasing the injectant temperature to model CO_2 decreases the film effectiveness on the pressure surface and increases it on the near suction surface. This is in contrast to the trend exhibited by the experimental data, where the air performs better on the suction surface but worse on the pressure surface. This may be due to species differences that the computer code is unable to model. The effect of increasing the injection angle from 30 deg to 45 deg is negligible on the suction surface and causes a slight decrease in film effectiveness on the pressure surface. However, very near the showerhead region the more normal injection performs markedly better. On the pressure surface, the 45 deg injection provides a better film to an x/d value of about 10, at which point the enhanced mixing caused by the more normal injection predominates and lowers the effectiveness.

Figure 6 shows the Nusselt number distributions for the same conditions as Fig. 5. The computations are in very good agreement with the experimental data, particularly on the suction surface. The effect of changing the hole angle is small, while CO_2 injection produces higher Nusselt numbers than air injection by a nearly constant offset of about 350. This trend is remarkably consistent with the experimental data, which also shows increased Nusselt numbers for CO_2 injection. These increases are likely due to density ratio differences rather than species differences since the code cannot model species differences.

Span-resolved data were recorded for all wake and blowing cases. Except for the $x/d=-8.0$ location, the film effectiveness distribution is nearly uniform. At $x/d=-8.0$ (Fig. 7), a large spanwise variation in film effectiveness is found. Spanwise gauge location 1 is repeated as location 9 to complete one spanwise unit cell. Data points are only shown for working gauges. The trends are consistent for all Strouhal number cases. The largest spanwise variations occur when the rotor is removed, due to the absence of wake-induced mixing of the film. As the Strouhal number is increased, not only does the span-average film effectiveness decrease, but the spanwise variations decrease as well, indicating that the higher wake passing speeds provide more spanwise mixing of the film. Spanwise locations 2 and 3 comprise the lowest film effectiveness region, and thus correspond to the gap between two adjacent film jets. It appears that the presence of a rotor wake actually increases the film effectiveness slightly in this region. This increase offsets the decrease in the high film effectiveness region (spanwise locations 5 through 8), so the span-average film effectiveness is not degraded by the presence of a rotor wake or by increasing Strouhal number up to about $St=0.250$. This helps explain the behavior seen on the suction side in Fig. 4, where the presence of a rotor has a greater effect at larger distances from the film holes. Near the film holes, the wake acts to effectively spread the film jet, reducing spanwise gradients but not the span-average film effectiveness since the gaps between the film jets are filled. Farther downstream, the effect of this spanwise mixing of the jet begins to reduce the span-average film effectiveness since the low

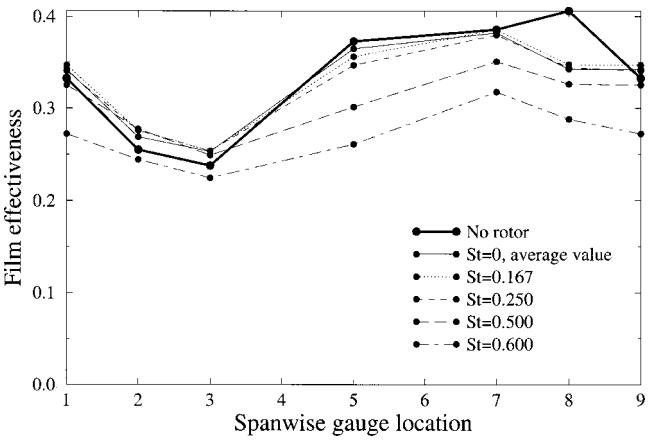

Fig. 7 Local film effectiveness, CO_2, $M=1.0$, $x/d=-8.0$

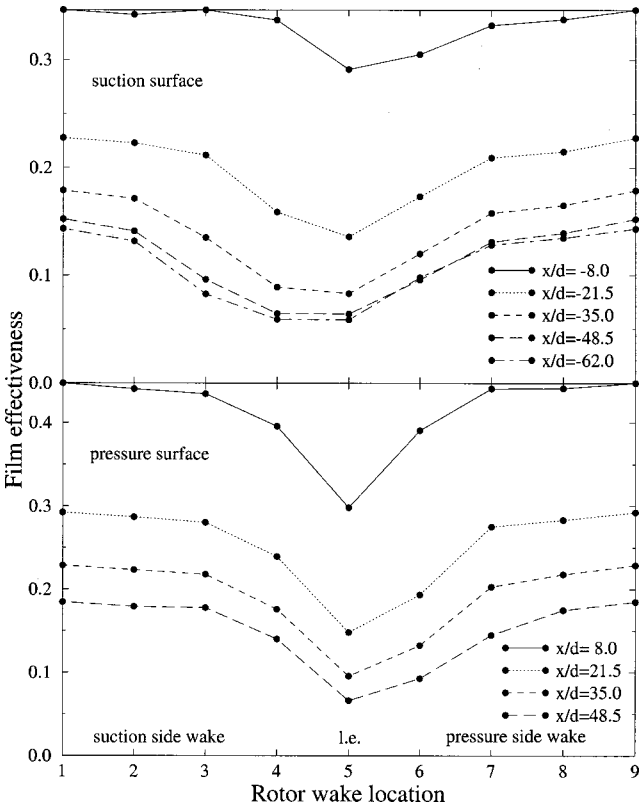

Fig. 8 Span-average film effectiveness, CO_2, $M=1.0$, St=0

film effectiveness gaps are already filled, and no additional benefit results from spanwise mixing. Nusselt number results indicate very little spanwise variation, even near the leading edge.

The gauges showed some time variations of film effectiveness, but these were random and lacked repeatability. The attempts to extract meaningful unsteady results are documented in detail by Heidmann [2]. Conduction effects in the substrate were the primary cause of this problem. Because of these difficulties, it was decided to scrutinize the results from the stationary wake data that was obtained as a limiting case of zero Strouhal number. Figure 8 shows the span-average steady film effectiveness variations with rotor wake location for the suction and pressure surfaces of the blade. Wake location 5 is for the wake aligned with the blade leading edge. Wake location 1 is the same as location 9, and is for the wake at mid-passage. These plots represent the limiting case of the rotating tests at zero rotational speed.

The suction surface results show a highly repeatable distribution for all streamwise locations. With the wake impinging on the blade (wake location 5), the film effectiveness is reduced by about 0.05 at $x/d=-8.0$ and almost 0.10 at the downstream locations. This result is expected due to the enhanced film mixing caused by the increased turbulence in the wake. It is surprising that the absolute reductions in film effectiveness are greater at the downstream locations, because the levels of film effectiveness are lower at these locations. However, this supports the explanation given for the behavior in Fig. 7. The impingement of the wake on the leading edge increases spanwise mixing of the film, but this action is actually favorable in the low effectiveness gaps between jets, which at $x/d=-8.0$ partially offsets the detrimental dissipation of the film. The pressure surface results indicate an even greater reduction in film effectiveness due to wake impingement than on the suction surface. Reductions of about 0.15 at $x/d=8.0$ and at least 0.10 downstream are noted. Both the suction and pressure surface data show an asymmetry of the film effectiveness profile. For both sides of the blade, the film effectiveness is reduced more for a wake location nearer that side, as expected. Thus the suction surface film effectiveness is reduced more at wake locations 3 and 4 than at wake locations 6 and 7, while the opposite is true on the pressure surface. The only streamwise location that indicates an effect of wake location on Nusselt number, is at $x/d=8.0$, which is the pressure surface leading edge. The wake exhibits a velocity defect that decreases the Nusselt number by about 20 percent because of lower velocity gradients at the wall.

Wake-Affected Film Cooling Model

Analytical film effectiveness correlations for slot injection are given by Goldstein [1], and are typically of the form:

$$\eta=\frac{C_1}{1.0+C_2\left(\frac{x}{MS}\right)^{C_3}} \tag{6}$$

where C_1, C_2, and C_3 are constants, x is the streamwise distance from the slot, M is the blowing ratio, and S is the slot width. For film cooling on a blade with discrete holes, an analytical description of the boundary layer is usually not available. For this case, empirical correlations are often used, although their applicability is limited to the geometry and conditions from which they were derived. Using the basic form given for slot injection, others have produced correlations of experimental data. For example, Takeishi et al. [29] have given an empirical correlation for film effectiveness on a low aspect ratio turbine nozzle with suction and pressure side circular hole film cooling. S now becomes the effective slot width, or the width of a slot having the same flow area as the hole pattern. For n rows of circular holes, $S=n\pi d^2/4p$, where p is the hole spanwise pitch.

The form of the correlation that proved to provide the best agreement with the experimental data for the present experiment is

$$\eta=\frac{C_1}{1.0+\left(\frac{C_2x}{MS(1.0\pm C_3M\pm C_4\mathrm{St})}\right)^{C_5\pm C_6}}C_7\mathrm{St} \tag{7}$$

Positive signs are taken for the pressure surface and negative for the suction surface. S is taken to be half of the effective slot width for all rows of holes. The form of Eq. (7) follows that of Eq. (6), but supplements it with additional terms to account specifically for suction/pressure surface and Strouhal number differences.

The primary effect of the wake unsteadiness on the film effectiveness is to reduce it as the rotational speed or Strouhal number increases. This is evident in Fig. 4. In addition, the change in film effectiveness for a given change in Strouhal number is fairly constant with downstream distance x on either the suction or pressure surface. The $-C_7\mathrm{St}$ term is used to model this effect. This term provides excellent agreement over the range of experimental data. In addition, the simplicity of this term allows for ease of interpretation. C_7 is the slope of the film effectiveness versus Strouhal number trend.

The Strouhal number effect, although nearly constant with x, differs on the suction and pressure surfaces due to the shifting of the attachment line. This phenomenon is addressed in the correlation through the $C_4\mathrm{St}$ term. This term arises from an assumption that the changes in injectant split are linear with Strouhal number. The quantity MS is an effective flow rate and is modified in the correlation to be $MS(1.0\pm C_3M\pm C_4\mathrm{St})$. This modification maintains the total flow rate on both sides of the blade at $2MS$.

The term C_3M arises from the observation that the difference between the pressure and suction surface film effectiveness is greater for $M=1.0$ than for $M=0.5$ for both air and CO_2 injection. The physical interpretation of the C_3M term is that the injectant split depends upon the blowing ratio. At low blowing ratios, the momentum of the injectant is low, and the split between pressure and suction surfaces depends primarily on the geometric location of the film holes. At high blowing ratios, the injectant

Table 1 Correlation coefficients for Eq. (7)

	Air	CO_2
C_1	0.761	0.948
C_2	0.054	0.094
C_3	0.139	0.241
C_4	0.286	0.144
C_5	0.792	0.762
C_6	0.033	0.014
C_7	0.093	0.095

penetrates more deeply into the freestream, and the split may be influenced by the angle of injection and freestream flow behavior. For the present experiment, the pressure surface is favored for higher blowing ratios, but this may be due to geometric considerations unique to this configuration.

It is not clear if the skewing of the coolant flow from suction to pressure side with increasing Strouhal number will actually occur for a true turbine stage. A turbine stage is designed for a specific rotational speed, which gives a desired attachment location. To attain a higher Strouhal number, the rotational speed must be increased, which would require a different design. Thus in an engine, a higher Strouhal number would not impart any additional swirl to the flow than for the lower Strouhal number with its respective design. However, the skewing seems plausible for increasing rotational for a fixed design, since the increased rotational speed would cause the stage to run off-design, moving the attachment line on the rotor blades as described for the present study.

The C_6 term represents the fact that the film effectiveness was found to decay more rapidly in the streamwise direction on the pressure surface than on the suction surface. This finding agrees with the analysis of Ito et al. [30], which predicts better film cooling performance on a convex wall than on a concave wall for streamwise momentum flux ratios less than 1.0. For the showerhead cooling of the present experiment, the injectant exits the hole with zero streamwise momentum, resulting in a streamwise momentum ratio of zero for all cases. Thus the convex (suction) surface should perform better than the concave (pressure) surface to the same degree for all blowing cases. The experimental data agrees with this prediction. Additionally, the analysis of Ito et al. [30] pertains to the performance of a fluid element once it has established a trajectory on either side of the blade. Because of this the C_6 term should be independent of blowing ratio for showerhead cooling, and is incorporated as such in the exponent.

The application of a least-squares algorithm on the experimental data produced the coefficients for Eq. (7) shown in Table I. The root mean square average of the error in film effectiveness using these coefficients is about 0.0068 for air and 0.0074 for CO_2.

In terms of their effect on the film effectiveness, C_5 and C_7 remain fairly constant between injectants. In particular, the magnitude of the Strouhal number effect (C_7) is almost the same for both injectants, having an average value near 0.094 for both air and CO_2. This may indicate a relative insensitivity of wake passing effects to injectant density ratio. The agreement between C_5 for air and CO_2 indicates that the film effectiveness decay rate is similar for both cases. The fact that the values are below 1.0 implies a more gradual decay of film effectiveness with downstream distance than for the cases of Takeishi et al. [29], which gave values of 1.0 and 1.6 for a nonshowerhead film cooled blade. This is to be expected for showerhead cooling, since the injectant has less opportunity to separate from the blade than does suction and pressure surface injection. C_3, C_4, and C_6 are the three coefficients associated with differences between suction and pressure surface film effectiveness values. All of these coefficients have the same sign for air and CO_2, which indicates that the trend between suction and pressure surface data is consistent for the two injectants. The magnitudes of these coefficients differ, however. It should be noted that the specific heat of CO_2 is 14 percent lower than that of air. As indicated by Mehendale et al. [6], this causes the measured film effectiveness values for CO_2 to be conservative by up to 14 percent, depending on the concentration of CO_2 at the wall. However, due to the generally small concentrations, this error is estimated to result in less than a 3 percent underprediction of the actual value over most of the blade.

Figure 4 shows comparisons between the experimental data and correlations for air at blowing ratios of 0.5 and 1.0 and CO_2 at blowing ratios of 0.5 and 1.0, respectively. It can be seen that the correlation is in excellent agreement with the experimental data for air injection at both blowing ratios. The change in film effectiveness with increasing Strouhal number is captured quite well. This indicates that the assumption of linear decay of film effectiveness with Strouhal number is proper. In general, the correlation agrees well with the CO_2 data. The magnitude of the Strouhal number effect is underpredicted for a blowing ratio of 1.0, particularly on the suction surface, and is overpredicted for a blowing ratio of 0.5, particularly on the pressure surface. This indicates that the correlation might properly require a blowing ratio influence on the C_7St term. However, in view of the excellent correlation achieved with the relatively simple correlation equation, the recommended correlation stands.

Mehendale et al. [6] have presented film effectiveness values for St=0.1 and 0.3. Their experiment was conducted for a more highly loaded turbine blade and consists of suction and pressure surface cooling in addition to the showerhead cooling of the present study, so direct comparisons are difficult. However, the Strouhal number effect is nearly constant in the streamwise direction as in the present study. The mean film effectiveness decrement predicted by the current model for a Strouhal number increase of 0.2 is 0.019. The Mehendale et al. [6] data set shows a decrement ranging from 0.025 at $M=0.8$ to slightly negative (enhancement) at $M=0.4$ on the pressure surface, with a mean value of about 0.013. The model predicts a smaller film effectiveness decrement on the pressure surface due to attachment line variations at higher Strouhal numbers. This effect is present, particularly at $M=0.4$ and $M=1.2$, although it is smaller than in the present study, presumably due to the presence of suction and pressure surface (nonshowerhead) cooling, which is unaffected by attachment line variations.

An additional study by Du et al. [8] corroborates the data of Mehendale et al. [6]. In the more recent study, a transient liquid crystal technique was used to repeat the no wake and St=0.1 cases from the earlier study. Approximately the same reduction in film effectiveness was found. Although more recent data exists relative to the effect of freestream turbulence level on film effectiveness, Mehendale et al. [6] still represents the most recent and best available data on the effect of Strouhal number on film cooling effectiveness, especially since Du et al. [8] did not extend their data to St=0.3.

Conclusions and Recommendations

A model has been developed which accounts for the primary effects of wake passing unsteadiness on film cooling effectiveness for a showerhead-cooled stationary turbine blade. The experimental film effectiveness as correlated by the model is seen to be reduced by wake passing unsteadiness for all cases by a nominal value of 0.094 St. The Strouhal number has a measurable effect on the flow split between the suction and pressure surfaces for showerhead cooling. A higher Strouhal number skews the coolant flow toward the pressure surface, producing better cooling on the pressure surface and worse on the suction surface. Nusselt numbers were found to remain fairly constant with changing Strouhal number, but to be higher for CO_2 than for air injection.

The unsteady experimental data proved difficult to execute and interpret. It is recommended that future experiments which aim to measure high frequency temperature fluctuations use double-sided gauges similar to those used by Abhari and Epstein [18]. Several important mechanisms of wake passing were isolated by other

methods. A clear and consistent reduction in film effectiveness was found for stationary wake locations near the blade leading edge. Reductions of up to 0.10 and 0.15 were exhibited on the suction and pressure surfaces, respectively. Nusselt number reductions of about 20 percent were found near the pressure side leading edge with the wake impinging on the blade. Based on the success of these data, stationary wake experiments are recommended in the absence of advanced instrumentation capable of resolving high frequency data. In addition, the averaging of these data more properly represent a limiting case for wake passing experiments than the more traditional no wake condition. Another unsteady mechanism identified by the steady experiments is the spanwise variation in film effectiveness near the suction side leading edge for various Strouhal numbers. The reduction in span-average film effectiveness is found to be primarily due to reductions near the peak film effectiveness value. This indicates that the wake passing influences the film jets by enhancing their spanwise mixing.

Nusselt numbers are predicted quite well by the steady computation. Film effectiveness prediction is not as successful. The computation predicts higher film effectiveness values than the experiments, which indicates an underprediction of film mixing. This is thought to be primarily due to not resolving the flow inside the film holes, as well as the absence of reliable turbulence models for film cooling.

A better understanding of the complex interactions between unsteady flows and film cooling flows is necessary to improve existing models and achieve better film cooling designs. It is hoped that the results of this study represent a step in this direction, and will lead to other research in the field.

Nomenclature

C = model coefficient
c = blade chord
D = cylindrical rod diameter
d = cooling hole diameter
h = heat transfer coefficient
k = thermal conductivity
L = cooling hole length
M = blowing ratio
N = rotor speed in rpm
n = number of rods in rotor
Nu = Nusselt number
q'' = heat flux per unit area
S = effective slot width
St = Strouhal number
T = temperature
V = velocity
x = streamwise distance from leading edge
y^+ = dimensionless distance from wall
η = film effectiveness
ρ = density

Subscripts

c = coolant conditions
f = film conditions
r = recovery conditions
w = wall conditions with heating
∞ = freestream conditions

References

[1] Goldstein, R. J., 1971, ''Film Cooling,'' Advances in Heat Transfer, **7**, pp. 321–379.
[2] Heidmann, J. D., 1996, ''The Effect of Wake Passing on Turbine Blade Film Cooling,'' NASA TM-107380 and Ph.D. Dissertation, Case Western Reserve University (1997).
[3] Heidmann, J. D., Rigby, D. L., and Ameri, A. A., 2000, ''A Three-Dimensional Coupled Internal/External Simulation of a Film-Cooled Turbine Vane,'' ASME J. Turbomach., **122**, pp. 348–359.
[4] Rigby, M. J., Johnson, A. B., and Oldfield, M. L. G., 1990, ''Gas Turbine Rotor Blade Film Cooling With and Without Simulated NGV Shock Waves and Wakes,'' ASME Paper No. 90-GT-78.
[5] Ou, S., Han, J.-C., Mehendale, A. B., and Lee, C. P., 1994, ''Unsteady Wake Over a Linear Turbine Blade Cascade With Air and CO_2 Film Injection: Part I-Effect on Heat Transfer Coefficients,'' ASME J. Turbomach., **116**, pp. 721–729.
[6] Mehendale, A. B., Han, J.-C., Ou, S., and Lee, C. P., 1994, ''Unsteady Wake Over a Linear Turbine Blade Cascade With Air and CO_2 Film Injection: Part II-Effect on Film Effectiveness and Heat Transfer Distributions,'' ASME J. Turbomach., **116**, pp. 730–737.
[7] Funazaki, K., Koyabu, E., and Yamawaki, S., 1996, ''Effect of Periodic Wake Passing on Film Effectiveness of Inclined Discrete Cooling Holes Around the Leading Edge of a Blunt Body,'' ASME Paper No. 96-GT-207.
[8] Du, H., Han, J. C., and Ekkad, S. V., 1998, ''Effect of Unsteady Wake on Detailed Heat Transfer Coefficient and Film Effectiveness Distributions for a Gas Turbine Blade,'' ASME J. Turbomach., **120**, pp. 808–817.
[9] Du, H., Ekkad, S. V., and Han, J. C., 1999, ''Effect of Unsteady Wake With Trailing Edge Ejection on Film Cooling Performance for a Gas Turbine Blade,'' ASME J. Turbomach., **121**, pp. 448–455.
[10] Teng, S., Sohn, D. K., and Han, J. C., 2000, ''Unsteady Wake Effect on Film Temperatures and Effectiveness Distributions for a Gas Turbine Blade,'' ASME J. Turbomach., **122**, pp. 340–347.
[11] Seo, H. J., Lee, J. S., and Ligrani, P. M., 1999, ''Effects of Bulk Flow Pulsations on Film Cooling From Different Length Injection Holes at Different Blowing Ratios,'' ASME J. Turbomach., **121**, pp. 542–550.
[12] Ekkad, S. V., Han, J. C., and Du, H., 1998, ''Detailed Film Cooling Measurements on a Cylindrical Leading Edge Model: Effect of Free-Stream Turbulence and Coolant Density,'' ASME J. Turbomach., **120**, pp. 799–807.
[13] Ames, F. E., 1998, ''Aspects of Vane Film Cooling With High Turbulence: Part I—Heat Transfer,'' ASME J. Turbomach., **120**, pp. 768–776.
[14] Ames, F. E., 1998, ''Aspects of Vane Film Cooling With High Turbulence: Part II—Adiabatic Effectiveness,'' ASME J. Turbomach., **120**, pp. 777–784.
[15] Kohli, A., and Bogard, D. G., 1998, ''Effects of Very High Free-Stream Turbulence on the Jet-Mainstream Interaction in a Film Cooling Flow,'' ASME J. Turbomach., **120**, pp. 785–790.
[16] Dring, R. P., Blair, M. F., and Joslyn, H. D., 1980, ''An Experimental Investigation of Film Cooling on a Turbine Rotor Blade,'' ASME J. Eng. Power, **102**, pp. 81–87.
[17] Takeishi, K., Aoki, S., Sato, T., and Tsukagoshi, K., 1992, ''Film Cooling on a Gas Turbine Rotor Blade,'' ASME J. Turbomach., **114**, pp. 828–834.
[18] Abhari, R. S. and Epstein, A. H., 1992, ''An Experimental Study of Film Cooling in a Rotating Transonic Turbine,'' ASME Paper No. 92-GT-201.
[19] Funazaki, K., Kitazawa, T., Koizumi, K., and Tanuma, T., 1997, ''Studies on Wake-Disturbed Boundary Layers Under the Influences of Favorable Pressure Gradient and Free-Stream Turbulence Part I: Experimental Setup and Discussions on Transition Model,'' ASME Paper No. 97-GT-451.
[20] Funazaki, K., Kitazawa, T., Koizumi, K., and Tanuma, T., 1997, ''Studies on Wake-Disturbed Boundary Layers Under the Influences of Favorable Pressure Gradient and Free-Stream Turbulence Part II: Effect of Freestream Turbulence,'' ASME Paper No. 97-GT-452.
[21] Chakka, P., and Schobeiri, M. T., 1999, ''Modeling Unsteady Boundary Layer Transition on a Curved Plate Under Periodic Unsteady Flow Conditions: Aerodynamic and Heat Transfer Investigations,'' ASME J. Turbomach., **121**, pp. 88–97.
[22] Kim, K., and Crawford, M. E., 2000, ''Prediction of Transitional Heat Transfer Characteristics of Wake-Affected Boundary Layers,'' ASME J. Turbomach., **122**, pp. 78–87.
[23] Dorney, D. J., Davis, R., and Edwards, D., 1992, ''Investigation of Hot Streak Migration and Film Cooling Effects on Heat Transfer in Rotor/Stator Interacting Flows,'' N00140-88-C-0677-Report 1, UTRC Report 91-29.
[24] Simoneau, R. J., Morehouse, K. A., VanFossen, G. J., and Behning, F. P., 1984, ''Effect of a Rotor Wake on Heat Transfer From a Circular Cylinder,'' NASA TM-83613.
[25] O'Brien, J. E., and Capp, S. P., 1989, ''Two-Component Phase-Averaged Turbulence Statistics Downstream of a Rotating Spoked- Wheel Wake Generator,'' ASME J. Turbomach., **111**, pp. 475–482.
[26] Heidmann, J. D., 1995, ''A Numerical Study of the Effect of Wake Passing on Turbine Blade Film Cooling,'' NASA TM-107077 and AIAA-95-3044.
[27] Chima, R. V., and Yokota, J. W., 1990, ''Numerical Analysis of Three-Dimensional Viscous Flows in Turbomachinery,'' AIAA J., **28**, No. 5, pp. 798–806.
[28] Bird, R. B., Stewart, W. E., and Lightfoot, E. N., 1960, *Transport Phenomena*, Wiley, New York.
[29] Takeishi, K., Matsuura, M., Aoki, S., and Sato, T., 1990, ''An Experimental Study of Heat Transfer and Film Cooling on Low Aspect Ratio Turbine Nozzles,'' ASME J. Turbomach., **112**, pp. 477–487.
[30] Ito, S., Goldstein, R. J., and Eckert, E. R. G., 1978, ''Film Cooling of a Gas Turbine Blade,'' ASME J. Eng. Power, **100**, pp. 476–481.

Film Cooling Downstream of a Row of Discrete Holes With Compound Angle

R. J. Goldstein

P. Jin

Department of Mechanical Engineering,
University of Minnesota,
Minneapolis, MN 55455

A special naphthalene sublimation technique is used to study the film cooling performance downstream of one row of holes of 35 deg inclination angle and 45 deg compound angle with 3d hole spacing and relatively small hole length to diameter ratio (6.3). Both film cooling effectiveness and mass/heat transfer coefficients are determined for blowing rates from 0.5 to 2.0 with density ratio of unity. The mass transfer coefficient is measured using pure air film injection, while the film cooling effectiveness is derived from comparison of mass transfer coefficients obtained following injection of naphthalene-vapor-saturated air with that of pure air injection. This technique enables one to obtain detailed local information on film cooling performance. General agreement is found in local film cooling effectiveness when compared with previous experiments. The laterally averaged effectiveness with compound angle injection is higher than that with inclined holes immediately downstream of injection at a blowing rate of 0.5 and is higher at all locations downstream of injection at larger blowing rates. A large variation of mass transfer coefficients in the lateral direction is observed in the present study. At low blowing rates of 0.5 and 1.0, the laterally averaged mass transfer coefficient is close to that of injection without compound angle. At the highest blowing rate used (2.0), the asymmetric vortex motion under the jets increases the mass transfer coefficient drastically ten diameters downstream of injection.
[DOI: 10.1115/1.1344905]

Introduction

Film cooling is one of the techniques used to reduce the potential large blade temperatures and thermal stresses that tend to occur with an increase of the inlet temperature to the first-stage turbine of high-performance gas turbine systems. Air bypassed from the compressor (often after the last stage) flows into the blades. Here it is used for internal cooling and then ejected through the blade surface (to provide film cooling) into the external boundary layer, where it reduces the temperature in the boundary layer and protect the surface over which the hot combustion gas flows.

Due to manufacturing and stress-related issues, discrete-hole film cooling is preferred over slot injection film cooling for external cooling. The discrete-hole geometry leads to three-dimensional flow and temperature fields downstream of injection. Jet lift-off, high turbulence intensity in the shear layer, and double counterrotating vortices are important features of film cooling cited by many researchers.

The performance of film cooling is usually characterized by adiabatic wall effectiveness and heat transfer coefficient. Various geometric and fluid dynamics parameters can affect the performance of discrete hole film cooling. Geometric factors include hole spacing (s/d), length of hole *(L/d)*, shape of hole, inclination angle *(IA)*, compound angle *(CA)*, surface curvature, and smoothness while the fluid dynamics parameters include blowing rate (M), momentum flux ratio (I), density ratio *(DR)*, velocity ratio *(VR)*, free-stream turbulence intensity *(Tu)* and length scale, and mainstream pressure gradient.

Many studies have been conducted on the performance of one row of discrete hole film cooling. Both heat transfer measurements [1,2] and mass transfer experiments [3,4] were widely used. However, in most studies, the detailed local values of film cooling effectiveness and heat transfer coefficient were not obtained due to the measurement methodology and averaged values were usually presented. Wall conduction errors in heat transfer experiments are often problematic. In a previous study of Goldstein et al. [5], a special naphthalene sublimation technique is used to obtain detailed local information of both film cooling effectiveness and mass/heat transfer coefficient downstream of one row of streamwise inclined holes.

Compared with research in other areas of film cooling, relatively fewer studies have been conducted on the effect of compound angle configuration on the fluid dynamics and film cooling performance. In late 60's, Goldstein et al. [6] obtained results for film cooling effectiveness with lateral injection. Honami et al. [7] made simultaneous velocity and temperature measurements with one row of laterally injected jet issuing into a turbulent boundary layer. An asymmetric flow structure with a large-scale vortex motion was detected, which resulted in low film cooling effectiveness at increased blowing rate. Lee et al. [8] investigated the flow structure of one inclined injection hole with various orientation angles. A surface flow model was suggested. They also detected the pair of counterrotating vortices turning into a single strong vortex as the compound angle is increased. While the film coverage becomes better with compound angle injection, more flow disturbances are also produced, resulting in larger aerodynamic loss.

Ligrani et al. [9] presented experimental results describing the flow structure and film cooling parameters downstream of a single row of holes with compound angle. Their results show that the compound angle injection configuration significantly improves the film cooling protection. In heat transfer measurements, Sen et al. [10] and Schmidt et al. [11] investigated the adiabatic wall effectiveness and heat transfer coefficient using a single row of inclined holes with different shapes, compound angles, and a hole length of $4d$. Their results showed that holes with a large compound angle had little effect on heat transfer rate for small momentum ratios, while heat transfer level is significantly increased for holes with compound angle at large momentum ratios. Ekkad et al. [12,13] presented film cooling effectiveness and heat transfer coefficient distributions over a flat surface with one row of

Contributed by the International Gas Turbine Institute and presented at the 45th International Gas Turbine and Aeroengine Congress and Exhibition, Munich, Germany, May 8–11, 2000. Manuscript received by the International Gas Turbine Institute February 2000. Paper No. 2000-GT-248. Review Chair: D. Ballal.

inclined holes for three different compound angles and density ratios at an elevated free-stream turbulence intensity (Tu=8.5 percent) using a transient liquid crystal technique proposed by Vendula and Metzger [14] to determine local effectiveness and heat transfer coefficient distribution simultaneously. They found that compound angle injection provides higher effectiveness than injection without compound angle.

Most recently, Cho et al. [15] and Seager and Liburdy [16] studied the effects of compound angle on film cooling performance using a naphthalene sublimation technique and a liquid crystal method, respectively. Cho's measurement was conducted on a single hole inclined at 30 deg to the flat surface with various compound angles. They concluded that to obtain higher effectiveness and wider film-cooled area, reasonable compound angle injection should be combined with moderate blowing rates. In their experiment, Seager and Liburdy [16] employed a row of holes with inclination angle of 35 deg and compound angle of 45 deg. A density ratio of 1.55 and an constant heat flux heat surface were also used. They also found improved performance with compound angle injection.

In the present study, one row of discrete film cooling holes on a flat plate with inclination angle of 35 deg, compound angle of 45 deg, and a length to diameter ratio of 6.3 is investigated using a naphthalene sublimation technique and mass/heat transfer analogy, by which the detailed local information of effectiveness and mass transfer coefficient can be attained. The blowing rate varies from 0.5 to 2.0 with a density ratio of 1.0 and the mainstream is a low turbulence intensity flow.

Experimental Method

Eckert [17] analyzed two approaches used in film cooling experiments. The first uses the adiabatic wall temperature (effectiveness) and a heat transfer coefficient only dependent on the fluid mechanics, which is, arguably, the most prevalent method used in research and industry. The second approach uses a dimensionless temperature and hence a heat transfer coefficient varying linearly with the dimensionless temperature. Both methods utilize the linear energy equation under the condition of constant fluid properties to enable the superposition of temperature field. Eckert [17] showed that the results of the two approaches are convertible under conditions of small temperature gradients on the film cooled wall. With large temperature (property) variations, care must be taken in assuming the validity of superposition.

The naphthalene sublimation method and the heat/mass transfer analogy were reviewed by Goldstein and Cho [18]; the advantages as well as the measurement technique were analyzed and compared to heat transfer results. Goldstein and Taylor [19] published mass transfer results for film cooling downstream of one row of holes using the naphthalene technique. Cho and Goldstein [20,21] measured film cooling effectiveness and mass/heat transfer coefficient for full coverage film cooling on a flat plate using naphthalene sublimation.

In summary, the naphthalene sublimation technique can be used to determine the convective component of heat transfer in the absence of wall conduction and radiation errors. A mass transfer problem can be converted to a heat transfer problem under the equivalent boundary conditions by mass/heat transfer analogy. Following Cho and Goldstein [20] and Goldstein et al. [5], using the naphthalene sublimation technique and the equivalent of isothermal conditions, the mass/heat transfer coefficient for film cooling on a flat plate downstream of injection can be obtained by measuring the mass transfer coefficient of the naphthalene wail with pure air injection,

$$h_m = h'_{m0} = \frac{\dot{m}_0}{\rho_{v,w} - \rho_{v,\infty}} \quad \text{when} \quad \rho_{v,2} = \rho_{v,\infty}$$

$$= \frac{\dot{m}_0}{\rho_{v,w}} \quad \text{since} \quad \rho_{v,\infty} = 0 \quad \text{in present study.} \qquad (1)$$

A dimensionless mass transfer coefficient, the Sherwood number, is used and often normalized by the mass transfer coefficient on the same flat plate without injection of secondary flow to cancel the effects of unheated starting length and Schmidt (Prandtl) number (Sc), making it comparable to the normalized heat transfer coefficient (h/h_0):

$$\frac{\mathrm{Sh}'_0}{\mathrm{Sh}_0} = \frac{h'_{m0}}{h_{m0}} \approx \frac{h}{h_0} \qquad (2)$$

The isothermal (isoconcentration) wall film cooling effectiveness, which is shown by Eckert [17] to be convertible to the adiabatic (impermeable) wall effectiveness, can be attained by comparing the mass transfer coefficient measured with injection of naphthalene-vapor–saturated air at the ambient temperature with the mass transfer coefficient measured with pure air injection,

$$h'_{m1} = \frac{m_1}{\rho_{v,w} - \rho_{v,\infty}} \quad \text{when} \quad \rho_{v,2} = \rho_{v,w}$$

$$= \frac{\dot{m}_1}{\rho_{v,w}} \quad \text{since} \quad \rho_{v,\infty} = 0 \quad \text{in present study} \qquad (3)$$

$$\eta_{iw} = \frac{\rho_{v,iw} - \rho_{v,\infty}}{\rho_{v,2} - \rho_{v,\infty}} = 1 - \frac{h'_{m1}}{h'_{m0}} = 1 - \frac{\mathrm{Sh}'_1}{\mathrm{Sh}'_0} \qquad (4)$$

These relations are used in the data reduction of the present investigation to obtain the effectiveness.

Experimental Apparatus

A large open-cycle, suction-type wind tunnel in the Heat Transfer Laboratory at the University of Minnesota is used to supply the mainstream for the film cooling test. Flow to the 2500-mm-long, 305.0-mm-high, and 610.0-mm-wide test section is preceded by a flow straightener and a 15:1 area contraction. The side and top wall of the test section are made of Plexiglas. The film cooling injection plate perforated with one row of holes and naphthalene test plate are installed in the bottom wall of the test section. The plan view of the test section is shown in Fig. 1. A 1.0-mm-dia trip wire followed by a 25.4 mm strip of sandpaper are placed at the exit of the contraction to trip and smooth the turbulent boundary layer developing on the flat wall. The center of the holes is 247.7 mm downstream of the trip and 10.3 mm upstream of the aluminum leading edge of the naphthalene plate (14.0 mm ahead of the starting edge of the naphthalene surface).

The details of the injection hole are shown in Fig. 2. The coordinate directions are also shown in the same figure. The one row of 12 holes of 6.35 mm diameter is rotated 45 deg from the direction of mainstream in the $+z$ direction and inclined at 35 deg with respect to test section surface with a 3d hole spacing. The injection plate is 22.9 mm thick and made of aluminum, providing a hole length of 6.3d. In previous studies, the origin of the coordinate system is often placed at the downstream (aft) tip of the hole. In the present study of compound angle configuration, the

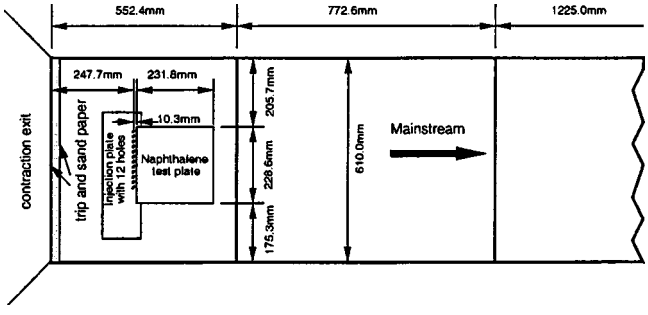

Fig. 1 Planview of test section

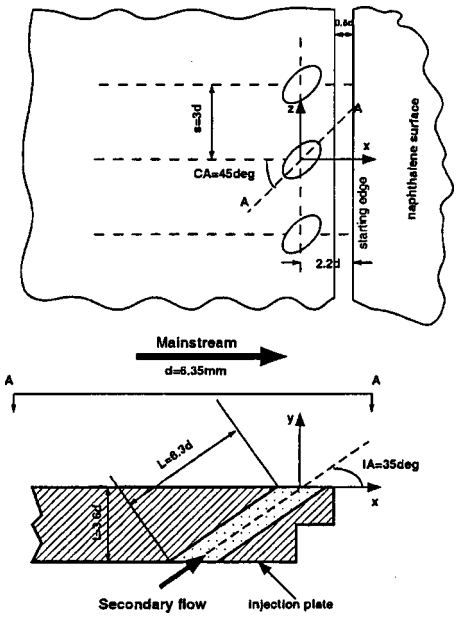

Fig. 2 Film cooling hole geometry

origin of the coordinates is more commonly placed at the center of hole. Then the value of *x/d* at the aft edge of the hole for the streamwise injection per Goldstein et al. [5] is 0.87 and for the present compound angle injection it is 0.62. When compared, results from other studies are corrected for this definition of *x*.

The aluminum naphthalene test plate is located immediately downstream of the holes to facilitate the investigation of film cooling performance near the hole. Figure 3 shows the geometry of the naphthalene plate. The naphthalene casting layer is 35*d* long, 34 *d* wide, and 2.54 mm thick, of which only a 9*d* wide strip around the centerline of the test section (covering three holes) is used to measure the mass transfer coefficient. Two thermocouples in the naphthalene monitor the surface temperature. The fill hole and air vent are used in casting naphthalene. The reference point and aluminum rim around the naphthalene layer are used as the references in the naphthalene profile measurement. The values of *x/d* at the leading edge of the naphthalene are 2.20 for both the streamwise injection of Goldstein et al. [5] and the present compound injection.

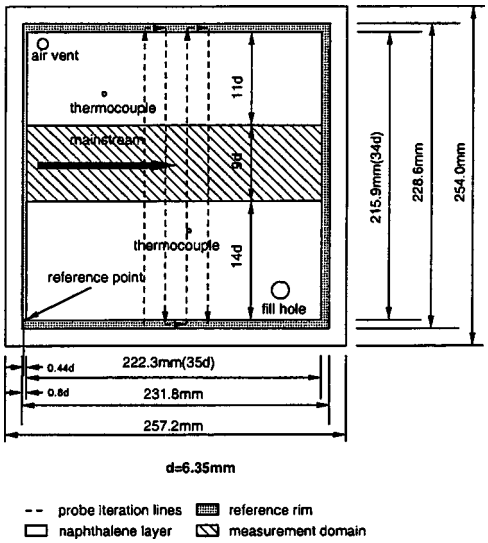

Fig. 3 Naphthalene sublimation test plate

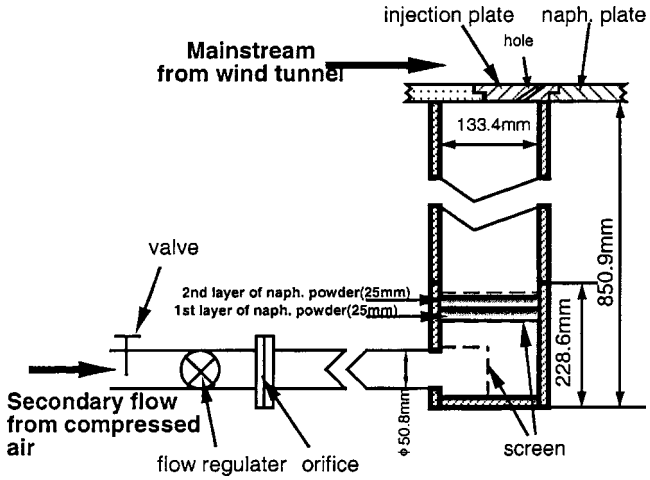

Fig. 4 Secondary flow injection system

Figure 4 shows the secondary air injection system. Compressed air from the building supply passes through a 50.8-mm-dia piping system equipped with valve, flow regulating orifice, tape heater, and thermocouple, which provide control of the secondary air flow rate and temperature. At the end of the pipe, the secondary air goes into a plenum chamber 133.4 mm wide, 414.7 mm long, and 850.9 mm high. The air first passes through a screen at the inlet of the plenum and then a flat screen for pure air injection or two layers of naphthalene powder (about 50 mm thick) in the naphthalene-vapor-saturated air injection case. Then the flow goes along the plenum passage and out through the injection holes into the mainstream. Thermocouples are installed to monitor the temperature of the flow in the mainstream, plenum, and surrounding air.

The T-type thermocouples and orifice meter used in the experiment were previously calibrated per Cho and Goldstein [20]. The thermocouples are integrated with a GPIB board-enabled Linux workstation to facilitate the temperature measurement of the system. Pressures are measured with a total pressure tube located 300 mm downstream of the holes and a static pressure tap 20 mm upstream of the total pressure tube. Both of these are connected to a micromanometer with a reading precision of 0.01 mm H_2O to give the mainstream velocity. The secondary air flow is determined from the pressure drop across the calibrated orifice in the pipe with a manometer system and is adjusted by the valve. The depth change of the naphthalene layer during the film cooling test is measured with an automated XY-table surface profile measuring system developed in the Heat Transfer Laboratory at the University of Minnesota. The details of the system and calibration procedure can be found in Jin [22].

The uncertainty in naphthalene wall temperature measurement is 0.09 percent in absolute temperature with 95 percent confidence level. The uncertainties in mainstream and secondary flow velocities are 1.0 and 2.6 percent, respectively. The uncertainty is 2.8 percent in blowing rate and within 0.80 percent in the naphthalene sublimation depth change, which includes the error of repositioning. The uncertainties in mass transfer coefficient and Sherwood number at 95 percent confidence level are 5.8 and 7.6 percent, respectively. The errors are mainly caused by the uncertainty in properties of naphthalene. The relative uncertainty in effectiveness is local-effectiveness dependent in this method and is 7.1 percent for higher effectiveness ($\sim$0.5) and less than 29 percent for low effectiveness of ($\sim$0.2). The naphthalene loss due to natural convection is estimated and included in the above-described uncertainty analysis. The experimental procedure is described in detail by Jin [22].

The turbulent boundary layer established downstream of the trip without secondary air injection is described in Table 1. The

Table 1 Film cooling geometry and operating conditions

d(mm)	s/d	L/d	IA	CA	x/d	$Re_2 \times 10^{-3}$
6.35	3	6.3	35°	45°	2.2-36	2.7 – 11
$U_\infty(m/s)$	$Tu(\%)$	δ^*/d	Re_d	M	D.R.	$Re_x \times 10^{-5}$
13.5	0.70	0.271	5500	0.5-2.0	1.0	4.4 – 6.2

boundary layer characteristics are measured at three different locations—upstream, near, and downstream of the injection holes —using a flat pitot tube with near wall correction. The interpolated displacement thickness and shape factor are 0.27l*d* and 1.45 at the center of holes, respectively. The mass transfer Stanton number downstream of (taped) holes without injection is measured and compared with heat transfer Stanton numbers with unheated starting length calculated from empirical equations. Good agreement is obtained. For a typical sublimation depth of 50 μm, the effect of thinner naphthalene wall on boundary layer thickness (of order of 10 mm) can be neglected. Since the pressure of saturated naphthalene vapor is four orders of magnitude less than the atmospheric pressure, the fluid properties for saturated-naphthalene-vapor injection are considered to be constant. Thus, the density ratio is essentially unity. The saturation of naphthalene vapor in the air is assured by comparing results for different thicknesses (25 and 50 mm) of the naphthalene layers used to add vapor to the injected flow at various blowing rates and is confirmed by the repeatability of the results. The repeatability of mass transfer coefficient for both pure air film injection and naphthalene-vapor-saturated air injection is demonstrated in Jin [22] and considered in the experiments uncertainty analysis according to the principles in Coleman and Steele [23].

Experimental Results and Discussion

The results from the present study are presented and compared with measurement from other groups in this section.

Mass/Heat Transfer Coefficient. As reported by Honami et al. [7] and Lee et al. [8], the flow near the wall is strongly affected by compound angle injection. Flow characteristics can be observed and interpreted from the mass transfer surface plots obtained in the present study. Contour plots of normalized Sherwood number for $M=0.5$, 1.0, and 2.0 are provided in Fig. 5.

At blowing rate of 0.5, the regions covered by the core of injected jets have a normalized Sherwood number less or equal to 1.0. The jets are deflected toward the mainstream direction due to their low momentum flux and the impact from the mainstream, which induces small regions of high mass transfer rate at the downstream tip ($z=1.0d$) of holes. Downstream of the upstream tip ($z=-0.5d$) of holes, the main flow passes over the jets and touches down the surface and creates large areas of relatively high mass transfer rate ($Sh'/Sh_0=1.1$). Between two neighboring jets, there are small regions unaffected by the jets, which have normalized Sherwood number about unity.

At blowing rate of 1.0 in Fig. 5, the areas covered by the core ($Sh'/Sh_0<1.0$) are shorter than for $M=0.5$ with compound angle injection, while the turbulent mixing, enhanced by the interaction with the mainstream, farther downstream widens the jets ($Sh'/Sh_0\leqslant 1.1$) than that at $M=0.5$ with compound angle injection. The bending of jets is less apparent due to the increased jet momentum flux. The strong interaction between the mainstream and the jets also expands the high mass transfer areas on the $+z$ side of jets immediately downstream of the holes. On the $-z$ side of jets, the surface is covered by the main flow passing over jets and touching down the naphthalene surface, similar to the situation mentioned at $M=0.5$ with compound angle injection.

At $M=2.0$, the areas covered by the core of jets only extend to $x/d=6$ and become narrower, which may indicate liftoff of the jets. At the same time, the spreading of jets above the surface is also enhanced and the jets merge at $x/d=20$. Asymmetric vortex motion formed by the down-sweeping of mainstream under the $-z$ side of jets can be interpreted from the naphthalene measurements. This is strengthened drastically due to the strong blockage of the mainstream by the jets and generates wide regions of high mass transfer rate between neighboring jets, attaining the maximum on the $-z$ side of the jets. These regions also merge with the narrowed high mass transfer region on the $+z$ side of neighboring jet in the $-z$ direction to give two peaks of normalized Sherwood number at $x/d = 4$ and $x/d = 9$, respectively.

From the above-described analysis and previous studies from

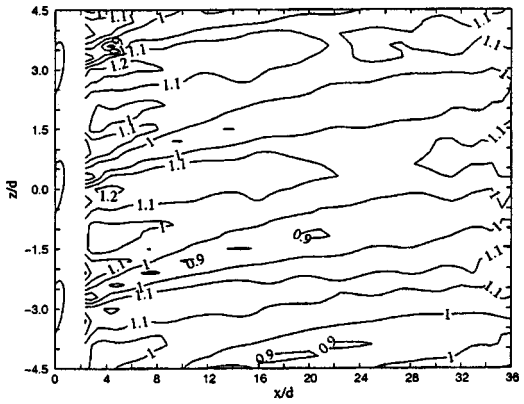

(a) M=0.5

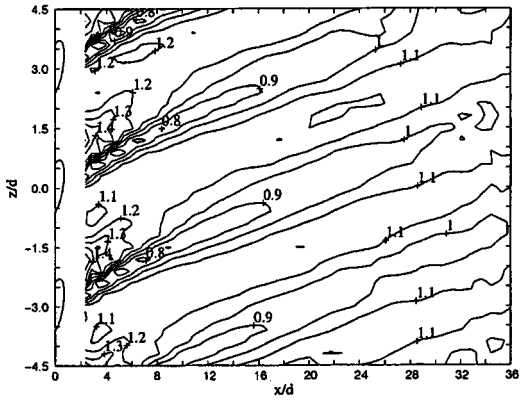

(b) M=1.0

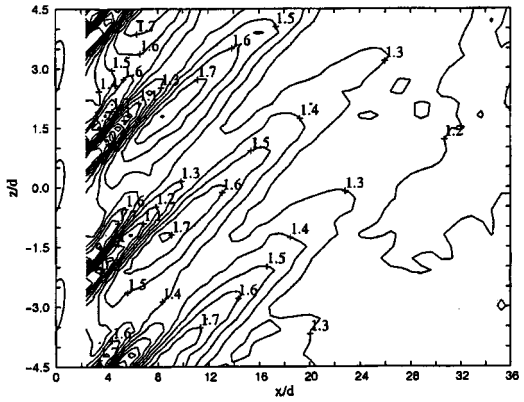

(c) M=2.0

Fig. 5 Local Sh_0'/Sh_0 contour

other groups, we can see that the strong interaction between mainstream and jets for compound angle injection keeps the core of jets attached to the wall. The jets are wider farther downstream compared with the situation for injection without compound angle, where the jets lift off at blowing rate above 0.5 for density ratio of unity. The flow structure becomes asymmetric due to compound angle orientation. The mainstream and the jet interaction intensifies mass transfer on the $+z$ side of the jets immediately downstream of the holes. However, on the $-z$ side of jets, the clockwise-rotating (looking downstream) vortex motion developed from down-sweeping of the mainstream after being blocked by and passing over the jets results in a wide region of high mass transfer rate at high blowing rates.

Comparisons of the data from the present study with the experimental results from other groups as well as from Goldstein et al. [5] are shown in Fig. 6 for blowing rates of 0.5, 1.0, and 2.0, respectively.

At a blowing rate of 0.5 in Fig. 6, the laterally averaged Sh'/Sh_0 for injection with compound angle shows no obvious difference comparing with that of injection without compound angle. The result of Ekkad et al. [12] is much higher apparently because of the high free-stream turbulence intensity (8.5 percent) used in their experiment. However, it could also relate to the uncertainty associated with the liquid crystal method.

At blowing rate of 1.0, the laterally averaged Sh'/Sh_0 for injection with compound angle is still close to that of injection without compound angle except immediately downstream of the injection holes, where the compound angle produces somewhat higher mass transfer rate. This is mainly due to the stronger interaction between mainstream and jets on the $+z$ side jets immediately downstream of the injection, as shown in Fig. 6. The results of Ekkad et al. [12] are still higher than other results.

At $M=2.0$, the mass transfer rate for injection with compound angle is much higher than that with injection without compound angle downstream of the holes up to $x/d=20$ because the strong asymmetric vortex increases the mass transfer rate on the $-z$ side of jets and causes a maximum in Sh at about $x/d=10$. Farther downstream of the injection holes, however, the mass transfer rate for injection with compound angle is lower than that for injection without compound angle. The results of Ekkad et al. [12] are a little closer to the present study for that blowing rate, perhaps because the strong interaction between mainstream and jets, as well as the vortex motion, greatly increases the turbulence intensity downstream of the holes.

In Fig. 7, comparison of local mass transfer coefficients at $x/d=10.4$ downstream of the injection at blowing rate of 0.5, 1.0, and 2.0 with the heat transfer results of Sen et al. [10] at the same location shows similar averaged results, but a variation with z for the present data, which is probably due to conduction in the wall in the heat transfer study.

Film Cooling Effectiveness. With compound angle injection, the film cooling performance is quite different from that by streamwise injection since the flow structure is changed downstream of the injection. We can observe the compound angle effect on film cooling clearly from the surface plot. A contour plot of effectiveness for $M=0.5$, 1.0, and 2.0 is provided in Fig. 8.

At a blowing rate of 0.5, the highest effectiveness is 0.5 at $x/d=3$ on the $+z$ side of holes. Regions of high effectiveness ($\geqslant 0.2$) are also on the $+z$ side of holes and extend to $x/d=18$ while on the $-z$ side of holes there exist regions of low effectiveness($\leqslant 0.1$). In other areas, the effectiveness is between 0.1 and 0.2. By comparison, the high effectiveness regions are much larger for injection with compound angle than without compound angle at the same blowing rate in Goldstein et al. [5]. The asymmetric distribution of effectiveness can be explained by the asymmetric flow structure of mainstream and jets interaction. On the $-z$ side of jets, the mainstream passes over the jets and covers the areas between the jets, resulting in low effectiveness. On the other hand, the interaction between mainstream and jets on the $+z$ side

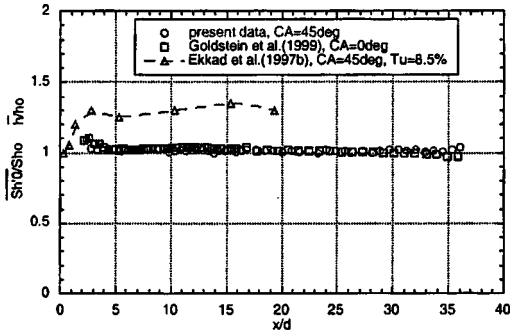

(a) M=0.5

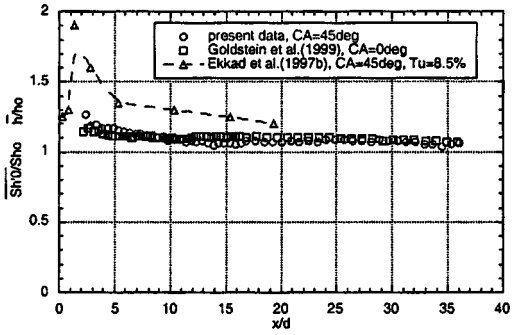

(b) M=1.0

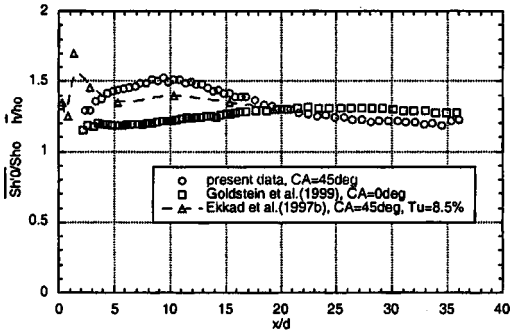

(c) M=2.0

Fig. 6 Comparison of $\overline{Sh'_0}/Sh_0$

keeps the jets attached to the wall and hence forms the high effectiveness area. The enhanced mixing also helps spread the jets farther downstream and gives rise to higher effectiveness than for injection without compound angle.

At a blowing rate of 1.0, the highest effectiveness decreases to 0.4 at $x/d=3$ and the high effectiveness regions on the $+z$ side of the jets become shorter (extends to $x/d=14$) and narrower compared with that for $M=0.5$, while the low effectiveness regions on the $-z$ side of jets also decrease. Although the film coverage at blowing rate of 1.0 is not as wide as that of $M=0.5$ due to the increased presence of mainstream between the neighboring jets, it is much better than that for streamwise injection at the same blowing rate.

At $M=2.0$, the high effectiveness regions on the $+z$ side of jets disappear immediately downstream of the holes while the low effectiveness regions extend to both sides of jets. At $x/d=10$, the

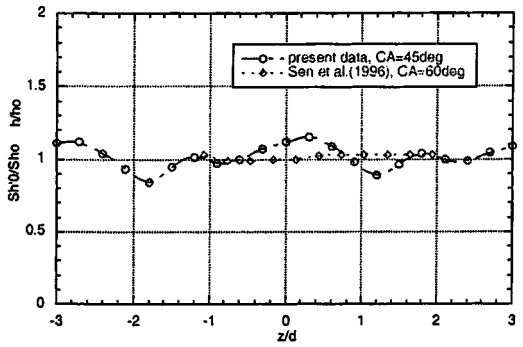

(a) M=0.5

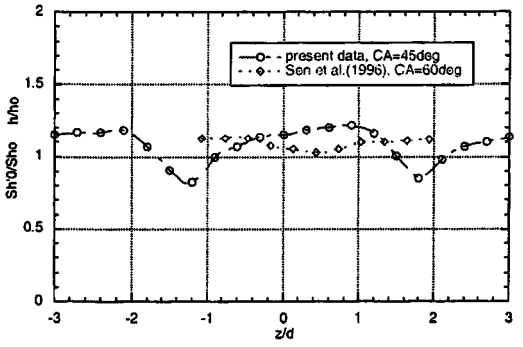

(b) M=1.0

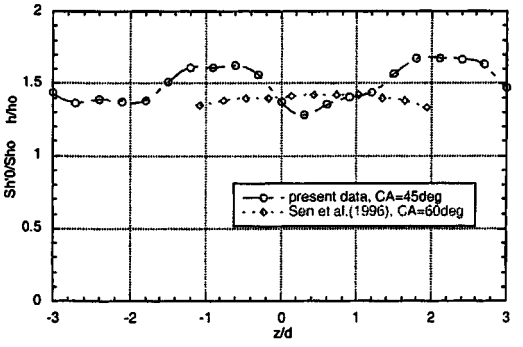

(c) M=2.0

Fig. 7 Comparison of local Sh_0'/Sh_0 at $x/d=10.4$

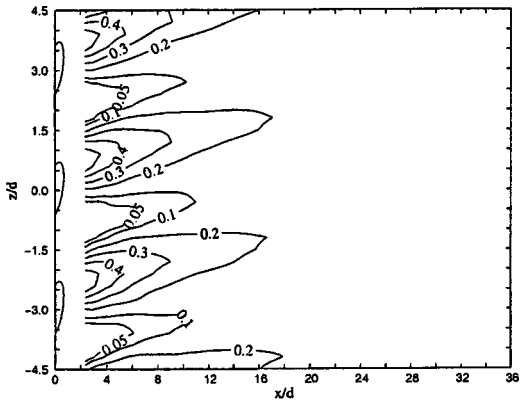

(a) M=0.5

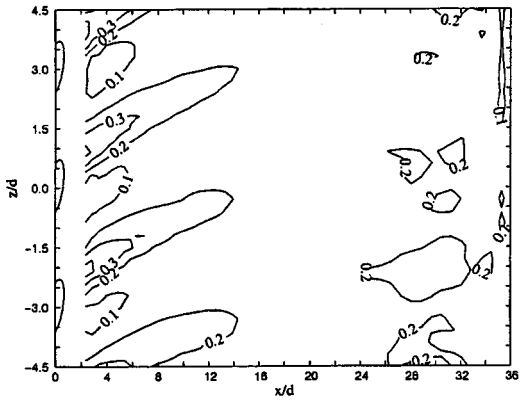

(b) M=1.0

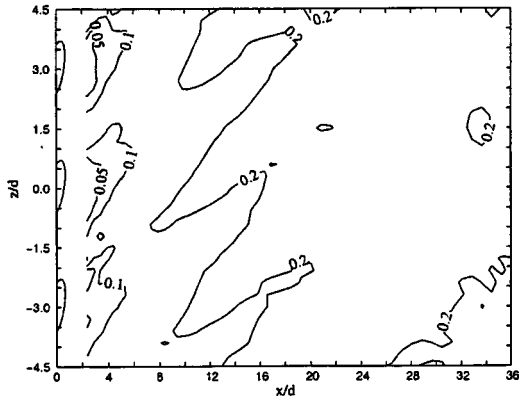

(c) M=2.0

Fig. 8 Local η_{iw} contour

areas of high effectiveness begin to merge and form a large area of high effectiveness farther downstream. This distribution of effectiveness at blowing rate of 2.0 indicates that the strong vortex motion formed by the down-sweeping of mainstream underneath the jets takes control immediately downstream of injection. At the same time, due to the strong interaction between mainstream and jets, the jets spread and re-attach to the wall after $x/d=10$, giving the merged area of high effectiveness.

As blowing rate increases over 1.0, the film cooling performance near the holes deteriorates for injection with compound angle because of the asymmetric vortex motion formed by the down-sweeping of mainstream on the $-z$ side of the jets. At blowing rates of 0.5 and 1.0, the film cooling performances are better than with streamwise injection without compound angle. The strong interaction between mainstream and jets also keeps the jets attached to the wall and generates enhanced turbulent mixing and spreading farther downstream.

Comparisons of laterally averaged effectiveness with previous measurements are plotted for $M=0.5$, 1.0, and 2.0 in Fig. 9, respectively.

At a blowing rate of 0.5 in Fig. 9, the averaged effectiveness in the present study is higher than for streamwise injection up to $x/d=10$ downstream of injection. Farther downstream the results

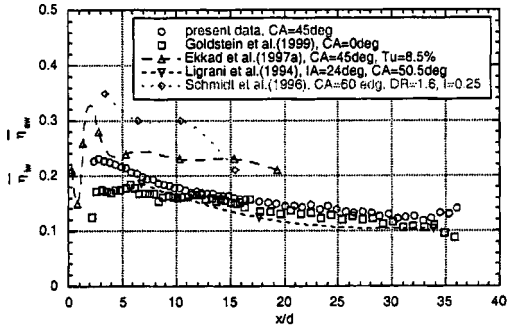

(a) M=0.5

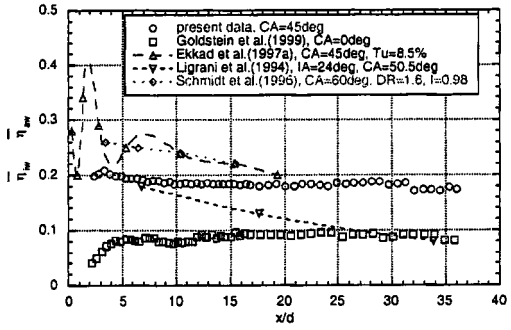

(b) M=1.0

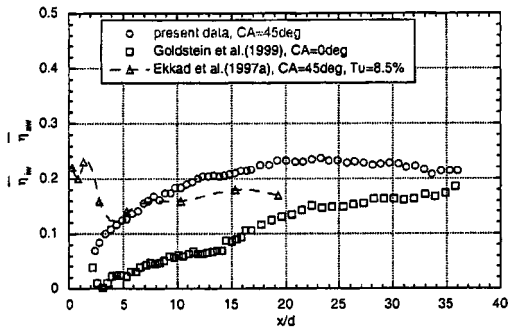

(c) M=2.0

Fig. 9 Comparison of $\overline{\eta_{iw}}$

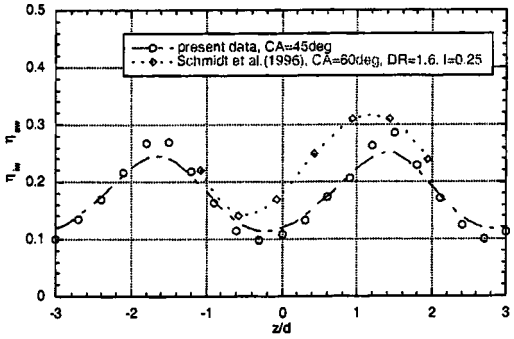

(a) M=0.5

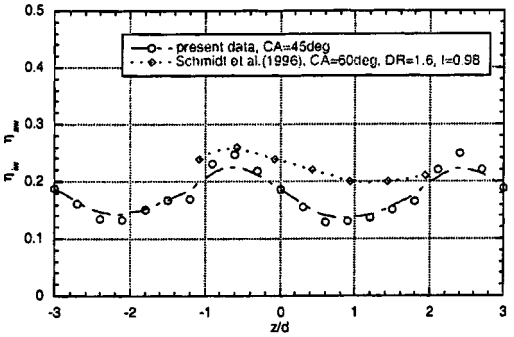

(b) M=1.0

Fig. 10 Comparison of local η_{iw} at $x/d=0.4$

of the present study are close to those of streamwise injection. The high effectiveness obtained by Ekkad et al. [13] cannot be attributed to its high free-stream turbulence level, which enhances the mixing and spreading of jets and reduces the average effectiveness. The higher effectiveness measured by Schmidt et al. [11] is apparently due to the high density ratio used, which gives jets a lower momentum flux-to-mainstream flux ratio at the same blowing rate.

At blowing ratio of 1.0 in the same figure, the effectiveness obtained by the present study is much higher at all streamwise locations than that obtained from Goldstein et al. [5] with streamwise injection. This can be explained by the absence of lift-off with compound angle and the wider spreading due to the strong interaction between jets and mainstream. For the same reasons mentioned above at $M = 0.5$, the results of Schmidt et al. [11] and Ekkad et al. [13] are also higher than in the current study. Results of Ligrani et al. [9] are close to the present study for $x/d<10$, but farther downstream they are close to the result of Goldstein et al. [5] with streamwise injection.

At $M=2.0$, data from the present study are higher than for streamwise injection, although in the near-hole region the effectiveness is close to that of Goldstein et al. [5]. The data of Ekkad et al. [13] are relatively close to the data of current study after $s/d=5$, probably due to the fact that at high blowing rate, the turbulence intensity is drastically increased by the strong interaction of the mainstream and jets.

The higher averaged effectiveness at all blowing rates for injection with compound angle than that of injection without compound angle can be explained by the better coverage of cooling film when using compound angle injection and the reduced jets liftoff effect at high blowing.

In Fig. 10, the local effectiveness is compared with results of Schmidt et al. [11] at $x/d=10.4$ for blowing rates of 0.5 and 1.0, respectively. At $M=0.5$, the data from Schmidt et al. [11] have the same trend as the current data except that the peak and the valley are not matched due to the differences in compound angle. The same trend is found at blowing rate of 1.0. In both cases, the results of Schmidt et al. [11] are a little higher than the current data due to the density ratio of 1.6 used in their case.

Conclusions

In the present study, the naphthalene sublimation technique and the heat/mass transfer analogy are used to measure the film cooling performance for one row of holes with 35 deg inclination angle and 45 deg compound angle. The mass transfer coefficient is measured using pure air film injection while the film cooling effectiveness is derived from comparison of mass transfer coefficients obtained following injection of naphthalene-vapor-saturated air with that of pure air. The following conclusions can be made:

1 In compound angle film cooling, the strong interaction between the mainstream and the jets on the $+z$ side of the jets keeps the injected film essentially attached to the wall at low blowing rates and reduces the liftoff effect at high blowing rates, compared with the jet liftoff as early as $M \approx 0.5$ for streamwise injection. On the $-z$ side of the jets, the asymmetric vortex motion developed from the down-sweeping of mainstream under the jets at high blowing rates strongly affects the mass transfer process and the jet coverage.

2 At blowing rates of 0.5 and 1.0, the laterally averaged $\mathrm{Sh}'/\mathrm{Sh}_0$ are close to that of injection without compound angle. At blowing rates of 2.0, the mass transfer rate increases drastically due to the asymmetric vortex motion under the jets on the $-z$ side of the jets.

3 The local mass transfer coefficients obtained in the present study differ from equivalent heat transfer results, perhaps due to conduction effects in the region of large temperature gradients with the heat transfer measurements.

4 The local film cooling effectiveness generally has the same trend as the results from other studies at similar positions downstream of injection. The laterally averaged film cooling effectiveness at all blowing rates studied are higher than those of streamwise injection because of the better coverage of cooling film in compound angle configuration due to the strong interaction between the mainstream and jets. At blowing ratios of 0.5 and 1.0, the effectiveness is better or comparable to that of streamwise injection at $M=0.5$. Regions of high and low effectiveness are formed on $+z$ and $-z$ sides of the jets, respectively, at these blowing rates. For blowing rate of 2.0, the down-sweeping of the asymmetric vortex motion under the jets deteriorates the film cooling performance downstream of injection. Farther downstream, merged regions of relative high effectiveness are attainable at these blowing rates.

Acknowledgments

This research was supported by the U.S. Department of Energy-Federal Energy Technology Center through the AGTSR program.

Nomenclature

$\dot{m}$ = mass transfer rate per unit area $=\rho_s(\delta y/\delta t)$
$\dot{m}_0$ = mass transfer rate per unit area for $\rho_{v,2}=\rho_{v,\infty}$
$\dot{m}_1$ = mass transfer rate per unit area for $\rho_{v,2}=\rho_{v,w}$
CA = compound angle of injection hole (cf. Fig. 2)=45 deg in present study
d = diameter of injection hole=6.35 mm in present study
DR = density ratio $=\rho_2/\rho_\infty$ in present study
D_{naph} = naphthalene vapor diffusivity in air $\approx 6.8\times10^{-6}$ m^2/s
h = heat transfer coefficient
h'_{m0} = mass transfer coefficient for $\rho_{v,2=\rho_{v,\infty}}$
h'_{m1} = mass transfer coefficient for $\rho_{v,2}=\rho_{v,w}$
h = lateral average (over z) of h
h_m = mass transfer coefficient
h_0 = heat transfer coefficient with our injection
h_{m0} = mass transfer coefficient without injection
I = momentum ratio $=(\rho_2U_2^2)/(\rho_\infty U_\infty^2)$
IA = inclination angle of injection hole in Fig. 2=35 deg in present study
L = length of injection hole in Fig. 2
M = blowing rate $=(\rho_2U_2)/(\rho_\infty U_\infty)$
Re_d = Reynolds number based on U_∞ and $d=\rho_\infty U_\infty d/\mu$
Re_2 = Reynolds number based on U_2 and $d=\rho_2U_2d/\mu$
s = space between the injection holes (cf. Fig. 2)=3d in present study
Sc = Schmidt number of naphthalene vapor in use $=\mu/\rho D_{\mathrm{naph}}\approx 2.29$ in present study
Sh'_0 = Sherwood number for $\rho_{v,2}=\rho_{v,\infty}$
$\overline{\mathrm{Sh}}'_0$ = lateral average (over z) of Sh'_0
Sh'_1 = Sherwood number for $\rho_{v,2}=\rho_{v,w}$
Sh_0 = Sherwood number based on $h_{m0}=h_{m0}d/D_{\mathrm{naph}}$
t = thickness of injection plate
Tu = free-stream turbulence intensity ≈ 0.54 percent in present study
U_2 = secondary flow velocity; mean velocity in injection holes
U_∞ = mainstream velocity
VR = velocity ratio $=U_2/U_\infty$
x = streamwise distance from center of injection hole (cf. Fig. 2)
y = distance normal to film cooling wall (cf. Fig. 2)
z = spanwise distance from center of injection hole (cf. Fig. 2)
δ^* = boundary layer displacement thickness
η_{iw} = impermeable wall film cooling effectiveness
$\overline{\eta_{iw}}$ = laterally averaged impermeable wall film cooling effectiveness
μ = air dynamic viscosity
ρ_2 = secondary flow density
ρ_∞ = mainstream density
$\rho_{v,2}$ = naphthalene vapor density in secondary flow
$\rho_{v\infty}$ = naphthalene vapor density in mainstream=0 in present study
$\rho_{v,iw}$ = naphthalene vapor density at impermeable wall
$\rho_{v,w}$ = naphthalene vapor density at wall

References

[1] Eriksen, V. L., and Goldstein, R. J., 1974, ''Heat Transfer and Film Cooling Following Injection Through Inclined Circular Tubes,'' ASME J. Heat Transfer, **96**, pp. 239–245.
[2] Sinha, A. K., Bogard, D. G., and Crawford, M. E., 1991, ''Film Cooling Effectiveness Downstream of a Single Row of Holes With Variable Density Ratio,'' ASME J. Turbomach., **113**, pp. 442–449.
[3] Pedersen, D. R., Eckert, E. R. G., and Goldstein, R. J., 1977, ''Film Cooling With Large Density Differences Between the Mainstream and the Secondary Fluid Measured by the Heat–Mass Transfer Analogy,'' ASME J. Heat Transfer, **99**, pp. 620–627.
[4] Foster, N. W., and Lampard, D., 1980, ''The Flow and Film Cooling Effectiveness Following Injection Through a Row of Holes,'' ASME J. Eng. Power, **102**, pp. 584–588.
[5] Goldstein, R. J., Jin, P., and Olson, R. L., 1999, ''Film Cooling Effectiveness and Mass/Heat Transfer Coefficient Downstream of One Row of Discrete Holes,'' ASME J. Turbomach., **121**, pp. 225–232.
[6] Goldstein, R. J., Eckert, E. R. G., Eriksen, V. L., and Ramsey, J. W., 1970, ''Film Cooling Following Injection Through Inclined Circular Tubes,'' Isr. J. Technol., **8**, pp. 145–154.
[7] Honami, S., Shizawa, T., and Uchiyama, A., 1994, ''Behavior of the Laterally Injected Jet in Film Cooling: Measurements of Surface Temperature and Velocity/Temperature Field Within the Jet,'' ASME J. Turbomach., **116**, pp. 106–112.
[8] Lee, S. W., Kim, Y. B., and Lee, J. S., 1997, ''Flow Characteristics and Aerodynamic Losses of Film-Cooling With Compound Angle Orientations,'' ASME J. Turbomach., **119**, pp. 310–319.
[9] Ligrani, E. M., Wigle, J. M., and Jackson, S. W., 1994, ''Film-Cooling From Holes With Compound Angle Orientations: Part II — Results Downstream of a Single Row of Holes With 6d Spanwise Spacing,'' ASME J. Heat Transfer, **116**, pp. 353–362.
[10] Sen, B., Schrnidt, D. L., and Bogard, D. G., 1996, ''Film Cooling With Compound Angle Holes — Heat Transfer,'' ASME J. Turbomach., **118**, pp. 800–806.
[11] Schmidt, D. L., Sen, B., and Bogard, D. G., 1996, ''Film Cooling With Compound Angle Holes—Adiabatic Effectiveness,'' ASME J. Turbomach., **118**, pp. 807–813.
[12] Ekkad, S. V., Zapata, D., and Han, J.-C., 1997b, ''Heat Transfer Coefficient Over a Flat Surface With Air and CO_2 Injection Through Compound Angle Holes Using a Transient Liquid Crystal Image Method,'' ASME J. Turbomach., **119**, pp. 580–586.
[13] Ekkad, S. V., Zapata, D., and Han, J.-C., 1997a, ''Film Effectiveness Over a Flat Surface With Air and CO_2 Injection Through Compound Angle Holes Using a Transient Liquid Crystal Image Method,'' ASME J. Turbomach., **119**, pp. 587–593.
[14] Vendula, R. J., and Metzger, D. E., 1991, ''A Method for the Simultaneous Determination of Local Effectiveness and Heat Transfer Distributions in Three-Temperature Convection Situations, '' ASME Paper No. 91-GT-345.
[15] Cho, H. H., Kim, B. G., and Rhee, D. H., 1998, ''Effects of Hole Geometry on Heat (Mass) Transfer and Film Cooling Effectiveness,'' *Proc. 11th IHTC*, **6**, pp. 499–504.
[16] Seager, D. J., and Liburdy, J. A., 1998, ''Film Cooling Heat Transfer: Shaped

and Compound Angle Hole Injection,'' ASME Paper No. 98-GT-134.
[17] Eckert, E. R. G., 1984, ''Analysis of Film Cooling and Full-Coverage Film Cooling of Gas Turbine Blades, '' ASME J. Eng. Gas Turbines Power, **106**, pp. 206–213.
[18] Goldstein, R. J., and Cho, H. H., 1995, ''A Review of Mass Transfer Measurements Using Naphthalene Sublimation, '' Exp. Therm. Fluid Sci., **8**, pp. 416–434.
[19] Goldstein, R. J., and Taylor, J. R., 1982, ''Mass Transfer in the Neighborhood of Jets Entering Crossflow,'' ASME J. Heat Transfer, **104**, pp. 715–721.
[20] Cho, H. H., and Goldstein, R. J., 1995, ''Heat (Mass) Transfer and Film Cooling Effectiveness With Injection Through Discrete Holes. I. Within Holes and on the Back Surface,'' ASME J. Turbomach., **117**, pp. 440–450.
[21] Cho, H. H., and Goldstein, R. J., 1995, ''Heat (Mass) Transfer and Film Cooling Effectiveness With Injection Through Discrete Holes. II. On the Exposed Surface,'' ASME J. Turbomach., **117**, pp. 451–460.
[22] Jin, P., 1998, ''Film Cooling Effectiveness and Mass-Heat Transfer Coefficient Downstream of One Row of Discrete Holes With 45° Compound Angle,'' Master's Thesis, University of Minnesota, Minneapolis, MN.
[23] Coleman, H. W., and Steele, W. G. S. J., 1989, *Experimentation and Uncertainty Analysis for Engineers*, Wiley, New York.

Scaling of Performance for Varying Density Ratio Coolants on an Airfoil With Strong Curvature and Pressure Gradient Effects

Marcia I. Ethridge
J. Michael Cutbirth
David G. Bogard

Mechanical Engineering Department,
The University of Texas at Austin,
Austin, TX 78712

An experimental study was conducted to investigate the film cooling performance on the suction side of a first-stage turbine vane. Tests were conducted on a nine times scale vane model at density ratios of DR=1.1 and 1.6 over a range of blowing conditions, 0.2 ≤M≤1.5 and 0.05≤I≤1.2. Two different mainstream turbulence intensity levels, Tu_∞ =0.5 and 20 percent, were also investigated. The row of coolant holes studied was located in a position of both strong curvature and strong favorable pressure gradient. In addition, its performance was isolated by blocking the leading edge showerhead coolant holes. Adiabatic effectiveness measurements were made using an infrared camera to map the surface temperature distribution. The results indicate that film cooling performance was greatly enhanced over holes with a similar 50 deg injection angle on a flat plate. Overall, adiabatic effectiveness scaled with mass flux ratio for low blowing conditions and with momentum flux ratio for high blowing conditions. However, for M<0.5, there was a higher rate of decay for the low density ratio data. High mainstream turbulence had little effect at low blowing ratios, but degraded performance at higher blowing ratios.
[DOI: 10.1115/1.1343457]

Introduction

The most common method for cooling turbine vanes and blades is discrete hole film cooling. Film cooling has been studied using a wide range of geometries, including flat plates, curved channels, and cylinders. These studies have been successful for isolating effects of pressure gradients, wall curvature, hole geometry, density ratio, and mainstream turbulence. However, a complete simulation of the combined effects requires use of an airfoil model. For turbine blades and vanes, regions such as the showerhead and the near suction side have distinct differences. One difference is the positioning of the region with the strongest curvature. For a turbine blade, the strongest curvature exists at the geometric leading edge, which also incorporates the stagnation streamline, yielding a low-Reynolds-number flow. This is contrasted with a vane in which the strongest curvature exists on the suction side of the stagnation line at a much higher Reynolds number flow.

Suction side turbine vane film cooling studies have been performed by Ames [1] with an adverse pressure gradient, Mehendale et al. [2] with a very mild favorable pressure gradient, and Lander et al. [3] with a strong favorable pressure gradient. All three of these studies were performed far downstream of the leading edge in a region with low convex curvature. In contrast, Ito et al. [4] presented results from a single row of coolant holes subject to strong convex curvature but zero pressure gradient, and Drost and Bölcs [5] present results from a single and double row of coolant holes, but subject to neither strong convex curvature nor strong pressure gradient. Studies by Abauf et al. [6] and Drost and Bölcs [7] both employ film cooling stations in regions with both high curvature and strong favorable pressure gradients. However, these studies used showerhead injection combined with coolant injection from the suction side holes.

For the present study, a turbine vane geometry was used, and the focus of the study was on the first row of coolant holes on the suction side of this vane. This row of holes was located in a region of very strong curvature and a strongly accelerating pressure gradient. Showerhead holes on the vane were blocked to isolate the adiabatic effectiveness performance of the suction side coolant holes. The unique location of these film cooling holes in a region of high acceleration and curvature for the current study does not allow for any direct comparison with previous studies. However, a number of studies have been made of the separate effects on film cooling of large pressure gradients and surface curvature. Relevant results from these previous studies are reviewed below.

The prevalent effect of a strong favorable pressure gradient on the adiabatic effectiveness is to extend the range of momentum flux ratios for which the coolant jet will remain attached or reattach downstream. This effect was seen in studies by Schmidt and Bogard [8] and Teekaram et al. [9]. Both studies indicate that for momentum flux ranges in which the jet is fully attached ($I<0.2$) or fully detached ($I>1.2$), the differences in the adiabatic effectiveness between the zero pressure gradient and nonzero pressure gradient are within the experimental uncertainty. However, for the range in which the jet is beginning to detach from the surface, the adiabatic effectiveness is 20–30 percent greater for the strong favorable pressure gradient at $x/d=3$. These levels of adiabatic effectiveness decay at a rate such that the increased effectiveness is negligible by $x/d=10$.

Curvature studies have been performed at the University of Minnesota by Ito et al. [4], Goldstein and Stone [10], and Schwarz et al. [11] for a range of curvatures, $46<2r/d<126$, with zero pressure gradient. These studies indicated that an increased convex curvature (decreasing $2r/d$) greatly enhances adiabatic effectiveness. Ito et al. [4] found that a convex curvature of $2r/d=46$ increased the maximum adiabatic effectiveness by more than a factor of two. The improved performance for a convex wall is due to a wall normal pressure gradient, which tends to keep the coolant jet attached to the wall for higher momentum flux ratios, and broadens the coolant distribution by pressing the jet to the wall.

Studies of high mainstream turbulence effects on film cooling, such as those of Campbell and Moffat [12] using a convex surface

Contributed by the International Gas Turbine Institute and presented at the 45th International Gas Turbine and Aeroengine Congress and Exhibition, Munich, Germany, May 8–11, 2000. Manuscript received by the International Gas Turbine Institute February 2000. Paper No. 2000-GT-239. Review Chair: D. Ballal.

with $2r/d=87$ and zero pressure gradient, and Ames [1] using the pressure side of a turbine vane, indicate 20–30 percent reduction of adiabatic effectiveness near the hole with high turbulence. This effect is more pronounced at low momentum flux ratios ($I<0.4$), where fully attached jets are expected. However, for high momentum flux ratios ($I>0.9$), where partially detached jets are expected, the adiabatic effectiveness is within 5 percent for both high and low turbulence levels. Ames [1] also indicated that for the suction side of the turbine vane with an adverse pressure gradient and elevated turbulence levels near the hole, the adiabatic effectiveness is enhanced 15–20 percent. Furthermore, both Campbell and Moffat [12] and Ames [1] indicate a faster rate of decay, 15–25 percent and 5–10 percent, respectively, of the adiabatic effectiveness at high turbulence levels.

Radomsky and Thole [13] examined the effect of high freestream turbulence on vane heat transfer using a turbine vane with identical geometric specifications to that of the current study. Results indicated that at the location of this study, the boundary layer is laminar for both low and high mainstream turbulence.

The current study presents data for the suction side film cooling of a turbine vane with 50 deg cylindrical holes subjected to a highly curved, highly accelerated flow. The results have been presented as spatially resolved, spanwise averaged, and centerline adiabatic effectiveness plots for various blowing ratios, turbulence levels of $Tu_\infty=0.5$ and 20 percent, and density ratios of $DR=1.1$ and 1.6. Particular attention is given to whether there is a matching of effectiveness performance for large and near-unity density ratio coolant when operating with similar mass flux ratio or momentum flux ratio.

Facilities and Experimental Techniques

The test facility consisted of a closed-loop, low-speed wind tunnel with the test section occupying one corner of the tunnel. A secondary flow loop was used to draw air from the main wind tunnel, pass the air through finned-tube heat exchangers, and drive this cooled air into interior plenums in the airfoil model. Liquid nitrogen was used as the coolant for the heat exchangers.

The test section, shown in Fig. 1, was a linear cascade, which consisted of three vane leading edges and two main passage flows. The correct flow through the two main passages was obtained by carefully adjusting flow rates through two bypass passages on the outside of the inner and outer airfoils so that the stagnation points on the inner and outer leading edges were correctly positioned. Furthermore, a movable outside wall on the pressure side of the outer leading edge and a movable tailboard allowed for proper positioning of the stagnation streamline on the central vane, where all adiabatic effectiveness measurements were made. This resulted in a uniformity of the velocity profile between the two passages within 0.4 percent. The test airfoil consists of two separable parts, a removable front section and a permanent trailing edge, allowing for research on different leading edge configurations.

The front section used in this study consisted of a low thermally conductive polyurethane foam representing a nine times scale advanced commercial first-stage turbine vane, seen in Fig. 2. Internal coolant flow in the front section was divided into three regions: the stagnation region, the pressure side, and the suction side.

The wall of the front section was 12.7 mm thick, simulating the appropriate film cooling hole length-to-diameter ratio for an actual vane. Impingement plates were installed inside the airfoil to correctly simulate the actual inlet flow to the cooling holes. Each impingement plate consisted of a nominally 1-mm-thick stainless steel plate fixed into place with a 5.5 mm gap between the impingement plate and the inner airfoil wall. The impingement plates had a full array of 7.8-mm-dia holes with the same pitch-to-diameter ratio as the cooling holes. In the vicinity of the film cooling holes, the impingement holes were located between the entrances to the film cooling holes. A full description of the airfoil and the test facility is given by Polanka et al. [14].

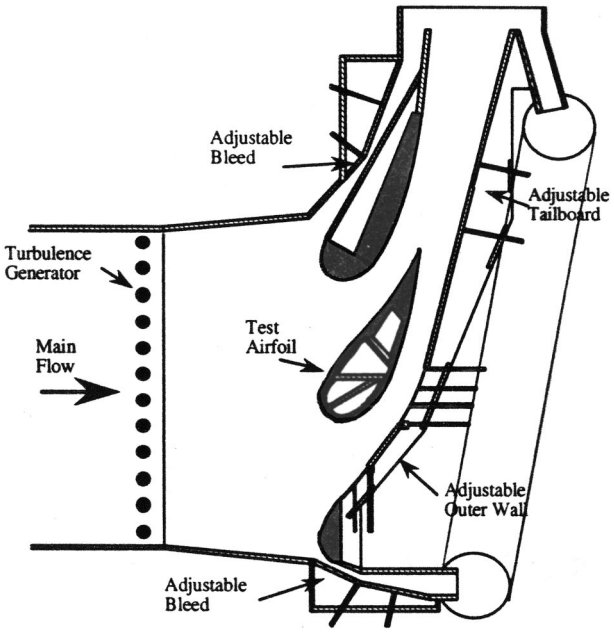

Fig. 1 Turbine vane facility

As shown in Fig. 2, the coolant holes for the suction side of the vane consisted of three rows of holes located at $30d$, $53d$, and $84d$ downstream from the stagnation line. For these tests, the showerhead film cooling holes were taped over. This study focused on the first row of holes on the suction side located at $30d$ downstream of the stagnation line. These holes had a diameter of $d=4.11$ mm with a pitch between holes of $p/d=5.6$ and were directed streamwise at a 50 deg injection angle with respect to the local surface. This section of the airfoil had a curvature of $2r/d=26$ at the coolant holes ($x/d=0$), decreasing to a curvature of $2r/d=53$ at a location $20d$ downstream of the holes. The pressure distribution around the airfoil is shown in Fig. 3. This pressure distribution shows that at the position of the cooling holes ($x/c=0.21$), there was an extremely strong acceleration of the mainstream with a nondimensional acceleration parameter of $K=8\times10^{-6}$ at the coolant holes, decreasing to $K=1.5\times10^{-6}$ by $20d$ downstream of the holes.

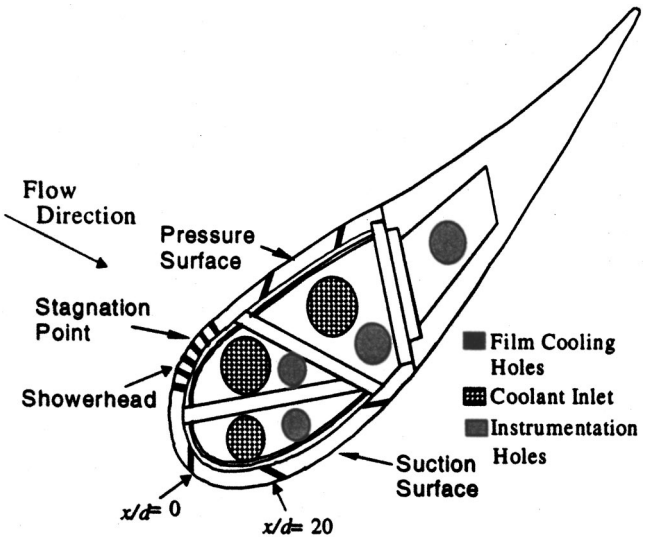

Fig. 2 Test airfoil

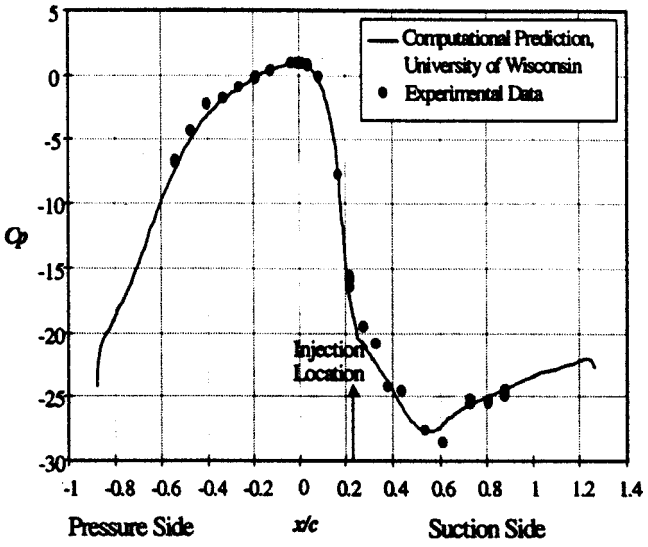

Fig. 3 Turbine vane pressure distribution

Surface instrumentation included pressure taps and thin ribbon thermocouples. The arrays of pressure taps were used to ensure that the proper pressure distribution around the airfoil was set by the adjustable outer wall. The thermocouples were used to calibrate the infrared camera and monitor operating temperatures. An Inframetries 600L infrared camera system was used to acquire the surface temperature distributions. Details of the data processing can be found in Witteveld et al. [15]. The resolution of the camera for these experiments was $0.6d \times 0.6d$, and the uncertainties of the surface temperatures were determined to be ± 0.3 K at $DR=1.1$ and ± 2.0 K at $DR=1.6$. A hot-wire anemometer was used to measure the mainstream characteristics, including turbulence intensity, spectra, and integral time scale.

The adiabatic effectiveness, defined in Eq. (1), was calculated by using the surface temperature, ejected coolant temperature, and the mainstream temperature. The uncertainty in effectiveness (95 percent confidence interval) was $\partial\eta = \pm 0.04$ for $\eta > 0.4$, $\partial\eta = \pm 0.02$ for $\eta < 0.4$, and $\partial\overline{\eta} = \pm 0.02$ for all $\overline{\eta}$. For $M < 1.3$, the uncertainty in blowing ratio is $\partial M = \pm 0.03$, while for $M > 1.3$ it is $\partial M = \pm 0.05$.

$$\eta \equiv (T_\infty - T_{aw})/(T_\infty - T_j) \tag{1}$$

Although the vane model was constructed of a low thermally conductive material, there was some conduction through the wall of the vane. A one-dimensional correction was applied to the adiabatic effectiveness data to account for this bias error. Midpitch values from a case with very low blowing were used to correct the data as follows:

$$\eta_{aw} = (1/(1-\eta_0))(\eta_{\text{meas}} - \eta_0) \tag{2}$$

where η_{aw} is the true effectiveness, η_0 is the conduction error and η_{meas} is the measured effectiveness. The value of η_0 was $0.05 \leqslant \eta_0 \leqslant 0.09$ for the low turbulence case and $0.02 \leqslant \eta_0 \leqslant 0.07$ with high turbulence.

The overall mass flow rate through the suction plenum was measured using a sharp-edged orifice meter. Although this overall mass flow rate was known, due to the presence of multiple rows, the mass flow rate through each individual row was unknown. Furthermore, due to the dependence of the discharge coefficient on the hole geometry and the pressure ratio between the plenum and external pressures, as well as the complex flow in the internal plenum, a simple discharge coefficient study was not attainable. However, at a given temperature, the flow rate exiting a single row of holes is dependent only on the plenum pressure. For this reason, two experiments were performed. The first measured the plenum pressure at a given flow rate with only the desired row of holes opened. This allowed for a relationship between the plenum pressure and the flow rate through a single row of holes. The second experiment measured the plenum pressure at a given total flow rate to the cooling plenum with all rows of holes open. This allowed for a relationship between the plenum pressure and the total flow rate. Combining these results yielded a relationship between the total flow rate and the flow rate exiting the single row of holes. Therefore, the mass flux ratio was determined using the flow rate exiting the single row of holes and the local mainstream velocity given by the measured pressure distribution.

Film cooling effectiveness experiments were conducted at a low mainstream turbulence level, $Tu_\infty = 0.5$ percent, and a very high turbulence level, $Tu_\infty = 20$ percent. The high turbulence level was generated by 12 vertical 3.8-cm-dia cylinders spaced 8.5 cm diameters apart and positioned 50.5 cm (13.3 rod diameters) upstream of the vane leading edge. The resulting turbulence intensity was $u_{\text{rms}}/U_\infty = 0.20$ at 8.5 cm ($0.14c$) upstream of the leading edge. At this position, the integral length scale was measured to be $\Lambda_f = 4.2$ cm or $\Lambda_f/d = 10$ (based on the convected length of integral time scales obtained from autocorrelation of U measurements with a hot-wire probe). Due to concern that a homogeneous and isotropic turbulence field had been developed at this relatively short distance from the cylinder array, characteristics of the turbulence field were thoroughly measured. Measurement of all three rms velocity components showed that the turbulence was reasonably isotropic. Spectra measurements of the streamwise component also showed a typical turbulence spectral distribution, with no energy spikes present at specific frequencies that would indicate vortex shedding from the cylinder array. More details of the validation of the turbulence field were presented in Polanka et al. [16,17].

Experiments used an approach velocity of $U_\infty = 5.8$ m/s. Tests were performed at two density ratios, $DR = 1.1$ and 1.6, and a range of momentum flux ratios, $I = 0.05-1.2$. The exit Reynolds number, based on the true chord length of $c = 59.4$ cm, was $\text{Re} = 1.2 \times 10^6$, which was typical for actual operating conditions of this vane. Boundary layer measurements by Radomsky [18] for an identical vane geometry and flow conditions showed that the boundary layer thickness approaching the film cooling holes would be expected to be $\delta = 0.6$ mm for low turbulence conditions and $\delta = 0.7$ mm for high mainstream turbulence conditions. Consequently the boundary layer thickness relative to the hole diameter was $\delta/d < 0.17$, which was a very thin boundary layer compared to most film cooling studies on flat plates.

Results

The film cooling performance of the suction side has been evaluated using measurements of adiabatic effectiveness. All tests were conducted with no showerhead film cooling, and with the showerhead holes taped over. In presenting these results we compare the adiabatic effectiveness performance with the performance for film cooling on flat and curved surfaces as found in previous studies. This is followed by analysis of the effects of coolant density ratio and mainstream turbulence on the vane suction side film cooling performance.

General Performance. Laterally averaged or spanwise averaged effectiveness values are presented for a range of blowing conditions at a density ratio of $DR = 1.1$ in Fig. 4. This figure illustrates three different regions of coolant jet performance. At low blowing ratios, $M < 0.3$, the effectiveness values are very low. The peak value near the hole is less than $\overline{\eta} = 0.2$ and decays very rapidly with downstream distance, reaching a value of $\overline{\eta} < 0.03$ for $15 \leqslant x/d \leqslant 20$. When the blowing ratio is increased from $M = 0.3$ to $M = 0.4$, however, there is a large increase in effectiveness near the hole, with the peak effectiveness increasing to about $\overline{\eta} = 0.27$ just downstream of the hole.

Peak laterally averaged effectiveness values immediately down-

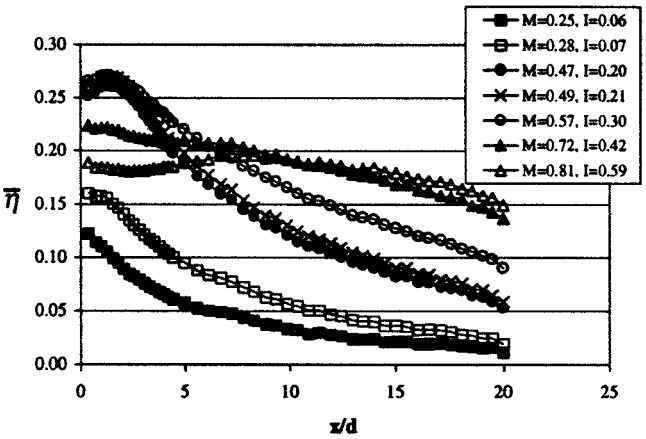

Fig. 4 Lateral average effectiveness, $Tu_\infty = 0.5$ percent, $DR = 1.1$

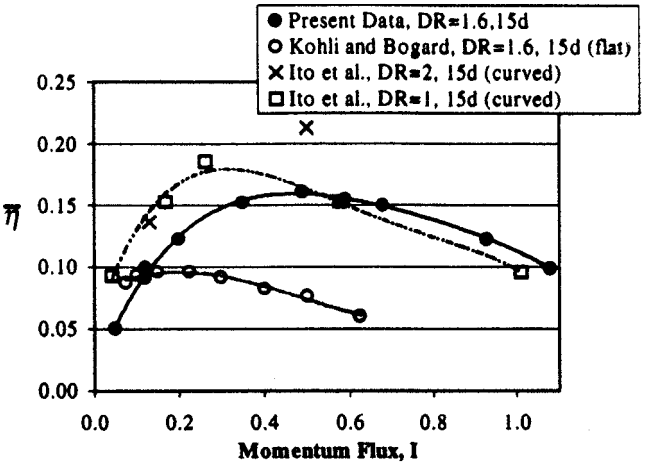

Fig. 6 Comparison of laterally averaged effectiveness with previous flat plate and curved wall studies at $x/d = 15$ and $Tu_\infty = 0.5$ percent

stream of the holes occurred for a blowing ratio $M = 0.6$ ($I = 0.3$). For $M > 0.6$, the effectiveness values decreased in the near hole region, but increased downstream. By $M = 0.8$ ($I = 0.6$), there was a slight dip in effectiveness about $2d$ from the trailing edge of the hole, then a recovery followed by a decay in effectiveness beyond $x/d = 7$. These results suggest that significant jet detachment occurred for $I > 0.6$, but reattachment caused a recovery of effectiveness farther downstream.

Results for laterally averaged effectiveness values for large density ratio conditions, $DR = 1.6$, are presented in Fig. 5. Comparing the general characteristics of these $\overline{\eta}$ distributions with that for $DR = 1.1$, essentially the same performance characteristics are evident. Near the hole, peak adiabatic effectiveness occurred at a blowing ratio of $M = 0.5$ ($I = 0.14$), a similar blowing ratio to the $DR = 1.1$ case. Decreases in $\overline{\eta}$ near the hole, presumably due to jet separation, become significant for momentum flux ratios greater than $I = 0.6$, again similar to the $DR = 1.1$ case.

The performance of the current geometry was compared with previous flat and curved surface studies in terms of the $\overline{\eta}$ distribution versus I at several different x/d locations. Comparisons at an intermediate distance downstream of the hole, $x/d = 15$, are shown in Fig. 6. Flat plate performance is taken from Kohli and Bogard [19] who used streamwise directed holes with a 55 deg injection angle on a flat plate with zero pressure gradient. Curved surface results are taken from Ito et al. [4] who used a convex curvature of $2r/d = 46$ at the hole injection point (compared to $2r/d = 26$ for the present vane geometry), zero pressure gradient and 35 deg injection. Results from Goldstein and Stone [10] indicate that varying the injection angle from 25 to 45 deg has little effect on performance on a curved surface, so differences in injection angle are not expected to significantly affect the comparison. Laterally averaged effectiveness results from Kohli and Bogard and Ito et al. were adjusted to account for different hole spacing. This is based on results from Schmidt et al. [20], who showed that increasing the spacing between holes by a factor of two causes a factor of two decrease in $\overline{\eta}$ values.

The current results show significantly higher $\overline{\eta}$ than for flat plate flows, but are similar to curved surface performance. Based on this, and recalling the studies that show pressure gradients do not increase $\overline{\eta}$ significantly (discussed in the Introduction), the large increase in $\overline{\eta}$ is attributed primarily to the surface curvature. The momentum flux ratio at which maximum $\overline{\eta}$ occurs near the hole shifts from $I = 0.1$ for the flat plate to $I = 0.2$ for the current vane geometry. This shift is consistent with the expected effect of a highly curved surface as seen in previous studies, e.g., Schwarz et al. [11].

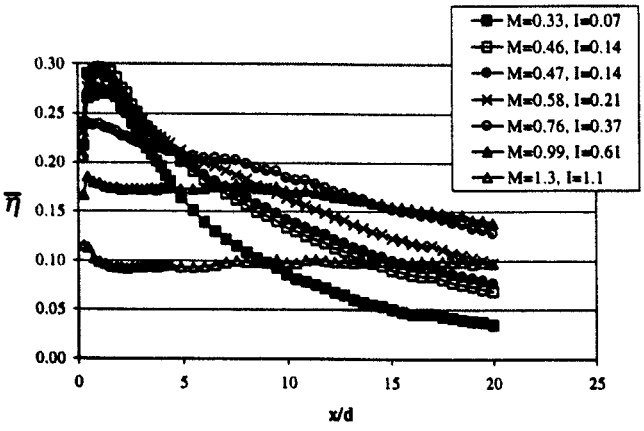

Fig. 5 Lateral average effectiveness, $Tu_\infty = 0.5$ percent, $DR = 1.6$

Effects of Density Ratio. To determine the appropriate scaling parameter for adiabatic effectiveness performance with varying density ratios, distributions of η_c and $\overline{\eta}$ values for small and large density ratios were compared as functions of momentum flux ratio and mass flux (blowing) ratio. Figures 7(*a*) and 7(*b*) show distributions of η_c, and Figs. 7(*c*) and 7(*d*) show distributions of $\overline{\eta}$. In each case, distributions are shown for a position relatively close to the hole, $x/d = 3$, and for a distance moderately far downstream, $x/d = 15$. Although neither M nor I give a complete matching of adiabatic effectiveness for small and large density ratio, there are ranges in which reasonable agreement is obtained. For low blowing ratios, $M < 0.7$, reasonable matching of performance occurs with matched M. One exception to this is for $M < 0.3$ where the $DR = 1.1$ coolant has significantly lower adiabatic effectiveness than the $DR = 1.6$ coolant. For high blowing ratios, $I > 0.4$, reasonable matching of performance occurs with matched I. These results are consistent with expectations since better scaling with M should occur at blowing ratios low enough that the coolant jets remain attached to the surface, while better scaling with I should occur when the jet begins to detach [21].

Similar scalings with M at low blowing ratios, and with I at high blowing ratios, were found for the high mainstream turbulence conditions (not shown). These results are discussed in more detail in the next section.

Although adiabatic effectiveness performance was nominally comparable for small and large density ratio when compared appropriately with either matched M or I, distinct differences were

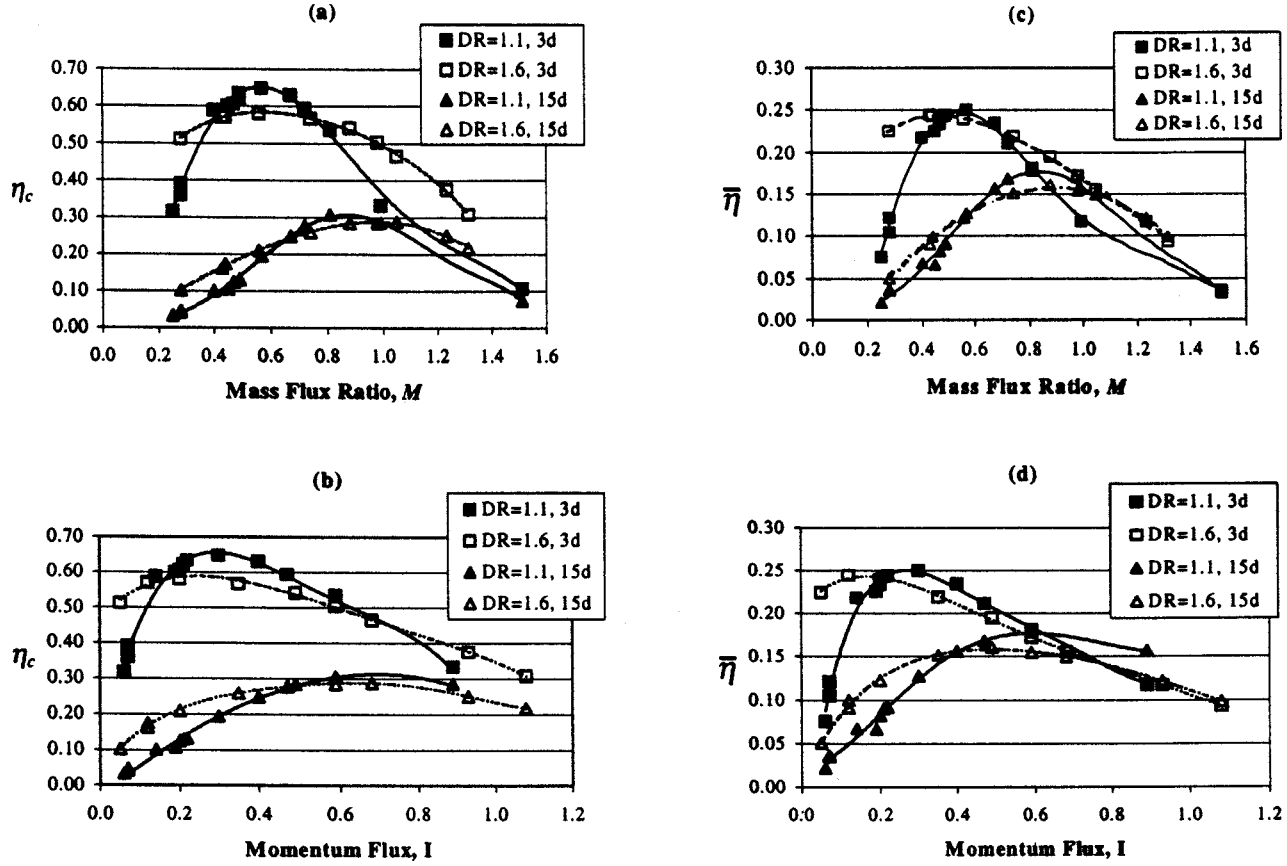

Fig. 7 Correlation of centerline effectiveness with: (*a*) *M* and (*b*) *I*, and laterally averaged effectiveness with (*c*) *M* and (*d*) *I*, for *DR*=1.1 and 1.6; Comparisons at *x*/*d*=3 and 15 with Tu_∞=0.5 percent

apparent in the spatial distribution of η for low blowing ratios. An example of this is evident in contour plots of η for small and large density ratios at $M=0.44$ as shown in Figs. 8(*a*) and 8(*b*). Besides the greater streamwise decay for $DR=1.1$, these contours show a broader, essentially flat peak for the $DR=1.1$ case. This flat and occasionally double peak pattern for the $DR=1.1$ case was found to be repeatable for $M<0.5$, but did not appear for the $DR=1.6$ case. The pattern suggests the existence of relatively strong trailing vortices, which tend to broaden the low density coolant jets and draw coolant from the centerline toward the edges of the jet. The resulting dispersal of the core of the coolant jet would account for the greater decay rate for the $DR=1.1$ case for $M<0.5$ evident in Fig. 7(*c*).

Effects of Mainstream Turbulence. The mainstream turbulence at a position immediately upstream of the turbine vane was $Tu_\infty=20$ percent for the high turbulence condition. However, due to the acceleration of the mainstream, the relative turbulence in-

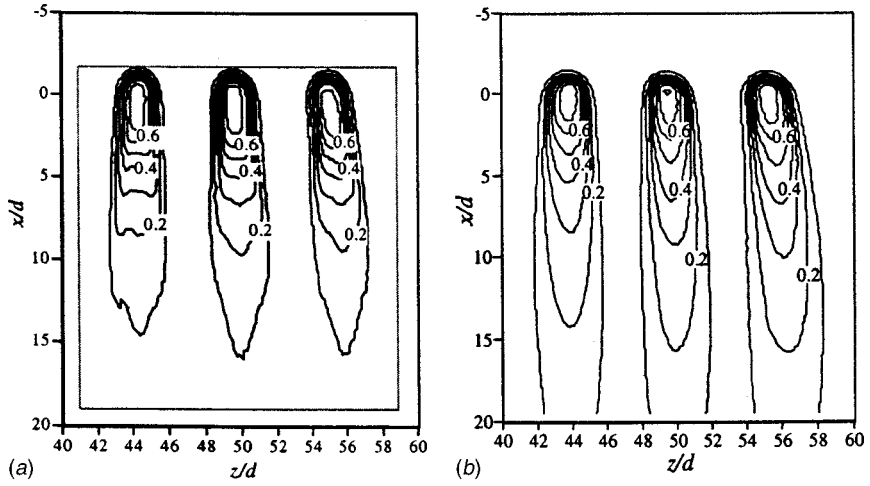

Fig. 8 Contour plots of local adiabatic effectiveness: (*a*) *DR*=1.1, *M*=0.45 (*I*=0.19), Tu_∞=0.5 percent; (*b*) *DR*=1.6, *M*=0.44 (*I*=0.12), Tu_∞=0.5 percent

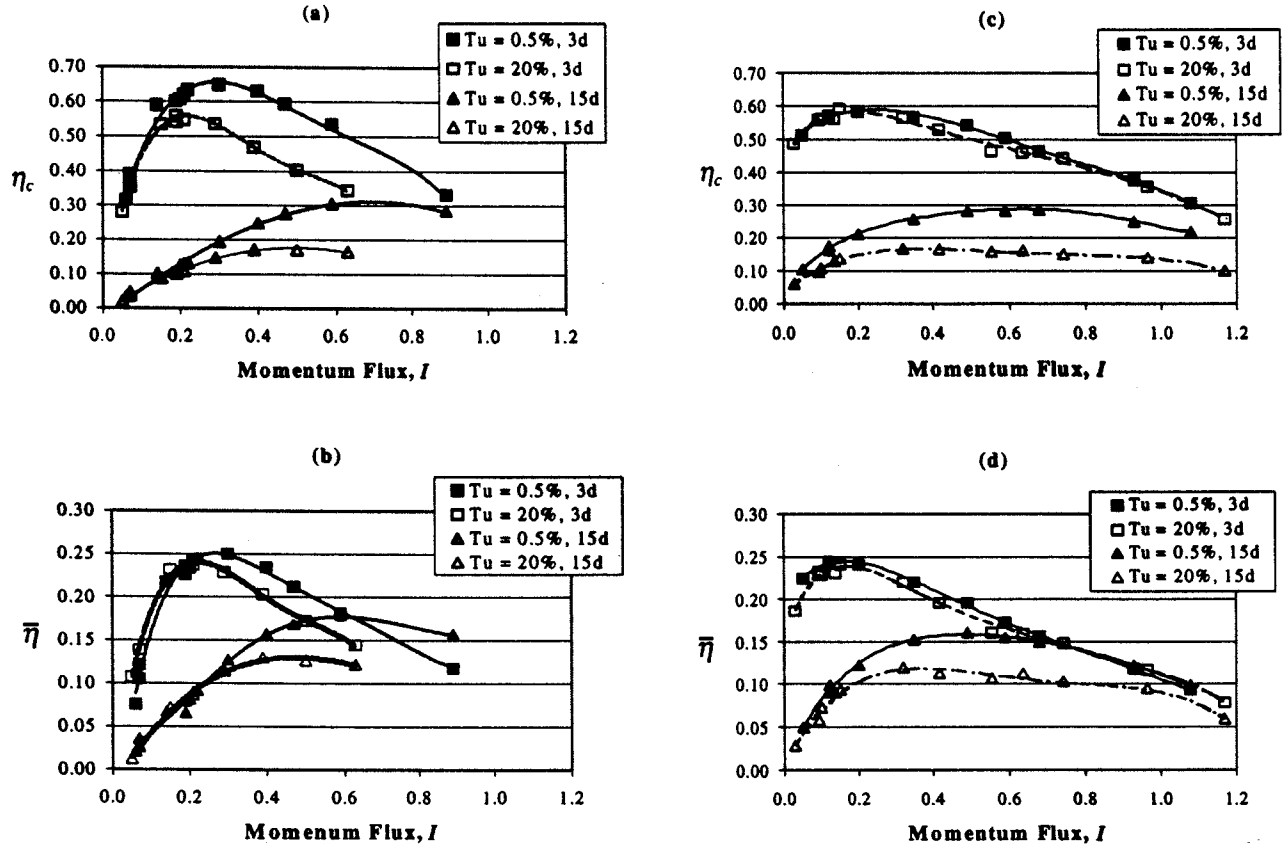

Fig. 9 Comparison of adiabatic effectiveness for low ($Tu_\infty = 0.5$ percent) and high ($Tu_\infty = 20$ percent) mainstream turbulence levels at $x/d = 3$ and 15: (*a*) and (*b*) for $DR = 1.1$, and (*c*) and (*d*) $DR = 1.6$

tensity ($\sqrt{2/3k}/U$) level at the location of the first suction side film cooling holes decreased substantially. Based on the turbulence kinetic energy measurements of Radomsky and Thole [22] using the same turbine vane geometry, and accounting for the increased mainstream velocity, the mainstream turbulence intensity at the cooling holes was $Tu_\infty = 5$ percent, reducing to $Tu_\infty = 4$ percent by $20d$ downstream. Radomsky and Thole also showed that, although high mainstream turbulence caused the suction side boundary layer to transition from laminar to turbulent much earlier, the boundary layer remained laminar at $x/c = 0.2$, i.e., the position of the film cooling holes. Furthermore, recent boundary layer profile measurements by Radomsky [18] showed that the boundary layer thickness at the location of the film cooling holes varied very little between the low and high mainstream turbulence conditions.

The effects of turbulence on the film cooling performance are presented in Figs. 9(*a*) and 9(*b*) for $DR = 1.1$ and Figs. 9(*c*) and 9(*d*) for $DR = 1.6$. In each case, distributions of η_c and $\overline{\eta}$ values are presented as a function of momentum flux ratio I for positions close to the hole and moderately far downstream. Close to the hole, $x/d = 3$, differences in mainstream turbulence caused essentially no difference in adiabatic effectiveness over the full range of I when using $DR = 1.6$ coolant. However, when using $DR = 1.1$ coolant, there was a noticeable decrease in η_c for the high turbulence case for conditions when $I > 0.2$. This difference highlights one of the few conditions for which scaling of the density ratio effects was not achieved, i.e., η_c distributions close to the hole for higher blowing ratios did not match with either M or I. Farther downstream, at $x/d = 15$, both $DR = 1.1$ and $DR = 1.6$ tests were consistent in showing little effects due to changes in mainstream turbulence for $I < 0.2$, but as much as a 30 percent decrease in adiabatic effectiveness due to high mainstream turbulence for higher blowing ratios.

The lack of an effect due to higher mainstream turbulence for $I < 0.2$ indicates that the higher mainstream turbulence does not influence adiabatic effectiveness when the coolant jets remain attached to the surface. This result is contrary to effects of high mainstream turbulence on flat plate film cooling found by Schmidt and Bogard [23] for mainstream turbulence levels of $Tu = 10$ and 20 percent, but consistent with the results of Drost et al. [24] for turbulence levels of $Tu = 8$ percent. Given these previous flat plate results, it is possible that the lack of influence of high mainstream turbulence for $I < 0.2$ is due to the lower local turbulence levels of $Tu = 5$ percent rather than pressure gradient or surface curvature effects. However, the differences among the studies are too numerous to make any definitive conclusions.

For higher blowing ratios, the decrease in adiabatic effectiveness downstream for the high mainstream turbulence conditions was consistent with the dispersion effects observed in previous studies. However, Schmidt and Bogard [23] and Drost et al. [24] both found an increase in adiabatic effectiveness for $I > 0.9$. Such an increase in adiabatic effectiveness was not evident in this study at momentum flux ratios as high as $I = 1.1$. The increase in adiabatic effectiveness found in previous flat plate studies was attributed to turbulent dispersion convecting some coolant back to the surface from coolant streams, which were detached from the surface. It is possible that for highly curved surfaces these detached coolant streams advect much farther from the surface so that high turbulence eddies are less effective in returning the coolant to the surface.

Conclusions

This study was conducted to investigate the film cooling performance on the suction side of a first-stage turbine vane. The performance of the first row of cooling holes on the suction side

was isolated by blocking the leading edge showerhead coolant holes. Experiments were conducted with both low and high density ratios and low and high levels of mainstream turbulence. A unique aspect of this study was that the holes were located in a position where there was a very strong curvature and a strong favorable pressure gradient. Consequently, the adiabatic effectiveness performance for these holes was much higher than holes with a similar injection angle of 50 deg on a flat plate. This performance was similar to previous studies using curved walls with low pressure gradients.

Evaluating and contrasting performance with small and large density ratios allowed a determination of appropriate scaling parameters. For $M<0.7$, performance is matched when scaled with mass flux ratio M, while for $I>0.4$, momentum flux ratio I was a more appropriate scaling parameter. However, for $M<0.5$, there was a higher decay rate for the small density ratio, which did not match the large density ratio performance when scaled with either M or I.

Increasing mainstream turbulence to $Tu_\infty=20$ percent had no effect at low blowing ratios for which the coolant jets remained attached to the surface. At high blowing ratios for which the coolant jets were somewhat detached, high mainstream turbulence caused a decrease in adiabatic effectiveness. This decrease in performance is consistent with an increase in dispersion of the coolant jet by the mainstream. However, the increase in adiabatic effectiveness for $I>0.9$ observed by previous studies did not occur. We attribute this difference to our highly curved surface, which could prevent high turbulence eddies from advecting coolant back to the surface once the coolant jets are detached.

Acknowledgments

We are most grateful to the sponsors of this work, Advanced Gas Turbine Systems Research Consortium and Pratt & Whitney. We would also like to thank Pratt & Whitney for supplying the turbine vane geometry.

Nomenclature

c = turbine vane true chord length = 59.4 cm
Cp = pressure coefficient = $(2(P-P_0)/\rho U_\infty^2)$
d = hole diameter
DR = density ratio = ρ_j/ρ_∞
I = momentum flux ratio = $\rho_j U_j^2/\rho_\infty U_\infty^2$
K = acceleration parameter = $(\nu/\rho U_\infty^3)(dP/dx)$
M = blowing ratio based on average velocity from suction row and local mainstream velocity = $\rho_j U_j/\rho_\infty U_\infty$
p = hole-to-hole pitch
P = local pressure
P_0 = upstream static pressure
r = radius of curvature of the turbine vane surface
Re = Reynolds number
T = temperature
Tu = turbulence intensity
U = streamwise velocity
x = streamwise coordinate along the surface; $x=0$ at trailing edge of coolant holes
z = spanwise coordinate; $z=0$ at center of bottom coolant hole in suction row
δ^* = boundary layer displacement thickness
η = adiabatic effectiveness
$\overline{\eta}$ = laterally (spanwise) averaged adiabatic effectiveness
Λ_f = integral length scale
ν = kinematic viscosity
ρ = density

Subscripts

c = centerline; $z/d=50$
j = conditions of the coolant jet
aw = adiabatic wall
∞ = conditions of mainstream

References

[1] Ames, F. E., 1998, ''Aspects of Vane Film Cooling With High Turbulence: Part II—Adiabatic Effectiveness,'' ASME J. Turbomach., **120**, pp. 777–784.
[2] Mehendale, A. B., Han, J.-C., Ou, S., and Lee, C. P., 1994, ''Unsteady Wake Over a Linear Turbine Blade Cascade With Air and CO_2 Film Injection: Part II—Effect on Film Effectiveness and Heat Transfer Distributions,'' ASME J. Turbomach., **116**, pp. 730–737.
[3] Lander, R. L., Fish, R. W., and Suo, M., 1972, ''External Heat-Transfer Distribution on Film Cooled Vanes,'' J. Aircr., **9**, pp. 707–714.
[4] Ito, S., Goldstein, R. J., and Eckert, E. R. G., 1978, ''Film Cooling of a Gas Turbine Blade,'' ASME J. Eng. Power, **113**, pp. 476–481.
[5] Drost, U., and Bölcs, A., 1999, ''Investigation of Detailed Film Cooling Effectiveness and Heat Transfer Distributions on a Gas Turbine Airfoil,'' ASME J. Turbomach., **121**, pp. 233–242.
[6] Abuaf, N., Bunker, R., and Lee, C. P., 1997, ''Heat Transfer and Film Cooling Effectiveness in a Linear Airfoil Cascade,'' ASME J. Turbomach., **119**, pp. 302–309.
[7] Drost, U., and Bölcs, A., 1999, ''Performance of a Turbine Airfoil With Multiple Film Cooling Stations—Part 1: Heat Transfer and Film Cooling Effectiveness,'' ASME Paper No. 99-GT-171.
[8] Schmidt, D. L., and Bogard, D. G., 1995, ''Pressure Gradient Effects on Film Cooling,'' ASME Paper No. 95-GT-18.
[9] Teekaram, A. J. H., Forth, C. J. P., and Jones, T. V., 1991, ''Film Cooling in the Presence of Mainstream Pressure Gradients,'' ASME J. Turbomach., **113**, pp. 484–492.
[10] Goldstein, R. J., and Stone, L. D., 1994, ''Row-of-Holes Film Cooling of a Convex and a Concave Wall at Low Injection Angles,'' *Heat Transfer in Gas Turbines*, ASME HTD-Vol. 300, pp. 15–29.
[11] Schwarz, S. G., Goldstein, R. J., and Eckert, E. R. G., 1990, ''The Influence of Curvature on Film Cooling Performance,'' ASME J. Turbomach., **113**, pp. 472–478.
[12] Campbell, R. P., and Moffat, R. J., 1994, ''Discrete Hole Film Cooling on a Convex Wall: Heat Transfer and Hydrodynamics With Free Stream Turbulence,'' in: *Heat Transfer in Gas Turbines*, ASME HTD-Vol. 300, pp. 45–33 [sic].
[13] Radomsky, R. W., and Thole, K. A., 1998, ''Effects of High Freestream Turbulence Levels and Length Scales on Stator Vane Heat Transfer,'' ASME Paper No. 98-GT-236.
[14] Polanka, M. D., Cutbirth, J. M., and Bogard, D. G., 1999, ''Turbine Vane Facility,'' University of Texas Report TTCRL 99-1.
[15] Witteveld, V. C., Polanka, M. D., and Bogard, D. G., 1999, ''Film Cooling Effectiveness in the Showerhead Region of a Gas Turbine Vane—Part II: Stagnation Region and Near-Suction Side,'' ASME Paper No. 99-GT-49.
[16] Polanka, M. D., Witteveld, V. C., and Bogard, D. G., 1999, ''Film Cooling Effectiveness in the Showerhead Region of a Gas Turbine Vane—Part I: Stagnation Region and Near-Pressure Side,'' ASME Paper No. 99-GT-48.
[17] Polanka, M. D., Ethridge, M. I., Cutbirth, J. M., and Bogard, D. B., 2000, ''Effects of Showerhead Injection on Film Cooling Effectiveness of Downstream Rows of Holes,'' ASME Paper No. 2000-GT-240.
[18] Radomsky, R. W., 2000, ''High Freestream Turbulence Studies on a Scaled-Up Turbine Vane,'' Ph.D. Dissertation, The University of Wisconsin at Madison.
[19] Kohli, A., and Bogard, D. G., 1997, ''Adiabatic Effectiveness, Thermal Fields, and Velocity Fields for Film Cooling With Large Angle Injection,'' ASME J. Turbomach., **119**, pp. 352–358.
[20] Schmidt, D. L., Sen, B., and Bogard, D. G., 1996, ''Film Cooling With Compound Angle Holes: Adiabatic Effectiveness,'' ASME J. Turbomach., **118**, pp. 807–813.
[21] Sinha, A. K., Bogard, D. G., and Crawford, M. E., 1991, ''Film Cooling Effectiveness Downstream of a Single Row of Holes With Variable Density Ratio,'' ASME J. Turbomach., **113**, pp. 442–449.
[22] Radomsky, R. W., and Thole, K. A., 2000, ''Flowfield Measurements for a Highly Turbulent Flow in a Stator Vane Passage,'' ASME J. Turbomach., **122**, pp. 255–262.
[23] Schmidt, D. L., and Bogard, D. G., 1996, ''Effects of Free-Stream Turbulence and Surface Roughness on Film Cooling,'' ASME Paper No. 96-GT-462.
[24] Drost, U., Bölcs, A., and Hoffs, A., 1997, ''Utilization of the Transient Liquid Crystal Technique for Film Cooling Effectiveness and Heat Transfer Investigations on a Flat Plate and a Turbine Airfoil,'' ASME Paper No. 97-GT-26.

Aerodynamic Loss Characteristics of a Turbine Blade With Trailing Edge Coolant Ejection: Part 1—Effect of Cut-Back Length, Spanwise Rib Spacing, Free-Stream Reynolds Number, and Chordwise Rib Length on Discharge Coefficients

Oguz Uzol

Cengiz Camci

Turbomachinery Heat Transfer Laboratory,
The Pennsylvania State University,
University Park, PA 16802

Boris Glezer

Heat Transfer Team Leader,
Solar Turbines, Inc.,
San Diego, CA 92186

The internal fluid mechanics losses generated between the blade plenum chamber and a reference point located just downstream of the trailing edge are investigated for a turbine blade trailing edge cooling system. The discharge coefficient C_d is presented as a function of the free-stream Reynolds number, cut-back length, spanwise rib spacing, and chordwise rib length. The results are presented in a wide range of coolant to free-stream mass flow rate ratios. The losses from the cooling system show strong free-stream Reynolds number dependency, especially at low ejection rates, when they are correlated against the coolant to free-stream pressure ratio. However, when C_d is correlated against a coolant to free-stream mass flow rate ratio, the Reynolds number dependency is eliminated. The current data clearly show that internal viscous losses due to varying rib lengths do not differ significantly. The interaction of the external wall jet in the cutback region with the free-stream fluid is also a strong contributor to the losses. Since the discharge coefficients do not have Reynolds number dependency at high ejection rates, C_d experiments can be performed at a low free-stream Reynolds number. Running a discharge coefficient experiment at low Reynolds number (or even in still air) will sufficiently define the high blowing rate portion of the curve. This approach is extremely time efficient and economical in finding the worst possible C_d value for a given trailing edge coolant system.
[DOI: 10.1115/1.1348017]

Introduction

The current project deals with an investigation of aerodynamic discharge coefficients obtained for the trailing edge coolant ejection system of a turbine blade. Due to increasing turbine inlet temperatures, internal and external cooling of turbine nozzle vanes and rotor blades including trailing edge ejection is becoming increasingly popular in modern systems. Improvements of 3–5 percent in direct operating cost and 8–10 percent in fuel efficiency of future gas turbine engines are possible. There are currently at least three major reasons for continued strong interest in turbine cooling research. According to Metzger et al. [1], ''the first and the foremost reason is the enormous turbine inlet temperature potential of around 2000 °C (3700 °F) set by stoichiometric combustion and the fact that use of higher temperatures (and corresponding higher pressure ratios) improves performance.'' Second is the underlying nature of both hot gas and coolant flows as highly turbulent, unsteady, three-dimensional, and geometry-dependent flows that have not yet yielded to general solutions. Third, although new aerodynamic advances and new manufacturing techniques generate new conceptual changes, their time-efficient analysis and design implementation are still in their infancy. Despite well-publicized advances in material capability, the current maximum allowable component metal temperatures are still only about 1000 °C (1800 °F). The current maximum turbine inlet temperatures are presently around 1450 °C (2600 °F). The difference of 800 °F has been primarily achieved through dramatic improvements in turbine cooling methods. Although the initial idea of an uncooled transonic turbine passage is very attractive because of the elimination of coolant ejection related aerodynamic penalties, the current level of maximum allowable metal temperatures clearly eliminates this approach. Our continued benefit from elevated inlet temperatures is only possible by effectively using cooling systems internally and externally. Understanding the internal flow physics due to trailing edge coolant ejection in turbine passages and generating an applicable and reliable set of discharge coefficient distributions is the main goal of this paper.

Related Past Studies

Several past investigators have studied the influence of coolant ejection on aerodynamic losses in turbine passages, including McMartin and Norbury [2], Prust [3], Lokai and Kumirov [4], Lawaczek [5], and Sturedus [6]. General observations indicate that different ejection geometries were used by different investigators with varying experimental uncertainty levels and their results are

Contributed by the International Gas Turbine Institute and presented at the 45th International Gas Turbine and Aeroengine Congress and Exhibition, Munich, Germany, May 8–11, 2000. Manuscript received by the International Gas Turbine Institute February 2000. Paper No. 2000-GT-258. Review Chair: D. Ballal.

somewhat inconclusive. A general trend was the excessive use of relatively thick trailing edges. A consistent set of discharge coefficients evaluated as a function of coolant to free-stream ejection rate, cutback length, free-stream Reynolds number, and rib geometry used inside the trailing edge does not exist.

Aerodynamic losses due to pressure side coolant ejection in a transonic turbine cascade are described by Moses et al. [7]. Although the ejection is on the pressure side of the blade, their configuration can best be described as trailing edge ejection system discharging near the pressure side. Only aerodynamic results are presented for an exit Mach number range of 0.7–1.4. Their results for the blowing rate range from 0 to 1.7 showed that there was little effect of the coolant ejection on the flow field and on the aerodynamic losses. Their conclusion was consistent with that of Venediktov [8] who used similar geometry and blowing conditions. Coolant ejection into local supersonic flow strongly influences the aerodynamic losses in a turbine, Kiock et al. [9]. Three rows of holes near the leading edge and a trailing edge ejection system were considered. They observed that the roughness due to the ejection holes near the leading edge did not influence the blade boundary layer behavior. However, local ejection near the leading edge and near the throat affects the transition. Typical ejections near the suction side throat almost doubles the momentum thickness near the trailing edge. Part of the wake is filled with trailing edge cooling jets so that the energy content in the exit plane increases with increasing coolant flow rate and can exceed the mainstream energy level at the inlet. The aerodynamic mixing effect of discrete cooling jets with mainstream flow on a highly loaded turbine blade is presented in Wilfert and Fottner [10]. A single row of holes located at 40 percent chord on the suction side is studied. The hole spacing is about 2.5 times that of the hole diameter. The maximum free-stream turbulence level was about 6.5 percent. The aerodynamic losses showed a minimum at a blowing rate of 1.5.

Experimental Facility

The experiments are conducted at the ''Cooled Turbine Cascade Facility'' at the Turbomachinery Heat Transfer Laboratory of the Pennsylvania State University. This is an open-loop wind tunnel that consists of an axial air blower, a diffuser with multiple screens, a plenum chamber, a high area ratio circular nozzle, a circular to rectangular transition duct, and the test section. The schematic of the facility is shown in Fig. 1. The air blower is a 45.7 cm tip diameter fan which is driven by a 7.5 kW electric motor. The fan has a potential to provide a pressure differential of 15 cm of water over a range of flow rates. The speed of the electric motor is controlled by an adjustable frequency AC drive, which gives the ability to control the air speed through the facility.

The three-bladed linear turbine cascade used in the present study is shown in Fig. 2. The original design of the blade profile, the cascade arrangement, and the typical velocity distribution around the airfoil is described in Gaugler and Russel [11] and

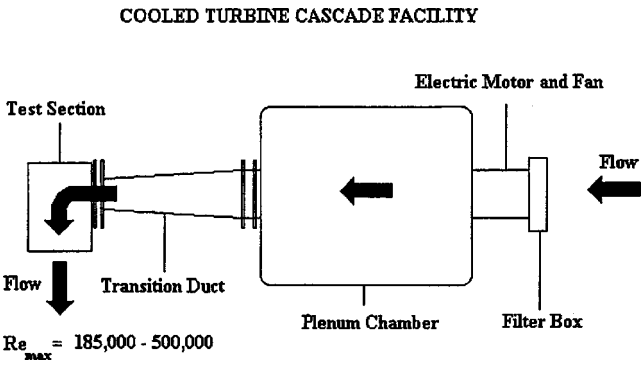

Fig. 1 Experimental facility

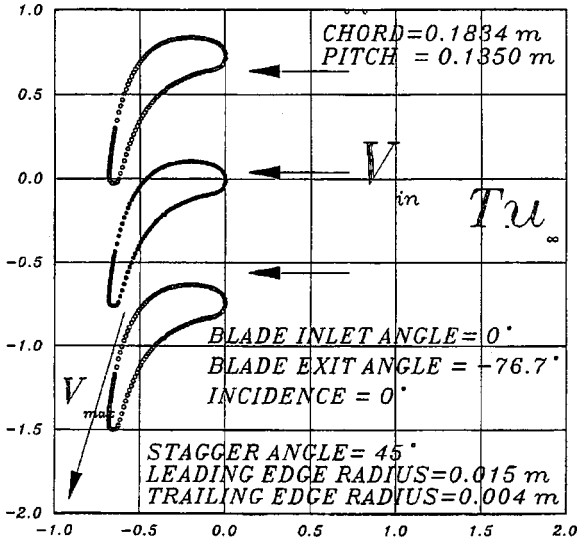

Fig. 2 Linear turbine cascade

Hippensteele et al. [12]. The chord length of the blades precision machined from wood is 0.1834 m and the pitch–chord ratio is 0.736. The blade inlet angle is 0 deg and blade exit angle is −76.7 deg. All experiments reported in this paper are performed at zero incidence. The cascade arrangement has a stagger angle of 45 deg. Since specific attention is paid to the flow physics near the cooled trailing edge section, the geometric details of the trailing edge area and the throat section of the turbine passage are shown in Fig. 3. The maximum velocity V_{max} at the exit of the cascade has been measured near the center of the throat circle. The location of the maximum velocity between the pressure side and the suction side has also been confirmed by Particle Image Velocimeter (PIV) measurements, described in Uzol and Camci [13].

A pressure side view of the trailing edge cooling system and the copper coolant feeding pipe is shown in Fig. 4. The metered coolant is fed into the system from both sides of the pipe. The copper pipe has 13 oblong openings, providing an effective area of 300.8 mm^2. The internal cavity of the cooling passage shown in Fig. 4 (without any ribs installed) is machined in a numerically con-

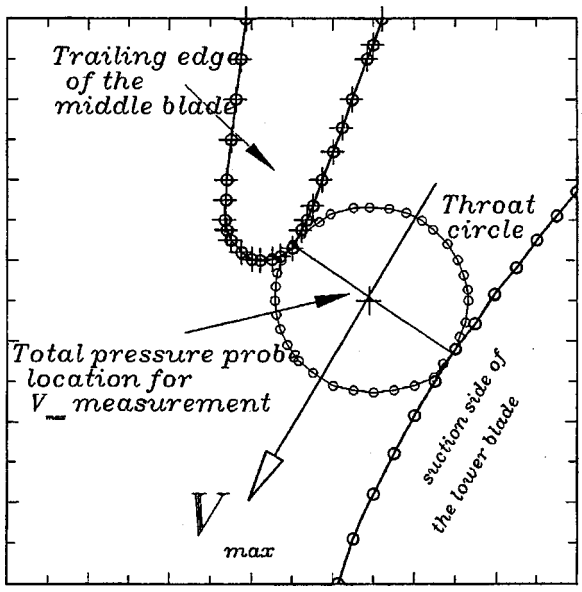

Fig. 3 Trailing edge details and throat section

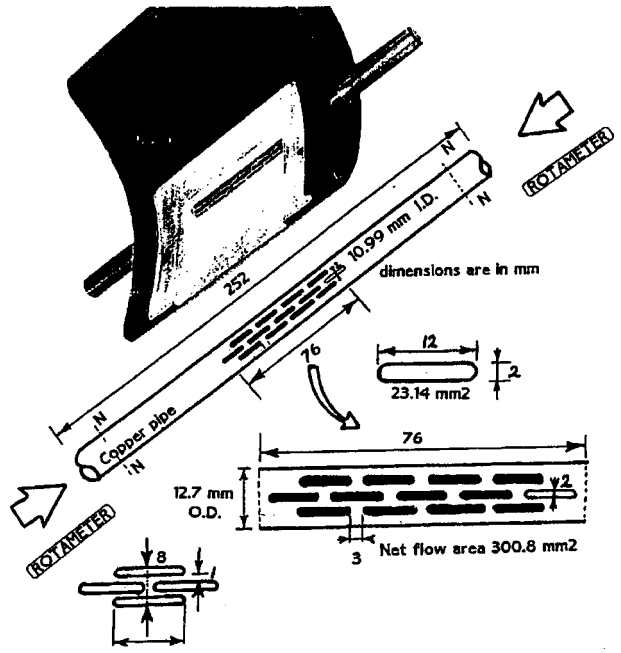

Fig. 4 Trailing edge cooling system and plenum chamber details

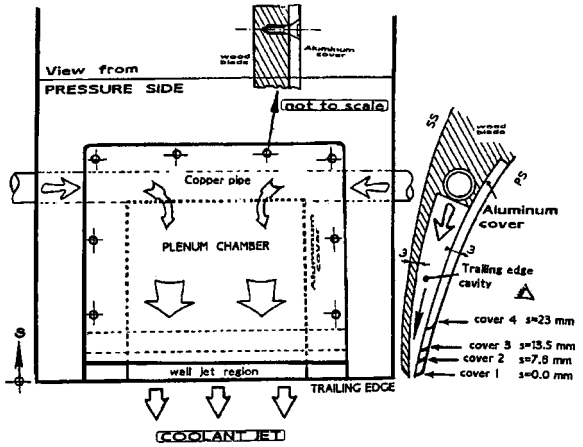

Fig. 5 Cut-back configurations and the trailing edge cavity

trolled milling machine. Special emphasis is paid to maintain a spanwise uniformity of coolant air downstream of the 13 holes. Four different aluminum covers carefully shaped to the original profile of the pressure side provide four different cut-back lengths used throughout the study.

Figure 5 presents the four individual cut-back configurations and the overall geometry of the trailing edge cavity without any ribs installed. The geometry of the wall jet region that occupies the region between the lip of the pressure side cover and the trailing edge point is extremely important because of its tremendous contribution to the final formation of the wake flow containing coolant fluid. This contribution is evident in the present computations explained in Part 2 [13]. It is apparent that the overall wake width controlling the total pressure losses can be reduced by carefully designing the cut-back trailing edge geometry on the pressure side. Figure 6 describes four different cut-back pressure side configurations obtained by altering the aluminum pressure side cover. Channel height h at the exit location is described in Fig. 6 for each cut-back length used in the study.

Figure 7 summarizes the three different rib configurations mounted inside the trailing edge cavity. Model *A* has the largest

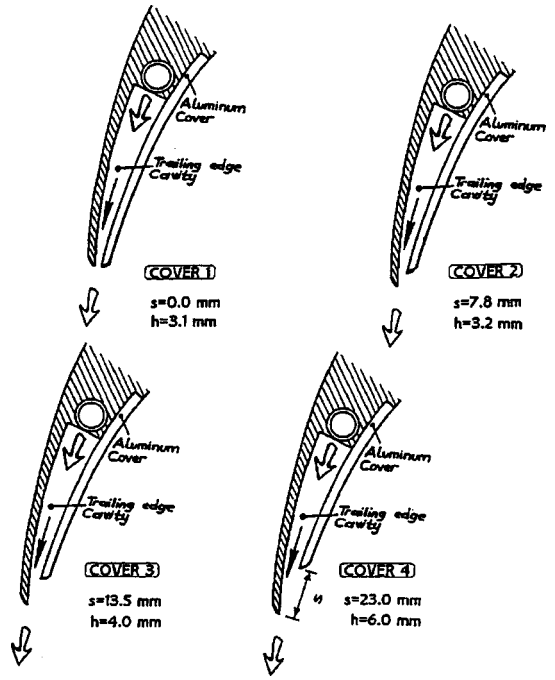

Fig. 6 Four different cut-back lengths

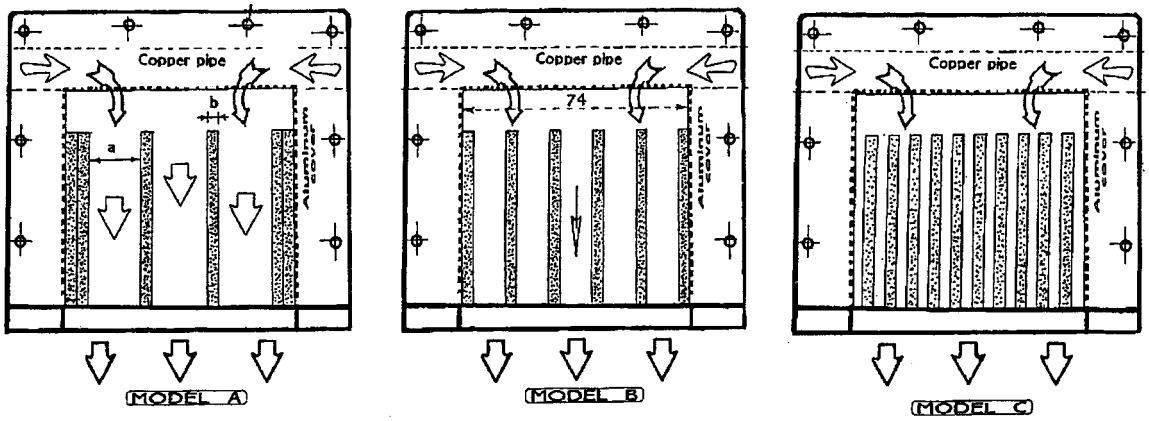

Fig. 7 Three different rib arrangements (Models *A*, *B*, *C*)

Table 1 Rib arrangement data (Models A, B, C)

MODEL A	COVER 1 h=3.1 mm	COVER 2 h=3.2 mm	COVER 3 h=4 mm	COVER 4 h=6 mm
Rib width in spanwise direction b=3.17 mm	b/h=1.02	b/h=0.99	b/h=0.79	b/h=0.53
Rib spacing in spanwise direction a=18.5 mm	a/h=5.97	a/h=5.78	a/h=4.62	a/h=3.08
Effective exit flow area A_{ex} (mm^2)	172	178	222	333

MODEL B	COVER 1 h=3.1 mm	COVER 2 h=3.2 mm	COVER 3 h=4 mm	COVER 4 h=6 mm
Rib width in spanwise direction b=3.17 mm	b/h=1.02	b/h=0.99	b/h=0.79	b/h=0.53
Rib spacing in spanwise direction a=10.88 mm	a/h=3.51	a/h=3.40	a/h=2.72	a/h=1.81
Effective exit flow area A_{ex} (mm^2)	169	174	218	326

MODEL C	COVER 1 h=3.1 mm	COVER 2 h=3.2 mm	COVER 3 h=4 mm	COVER 4 h=6 mm
Rib width in spanwise direction b=3.17 mm	b/h=1.02	b/h=0.99	b/h=0.79	b/h=0.53
Rib spacing in spanwise direction a=4.55 mm	a/h=1.47	a/h=1.42	a/h=1.14	a/h=0.76
Effective exit flow area A_{ex} (mm^2)	127	131	164	246

spanwise rib spacing of $a=18.5$ mm in a three-channel configuration. Spanwise rib width for all three cases is the same at $b=3.17$ mm. Although all three configurations in Fig. 7 are shown with ''Cover 2,'' the effective exit flow areas evaluated at the pressure side lip point for ''Cover 1,'' ''Cover 3,'' ''Cover 4'' (Fig. 6) are numerically tabulated in Table 1 and ''h'' is defined as the distance between the suction side shell and the pressure side shell at the cut-back lip location. ''Model B'' and ''Model C'' have 5 and 11 channels, respectively.

Discharge Coefficient Measurements

The free-stream total and static pressures are measured at the inlet of the test section using a Pitot probe by recording the outputs of the probe through separate channels. The total temperature of the free stream is measured using a thermistor based temperature sensor. In addition to free stream measurements, the maximum velocity inside the passage is also measured at the minimum area location (throat) between the pressure side of the middle blade and the suction side of the lower blade using a Pitot probe (Fig. 3).

The discharge coefficient for the trailing edge cooling system can be defined as the ratio of the actual mass flux rate to the isentropic mass flux rate that is the maximum possible value for one-dimensional flow. Therefore,

$$C_d=(\rho_c u_c)_{\text{act}}/(\rho_c u_c)_{is} \tag{1}$$

The actual mass flux rate is calculated using the measured coolant mass flow rate $\dot{m}_{\text{act}}$ and the exit area A_{ex} at the end of the trailing edge coolant cavity. The point at which A_{ex} is calculated for each of the four different cut-back lengths coincides with the lip of the pressure side as shown in Fig. 5. The actual coolant mass flux rate can then be calculated as,

$$(\rho_c u_c)_{\text{act}}=\dot{m}_{\text{act}}/A_{ex} \tag{2}$$

The isentropic mass flux rate can be calculated from one-dimensional momentum equation and the equation of state for air,

$$(\rho_c u_c)_{is}=P_{c_{ex}}\left(\frac{P_{t_c}}{P_{c_{ex}}}\right)^{(\gamma-1)/\gamma}\cdot\left\{\frac{2\gamma}{\gamma-1}\cdot\frac{1}{RT_{t_c}}\times\left[1-\left(\frac{P_{t_c}}{P_{c_{ex}}}\right)^{(\gamma-1)/\gamma}\right]\right\}^{1/2} \tag{3}$$

Equation (3) provides the maximum possible flux rate of coolant air between a coolant total pressure of P_{t_c} and the coolant exit static $P_{c_{ex}}$. The exit static pressure in the coolant stream is measured at 3 mm downstream of the trailing edge point of the blade using a 1.8-mm-dia Pitot-Static probe. The coolant total pressure P_{t_c} and coolant static pressure P_c are measured inside the copper pipe at section N–N as shown in Fig. 4. The copper plenum chamber is fed by two air supply pipes that have individual precision rotameters for volumetric flow rate measurements. The density of air at the rotameter location is calculated from the measured temperature and pressure values at the metering stations. Effective passage exit area A_{ex} for each configuration is measured at the pressure side lip location for each cut-back length and rib configuration. Twelve individual A_{ex} values obtained from three rib spacings and four different cutback lengths are tabulated in Table 1. The experimental uncertainties on the different measured quantities have been estimated as follows, based on a 20:1 confidence interval:

$\delta p=\pm 0.5$ percent at $p=105{,}000$ N/m^2 (typical atmospheric value)
$\delta T=\pm 0.2$ percent at $T=300$ K (typical inlet value)
$\delta\dot{m}_c=\pm 1.2$ percent at $\dot{m}_c=0.005$ kg/s
$\delta(\dot{m}_c/\dot{m}_\infty)=\pm 1.6$ percent at $(\dot{m}_c/\dot{m}_\infty)=0.02$
$\delta C_d=\pm 2.8$ percent at $C_d=0.60$

Experimental Results and Discussion

Table 2 summarizes the free-stream flow conditions during the experiments performed at three different Reynolds numbers defined by the true chord and exit velocity ($V_{ex}=V_{\max}$). Low, medium, and high Reynolds numbers based on exit velocity were 185,701, 358,029, and 505,868, respectively. The coolant ejection experiments were also performed in the absence of free-stream flow as a reference case. Free-stream turbulence intensity was kept at approximately $Tu_\infty=1.2$ percent for all experiments.

Discharge Coefficients (Model *A*). Figures 8–10 show the variation of discharge coefficients against the coolant to free-stream static pressure ratio P_{tc}/P_{cex}. The second column in each figure presents C_d data against coolant to free-stream mass flow rate ratio for Models *A*, *B*, and *C*. The three models represent three different rib spacings as described in Fig. 7. Four different cut-back lengths for each model are simulated by four different individual pressure side covers as shown in Fig. 6. A wide coolant to free-stream mass flow rate range from 0 to 5 percent is used in experiments. This range is sufficient to cover most gas turbine trailing edge cooling applications.

The results from the three models show that there is always a threshold coolant pressure above which the discharge coefficients do not have any free-stream Reynolds number dependency. For Covers 1, 2, and 3, this threshold level is about $P_{tc}/P_{cex}=1.003$. This threshold value is around 1.010 when Cover 4 is used. The flow losses in the trailing edge cavity are Reynolds

Table 2 Typical free-stream flow conditions at the cascade inlet and exit (exit is defined as the maximum velocity point at the throat area and Reynolds numbers are based on true chord length)

		INLET VELOCITY V_{inlet}	INLET REYNOLDS NUMBER Re_{inlet}	EXIT VELOCITY V_{exit}	EXIT REYNOLDS NUMBER Re_{exit}	SYMBOL
		m/s		m/s		
HIGH REYNOLDS NUMBER	Re_H	7.8	90334	44.1	505868	△
MEDIUM REYNOLDS NUMBER	Re_M	4.7	55187	30.9	358029	○
LOW REYNOLDS NUMBER	Re_L	1.9	21607	16.1	185701	▼
NO MAINSTREAM FLOW	Re_O	0	0	0	0	+

number dependent in the low P_{tc}/P_{cex} range shown in the figures. The effective exit area of the trailing cooling cavity is the largest when Cover 4 is used.

The dependency of the discharge coefficient data on the coolant to free-stream pressure ratio can easily be removed by plotting C_d against coolant to free-stream mass flow rate ratio instead of the pressure ratio. The independence of C_d from Reynolds number for this case is regardless of the rib spacing ''*a*'' or the cut-back length ''*s*'' used in the experiments summarized in Figs. 8–10. One explanation for this observation may be the strong functional dependency of the coolant mass flux rate to the coolant to free-stream pressure ratio P_{tc}/P_{cex} as described in Eq. (3). For small coolant to free-stream pressure ratio values at which this functional dependency is strong, a high level of dependency of C_d to pressure ratio is observed. Using mass flow rate ratio also stretches the horizontal axis.

The data presented in Figs. 8–10 show the no-free-stream flow case as a reference case. In all plots, a plus sign is assigned to no-free-stream flow experiments in which coolant jet issued from the trailing edge directly ejects into still air at atmospheric pressure. Covers 1, 2, and 3 produces the lowest C_d coefficients when

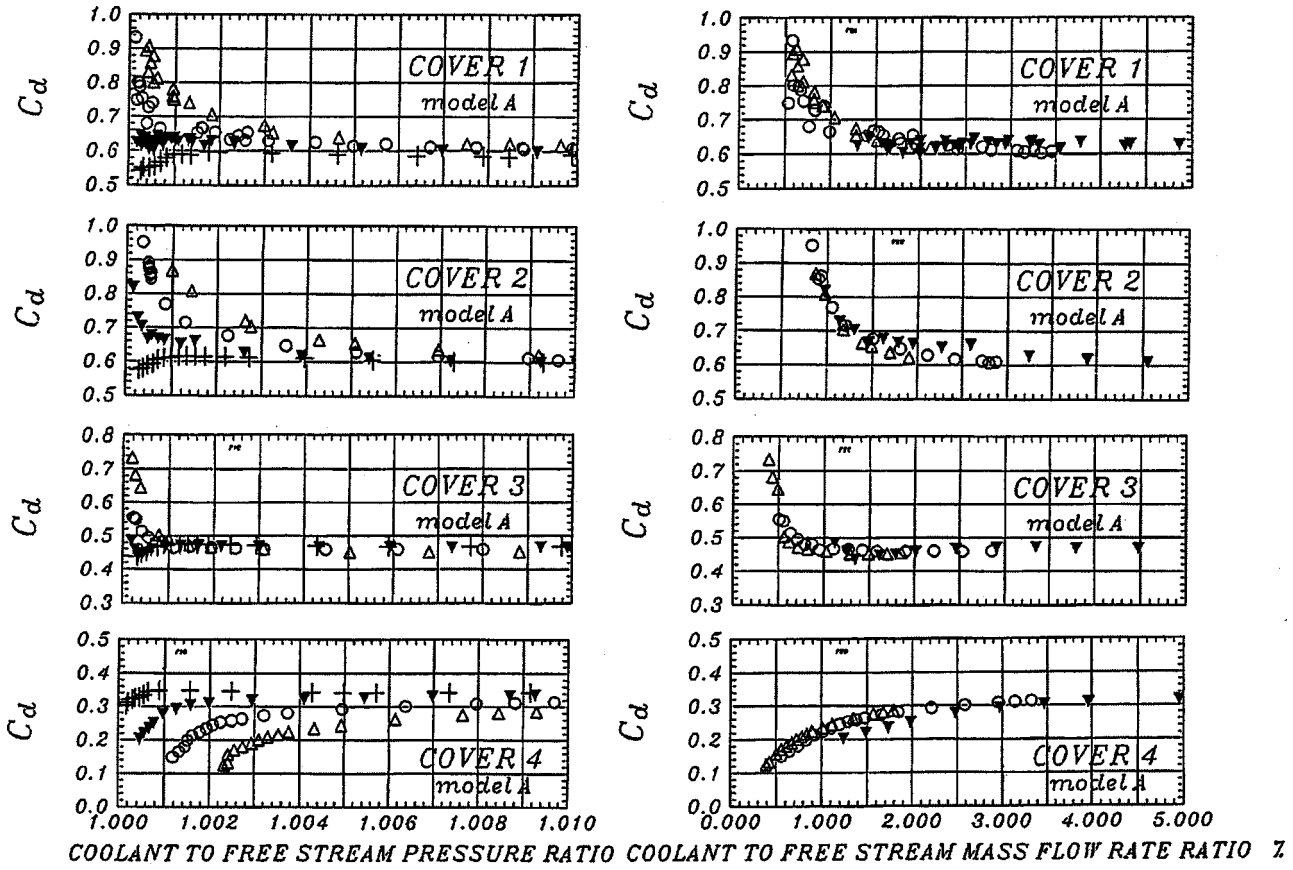

Fig. 8 Discharge coefficients for Model *A*

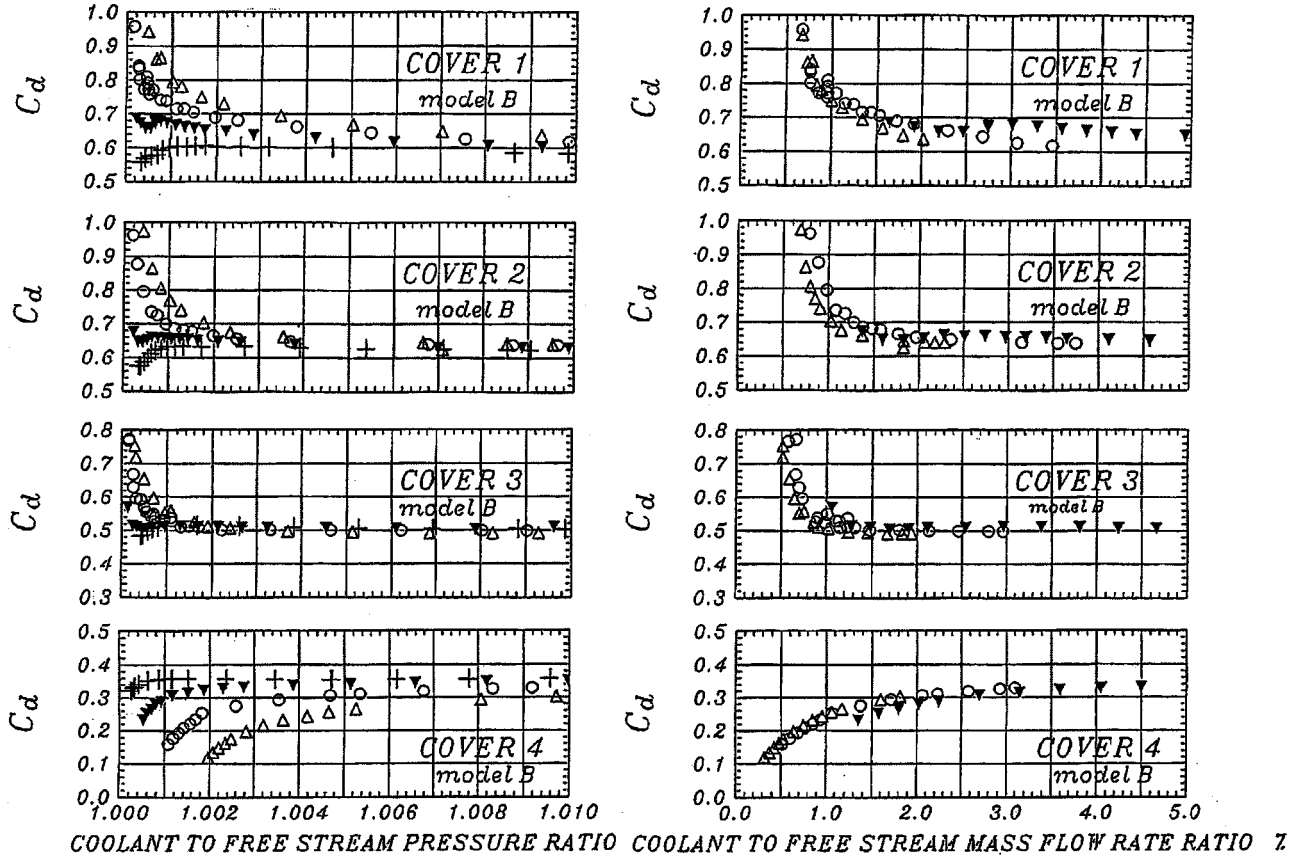

Fig. 9 Discharge coefficients for model *B*

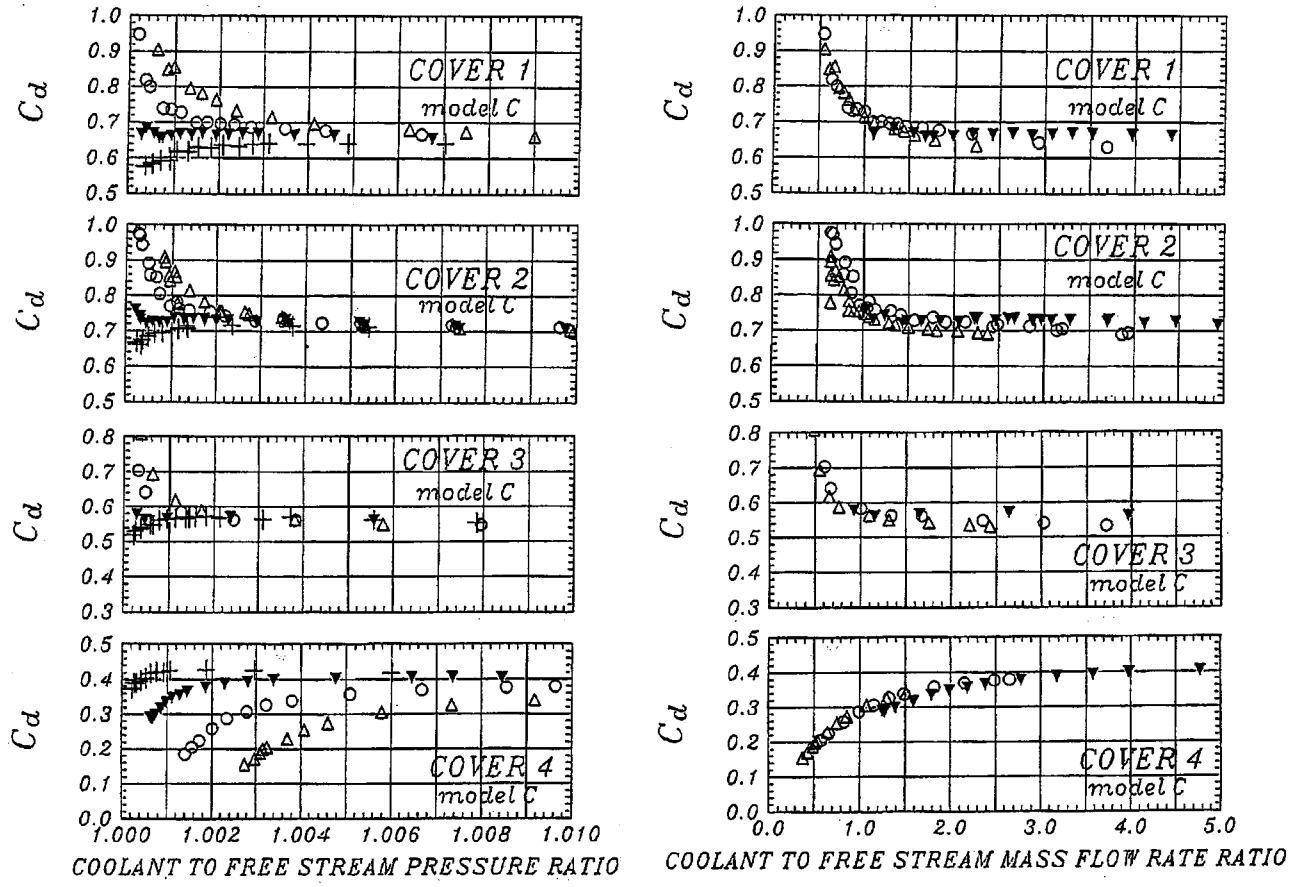

Fig. 10 Discharge coefficients for model *C*

the pressure ratio is less than the previously mentioned threshold level of approximately $P_{tc}/P_{cex}=1.003$. For this case, the exit pressure is atmospheric in still air and relatively higher than the exit pressure levels imposed by the ''low,'' ''medium,'' and ''high'' Reynolds number experiments.

In general, the discharge coefficients from ''Cover 4,'' which has the longest cut-back length, have the lowest values. This observation could be attributed to the fact that the effective exit area measured at the pressure side lip is the largest (when compared to other shorter cut-back lengths). The larger exit area results in a relatively low momentum wall jet near the trailing edge. Since the downstream pressure probe is located about 3 mm downstream of the trailing edge point, the C_d values measured in this study naturally include the losses in the trailing edge cavity and in the wall jet located between the pressure side lip and the probe location. The wall jet is bounded by the suction side shell of the blade on one side; however, the free shear layer existing between the free-stream and the wall jet is a major aerodynamic loss generation element in this configuration. The relatively low momentum coolant jet character imposed by the largest ($h=6$ mm) exit area creates a ''loss prone'' wall jet. For covers 1, 2, and 3, decreasing the coolant to free-stream pressure ratio causes an increase in the discharge coefficient. However, for Cover 4 this causes a decrease in the discharge coefficient, which indicates more losses are created. This change in the character of the loss generation mechanism is mainly due to the formation of a strong recirculatory flow inside the cut-back region for low ejection rates, as the cut-back length increases. As the ejection rate is increased, the recirculatory flow disappears and the ejected coolant flow starts to dominate the cut-back region. Hence, the discharge coefficient values are less influenced by this effect. The formation and the disappearance of the recirculatory region inside the cut-back length are visualized with the computational simulations discussed in Uzol and Camci [13]. Consequently the low momentum wall jet guided by the suction side shell makes ''Cover 4'' (or the longest cut-back length case) the least ideal case as far as the discharge coefficients are concerned.

Figures 8–10 clearly show that the discharge coefficients are continually improved below the threshold coolant pressure when the free-stream Reynolds number is gradually increased, from zero to low, medium, and high values for Covers 1, 2, and 3. Varying the Reynolds number at a constant coolant pressure ratio of P_{tc}/P_{cex}, only affects the losses in the wall jet region because at each Reynolds number case the free-stream velocity at the edge of the free shear layer is different. The shear-generating velocity difference between the wall jet and the free-stream flow is the main contributor to the loss generation. The discharge coefficient assumes its lowest value when the coolant is ejected into still air. The shear generated in the wall jet region of the coolant stream is maximum for this case because of the maximum possible velocity differential between the coolant and the free-stream flow.

When Cover 4, which has the longest cut-back length, is installed, the momentum of the wall jet issued at the exit plane (pressure side lip) is extremely low due to the large effective exit area ($h=6$ mm). Figures 8–10 show extremely low values of C_d for the cooling system because of the interaction of a low momentum (possibly laminar coolant jet) with the free-stream flow. For this case, increasing the free-stream Reynolds number does not improve the discharge coefficients. The losses become larger as the free-stream Reynolds number is increased at a fixed coolant pressure.

A plot of the $C_d$values against the ''coolant to free-stream pressure ratio'' is extremely illuminating to understand the contribution of free-stream to aerodynamic losses of a trailing edge cooling system. When the coolant pressure is gradually increased at a fixed free-stream Reynolds number, a practically constant C_d value is reached quickly. For example, for Covers 1, 2, and 3, when P_{tc}/P_{cex} values are greater than 1.003, further increases in the plenum chamber pressure does not affect the overall aerodynamic losses. A nearly constant C_d value for high blowing rates is about 0.61 for Cover 1, Fig. 8. Cover 2 has slightly higher loss, possibly because of the relatively shorter wall-jet region that exists for this model. Once the coolant jet reaches a momentum level equal to or higher than that of the free stream, further increases in the coolant pressure do not influence the losses in a significant manner. The nearly constant value of C_d is determined by the internal fluid mechanic features of the trailing edge cavity but not by the wall jet contributions occurring outside trailing edge cavity. However, in the given coolant mass flow range, the influence of varying coolant pressure is not significant as far as the final level of C_d is concerned. The main reason for the nearly constant C_d level could be attributed to the fact that once the coolant jet reaches a certain momentum level, the free-stream flow cannot easily modify the jet. The main loss contributing parameters of the cavity may be the overall volume of the cavity, the effective exit area, the open friction area defined by the ribs, and the free-stream static pressure at the pressure side lip location.

The aerodynamic losses are at the same level when the discharge coefficient C_d is evaluated for various free-stream Reynolds numbers at the same coolant to free-stream mass flow ratio. The independence from the Reynolds number is because the relative velocity ratios between the free stream and coolant jet are kept the same when the coolant mass flow rate ratio is employed as the horizontal axis. When the coolant to free-stream mass flow rate ratios are the same, the coolant to free-stream pressure ratios assigned to each free-stream Reynolds number experiment are naturally different. The second column in Figs. 8–10 contains C_d data as functions of the coolant to free-stream mass flow rate ratio. The observed collapsing character of various C_d distributions obtained in a wide free-stream Reynolds number range is an extremely useful property for the cooling designer. In a wide free-stream Reynolds number range from 185,701 to 505,868, the discharge coefficients show minimal Reynolds number dependency, which is well within the experimental measurement error on discharge coefficient ($\delta C_d=\pm 2.8$ percent).

Discharge Coefficients (Model *B*). Similar results are observed for Model *B*, which has a closer rib spacing ($a=10.88$ mm) with five distinct internal flow channels, as described in Fig. 7. Although the net flow friction area is increased by the addition of two more ribs, it is likely that the fluid mechanic losses in each of the five channels are reduced when compared to model *A*. The effective exit area value for each of the covers is also slightly reduced because of rib addition when compared to Model *A*. The discharge coefficient values obtained for high blowing rates for Model *B* are about 7 percent higher than those of Model *A* (on average) for all four cut-back lengths, as shown in Fig. 9.

Discharge Coefficients (Model *C*). Figure 10 presents the discharge coefficients from Model *C* for a ten-ribbed internal configuration that has 11 individual flow passages. Although the cavity friction area is increased significantly (about 25 percent compared to Model *A*), the overall losses are reduced. The effective exit area is reduced by about 26 percent, resulting in a higher momentum coolant jet at the pressure side lip. The measured discharge coefficients are about 15 percent higher on the average for Model *C* when compared to Model *A*. The increased rib spacing used in Model *C* results in the best overall discharge coefficient over a wide coolant mass flow rate range.

Low Re Experiments and the Worst Case Discharge Coefficients. The data presented in Figs. 8–10 suggest that discharge coefficients for a cooled trailing edge system with a cut-back length can be obtained from experiments performed at low Reynolds numbers without sacrificing accuracy. This approach eliminates the requirement of operating a test facility at full Reynolds number. Tremendous energy and time savings can be obtained from the acquisition of C_d data in low Reynolds number experiments. A very quick estimate of the trailing edge cooling system

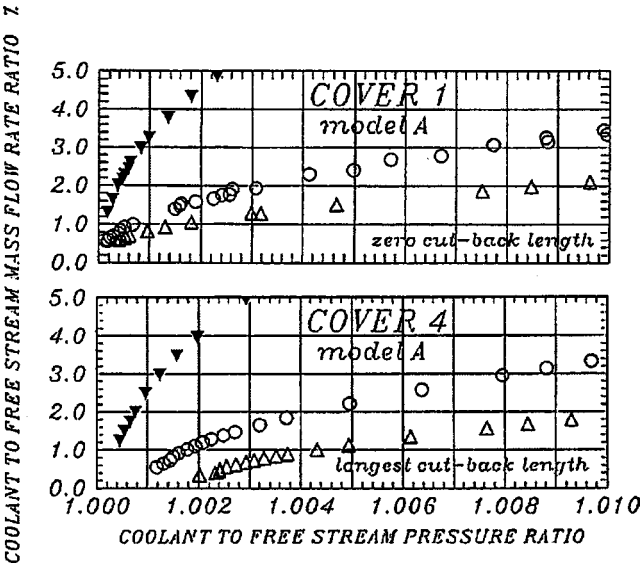

Fig. 11 Actual coolant mass flow rate ratio versus pressure ratio (model *A*, Covers 1 and 4)

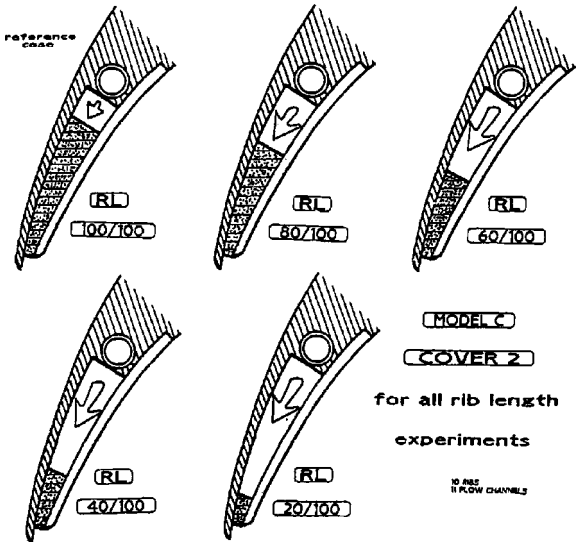

Fig. 12 Five different rib lengths (Model *C*, Cover 2)

performance can even be obtained by simply running the C_d experiment at zero free-stream Reynolds number. This approach can be realized even outside the test section of a wind tunnel by just ejecting the cooling air into still air. All experiments performed in still air shown in Figs. 8–10 with many rib spacings and cut-back lengths clearly show that the zero Reynolds number discharge coefficients (as shown by + signs) always merge to actual Reynolds number results when the threshold coolant to free-stream pressure level is exceeded. If the horizontal axis is chosen as the ''coolant to free-stream mass flow rate ratio,'' any experiment over $\dot{m}_c/\dot{m}_\infty = 2.5$ percent produces the asymptotic value of C_d that may be used as a worst-case discharge coefficient estimate. The trailing edge ejection system with Covers 1, 2, and 3 cannot perform worse than this asymptotic value. The system may actually perform much better than this limiting value at low coolant mass flow rate ratio values that are less than 1 percent.

Coolant Mass Flow Versus Pressure Ratio. Figure 11 shows the capability of Model *A* to pass coolant mass flow rate for a given coolant to free-stream pressure ratio. The results for the shortest cutback length (Cover 1, $s = 0.0$ mm) and the longest cut-back length (Cover 4, $s = 23.0$ mm) indicate that a shortening of the cut-back region length improves the coolant mass flow rate passing capability of the ejection system at a fixed pressure ratio. When the shortest cutback length data show a 5 percent coolant mass flow rate ratio at $P_{t_c}/P_{c_{ex}} = 1.0023$, the maximum cutback length configuration gives a coolant mass flow ratio of 4.2 percent. This reduction is related to the additional shear layer related losses generated in the wall jet section. When the same experiment is repeated with the same cover and rib configuration (Cover 1, Model *A*) for different free-stream Reynolds numbers, the low Reynolds number experiment provides the highest coolant mass flow rate at a fixed P_{tc}/P_{cex}. The highest Reynolds number experiment results in the lowest coolant mass flow rate ratio at the same coolant pressure ratio. Since the ratio P_{tc}/P_{cex} is kept constant, the relatively low free-stream static pressure of the high free-stream Reynolds number experiment require a lower coolant pressure than the low Reynolds number experiment. During a high free-stream Reynolds number experiment, the coolant pressure needs to be reduced in order to keep the pressure ratio the same.

Influence of Rib Length on Discharge Coefficients. The viscous flow losses in the trailing edge cavity need to be quantified for the length of the ribs used inside the cooling system. The rib length experiments performed in this study use the most successful aerodynamic configuration as far as the rib spacing and cut-back length is concerned. Figure 12 presents five different relative rib lengths ranging from 20 to 100 percent using Cover 2 and Model *C*. The corresponding cut-back length is fixed at 7.8 mm. The rib spacing is 4.55 mm with 11 flow channels. There are two major parameters to be considered in discussing the influence of rib length on the discharge coefficients: the specific three-dimensional flow in the chamber between the coolant pipe and the rib and the flow between the ribs described in Fig. 12.

Figure 13 presents measured discharge coefficients obtained from five different rib lengths at two different free-stream Reynolds numbers. The experimental results with no free-stream flow are also included. An immediate observation made from Fig. 13 is that varying rib length does not significantly affect the discharge coefficients for a constant free-stream Reynolds number. In all three experiments performed at different Reynolds numbers, the longer rib configurations result in slightly lower C_d values. However, when the data from all five rib lengths are plotted together, the maximum variation in the discharge coefficient values are less than ± 1.5 percent on C_d, Fig. 14. When low and high free-stream Reynolds number C_d data for all five rib lengths are plotted against the coolant to free-stream mass flow rate ratio, it can be concluded that the influence of rib length on the discharge coefficient of the trailing edge cooling systems considered is not significant. Figure 14 indicates that the discharge coefficient variation with respect to coolant mass flow rate ratio is only significant when the coolant flow rate ratio is less than 1.5 percent. Above 1.5 percent, the C_d has a constant value that can be taken as the worst possible discharge coefficient that can be assigned to a given cooling system. Figure 14 is an independent confirmation of the similar results presented in Figs. 8–10. All of the experiments performed in this study show that the nearly constant C_d value from the high blowing rate experiments can be accurately obtained from a zero free-stream Reynolds number experiment setup with a cooled blade discharging into still air.

The coolant mass flow rate passing capability of the trailing edge cooling system with five different rib lengths is shown in Fig. 15. The results obtained for low and high Reynolds numbers show no rib-length dependency in a wide coolant to free-stream pressure ratio range.

Spanwise Uniformity Tests. Spanwise uniformity of the coolant ejection at the trailing edge is checked by traversing along the spanwise direction 20 mm downstream of the trailing edge. Model *B* with Cover 2 is used for the test and a kiel probe with a

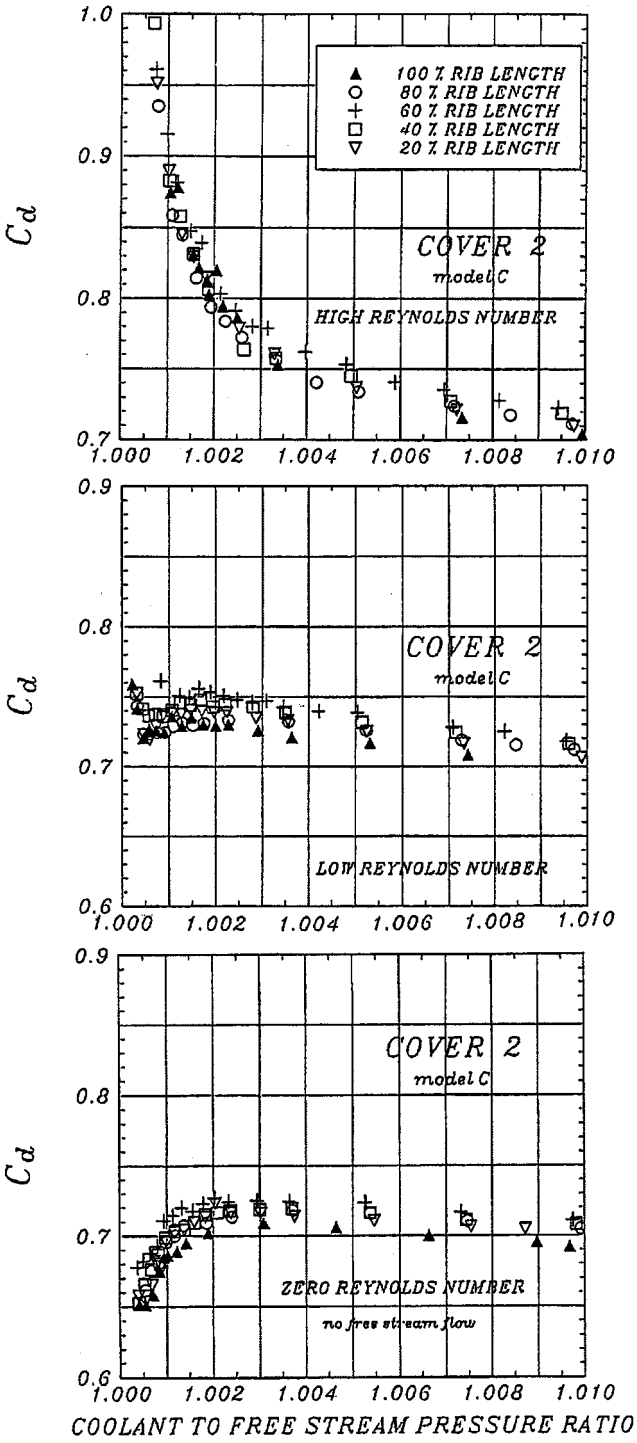

Fig. 13 Influence of rib length on discharge coefficients (Model *C*, Cover 2)

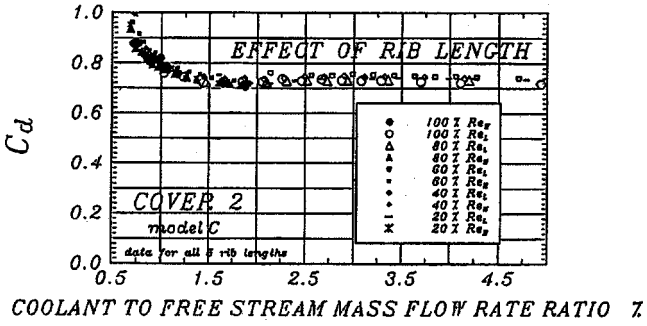

Fig. 14 Discharge coefficients versus coolant to free-stream mass flow rate ratio (model *C*, Cover 2, data for all five rib lengths)

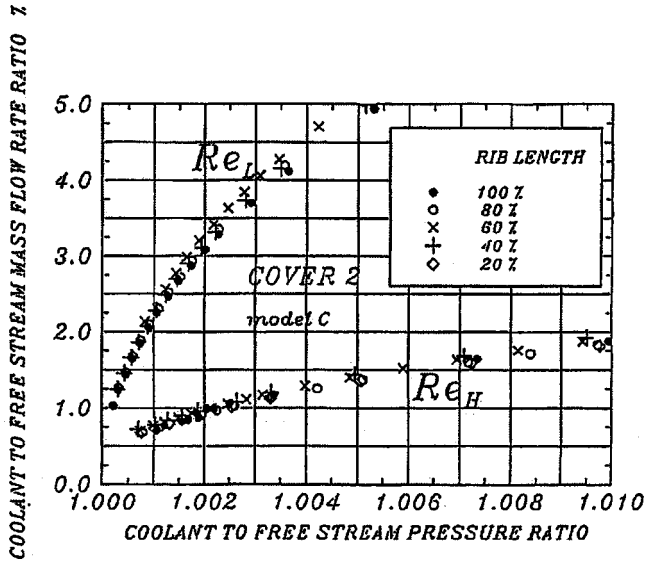

Fig. 15 Actual coolant mass flow rate versus pressure ratio (Model *C*, Cover 2, data for all five rib lengths)

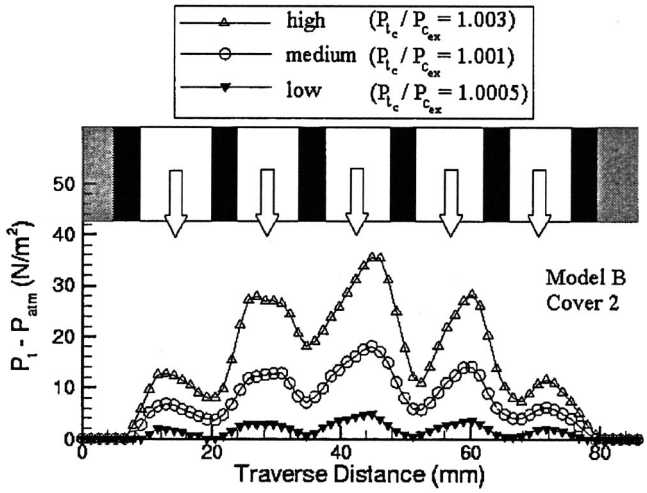

Fig. 16 Spanwise total pressure uniformity at the trailing edge

3.175 mm shield diameter is used for the traverse. The tests are conducted for three different coolant to free-stream pressure ratios representing the mass flow range used throughout this study. The coolant is injected into a still environment in order to reveal possible spanwise nonuniformities due to internal cooling system design.

The results of the spanwise traverse are shown in Fig. 16. The coolant ejection from the trailing edge stays reasonably uniform along the span for low coolant to free-stream pressure ratios. More coolant mass flow is directed through the central channels, whereas the channels toward the sides of the ejection system can deliver less mass flow as the coolant to free-stream pressure ratio is increased. This is a natural trend for the specific coolant delivery system defined in Fig. 4. Equivalent mass flow rates introduced from the left and right side of the coolant feed pipe result in

a higher coolant total pressure in the central region of the cavity. These results indicate that the specific coolant ejection system with the copper coolant feed pipe was successful in producing a good spanwise uniformity of coolant mass flow rate.

Conclusions

An experimental study of the internal fluid mechanic loss characteristics of a turbine blade with trailing edge coolant ejection is presented. The main emphasis is placed on the determination of the discharge coefficients under realistic gas turbine conditions. The effect of cut-back length, spanwise rib spacing, free-stream Reynolds number, and chordwise rib length on discharge coefficients is studied in detail. The discharge coefficients are obtained in a wide range of coolant to free-stream mass flow rate values.

The cooling experiments were performed at three different free-stream Reynolds numbers. Discharge experiments were also conducted in still air. The discharge coefficients are presented as functions of the coolant to free-stream pressure ratio. When the C_d results are plotted against the coolant to free-stream mass flow rate ratio, the free-stream Reynolds number dependency of the data can be removed.

The C_d has a smoothly varying character at low coolant to free-stream pressure levels. However, after reaching a threshold P_{tc}/P_{cex} value, the discharge coefficients reach a constant level.

Since the discharge coefficients do not have Reynolds number dependency, C_d experiments can be performed at a low free-stream Reynolds number. Running a discharge coefficient experiment at low Reynolds number (or even in still air) will sufficiently define the high blowing rate portion of the curve. This approach is extremely time efficient and economical in finding the worst possible C_d value for a given trailing edge coolant system.

Experiments performed at three different rib spacing values show that Model *C* with 11 ribs and 10 passages is aerodynamically superior to Models *A* and *B*, which have smaller numbers of ribs and larger rib spacing.

Four different pressure side covers representing different cut-back lengths on the pressure side show that Cover 1 ($s=0.0$ mm) and Cover 2 ($s=7.8$ mm) are the two most effective cases as far as the C_d levels are concerned. Covers 3 and 4 always produced higher aerodynamic losses in the cooling system. Higher losses for this case are associated with the increasing free-stream interaction length of the wall shear layer defined after the pressure side lip.

The increased effective exit area from the coolant cavity is also responsible from the relatively lower momentum levels in the coolant jet. The discharge coefficients obtained from Covers 4 and 3 have magnitudes less than the values obtained with Covers 1 and 2.

The most successful configuration producing the highest discharge coefficients is Cover 2 with the highest number of ribs (Model *C*).

Cover 2 with Model *C* has been used for rib length experiments. Five different rib lengths ranging from 20 to 100 percent indicate that the influence of the rib length on measured aerodynamic losses is minimal. Slight variations of C_d are well within the estimated uncertainty band for the discharge coefficient.

Acknowledgments

This paper is based on a research project funded by Solar Turbines Inc. The turbine cascade used in the current study was provided by NASA Lewis (Glenn) Research Center. The authors would like to acknowledge the equipment support provided by S. A. Hippensteele and Dr. R. E. Gaugler of NASA (Glenn) Research Center, Cleveland, OH. The authors are also grateful for the equipment grant provided by the College of Engineering of the Pennsylvania State University. The grant was used for the acquisition of the PIV equipment extensively used in this study.

Nomenclature

A = effective flow area
a = spanwise rib spacing
b = spanwise rib width
c = blade chord length
C_d = discharge coefficient
h = effective channel height at exit plane (pressure side lip location)
k = turbulent kinetic energy
$\dot{m}$ = mass flow rate
$(\dot{m}_c/\dot{m}_\infty)$ = coolant to free-stream mass flow rate ratio
p = static pressure
p^* = nondimensional static pressure $=(p-p_{\text{ref}})/\rho u_0^2$
$\text{Re}_{\max}$ = maximum Reynolds number calculated using maximum velocity at throat and blade chord
R = gas constant
RL = relative rib length (20, 40, 60, 80, and 100 percent)
s = cut-back length measured from trailing edge point
Tu_∞ = free-stream turbulence intensity
u = streamwise velocity
$V_{\max}$ = maximum velocity at throat
γ = specific heat ratio
δ = uncertainty of measured quantity
μ_0 = absolute viscosity
μ_t = turbulent viscosity
ρ = density

Subscripts

c = coolant
act = actual
H = high Reynolds number
is = isentropic
L = low Reynolds number
M = medium Reynolds number
0 = without mainstream flow
ex = exit reference location 3 mm downstream of trailing edge
t = total condition

References

[1] Metzger, D. E., Kim, Y. W., and Yu, Y., 1993, ''Turbine Cooling: An Overview and Some Focus Topics,'' *Proc. 1993 International Symposium on Transport Phenomena in Thermal Engineering*.
[2] McMartin, I. P., and Norbury, J. F., 1974, ''The Aerodynamics of a Turbine Cascade With Supersonic Discharge and Trailing Edge Blowing,'' ASME Paper No. 74-GT-120.
[3] Prust, H. W., 1975, ''Cold Air Study of the Effect on Turbine Stator Blade Aerodynamic Performance of Coolant Ejection from Various Trailing Edge Slot Geometries, Part II: Comparison of Experimental and Analytical Results,'' NASA Paper No. TM-X-3190.
[4] Lokai, V. I., and Kumirov, B. A., 1973, ''Losses in Turbine Cascades With Cooling Air Discharge and Various Trailing Edge Geometries,'' Soviet Aeronautics (English translation of Izvestiya VUZ Aviatsionnaya Tekhnika), **16**, No. 3, pp. 64–67.
[5] Lawaczek, O., 1977, ''The influence of Jets of Cooling Air Exhausted From the Trailing Edges of a Supercritical Turbine Cascade on the Aerodynamical Data,'' AGARD CP229, Paper No. 30.
[6] Sturedus, C. J., 1979, ''Aerodynamic Effects of Surface Cooling-Flow Injection on Turbine Transonic Flow Fields,'' AIAA paper No. 79-1210.
[7] Moses, H. L., Kiss, T., Bertsch, R., and Gergory, B. A. 1991, ''Aerodynamic Losses Due to Pressure Side Coolant Ejection in a Transonic Turbine Cascade,'' AIAA Paper No. 91-2032.
[8] Venediktov, V. D., 1972, ''Investigating a Turbine Stage With Cooling Air Leaving Through Slots in the Concave Surfaces of the Nozzle Blades,'' Thermal Engineering (English translation of Teploenergetika), **19**, No. 7, pp. 20–25.
[9] Kiock, R., Hoheisel, H., Dietrichs, H. J., and Holmes, A. T., 1985, ''The Boundary Layer Behavior of an Advanced Gas Turbine Rotor Blade Under the Influence of Simulated Film Cooling,'' *AGARD Conf. Proc. No. 390, Heat Transfer and Cooling in Gas Turbines*, pp. 42-1–42-19.
[10] Wifert, G., and Fottner, L., 1996, ''The Aerodynamic Mixing Effect of Dis-

crete Cooling Jets With Mainstream Flow on a Highly Loaded Turbine Blade,'' ASME J. Turbomach., **118**, pp. 468–477.
[11] Gaugler, R. E., and Russell, L. M., 1980, ''Streakline Flow Visualization Study of a Horseshoe Vortex in a Large-Scale, Two-Dimensional Turbine Stator Cascade,'' ASME Paper No. 80-GT-4.
[12] Hippensteele, S. A., Russell, L. M., and Torres, F . J., 1985, ''Local Heat Transfer Measurements on a Large, Scale-Model Turbine Blade Airfoil Using a Composite of a Heater Element and Liquid Crystals,'' NASA T M 86900.
[13] Uzol, O., and Camci, C., 2000, ''Aerodynamic Loss Characteristics of a Turbine Blade With Trailing Edge Coolant Ejection: Part 2—External Aerodynamics, Total Pressure Losses, and Predictions,'' ASME J. Turbomach., **123**, this issue, pp. 249–257.

Aerodynamic Loss Characteristics of a Turbine Blade With Trailing Edge Coolant Ejection: Part 2—External Aerodynamics, Total Pressure Losses, and Predictions

Oguz Uzol

Cengiz Camci

Turbomachinery Heat Transfer Laboratory,
The Pennsylvania State University,
University Park, PA 16802

Investigation of the internal fluid mechanic losses for a turbine blade with trailing edge coolant ejection was present in Uzol et al. (2001). The current study is a detailed experimental investigation of the external subsonic flowfield near the trailing edge and the investigation of the external aerodynamic loss characteristics of the turbine blade with trailing edge coolant ejection system. Particle Image Velocimetry experiments and total pressure surveys in the near wake of the blade are conducted for two different Reynolds numbers and four different ejection rates. Two different trailing edge configurations with different cut-back lengths are also investigated. Numerical simulations of the flowfield are also performed for qualitative flow visualization purposes. Two-dimensional, incompressible, and steady solutions of Reynolds-averaged Navier–Stokes equations are obtained. A two-equation standard $k-\epsilon$ turbulence model coupled with an Algebraic Reynolds Stress Model is used for the simulation of the turbulent flowfield. The results show that the aerodynamic penalty levels in the wake region near the trailing edge are increased due to the mixing of the coolant and mainstream flows for 0–3 percent ejection rates. However, after a threshold level (5 percent ejection rate), the ejected coolant flow has enough momentum to fill the wake of the blade, which in turn results in a decrease in the aerodynamic penalty levels. [DOI: 10.1115/1.1351817]

Introduction

In order to increase the specific thrust and to reduce the specific fuel consumption of gas turbine engines, higher turbine inlet temperatures are needed. This need for high temperatures results in a demand for effective cooling of high-pressure turbine blades. Many of the blade cooling systems involve ejection of cooling flows into the hot gas stream at various points on the blade. One of the most critical locations on the blade where coolant ejection is performed is the trailing edge. The mixing of high-density coolant with hot mainstream gases can result in aerodynamic losses, which will influence the engine performance.

Aerodynamic aspects associated with trailing edge coolant ejection in steady two-dimensional blade-to-blade flow over a range of exit Mach numbers and coolant pressure ratios were studied by Deckers and Denton [1]. The tests were carried out on flat plate models representing the region of uncovered turning downstream of the throat. It was concluded that the effect of coolant ejection is a substantial increase in the base pressure and a reduction in overall loss. Pappu and Schobeiri [2] investigated the aerodynamic effects of trailing edge ejection on mixing losses downstream of cooled gas turbine blades. The results indicate that for an ejection velocity ratio of unity, the trailing edge ejection reduces the mixing losses. An investigation of the flow field downstream of a turbine trailing edge cooled nozzle guide vane is described in Sieverding et al. [3]. A cutback trailing edge ejection system discharging on the pressure side of the blade is used. It was concluded that the coolant flow ejection did not produce any unusual wake flow patterns in the measurement planes. This feature was explained with very rapid mixing of the coolant with mainstream flow. Mee [4] discussed the experimental methods required to compare different trailing edge region coolant ejection geometries. It is suggested that if the additional complexity associated with foreign gas ejection or cooled air injection is to be avoided, more accurate results may be obtained by simulating the momentum flux ratio rather than the ejection rate of the coolant. Aerodynamic penalties of coolant ejection for two different trailing edge geometries were investigated by Kost and Holmes [5]. A blade with a thick trailing edge where coolant is ejected through slots in the trailing edge and a blade with a thin trailing edge where coolant is ejected through a row of holes on the pressure and suction sides were tested. Their results indicate that for coolant to mainstream mass flow rate ratios larger than 2.5 to 3 percent, the coolant momentum has a positive effect on total loss. Kapteijn et al. [6] tested an inlet guide vane with two different trailing edge shapes to investigate the aerodynamic effects of trailing edge ejection. A fully enclosed trailing edge ejection system and a cut-back trailing edge ejecting on the pressure side were compared. The cut-back trailing edge generates higher losses than the fully enclosed ejection system, especially in the supersonic range.

This study is an extension of the internal loss investigation and discharge coefficient measurements performed by Uzol et al. [7]. The objective is to understand the effect of trailing edge coolant ejection on the external aerodynamic loss characteristics of the turbine blade with the trailing edge coolant ejection system. For this purpose Particle Image Velocimetry (PIV) experiments and total pressure surveys are conducted in the near wake region of the trailing edge. High-resolution flow field maps are obtained for two different Reynolds numbers, namely $Re_{max}=500{,}000$ and 350,000, which is calculated using the chord length and the maximum velocity at the throat. The coolant to free-stream mass flow rate ratio, i.e., ejection rate, is varied between 0 and 5 percent. The effect of the trailing edge ejection configuration is also investigated by testing two different cut-back lengths at the trailing edge.

Contributed by the International Gas Turbine Institute and presented at the 45th International Gas Turbine and Aeroengine Congress and Exhibition, Munich, Germany, May 8–11, 2000. Manuscript received by the International Gas Turbine Institute February 2000. Paper No. 2000-GT-557. Review Chair: D. Ballal.

One configuration was a zero cut-back length blade in which the trailing edge ejection occurs right at the trailing edge. The second configuration had a cut-back length of 23 mm (12.5 percent chord) from the trailing edge and the coolant ejection was from the pressure side. Computational simulations of the flowfield are also obtained by solving two-dimensional, incompressible, steady Reynolds-averaged Navier–Stokes equations using a finite element scheme. The numerical results obtained are used for qualitative flow visualization purposes.

Experimental Facility

The experiments are conducted at the ''Cooled Turbine Cascade Facility'' at the Turbomachinery Heat Transfer Laboratory of the Pennsylvania State University. Detailed information about the facility was presented in Uzol et al. [7]

The test section consists of two flow passages that are formed by a linear cascade of three generic high-pressure turbine blade profiles with high trailing edge thickness as explained in Uzol et al. [7] (Fig. 1). The turbine blades have a chord length of 0.1834 m and the pitch is 0.135 m, which gives a pitch-to-chord ratio of 0.736. The blades are placed with a 45 deg stagger angle with an inlet flow angle of 0 deg and an exit flow angle of −76.7 deg. Typical velocity distribution around the airfoil and additional details of the specific cascade can be found in Gaugler and Russell [8] and Hippensteele et al. [9]

The middle blade in the cascade is instrumented to simulate trailing edge coolant ejection. The trailing edge is also modified to allow testing of different trailing edge coolant ejection configurations. The geometry and the details of the trailing edge coolant ejection system are explained in detail in Uzol et al. [7]. The specific geometry used in this study has six ribs between the suction side and the pressure side shells, which are enclosed with an aluminum cover plate. The two trailing edge configurations tested

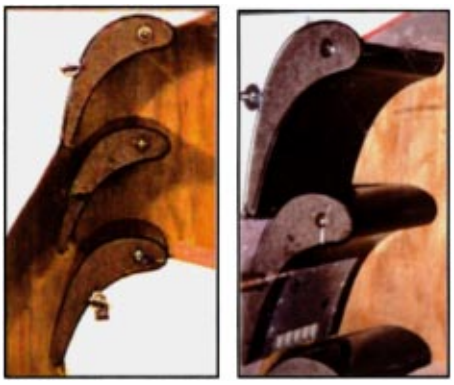

Fig. 1 View of test section

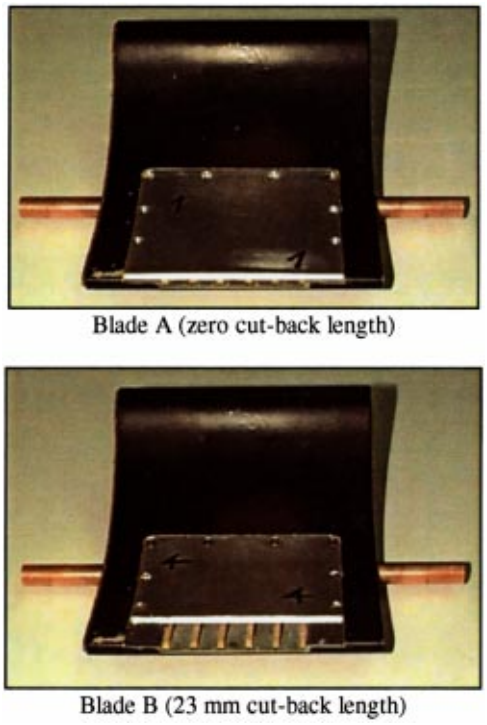

Fig. 2 Trailing edge coolant ejection configurations

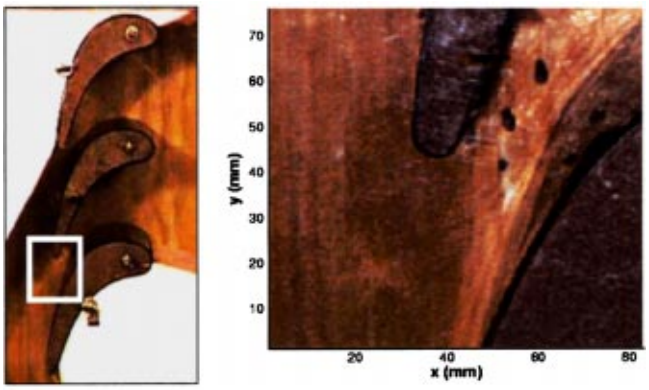

Fig. 3 PIV measurement domain

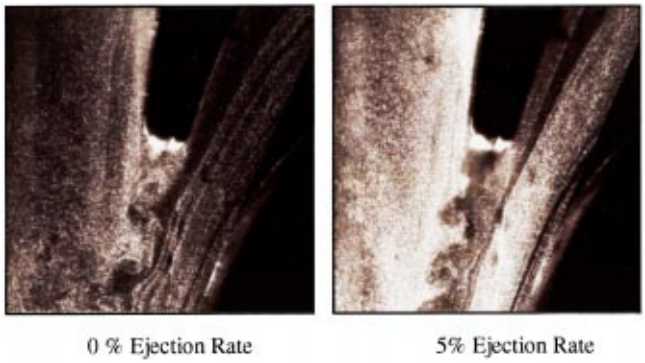

Fig. 4 Typical speckle images for PIV measurements (Blade A)

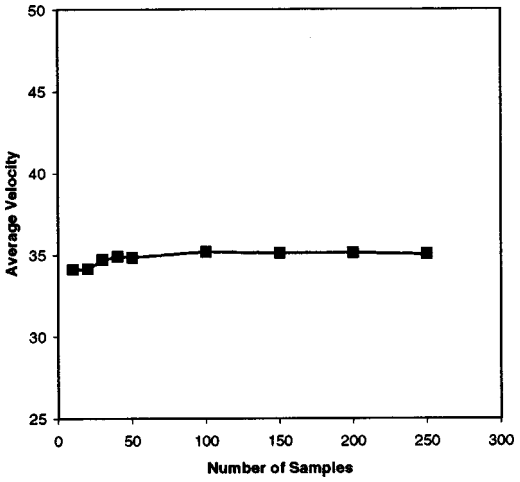

Fig. 5 Variation of the mean velocity inside the wake with number of samples

are a zero cut-back length (Blade A) and a cut-back length of 23 mm on the pressure side (Blade B) (Fig. 2). The blade span is 152.4 mm, which is equal to the endwall to endwall distance in the test section.

Pressurized air is supplied through from both sides of the instrumented blade in order to have a uniform coolant ejection from the trailing edge. The volumetric flow rate of the coolant is controlled by a rotameter. The total pressure and the total temperature of the coolant are also measured just before the coolant goes inside the blade; these measurements are used to calculate the ejection rate. The mainstream flow velocity, total pressure, and total temperature at the inlet of the test section were also measured to obtain the inlet mass flow rate. For a given inlet Reynolds number, the coolant mass flow rate is varied until the desired ejection rate is reached. Once it is reached, 250 PIV speckle images are collected. A miniature total pressure probe mounted on a traverser is also used to measure total pressure losses in addition to velocity field measurements from PIV.

PIV Measurements

Particle Image Velocimetry experiments are conducted for the investigation of the flowfield near the trailing edge of the middle blade (Fig. 1), which was instrumented for creating a coolant ejection from its trailing edge with different trailing edge configurations. The PIV measurement domain is illustrated in Fig. 3.

The flow field is seeded with fog particles and the PIV measurement domain is illuminated by two frequency doubled pulsating Nd:YAG laser sheets, which have an emitted radiation wave-

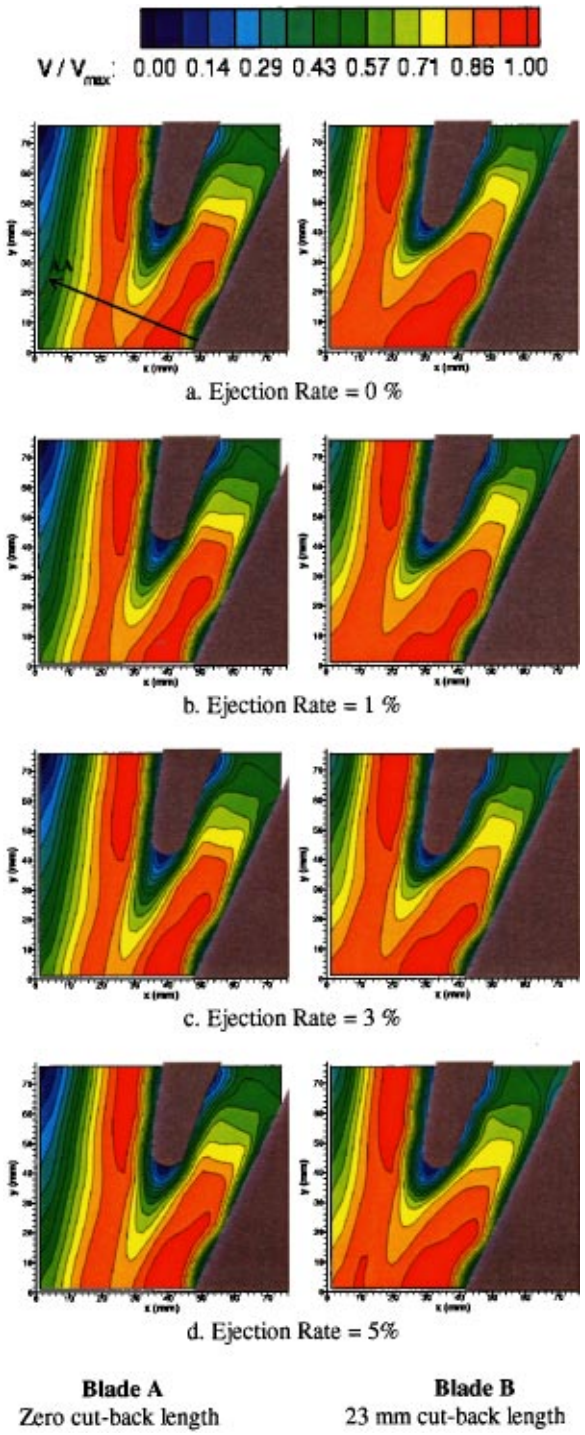

Fig. 6 Measured PIV speed contours at Re_{max}=350.000

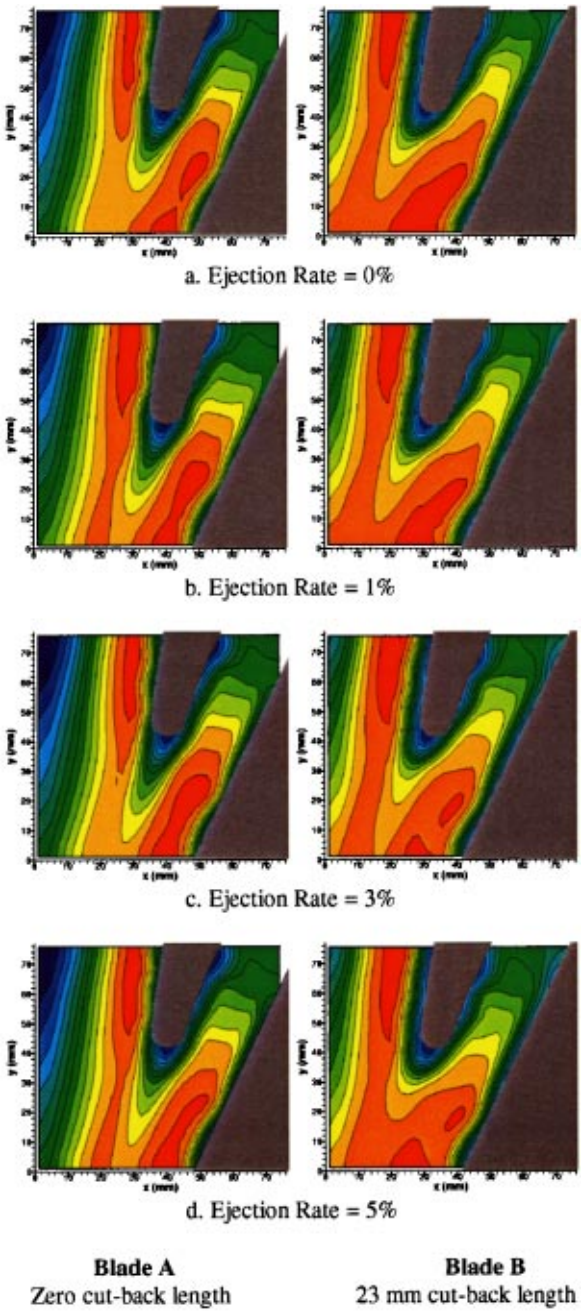

Fig. 7 Measured PIV speed contours at Re_{max}=500,000

length of 532 nm. The pulsed Nd:YAG laser power is 50 mJ and the laser sheet is placed between the third and fourth ribs, which corresponds to the midspan location on the blade. Pairs of speckle images of the PIV domain are then captured using a CCD cross-correlation camera, which is fully synchronized with the pulsating laser sheets. The minimum time delay between the two frames in an image pair that can be obtained in this system is 1 μs. Two different time delay settings of 15 μs and 11 μs are used for two different Re_{max} values of 350,000 and 500,000, respectively. All the synchronization and image-capturing processes are controlled by a DANTEC PIV 2000 processor. The cross-correlation and data reduction processes as well as the control of the PIV 2000 processor are managed by a personal computer. Figure 4 shows typical speckle images of the PIV domain captured with the CCD camera. Although the instantaneous flow details in the wake region in the absence and presence of coolant ejection are illuminated in these images, obtaining information about the unsteady nature of the flow field using these visualizations is beyond the scope of this study. The main purpose is to obtain the true-mean velocity field information, which will be used in the external loss investigation.

For each measurement case (i.e., for a specific combination of Re_{max}, a trailing edge configuration, and an ejection rate), 250 pairs of images are collected. After each pair is cross-correlated

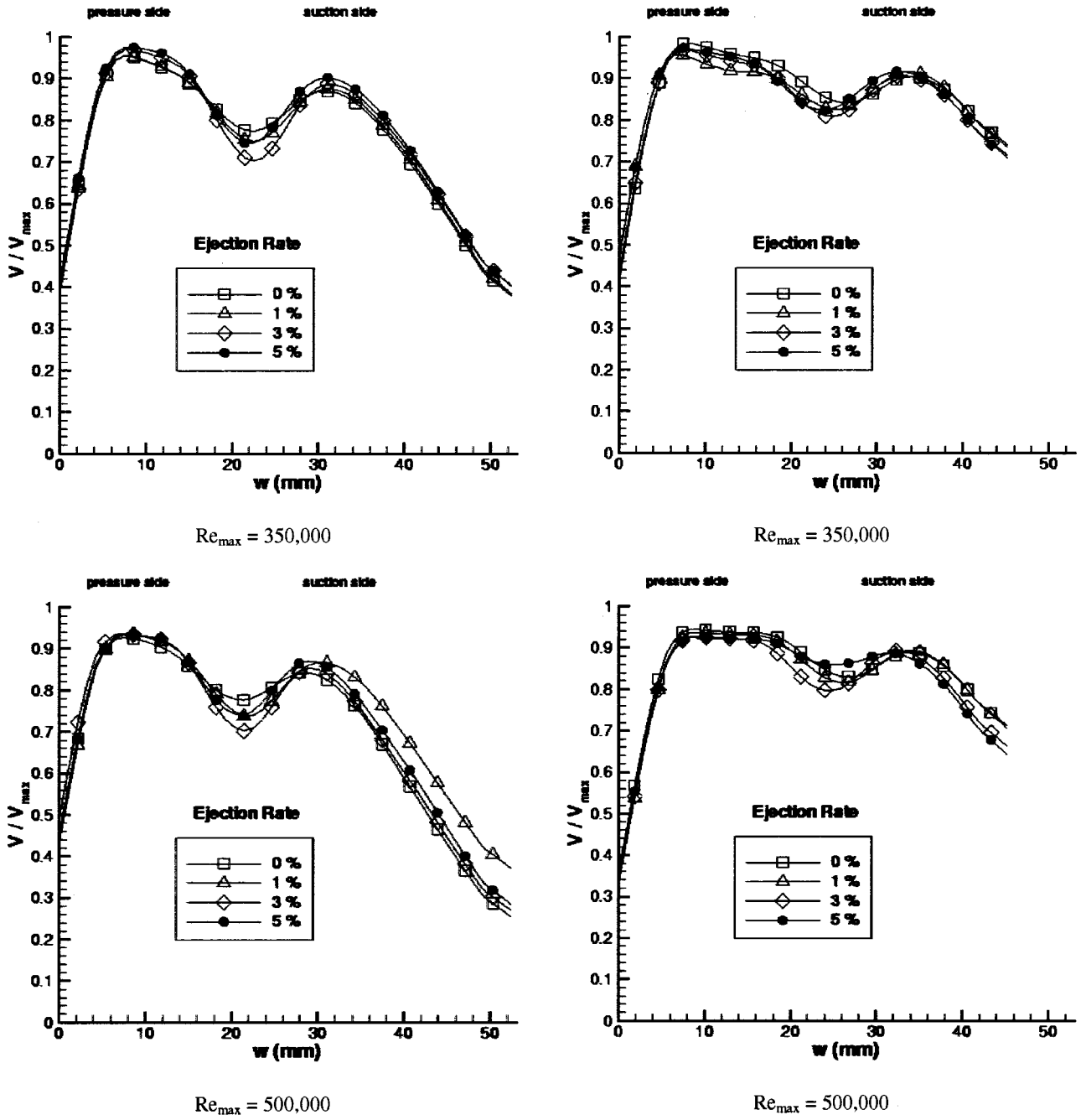

Fig. 8 Measured velocity profiles inside the wake along line *AA*

and the raw velocity fields are moving-averaged/filtered, the mean flow field is obtained by ensemble-averaging over 250 samples. The variation of the mean velocity, which was obtained by taking the average along a certain line (line *AA* in Fig. 6(*a*) inside the wake of the blade, with number of samples is shown in Fig. 5. It is clear that a stationary measurement is obtained after the number of acquired samples exceeds 150. The experimental uncertainty level for the velocity measurements using 250 samples is estimated to be ± 0.5 percent.

Figures 6 and 7 show the speed contours inside the PIV domain for Blades A and B at $Re_{max} = 350{,}000$ and 500,000, respectively. The term speed is used for the magnitude of the velocity vector from PIV measurements throughout this paper. The results are presented for ejection rates of 0, 1, 3, and 5 percent. As can be seen from the plots, it was not possible to obtain physically meaningful data from the right-hand side of the PIV domain because of the blockage of the laser sheet by the trailing edge of the lower blade. That portion of the domain is illustrated as gray triangles in Figs. 6 and 7. The actual laser sheet blockage can be seen in Fig. 4. The rest of the flowfield, however, had sufficient laser illumination, which was used to produce the wake characteristics of the middle blade.

The maximum velocity is reached at the cross section that has the minimum area between the pressure side of the middle blade and the suction side of the lower blade. The quantitative results for the maximum velocity obtained from the PIV measurements are observed to be in close agreement with the data obtained from pitot-static probe measurements acquired at the minimum area plane, as explained in Uzol et al. [7]. It is also observed that there is no separation on the suction side of the middle blade for both Reynolds numbers and both trailing edge configurations. The suction side boundary layer stays attached and mixes with the pressure side boundary layer at the trailing edge. This mixing of the suction and pressure side wall shear layers create an almost symmetric low-momentum field, in the region close to the trailing edge of Blade A (zero cut-back length). The small asymmetry that still exists is due to the difference in the thickness of these boundary layers. The near-wake region of Blade B, however, shows a greater asymmetry, which can easily be depicted in Fig. 6. This is mainly due to the effect of the cut-back region, which behaves as a backward-facing step and modifies the boundary layer behavior on the pressure side. The existence of the cut-back region diverts the speed contours toward the suction side at the trailing edge.

As the ejection rate is increased from 0 to 5 percent, some changes in the wake patterns occur. For both trailing edge configuration, the low-momentum region extends more and more as the ejection rate is increased from 0 to 3 percent. However, for 5 percent coolant ejection, the low-momentum region becomes smaller. This behavior of the wake pattern is evident in Fig. 8 in which the velocity profiles inside the wake along line *AA* (Fig. 6(*a*)) are illustrated. For both Reynolds numbers and trailing edge configurations, the velocity defect in the velocity profile becomes more significant up to 3 percent ejection rate. However, again for all cases, a decrease of the velocity defect inside the wake is observed for 5 percent coolant ejection. This particular variation of the wake patterns with varying ejection rates will have a significant effect on the blade total pressure loss characteristics.

Effect of Cut-Back Length

The effect of the cut-back length is illustrated in Fig. 9, which shows the velocity profiles along line *AA* for blades A and B, at a free-stream Reynolds number of 500,000 and for a 0 percent ejection rate. A shift in the position of the velocity defect in the velocity profile inside the wake can be observed from this figure. The minimum velocity region is shifted toward the suction side for Blade B. Although the results shown are for 0 percent ejection rate, the same shift pattern is also observed for all the other ejection rates. This shift in the velocity defect is mainly due to the reason that the pressure side shell is not complete for Blade B.

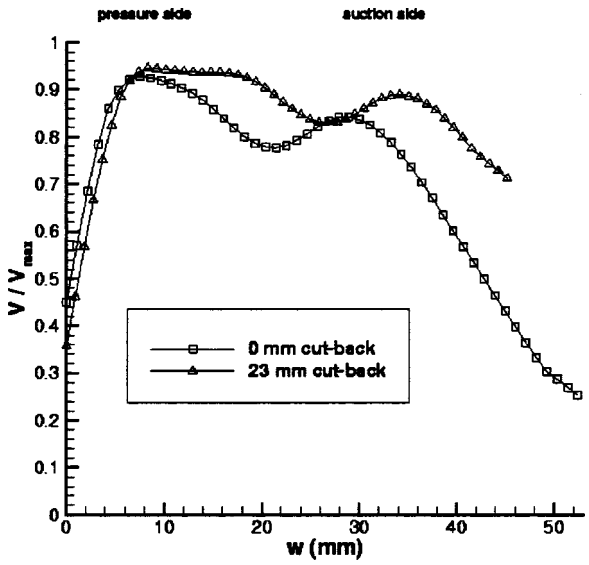

Fig. 9 Effect of cut-back length on wake velocity defect (0 percent ejection rate)

Therefore, in the near-wake region the velocity defect for Blade B is just because of the suction side shell, which clearly has a smaller defect because of the smaller thickness at the trailing edge.

Total Pressure Loss Measurements

As a complementary study for the PIV measurements, a total pressure traverse inside the near wake of the middle blade, again along line *AA*, is performed independently using a total pressure probe. The uncertainty level for the pressure measurements is estimated to be ± 0.5 percent at 105,000 N/m^2 (typical atmospheric value). The results are shown in Fig. 10, and show similar wake characteristics to the PIV results. The total pressure loss levels increase with increasing ejection rate up to 3 percent, and at 5 percent coolant ejection the losses are minimized. Furthermore, at 5 percent ejection the local total pressure increase due to the high-momentum coolant jet ejection can be seen in Fig. 9. Consequently, both the PIV results and the total pressure traverse results show that the coolant ejection has a negative effect, in terms of total pressure losses, until a certain ejection rate is reached. This behavior was also observed by previous researchers. Kost and Holmes [5] indicate that for coolant to mainstream mass flow rate ratios larger than 2.5 to 3 percent, the coolant momentum has a positive effect on total loss, both for pressure side coolant ejection and for the ejection from a slot at the trailing edge. Their results are for a cascade operating at an exit Mach number of 0.76, which is below the design condition. It is concluded that by ejecting a moderate amount of coolant from a row of holes into subsonic local flow, a decrease of profile loss will be achieved if the coolant momentum has a component in the main flow direction. Pappu and Schobeiri [2] also indicate that increasing the coolant to mainstream velocity ratio yields a deeper wake in comparison to the no-injection case and consequently in higher total pressure losses for a turbine blade trailing edge coolant ejection system without a cut-back length. The main physical reason for this phenomenon is explained thus: The ejected coolant jet does not have enough momentum to overcome the strong dissipative nature of the wake at the trailing edge, which results in the dissipation of the kinetic energy of the jet. This dissipation yields a deeper wake than for the no-injection case. The aerothermodynamic modeling and performance analysis of Kim et al. [10] for a turbine stage having cooled nozzle blades also show that ejection of coolant causes total pressure losses up to 2–3 percent of the ejection rate. How-

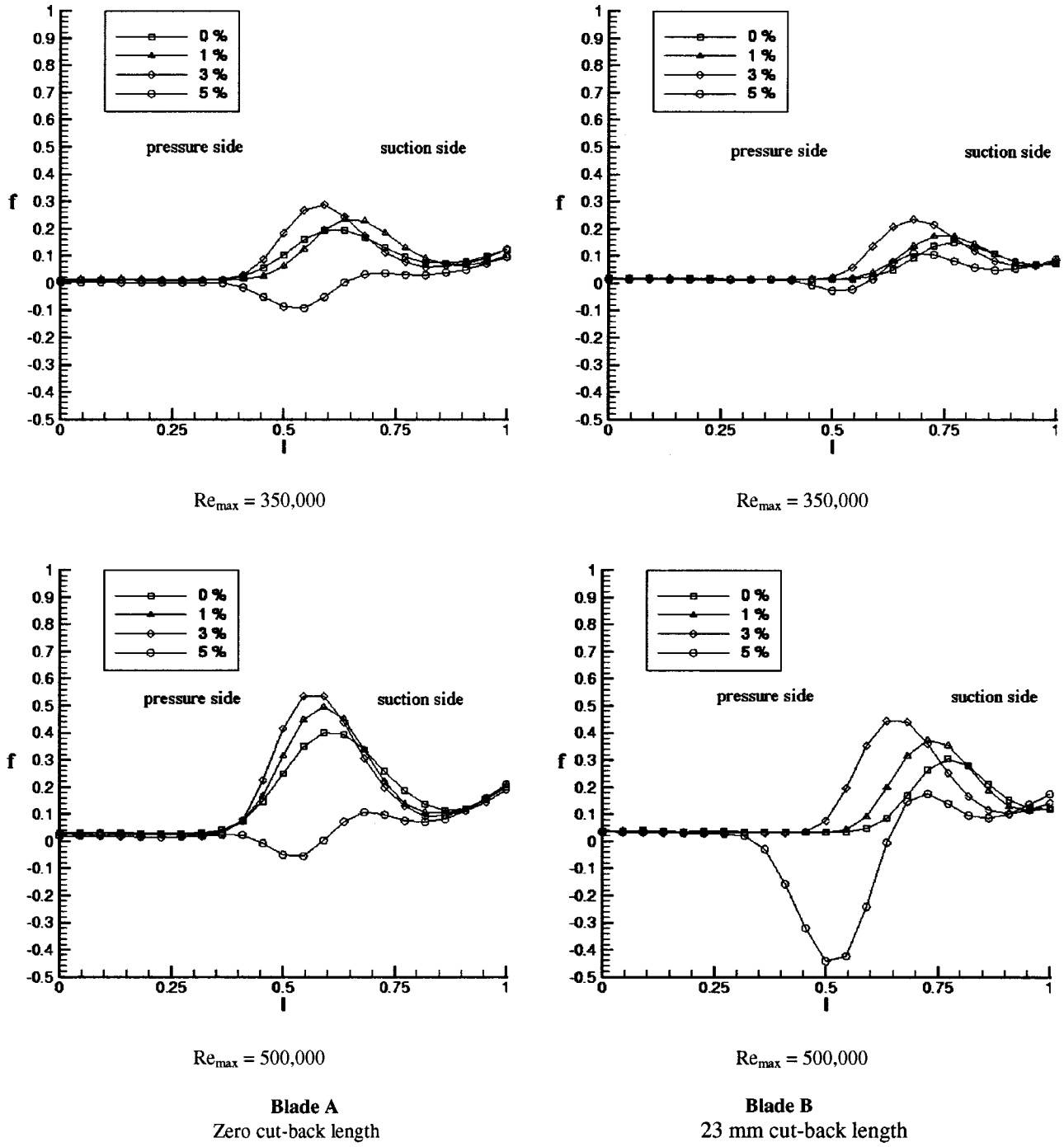

Fig. 10 Measured total pressure loss profiles along line *AA*

ever, when the momentum contribution of the coolant becomes significant, a total pressure gain is predicted when compared to the no-injection case.

The main reason for this increase in loss for low ejection rates is that the ejected coolant has a very low momentum when compared to the mainstream flow. Therefore, when the low-momentum coolant jet mixes with the high-momentum mainstream, mixing losses are created by high shear regions, which cause increases in the turbulence production in these regions. Hence, some part of the kinetic energy of the main flow is wasted through this turbulence production mechanism and this reflects as an increase in the total pressure loss levels in the wake. However, for high ejection rates like 5 percent, the ejected coolant jet has comparable momentum with the mainstream and it fills the low-momentum region inside the wake, yielding lower loss levels. This kind of behavior of the loss mechanism is observed for both trailing edge configurations and Reynolds numbers.

The total pressure loss levels for Blade B, which has a 23 mm cut-back length, are also observed to be less than that of Blade A, which has a zero cut-back length. This is due to the fact that the low-momentum region inside the wake coming from the pressure side wall shear layer of Blade A (zero cut-back length) is filled with the momentum of the coolant jet in case of Blade B. Even when there is no ejection, this region is again filled with the momentum of the mainstream coming over the back-step region. Hence this results in a reduction in the total pressure loss levels for Blade B (23 mm cut-back length).

Computational Simulations

Solutions of the two-dimensional, steady, and incompressible Reynolds-averaged Navier–Stokes equations are obtained for the test section geometry using a finite element methodology. These results are basically used for qualitative flow visualization of the flow field. A standard $k-e$ turbulence model coupled with Lander's [11] Algebraic Reynolds Stress Model is used for the simulation of the turbulent flow field. The governing equations for the flow field are:

$$u_{i,i}^* = 0 \tag{1}$$

$$\frac{\partial u_i^*}{\partial t} + u_j^* u_{i,j}^* = -p_{,i}^* + \frac{1}{\mathrm{Re}}[\mu^*(u_{i,j}^* + u_{j,i}^*)]_j \tag{2}$$

$$\frac{\partial k^*}{\partial t^*} + u_j^* k_{,j}^* = \left(\frac{\mu_t^*}{\sigma_k} k_{,j}^*\right)_j - \varepsilon^* + \mu_t^* \Phi^* \tag{3}$$

$$\frac{\partial \varepsilon^*}{\partial t^*} + u_j^* \varepsilon_{,j}^* = \left(\frac{\mu_t^*}{\sigma_k} \varepsilon_{,j}^*\right)_{,j} + C_1 \left(\frac{\varepsilon^*}{k^*}\right) \mu_t^* \Phi^* - c_2 \frac{\varepsilon^{*2}}{k^*} \tag{4}$$

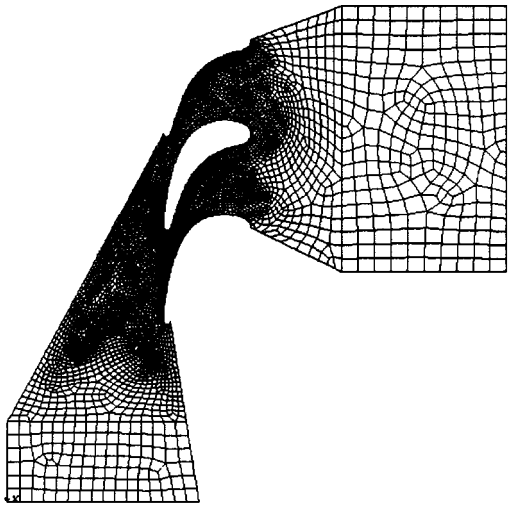

Blade A

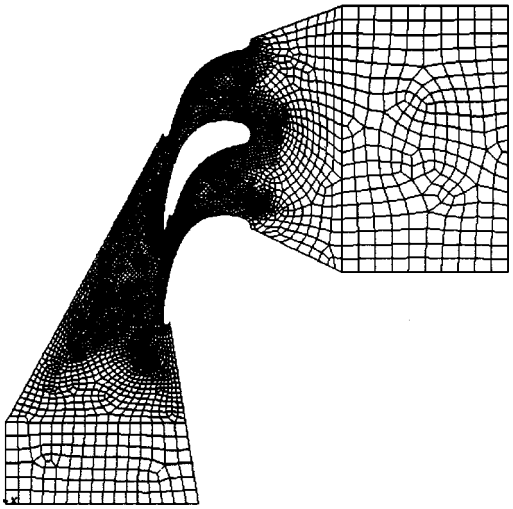

Blade B

Fig. 11 Computational meshes for Blades A and B

A finite element-based fluid dynamics analysis package, FIDAP [12], is used to solve the governing equations. The flow domain is discretized by using nine-node quadrilateral elements, which give a biquadratic velocity and bilinear pressure variation within each element. Velocity components are specified as zero on the walls and on the blade in order to satisfy the no-slip condition. At the inlet of the test section, the x component of the velocity is specified as a uniform steady profile and the y component is specified as zero. At the trailing edge of the blade, the coolant ejection velocity is specified as a uniform profile that corresponds to the desired coolant ejection rate. Values for the turbulent kinetic energy and for the dissipation rate of turbulent kinetic energy corre-

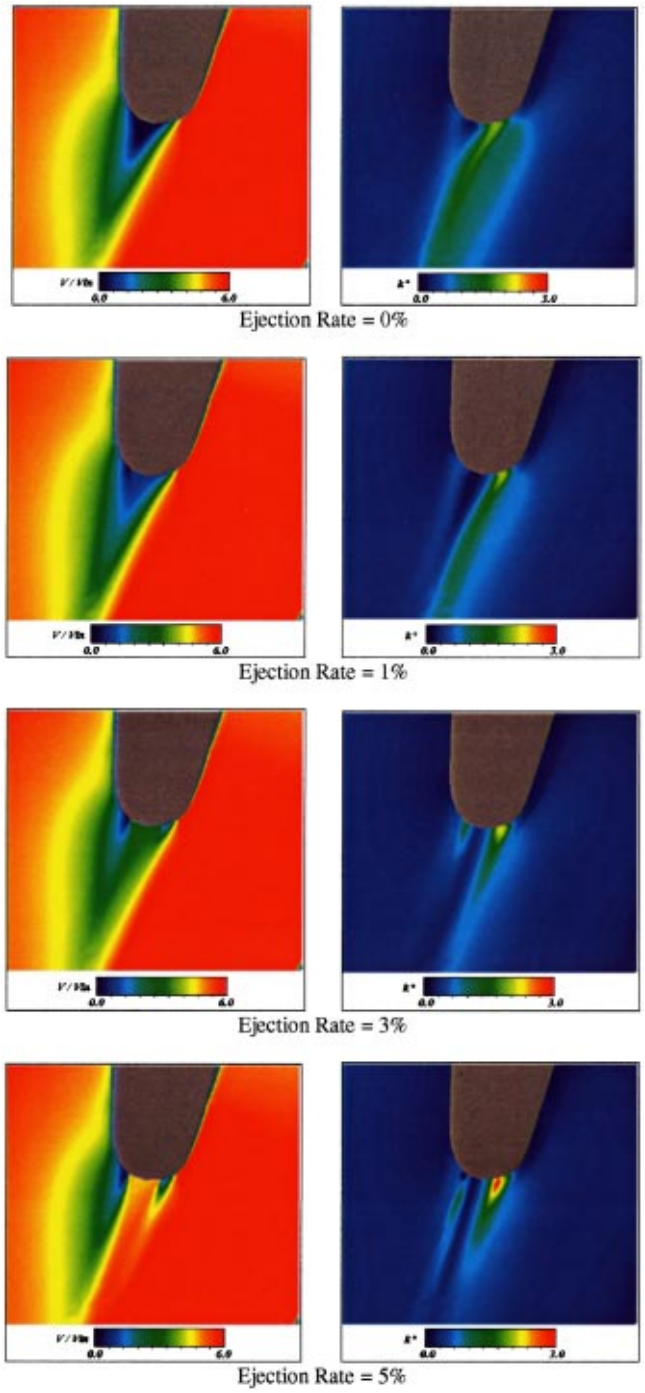

Fig. 12 Speed contours and turbulent kinetic energy contours for Blade A

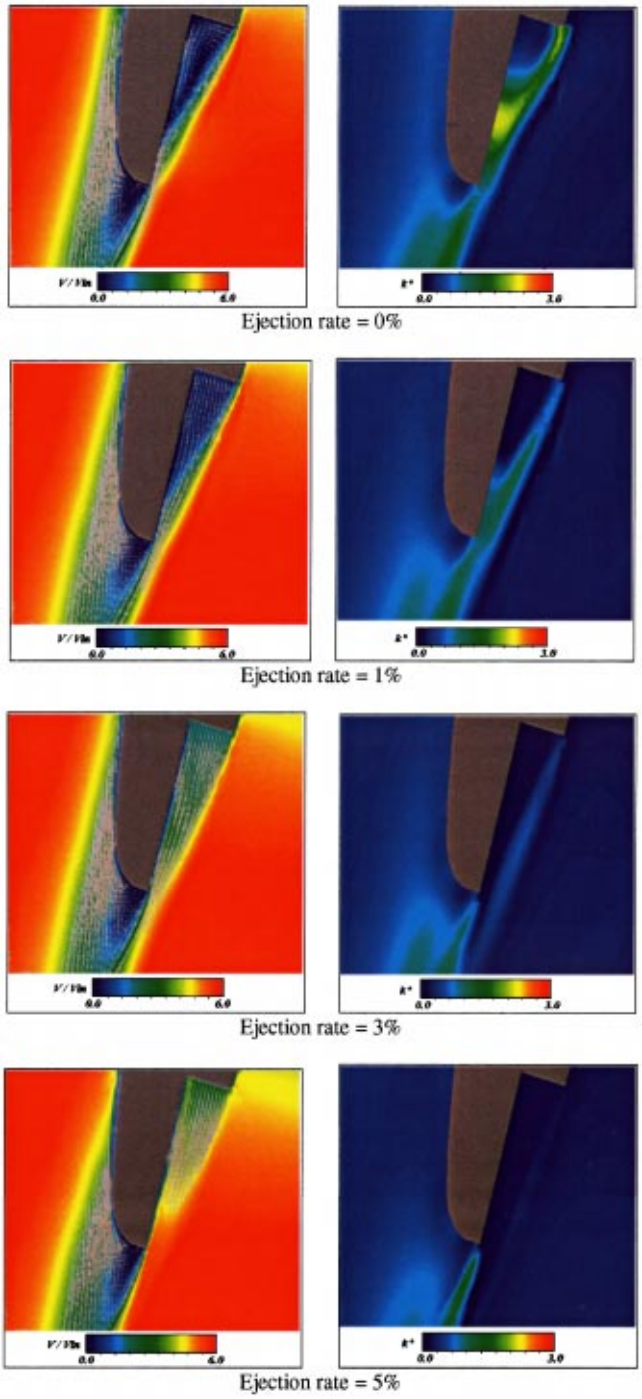

Fig. 13 Speed contours and turbulent kinetic energy contours for Blade B

sponding to a 1.2 percent turbulence intensity level are also specified at the test section inlet. This level of turbulence intensity is obtained from single sensor hot-wire measurements at that location. For the Blade A case, 6640 second-order finite elements are created, which resulted in 24,776 nodes. For Blade B, 6555 second-order elements are used, which gives 24442 nodes. The computational meshes used for Blade A and B are illustrated in Fig. 11.

Figures 12 and 13 illustrate the results of the computational analysis near the trailing edges of Blades A and B, respectively. The speed contours and the turbulent kinetic energy distribution of the flow field are shown in these figures. The recirculatory region inside the cut-back length of Blade B is clearly seen in Fig. 13 for 0 percent ejection rate. As the ejection rate is increased, this region vanishes, and the coolant ejection starts to dominate the cut-back region on the trailing edge. The formation of this strong recirculatory region at low ejection rates is the main reason for the increase in losses, which in turn result in low discharge coefficients for a trailing edge with a long enough cut-back length [7]. As can be seen from the turbulent kinetic energy plots, the turbulent kinetic energy production inside the high shear regions is high for 0 and 1 percent ejection rates when compared to the higher ejection rates. However, as the ejection rate increases, the turbulent kinetic energy generation goes down because of the reduction of the shear between the ejected coolant and the main flow. This behavior is closely related to the total pressure loss characteristics of the blade because it is the shear between the coolant and the mainstream that determines the kinetic energy losses. These in turn result in the creation of total pressure losses inside wake as observed from PIV and total pressure loss measurements.

Conclusions

The subsonic external flow field physics near the trailing edge of a turbine blade with a coolant ejection system is investigated in order to determine the external aerodynamic loss behavior of the blade due to trailing edge coolant ejection for different ejection rates. Particle Image Velocimetry (PIV) and total pressure loss measurement results show that the mixing of the coolant flow with the mainstream result in an increase in loss levels for 0–3 percent ejection rates. However, when the coolant ejection rate reaches 5 percent, the loss levels are minimized and even local total pressure increases are observed due to the high-momentum coolant jet. This behavior of the loss mechanism is observed both for the blade with a zero cut-backlength and for the blade with a 23 mm cut-back length at the trailing edge. The main possible reason for this kind of behavior at low ejection rates is the creation of mixing losses due to the mixing of high-momentum mainstream and the low-momentum coolant flow. The effect of the cut-back length was determined to be a shift in the velocity defect region in the wake velocity profile. Additionally, the blade with the cut-back length at the trailing edge is observed to have a smaller velocity defect in the profile that will lead to less aerodynamic loss. The results of the computational simulations reveal the existence of a recirculatory region inside the cut-back length of Blade B for 0 percent ejection, which results in a reduction in the discharge coefficient values for this specific trailing edge arrangement. The turbulence generation is also numerically visualized as the ejection rate is changed from 0 to 5 percent. It is observed that the behavior of the shear generated between the mainstream and the coolant flow mainly determines most of the loss characteristics of the blade. Numerical simulation results illuminate the details of the flow field that could not be captured by PIV.

Acknowledgments

The turbine cascade used in the current study was provided by NASA Lewis (Glenn) Research Center. The authors would like to acknowledge the equipment support provided by S. A. Hippensteele and Dr. R. E. Gaugler of NASA (Glenn) Research Center, Cleveland, Ohio. The authors are also grateful for the equipment grant provided by the College of Engineering of the Pennsylvania State University. The grant was used for the acquisition of the PIV equipment extensively used in this study.

Nomenclature

f = total pressure loss coefficient $=(P_{tin}-P_{tex})/P_{tin}\times 100$
k = turbulent kinetic energy
k^* = k/u_0^2=nondimensional turbulent kinetic energy
l = $w/w_{\max}$=nondimensional total pressure traverse distance parameter

p = static pressure
p^* = $(p-p_{ref})/\rho u_0^2$=nondimensional static pressure
Re_{max} = maximum Reynolds number calculated using maximum velocity at throat and blade chord
u_i = ith component of velocity vector
u_i^* = u_i/u_0=nondimensional velocity
V = magnitude of velocity vector
V_{in} = velocity at inlet of test section
V_{max} = maximum velocity at throat
w = distance parameter along line AA, mm
w_{max} = maximum distance on AA, mm
x_i = ith component of spatial coordinate
x_i^* = x_i/D=nondimensional coordinate
ε = viscous dissipation rate of turbulent kinetic energy
ε^* = $\varepsilon D/u_0^3$=nondimensional viscous dissipation rate of turbulent kinetic energy
Φ = viscous dissipation function
Φ^* = $\Phi D^2/u_0^2$=nondimensional viscous dissipation function
μ_0 = absolute viscosity
μ_t = turbulent viscosity
μ_t^* = $\mu_t/(\rho u_0/D)$=nondimensional turbulent viscosity
μ^* = $1+\mu_t/\mu_0$=nondimensional viscosity
ρ = density

References

[1] Deckers, M., and Denton, J. D., 1997, ''The Aerodynamics of Trailing-Edge-Cooled Transonic Turbine Blades: Part 1—Experimental Approach,'' ASME Paper No. 97-GT-518.

[2] Pappu, K. R., and Schobeiri, M. T., 1997, ''Optimization of Trailing Edge Ejection Mixing Losses: A Theoretical and Experimental Study,'' ASME Paper No. 97-GT-523.

[3] Sieverding, C. H., Arts, T., Dénos, R., and Martelli, F., 1996, ''Investigation of the Flow Field Downstream of a Turbine Trailing Edge Cooled Nozzle Guide Vane,'' ASME J. Turbomach., **118**, pp. 291–300.

[4] Mee, D. J., 1992, '''Techniques for Aerodynamic Loss Measurement of Transonic Turbine Cascades With Trailing-Edge Region Coolant Ejection,'' ASME Paper No. 92-GT-157.

[5] Kost, F. H., and Holmes, A. T., 1985, ''Aerodynamic Effect of Coolant Ejection in the Rear Part of Transonic Rotor Blades,'' in: *Heat Transfer and Cooling in Gas Turbines*, AGARD Conference Proceedings No. 390, pp. 41-1–41-12.

[6] Kapteijn, C., Amecke, J., and Michelassi, V., 1996, ''Aerodynamic Performance of a Transonic Turbine Guide Vane With Trailing Edge Coolant Ejection: Part 1—Experimental Approach,'' ASME J. Turbomach., **118**, pp. 519–528.

[7] Uzol, O., Camci, C., and Glezer, B., 2001, ''Aerodynamic Loss Characteristics of a Turbine Blade With Trailing Edge Coolant Ejection: Part 1—Effect of Cut-Back Length, Spanwise Rib Spacing, Free-Stream Reynolds Number, and Chordwise Rib Length on Discharge Coefficients,'' ASME J. Turbomach., **123**, pp. 238–248.

[8] Gaugler, R. E., and Russell, L. M., 1980, ''Streakline Flow Visualization Study of a Horseshoe Vortex in a Large-Scale, Two-Dimensional Turbine Stator Cascade,'' ASME Paper No. 80-GT-4.

[9] Hippensteele, S. A., Russell, L. M., and Torres, F. J., 1995, ''Local Heat Transfer Measurements on a Large, Scale-Model Turbine Blade Airfoil Using a Composite of a Heater Element and Liquid Crystals,'' NASA TM 86900.

[10] Kim, J. H., Kim, T. S., Lee, J. S., and Ro, S. T., 1996, ''Performance Analysis of a Turbine Stage Having Cooled Nozzle Blades With Trailing Edge Ejection,'' ASME Paper No. 96-TA-12.

[11] Launder, B. E., 1993, ''Lecture Notes on Turbulence Modeling in Industrial Flows,'' Les Houches Summer School on Computational Fluid Dynamics; also in FIDAP, 1993.

[12] Fluid Dynamics International, Inc., 1993, FIDAP 7.0 Users' Manual.

A Method for Correlating the Influence of External Crossflow on the Discharge Coefficients of Film Cooling Holes

D. A. Rowbury
Rolls-Royce plc,
Bristol, UK

M. L. G. Oldfield
Department of Engineering Science,
University of Oxford,
Oxford, UK

G. D. Lock
Department of Mechanical Engineering,
University of Bath,
Bath, UK

An empirical means of predicting the discharge coefficients of film cooling holes in an operating engine has been developed. The method quantifies the influence of the major dimensionless parameters, namely hole geometry, pressure ratio across the hole, coolant Reynolds number, and the freestream Mach number. The method utilizes discharge coefficient data measured on both a first-stage high-pressure nozzle guide vane from a modern aero-engine and a scale (1.4 times) replica of the vane. The vane has over 300 film cooling holes, arranged in 14 rows. Data was collected for both vanes in the absence of external flow. These noncrossflow experiments were conducted in a pressurized vessel in order to cover the wide range of pressure ratios and coolant Reynolds numbers found in the engine. Regrettably, the proprietary nature of the data collected on the engine vane prevents its publication, although its input to the derived correlation is discussed. Experiments were also conducted using the replica vanes in an annular blowdown cascade which models the external flow patterns found in the engine. The coolant system used a heavy foreign gas (SF_6/Ar mixture) at ambient temperatures which allowed the coolant-to-mainstream density ratio and blowing parameters to be matched to engine values. These experiments matched the mainstream Reynolds and Mach numbers and the coolant Mach number to engine values, but the coolant Reynolds number was not engine representative (Rowbury, D. A., Oldfield, M. L. G., and Lock, G. D., 1997, ''Engine-Representative Discharge Coefficients Measured in an Annular Nozzle Guide Vane Cascade,'' ASME Paper No. 97-GT-99, International Gas Turbine and Aero-Engine Congress & Exhibition, Orlando, Florida, June 1997; Rowbury, D. A., Oldfield, M. L. G., Lock, G. D., and Dancer, S. N., 1998, ''Scaling of Film Cooling Discharge Coefficient Measurements to Engine Conditions,'' ASME Paper No. 98-GT-79, International Gas Turbine and Aero-Engine Congress & Exhibition, Stockholm, Sweden, June 1998). A correlation for discharge coefficients in the absence of external crossflow has been derived from this data and other published data. An additive loss coefficient method is subsequently applied to the cascade data in order to assess the effect of the external crossflow. The correlation is used successfully to reconstruct the experimental data. It is further validated by successfully predicting data published by other researchers. The work presented is of considerable value to gas turbine design engineers as it provides an improved means of predicting the discharge coefficients of engine film cooling holes.
[DOI: 10.1115/1.1354137]

Introduction

The rotor and nozzle guide vane (NGV) stages of the high-pressure turbine often incorporate discrete hole film cooling in an attempt to ''insulate'' the components from the hot mainstream gas. Such a film cooling design will, ideally, result in a uniform airfoil metal temperature, as this minimizes the thermal stresses within the airfoil, thereby maximizing component life. For the sake of engine specific fuel consumption (sfc), this has to be achieved with the minimum coolant flow possible. Given that the coolant-to-mainstream pressure ratio is usually set by the compressor exit pressure and the combustor pressure drop, the design problem hinges on correct hole sizing and positioning in order to provide the requisite coolant flow. This requires the accurate prediction of the discharge coefficients of the film cooling holes.

The measurement of film-cooling hole discharge coefficients is a subject widely reported in the literature, although there is a general lack of data gathered under conditions comparable to the engine environment. Research of this nature is needed in order to validate and improve upon existing CFD codes and, ultimately, to aid the attainment of greater component durability. An excellent review of work in this field has been produced by Hay and Lampard [1]. The review concentrates on the various methods of predicting the discharge coefficient, C_d, of a film cooling hole, concluding that ''potential flow analyses can give acceptable accuracy for simple geometries with crossflows, while more complex cases require the use of correlated data which may be incorporated in a range of predictive schemes.''

The C_d depends on both the local geometry and the flow conditions upstream and downstream of the hole. Hole geometries are chosen such that cooling effectiveness is maximized, with inclined holes often being used as higher effectiveness levels are achieved for shallow injection angles than for normal injection (see, for example, Sasaki et al. [2] or Foster and Lampard [3]). Furthermore, ''flared'' or ''fan-shaped'' holes are often used in film cooling arrays as they reduce the momentum of the jet at exit, thereby improving the film cooling performance further [4].

The work discussed in this paper provides a numerical means of

Contributed by the International Gas Turbine Institute and presented at the 45th International Gas Turbine and Aeroengine Congress and Exhibition, Munich, Germany, May 8–11, 2000. Manuscript received by the International Gas Turbine Institute February 2000. Paper No. 2000-GT-294. Review Chair: D. Ballal.

predicting the discharge coefficient of a film cooling hole, allowing for external but not internal crossflow, from the hole geometry and the flow conditions present. Data collected has been used to develop a generalized design methodology, so that new hole geometries or flow conditions can be readily investigated without the need for additional experimental work. When accounting for the influence of external crossflow, the correlation is broken down to cylindrical or fan-shaped holes in the pressure surface, suction surface, or leading edge regions of the airfoil.

Test Facility

The with-crossflow experimental data presented in this paper was gathered on the cold heat transfer tunnel (CHTT; Martinez-Botas et al. [5]) in Oxford. The CHTT incorporates an annular cascade of 36 film cooled NGVs at 1.4 times larger than engine size, resulting in good spatial resolution on all measurements taken. A detailed description of the tunnel, shown schematically in Fig. 1, can be found in Rowbury et al. [6].

The CHTT is a short duration (typically 5–7 s), transonic test facility which not only provides engine representative Reynolds and Mach numbers, but also, being an annular cascade of NGVs, models the three-dimensional flow patterns found in modern aero-engines, including all secondary flow phenomena. Moreover, the coolant system design, employing a ''foreign gas'' coolant (30.2 percent SF_6, and 68.8 percent Ar by weight, which has a ratio of specific heats of 1.4 and gives a density ratio 1.77), allows the engine coolant-to-mainstream density ratio, ρ_{0c}/ρ_{0m}, blowing parameter, $\rho_c u_c/\rho_m u_m$, and momentum flux ratio, $\rho_c u_c^2/\rho_m u_m^2$, to be varied about actual engine design values. Indeed, when the test vanes are cooled with foreign gas, all of the major flow parameters except the temperature ratio and the coolant Reynolds number are then simultaneously matched to the engine condition (Rowbury et al. [7]). The total and static pressure ratios, blockage at the mainstream throat, density ratios, mainstream Reynolds number, and the local Mach numbers in the coolant and mainstream are all matched.

Geometric and Flow Parameters

The NGV row being studied in the CHTT is representative of that found in the high pressure turbine of a modern aero-engine. The cooling geometry consists of fourteen rows of holes, fed from one of two internal cavities, as illustrated in Fig. 2. The four rows of cooling holes around the leading edge (rows 7–10 inclusive) and the first two rows of film cooling holes on the pressure surface (rows 5 and 6) are cylindrical while each of the remaining rows (except row 11) have been investigated with both a cylindrical and a fan-shaped (see, for example, Gritsch et al. [8]) geometry. There are, therefore, a total of 20 data sets.

The attainment of each data set involved flowing a single row of holes both with and without the presence of external crossflow. As the rows were flowed singly, the internal crossflow Mach number, M_c, was negligible, so the influence of internal crossflow could not be investigated. The noncrossflow experiments were conducted in a pressurized vessel in order to cover the wide range of pressure ratios and coolant Reynolds numbers expected in the engine [6]. As already mentioned, the with-crossflow experiments were carried out on the CHTT.

Of the 20 data sets, only three representative sets are presented, as the main aim of the paper is to highlight the success of the correlation rather than the mass-presentation of experimental data.

By testing an actual engine vane cooling configuration, the range of flow conditions (mainstream Mach number, M_m, and pressure ratio across the holes, PR) encountered around the vane surface is significant, as seen in Table 1. At the same time, the two commonly defined hole angles (Fig. 3), the angles of inclination, θ, and orientation, α, vary within the ranges $20°<\theta<90°$ and $0°<\alpha<60°$, respectively.

The fan-shaped holes have a fan angle of 12.5°, leading to area ratios in the range 2.9 to 4.0. These values are comparable to those of the fan-shaped holes tested at Karlsruhe [8].

There is one significant difference between the CHTT and engine vanes—whereas the CHTT holes are drilled on a CNC machine, resulting in sharp inlets and hydraulically smooth walls, the engine vanes are laser drilled or spark eroded, leading to a shaping of the hole inlets and rough walls. The radiusing of the hole inlets, due to ''unclean breakthrough,'' has to be accounted for within the noncrossflow discharge coefficient, $C_{d,\mathrm{no}}$, correlation. The difference in surface roughness between CHTT and engine holes means that an insight into its effect on $C_{d,\mathrm{no}}$ has been completed. Although the proprietary nature of the engine vane data prevents

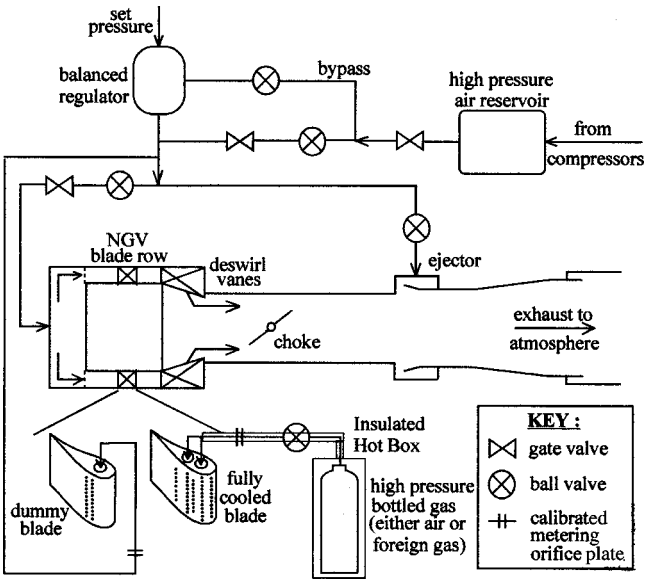

Fig. 1 Schematic diagram of the CHTT

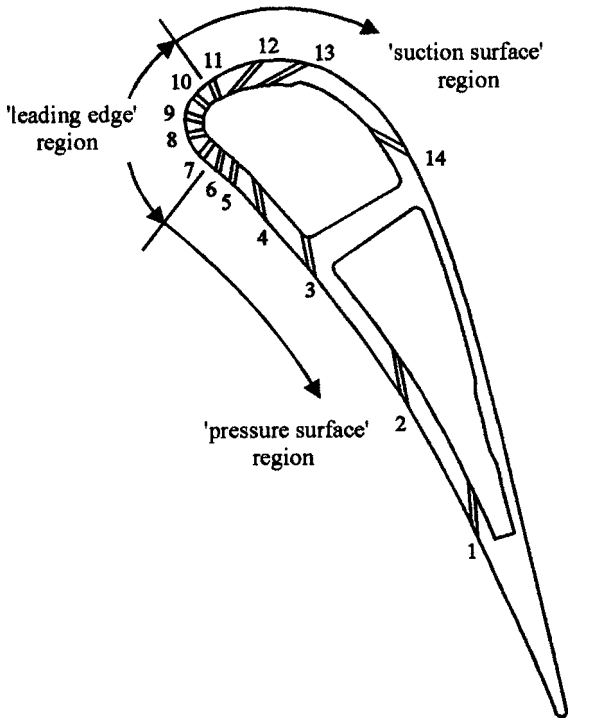

Fig. 2 Vane cross-section, illustrating the ''regions'' referred to in the declaration of coefficients for the ''$\delta_{\mathrm{out}} = A k_{\mathrm{out},\perp}^{-B} - C$'' relationships (Table 2)

Table 1 CHTT vane hole geometries and flow conditions

Row No.	Angle of Inclination, θ	Angle of Orientation α	External Mach Number	Design *PR*	CHTT *l/d*
1	21°	0°	0.39	1.12	9.8
2	20°	7°	0.21	1.05	10.3
3	28°	7°	0.12	1.03	7.5
4	30°	7°	0.08	1.02	7.0
5	58°	0°	0.06	1.02	3.6
6	58°	0°	0.05	1.02	3.6
7	90°	60°	0.04	1.02	6.1
8	89°	60°	0.07	1.02	6.1
9	84°	60°	0.17	1.04	6.1
10	83°	60°	0.25	1.06	6.1
11	78°	0°	0.32	1.09	3.6
12	39°	0°	0.49	1.18	5.5
13	40°	0°	0.61	1.28	5.4
14	30°	6°	0.96	1.77	7.0

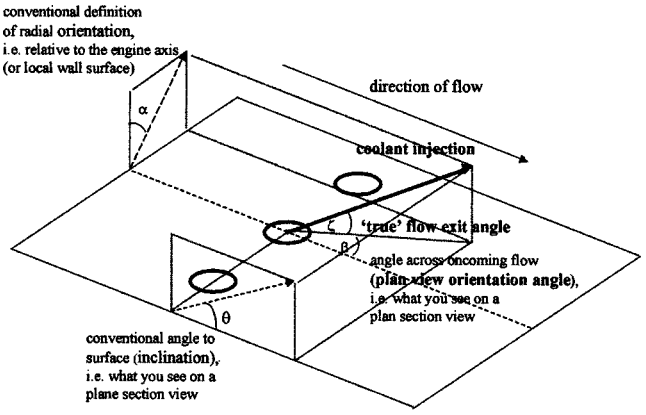

Fig. 3 Definition of film cooling hole angles

its presentation, it is worth highlighting that the noncrossflow correlation aimed to mimic the engine vane data as closely as possible. Hole roughness is not expected to affect the influence of the external crossflow on the hole discharge coefficients. Needless to say, hole roughness also leads to a large uncertainty in hole area, although this simply alters the magnitude of C_d rather than trends witnessed.

It is worth noting that the important dimensionless groups when studying C_d data, both with and without external crossflow, are PR and Re_h [6].

Predicting Hole Discharge Coefficients

The prediction of film cooling hole discharge coefficients during the design process can, and should, be broken down into two distinct steps: the prediction of the hole C_d without crossflow present, followed by a modification of this ''baseline'' prediction to allow for the influence of external crossflow. As explained earlier, the experimental method used in the present study was for no internal crossflow present, so the recommendations provided here are purely on how to obtain accurate predictions of the hole C_d *without internal* or *external* crossflow, and how to modify this for the influence of *external* crossflow.

Noncrossflow Correlations. Given that this correlation has been developed for employment as a design tool, the accuracy of its predictions is paramount. The predictive schemes proposed by Rogers and Hersh [9], Andrews and Mkpadi [10], Tay Chu et al. [11], Adkins and Gueroui [12], and Parker and Kercher [13] were all studied in an attempt to obtain a noncrossflow correlation that accurately reproduced the engine vane data. However, the correlations presented by McGreehan and Schotsch [14] and Lichtarowicz et al. [15] were found to be vastly superior. The recommendations of Lichtarowicz et al., allowing for l/d and Re_h effects, were adopted, allowing for inlet radius effects by means of the correction proposed of Schoder and Dawson [16]. This provided the noncrossflow discharge coefficient, $C_{d,\mathrm{no}}$, values from which the with-crossflow predictions could be produced.

Lichtarowicz et al. [15] recommend/conclude:

(a) Avoid $l/d<1.5$, as the C_d varies rapidly with l/d below this value.

(b) For $2<l/d<10$, $C_{d,\mathrm{no}}$ can be assumed to be constant for $\mathrm{Re}_h>2\times10^4$, and is given by

$$C_{du}=0.827-0.0085(l/d) \tag{1}$$

with an accuracy of 1.25 percent. (N.B.: This is not consistent with the data collected on the CHTT vanes but is supported by the engine vane data.) This is referred to as the ''limiting C_d'' or ''limit,'' denoted C_{du}. For $1.5<l/d<2$, $C_{du}=0.810$ to the same accuracy.

(c) For $10<\mathrm{Re}_h<2\times10^4$, $C_{d,\mathrm{no}}$ is given to an accuracy of ~2.5 percent by

$$\frac{1}{C_{d,\mathrm{no}}}=\frac{1}{C_{du}}+\frac{20}{\mathrm{Re}_h}\left(1+2.25\frac{l}{d}\right)-\frac{0.005l/d}{1+7.5(\log 0.0015\,\mathrm{Re}_h)^2} \tag{2}$$

While Schoder and Dawson [16] suggest correcting for inlet radius effects by means of

$$\Delta C_d=3.10(r/d)C_d\,. \tag{3}$$

Given that we require a predictive scheme for application to engine hardware, it is worth noting that all the engine vane data is predicted to within ~6 percent using this method (although it is less successful in reproducing the CHTT vane data). At the design PR, the engine data is generally predicted within ~1 percent.

With-Crossflow Correlations

Karlsruhe Method. The authors feel that the additive loss coefficient method provides a sensible means of accounting for the influence of external crossflow as it is based on the physical reality that the external flow leads to a modification of the local static pressure field, thereby altering the pressure drop driving the fluid (Rowbury et al. [17]). However, there has been a large amount of C_d research carried out at the University of Karlsruhe in recent years [8,18–20], culminating in the proposal of a method for correlating discharge coefficients [21]. These authors found that the with-crossflow data collected for a number of different mainstream Mach numbers and pressure ratios collapses to a single curve if it is normalized by $C_{d,\mathrm{no}}$ at the same PR and is then plotted against the jet-to-crossflow momentum flux ratio. The use of a least-squares curve-fit to this data then provided an accurate means of predicting the with-crossflow discharge coefficients.

Although successful, the method has yet to be ''generalized'' into a numerical correlation that can be applied accurately to untested geometries and flow conditions, so test data needs to be collected for each new geometry considered. The authors feel that this may prove more difficult than it has for the additive loss coefficient approach (see ''Generalizing the Predictive Scheme'' below) as the modification of the pressure drop across the hole, the basis of the approach, could be readily related to the cooling hole flow angles [17]. Needless to say, this is of fundamental importance if the correlation is to become a viable tool for the engine designer.

Additive Loss Coefficient Approach. As already mentioned, the influence of internal crossflow was not investigated on the CHTT vanes, so only the outlet loss coefficient approach will be discussed here. However, it is worth realizing that the inlet loss coefficient approach is analogous to that for outlet, and, since film

cooling holes invariably have length-to-diameter ratios greater than 3.5, the influence of inlet and exit crossflow effects on the hole C_d can be assumed to be independent of each other. This is equivalent to assuming that the mainstream external flow alters the localized external pressure but does not significantly affect the flow structure within the hole, a commonly made assumption that is supported by the accuracy of predictions by Hay et al. [22] and Hay et al. [23]. Consequently, the loss coefficient approach can be used to account for internal and external crossflow effects simultaneously. However, the work of Thole et al. [19], Walters and Leylek [24], and Burd and Simon [25,26] implies that, under some circumstances, δ_{out} can be influenced by the coolant crossflow Mach number, and so this assumption is not universally valid.

When presenting results pertaining to the influence of internal or external crossflow on the discharge coefficients of film cooling holes, it is common to do so in terms of the ''additive loss'' approach first proposed by Sasaki et al. [2] and extended by Tillman and Jen [27]. The approach assumes that the presence of crossflow will require an increase in the pressure drop across the hole in order to maintain the coolant mass flow rate. The additional pressure drop is nondimensionalized using the hole flow dynamic pressure, and is assumed to correlate with the ratio of the hole exit-to-crossflow momentum flux ratio. The data presented by Rogers and Hersh [9] provided evidence supporting a physical model based on momentum transfer, implying that it is physically realistic to correlate loss coefficients with momentum flux ratio.

The external additive loss coefficient, δ_{out}, is defined as

$$\delta_{\text{out}}=\frac{[(p_{0c}-p_m)_{\text{with crossflow}}-(p_{0c}-p_m)_{\text{without crossflow}}]_{\rho_h,u_h}}{\frac{1}{2}\rho_h u_h^2}. \tag{4}$$

Note that the pressure drops are measured at the same coolant mass flow rate (or Re_h). In order to match Re_h, the mainstream static pressure must be maintained, so the dynamic pressure within the hole will remain constant. Consequently, if the hole discharge coefficient changes from $C_{d,\text{no}}$ without crossflow to C_d with crossflow, the volume flow rate, Q, for incompressible flow, can be expressed as

$$Q=Au_h=C_dA\sqrt{\frac{2}{\rho_h}(p_{0c}-p_m)_{\text{with crossflow}}}, \tag{5}$$

or as

$$Q=Au_h=C_{d,\text{no}}A\sqrt{\frac{2}{\rho_h}(p_{0c}-p_m)_{\text{without crossflow}}}, \tag{6}$$

and a comparison between Eqs. (4), (5), and (6) illustrates the close relationship between δ_{out} and C_d (or, by analogy, between δ_{in} and C_d):

$$\delta_{\text{out}}=\frac{1}{C_d^2}-\frac{1}{C_{d,\text{no}}^2} \tag{7}$$

It is important to realize that any experimental data gathered, for the particular hole geometry and flow conditions encountered, can always be used to obtain a relationship that defines δ_{out} as a function of the outlet momentum flux ratio, $k_{\text{out}}=(\rho_h u_h^2)/(\rho_m u_m^2)$. Hay et al. [22,23] illustrate how the correlation between these parameters depends on radiusing of the hole outlet, hole orientation, and the mainstream crossflow Mach number. This is to be expected as the hole C_d is known to depend on each of these parameters, and, from Eq. (7), δ_{out} is closely related to C_d.

The $\delta_{\text{out}}-k_{\text{out}}$ relationship can then be used to predict the cooling hole C_d (and, hence, the coolant mass flow rate). This is usually achieved computationally by means of an iterative procedure. Such a computer program requires the input of T_{0c}, T_{0m}, p_m, M_m, δ_{out} as a function of k_{out}, and $C_{d,\text{no}}$ as a function of Re_h.

Firstly, the ideal mass flow rate of coolant is calculated from the design PR by assuming isentropic expansion. By guessing a sensible value for the hole C_d, an initial estimate of the actual mass flow through the hole can be calculated, which then allows the calculation of Re_h and k_{out}. In turn, k_{out} is used to calculate δ_{out}, and the associated pressure loss can be determined. That is, in effect, one ''loop'' of the iterative procedure. The modified pressure ratio leads to a new ''ideal'' mass flow rate, while the Re_h from the previous loop allows a more accurate prediction of $C_{d,\text{no}}$ (from the $C_{d,\text{no}}-\text{Re}_h$ relationship). Together these provide a better approximation to the actual mass flow rate of coolant, leading to new values for Re_h, k_{out}, δ_{out}, and the pressure drop. Iteration continues until convergence is achieved. The C_d in the presence of external crossflow can then be calculated as the ratio of the actual to the ideal (*i.e.*, calculated from the design PR) mass flow rates. This is, ultimately, the same method as used by Sasaki et al.[2] and Tillman and Jen [26].

Hay et al. [22,23] present data illustrating the excellent agreement between film cooling hole C_d measurements and predictions using the loss coefficient approach. More recently, Burd and Simon [26] have used the approach to present the influence of crossflows on cooling hole discharge coefficients. Apart from discussing and providing evidence for the importance of the location of the emerging jet, the authors also present data supporting the claims of Rowbury et al. [7] that laterally injected flow is more likely to result in negative loss coefficients.

Although it may seem obvious, it is worth realizing that *negative* loss coefficients, as reported by Sasaki et al. [2], Tillman and Jen [27], Hay et al. [22], Hay et al. [23], and Burd and Simon [26], correspond to flow enhancement with crossflows present, *i.e.*, the crossover phenomenon. For incompressible flow, this can be seen from Eq. (7). It was suggested by Rowbury et al. [7] that the extent of the enhancement depends on many factors, including the internal and external crossflow Mach numbers, and the inclination and orientation of the hole to the flow. This subject is discussed further by Rowbury et al. [17].

It is important to realize that full integration of the additive loss approach into design work relies on the assumption that the inlet and exit losses are, essentially, decoupled. For obvious reasons, this becomes increasingly more valid as the length-to-diameter ratio increases.

Application of the Additive Loss Coefficient Approach to the CHTT. In this section the additive loss coefficient approach will be applied to the CHTT in order to produce predictions of the with-crossflow C_d data. Data collected for row 1 as cylindrical holes will be used to illustrate the process.

As mentioned above, the method requires experimental data that quantifies the hole C_d both with and without external flow. In addition to providing a relationship defining $C_{d,\text{no}}$ as a function of Re_h, this information is also converted into a $\delta_{\text{out}}-k_{\text{out}}$ relationship.

$C_{d,\text{no}}$ vs. Re_h Relationships. The additive loss approach requires $C_{d,\text{no}}$ to be defined as a function of Re_h. As discussed earlier, the noncrossflow correlation amalgamating the recommendations of Lichtarowicz et al. [15] and Schoder and Dawson [16] is recommended as it accurately (within ~6 percent) predicts the $C_{d,\text{no}}$ data for the engine vanes. However, purely to demonstrate the accuracy of the loss coefficient approach in accounting for the influence of external crossflow, this section will utilize $C_{d,\text{no}}-\text{Re}_h$ relationships obtained from a polynomial curve-fit through the relevant CHTT data.

δ_{out} vs. k_{out} Relationships. For each with-crossflow experiment carried out on the CHTT, an outlet momentum flux ratio, k_{out}, and, using the appropriate noncrossflow data, an external additive loss coefficient, δ_{out}, can be calculated. A relationship

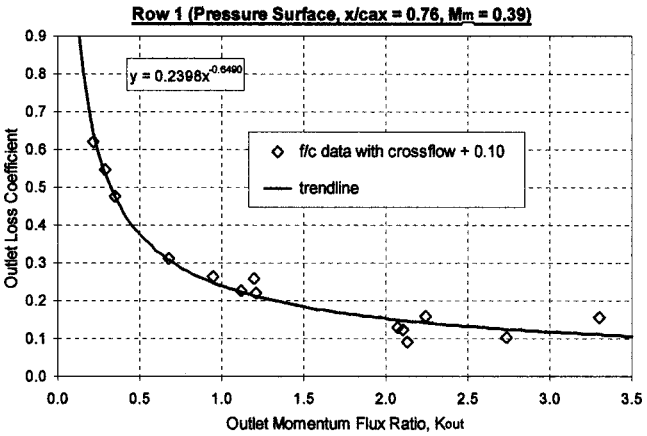

Fig. 4 δ_{out} vs. k_{out} for CHTT row 1 as cylindrical holes

defining δ_{out} as a function of k_{out} can then be obtained for each row of film cooling holes. This was achieved using a power-law curve-fit to the δ_{out} vs. k_{out} data by a least-squares method. Figure 4 illustrates the form taken and the accuracy achievable using this method, presenting data for cylindrical film cooling holes in row 1. In this manner, a unique $\delta_{out}-k_{out}$ relationship can be obtained for each of the twenty data sets. It should be noted that k_{out} for the fan-shaped holes is calculated using the coolant momentum flux at the hole exit plane, perpendicular to the hole axis.

As one might expect, the derivation of a unique $\delta_{out}-k_{out}$ relationship for each new geometry encountered results in the technique being unwieldy as a design tool. This is addressed in the section entitled ''Generalizing the Predictive Scheme.''

Comparison Between With-Crossflow Data and ''Predictions'' Using the Additive Loss Coefficient Approach. In order to check the accuracy of the additive loss coefficient method, the PR corresponding to each with-crossflow data point was used as the input to the loss coefficient predictive scheme, and iteration continued until convergence was achieved.

Figure 5 illustrates the success of the predictive method in accounting for the influence of external crossflow, presenting the data for cylindrical film cooling holes in row 1. The excellent agreement between measured and predicted with-crossflow discharge coefficients is reproduced for all twenty rows of film cooling holes investigated on the CHTT. This is to be expected as accurate curve-fits to the original data are employed in order to ''predict'' the noncrossflow data. It would be a major cause for concern if this method were failing to accurately predict the results! However, we will now generalize the methodology by replacing the $C_{d,no}-Re_h$ curve-fits with the noncrossflow correlation and through the development of a numerical means of producing the $\delta_{out}-k_{out}$ relationship.

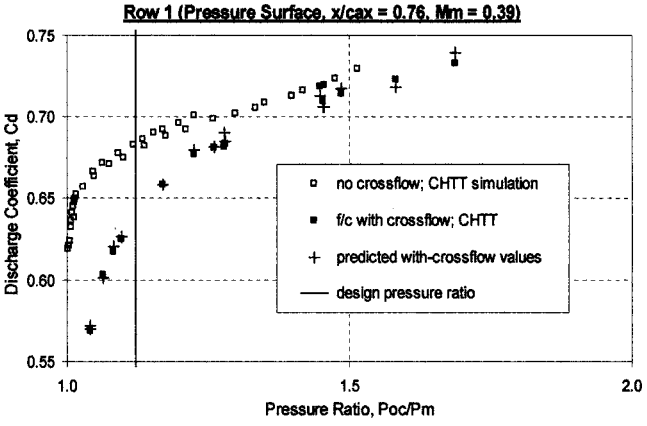

Fig. 5 Comparison between with-crossflow measurements and additive loss coefficient predictions for CHTT row 1 as cylindrical film cooling holes

Generalizing the Predictive Scheme

In order to produce a useful design tool, the methodology must be entirely numerical and be ''generalized'' so as to encompass the full range of geometric and flow parameters. Consequently, correlations defining the $C_{d,no}-Re_h$ and $\delta_{out}-k_{out}$ relationships in terms of the geometric and flow parameters are required, in order to eliminate the need for further experimental work whenever a new vane design is encountered.

The C_d of a hole is expected to depend primarily on

- the pressure ratio across the hole, PR, or, alternatively, the hole Reynolds number, Re_h,
- the length-to-diameter ratio, l/d,
- the entry/exit profile, which may result from the method of manufacture (*e.g.*, the ratio of inlet/exit hole radiusing to orifice diameter, r/d, or the ratio of chamfer depth to orifice diameter, w/d),
- the internal and external crossflow Mach numbers, M_c and M_m (respectively),
- the angles of inclination, θ, and orientation, α, of the hole (Fig. 3), and
- the exit geometry (*e.g.*, ''fanning'' of the hole).

In relation to the $C_{d,no}-Re_h$ relationship, it was shown earlier how the influence of Re_h and l/d can be accounted for by means of the correlation proposed by Lichtarowicz et al. [15], and that inlet radius effects can be allowed for by means of the factor proposed by Schoder and Dawson [16]. However, a noncrossflow correlation accounting for the influence of exit geometry (*i.e.*, fanning of the exit) is, unfortunately, beyond the scope of the present study. In terms of predicting the engine data, this is not a problem as the above method accurately predicts $C_{d,no}$ for the fan-shaped holes (all engine vane data predicted within ~5.5 percent, generally within 2 percent).

Given that separate $\delta_{out}-k_{out}$ correlations can be derived for cylindrical and fan-shaped hole geometries, and that the influence of PR and M_m are allowed for by correlating against the outlet momentum flux ratio, k_{out}, the flow angles can be expected to be pivotal to the formulation of the generalized coefficients. This is also in keeping with the data collected on the CHTT vanes and in the ''large-scale'' tests [17]. This data demonstrated how, given crossover, the level of flow enhancement with external crossflow is strongly dependent on the flow angles. Indeed, crossover is seen to increase with increasing θ and α, *i.e.*, with increasing blockage presented to the approaching mainstream flow.

Having concluded that the flow angles are pivotal to the influence of external crossflow on the discharge coefficients of film cooling holes, their influence was incorporated in two ways. Firstly, a ''perpendicular'' outlet momentum flux ratio, $k_{out,\perp}$, was defined as $k_{out,\perp}=(\rho_h u_h \cdot u_{h,\perp})/(\rho_m u_m^2)$, where $u_{h,\perp}$ is the component of the coolant velocity perpendicular to the vane surface. The modified coolant momentum flux is then proportional to the coolant mass flow rate along the hole axis, yet incorporates a dependence on the jet-mainstream interaction. Secondly, it was assumed that the generalized coefficients in the $\delta_{out}-k_{out}$ relationships could be derived from functions of the two flow angles alone. To this end, the relationships obtained from the power-law curve-fits to the $\delta_{out}-k_{out}$ data could be generalized in the form:

$$\delta_{out}=Ak_{out,\perp}^{-B}-C \tag{8}$$

It was decided to adopt this form as a first approximation. Functions minimizing the deviation from the variations defined by the power-law curve-fits were sought, with accuracy optimized in the design region. It was found that acceptable accuracy could be achieved by formulating different functions for the coefficients in

Table 2 Coefficients in "$\delta_{out} = A k_{out}^{-B} - C$" relationships for cylindrical and fan-shaped film cooling holes in the different regions (see Fig. 2) of the vane.

	Cylindrical Holes	Fan-Shaped Holes
(a) Pressure Surface (Rows 1-6):		
A	$(2.95\sin\theta - 0.88)(1+\sin\alpha)$	$(0.435\sin\theta - 0.140)(1+\sin\alpha)$
B	$(0.714\sin\theta + 0.393)(1+\sin\alpha)$	$(0.350\sin\theta + 0.570)(1+\sin\alpha)$
C	0.10	0. 02
(b) Leading Edge (Rows 7-10):		
A	$0.079\sin\theta(1+\sin\alpha)$	N/A
B	$(4.795\sin\theta - 4.487)(1+\sin\alpha)$	
C	0.28	
(c) Suction Surface (Rows 11-14):		
A	$(0.682\sin\theta - 0.24)(1+\sin\alpha)$	$(0.225\sin\theta - 0.110)(1+\sin\alpha)$
B	$(0.777\sin\theta + 0.405)(1+\sin\alpha)$	$(0.350\sin\theta + 0.570)(1+2.8\sin\alpha)$
C	0.10	0.05

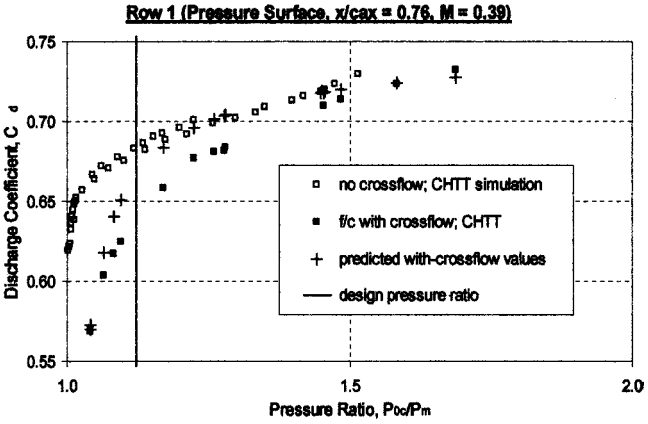

Fig. 6 Rig measurements and "generalized" predictions for row 1 as cylindrical film cooling holes

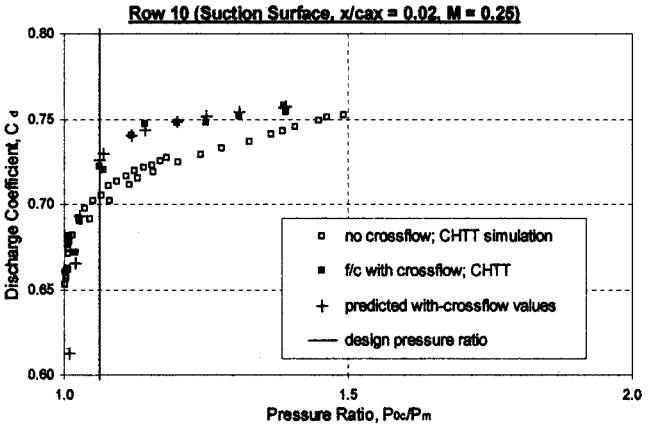

Fig. 7 Rig measurements and "generalized" predictions for row 10 (cylindrical film cooling holes)

the different "regions" of the vane. The "regions" referred to are illustrated in Fig. 2. Hence, the pressure surface, suction surface, and leading edge regions of the vane were correlated separately. The two hole geometries encountered also had to be correlated separately. The resulting equations for the coefficients are presented in Table 2.

These "generalized" coefficients can now be used to obtain the $\delta_{out} - k_{out}$ relationships for film cooling rows in the different regions of the vane. These are used to "predict" the CHTT measurements made with external crossflow. The accuracy attainable

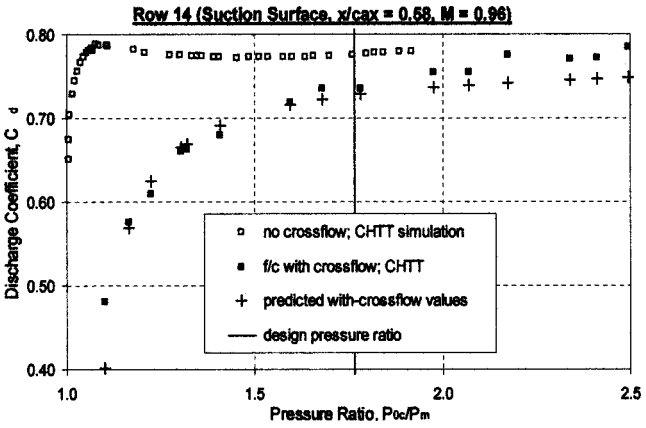

Fig. 8 Rig measurements and "generalized" predictions for row 14 as fan-shaped film cooling holes

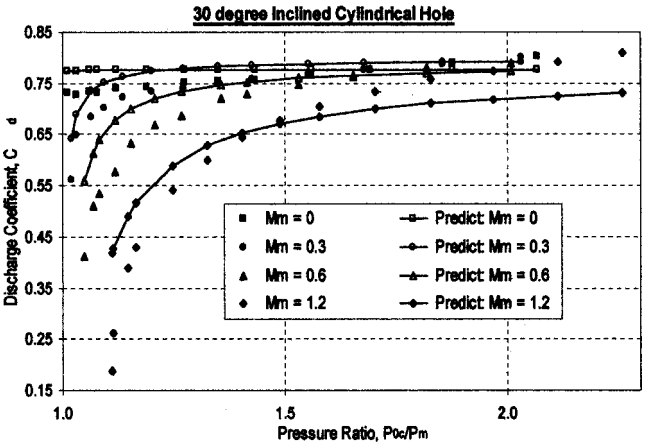

Fig. 9 Comparison between Karlsruhe experimental data for an inclined 30 deg cylindrical film cooling hole and predictions using the proposed methodology

is demonstrated by the data for the cylindrical holes in rows 1 and 10 and the fan-shaped holes in row 14, presented in Figs. 6, 7, and 8, respectively. Not surprisingly, the accuracy achieved is not generally as good as when using the row-specific δ_{out} vs. k_{out} relationships discussed previously. However, as a generalized design tool it is very successful.

Prediction of Karlsruhe Data

As already mentioned, there has been a large amount of discharge coefficient research carried out at the University of Karlsruhe in recent years, culminating in a proposed methodology for correlating the discharge coefficient of a 30 deg inclined cylindrical film cooling hole by Gritsch et al. [21]. In this section, the cooling hole geometry encountered in that paper will be used as the input to the predictive scheme proposed in the previous section, with the aim of testing the robustness of the methodology.

The data reported by Gritsch et al. [21] with no internal crossflow but mainstream crossflow Mach numbers, M_m, of 0, 0.3, 0.6, and 1.2 is presented in Fig. 9, along with the equivalent predictions using the design methodology proposed in the previous section. The predictions use coefficients A, B, and C calculated from the relationships defined for cylindrical holes on the suction surface of the airfoil. It can be seen that the agreement is reasonably good. The baseline (noncrossflow) prediction overpredicts in the low PR region, but under-predicts the test data for PR$\sim$2. This discrepancy has a knock-on effect for the predictions with exter-

nal crossflow, as highlighted by the overprediction in the low PR region for each of the crossflow Mach numbers considered.

However, overall the agreement is good, increasing faith in the potential robustness of the proposed design methodology.

Conclusions

The discharge coefficients of cylindrical and fan-shaped film cooling holes have been measured on a fully film cooled NGV in an annular cascade tunnel, where all of the major flow parameters except the coolant Reynolds number are simultaneously matched to the engine condition.

The data collected have been used to derive a proposed means of predicting the discharge coefficients of film cooling holes under engine operating conditions. The proposed scheme predicts $C_{d,\mathrm{no}}$, allowing for Re_h, l/d, and inlet radiusing effects, which is then modified to allow for the influence of external crossflow by means of the additive loss coefficient approach. Noncrossflow data, collected on NGVs from a modern day aero-engine, was used to highlight correlations from the literature [15,16] that successfully predicted the dependencies witnessed. Data collected on the CHTT, thereby incorporating external crossflow, was then used to derive a means of accounting for the influence of the mainstream flow. The method adopted used the additive loss coefficient approach, with the relationship between the outlet loss coefficient, δ_{out}, and the ''perpendicular'' outlet momentum flux ratio, k_{out}, dependent on the coolant flow angles relative to the oncoming mainstream and the hole exit geometry.

It should be emphasized that once the hole exit geometry (cylindrical or fan-shaped) and the location on the airfoil (pressure surface, suction surface, or leading edge region) have been specified, the proposed design method is geometry unspecific—it is readily applicable to new hole geometries and external flow conditions.

In addition to demonstrating the success of the ''generalized'' scheme in predicting the C_d data gathered on the CHTT, it has also been successfully applied in the prediction of cylindrical hole data collected at the University of Karlsruhe.

This experimental research and, in particular, the predictive scheme developed will be of interest to aero-engine designers as they provide a means of modifying their cooling hole C_d predictions.

Acknowledgments

This work has been carried out with the support of Rolls-Royce plc, DERA, MoD, and DTI. The authors would also like to thank Professor T.V. Jones, Dr. C.R.B. Day, and A. Rawlinson for their help and guidance, and K. Walton, T. Godfrey, and D. O'Dell for their practical assistance.

Nomenclature

Symbols

A = cooling hole area
C_d = discharge coefficient $= \dot{m}_{\mathrm{actual}}/\dot{m}_{\mathrm{ideal}}$
$C_{d,\mathrm{no}}$ = discharge coefficient without crossflow
C_{du} = ''limiting'' (i.e., high Re_h) discharge coefficient
d = hole diameter
k_{out} = outlet momentum flux ratio $= \rho_h u_h^2/\rho_m u_m^2$
$k_{\mathrm{out},\perp}$ = ''perpendicular'' momentum flux ratio $= \rho_h u_h . u_{k,\perp}/\rho_m u_m^2$
l = hole length
$\dot{m}$ = mass flow rate
M = Mach number
p = pressure
PR = pressure ratio across hole $= p_{0c}/p_m$
Q = volume flow rate
r = radius of curvature of hole inlet/exit
Re = Reynolds number $= \rho u d/\mu = 4\dot{m}/\pi d\mu$
T = temperature
u = velocity
$u_{h,\perp}$ = component of coolant exit velocity perpendicular to the vane surface
w = chamfer depth

Greek

α = angle of orientation (see Fig. 3)
β = plan view orientation angle (see Fig. 3)
δ_{out} = outlet additive loss coefficient
μ = dynamic viscosity
θ = angle of inclination (see Fig. 3)
ρ = density
ζ = ''true'' flow exit angle (see Fig. 3)

Subscripts

c = coolant
h = coolant at the hole exit plane
m = mainstream
0 = total

References

[1] Hay, N., and Lampard, D., 1998, ''Discharge Coefficients of Turbine Cooling Holes: A Review,'' ASME J. Turbomach., **120**, pp. 314–390.
[2] Sasaki, M., Takahara, K., Sakata, K., and Kumagai, T., 1976, ''Study on Film Cooling of Turbine Blades: Experiments on Film Cooling With Injection Through Holes Near the Leading Edge,'' Bull. JSME, **19**, No. 137, pp. 1344–1352.
[3] Foster, N. W., and Lampard, D., 1980, ''The Flow and Film Cooling Effectiveness Following Injection Through a Row of Holes,'' ASME J. Eng. Power, **102**, No. 3, pp. 584–588.
[4] Hay, N., and Lampard, D., 1995, ''The Discharge Coefficient of Flared Film Cooling Holes,'' *ASME Paper No. 95-GT-15*, International Gas Turbine and Aero-Engine Congress and Exposition, Houston, Texas, June 1995.
[5] Martinez-Botas, R. F., Main, A. J., Lock, G. D., and Jones, T. V., 1993, ''A Cold Heat Transfer Tunnel for Gas Turbine Research on an Annular Cascade,'' *ASME Paper No. 93-GT-248*, International Gas Turbine and Aero-Engine Congress and Exposition, Cincinnati, Ohio, May 1993.
[6] Rowbury, D. A., Oldfield, M. L. G., Lock, G. D., and Dancer, S. N., 1998, ''Scaling of Film Cooling Discharge Coefficient Measurements to Engine Conditions,'' *ASME Paper No. 98-GT-79*, International Gas Turbine and Aero-Engine Congress & Exhibition, Stockholm, Sweden, June 1998.
[7] Rowbury, D. A., Oldfield, M. L. G., and Lock, G. D., 1997, ''Engine-Representative Discharge Coefficients Measured in an Annular Nozzle Guide Vane Cascade,'' *ASME Paper No. 97-GT-99*, International Gas Turbine and Aero-Engine Congress & Exhibition, Orlando, Florida, June 1997.
[8] Gritsch, M., Schulz, A., and Wittig, S., 1998, ''Discharge Coefficient Measurements of Film-Cooling Holes With Expanded Exits,'' ASME J. Tribol., **120**, pp. 560–567.
[9] Rogers, T., and Hersh, A. S., 1975, ''The Effect of Grazing Flow on the Steady State Resistance of Square-Edged Orifices,'' *American Institute of Aeronautics and Astronautics (AIAA) 2nd Aero-Acoustics Conference, Paper No. 75-493*.
[10] Andrews, G. E., and Mkpadi, M. C., 1983, ''Full Coverage Discrete Hole Wall Cooling: Discharge Coefficients,'' *ASME Paper No. 83-GT-79*, International Gas Turbine Conference and Exhibit, Phoenix, Arizona, March 1983.
[11] Tay Chu, Brown, A., and Garrett, S., 1985, ''Discharge Coefficients of Impingement and Film Cooling Holes,'' *ASME Paper No. 85-GT-81*, International Gas Turbine Conference and Exhibit, Houston, Texas, March 1985.
[12] Adkins, R. C., and Gueroui, D., 1986, ''An Improved Method for Accurate Prediction of Mass Flows Through Combustor Liner Holes,'' ASME J. Eng. Gas Turbines Power, **108**, pp. 491–497.
[13] Parker, D. M., and Kercher, D. M., 1991, ''An Enhanced Method to Compute the Compressible Discharge Coefficient of Thin and Long Orifices With Inlet Corner Radiusing,'' *ASME Winter Annual Meeting (Heat Transfer in Gas Turbines)*, Heat Transfer Division, **188**, pp. 53–63.
[14] McGreehan, W. F., and Schotsch, M. J., 1988, ''Flow Characteristics of Long Orifices With Rotation and Corner Radiusing,'' ASME J. Turbomach., **110**, pp. 213–217.
[15] Lichtarowicz, A., Duggins, R. K., and Markland, E., 1965, ''Discharge Coefficients for Incompressible Non-Cavitating Flow Through Long Orifices,'' J. Mech. Eng. Sci., **7**, No. 2, pp. 210–219.
[16] Schoder, E. W., and Dawson, F. M., 1934, *Hydraulics*, McGraw-Hill, New York, p. 408.
[17] Rowbury, D. A., Oldfield, M. L. G., and Lock, G. D., 2000, ''Large-Scale Testing to Validate the Influence of External Crossflow on the Discharge Coefficients of Film Cooling Holes,'' *ASME Paper No. 2000-GT-0293*, International Gas Turbine and Aero-Engine Congress & Exhibition, Munich, Germany, May 2000.
[18] Wittig, S., Schulz, A., Gritsch, M., and Thole K. A., 1996, ''Transonic Film-Cooling Investigations: Effects of Hole Shapes and Orientations,'' *ASME Pa-*

per No. 96-GT-222, International Gas Turbine and Aero-Engine Congress & Exhibition, Birmingham, UK, June 1996.
[19] Thole, K. A., Gritsch, M., Schulz, A., and Wittig, S., 1997, ''Effect of a Crossflow at the Entrance to a Film-Cooling Hole,'' ASME J. Fluids Eng., **119**, pp. 533–541.
[20] Thole, K. A., Gritsch, M., Schulz, A., and Wittig, S., 1998, ''Flowfield Measurements for Film-Cooling Holes With Expanded Exists,'' ASME J. Turbomach., **120**, pp. 327–336.
[21] Gritsch, M., Schulz, A., and Wittig, S., 1998, ''Method for Correlating Discharge Coefficients of Film-Cooling Holes,'' AIAA J., **36**, No. 6, pp. 976–980.
[22] Hay, N., Khaldi, A., and Lampard, D., 1987, ''Effect of Crossflows on the Discharge Coefficients of Film Cooling Holes With Rounded Entries or Exists,'' *Proceedings of the 2nd ASME-JSME Thermal Engineering Joint Conference*, Honolulu, Hawaii, Vol. 3, pp. 369–374.
[23] Hay, N., Lampard, D., and Khaldi, A., 1994, ''The Coefficient of Discharge of 30° Inclined Film Cooling Holes With Rounded Entries or Exits,'' *ASME Paper No. 94-GT-180*, International Gas Turbine and Aero-Engine Congress and Exposition, The Hague, Netherlands, June 1994.
[24] Walters, D. K., and Leylek, J. H., 2000, ''A Detailed Analysis of Film-Cooling Physics, Part 1: Streamwise Injection With Cylindrical Holes,'' ASME J. Turbomach., **122**, pp. 102–112.
[25] Burd, S. W., and Simon, T. W., 1997, ''The Influence of Coolant Supply Geometry an Film Coolant Exit Flow and Surface Adiabatic Effectiveness,'' *ASME Paper No. 97-GT-25*, International Gas Turbine and Aero-Engine Congress & Exhibition, Orlando, Florida, June 1997.
[26] Burd, S. W., and Simon, T. W., 1999, ''Measurements of Discharge Coefficients in Film Cooling,'' ASME J. Turbomach., **121**, No. 2, pp. 243–248.
[27] Tillman, E. S., and Jen, H. F., 1984, ''Cooling Airflow Studies at the Leading Edge of a Film-Cooled Airfoil,'' ASME J. Eng. Gas Turbines Power, **106**, pp. 214–221.

Flow Characteristics Inside Circular Injection Holes Normally Oriented to a Crossflow: Part I — Flow Visualizations and Flow Data in the Symmetry Plane

Sang Woo Lee

Sang Won Park

School of Mechanical Engineering,
Kumoh National University of Technology,
Kumi, Kyungbook 730-701, Korea

Joon Sik Lee
School of Mechanical
and Aerospace Engineering,
Seoul National University,
Seoul 151-742, Korea

Experimental results are presented that describe flow behavior inside circular injection holes with a sharp square-edged inlet. Oil-film flow visualizations and mean flow data are obtained in the flow symmetry plane of injection holes that are normally oriented to a crossflow. Additional visualizations inside inclined holes are also performed for inclination angles of 30 and 60 deg. Data are presented for three different length-to-diameter ratios: L/D = 0.5, 1.0, and 2.0. The blowing ratio is fixed at M = 2.0 in the flow visualizations and takes the values M = 0.5, 1.0, and 2.0 in the flow measurements. The normal-injection flow visualization in the case of L/D = 2.0 clearly demonstrates the existence of four distinct near-wall flow regions: an inlet separation region, a reattachment region, a developing region, and a near-exit flow region. When L/D = 1.0 and 2.0, an inlet separation bubble is apparent with a clear imprint of recirculating flow traces, especially on the windward side, even though it is not so well organized on the opposite side. For a short hole such as L/D = 0.5, however, the separation bubble with flow recirculation seems to be suppressed by the crossflow. Due to the presence of the inlet separation bubble, actual flow passage is in the form of a converging–diverging channel, regardless of the L/D values. In general, the crossflow stabilizes the inside flow on the leeward side, meanwhile destabilizes it on the windward side. On the contrary, the inclination of the injection hole in the leeward direction of the crossflow stabilizes the flow near the windward wall but destabilizes it near the leeward wall. Relatively short holes such as L/D = 0.5 and 1.0 do not allow the boundary-layer development on the wall. Particularly in the case of L/D = 0.5, a direct interference is observed between the complicated inlet and exit flows. The inlet flow, however, seems to be isolated from the exit flow for a long hole such as L/D = 2.0. It is also found that the potential-core inside the normal injection hole comprises a converging flow region, a diverging flow region, a developing flow region, and a flow region deflected by the crossflow.
[DOI: 10.1115/1.1344876]

Introduction

Jets in a crossflow have extensive industrial applications, such as gas turbine hot-component cooling, dilution in a turbine combustor, pollution control, drying processes, electronic component cooling, etc. Open literatures on jets in a crossflow can be classified into two broad categories: normal and inclined injections. Typical examples of normal injections are dilution-air injections in the gas turbine combustor and impinging jets in the internal cooling passage of turbine blades. Film-cooling jets are usually injected with inclination angles to the hot crossflow.

Much research has been performed in regard to jets in a crossflow since Morton [1]. Among this work, Andreopoulos and Rodi [2], and Andreopoulos [3] provided significant contributions to the understanding of a normally injected jet in a crossflow boundary layer when the hole length-to-diameter ratio, L/D, is 12. In turbine combustor applications, Carrotte and Stevens [4] measured the temperature fields and three-dimensional flows in the exit plane as well as in the downstream region of three plunged dilution holes with L/D of about 0.4. Holdeman et al. [5] investigated the mixing characteristics of multiple jets injected normally into the confined crossflow in the case of very short L/D's less than 0.25. According to Burd et al. [6], who investigated the effects of the length-to-diameter ratio and turbulent intensity on the flow field downstream of a row of film cooling holes, downstream flow structures are substantially different between L/D's of 2.3 and 7.0 under lower free-stream turbulence conditions. In addition, the short L/D injection causes ''jetting'' of the coolant farther into the free-stream flow and enhanced mixing. In an investigation of the flow characteristics and aerodynamic losses of film-cooling jets with compound angle orientations, Lee et al. [7] proposed a near-wall flow model, which comprises five flow regions, and discussed various flow characteristics in each region in detail. Lee et al. [8] and Burd et al. [6] summarized previous studies related to jet flows for both normal and inclined injections. These prior studies are interested mainly in the downstream flow field behind the injection hole.

Of the previous investigations of flow in the injection hole, Andreopoulos [9] was the first to measure mean velocities and turbulent fluctuations inside the normal injection pipe of $L/D = 12$ with a contoured inlet. He showed that nonuniformity in the velocity profiles inside the pipe extends as far as $3D$ upstream of the jet exit at low blowing ratios, while the crossflow effect is insignificant at higher blowing ratios. Lloyd and Brown [10] carried out an experimental investigation into the velocity and turbulence fields in the entrance region of a long circular pipe with a

Contributed by the International Gas Turbine Institute and presented at the 45th International Gas Turbine and Aeroengine Congress and Exhibition, Munich, Germany, May 8–11, 2000. Manuscript received by the International Gas Turbine Institute February 2000, Paper No. 2000-GT-256. Review Chair: D. Ballal.

plenum crossflow at the entry. The pipe was normally oriented to the plenum crossflow and had a sharp square-edged entry. They found a separated nonaxisymmetric flow at the entry followed by a skewed flow that progressively smoothed out with distance along the pipe. Other related studies are described by Leylek and Zerkle [11], who performed three-dimensional computations for a row-of-hole film cooling with a streamwise inclination angle of 35 deg. They obtained simultaneous numerical solutions of fully coupled flows in plenum, film-hole, and crossflow regions for $L/D=1.75$ and 3.5. They described complex flows within the inclined hole such as a ''jetting'' of injectant, a low-momentum region, and a counterrotating vortex. Cho and Goldstein [12] measured local mass (heat) transfer for a jetstream entering a crossflow through normal film-cooling holes of $L/D=1.5$. They classified the inside-hole flow into four different regions, showing that the separation zone near the hole entrance is greatly shrunk by the crossflow at low blowing ratios, but this zone increases to the same length as in the case of no crossflow at high blowing ratios. In addition, the zone affected directly by the crossflow inside the injection hole was confined to the exit of the hole even at the low blowing ratio. Thole et al. [13] studied the effect of a plenum crossflow on the flow inside a film-cooling hole of $L/D=6$, which was inclined at 30 deg with respect to the crossflow. The main and plenum crossflows were parallel and in the same direction. They showed that as Mach number of the plenum crossflow increases from 0 to 0.5, a separation region located on the leeward side of the cooling hole entrance shifts to the windward side. In electronics cooling applications, Morris and Garimella [14] performed a numerical work on the flow within the injection hole and in the confinement region for a normally impinging, axisymmetric, confined, and submerged liquid jet with no crossflow. They reported the reattachment length at the inlet as well as the pressure loss data through the hole for a perfluorinated dielectric fluid, FC-77, as a function of L/D.

As described above, different values of L/D are considered depending on its application. For example, L/D has values less than unity in the application to the dilution holes of gas turbine combustors. On the other hand, their values are larger than unity for most of the film cooling and impinging holes. In general, the downstream flow after coming out from the injection hole is related closely to the aerodynamic behavior of the injectant within the injection hole. Thus, it is important to figure out flow characteristics inside the injection hole, which seem to depend strongly on L/D as well as the blowing ratio, M. Some other studies can be found on the flow within an inclined injection hole in a crossflow [11,13]. However, it is hard to find literature describing complicated flows inside the injection hole, which is normally oriented to the crossflow, especially for relatively short $L/D's$. In the present study (Part I), flow visualizations and mean flow measurements in the flow symmetry plane, the x-y plane at $z=0$, have been conducted inside normal injection holes with a sharp square-edged inlet. Three-dimensional mean velocity components and aerodynamic loss data are presented in the companion paper [15].

Experimental Apparatus and Procedure

The wind tunnel used in this experiment is an open-circuit type with a cross section of 0.6 m$\times$0.4 m. At a mean velocity of 15 m/s, spatial nonuniformities of the mean velocity and turbulence level are 1.0 and 0.5 percent, respectively. The uniform flow streaming from the wind-tunnel contraction is developing to a turbulent boundary-layer flow on the floor of the test section after a trip wire of 1.8 mm in diameter. As shown in Fig. 1, an injection hole made of aluminum is located 740 mm downstream of the trip wire at the mid-span of the wind-tunnel floor and has a sharp square-edged inlet. Its diameter, D, is fixed as 60 mm, but its length, L, varies as 30, 60, and 120 mm, which provide L/D values of 0.5, 1.0, and 2.0, respectively. The secondary air from a blower is supplied to the injection hole through a heat exchanger, an orifice, a flow control valve, a settling chamber, and a cylindrical plenum in sequence. An inlet mesh screen, a honeycomb, and three mesh screens are installed in turn inside a plenum with an inner diameter 195 mm. The area reduction ratio of the present injection hole to the cylindrical plenum is about 0.095. The nearest mesh screen is situated $2D$ apart from the inlet of the injection hole, regardless of L/D values. This study employs a corner-tapping orifice based on ISO 5167 [16]. The centerline of the injection hole coincides exactly with that of the cylindrical plenum, so that with no crossflow, the flow within the injection hole should be axisymmetric. The origin of the present coordinates is at the center of the injection-hole exit, and x, y, and z are streamwise (leeward), normal, and spanwise coordinates, respectively (Fig. 1).

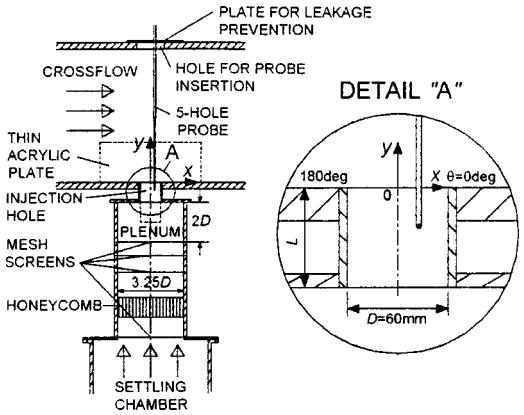

Fig. 1 Experimental apparatus

A cone-type five-hole probe of 3.18 mm (0.125 in.) in tip diameter, custom-made by United Electric Controls, is used to measure three-dimensional velocity components inside the injection hole. As shown in Fig. 1, the five-hole probe has a straight probe stem of about 1.1 m in total length, and its reinforced portion is 6.35 mm (0.25 in.) in diameter and 0.86 m long. The probe tip shape is the same as its DC125 model. In order to minimize flow leakage into the crossflow, a circular acrylic plate 1 mm in thickness is placed on the top wall of the wind tunnel, as in Fig. 1. The five-hole probe is traversed in the y-direction through a hole 8 mm in diameter drilled at the center of the thin plate. In the x- and z-directions, it moves with the plate on the wind-tunnel top wall. A three-dimensional automatic probe traverse system, equipped with linear motion guides (Samik, SAR1615T), stepping motors (Oriental Motor, UPH599-A), and stepping motor drivers (Oriental Motor, UDX5114), is used for probing. All the measurements are controlled by a personal computer (IBM, AT 486) equipped with plug-in boards such as a Multi-Function DI/O Board (National Instruments, AT-MIO-16D-H-9) and a GPIB adapter (National Instruments, AT-GPIB). Measured pressures are transformed into DC voltages by a high-accuracy differential pressure transducer (MKS, Type 120AD-00010RDB) and a power-supply readout (MKS, Type 510B). The electric signals are sampled by a 12-bit A-D converter in the Multi-Function DI/O Board, and transferred into the computer. The temperatures of the crossflow and jet flow are measured by T-type thermocouples connected to a temperature scanner (Keithley, Model 2001TSCAN), which is also controlled by the computer through the GPIB. The automatic probe traverse system as well as a pressure scanning box (Furness Controls, FC091-6) for sequential switching of pressure holes are controlled by digital-out pulses from the Multi-Function DI/O Board. The whole measurement system is controlled in a proper sequence by a stand-alone C-language program.

Experimental Conditions and Uncertainties

Throughout the experiments free-stream velocity, U_∞ is maintained at 15 m/s. In the absence of the injection hole, the boundary

layer thickness at the location of the hole center is about 17.5 mm and the displacement and momentum thicknesses are 2.3 and 1.8 mm, respectively. The two dimensionality of the crossflow boundary layer is assured by measuring velocity profiles at four locations in the z direction. The Reynolds number based on the free-stream velocity and the momentum boundary-layer thickness, $\mathrm{Re}_{\delta 2}$, is 1.7×10^3 and the Reynolds number defined using the spatially averaged injection velocity, V_j, and the injection-hole diameter, Re_D, is 5.7×10^4 at $M=1.0$. The temperature difference between the crossflow and injectant is controlled to within 0.5°C, so that the density ratio of the two fluids is unity. In the flow visualizations, the blowing ratio, M, and the momentum flux ratio, J, are fixed at 2.0 and 4.0, respectively. The length-to-diameter ratio varies to be $L/D=0.5$, 1.0, and 2.0 for the normal injection. For 30 and 60 deg inclined injections, the thickness-to-diameter ratio is fixed as $t/D=1.0$. Thus, L/D's for the 30 and 60 deg inclined holes are about 2.0 and 1.15, respectively. The velocity fields are measured only for the normal injection with three L/D values of 0.5, 1.0, and 2.0. The blowing ratios considered are $M=0.5$, 1.0, and 2.0, and the corresponding momentum flux ratios are $J=0.25$, 1.0, and 4.0, respectively. The flow in the symmetry plane within the injection hole is measured at 9×6 points at $z/D=0.0$ in the case of $L/D=0.5$ and at 9×11 points when $L/D=1.0$, with an interval of $D/10$ in both x and y directions. At $L/D=2.0$, measuring points are 9×9 in the $x-y$ plane with intervals of $D/10$ in the x direction and of $D/4$ in the y direction with additional nine locations $0.1D$ downstream of the inlet.

We develop a non-nulling calibration program based on Treaster and Yocum [17] to determine flow angles, total pressure, and static pressure from calibration data. In order to minimize the effect of the probe Reynolds number, the calibrations are made for the three mean velocities of 7.5, 15, and 30 m/s, which are the same as V_j's at $M=0.5$, 1.0, and 2.0, respectively. Each calibration is made for both pitch and yaw angles in the range from -40 to $+40$ deg with increments of 5 deg. The location of the closest near-wall measurements is $D/10$ (about two times the probe tip diameter) apart from the wall, which is believed to deliver negligible wall-proximity effects of the five-hole probe [18]. The blockage ratio due to the presence of the five-hole probe inside the injection hole is evaluated to be only 0.28 percent.

The uncertainty intervals are evaluated with 95 percent confidence. Uncertainties associated with the probe location are given by ±0.1 mm in both x and z directions, and ±0.2 mm in the y direction. In pressure measurements, the uncertainty is estimated to be ±0.7 percent of the crossflow dynamic pressure. The uncertainty interval in the injection flow measurements based on the uncertainty analysis of the ISO 5167 [16] is ±0.5 percent of the mass flow rate. In the five-hole probe measurements, uncertainty intervals based on Abernethy et al. [19] are calculated to be ±1.1 deg in the pitch and yaw angles and ±1.4 percent of U_∞ in the velocity magnitude, in the absence of additional uncertainties resulted from local turbulence and velocity gradient. After completion of experiments, repeatability is checked when $L/D=1.0$ at $M=1.0$. The uncertainty intervals from the repeatability test are ±1.6 deg for the flow angles and ±1.8 percent of U_∞ for the velocity magnitude.

Results and Discussion

Flow Visualization. Because of the relatively high injection velocity and opacity of the hole wall, it is not easy to obtain a detailed picture of the complicated inside flow within the injection hole. After some trials, an oil film is applied to a thin acrylic plate 1 mm in thickness, which is carefully installed in the flow symmetry plane. In this oil-film method, a mixture of carbon black and kerosene is covered on the thin plate with ''T'' shape, which extends from the upstream cylindrical plenum to the downstream crossflow region as in Fig. 1. Therefore, a good oil-film trace is obtained without any discontinuities at the inlet and exit of the injection hole. In this visualization, however, it is impossible to avoid flow retardation due to the additional wall friction.

When a sudden reduction in the flow cross section is introduced into a flow, a separation region is always formed at the inlet of the smaller-diameter pipe, resulting in a vena contracta. In addition, the discharging flow at the injection-hole exit tends to be significantly disturbed by the crossflow. Figure 2 shows the oil-film flow visualizations in the flow symmetry plane of the normal injection hole at $M=2.0$. These pictures are believed to be the first that reveal the entire complicated flow pattern, including the entrance and crossflow effects simultaneously. According to Cho and Goldstein [12], the inside flow can be classified into four near-wall flow regions: a separation/recirculation region at the inlet, a reattachment region, a developing region, and a region affected directly by the crossflow. Their conclusion is based on mass transfer rate distributions on the wall surface and the fog flow visualization in the exit area by Foss [20]. The present oil-film trace in the case of $L/D=2.0$ (Fig. 2(c)) clearly demonstrates these four near-wall flow regions, which are denoted by ''A'' to ''D''. The extent of each flow region in Fig. 2(c) is determined with the aid of the flow measurement data as well as the oil-film traces. Region A, a separation/recirculation region, is apparently seen near the wall at the entrance, and it extends roughly up to $0.55D$ from the square-edged inlet. A recirculating flow pattern is distinctly imprinted in the separation bubble on the windward side (on the negative x side), even though it is not clear on the leeward side (on the positive x side). Thus, the presence of the crossflow destabilizes the inside flow on the windward side; meanwhile it has a stabilizing tendency on the opposite side. This will also be discussed later with static pressure data. Due to the presence of the inlet separation bubble, actual flow passage is in the form of a converging–diverging channel. The recirculation zone is growing rapidly toward the hole centerline at a short distance from the inlet edge, and then its thickness gradually decreases after passing the throat of the converging–diverging passage. In the negative x region, the vortex center of the recirculating flow is located about $0.025D$ apart from the wall and about $0.18D$ downstream of the inlet edge. In the inlet potential-core region, the oncoming flow may accelerate along the short converging part up to the throat. Subsequently, the flow gradually decelerates along the diverging part until the developing region (Region C) is reached. In the reattachment region (Region B), the diverging flow collides obliquely with the wall and the recirculating flow vanishes. In Region C, the reattached flow starts to develop into a boundary-layer type. The accumulated carbon black near the wall in Region C is caused by flow retardation due to the wall friction in the boundary layer. Finally, Region D shows the injectant interaction with the crossflow where it is deflected in the positive x direction.

The oil-film trace at $L/D=1.0$ (Fig. 2(b)) shows very similar flow to the entry flow at $L/D=2.0$. As in the case of $L/D=2.0$, a recirculating flow is clearly imprinted in the windward separation bubble; meanwhile it is not clear on the opposite side. However, the hole is so short that the boundary-layer flow is not seen developing along the wall. Instead, the decelerated diverging flow after passing the throat suffers a direct influence of the crossflow, which results in strong mutual interactions between the two flows, especially on the windward side of the exit. In the case of $L/D=0.5$ in Fig. 2(a), the well-organized recirculating flow observed in Fig. 2(b) or 2(c) is not apparent anymore. The separation bubble seems to be suppressed by the crossflow, and it is thus confined to the restricted region adjacent to the wall with a considerable reduction in its size. Even in this case, however, overall flow in the central potential-core region has a similar tendency to that in the case of $L/D=1.0$ or 2.0. From the viewpoint of fluid mechanics, the inlet separation bubble brings about a considerable aerodynamic loss. This will be discussed in Part II [15]. In the heat transfer viewpoint, the inlet separation bubble, which serves as a ''thermal pocket,'' tends to provide lower heat transfer coefficient, as indicated by Cho and Goldstein [12].

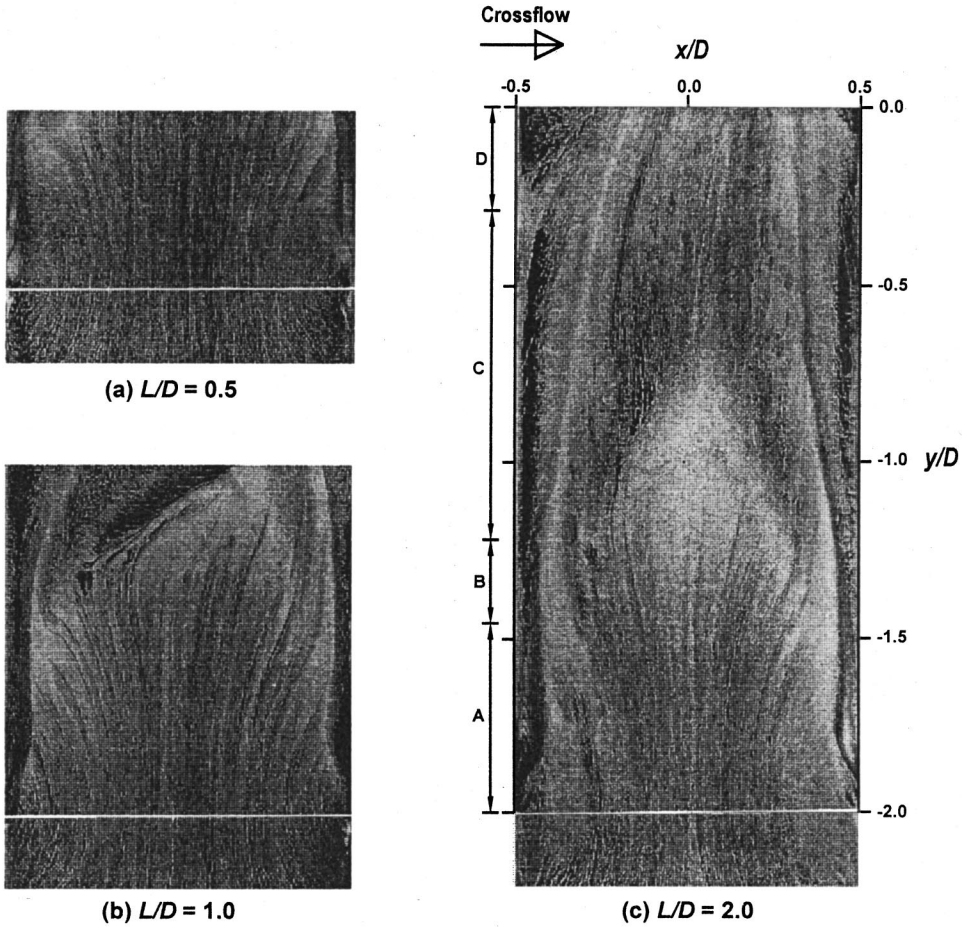

Fig. 2 Oil-film flow visualizations in the symmetry plane in the normal injection hole at $M=2.0$

Additional flow visualizations are conducted for 30 and 60 deg inclined holes with $t/D=1.0$ at $M=2.0$, and the flow pattern is compared with the corresponding normal injection case (Fig. 2(*b*)). Figure 3 shows an oil-film trace of the 60 deg inclined injection. Compared to the normal injection, the inlet separation region is subjected to a remarkable contraction on the windward side, but a dramatic expansion on the leeward side. In the case of the 30 deg inclined injection (Fig. 4), this trend is more accentuated. The separation bubble is not observed near the windward inclined wall; meanwhile the largest separation region can be seen on the leeward side. Due to the considerable reduction in the flow passage area, the windward side flow accelerates greatly to produce a '' jetting effect,'' as indicated by Leylek and Zerkle [11]. As noted from these discussions, inclined injections demonstrate totally different inside flow patterns compared to the normal injection. The solid lines indicated in Figs. 3 and 4 are the boundaries between the jetting region and the low-momentum region. The jetting effect originates from a sudden reduction in the flow area, due to the expansion of the low-momentum region. Our preliminary tests show that even in the absence of the crossflow, a large separation region is still found within the inclined injection holes. Moreover, the boundary (the solid line in Figs. 3 or 4) in the presence of the crossflow moves closer to the wall on the leeward side compared to that with no crossflow. This implies that the crossflow has a stabilizing effect on the leeward separated flow. This effect is also found in the normal injection case, as noted earlier in Fig. 2. Contrary to the crossflow effect, because of the inclination of the injection hole in the leeward direction, the flow on the windward side is stabilized, but it is destabilized on

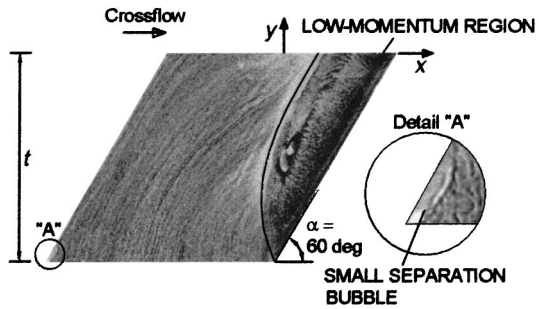

Fig. 3 Oil-film flow visualization in the symmetry plane in the 60 deg inclined hole of $t/D=1.0$ at $M=2.0$

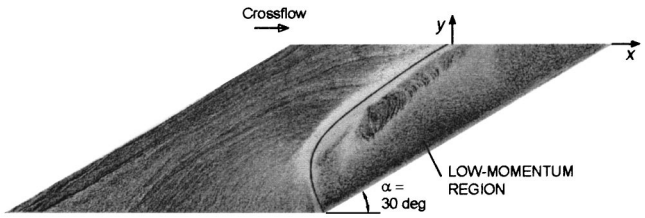

Fig. 4 Oil-film flow visualization in the symmetry plane in the 30 deg inclined hole of $t/D=1.0$ at $M=2.0$

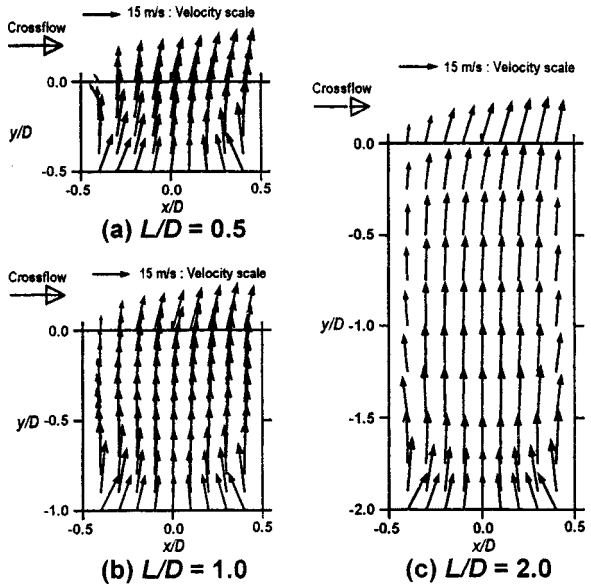

Fig. 5 Velocity vectors in the symmetry plane at $M=1.0$

the leeward side. This tendency is also true for the case with no crossflow. It is noted that the inclination of the injection hole plays a more dominant role than the crossflow does. From Figs. 2(*b*), 3, and 4, it can be said that the low-momentum region inside the inclined hole, and the separation bubble inside the normal hole, both resulted from the same origin, that is, the sharp inlet edge, even though the detailed flow structures are considerably different from each other.

Flow Measurement Data. In the velocity measurements, the position of the five-hole probe center can be traversed as close as 6.0 mm apart from the wall. This is because the largest recirculation zone is observed in the flow visualizations at $M=2.0$ in the case of $L/D=2.0$, whose thickness is about $0.064D$ (3.8 mm). Considering the probe radius of 1.59 mm, the five-hole probe could safely be positioned away from the recirculation zone.

Velocity vectors in the flow symmetry plane at $M=1.0$ are presented in Fig. 5. Velocity vectors in the case of $L/D=2.0$ (Fig. 5(*c*)) apparently show the existence of the converging flow at the hole entrance and the subsequent diverging flow. This implies the occurrence of the inlet flow separation near the wall. The velocity at the hole inlet is lowest at the hole center and highest near the wall. This is attributed to the flow acceleration near the boundary between the potential-core region and the separation bubble. In the downstream region, the velocity becomes highest along the centerline, and then the location of highest velocity shifts toward the positive *x* region near the hole exit. These overall trends are also true for $L/D=0.5$ and 1.0 (Figs. 5(*a*, *b*)). However, shorter L/D results in stronger interactions of the injectant with the crossflow and considerable disturbances in the exit flow. Particularly in the case of $L/D=0.5$, the diverging flow on the windward side collides directly with the crossflow, so that the flow near the wall rapidly slows down. At $M=0.5$, unfortunately, there are regions where the flow angles are beyond the calibration range of the five-hole probe. These regions are always found in Region D, regardless of L/D.

The velocity vectors at different blowing ratios in the case of $L/D=1.0$ are illustrated in Fig. 6. In Fig. 6(*a*), there are two measurement points beyond the calibration range at $M=0.5$, which are denoted by solid circles. At this low blowing ratio, the injectant is significantly affected by the crossflow near the hole exit. Most of the injectant approaching the exit turns in the leeward direction. The flow on the windward side is rapidly retarded while the injectant on the opposite side accelerates greatly, so that

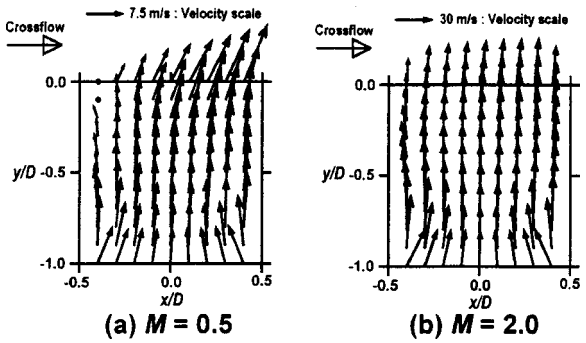

Fig. 6 Velocity vectors in the symmetry plane at $L/D=1.0$

the velocity profile at the exit shows linear variation in the positive *x* direction. An interesting thing is that most of the exit velocity vectors seem to have the same flow angle of about 65 deg. At $M=2.0$ (Fig. 6(*b*)), even the exit flow retains a nearly symmetric profile with respect to the centerline.

The distributions of the velocity component in the *x* direction, U/V_j, in the flow symmetry plane at $M=1.0$ are plotted in Fig. 7. The V_j stands for the mean injectant velocity averaged over the cross-sectional area of the injection hole, which is obtained from the mass flow rate measured by the orifice flow meter. Regardless of L/D, there exists a converging flow toward the centerline at the entrance, and a positive *x*-directional flow at the exit. At the majority of measuring points, the velocities have positive values except for two confined regions for all three L/D'*s*. The first one is at about $0.5D$ downstream of the inlet near the wall on the windward side. This is the region where the separation bubble ends or the reattachment starts. The second is situated at the inlet on the leeward side. It is noticeable that the maximum values of U/V_j at the exit, and their *x*-directional locations are nearly the same independent of L/D. In the case of $L/D=2.0$, the exit flow disturbed by the crossflow is completely isolated from complicated flow at the inlet, and there seems thus no direct interaction between the two flow fields. When $L/D=0.5$, however, the inlet and exit flows are coupled strongly.

The effects of the blowing ratio on the distributions of U/V_j for $L/D=1.0$ are presented in Fig. 8. The shaded rectangular box in Fig. 8(*a*) indicates two measurement points where the flow angles

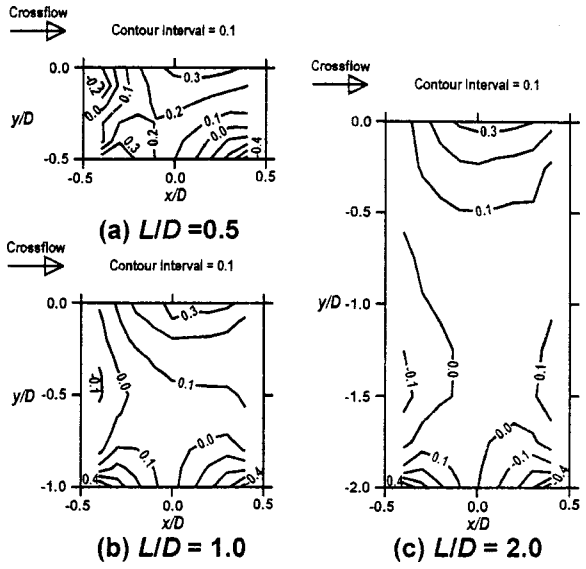

Fig. 7 Contours of the *x*-directional velocity component, U/V_j, in the symmetry plane at $M=1.0$

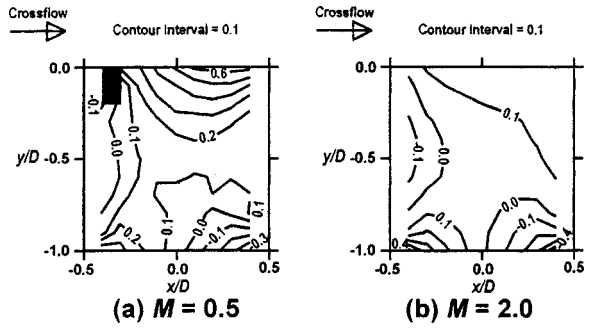

Fig. 8 Contours of the *x*-directional velocity component, U/V_j, in the symmetry plane at $L/D=1.0$

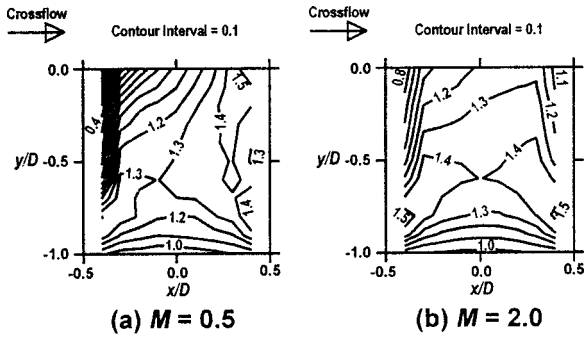

Fig. 10 Contours of the *y*-directional velocity component, V/V_j, in the symmetry plane at $L/D=1.0$

are beyond the present calibration range as in Fig. 6(*a*). The U/V_j distribution at the low blowing ratio, $M=0.5$ (Fig. 8(*a*)), shows a considerable difference from that in Fig. 7(*b*). First of all, there exists much steeper velocity gradient near the exit, and the maximum value of U/V_j is about two times larger than that at $M=1.0$ because of a strong shearing interaction between the crossflow and the injectant. In addition, the crossflow effect reaches deeply into the injection hole. At $M=2.0$, however, U/V_j at the entrance shows a similar distribution to that at $M=1.0$, but has very mild velocity gradient near the exit.

The distributions of the velocity component in the *y* direction, V/V_j, in the symmetry plane are introduced in Fig. 9 at $M=1.0$. In the case of $L/D=2.0$ (Fig. 9(*c*)), the on-coming flow strongly accelerates in the inlet potential-core region, and then it gradually decelerates up to the developing region along the hole centerline. This is because the actual flow passage is in the form of a converging–diverging channel as discussed in the flow visualization. From the inlet to $y/D=-1.0$, the *y*-directional velocity component shows a symmetric distribution with respect to the centerline. At far downstream locations, the reattached flow starts to develop into a boundary-layer flow near the wall, losing its flow symmetry. Finally, the injectant suffers a considerable retardation in Region D on the windward side of the injection hole. On the other hand, a region with high discharge velocity is still observed on the leeward side. The overall flow trend when $L/D=1.0$ (Fig. 9(*b*)) is approximately the same as when $L/D=2.0$. However, there is strong flow deceleration near the wall on the windward side, and the flow even in the entrance region does not show a symmetric distribution. In the case of $L/D=0.5$ (Fig. 9(*a*)), the discharge velocity profile at the exit shows very intensive variation in the *x* direction, and its minimum value is only $0.2V_j$ near the windward side. The effects of the blowing ratio on the distributions of V/V_j in the case of $L/D=1.0$ are illustrated in Fig. 10. At $M=0.5$ (Fig. 10(*a*)), the crossflow induces a considerable variation in the exit discharge velocity distribution along the *x* direction. The maximum value of the discharge velocity is more than $1.5V_j$ near the right edge and it sharply decreases in the negative *x* direction. On the contrary, the inside flow at $M=2.0$ shows symmetric distributions because the crossflow effect becomes much weaker (Fig. 10(*b*)).

Flow data in the absence of the crossflow is shown in Fig. 11 at $V_j=15$ m/s in the case of $L/D=1.0$, which is collected as baseline data. As expected, the flow vectors are symmetric with respect to the hole centerline, and the converging–diverging flow is also found in the entrance region. Direct comparisons of the results in Figs. 11(*a*, *b*) with those in Figs. 5(*b*) and 9(*b*) in turn can provide the net variations of the inside flow due to the crossflow. In the entrance region, the two flows are nearly the same in both flow direction and magnitude. In the exit region, however, the presence of the crossflow results in the retardation of the windward-side flow, but enhances the discharge of the injectant on the leeward side.

The static-pressure coefficient inside the injection hole, C_{PS}, is defined as follows:

$$C_{PS}=\frac{P_S-P_{S,0}}{\rho_j V_j^2/2} \tag{1}$$

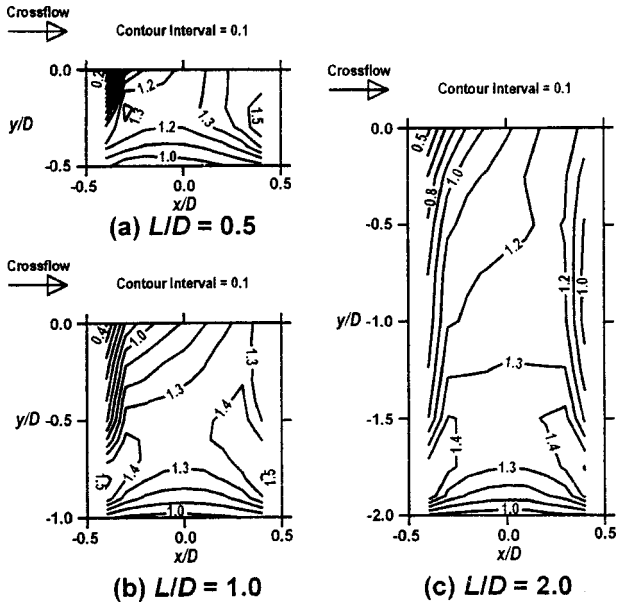

Fig. 9 Contours of the *y*-dirctional velocity component, V/V_j, in the symmetry plane at $M=1.0$

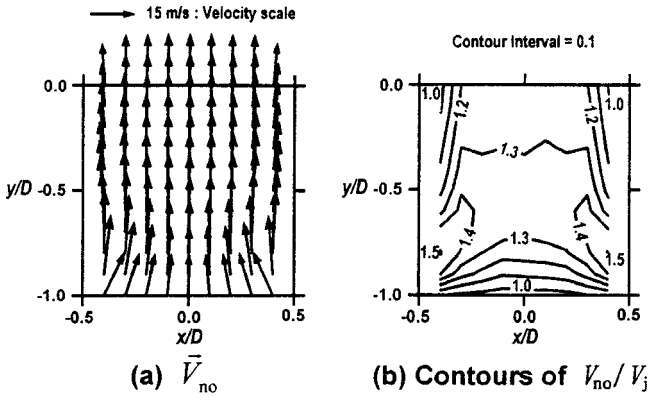

Fig. 11 Flow data in the symmetry plane with no crossflow at $L/D=1.0$

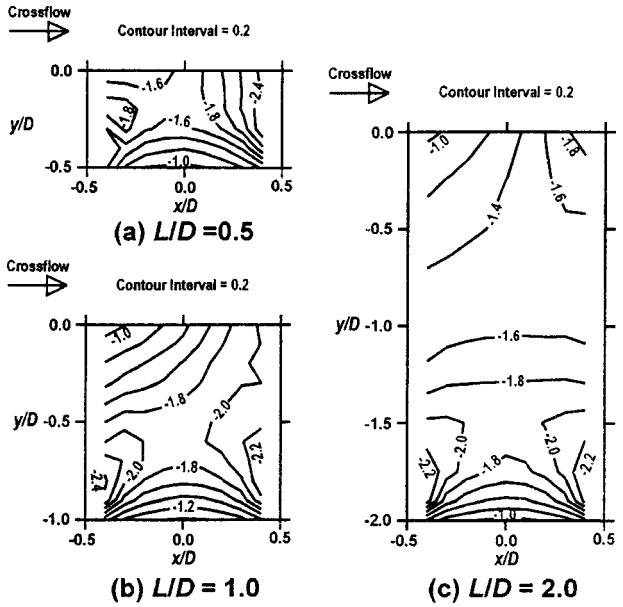

Fig. 12 Contours of the static-pressure coefficient, C_{Ps}, in the symmetry plane at $M=1.0$

where P_S denotes the local static pressure measured inside the injection hole, and $P_{S,0}$ is the plenum static pressure measured $1.0D$ upstream of the hole inlet. The static-pressure coefficients in the symmetry plane at $M=1.0$ are plotted in Fig. 12. The static-pressure coefficient value should be negative, since $P_{S,0}$ is always larger than P_S in any case. In the y direction along the centerline at $L/D=2.0$ (Fig. 12(c)), there exists a strong favorable pressure gradient at the entrance, and then a relatively weak adverse pressure gradient in the far downstream region. These static-pressure distributions clearly explain the strong acceleration and subsequent gradual deceleration of the oncoming flow in the potential-core region. Due to the crossflow effect, the adverse pressure gradient becomes steeper on the windward side near the exit, while there is another favorable pressure gradient region on the leeward side (Fig. 12(c)). The crossflow thus stabilizes the exit flow on the leeward side, and meanwhile destabilizes the opposite exit flow. Regardless of L/D, there always exists a favorable pressure gradient in the positive x direction at the hole exit. The static pressure is found to be minimal near the vortex center of the inlet separation bubble. A closer examination shows that the values of C_{PS} on the windward side in the cases of $L/D=1.0$ and 2.0 are smaller than those on the opposite side, which assures that the flow near the wall on the windward side is destabilized even in the entrance region. In the case of $L/D=0.5$, the static pressure distribution is greatly altered because the crossflow directly interacts with the inlet separated flow.

Summary and Conclusions

Oil-film flow visualizations and mean flow measurements in the flow symmetry plane have been conducted inside a circular injection hole with a sharp square-edged inlet. The focus is on normally oriented injections to a crossflow, but additional visualizations are also performed inside inclined holes with inclination angles of 30 and 60 deg. Because of their importance to flow behavior, three different length-to-diameter values of 0.5, 1.0, and 2.0, and the blowing ratios of 0.5, 1.0, and 2.0 are investigated. In the long L/D case such as $L/D=2.0$, the near-wall flow inside the normal-injection hole is classified as four flow regions: an inlet separation region, a reattachment region, a developing region, and a near-exit flow region. On the other hand, the potential-core flow comprises a converging flow region, a diverging flow region, a developing flow region, and a deflected flow region by the crossflow.

Flow visualizations for the normal injection show that the inlet separation bubbles in the cases of $L/D=1.0$ and 2.0 are apparent with a clear imprint of recirculating flow patterns on the windward side, even though the recirculation is not distinct on the opposite side. This fact implies that the crossflow stabilizes the inside flow on the leeward side, and meanwhile destabilizes it on the windward side, which is also assured from the static-pressure data. In the case of $L/D=0.5$, the separation bubble undergoes a considerable contraction, and its recirculating flow structure seems to be suppressed by the crossflow. Regardless of the L/D values, actual flow passage is in the form of a converging–diverging channel due to the presence of the inlet separation bubble.

Contrary to the crossflow effect, the inclination of the normal injection hole in the leeward direction of the crossflow stabilizes the inside flow near the windward wall but destabilizes that near the leeward one. Particularly for 30 deg inclined injection, the separation bubble is no longer observed on the windward side, while the low-momentum region on the opposite side is dramatically expanded. Due to the sudden reduction in the flow passage area, a jetting effect appears near the windward wall. Both the low-momentum region inside the inclined hole and the separation bubble inside the normal hole are attributed basically to the same origin, that is, the sharpness of the inlet edge, although the resulting inside flows are strikingly different.

Flow measurement data at $L/D=2.0$ show that regardless of M, there exists a converging–diverging flow in the entrance region, and that the oncoming flow in the inlet potential-core region strongly accelerates and then gradually decelerates until the developing region is reached. The reattached flow starts to develop in a boundary-layer form in the developing region, and finally the injectant undergoes a strong interaction with the crossflow. Relatively short holes such as $L/D=1.0$ and 0.5, however, do not allow the boundary-layer flow development on the wall. Instead, the diverging flow after the throat of the converging–diverging part interacts directly with the crossflow on the windward side at the exit, especially in the case of $L/D=0.5$. In this short L/D case, the inlet flow is directly influenced by the exit flow. When $L/D=2.0$, however, the inlet flow is completely isolated from the exit flow. At $M=0.5$, the injectant is significantly disturbed by the crossflow near the exit, resulting in a considerable variation in the discharge velocity profile. At $M=2.0$, however, the crossflow effect is found to be minute.

Acknowledgments

The research herein was supported by the Korea Science and Engineering Foundation (KOSEF Grant No. 95-0200-12-01-3), and was also supported, in part, by the Turbo and Power Machinery Research Center.

Nomenclature

C_{PS} = static pressure coefficient, Eq. (1)
D = injection hole diameter
J = momentum flux ratio $=\rho_j V_j^2/\rho_\infty U_\infty^2$
M = blowing ratio $=\rho_j V_j/\rho_\infty U_\infty$
P_S = local static pressure
$P_{S,0}$ = plenum static pressure measured $1D$ upstream of the hole inlet
Re_D = Reynolds number $=V_j D/\nu_j$
$\mathrm{Re}_{\delta 2}$ = Reynolds number $=U_\infty \delta_2/\nu_\infty$
t = injection plate thickness, Fig. 3
U = x-directional velocity component
U_∞ = free-stream velocity
V = y-directional velocity component
V_j = spatially averaged injection velocity over cross section of injection hole

V_{no} = y-directional velocity in absence of crossflow
$\vec{V}_{no}$ = velocity vector in absence of crossflow
x = coordinate in streamwise (leeward) direction, Fig. 1
y = coordinate in normal direction, Fig. 1
z = coordinate in spanwise direction, Fig. 1
α = inclination angle of injection hole
δ_2 = momentum boundary-layer thickness
ν_j = injectant kinematic viscosity
ν_∞ = kinematic viscosity of crossflow fluid
ρ_j = injectant density
ρ_∞ = crossflow density

References

[1] Morton, B. R., 1961, ''On a Momentum-Mass Flux Diagram for Turbulent Jets, Plumes and Wakes,'' J. Fluid Mech., **10**, pp. 101–108.
[2] Andreopoulos, J., and Rodi, W., 1984, ''Experimental Investigation of Jets in a Crossflow,'' J. Fluid Mech., **138**, pp. 93–127.
[3] Andreopoulos, J., 1985, ''On the Structure of Jets in a Crossflow,'' J. Fluid Mech., **157**, pp. 163–197.
[4] Carrotte, J. F., and Stevens, S. J., 1990, ''The Influence of Dilution Hole Geometry on Jet Mixing,'' ASME J. Eng. Gas Turbines Power, **112**, pp. 73–79.
[5] Holdeman, J. D., Liscinsky, D. S., Oechsle, V. L., Samuelsen, G. S., and Smith, C. E., 1997, ''Mixing of Multiple Jets With a Confined Subsonic Crossflow: Part 1—Cylindrical Duct,'' ASME J. Eng. Gas Turbines Power, **119**, pp. 852–862.
[6] Burd, S. W., Kaszeta, R. W., and Simon, T. W., 1998, ''Measurements in Film Cooling Flow: Hole L/D and Turbulence Intensity Effects,'' ASME J. Turbomach., **120**, pp. 791–798.
[7] Lee, S. W., Kim, Y. B., and Lee, J. S., 1997, ''Flow Characteristics and Aerodynamic Losses of Film-Cooling Jets With Compound Angle Orientations,'' ASME J. Turbomach., **119**, pp. 310–319.
[8] Lee, S. W., Lee, J. S., and Ro, S. T., 1994, ''Experimental Study on the Flow Characteristics of Streamwise Inclined Jets in Crossflow on Flat Plate,'' ASME J. Turbomach., **116**, pp. 97–105.
[9] Andreopoulos, J., 1982, ''Measurements in a Jet-Pipe Flow Issuing Perpendicularly Into a Cross Stream,'' ASME J. Fluids Eng., **104**, pp. 493–499.
[10] Lloyd, S., and Brown, A., 1986, ''Velocity and Turbulence Fields in Pipe Entrance Regions in the Presence of Cross Flows,'' ASME J. Eng. Gas Turbines Power, **108**, pp. 499–503.
[11] Leylek, J. H., and Zerkle, R. D., 1994, ''Discrete-Jet Film Cooling: A Comparison of Computational Results With Experiments,'' ASME J. Turbomach., **116**, pp. 358–368.
[12] Cho, H. H., and Goldstein, R. J., 1995, ''Heat (Mass) Transfer and Film Cooling Effectiveness With Injection Through Discrete Holes: Part I — Within Holes and on the Back Surface,'' ASME J. Turbomach., **117**, pp. 441–450.
[13] Thole, K. A., Gritsch, M., Schulz, A., and Wittig, S., 1997, ''Effect of a Crossflow at the Entrance to a Film-Cooling Hole,'' ASME J. Fluids Eng., **119**, pp. 533–540.
[14] Morris, G. K., and Garimella, S. V., 1998, ''Orifice and Impingement Flow Fields in Confined Jet Impingement,'' ASME J. Electron. Packag., **120**, pp. 68–72.
[15] Lee, S. W., Joo, S. K., and Lee, J. S., 2001, ''Flow Characteristics Inside Circular Injection Holes Normally Oriented to a Crossflow: Part II — Three-Dimensional Flow Data and Aerodynamic Loss,'' ASME J. Turbomach., **123**, this issue, pp. 274–280.
[16] ISO 5167-1:1991(E), 1991, ''Measurement of Fluid Flow by Means of Pressure Differential Devices — Part 1: Orifice Plates, Nozzles and Venturi Tubes Inserted in Circular Cross-Section Conduits Running Full,'' International Organization for Standardization.
[17] Treaster, A. L., and Yocum, A. M., 1979, ''The Calibration and Application of Five-Hole Probes,'' ISA Trans., **18**, pp. 23–34.
[18] Lee, S. W., and Yoon, T. J., 1999, ''An Investigation of Wall-Proximity Effect Using a Typical Large-Scale Five-Hole Probe,'' KSME Int. J., **13**, No. 3, pp. 273–285.
[19] Abernethy, R. B., Benedict, R. P., and Dowdell, R. B., 1985, ''ASME Measurement Uncertainty,'' ASME J. Fluids Eng., **107**, pp. 161–164.
[20] Foss, J. F., 1980, ''Interaction Region Phenomena for the Jet in a Cross-flow Problem, '' Rep. SFB 80/E/161, Univ. Karlsruhe.

Flow Characteristics Inside Circular Injection Holes Normally Oriented to a Crossflow: Part II—Three-Dimensional Flow Data and Aerodynamic Loss

Sang Woo Lee

Seong Kuk Joo

School of Mechanical Engineering,
Kumoh National University of Technology,
Kumi, Kyungbook 730-701, Korea

Joon Sik Lee
School of Mechanical and Aerospace Engineering,
Seoul National University,
Seoul 151-742, Korea

Presented are three-dimensional mean velocity components and aerodynamic loss data inside circular injection holes. The holes are normally oriented to a crossflow and each hole has a sharp square-edged inlet. Because of their importance to flow behavior, three different blowing ratios, $M=0.5$, 1.0, and 2.0, and three hole length-to-diameter ratios, $L/D=0.5$, 1.0, and 2.0, are investigated. The entry flow is characterized by a separation bubble, and the exit flow is characterized by direct interaction with the crossflow. The uniform oncoming flow at the inlet undergoes a strong acceleration and a subsequent gradual deceleration along a converging–diverging flow passage formed by the inlet separation bubble. After passing the throat of the converging–diverging passage, the potential core flow, which is nearly axisymmetric, decelerates on the windward side, but tends to accelerate on the leeward side. The presence of the crossflow thus reduces the discharge of the injectant on the windward side, but enhances its efflux on the leeward side. This trend is greatly accentuated at $M=0.5$. In general, there are strong secondary flows in the inlet and exit planes of the injection hole. The secondary flow within the injection hole, on the other hand, is found to be relatively weak. The inlet secondary flow is characterized by a strong inward flow toward the injection-hole center. However, it is not completely directed inward since the crossflow effect is superimposed on it. Past the throat, secondary flow is observed such that the leeward velocity component induced by the crossflow is superimposed on the diverging flow. Short L/D usually results in an exit discharging flow with a steep velocity gradient as well as a strong deceleration on the windward side, as does low M. The aerodynamic loss inside the injection hole originates from the inlet separation bubble, wall friction and interaction of the injectant with the crossflow. The first one is considered as the most dominant source of loss, even in the case of $L/D=2.0$. At $L/D=0.5$, the first and third sources are strongly coupled with each other. Regardless of L/D, the mass-averaged aerodynamic loss coefficient has an increasing tendency with increasing M. [DOI: 10.1115/1.1348016]

Introduction

Normally injected jets in a crossflow have wide industrial applications, such as gas turbine hot-component cooling, pollution control, drying processes, electronic component cooling, etc. Numerous researches on this subject are reviewed in the companion paper of this work, Part I [1]. The hole length-to-diameter ratio values, L/D, are different depending on the specific applications. The L/D values are usually less than unity when applied to the dilution in gas turbine combustors. On the contrary, their values are larger than unity for film or impingement cooling applications. In general, the downstream three-dimensional flow field after coming out of an injection hole is related closely to the aerodynamic behavior of the injectant inside the injection hole. Moreover, the aerodynamic loss inside the injection hole is very important for the design of cooling- and dilution-air supply systems of gas turbines. There are several studies, such as that of Leylek and Zerkle [2], on the three-dimensional flow within an inclined injection hole in a crossflow. However, it is not easy to find literature which reports three-dimensional flow and aerodynamic loss data inside the injection hole normally oriented to the crossflow, especially for relatively short L/D's.

In Part I [1], both flow visualizations and flow data in the symmetry plane are presented inside the injection hole. For a further insight, this paper describes a full three-dimensional nature of the flow in injection holes, which are normally oriented to a crossflow. In this Part II, three-dimensional flow and aerodynamic loss data are presented for various hole length-to-diameter ratios and blowing ratios.

Experiment

The present experimental apparatus and procedures are basically the same as those described in Part I [1]. The hole diameter, D, is fixed at 60 mm, but its length varies as $L=30$, 60, or 120 mm, providing L/D values of 0.5, 1.0, and 2.0, respectively. The blowing ratios considered are $M=0.5$, 1.0, and 2.0 for all three L/D values. Additional measurements are performed at $M=1.5$ only in the hole exit plane in order to evaluate $\overline{C_{Pt}}$. The origin of the present coordinates is located at the center of the injection-hole exit, and x, y, and z are the streamwise (leeward), normal, and spanwise coordinates, respectively (Fig. 1). A cone-type five-hole probe 3.18 mm (0.125 in.) in its tip diameter is used to measure three-dimensional velocity components inside the injection hole.

The Reynolds number based on the free-stream velocity and the momentum boundary-layer thickness at the hole center, Re_{δ_2}, is

Contributed by the International Gas Turbine Institute and presented at the 45th International Gas Turbine and Aeroengine Congress and Exhibition, Munich, Germany, May 8–11, 2000. Manuscript received by the International Gas Turbine Institute February 2000. Paper No. 2000-GT-257. Review Chair: D. Ballal.

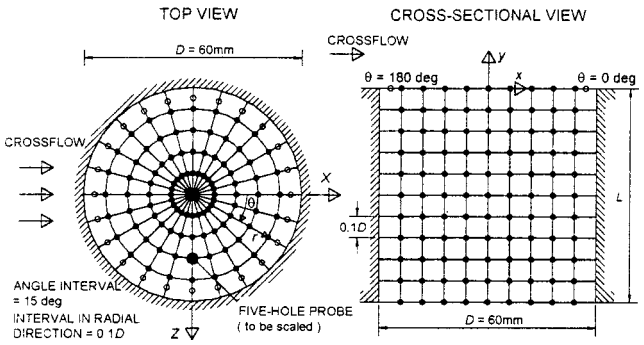

Fig. 1 Measurement locations in the case of $L/D=1.0$

1.7×10^3, and the injectant Reynolds number based on the spatially averaged injection velocity, V_j, and the hole diameter, Re_D, is 5.7×10^4, when the blowing ratio is unity. Three-dimensional velocity components in the injection holes are measured in the six x–z planes when $L/D=0.5$, and in the eleven x–z planes when $L/D=1.0$ with an interval of $D/10$ in both cases. At $L/D=2.0$, the flow velocity is measured in the nine x–z planes with an interval of $D/4$. In each x–z plane, data are obtained at five points in the r direction with an interval of $D/10$, starting from $r/D=0.0$, and at 25 points in the θ direction with an interval of 15 deg. These measuring points at $M=1.0$ are indicated by small solid circles in Fig. 1. In particular, at the exit plane ($y/D=0.0$), an additional 25 measurements are performed at $r/D=0.45$ for more accurate evaluation of mass-averaged total pressure loss coefficients. The open circles in Fig. 1 stand for these additional points.

The closest near-wall measurement is always carried out $D/10$ (about two times the probe tip diameter) apart from the wall except for the hole-exit measurement as in Fig. 1, to minimize additional error due to the wall proximity [3]. The uncertainty intervals are basically the same as those listed in Part I [1]. In order to examine the accuracy of the present measurement data, the mass flow rate through the exit plane is obtained by integrating the measured y-directional velocity components at the exit. The result shows that the difference between the evaluated mass flow rate, $\dot{m}$, and the mass flow rate measured with the orifice flow meter, $\dot{m}_{orif}$, falls within only 1.4 percent of $\dot{m}_{orif}$ at $M=2.0$, even though the flow is highly turbulent with steep velocity gradients.

Results and Discussion

Three-Dimensional Velocity Data. In Fig. 2, contours of the y-directional velocity component, V/V_j, are plotted in selected x–z planes at $M=1.0$ in the case of $L/D=1.0$. First of all, the flow inside the injection hole shows fully three-dimensional characteristics. As can be seen in Fig. 2(a), the contours do not show an axisymmetric flow pattern even at the inlet. Moving from the inlet ($y/L=-1.0$) to where $y/L=-0.8$ delivers a significant change in the velocity distribution. The nearly uniform flow at the inlet accelerates rapidly over the whole cross section, particularly at $r/D=0.4$, and develops into a flow with concentric distribution where the minimum value of V/V_j occurs at the hole center (Fig. 2(b)). The near-wall value of V/V_j at $y/L=-0.8$ is about 1.5, which is found to be largest all over the measurement x–z planes in Fig. 2. This flow behavior is due mainly to the presence of the inlet separation bubble, as discussed by Lee et al. [1]. The nearly axisymmetric flow at $y/L=-0.8$ begins to show a three-dimensional nature at $y/L=-0.6$, and the location with a peak value of V/V_j seems to shift radially toward the hole center (Fig. 2(c)). From this position, the near-wall flow starts to decelerate on the windward (negative x) side, but accelerates on the leeward (positive x) side on the whole. As it approaches the hole exit

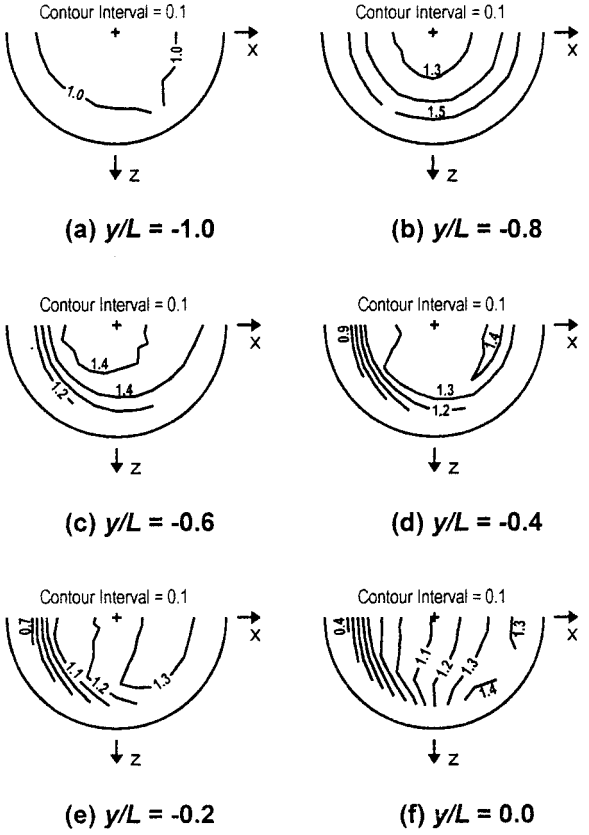

Fig. 2 Contours of the y-directional velocity component, V/V_j, in the $x-z$ plane at $M=1.0$ in the case of $L/D=1.0$

($y/L=0$) from $y/L=-0.6$, the flow in the windward region experiences a strong deceleration along the y direction, which results in a steep velocity gradient on the windward side at each x–z plane. In the exit plane (Fig. 2(f)), the V/V_j value varies widely from 0.4 at the far windward location to 1.4 on the leeward side. This implies that the crossflow has an adverse effect on the discharge of the injectant on the windward side, and at the same time augments discharge on the opposite side.

The distribution of V/V_j at $M=2.0$ when $L/D=1.0$ is shown in Fig. 3. Now the inside flow becomes more uniform in the central region, and the velocity gradient is less steep in each x–z plane compared with that at $M=1.0$. However, the two cases basically show a very similar flow trend. The contours in the exit planes (Figs. 2(f) and 3(f)) explain that a larger portion of the injectant is discharged through the leeward region at $M=1.0$, but through the central area at $M=2.0$. The flow visualization at $M=2.0$ for $L/D=1.0$ [1] reveals that the throat of the converging–diverging passage formed by an inlet separation bubble is located approximately at $y/D=-0.81$. In addition, the thickness of the separation bubble at $y/D=-0.81$ on the windward side is measured about 3.6 mm ($0.06D$). The reduction in the flow cross-sectional area at the throat results in a strong acceleration of the on-coming flow, especially near the boundary of the inlet separation bubble. This is the reason that V/V_j contours in Fig. 3(b) appear nearly concentric.

The projections of velocity vectors on each selected x–z plane are presented in Fig. 4 at $M=1.0$ for $L/D=1.0$. The secondary flow is, on the whole, very strong at the inlet and exit planes of the injection hole, but it is relatively weak at other locations. The inlet secondary flow is characterized by a strong inward flow toward the hole center as in Fig. 4(a) due to the sharp square inlet edge. As r/D increases, the velocity magnitude increases significantly. The strong inward flow near the wall at $y/D=-1.0$ is altered

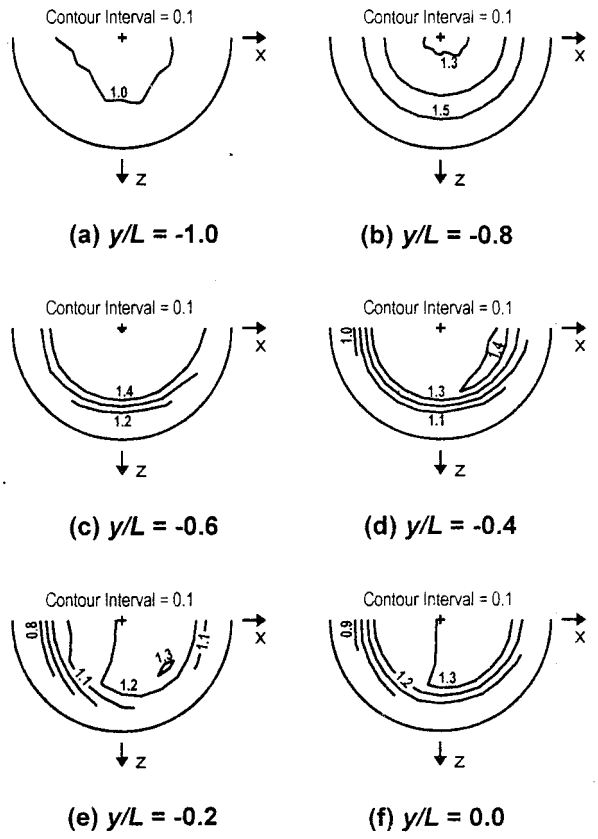

Fig. 3 Contours of the *y*-directional velocity component, V/V_j, in the *x*–*z* plane at $M=2.0$ in the case of $L/D=1.0$

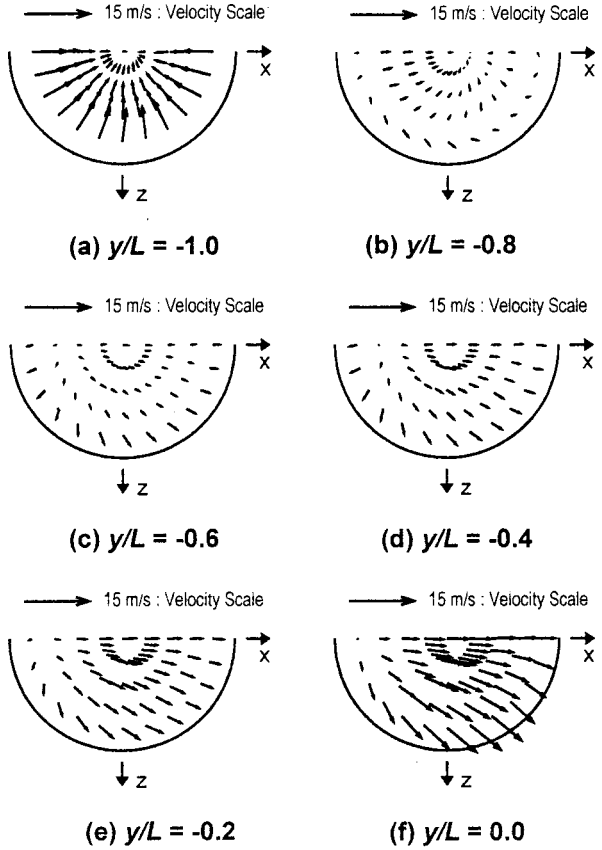

Fig. 4 Projection of velocity vectors on the *x*–*z* plane at $M=1.0$ in the case of $L/D=1.0$

greatly to a somewhat irregular flow at $y/L=-0.8$ (Fig. 4(*b*)). Even at this location, the flow around the center of the injection hole still has an inward motion similar to the inlet secondary flow, but the crossflow effect becomes more noticeable. At $y/L=-0.6$, no converging flow is observed even in the central potential-core region. Instead, the secondary flow is built up in such a way that a diverging flow is superimposed upon the leeward flow, which results from the shearing with the crossflow. The qualitative flow feature at $y/D=-0.6$ is sustained up to the downstream location of $y/D=-0.2$, even if the secondary flow shows an increasing trend in its magnitude along the *y* direction. At the exit plane (Fig. 4(*f*)), the secondary flow is remarkably magnified compared to those in other measurement planes. It is interesting to note that most of the velocity vectors near the wall have flow angles around $\theta=45$ deg.

The projections of velocity vectors on the *x*–*z* plane at $M=2.0$ in the case of $L/D=1.0$, are shown in Fig. 5. Comparing these secondary flow vectors with those at $M=1.0$, the two flow patterns are qualitatively the same. Independent of the blowing ratio, velocity vectors show in sequence a strong inward flow at the inlet, a complicated secondary flow near the throat of the converging–diverging passage, a subsequent diverging flow affected by the crossflow, and a relatively strong exit secondary flow. The secondary-flow magnitudes at the inlet at $M=2.0$, however, are observed to be much larger than those at $M=1.0$. This is simply because the average injection velocity, V_j, at $M=2.0$ is twice as large as that at $M=1.0$. The secondary flow in Fig. 5(*b*) is also attributed to the inlet separation bubble, as discussed in Fig. 4(*b*). As noted earlier, the throat of the converging–diverging passage is located at about $y/D=-0.81$ at $M=2.0$ when $L/D=1.0$. The measurement plane at $y/D=-0.8$ (Fig. 5(*b*)) is thus located immediately downstream of the throat. Therefore, the flow near the wall is liable to diverge, even though the converging flow still appears in the central potential-core region (Fig. 5(*b*)).

Figures 6 and 7 show the *x*- and *z*-directional velocity components, U/V_j and W/V_j, in the exit plane at $M=1.0$ and 2.0 when $L/D=1.0$. Figure 6 illustrates that the *x*-directional velocity component has a steep velocity gradient in the windward region, but a mild velocity gradient in the leeward region. Regardless of the blowing ratios, U/V_j has its maximum value away from the hole center. The maximum value of U/V_j seems to occur because of the shearing with the crossflow. The location of the maximum U/V_j near the wall is moved from $\theta=75$ deg at $M=1.0$ to $\theta=90$ deg at $M=2.0$. The *z*-directional velocity component, W/V_j, in Fig. 7 vanishes near the symmetry line and shows an increasing trend in the positive *z* direction. Its maximum value is located near the wall at $\theta=80$ deg when $M=1.0$ and at 90 deg when $M=2.0$. The crossflow usually forces the injectant not only to be deflected in the positive *x* direction but also to be pushed down in the negative *y* direction. Because of this crossflow effect, the injectant is inevitably directed away from the symmetry line into the *z* direction as in Fig. 7.

In Fig. 8, the contours of the *y*-directional velocity component, V/V_j, and secondary flow vectors are shown in the exit plane at $M=0.5$ in the case of $L/D=1.0$. For a small blowing ratio such as $M=0.5$, unfortunately, the flow in the shaded region of Fig. 8(*a*) is beyond the present calibration flow-angle ranges. There seems to be a very complicated vortical flow, such as a crossflow horseshoe vortex, as discussed by Cho and Goldstein [4], and a periodic unsteady motion proposed by Andreopoulos [5]. From Figs. 8(*a*), 2(*f*), and 3(*f*), it can be seen that regardless of *M*, the contours of the discharge velocity are far from a concentric distribution, and with an increase in the blowing ratio the discharge velocity gradient is getting less steep. Particularly for $M=0.5$, V/V_j varies

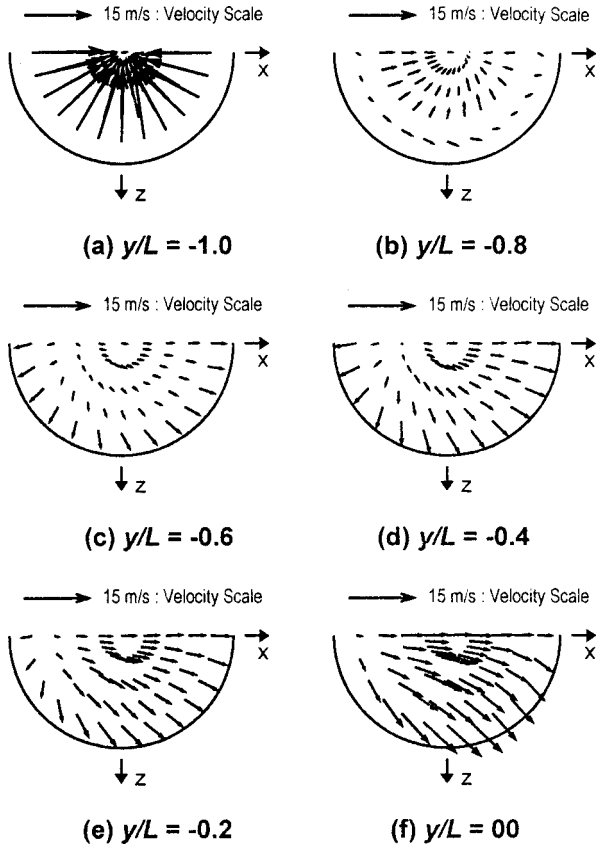

Fig. 5 Projection of velocity vectors on the $x-z$ plane at $M=2.0$ in the case of $L/D=1.0$

significantly from its minimum value of about $V/V_j=0.5$ on the windward side to its maximum value of about $V/V_j=1.6$ on the leeward side. This means that at this lowest blowing ratio, most of the injectant is discharged through the leeward side. The small solid circles in Fig. 8(*b*) also denote the points where the flow angle is beyond the calibration range. Comparison of Fig. 8(*b*) with Figs. 4(*f*) and 5(*f*) reveals that the velocity vectors at the exit, in general, have a qualitatively similar pattern independent of the blowing ratios. However, a closer examination shows that the lower the blowing ratio, the smaller the flow turning angles in the θ direction in the exit plane.

Exit velocities in the absence of the crossflow are presented in Fig. 9 where $V_j=15$ m/s and $L/D=1.0$. In this case, the *y*-directional velocity component is in an axisymmetric distribution. Moreover, the secondary velocity vectors are always directed toward the wall, and their magnitude is largest when r/D is 0.4.

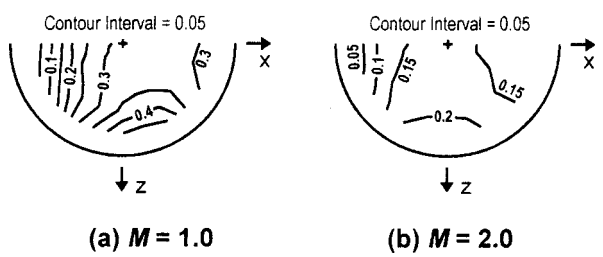

Fig. 6 Contours of the *x*-directional velocity component, U/V_j, in the exit plane in the case of $L/D=1.0$

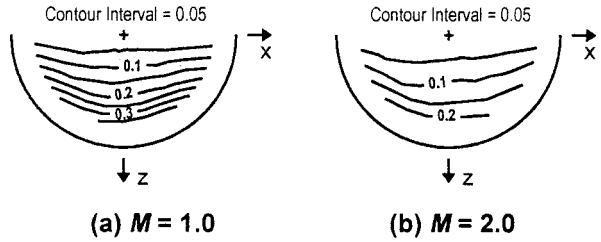

Fig. 7 Contours of the *z*-directional velocity component, W/V_j, in the exit plane in the case of $L/D=1.0$

Comparisons of the results in Fig. 9(*a*) with Figs. 8(*a*), 2(*f*), and 3(*f*) clearly indicate significant change in the exit flow due to the presence of the crossflow.

In Fig. 10, the *y*-directional velocity components in the exit plane at $M=1.0$ are introduced in the case of $L/D=0.5$ and 2.0. From Figs. 10 and 2(*f*), it is found that the steep velocity gradient exists in the windward region and mild velocity gradient on the opposite side, and as L/D increases the velocity gradient is less steep. When $L/D=0.5$, the velocity gradient is steepest in the windward near-wall region, and the value of V/V_j varies considerably from the minimum of 0.2 to the maximum of 1.5. Therefore, a short L/D has the same effect on the discharge of the injection fluid as low M does.

The effect of L/D on the exit secondary flow at $M=1.0$ is illustrated in Fig. 11. The secondary flow patterns have the same general trend except for the region around $x/D=-0.4$. The flow difference observed in the far windward region is due mainly to the different strength of the diverging flows downstream of the inlet separation bubble. It is noted that contrary to the large variations in V/V_j with L/D as discussed in Fig. 10, the changes in the secondary flow are not considerable.

When $M=2.0$, the inlet secondary flow at $L/D=0.5$ is compared with that at $L/D=2.0$ in Fig. 12. In the case of $L/D=2.0$ (Fig. 12(*b*)), most of the velocity vectors are directed toward the center of the injection hole because of the negligible crossflow effect. When $L/D=0.5$ (Fig. 12(*a*)), however, because of the

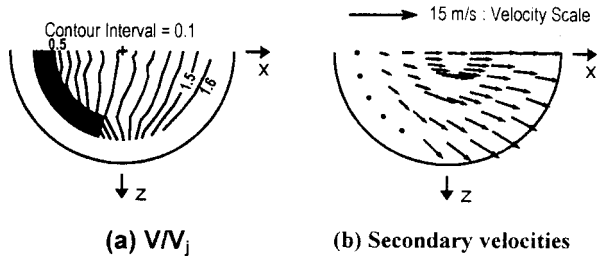

Fig. 8 Velocity data in the exit plane at $M=0.5$ in the cse of $L/D=1.0$

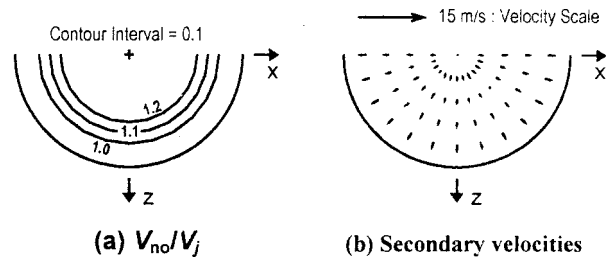

Fig. 9 Velocity data in the exit plane with no crossflow at $V_j=15$ m/s in the case of $L/D=1.0$

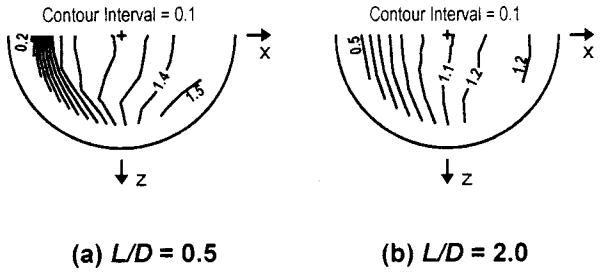

Fig. 10 Contours of the *y*-directional velocity component, V/V_j, in the exit plane at $M=1.0$

crossflow, the secondary flow is altered from the axisymmetric inward flow in the near-wall region particularly in between $\theta=75$ and 150 deg.

The circumferential distributions of V/V_j in $\theta-y$ planes at $r/D=0.4$ for $M=1.0$ are presented in Fig. 13. The grid points in each figure represent the measurement points. In the y direction, V/V_j in the case of $L/D=2.0$ (Fig. 13(*c*)) rapidly accelerates in the inlet region, has a peak value near $y/D=-1.75$, and then decelerates gradually. From the inlet to the location where $y/D=-1.5$, the variation of V/V_j is independent of θ. In the farther downstream region, however, contours show a noticeable change in the θ direction. From $y/D=-1.25$ to -0.75, V/V_j has a nearly constant value of about 1.0. Near the exit, the flow is retarded in the range between $\theta=90$ and 180 deg, while it accelerates between $\theta=0$ and 90 deg. As L/D becomes shorter, the crossflow effect becomes more important, and the adverse pressure gradient on the windward side is considerably steepened; meanwhile the favorable pressure gradient on the leeward side remains mild. Particularly in the case of $L/D=0.5$, the variation of V/V_j in the θ direction is already developed at the inlet, and a broad region with the peak value of $V/V_j(=1.5)$ is found on the leeward side.

Aerodynamic Loss. Aerodynamic loss, a measure of total pressure deficit, is usually expressed in the form of the total-pressure loss coefficient, defined as:

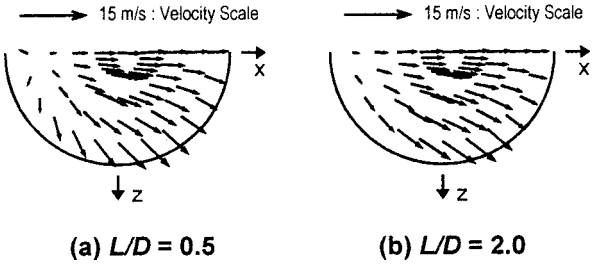

Fig. 11 Projection of velocity vectors in the exit plane at $M=1.0$

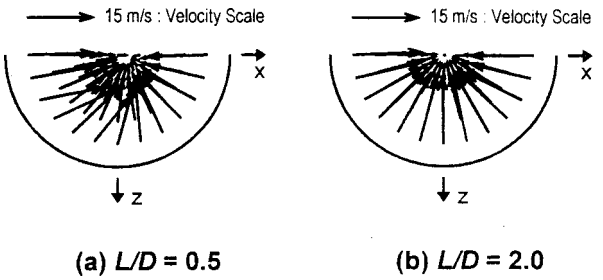

Fig. 12 Projection of velocity vectors in the inlet plane at $M=2.0$

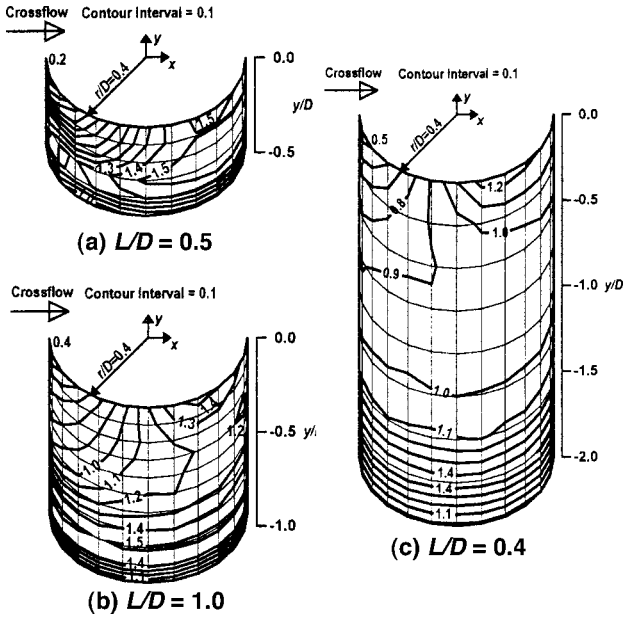

Fig. 13 Contours of the *y*-directional velocity component, V/V_j, at $M=1.0$ in the $\theta-y$ plane at $r/D=0.4$

$$C_{Pt}=\frac{P_{t,0}-P_t}{\rho_j V_j/2} \tag{1}$$

where P_t represents the measured local total pressure inside the injection hole, and $P_{t,0}$ denotes the plenum total pressure measured $1.0D$ upstream of the injection hole inlet.

In Fig. 14, the distributions of the total-pressure loss coefficient in the flow symmetry plane are reported with the variation of L/D at $M=1.0$. In the case of $L/D=2.0$ (Fig. 14(*c*)), C_{Pt} starts to increase at the near-wall location about $0.25D$ downstream of the inlet. This increase in the aerodynamic loss is apparently attributed to the presence of the inlet separation bubble. The largest value of C_{Pt} is found $0.5D$ downstream of the inlet. This location coincides approximately with the end point of the separation bubble, as can be seen in the flow visualization by Lee et al. [1]. Except for $L/D=2.0$ (Fig. 14(*c*)), the C_{Pt} value on the windward

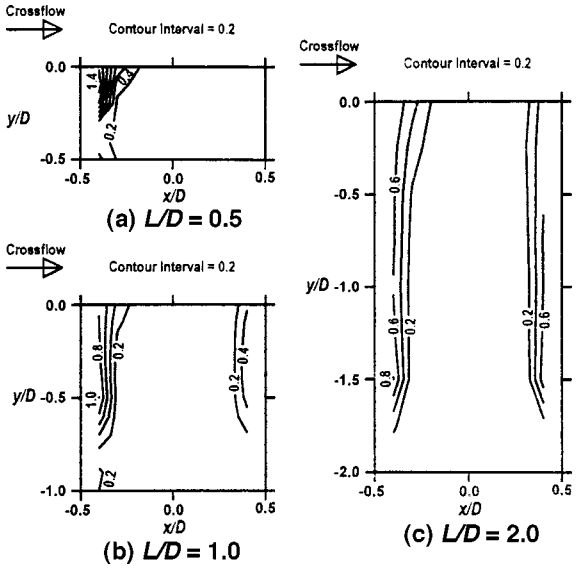

Fig. 14 Contours of the total-pressure loss coefficient, C_{Pt}, in the flow symmetry plane at $M=1.0$

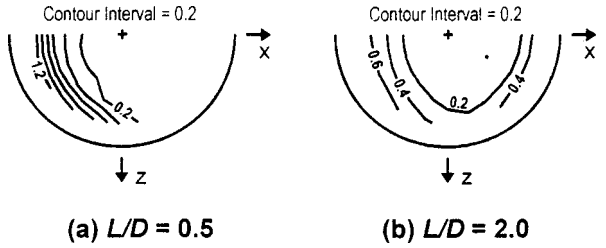

Fig. 15 Contours of the total-pressure loss coefficient, C_{Pt}, in the exit plane at $M=1.0$

side is larger than that on the opposite side, since the destabilized flow tends to generate more aerodynamic loss. In the developing flow region in Fig. 14(*c*), the area with large C_{Pt} gradually expands due to the wall friction, but its contribution is relatively small compared to that by the inlet flow separation. Near the exit of the injection hole, C_{Pt} has an asymmetric and broad distribution. The aerodynamic loss on the windward side near the exit increases; on the other hand it decreases slightly on the opposite side. The overall trend in the case of $L/D=2.0$ is also true for the different L/D cases. As the hole length becomes shorter, however, C_{Pt} in the windward region has a tendency to increase, but C_{Pt} on the leeward side tends to decrease. When $L/D=0.5$ (Fig. 14(*a*)), aerodynamic loss is negligible on the leeward side, but significant loss is generated near the windward wall. In summary, the aerodynamic loss inside the injection hole results from the inlet flow separation, wall friction, and interaction with the crossflow. The relative importance of these sources depends in general on L/D. In the case of $L/D=0.5$, the effects of these three sources can hardly be identified. Even in the case of $L/D=2.0$, the second one seems to have a minor effect. The total-pressure loss coefficient data in the exit plane at $M=1.0$ are shown in Fig. 15. When $L/D=0.5$, the aerodynamic loss is always found on the windward side (Fig. 15(*a*)). In the case of $L/D=2.0$, however, it is usually found near the wall, but C_{Pt} still shows a considerable circumferential variation. In particular, C_{Pt} near the wall has a minimum at $\theta=75$ deg. This position coincides with the location with a maximum discharge velocity as shown in Fig. 13(*c*).

The mass-averaged total pressure loss coefficient is defined as follows:

$$\overline{C}_{Pt}=\frac{\int_0^{D/2}\int_0^{2\pi}C_{Pt}\rho Vr\,d\theta dr}{\int_0^{D/2}\int_0^{2\pi}\rho Vr\,d\theta dr} \tag{2}$$

In Fig. 16, the mass-averaged total pressure loss coefficient, $\overline{C}_{Pt}$, at the exit is provided as a function of M for three L/D's. In general, $\overline{C}_{Pt}$'s have their values in between about 0.2 and 0.4, and

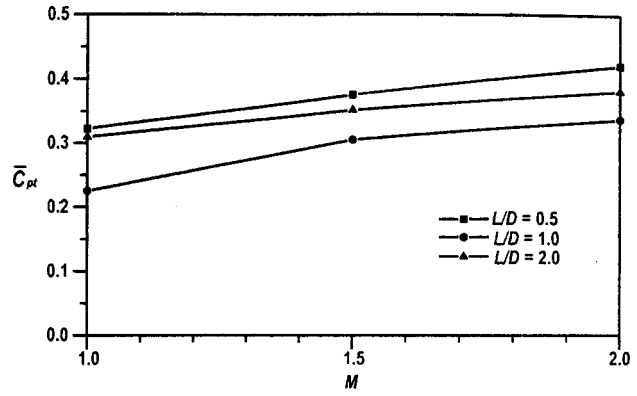

Fig. 16 Mass-averaged total pressure loss coefficient, $\overline{C}_{Pt}$, in the exit plane for a normal hole in crossflow

the $\overline{C}_{Pt}$ value increases with increasing M. The $\overline{C}_{Pt}$ values at $L/D=0.5$ and 2.0 are larger than that at $L/D=1.0$. This is because for short L/D there is a strong interaction between the diverging flow in the hole and the crossflow, especially on the windward side, and long L/D provides a larger frictional loss. As M increases, the inlet separation bubble may play a more important role than other sources of the aerodynamic loss. Thus, with increasing M, the $\overline{C}_{Pt}$ value at $L/D=2.0$ approaches that at $L/D=1.0$.

Summary and Conclusions

Three-dimensional mean flow measurements have been conducted inside normal injection holes with a sharp square-edged inlet. The blowing ratios considered are $M=0.5$, 1.0, and 2.0, and the hole length-to-diameter ratios are $L/D=0.5$, 1.0, and 2.0.

The flow is characterized by an inlet flow separation in the entrance region, and by a strong interaction with the crossflow near the exit of the injection hole. The relative importance of these depends on M and L/D. The uniform oncoming flow at the inlet undergoes a strong acceleration and a subsequent gradual deceleration along a converging–diverging flow passage formed by the inlet separation bubble. After passing the throat of the converging–diverging passage, the nearly axisymmetric potential-core flow turns to a fully three-dimensional one. In the near-exit region, flow decelerates on the windward side, while it accelerates on the leeward side. Therefore, the presence of the crossflow reduces the discharge of the injectant the windward side, but augments its efflux on the leeward side. These qualitative flow characteristics are observed regardless of M and L/D.

For the tested blowing ratios, there are strong secondary flows in the inlet and exit planes of the injection hole; meanwhile, the secondary flow within the injection hole is found to be relatively weak. The inlet secondary flow shows a strong inward motion to the injection-hole center. The magnitude of the inward flow velocity decreases rapidly as it approaches the hole center. However, it is not a complete inward flow since the crossflow effect is superimposed on it. This effect is most noticeable in the case of $L/D=0.5$. Past the throat, the flow near the separation bubble is liable to diverge, showing an irregular flow pattern, while in the central potential-core region, the flow is still converging. In the far-downstream region, the secondary flow develops in such a way that the leeward velocity component induced by the crossflow is superimposed on the diverging flow. This flow pattern is qualitatively sustained to the exit plane.

As the blowing ratio increases, the crossflow effect, in general, is reduced, but the inlet converging–diverging flow is intensified. At $M=0.5$, the variation of the discharge velocity across the exit plane is observed to be largest, and at this low blowing ratio the inside flow shows a full three-dimensional nature. The secondary flow in the exit plane seems to be independent of the blowing ratio in its magnitude as well as in the overall flow direction. On the contrary, the exit discharge velocity is dependent strongly on the blowing ratio.

In the cases of $L/D=1.0$ and 2.0, the crossflow effect on the inlet flow is relatively small. When $L/D=0.5$, however, the inlet secondary flow is greatly altered from the axisymmetric inward flow because of the crossflow effect. For a short hole such as $L/D=0.5$, both a steep velocity gradient and a strong deceleration of the exit discharging flow are usually observed on the windward side, as in the case of low M. On the other hand, the exit secondary flow seems to depend weakly on L/D, in contrast to the large variation of the exit discharging velocity with L/D.

The aerodynamic loss inside the injection hole is originated from the inlet separation bubble, wall friction, and interaction with the crossflow. The relative contribution of these sources depends on M and L/D. In general, the first one is considered as the most dominant source, even in the case of $L/D=2.0$. When $L/D=0.5$, the aerodynamic loss results mainly from a strong interaction between the diverging flow and the crossflow on the

windward side. Therefore, the mass-averaged aerodynamic loss is larger than that at $L/D=1.0$, although the short hole length reduces the frictional loss. In the case of $L/D=0.5$, the first and third sources are coupled strongly with each other. Independent of L/D, the mass-averaged aerodynamic loss coefficient shows an increasing tendency with increasing M, since the higher M enhances the inlet flow separation.

Acknowledgment

The research herein was supported by the Korea Science and Engineering Foundation (KOSEF Grant No. 95-0200-12-01-3) and was also supported, in part, by the Turbo and Power Machinery Research Center.

Nomenclature

$\underline{C}_{pt}$ = total pressure loss coefficient with injection, Eq. (1)
C_{pt} = mass-averaged total pressure loss coefficient, Eq. (2)
D = injection hole diameter
L = injection hole length
$\dot{m}$ = mass flow rate evaluated with y-directional velocity component data
$\dot{m}_{\text{orif}}$ = mass flow rate measured by orifice
M = blowing ratio $=\rho_j V_j/\rho_\infty U_\infty$
P_t = local total pressure
$P_{t,0}$ = plenum total pressure measured at $1.0D$ upstream of hole inlet
r = radial coordinate, Fig. 1
Re_D = injectant Reynolds number $=V_j D/\nu_j$
$\text{Re}_{\delta 2}$ = crossflow Reynolds number $=U_\infty \delta_2/\nu_\infty$
U = x-directional velocity component
U_∞ = free-stream velocity in crossflow
V = y-directional velocity component
V_{no} = y-directional velocity in absence of crossflow
V_j = spatially averaged injection velocity across cross section of hole
W = z-directional velocity component
x = coordinate in streamwise (leeward) direction, Fig. 1
y = coordinate in normal direction, Fig. 1
z = coordinate in spanwise direction, Fig. 1
δ_2 = momentum boundry-layer thickness of crossflow
ν_j = kinematic viscosity of injectant
ν_∞ = kinematic viscosity of crossflow fluid
ρ_j = density of injectant
ρ_∞ = density of crossflow fluid
θ = azimuthal coordinate, Fig. 1

References

[1] Lee, S. W., Park, S. W., and Lee, J. S., 2001, ''Flow Characteristics Inside Circular Injection Holes Normally Oriented to the Crossflow: Part I—Flow Visualizations and Flow Data in the Symmetry plane,'' ASME J. Turbomach., **123**, pp. 266–273.
[2] Leylek, J. H., and Zerkle, R. D., 1994, ''Discrete-Jet Film Cooling: A Comparison of Computational Results With Experiments,'' ASME J. Turbomach., **116**, pp. 358–368.
[3] Lee, S. W., and Yoon, T. J., 1999, ''An Investigation of Wall-Proximity Effect Using a Typical Large-Scale Five-Hole Probe,'' KSME Int. J., **13**, pp. 273–285.
[4] Cho, H. H., and Goldstein, R. J., 1995, ''Heat (Mass) Transfer and Film Cooling Effectiveness With Injection Through Discrete Holes: Part II—On the Exposed Surface,'' ASME J. Turbomach., **117**, pp. 451–460.
[5] Andreopoulos, J., 1982, ''Measurements in a Jet-Pipe Flow Issuing Perpendicularly Into a Cross Stream,'' ASME J. Fluids Eng., **104**, pp. 493–499.

Influence of Crossflow-Induced Swirl and Impingement on Heat Transfer in a Two-Pass Channel Connected by Two Rows of Holes

Gautam Pamula

Srinath V. Ekkad
e-mail: ekkad@me.lsu.edu

Sumanta Acharya

Mechanical Engineering Department,
Louisiana State University,
Baton Rouge, LA 70803

Detailed heat transfer distributions are presented inside a two-pass coolant square channel connected by two rows of holes on the divider walls. The enhanced cooling is achieved by a combination of impingement and crossflow-induced swirl. Three configurations are examined where the crossflow is generated from one coolant passage to the adjoining coolant passage through a series of straight and angled holes and a two-dimensional slot placed along the dividing wall. The holes/slots deliver the flow from one passage to another. This is typically achieved in a conventional design by a 180 deg U-bend. Heat transfer distributions will be presented on the sidewalls of the passages. A transient liquid crystal technique is applied to measure the detailed heat transfer coefficient distributions inside the passages. Results for the three-hole supply cases are compared with the results from the traditional 180 deg turn passage for three channel flow Reynolds numbers ranging between 10,000 and 50,000. Results show that the new feed system, from first pass to second pass using crossflow injection holes, produces significantly higher Nusselt numbers on the second pass walls. The heat transfer enhancements in the second pass of these channels are as much as two to three times greater than that obtained in the second pass for a channel with a 180 deg turn. Results are also compared with channels that have only one row of discharge holes. [DOI: 10.1115/1.1343467]

Introduction

Improvement in heat transfer augmentation technology inside airfoil internal channels has significant impact on overall gas turbine engine performance. Several strategies, including combinations of turbulated serpentine passage cooling, impingement cooling, double wall cooling, and film cooling, are utilized in modern airfoil designs. The present study focuses on new improved internal channel designs to provide higher heat transfer enhancement with relatively small changes to the airfoil internal cooling channel geometry. This strategy consists of replacing the conventional 180 deg **U**-bend connecting the two passages with a pattern that includes rows of cylindrical holes or slots along the dividing wall. The cylindrical holes permit lateral injection from the first passage to the second passage; this leads to a combination of impingement and crossflow-induced swirl in the second passage. This combination of impingement and swirl provides a higher and more uniform heat transfer in the second passage. A two-dimensional slot is also investigated to reduce the nonuniform heat transfer distributions generated by impingement.

There have been several studies on two-pass channels reported in the literature. Boyle [1], Metzger and Sahm [2], Abuaf et al. [3], Fan and Metzger [4], Chyu [5], and Ekkad and Han [6] provided heat transfer information in two-pass channels connected by a 180 deg bend. They all indicated that bend-induced secondary flows produce heat-transfer nonuniformities in the second-pass immediately after the turn. Several other researchers [7–10] presented enhanced heat transfer measurements in both the first and second passes using rib turbulators. Additional use of rib turbulators in the two-pass channel design increased both heat transfer enhancement and pressure drop. An optimal design of rib turbulator produces the highest heat transfer enhancement with minimal increases in pressure drop.

Contributed by the International Gas Turbine Institute and presented at the 45th International Gas Turbine and Aeroengine Congress and Exhibition, Munich, Germany, May 8–11, 2000. Manuscript received by the International Gas Turbine Institute February 2000. Paper No. 2000-GT-235. Review Chair: D. Ballal.

Recent studies by Glezer et al. [11], Ligrani et al. [12], and Moon et al. [13] investigated the advantages of induced swirl in tubular channels for heat transfer enhancement. They create swirl by injecting air into the tube through tangential jets along the wall. Hedlund et al. [14] presented heat transfer measurements inside a tubular swirl chamber for simulating turbine blade internal cooling. All the above-mentioned studies used tubular channels. The importance of these studies is in the indication that inducing swirl contributes to significantly higher heat transfer.

The present study generates swirl inside airfoil internal channels by eliminating the 180 deg turn and passing the coolant from one pass to the second pass through discrete rows of holes. The jets ricochet off the surfaces of the second pass channel and produce a swirling flow that is carried downstream by the crossflow generated by the spent air. The complex interactions of the jets and the crossflow produces significantly high heat transfer coefficients on the sidewalls. These sidewalls represent the insides of the pressure and suction surface walls of the channel. Typically, these walls are ribbed with different turbulator geometries for heat transfer enhancement. Ekkad et al. [15] presented detailed heat transfer distributions in channels connected by one row of holes. They varied the angle of the hole and also the location of the hole to determine the most effective geometry. They determined that the single hole row design provides significantly (up to eight to ten times) higher heat transfer coefficients than the 180 deg turn geometry. However, the pressure drop across the holes is also significant resulting in slightly higher thermal performance $(\mathrm{TPP}=\overline{\overline{\mathrm{Nu}}}/\mathrm{Nu}_0)/(\bar{f}/f_0)^{1/3}$. They compared straight injection with inclined injection holes. Although the inclined injection provided much higher heat transfer coefficients, the pressure drop was also significant, resulting in almost similar thermal performance numbers. Another important facet in the results presented by Ekkad et al. [15] was the significantly different heat transfer distributions on the two sidewalls. The effect of impingement on one sidewall caused much higher heat transfer coefficients on that wall. The ricocheted flow produced relatively lower heat transfer coefficients on the other sidewall. The cases present in this study are an

extension of the study by Ekkad et al. [15]. The hole geometry and location of holes on the divider wall are similar in both studies.

In the present study, three different configurations are studied. The first two configurations use two rows of discrete holes evenly spaced all along the divider wall. It is expected that the two rows of holes will produce uniform heat transfer distributions on both sidewalls and also produce lower pressure drop due to increased flow area. The discrete holes produce three-dimensional effects in flow and heat transfer distributions. The third case uses a varying two-dimensional slot geometry to channel the flow from first pass to the second pass. For each case, three channel flow Reynolds numbers of 10,000, 25,000, and 50,000 are tested. There are 24 holes in this study, compared to 12 holes of same diameter used by Ekkad et al. [15]. This provides less resistance to flow resulting in lower jet velocities and reduced overall pressure drop. The present results for two rows of holes are compared to the single row data from Ekkad et al. [15]. A transient liquid crystal technique was used to measure the detailed heat transfer coefficients [6,9,15].

Experimental Setup

Figure 1 presents a schematic of the experimental setup. The experimental setup consists of an image processing system (RGB Color CCD Camera, 24-bit Color Frame Grabber Card, PC and Imaging Software), temperature measurement system, flow loop, and the test section. The RGB camera is focused on the test section and the color FG card is programmed through the software to analyze real-time images for color signals during a transient heat transfer test.

The flow circuit consists of an air supply from a 300-psi compressor. The air is regulated and metered through a standard orifice meter to measure the flow rate through the test section. The air is then routed through an in-line 3 kW air heater controlled by a temperature controller system. The air from the heater is then diverted away from the test section with a three-way ball diverter valve. The heated air temperature is monitored by the temperature control unit by measuring the heated air temperature immediately downstream of the heater. When the valve is flipped, the air is routed through the test section. A series of honeycomb strips and a mesh help produce a uniform flow at the entrance into the test section.

Figure 2 shows the schematic of the test channels. Case 1 shows the schematic of the two-pass channel with 180 deg turn. Cases 2 and 3 are channels with single row of holes on the divider

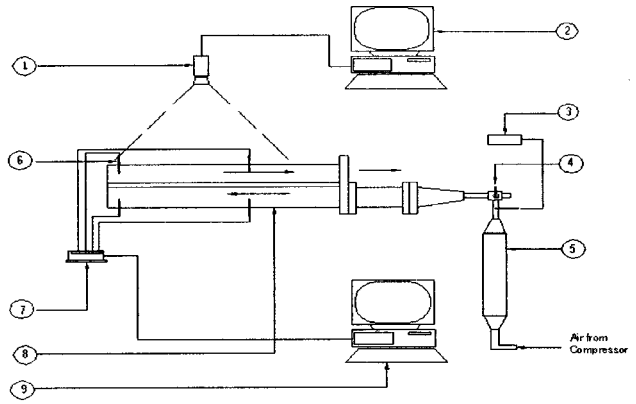

Fig. 1 Experimental setup

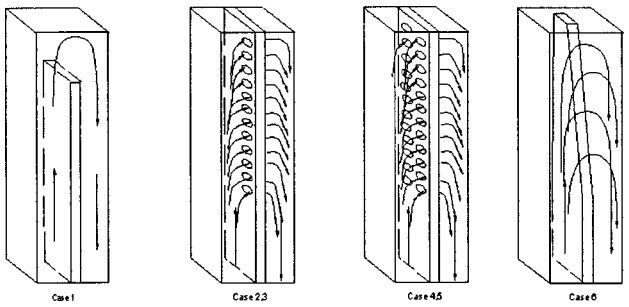

Fig. 2 Schematic of the test sections with proposed divider wall geometries

wall along one sidewall from Ekkad et al. [15]. Cases 4 and 5 represent the channels with two rows of holes along sidewall. Case 6 is the channel with two-dimensional slots that vary in width from middle of the channel to the endwall along the sidewalls. The plate separating the two passages is called the divider wall. The sidewalls are the outer surfaces on the both passages orthogonal to the divider wall. The sidewalls are the primary heat transfer surfaces for which the results are presented. The outer walls of the test section are parallel to the divider wall. The wall of the test section that bounds the flow inside the passage where the flow is forced to enter the second passage is called the endwall.

The test channel is a 5.08 cm square cross section through the 60.96 cm length. The channel length to hydraulic diameter ratio (L/D) is 12. There is no 180 deg turn for the channels connected by the holes or slots. All of the flow goes through the holes or slots. The ratio of holes to 180 deg turn for Cases 2 and 3 was 0.6. For the present study, the ratio of the total area of all the holes/slots (Cases 4–6) to the turn region area in the 180 deg turn case was 1.2. For the channels with holes, there are 24 holes of 1.27 cm diameter each, with 12 holes in each row. Each hole row centerline is 1.27 cm from the sidewall. There are no holes along the divider wall for the first 30.48 cm of the channel length from entrance. The 12 holes in each row are then evenly distributed over the next 30.48 cm of the channel length. The holes are spaced two hole diameters (centerline to centerline) apart from each other. The hole locations on the divider wall were also designed to produced a swirling flow. For the slotted divider wall, there are no slots for the first half of the channel length. The slots along the sidewalls increase in width from half the channel length to about 0.96 cm width at the endwall. The slots are identical along both sidewalls, resulting in similar flow distributions along both sidewalls (1.27 cm thick).

Figure 3 shows the channel geometries studied. Cases 2 and 3 are the geometries presented by Ekkad et al. [15]. Case 4 shows the straight injection configuration. The holes are 1.27 cm in diameter and the hole centerlines are 1.27 cm from the sidewalls. Case 5 shows the inclined hole geometry. The holes are inclined at 45 deg to the vertical direction and the hole exit centerlines on the divider wall are 1.27 cm from the sidewalls. Case 6 shows the slot geometry. The slots along both the sidewalls begin from the middle of the channel and increases in width to about 0.96 cm at the endwall location. The two-dimensional slots were chosen instead of a uniform slot width to create more uniform flow through the slot from inlet to the endwall.

The heat transfer measurements are made only on one of the sidewalls of the plexiglass test section. For Cases 2 and 3, the heat transfer measurements were made on both sidewalls as the holes are along only one sidewall [15]. The surface is coated on the inside with a thin layer of thermochromic liquid crystals. A black paint coating is sprayed over the liquid crystal coating to ensure visibility of the liquid crystal color changes when viewed from the outside. Once the test section is coated with both the liquid crystal

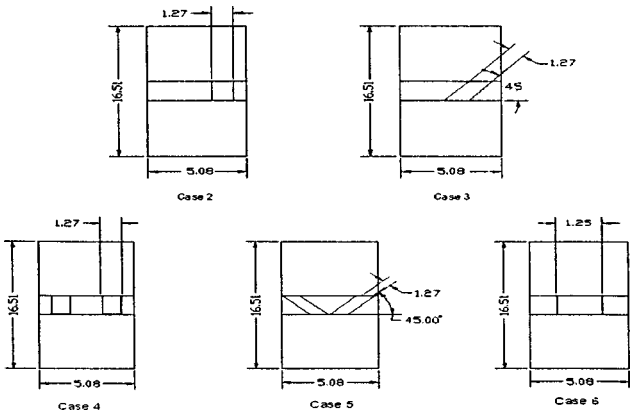

Fig. 3 Schematic of the test section cross section

and black paint layers, the insides of the channel are opaque. Thermocouples are placed at inlet and outlet of each passage (a total of four) to measure the local temperatures of the heated air. The transient thermocouple outputs are digitized during the test using an eight-channel A/D system.

The air mass flow rate is set for the required inlet channel Reynolds number condition, and then heated through the in-line air heater. The temperature at the exit of the heater is set based on some qualification tests to produce acceptable liquid crystal color change times during the transient test. The heated air is routed away from the test section. The temperature measurement system and the image processing system are set to initiate data measurement at the same instant as the diverter valve is flipped. The test section is ready for running when the air is heated to the steady required temperature. The diverter valve is flipped to let the hot air into the test section. The thermochromic liquid crystal coating is heated by the hot air and changes color when it reaches its display color range. Liquid crystal color temperatures are preset and are calibrated under lab lighting conditions. The liquid crystal used in this study has a narrow band with the initial red color appearing at 35.1°C, then green color appearance at 35.4°C, and finally blue color at 35.9°C. The total band is 1°C. The image processing system divides the test section into tiny pixel locations and monitors each location individually for color changes. The test section in this study was divided into 500×200 pixels. The reference point in this study is set as the appearance of green color during the transient. This indicates that the image processing system will provide time of color changes at every pixel when it reaches 35.4°C. The test duration is typically a maximum of 150 seconds. The air temperature is set such that the times of color changes at all pixels are between 10 and 150 seconds. The reason for this is that the test section wall should not violate the semi-infinite solid assumption. The test section is made of plexiglass so that a one-dimensional semi-infinite solid assumption can be applied on the test section wall [6,9]. The local air bulk temperature for each axial pixel location is interpolated from the measured thermocouple locations. The time-step changes are then included in the equation to obtain a function of the form

$$T_w - T_i = \sum_{j=1}^{N} \left\{ 1 - \exp\left[\frac{h^2\alpha(t-\tau_j)}{k^2}\right] \mathrm{erfc}\left[\frac{h\sqrt{\alpha(t-\tau_j)}}{k}\right] \right\} \times [\Delta T_{m,(j,j-1)}]$$

where $T_m,(j,j-1)$ and τ_j are the mainstream temperature and time step changes interpolated from the digitized temperature outputs. The equation is solved at every pixel location to obtain the local heat transfer coefficient, h. Ekkad and Han [6,9] and Ekkad et al. [15] used a similar approach. The average experimental uncertainty based on the methodology of Kline and McClintock [16] is on the order of ±7.4 percent. The individual uncertainties in the measurement are listed as: time of color change, t, ±3 percent; thermal properties of wall, (α,k), ±5 percent; mainstream temperature, T_m, ±3 percent; color change temperature, T_w, ±2 percent; initial temperature, T_i, ±3 percent. The shortest color changes (if time of color change is lower than 5 seconds) produce uncertainty levels as high as ±14.5 percent. The uncertainty in friction factor measurement is on the order of ±8.0 percent.

Results and Discussion

Flow Visualization. A series of smoke flow visualization experiments was performed to determine the jet-crossflow structures. The test section was injected with smoke instead of compressed air. The smoke flow rate is much smaller than the actual air flow rate into the test section. The image processing system was triggered to grab a set of sequential frames during the smoke injection. The frames were then analyzed to determine the frames that provide the most details on the flow patterns inside the channels. The test sections were viewed from the endwall. Figure 4 shows the smoke flow patterns for each of Cases 4–6. The flow patterns clearly show the swirling flow and the vortices generated by the new geometry. The straight hole injection in Case 4 indicates that the flow impinges against the top wall and breaks up into two structures, one along the sidewall and the other into the core of the channel. The angled injection generates primary impingement on the sidewalls and the flow ricochets back into the core and is pushed toward exit by the crossflow. For the slot case, the flow pattern indicates four vortices: two smaller ones near the divider wall in the second pass, and two in the upper corners near the top wall. The heat transfer distributions are significantly affected by the flow patterns in these channels. The flow visualizations are qualitative in nature and are presented at very low Reynolds numbers. The flow behavior may be different at higher Reynolds number conditions.

Heat Transfer Measurements. Detailed Nusselt number (Nu) distributions were measured on the sidewalls of both passes of the test channel. Results are presented on only one sidewall. It is assumed, due to impingement, that the results on both sidewalls will be similar. Results are presented for the 180 deg turn channel and the channels with hole/slot geometries at Reynolds numbers of 10,000, 25,000, and 50,000. All local Nusselt numbers on the wall are normalized using the turbulent Nusselt number correlation for flow inside a pipe. All results are presented in the form of Nusselt number ratio ($\mathrm{Nu/Nu_0}$).

Figure 5 presents the detailed Nusselt number ratio ($\mathrm{Nu/Nu_0}$) distributions on the sidewall of each channel (Case 1, Cases 4–6) for $\mathrm{Re}=25{,}000$. The first pass distributions show little differences for all four cases shown in the figure, except in the case of the slotted divider plate. This result is encouraging, indicating that heat transfer enhancement in the second pass is not affecting the first pass heat transfer distributions. The results and discussion

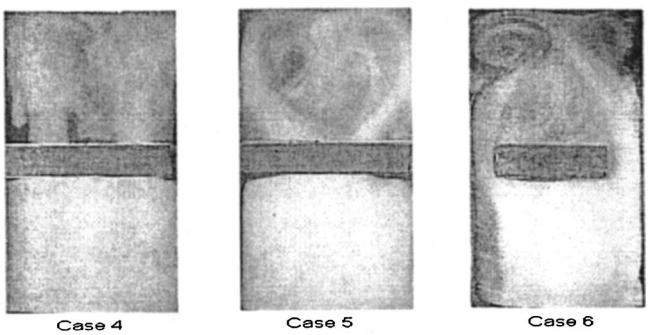

Fig. 4 Smoke flow visualization of the flow inside the channels

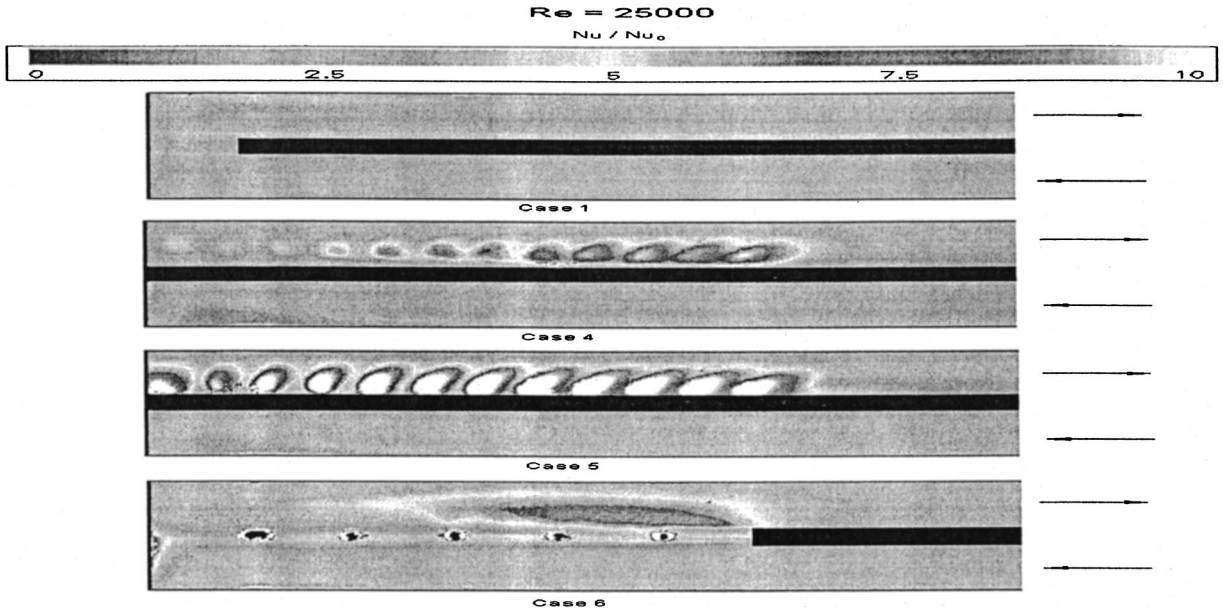

Fig. 5 Detailed Nu/Nu$_0$ distributions for the tested geometry

presented are therefore concentrated on the second pass heat transfer distributions. For Case 1, there is strong nonuniformity in Nusselt number ratio distributions in the second pass immediately after the 180 deg turn. This is because the flow is affected by flow separation, reattachment, and bend effects. Ekkad and Han [15] present a detailed description of the turn region heat transfer.

Figure 5(*b*) shows the case where the flow is through straight holes (Case 4). Heat transfer distributions show significant jet impingement effects from the first few holes in the row. One set of roll-cells impinges on the sidewall and the other roll-cell is pushed into the core of the channel and becomes part of the crossflow. The jets are stronger for flow through the first few holes in each row due to larger pressure differential. The jets become progressively weaker toward the endwall. In the second pass, the crossflow becomes stronger toward the exit of the channel. This strong crossflow rides the jets and pushes the impingement location downward for the jets closer to the channel exit. Thus, the roll-cells are displaced by the strong crossflow generated by the upstream jet injection. Nusselt number ratios are as high as 7–10 inside the impingement core.

Figure 5(*c*) shows the case where injection is through inclined holes (Case 5). In this case, the flow from the first pass is directed and angled toward the sidewalls. The jet impingement is strongly evident with extremely high Nusselt numbers at impingement locations. The jets are weaker as the flow moves closer to the endwall. The enhancement produced by the jet impingement produces Nusselt number ratio values greater than 10 inside the impingement core. Unlike Case 4, the high heat transfer on the sidewall is caused by primary impingement. The spent air after impingement rolls up and swirls into the core of the channel and becomes the crossflow. The crossflow gains strength from the endwall to the channel exit. The stronger crossflow then pushes the impingement location of the jets downward and toward the exit.

Figure 5(*d*) shows the case where the flow enters the second channel through two-dimensional slots. The highest Nusselt numbers are obtained where the slot is narrow. The higher velocity of the flow across the slot produces significantly high Nusselt numbers in this region. As the slot widens, the local velocity of the flow is reduced and the resultant Nusselt numbers are lower. It appears that the endwall region in the first pass has some enhancement due to main flow impingement on the endwall. The circular regions along the divider wall represented screw holes on the sidewalls used for fixing the divider plate. They do not represent heat transfer data.

Figure 6 presents the effect of channel Reynolds number on spanwise-averaged Nusselt number ratios. The middle of the turn is marked as $X/D=0$, with the first pass as negative X/D and second pass as positive X/D. For all the cases, the effect of Reynolds number is significant in the second pass. For Case 1, Nusselt number ratios decrease as the flow moves downstream in the first pass toward the 180 degturn region. The Nusselt numbers immediately downstream are enhanced due to the turn effects. Farther downstream, due to cross-stream mixing, the Nusselt numbers decrease and the turn effects are mitigated. For Case 4, the first pass results look similar to that for Case 1. In the second pass, the Nusselt number ratio increases from the endwall toward the exit until the last ejection hole at $X/D=6$ and then begins to decrease again. The local wiggles indicate the highs and lows between the impinging jets. For Case 5, the first pass Nusselt numbers are unaffected by the holes on the divider wall. The impingement heat transfer enhancement in the second pass is significant. The highs and lows under and between the jets are stronger than for Case 4. The effect of Reynolds number is also significant with the enhancement ratio as high as 6–8 for Re=10,000 and drops to 3–4 for Re=50,000. The Nusselt number ratios are uniform underneath all the jets. For Case 6, the Nusselt number ratios in the first pass appear to increase from entrance to endwall unlike Cases 1, 4, and 5. The local peak at $X/D=0$ is due to the first pass flow impingement on the endwall causing a local high heat transfer region along the endwall. In the second pass, the Nusselt number ratios increase from the endwall toward the exit until about $X/d=6$ where the slot ends and then reduces rapidly toward the channel exit. It appears that the heat transfer enhancement for Case 6 may be caused purely by the production of swirl-induced vortices, unlike Cases 2–5, where the effect is a combination of impingement and crossflow induced swirl.

Figure 7 presents the effect of channel geometry on spanwise-averaged Nusselt number ratio distributions at each Reynolds number. At Re=10,000, there is significant variation in the levels of enhancement between all the geometries. Nusselt number ratios decrease gradually from inlet to $X/D=0$ (turn or endwall) for Cases 1, 4, and 5. For Case 6, there is some enhancement from

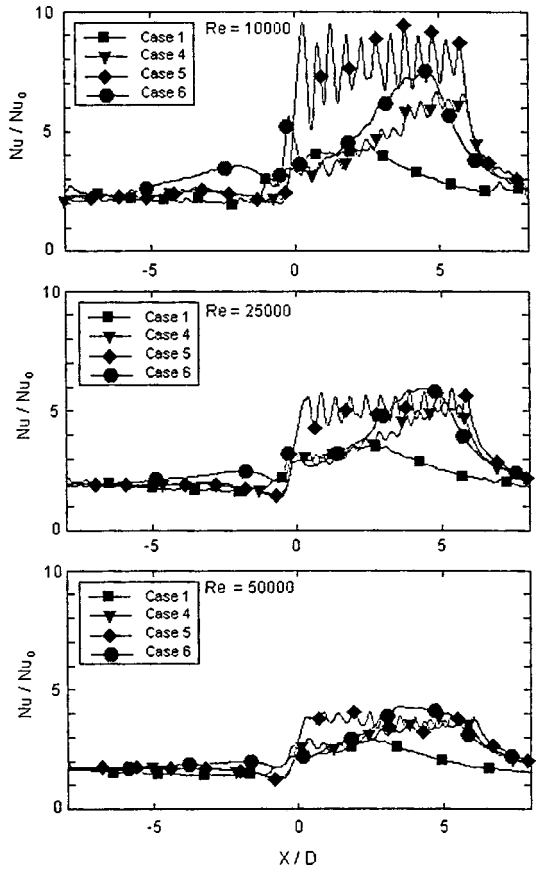

Fig. 6 Effect of channel Reynolds number on spanwise averaged Nusselt number ratio distributions

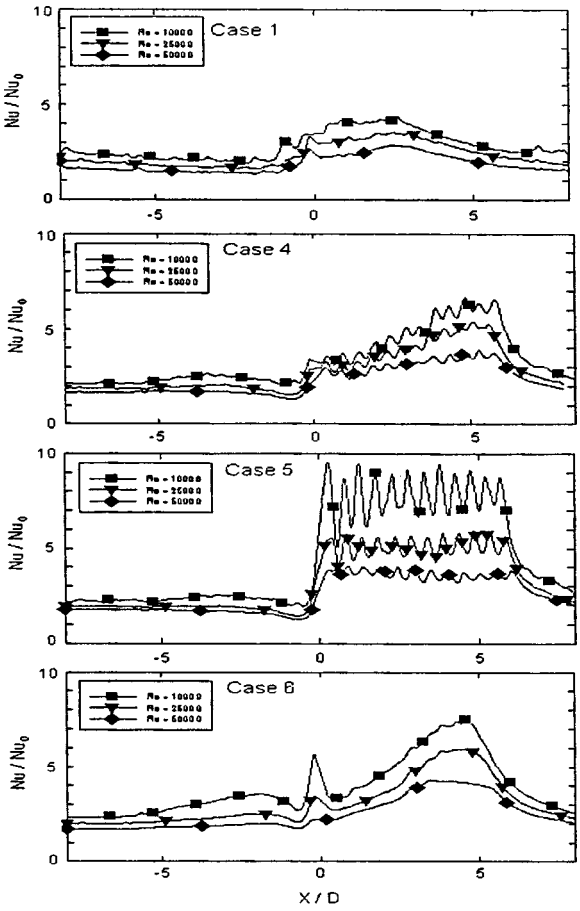

Fig. 7 Effect of divider wall geometry on spanwise averaged Nusselt number distributions

inlet to endwall in the first pass. In the second pass, Case 5 with inclined injection produces the highest enhancement in the injection region. Cases 4 and 6 show similar distributions with Case 6 being higher than Case 4. The 180 deg turn channel shows enhancements up to 2.5 immediately after the turn and then decreases toward the exit. The variations in the Nusselt number ratios between the channels decreases with increasing Reynolds number.

Figure 8 compares the effect of single row of holes data from Ekkad et al. [15] and the present data for two rows of holes at Re=25,000. Single row of holes along the divider walls provide stronger jet velocities as the area ratio for the same flow rate is half that for two hole rows. The increased jet impingement produces significant high heat transfer enhancement values in the impingement regions. Enhancement values are between 8 and 10 for Cases 2 and 3 compared to between 3 and 4 for Cases 4–6. However, it is important to note that it requires greater pressure differential to push the same flow through a smaller area than a larger area. This makes it important to determine the thermal performance parameter $(\mathrm{TPP}=\overline{\overline{\mathrm{Nu}}}/\mathrm{Nu}_0)/(\bar{f}/f_0)^{1/3}$ for each case. Ekkad et al. [15] clearly show that the enhancement levels alone are not sufficient to determine the cooling effectiveness for a particular enhancement geometry. Highest enhancement at reduced pressure losses contributes the most effective cooling scheme [17].

Figure 9 compares the overall averaged Nusselt number ratios $(\overline{\overline{\mathrm{Nu}}}/\mathrm{Nu}_0)$ on the second pass of the channels in this study and compares with results for rib-turbulated second pass of a two-pass channel with 180 deg turn. The present results are compared with results from Chandra et al. [8] and Ekkad and Han [9]. Both Chandra et al. [8] and Ekkad and Han [9] did not provide any results for pressure drop to compare overall performance results. The results for 90 deg rib turbulated channel from Chandra et al. [8] are higher than Ekkad and Han [9] but lower than Cases 4–6. Ekkad and Han [9] have only one sidewall ribbed whereas Chandra et al. [8] have both sidewalls ribbed in their study. It is clear that all the three geometries introduced in this present study outperform the 90 deg rib effect in the second pass. The 60 deg case presented from Ekkad and Han [9] is slightly higher than Case 4 at higher Reynolds numbers. But Cases 5 and 6 are significantly higher than the 60 deg rib results. A 20 percent higher Nusselt number ratio is expected for the two-wall ribbed case that may still be lower than Cases 5 and 6. These comparisons clearly show the effectiveness of these new cooling geometry channels compared to conventional designs.

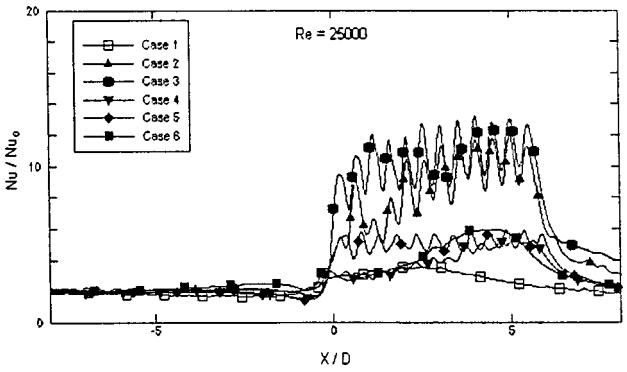

Fig. 8 Comparison of different cases from present study with cases studied by Ekkad et al. [15]

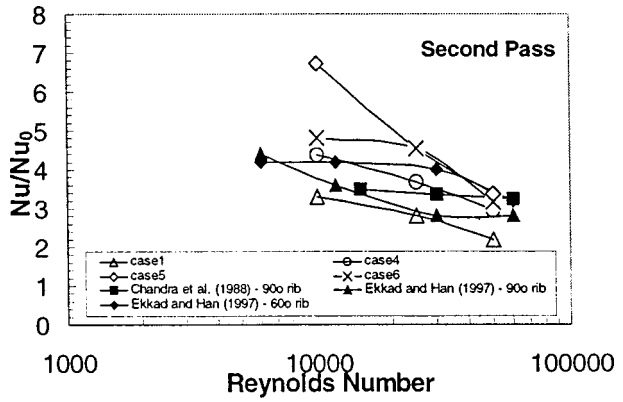

Fig. 9 Comparison of second pass overall averaged Nusselt number ratios to published rib turbulator studies

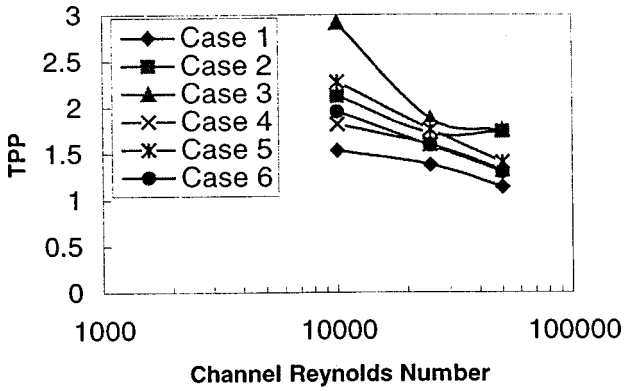

Fig. 11 Thermal Performance Parameter (TPP) versus channel Reynolds number for all six channels

Overall pressure drops through each of the channels were measured using static pressure taps. The pressure differential from inlet to exit for the channels was measured in inches of water using a precision manometer. The Darcy friction factor (f) is computed using the known pressure drop (ΔP) across the entire two-pass channel and the mass flux ($\rho \bar{v}$) through the channel. The Darcy friction factor is normalized by the Darcy friction factor correlation in an all-wall smooth channel given as $f_0 = 0.046\,\mathrm{Re}^{-0.2}$. The friction factor ratio (f/f_0) is computed for each channel at a particular Reynolds number. The overall averaged Nusselt number ratio ($\overline{\overline{\mathrm{Nu}}}/\mathrm{Nu}_0$) is obtained by averaging the detailed Nusselt number distributions for both passes so as to obtain a single Nusselt number enhancement value for the entire channel irrespective of the channel configuration. The $\overline{\overline{\mathrm{Nu}}}/\mathrm{Nu}_0$ value is plotted against the corresponding f/f0 for the channel in Fig. 10. The single row hole cases (Cases 2 and 3) from Ekkad et al. [15] provide significantly higher Nusselt number ratios than the other four cases. However, the increase in friction factor is also significant due to the low area ratio of 0.6 compared to the 180 deg turn channel for Cases 2 and 3. Cases 4–6 show friction factor ratios ranging between 5 and 10 and Nusselt number ratios between 2 and 3. Case 1 for the 180 deg turn channel produces the lowest pressure drop and the lowest overall heat transfer enhancement.

The thermal performance parameter (TPP) is calculated for each channel and plotted against the Reynolds number in Fig. 11. At low Reynolds numbers, Case 3 outperforms the other cases due to the extremely high Nusselt number ratios. However, at Re $=25{,}000$, the thermal performance parameter values are similar for all five channels connected by holes. The 180 deg turn channel has the lowest thermal performance values. At Re$=50{,}000$, Cases 2 and 3 show higher TPP values. It is evident that a huge penalty in terms of pressure drop is paid for high heat transfer enhancement as in the cases of the single row geometry. However, the two-hole cases may be considered a better alternative due to the reduced friction losses and lower pressure differential required to push the flow through the channel and still produce relatively higher heat transfer enhancement values of around 3. Also, these new designs produce higher heat transfer enhancement over most of the channel length where the holes are present, and could possibly help in eliminating the need for complex geometry modifications such as rib turbulators in the second pass. Typically, rib-turbulated channels provide thermal performance parameter values around 1.5 due to the higher pressure-drop associated with ribs [7,8]. However, there are fewer data available for TPP values inside two-pass channels with 180 deg turns and rib turbulators. The first pass heat transfer can be enhanced using rib turbulators as in conventional designs to avoid overcooling in the second pass compared to the first pass.

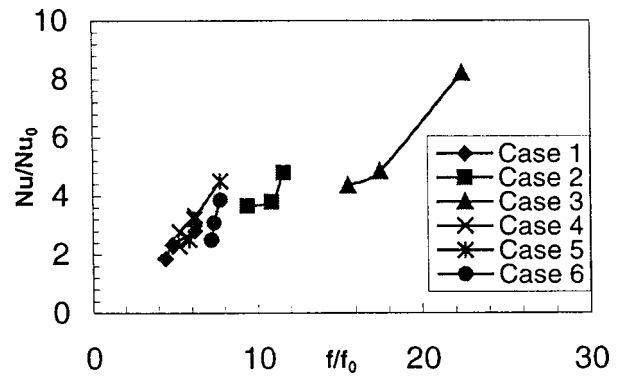

Fig. 10 Overall averaged Nusselt number ratio versus friction factor ratio for all six channels

Conclusions

Results are presented for a two-pass channel geometry where flow is transported from one pass to the next through discrete hole rows. This geometry appears promising due to the high heat transfer enhancement obtained in the second pass compared to the 180 deg turn channel. Typically, the 180 deg turn channels are ribbed with strip turbulators to further enhance heat transfer. However, the second pass heat transfer is enhanced two to three times over the 180 deg turn channel for the new geometry without using rib turbulators. This geometry may help designers eliminate the need for ribs in the second pass without compromising on heat transfer enhancement. The present data produce higher heat transfer enhancement than with turbulated 180 deg turn channel data. Also, the associated pressure drop may be lower than in ribbed channels, resulting in higher thermal performance of the coolant channel. This type of channel may reduce complications in blade fabrication processes where the ribs are typically 0.04 cm in height and width. Holes on the divider channels can be easily fabricated compared to rib turbulators on all heat transfer walls. Overall, in conclusion, the new design for the internal cooling channel inside a turbine airfoil appears promising. However, more data at a variety of stationary and rotating conditions are required before the geometry can be utilized in real engine design.

Acknowledgments

The authors wish to acknowledge the support for the project funded by Louisiana Board of Regents through the NASA-LaSPACE REA under contract No. NASA/LEQSF (1996–2001). The program manager is Dr. John Wefel.

Nomenclature

b = divider wall thickness
d = hole diameter
D = square channel width or height
D_h = channel hydraulic diameter
f = Darcy friction factor
$= 2\Delta P(D_h/L)/(\rho \overline{V}^2)$
f_0 = Darcy friction factor in all-smooth wall channel $= 0.046\,\mathrm{Re}^{-0.2}$
h = convective heat transfer coefficient
k = thermal conductivity of test surface material
k_a = thermal conductivity of air
L = length of each pass
$\dot{m}$ = mass flow rate
Nu = Nusselt number $= hD/k_a$
Nu_0 = fully developed flow Nusselt number $= 0.023\,\mathrm{Re}^{0.8}\,\mathrm{Pr}^{0.4}$
p = hole spacing
P = pressure
Pr = Prandtl number
Re = channel Reynolds number $= \rho \overline{V} D/\mu$
t = time of color change
T = temperature
TPP = thermal performance parameter
$= (\overline{\overline{\mathrm{Nu}}}/\mathrm{Nu}_0)/(\overline{f}/f_0)^{1/3}$
$\overline{v}$ = average flow velocity
X = axial distance from middle of turn
α = thermal diffusivity of test surface material
μ = dynamic viscosity of air
ρ = density

Subscripts

0 = correlation based
in = inlet condition
j = time step based

Errata

The f/f_0 values are off by a factor of 4 (should be higher than shown in the figure) and the TPP values should be lower by a factor of 1.587 in this paper and Ref. [15].

References

[1] Boyle, R. J., 1984, ''Heat Transfer in Serpentine Passages With Turbulence Promoters,'' ASME Paper No. 84-HT-24.
[2] Metzger, D. E., and Sahm, M. K., 1986, ''Heat Transfer Around Sharp 180 deg Turns in Smooth Rectangular Channels,'' ASME J. Heat Transfer, **108**, pp. 500–506.
[3] Abuaf, N., Gibbs, R., and Baum, R., 1986, ''Pressure Drop and Heat Transfer Coefficient Distributions in Serpentine Passages With and Without Turbulence Promoters,'' *Proc. 8th International Heat Transfer Conference*, pp. 2837–2845.
[4] Fan, C. S., and Metzger, D. E., 1987, ''Effect of Channel Aspect Ratio on Heat Transfer in Rectangular Passage Sharp 180-deg Turns,'' ASME Paper No. 87-GT-113.
[5] Chyu, M. K., 1991, ''Regional Heat Transfer in Two-Pass and Three-Pass Passages With 180-deg Sharp Turns,'' ASME J. Heat Transfer, **113**, pp. 63–70.
[6] Ekkad, S. V., and Han, J. C., 1995, ''Local Heat Transfer Distributions Near a Sharp 180° Turn of a Two-Pass Square Channel Using a Transient Liquid Crystal Image Technique,'' J. Flow Visualization Image Processing, **2**, No. 3, pp. 287–298.
[7] Han, J. C., Chandra, P. R., and Lau, S. C., 1988, ''Local Heat/Mass Transfer Distributions Around Sharp 180 deg Turns in Two-Pass Smooth and Rib-Roughened Channels,'' ASME J. Heat Transfer, **110**, pp. 91–98.
[8] Chandra, P. R., Han, J. C., and Lau, S. C., 1988, ''Effect of Rib Angle on Local Heat/Mass Transfer Distribution in a Two-Pass Rib-Roughened Channel,'' ASME J. Turbomach., **110**, pp. 70–79.
[9] Ekkad, S. V., and Han, J. C., 1997, ''Detailed Heat Transfer Distributions in Two-Pass Square Channels With Rib Turbulators,'' Int. J. Heat Mass Transf., **40**, No. 11, pp. 2525–2537.
[10] Hibbs, R., Acharya, S., Chen, Y., Nikitopoulos, D., and Myrum, T., 1998, ''Heat Transfer in a Two-Pass Internally Ribbed Turbine Blade Coolant Channel With Cylindrical Vortex Generators,'' ASME J. Turbomach., **120**, pp. 724–734.
[11] Glezer, B., Moon, H. K., and O'Connell, T., 1996, ''A Novel Technique for the Internal Blade Cooling,'' ASME Paper No. 96-GT-181.
[12] Ligrani, P. M., Hedlund, C. R., Thambu, R., Babinchak, B. T., Moon, H. K., and Glezer, B., 1997, ''Flow Phenomena in Swirl Chambers,'' ASME Paper No. 97-GT-530.
[13] Moon, H. K., O'Connell, T., and Glezer, B., 1998, ''Heat Transfer Enhancement in a Circular Channel Using Lengthwise Continuous Tangential Injection,'' *Proc. Int. Heat Transfer Conference*, Seoul, South Korea.
[14] Hedlund, C. R., Ligrani, P. M., Moon, H. K., and Glezer, B., 1999, ''Heat Transfer and Flow Phenomena in a Swirl Chamber Simulating Turbine Blade Internal Cooling,'' ASME J. Turbomach., **121**, pp. 804–813.
[15] Ekkad, S. V., Pamula, G., and Acharya, S., 1999, ''Influence of Cross-Flow Induced Swirl and Impingement on Heat Transfer in an Internal Coolant Passage of a Turbine Airfoil,'' in: *Heat Transfer in Gas Turbines*, ASME HTD-Vol. 364-1; ASME J. Heat Transfer, **122**, pp. 587–597.
[16] Kline, S. J., and McClintock, F. A., 1953, ''Describing Uncertainties in Single Sample Experiments,'' Mech. Eng. (Am. Soc. Mech. Eng.), **75**, Jan., pp. 3–8.
[17] Gee, D. L., and Webb, R. L., 1980, ''Forced Convection Heat Transfer in Helically Rib-Roughened Tubes,'' Int. J. Heat Mass Transf., **23**, pp. 1127–1136.

Heat Transfer in Rotating Narrow Rectangular Ducts With Heated Sides Oriented at 60° to the *r-z* Plane

Fred T. Willett[1]

Arthur E. Bergles

Rensselaer Polytechnic Institute,
Troy, NY 12180

Gas turbine blade life is often limited by the effectiveness of the cooling in the trailing edge convective cavity, which generally has a narrow cross-section. Previous research on rotational effects considered cavity shapes quite different from those of typical trailing edge cavities. In this research, experiments were conducted to determine the effect of rotation on heat transfer in ducts of narrow cross-section (height-to-width ratio of 1:10), oriented with the heated sides at 60° to the r-z plane. In the experiment, a high-molecular-weight gas (Refrigerant-134A) at ambient pressure and temperature conditions was used to match the dimensionless parameters at engine conditions. Thin foil heaters were used to produce a constant heat flux at the long sides of the duct; the narrow sides were unheated. Duct Reynolds numbers were varied up to 20,000; rotation numbers were varied up to 0.25. The test results show the effect of rotation and aspect ratio on duct leading and trailing side heat transfer. In addition, the results show the variation in heat transfer coefficient with transverse location in the duct, demonstrating the effect of rotation not only on lead and trail side heat transfer, but also on forward and aft end heat transfer. [DOI: 10.1115/1.1354189]

Introduction

The demand for more power, whether it be thrust from an aircraft engine or shaft horsepower from an industrial gas turbine, provides incentive for gas turbine manufacturers to continually seek improvements in gas turbine performance. Turbine performance can be increased by raising the turbine inlet temperature. It can also be increased by decreasing the amount of air from the compressor that is dedicated to turbine cooling. In general, turbine blades, in order to survive in higher performance turbines, must either be made from superior materials or have superior cooling designs, or both. Insufficiently cooled blades are subject to oxidation, creep rupture, and, in extreme cases, melting.

Turbine efficiency is dependent on trailing edge thickness, with efficiency improving as trailing edge thickness is reduced. This, combined with the constraints imposed by manufacturing process capability, makes for a difficult cooling design. Knowledge of the local heat transfer in the trailing edge cooling passage is essential to a successful design. The heat transfer in a rotating heated channel is complex. The action of rotation on the coolant results in a nonuniform distribution of the heat transfer coefficient at any cross-section. Numerical solutions are not yet reliable or accurate enough for use in design. Experimental data are required to help gain a better understanding of the effects of rotation on heat transfer in a heated channel.

Figure 1 describes the rotation-induced forces acting on radially outward-flowing coolant in a heated channel. The buoyancy force is governed by both the centrifugal force acting on the fluid and the density gradient in the fluid. The density gradient is a function of the difference in temperatures of the fluid near the heated walls and the fluid in the core of the passage.

Mori et al. [1] did an investigation of the Coriolis effect, studying flow in round tubes both experimentally and analytically. Wagner and Johnson [2] investigated both Coriolis and buoyancy effects in their work, which used square passages and nondimensional flow parameters typical of gas turbine blades. Later work by Johnson and Wagner [3] studied the effects of rotation on inward flow as well as outward flow. Soong et al. [4], and later Kuo and Hwang [5] expanded the investigation of secondary flow effects due to rotation by considering smooth-walled rectangular ducts, and concluded that aspect ratio is a critical parameter. They observed that the greatest Coriolis effect occurs in square ducts, i.e., an aspect ratio of 1:1.

Zhang et al. [6] experimented with a three-pass serpentine circuit with turbulators oriented normal to the flow, concluding that the normalized Nusselt number is insensitive to Reynolds-number variation. The effects of rotation they observed were consistent

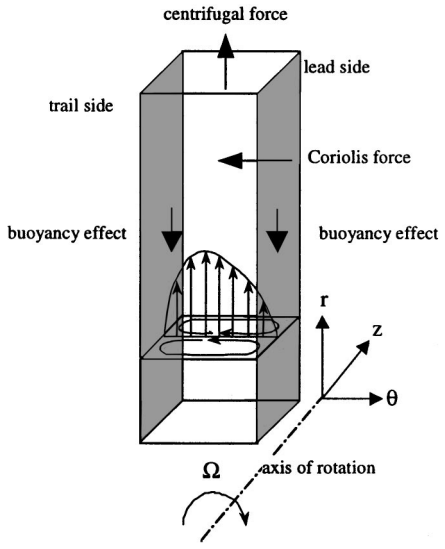

Fig. 1 Outward flowing channel in rotation

[1]Permanent affiliation: GE Power Systems, Schenectady, NY.

Contributed by the International Gas Turbine Institute and presented at the 45th International Gas Turbine and Aeroengine Congress and Exhibition, Munich, Germany, May 8–11, 2000. Manuscript received by the International Gas Turbine Institute February 2000. Paper No. 2000-GT-224. Review Chair: D. Ballal.

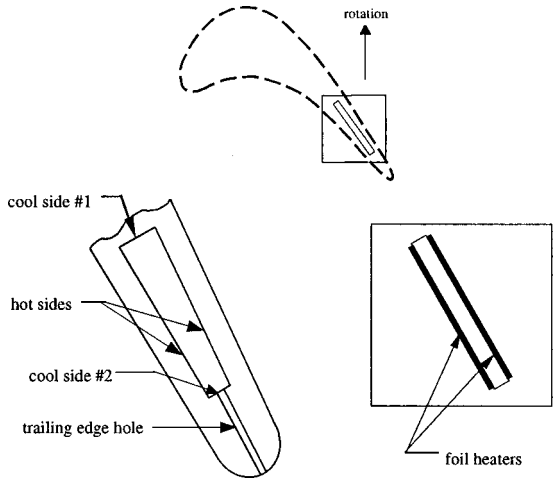

Fig. 2 Test duct orientation and comparison to turbine blade trailing edge cavity

with the work of Wagner and Johnson [2]. Further work on two-pass cooling channels was done by Han et al. [7,8] who considered the effect of uneven wall temperature in a square, smooth-walled passage. A three-pass, smooth-walled, serpentine passage was studied by Mochizuki et al. [9] who noted the strong three-dimensional structure in the flow through the 180° bends.

Parsons et al. [10,11] investigated the effect of model orientation and wall heating condition on heat transfer in a rotating two-pass square channel. Dutta et al. [12] considered the effects of orientation and rotation on heat transfer in a smooth triangular-shaped passage. Morris and Chang [13], and Park and Lau [14] attempted to uncouple the buoyancy and Coriolis effects, using extrapolation of experimental data to the implied zero-buoyancy condition and naphthalene sublimation experiments, respectively. Willett [15] presents a more detailed summary of the previous work. The configuration studied in this research is a smooth-walled rectangular passage with a 1:10 aspect ratio, oriented such that the long sides of the duct cross-section are at a 60° angle to the direction of blade tangential velocity, i.e., 60° to the r-z plane. This is an important case, because it models the trailing edge passage of a turbine blade. Figure 2 shows an airfoil cross-section with the subject configuration superimposed as though it were a cooling passage.

Test Apparatus

Review of Experimental Model. In the general case, all walls of the channel are heated, and there is a buoyancy force in effect on each wall. In the specific case investigated in this experiment, only the wide sides of the duct are heated. The heat input to the narrow sides of the duct is assumed to be small compared to the heat into the wide sides. Figure 2 shows cross-sections of the turbine blade trailing edge cavity and the experimental model. In the turbine blade, the longer walls of the cavity, denoted as ''hot sides,'' are close to the external surface or the turbine airfoil. The shorter walls, denoted as ''cool sides,'' are roughly perpendicular to the external surface of the airfoil. Cool side #1 is an internal rib. In a serpentine-cooled turbine blade, the other side of the rib is also cooled. Cool wall #2 is typically intersected by holes cast or drilled into the trailing edge of the airfoil. In an actual turbine blade, no heat enters the cavity through cool wall #1, and very little through cool wall #2. The experimental model was built with this in mind.

Rotational Test Rig. The test facility consisted of a rotor and stator enclosed in a closed loop system using R-134a as the test fluid. The refrigerant was supplied as a gas to the test sections to

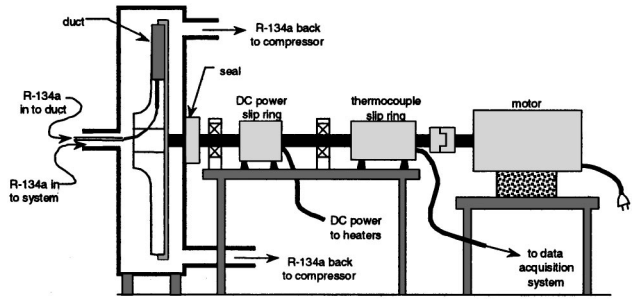

Fig. 3 Rotating test rig diagram

be evaluated. The use of a high-molecular-weight gas, e.g., a refrigerant, means that the dimensionless parameters relevant to gas turbine operating conditions can be matched at ambient pressure and relatively low rotational speeds. A diagram describing the test rig is given in Fig. 3.

The test sections, or ducts, were installed in a 24.5 in. (622 mm) diameter rotor. The rotor was constructed of mahogany and framed by an aluminum disk. The duct coolant was fed through the rotor via a rotating union and a radial supply passage in the disk. An inlet plenum was used to connect the supply tube to the rotor with an O-ring seal. Two inlet screens were used in the plenum to provide a uniform velocity at the inlet to the test duct. The inlet plenum was made of aluminum and was fitted into the supply tube at the inlet to the test duct. The inlet gas temperature was measured between the two inlet screens. The duct inlet was located at a radius of 6.61 in. (168 mm).

Test Sections. The duct was a two-piece construction and was made of mahogany. The flow passage in the test section was created by removing material from one half of the section, then cementing the two halves together. The external dimensions of the test section are 1.05 inches×0.95 in. (26.7 mm×24.1 mm), which allows it to fit in the inlet plenum. Continuous thin (0.0005 in., 0.013 mm) film nickel-based alloy heaters were attached to the wide sides of the duct. The heaters were backed with a very thin polymer film, which prevents the foil from tearing easily, but more importantly, electrically insulates the foil heater from the thermocouples. A specially formulated epoxy cement was used to fasten the polymer backing of the heaters to the walls of the duct. This very thin layer of epoxy provided additional electrical insulation for the thermocouples. As noted above, the narrow sides of the duct were not heated. The heated length of the duct was 4.50 in. (114.3 mm). The two pieces of the duct were cemented together with gasket cement and wrapped with tape to prevent leaks. The flow area of the duct was 0.10 in.×1.00 in. (2.54 mm×25.4 mm).

Instrumentation and Data-Acquisition

The duct was instrumented with Type-K thermocouples. The insulated thermocouple beads were in contact with the back of the heater. The thermocouple wires were 0.010 in. (0.25 mm) diameter and were covered with 0.006 in. (0.15 mm) thick insulation. The thermocouples were fed through the duct wall, perpendicular to the heater surface. The thermocouples were connected to a slip ring, which allowed transmission of data to the data-acquisition system. One side of the duct was well instrumented; the other side had only three thermocouples, used for measuring heater temperature and regulating the power to the heaters. The total number of thermocouples was limited by the slip ring capacity. A total of thirty-one thermocouples was used on the well-instrumented side, eleven in the developing region and twenty in the fully developed region. An additional thermocouple was placed on the outer wall of the test section. Because of the limited number of slip ring channels available, lead side and trail side data could not be ob-

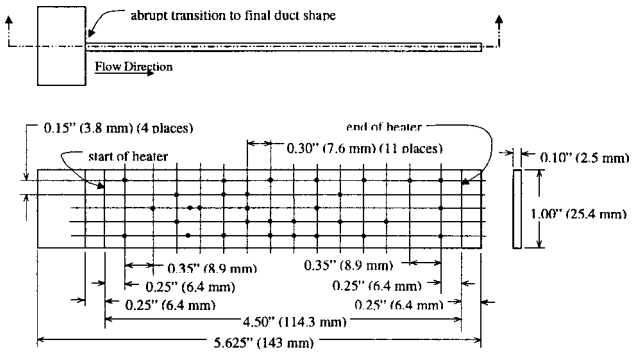

Fig. 4 Test duct and thermocouple locations

tained simultaneously. The test rig was operated in both forward and reverse rotation to obtain data for both sides. Figure 4 describes the test duct.

A program written using commercially available software enabled continuous readout of the data. The data were displayed on the computer screen in a virtual instrument format configured especially for the experiment. The user could write the data from the virtual instrument to a file command. Flow levels were set manually using a flow gage and monitored by the program. Rotating speed was measured with a tachometer and was set by the test operator using a variable-speed electric motor. Current to the heaters was controlled by the user via a DC power supply and displayed along with the other data. Heat input to the test section was entirely from resistance heating; the same current was supplied to both heated sides of the duct. The uniform-heat-flux boundary condition was applied on two sides of the duct. Uniform heat flux is a reasonable first-order representation of the heat transfer in an actual turbine blade. The nickel-based alloy heaters have a very low temperature coefficient of resistance (TCR), so the resistance is relatively constant over the range of operation, however, a correction was made to the resistance for the calculation of heat input to the duct.

The known or measured quantities for this experiment were (1) the heat into the test-section, (2) the R-134a flow rate, (3) the wall temperature, (4) the R-134a inlet temperature, (5) the fluid properties, and (6) the duct geometry.

The heat transfer coefficient is defined as:

$$h = \frac{Q_{\text{in}} - Q_{\text{loss}}}{A(T_{\text{wall}} - T_{\text{bulk}})} \tag{1}$$

In the experiment described here, Q, T_{wall}, and A are known. T_{bulk} can be calculated knowing the inlet temperature and the heat supplied to the heaters. With the calculated value of T_{bulk}, the local heat transfer coefficient can be determined at any thermocouple location. Q_{loss}, the heat lost from the heaters by conduction out of the test section, was determined using temperatures measured at the outside wall of the test section and a 2D finite-element model of the test section. Because the test section is-made of nonconducting material, this loss is small, between 5 percent and 10 percent of the total heat supplied by the heaters, depending on test conditions.

The duct-average heat transfer coefficient can also be determined for each heated wall. When determining the duct-average heat transfer coefficient, only the fully developed region is considered. In this experiment, it is expected that the flow be fully developed after ten hydraulic diameters from the duct inlet. The duct-average heat transfer coefficient is based on average temperatures, i.e.,

$$\overline{h} = \frac{Q_{\text{in}} - Q_{\text{loss}}}{A(T_{\text{wall}} - T_{\text{bulk}})} \tag{2}$$

The average Nusselt number is calculated as

$$\overline{\text{Nu}} = \frac{\overline{h} d_h}{k} \tag{3}$$

The Nusselt number is normalized to the Nusselt number for fully developed turbulent flow in a smooth duct as correlated by Dittus and Boelter/McAdams,

$$\text{Nu}_0 = 0.023\,\text{Re}^{0.8}\,\text{Pr}^{0.4} \tag{4}$$

A series of tests were conducted, over the range of Re anticipated for the rotating tests, with the duct in a static, i.e., nonrotating, condition to validate the use of this correlation for the 1:10 aspect ratio duct. The stationary duct results were compared to the values predicted by the Dittus/Boelter/McAdams equation and were found to correlate well; the value of R^2 calculated was 98.3 percent. These results validate not only the use of the Dittus/Boelter/McAdams equation for normalization, but also the use of hydraulic diameter as a characteristic length for the 1:10 aspect ratio duct. Additional data were taken to validate the assumption of fully developed flow for $L/d_{\text{H}} > 10$. The developing heat transfer data were compared with the results of Boelter, Young, and Iversen as reported by Kays and Crawford [16], for air flowing in a circular tube with constant surface temperature. The results from the present experiment are reported by Willett [15] and match well with the previous results.

The duct-averaged normalized Nusselt number is calculated as

$$\frac{\overline{\text{Nu}}}{\text{Nu}_0} = \frac{\overline{\text{Nu}}}{\frac{1}{n}\Sigma_{i=1}^{n}(\text{Nu}_0)_i} \tag{5}$$

where n is the number of thermocouples in the section of the duct over which the average is taken and $(\text{Nu}_0)_i$ is the calculated smooth, non-rotating, duct Nusselt number corresponding to the thermocouple location. The variation in Nu_0 with axial distance is quite small, and is due to the dependence of viscosity and Prandtl number on bulk fluid temperature.

Normalized Nusselt number was studied as a function of both rotation number, $\text{Ro} = \Omega d_h / V$, and buoyancy number, $\text{Buo} = \text{Gr}/\text{Re}^2$. Rotation number was controlled by adjusting the mass flow through the duct. Buoyancy number was controlled by adjusting mass flow and wall temperature. Rotational speed was 2400 rpm in all cases.

An uncertainty analysis was performed using the method described by Kline and McClintock [17]; the experimental uncertainty in normalized Nusselt number was calculated to be ± 10 percent. The largest sources of uncertainty were the temperature measurement and the measurement of heater area. Willett [15] describes the apparatus, procedure, and data reduction in greater detail.

Smooth Duct With Heated Sides Oriented at 60° to the *r-z* Plane. With the duct rotated out of the r-z plane, i.e., heated sides not perpendicular to the θ-direction, the lead-side and trail-side designations are no longer sufficient. It is necessary now to add forward and aft designations. The transverse location in the duct is referenced to the forward and aft positions, with aft corresponding to the end at the turbine blade trailing edge. Data were collected at five equally spaced transverse locations, one at the center and two each on either side of the duct center line. The five positions are designated as: far forward, center forward, center line, center aft, and far aft; these are shown in Fig. 5. By separating lead and trail-side data and by segregating data as described above, it is possible to gain a more thorough understanding of the effects on heat transfer, not only of rotation and duct orientation, but also of local position within the duct.

Trail-Side Data. Average Nu/Nu_0 was determined from the trail side data for each test point. There were four sets of data, corresponding to $\text{Ro} = 0.128$, 0.160, 0.197, and 0.255. Over the range of buoyancy number evaluated, the duct-average normal-

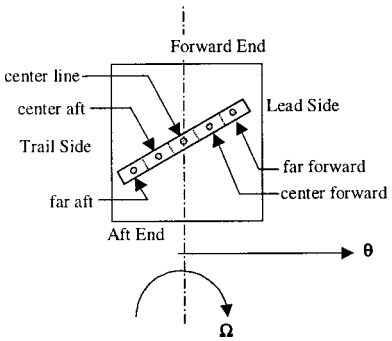

Fig. 5 Transverse locations within the test duct

ized Nusselt number is nearly constant, ranging between 1.37 and 1.52, as the enhancement of heat transfer coefficient at the aft end is offset by degradation at the forward end.

An interesting view of the data is presented in Figs. 6 and 7, where the data are arranged by transverse location and rotation number. Figure 7 shows the results for Ro=0.128, the lowest value of rotation number studied. The data are tightly grouped, especially at lower buoyancy number. As buoyancy number and rotation number are increased, more heat transfer enhancement is observed at the aft end than at the center line or the forward end, i.e., the effect of transverse location on normalized Nusselt number becomes more pronounced. This is much clearer in Fig. 7, which shows results for Ro=0.255, the highest value of rotation number considered. At Ro=0.255, the Coriolis effect results in more heat transfer enhancement at the center aft and especially the far aft location.

The full set of data, for all rotation numbers (Ro=0.128, 0.160, 0.197, and 0.255), is plotted in Fig. 8 and shows the marked influence of transverse location on heat transfer in the duct. This is due to a combination of factors. The Coriolis force is acting at an angle to the trail-side wall, with a force component in the aft direction which produces (1) a skewed flow profile resulting in higher velocity at the far aft end, (2) secondary flow in the tangential direction bringing cooler core fluid to the aft end, and (3) aft-end boundary layer thinning due to the Coriolis force. The buoyancy effect contributes to heat transfer enhancement at higher rotation numbers, as buoyancy-driven counterflow near the wall results in more turbulent mixing.

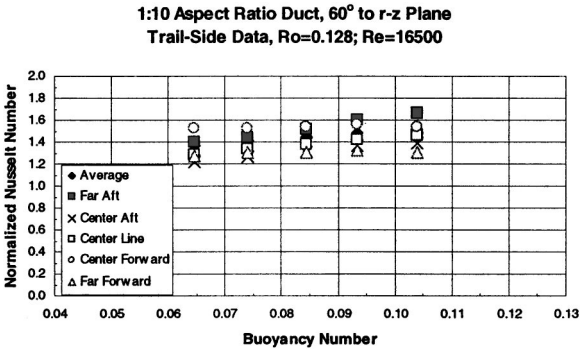

Fig. 6 Trail-side data for Ro=0.128

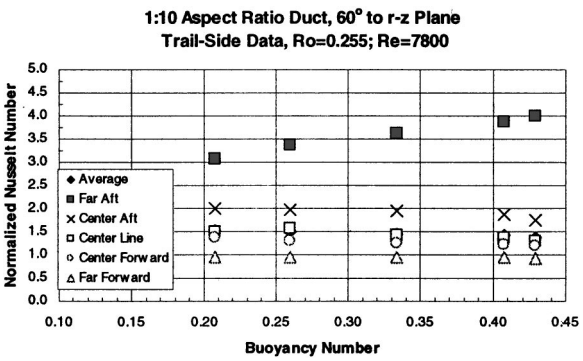

Fig. 7 Trail-side data for Ro=0.255

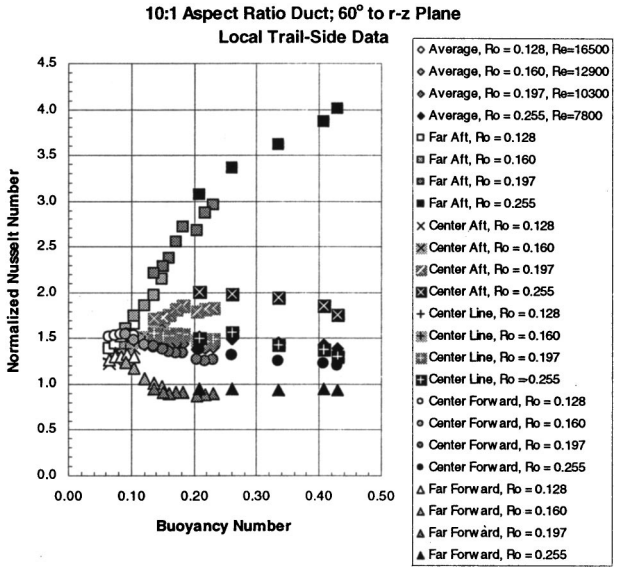

Fig. 8 Local trail-side normalized Nusselt number vs. Buo

There is a change in the slope of the data apparent at Buo=0.2, suggesting a change in the interaction of the secondary flows. The far-forward end data show a decrease in normalized Nusselt number with increasing buoyancy number, with Nu/Nu_0 below 1.0 in the range of buoyancy number from 0.15–0.2, followed by a recovery to an asymptotic value of 1.0. The data at the center-aft, center-forward, and center-line locations also stabilize, and even decrease slightly, above Buo=0.2, which suggests cell formation and transverse mixing of the flow. Test-rig limitations prevented further study at higher buoyancy number that would be necessary to find the asymptotic limit for the aft end Nu/Nu_0.

The full set of far-aft-end data was fit to an equation of the form in Eq. (6).

$$Nu/Nu_0 = A + B\,Ro^2 + C\,Buo + D\,RoBuo^2 \tag{6}$$

A regression analysis was used, and the resultant equation was forced to a normalized Nusselt number close to 1.0 when Ro and Buo were reduced to zero. The resultant regression equation for the trail-side aft end is

$$Nu/Nu_0 = 0.962 + 13.5Ro^2 + 5.94Buo - 7.26RoBuo^2 \tag{7}$$

and R^2, the coefficient of determination, is 98.1 percent.

The effects of both centrifugal force and density gradient are contained in the buoyancy number due to its relationship to rotation number. The effect of density gradient alone can be illustrated using density ratio. Figure 9 presents the normalized Nusselt number plotted as a function of density ratio, i.e., $\Delta\rho/\rho = (\rho_{bulk} - \rho_{wall})/\rho_{bulk}$, for the far aft end location. The Coriolis effect is clear, as the data show an increasing Nu/Nu_0 with increasing rotation number. The effect of density ratio can be inferred from the slopes of the data, with the sharpest slope observed for Ro=0.255. The data at the far forward end also showed the effect of increasing rotation number, as Nu/Nu_0 was found to be highest at Ro=0.128 and decreased with increasing rotation number. The effect of density ratio was almost negligible at the

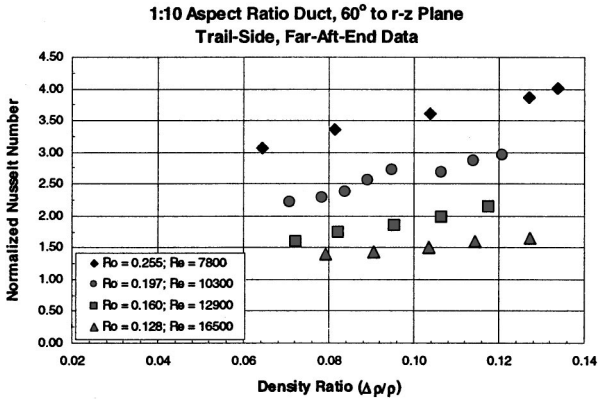

Fig. 9 Trail-side, far-aft-end Nu/Nu_0 vs. density ratio

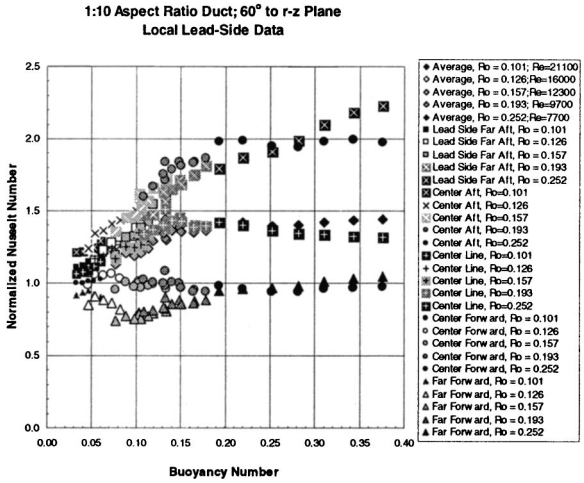

Fig. 11 Local lead-side normalized Nusselt number vs. Buo

far-forward end and at the center line for the lower Ro case. These results show that rotation, not density ratio, is the dominant factor influencing heat transfer.

Lead-Side Data. Five sets of data, corresponding to different values of rotation number, were collected for the lead side of the duct. The duct-average normalized Nusselt number was found to increase linearly with Buo up to a buoyancy number between 0.15 and 0.2. For buoyancy number greater than 0.2, the normalized Nusselt number is nearly constant at 1.4. The pattern is greatly influenced by the behavior at the far-forward end.

The five values of rotation number tested were 0.100, 0.126, 0.157, 0.193, and 0.252. Data for the lowest and highest rotation numbers are shown in Figs. 10 and 11. As was the case for the trail-side data, the influence of transverse location on normalized Nusselt number is apparent. Also clear is the effect of the duct orientation. At 60° to the *r-z* plane, the component of Coriolis force parallel to the heated walls becomes significant. The aft end of the duct displays lead-side heat transfer behavior normally characteristic of the trail side.

Figure 12 shows the results for Ro=0.100, the lowest value of rotation number studied. The data are tightly grouped, especially at lower buoyancy number. As buoyancy number is increased, more enhancement is observed at the aft end than at the center line or the forward, but at low Ro and Buo, the difference is rather small.

Figure 10 shows the results for Ro=0.252, the highest value of Ro tested. The effect of transverse location on heat transfer is much more apparent, and a nearly linear increase in normalized Nusselt number with increasing buoyancy number is observed at the far-aft end of the duct. Normalized Nusselt elsewhere in the duct is relatively constant.

The full set of lead-side data, for all rotation numbers tested (Ro=0.100, 0.126, 0.157, 0.193, and 0.252), is plotted in Fig. 11. The data segregate, at higher buoyancy numbers, into forward, center, and aft groupings. At the far aft end of the duct, the normalized Nusselt behavior is similar to that observed at the far aft end of the trail side. A similar regression fit was found, and as with the trail side, the resultant equation was forced to a normalized Nusselt number close to 1.0 when Ro and Buo were reduced to zero. The resultant regression equation for the lead-side aft end is

$$Nu/Nu_0 = 0.952 + 1.82Ro^2 + 4.67Buo - 17.6RoBuo^2 \qquad (8)$$

In this case $R^2 = 97.2$ percent. The regression curves for lead and trail side far-aft-end are plotted, along with the data, in Fig. 13.

At the far forward end of the duct, the normalized Nusselt number dips well below 1.0 around Buo=0.10, then gradually increases to 1.0 at higher buoyancy numbers. This is similar to the behavior observed in square ducts, first published by Wagner and Johnson [2]. The center line and average data show an increase in normalized Nusselt number at nearly the same rate as the aft end data, until around Buo=0.15, when Nu/Nu_0 levels off and begins to decrease with increasing Buo. The trend shows a convergence of center-line and forward-end data at high Buo.

Figure 14 presents the lead-side normalized Nusselt number plotted as a function of density ratio for the far-aft end location, where the Coriolis effect is strongest. The data show a sharp increase in Nu/Nu_0 with increasing rotation number at constant density ratio. The data also shows an increase in Nu/Nu_0 with increasing density ratio, especially at high rotation numbers. The results

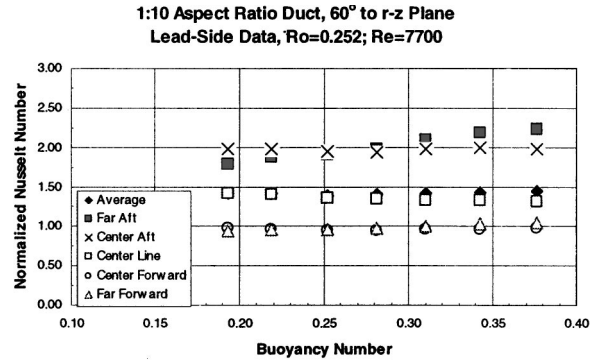

Fig. 10 Local lead-side data for Ro=0.252

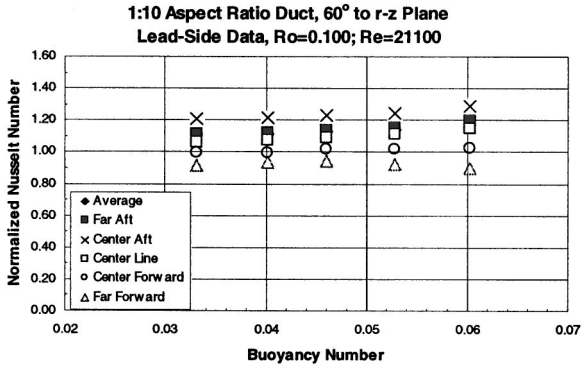

Fig. 12 Local lead-side data for Ro=0.100

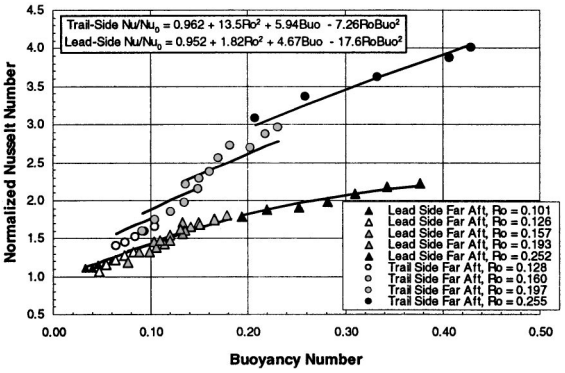

Fig. 13 Nu/Nu_0 vs. Buo at the far aft end of the duct

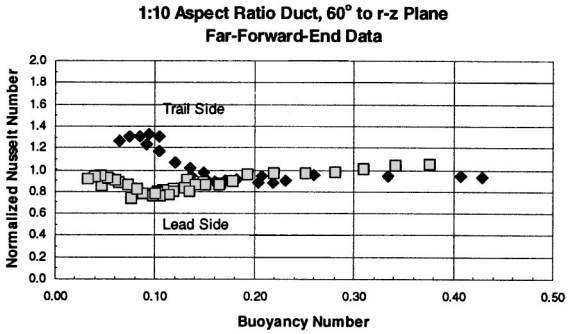

Fig. 15 Nu/Nu_0 vs. Buo at the far forward end of the duct

are similar to those observed for the trail side and demonstrate the relative strengths of Coriolis and buoyancy effects.

Forward and Aft End Data. The Coriolis force in the duct oriented 60° to the *r-z* plane has two components relative to the heated walls. The perpendicular component is similar to the case of a duct oriented parallel to the *r-z* plane. The parallel component forces flow towards the aft end of the duct, and is a factor in the transverse variation in heat transfer coefficient. The resultant effect is that at the aft end of the duct, lead-side heat transfer behavior is similar to that observed at the trail side in ducts oriented parallel to the *r-z* plane. Also, at the forward end of the duct, the trail-side heat transfer is reduced compared to the trail-side heat transfer in ducts oriented at parallel to the *r-z* plane. The trail-side heat transfer at the forward end of the duct is more like that observed at the lead side in ducts oriented at 0 deg to the *r-z* plane. Figure 13 compares the lead and trail-side normalized Nusselt numbers at the far aft end of the duct. The heat transfer enhancement at the trail side is higher than that at the lead side, but the normalized Nusselt number at the lead side is greater than 1.0 over the entire range of Buo tested and follows the same trend as the trail-side data. The trail side benefits from the full Coriolis effect and the resultant boundary layer thinning, which accounts for the difference in normalized Nusselt number between lead and trail sides.

It can be inferred from the results that thinning and thickening of the boundary layer is occurring in the corners, directly in line with the Coriolis force. This accounts for the more pronounced increase in heat transfer at the aft end of the trail side, as well as the increase in heat transfer with increasing Buo, as the buoyancy-driven counterflow increases turbulence near the wall. Likewise, a thick boundary layer at the lead-side forward end of the duct results from the pressure gradient created by the Coriolis effect. Reduced turbulent transport at the lead-side forward end gives rise to reduced heat transfer. The increase in Ro also increases the cross-stream flow, which impinges cool core fluid on the trail side and brings heated fluid from the trail side to the lead side. Heat transfer near the center-line is less affected by boundary layer thinning and thickening, as the region is not directly in line with the Coriolis force. The pressure gradient and cross-stream flows have less influence on the heat transfer, and, as a result, the lead and trail-side normalized Nusselt numbers are expected to be similar.

A similar comparison is made for the far forward end of the duct. Figure 15 is a plot of normalized Nusselt number vs. Buo for both the lead and trail-side data collected at the far-forward location. At low Buo, the difference between lead and trail-side data is significant, and is due to the boundary layer expansion on the lead side due to the Coriolis-induced pressure gradient. The trail side benefits from cross-stream flow of cooler fluid from the core. At higher rotation and buoyancy numbers, the formation of secondary flow cells promotes mixing and uniform heat transfer at the forward end.

Comparison With Previous Research. The data collected for the smooth duct oriented with its heated walls at a 60° angle to the *r-z* plane is unique in the field of rotational heat transfer research. The duct aspect ratio, the orientation relative to the *r-z* plane, and the interest in transverse location are each different from any research previously reported. Accordingly, comparisons with previous data are difficult to interpret. The work of Park and Lau [14] reported on a two-pass channel oriented at 45° to the *r-z* plane, but their work studied mass transfer using naphthalene sublimation, so there was no buoyancy effect to evaluate. Other investigations into the effects of orientation were conducted on ducts with turbulator ribs [10] and are not appropriate for comparison.

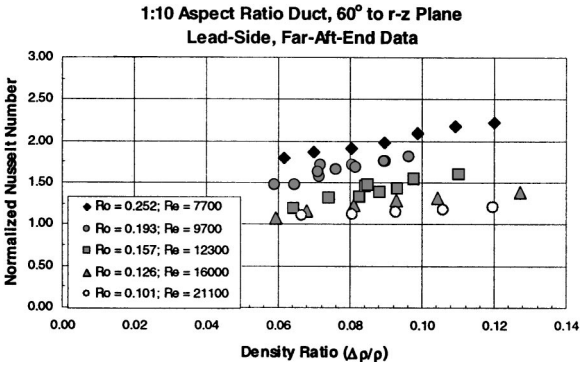

Fig. 14 Lead-side, far-aft-end Nu/Nu_0 vs. density ratio

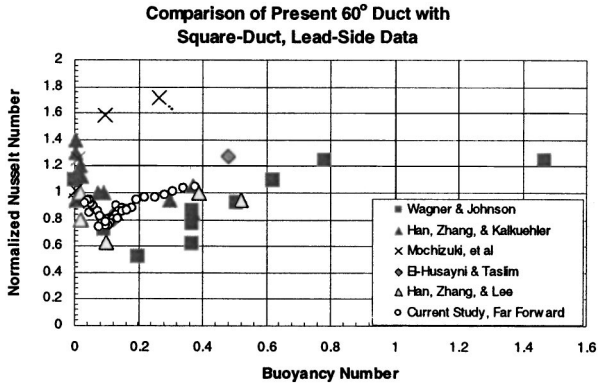

Fig. 16 Comparison of present 60° duct local-lead-side data with lead-side data for square ducts

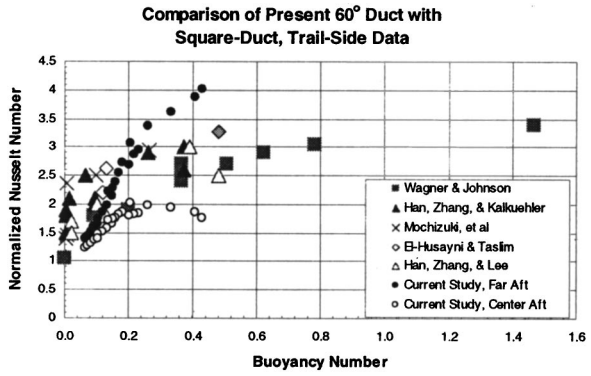

Fig. 17 Comparison of present 60° duct local trail side data with trail-side data for square ducts

The majority of previous research considered a square duct in rotation. A comparison of the present far-forward-end data with the data for the lead side of a square duct is given in Figure 16. As mentioned above, the data trend is similar to that observed in the square duct by previous investigators. The reversal at lower buoyancy number in the present duct is due to better flow mixing. Figure 17 compares the trail-side-far-aft data and center-aft data with the square duct trail side data reported by previous researchers. A good comparison of the trends is observed. The normalized Nusselt number at the far-aft end of the duct is higher than the average observed for the square duct. Previous research comparing ducts of different aspect ratios concluded that the trail side heat transfer was greatest in square ducts. The results presented here, however, show that orientation of the duct has a strong influence on local heat transfer.

Conclusions

(a) Because of the duct orientation, there is significant variation in heat transfer coefficient with transverse location on both the lead and trail sides. The investigation of forward and aft-end heat transfer coefficient is as important as that of lead and trail-side heat transfer coefficient.

(b) Normalized Nusselt number at the far-aft-end of the trail side of the duct, which represents the very trailing edge in an actual turbine blade, is a strong function of rotation number and buoyancy number. The normalized Nusselt number increases with increasing buoyancy number at a steeper rate than the rate reported for a square duct by previous researchers.

(c) Normalized Nusselt number at the far-aft-end of the lead side of the duct increases with buoyancy number in a manner typical of square-duct trail-side $\mathrm{Nu}/\mathrm{Nu}_0$.

(d) Normalized Nusselt number at the forward end of the duct is much lower than at the aft end, and is less than 1.0 at buoyancy numbers below 0.20 on the lead side. This is due to boundary layer thickening at the lead side and is caused by the Coriolis effect. It is similar to results observed in square-duct lead-side rotational heat transfer reported by previous researchers.

(e) Lead-side and trail-side heat transfer coefficients at the far-aft end of the duct can be correlated to simple relationships of the form $\mathrm{Nu}/\mathrm{Nu}_0 = A + B\,\mathrm{Ro}^2 + C\,\mathrm{Buo} + D\,\mathrm{RoBuo}^2$.

Acknowledgments

This effort has benefited greatly from technical discussions with Fred Staub of GE's Corporate Research and Development Center. The authors also gratefully acknowledge the support of Karl Hardcastle, also of GE CR&D, during the data-gathering phase of this research. The rotating test rig used for this research is located at GE's Corporate Research and Development Center. Dr. Norm Shilling, Dr. Kent Cueman, and Gene Kimura graciously made the rig available for this work; their interest and encouragement is much appreciated.

Nomenclature

A = heater surface area
Buo = buoyancy number ($=\mathrm{Gr}/\mathrm{Re}^2$)
d_H = hydraulic diameter
Gr = Grashof number ($=\Omega^2 R_m \beta \Delta T d_\mathrm{H}^3 \rho^2/\mu^2$)
h = convective heat transfer coefficient
k = thermal conductivity
Nu = Nusselt number ($=h d_\mathrm{H}/k$)
Nu_0 = Nusselt number in a stationary duct ($=0.023\,\mathrm{Re}^{0.8}\mathrm{Pr}^{0.4}$)
Q_in = total heat flow through the heaters
Q_loss = heat loss from the test section
Pr = Prandtl number ($=C_p\mu/\mathrm{k}$)
R_m = mean duct radius
Re = Reynolds number ($=\rho V d_\mathrm{H}/\mu$)
Ro = rotation number ($=\Omega d_\mathrm{H}/V$)
T_bulk = bulk fluid temperature
T_inlet = fluid temperature measured at the duct inlet
T_wall = duct wall temperature
V = average fluid velocity
Ω = rotational speed
ρ_bulk = bulk fluid density
ρ_wall = fluid density near the heated wall
μ = absolute viscosity
β = coefficient of volumetric expansion

References

[1] Mori, Y., Fukada, T., and Nakayama, W., 1971, ''Convective Heat Transfer in a Rotating Radial Circular Pipe (2nd Report),'' Int. J. Heat Mass Transf., **14**, pp. 1807–1824.
[2] Wagner, J. H., Johnson, B. V., and Hajek, T. J., 1989, ''Heat Transfer in Rotating Passages With Smooth Walls and Radial Outward Flow,'' ASME Paper No. 89-GT-272.
[3] Johnson, B. V., Wagner, J. H., and Kopper, F. C., 1990, ''Heat Transfer in Rotating Serpentine Passages With Smooth Walls,'' ASME Paper No. 90-GT-331.
[4] Soong, C. Y., Lin, S. T., and Hwang, G. J., 1991, ''An Experimental Study of Convective Heat Transfer in Radially Rotating Rectangular Ducts,'' ASME J. Heat Transfer, **113**, pp. 604–611.
[5] Kuo, C. R., and Hwang, G. J., 1994, ''Aspect Ratio Effect on Convective Heat Transfer of Radially Outward Flow in Rotating Rectangular Ducts,'' *5th International Symposium on Transport Phenomena and Dynamics of Rotating Machinery*, Kaanapali, HI.
[6] Zhang, N., Chiou, J., Fann, S., and Yang, W.-J., 1993, ''Local Heat Transfer Distribution in a Rotating Serpentine Rib-Roughened Flow Passage,'' ASME J. Heat Transfer, **115**, pp. 560–567.
[7] Han, J. C., Zhang, Y.-M., and Kalkuehler, K., 1993, ''Uneven Wall Temperature Effect on Local Heat Transfer in a Rotating Two-Pass Square Channel With Smooth Walls,'' ASME J. Heat Transfer, **115**, pp. 912–920.
[8] Han, J. C., Zhang, Y.-M., and Lee, C. P., 1994, ''Influence of Surface Heating Condition on Local Heat Transfer in a Rotating Square Channel With Smooth Walls and Radial Outward Flow,'' ASME J. Turbomach., **116**, pp. 149–158.
[9] Mochizuki, S., Takamura, J., Yamawaki, S., and Yang, W.-J., 1994, ''Heat Transfer in Serpentine Flow Passages With Rotation,'' ASME J. Turbomach., **116**, pp. 133–140.
[10] Parsons, J. A., Han, J. C., and Zhang, Y., 1995, ''Effect of Model Orientation and Wall Heating Condition on Local Heat Transfer in a Rotating Two-Pass Square Channel With Rib Turbulators,'' Int. J. Heat Mass Transf., **38**, No. 7, pp. 1151–1159.
[11] Parsons, J. A., Han, J. C., and Zhang, Y., 1994, ''Wall Heating on Local Heat Transfer in a Rotating Two-Pass Square Channel With 90 deg Rib Turbulators,'' Int. J. Heat Mass Transf., **37**, No. 9, pp. 1411–1420.
[12] Dutta, S., Han, J.-C., and Lee, C. P., 1995, ''Experimental Heat Transfer in a Rotating Triangular Duct: Effect of Model Orientation,'' ASME J. Heat Transfer, **117**, pp. 1058–1061.

[13] Morris, W. D., and Chang, S. W., May 1998, ''Heat Transfer in a Radially Rotating Smooth-Walled Tube,'' Aeronautical J., **102**, pp. 277–285.
[14] Park, C. W., and Lau, S. C., 1998, ''Effect of Channel Orientation on Local Heat (Mass) Transfer Distributions in a Rotating Two-Pass Square Channel With Smooth Walls,'' ASME J. Heat Transfer, **120**, pp. 624–632.
[15] Willett, F. T., 1999, ''An Experimental Study of the Effects of Rotation on Convective Heat Transfer in Smooth and Pin Fin Ducts of Narrow Cross-section,'' Ph.D. thesis, Rensselaer Polytechnic Institute.
[16] Kays, W. M., and Crawford, M. E., 1980, *Convective Heat and Mass Transfer*, McGraw-Hill, New York.
[17] Kline, S. J., and McClintock, F. A., January 1953, ''Describing Uncertainties in Single-Sample Experiments,'' Mechanical Engineering, Jan., pp. 3–8.

Tip Clearance Effects in a Turbine Rotor: Part I—Pressure Field and Loss

Xinwen Xiao
Graduate Assistant

Andrew A. McCarter
Graduate Assistant

Budugur Lakshminarayana
Evan Pugh Professor and Director
b1laer@engr.psu.edu

Center for Gas Turbines and Power,
Pennsylvania State University,
153-J Hammond Bldg.,
University Park, PA 16802

This paper presents an experimental investigation of the effects of the tip clearance flow in an axial turbine rotor. The effects investigated include the distribution and the development of the pressure, the loss, the velocity, and the turbulence fields. These flow fields were measured using the techniques of static pressure taps, rapid response pressure probes, rotating five-hole probes, and Laser Doppler Velocimeter. Part I of this paper covers the loss development through the passage, and the pressure distribution within the passage, on the blade surfaces, on the blade tip, and on the casing wall. Regions with both the lowest pressure and the highest loss indicate the inception and the trace of the tip leakage vortex. The suction effect of the vortex slightly increases the blade loading near the tip clearance region. The relative motion between the turbine blades and the casing wall results in a complicated pressure field in the tip region. The fluid near the casing wall experiences a considerable pressure difference across the tip. The highest total pressure drop and the highest total pressure loss were both observed in the region of the tip leakage vortex, where the loss is nearly twice as high as that near the passage vortex region. However, the passage vortex produces more losses than the tip leakage vortex in total. The development of the loss in turbine rotor is similar to that observed in cascades. Part II of this paper covers the velocity and the turbulence fields.
[DOI: 10.1115/1.1368365]

Introduction

The effects of the clearance flow have been fully investigated in turbine cascades. However, some rotation-related features may not be simulated in cascades even with moving walls. These features include the centrifugal force, the Coriolis force, and the inlet boundary conditions from the upstream nozzle. Their importance on the tip clearance flow in real axial turbines has yet to be fully investigated. The two most significant aspects affected by the tip clearance flow are probably the blade loading and the loss.

A detailed literature review on the studies of the tip clearance flow in axial turbines has been made available by Sjolander [1]. Blade unloading is a major feature of the pressure field near the blade tip and is strongly dependent on the tip clearance height, as observed by Graham [2] in a water analogy rig with variable tip clearance heights and variable casing wall moving speeds. Tip unloading is reduced at larger clearances and faster casing wall moving speeds. A more detailed measurement of the blade loading near the blade tip was obtained by Sjolander & Amrud [3]. The local blade loading actually increases as the tip is approached, due primarily to a strong suction peak induced by the tip vortex on the suction surface. The pressure variations along the blade tip surface and on the casing wall were examined in a cascade by Bindon [4] using a high resolution measurement technique. An ultra low pressure could result at the pressure side entry due to the sharp radius of curvature the leakage flow undergoes at gap entry. A large low-pressure zone was found at the suction corner on the casing wall. This low pressure zone could then induce an added pressure differential across the tip and result in higher leakage velocity. Even for a relatively large tip clearance (3.2 percent chord), the fluid near the casing wall still experiences a pressure difference across the tip gap comparable with that on the blade [5]. The variation of the casing wall pressure distribution with different incidence angles was investigated in a low-speed turbine rig by Yamamoto et al. [6].

The loss development within the passage due to the tip clearance flow was studied in cascades by Bindon [7], as well as Yaras & Sjolander [8]. The majority of the loss is due to the mixing between the flows from the tip gap and within the passage. Yamamoto et al. [9] and Peter & Moore [10] also measured the total pressure loss at a couple of axial locations within a rotor and downstream of a linear cascade, respectively.

Almost all of the above studies were performed in turbine cascades. The objective of this paper is to clarify the behavior and the effects of the tip clearance flow in rotating axial flow turbines. The approaches were detailed experimental investigation of the pressure field, the blade loading, the loss field, the velocity and vorticity fields, and the turbulence field, in a state-of-art single-stage axial flow turbine rig. Experimental techniques include static pressure taps, rapid responding pressure probe, rotating five-hole probe, and Laser-Doppler Velocimeter. The measurement covered the pressure surface, the suction surface, the blade tip, the casing wall, and inside the passage near the tip region. Part I of this paper covers the effects on the blade loading and the losses of the tip clearance flow. The blade loading was derived from the pressure data measured on the blade surfaces. The loss was derived from the total pressure data measured in various axial locations within the passage. The pressure and loss distributions indicate the rollup of the tip leakage vortex, and shows the inception point and trajectory. A passage vortex and a possible scraping vortex were also clearly observed. Part II of this paper presents the velocity fields within the passage, including the vorticity, the secondary flow, and the turbulence fields. Part II also discusses the physics of the tip clearance flow. Data presented in this paper could be used to reduce the effects of the tip clearance flow in axial turbines.

Experimental Apparatus and Tip Clearance Geometry

The experimental apparatus used in this study was a low-speed single-stage axial flow turbine research facility in the Pennsylva-

Contributed by the International Gas Turbine Institute and presented at the 45th International Gas Turbine and Aeroengine Congress and Exhibition, Munich, Germany, May 8–11, 2000. Manuscript received by the International Gas Turbine Institute February 2000. Paper No. 2000-GT-476. Review Chair: D. Ballal.

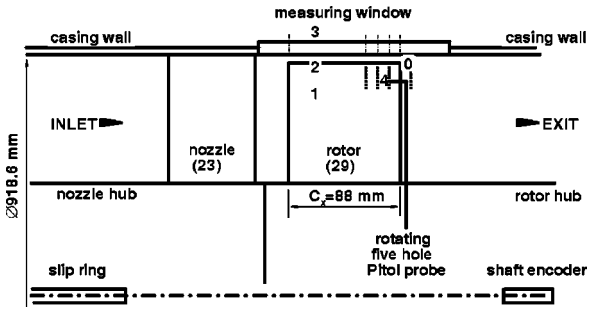

Fig. 1 Schematic of facility test section and measurement positions. 0 tip gap height: 0.76% chord at tip; 1 static pressure measurement on suction and pressure surfaces; 2 static pressure measurement at the corner of the blade tip; 3 transient pressure measurement on the casing wall from leading edge (X=0) to trailing edge (X=1) using kulite; 4 pressure measurement within the passage at X=0.7, 0.8, 0.9, and 1.1 using rotating five-hole Pitol probe and LDV.

Table 1 Parameters of facility at design condition

Corrected rotation speed (rpm)	1300
Radius at tip (millimeter)	458.3
Hub-to-tip radius	0.7269
No. of rotor blades	29
Blade turning angle at tip (degree)	95.42
Blade maximum thickness-to-chord at tip	17.1%
Blade chord at tip (millimeter)	128.7
Blade axial chord at tip (millimeter)	88.0
Pitchline loading coefficient $(P_{t1}-P_{t3})/(0.5\rho U_m^2)$	3.4
Rotor Zweifel coefficient	0.90
Pitchline reaction	0.4~0.5
Maximum relative mach number at tip	0.240
Re# based on inlet relative velocity ($x10^6$)	0.25~0.45
Re# based on exit relative velocity ($x10^6$)	0.50~0.7

Table 2 Geometry parameters of blade tip clearance

	Mean	Min.	Max.
Tip clearance (τ, millimeter)	0.978	0.811	1.120
τ/chord at tip	0.76%	0.63%	0.87%
τ/max. blade thickness at tip	4.44%	3.69%	5.09%
τ/span	0.78%	0.65%	0.90%
Standard error of τ/chord at tip	< 0.1%		
Radius of the blade tip corners	< 0.10 millimeter		

nia State University. The details of the facility have been reported by Lakshminarayana et al. [11]. The test section of the facility is representative of the features of a current or near future high-pressure turbine stage. Figure 1 shows schematically the test section with the measurement positions selected. Some of the most significant turbine parameters related to the present study are summarized in Table 1. All measurements were performed at the design condition.

The blade tip clearance geometry is described in Table 2. The heights of the tip clearances were measured while the turbine was stationary. The slight differences in heights are due to the out-of-roundness of the casing wall, and are experienced by each blade as it rotates. The facility runs at a low speed (1300 rpm). The turbine blisk is much thicker than the blisks in real engines. The variation of the tip gap heights with the rotation speed is therefore assumed to be insignificant. Compared with the tip clearance height (1~5 percent chord) investigated in cascades, the tip clearance height for this facility is almost constant. Each blade effectively experienced the mean value of the tip clearance (0.76 percent tip clearance-to-chord).

Experimental Techniques

Three different experimental techniques were used in this study to measure the static pressure distribution on the blade surfaces, on the blade tip, on the casing wall, and within the passage, as well as the loss development through the passage. These measurement locations are shown in Fig. 1 as ''1,'' ''3,'' and ''4.''

Static Pressure Measurement on Blade Surfaces. The static pressure distribution on the blade surfaces (shown as ''1'' in Fig. 1) were measured using the static pressure taps (22 axial×12 radial) incorporated into both the pressure and suction blade surfaces. To clarify the tip clearance flow, more taps were located at the region near the blade tip. Spanwise locations near the tip were $H=0.995$, 0.98, 0.965, 0.95, 0.925, and 0.90. Another 22 pressure taps were incorporated on the blade tip surface ($H=1.00$ as shown in Fig. 6). All static pressure taps were connected to a Pressure Measurement System Inc. model ESP-32 pressure transducer array, which was installed inside the turbine rotor. Pressure signals were transmitted to the stationary frame through a slip ring. Data was acquired at a rate of 20,000 samples per second, and averaged to get the mean pressure data. The absolute accuracy of the acquired pressure data was within ±18.6 Pascal (0.0027 psi). The probe head and the pressure transducer were at the different radii; corrections needed for the centrifugal force were made.

Dynamic Pressure Measurement on Casing Wall. The transient static pressure on the casing wall (shown as ''3'' in Fig. 1) was investigated at 11 axial locations equally distributed from the leading edge to the trailing edge of the rotor, using a miniature dynamic pressure sensor (Kulite XCS-093-5D with a frequency response of 150 kHz). The diameter of the sensor head is less than 1.0 percent of the axial rotor chord, about 1.007 percent of the rotor spacing at the tip. The pressure variation along the tangential direction of the rotor was determined using a phase-locked technique. A shaft encoder with 6000 lines per resolution (about 207 data points per rotor spacing) was used as the trigger and the clock for the phase-locked technique. The data was ensemble-averaged using about 173 revolutions. The absolute accuracy of the sensor was ±103.4 Pascal (0.015 psi), and the relative accuracy of the data is about 1 percent.

Pressure Measurement Within Passage. The static and total pressure within the passage (shown as ''4'' in Fig. 1) was measured using a miniature five-hole probe (1.67 mm probe diameter). The probe was traversed in the rotating frame (Fig. 1). The probe was connected to the ESP-32 pressure transducer array. A minimum step of 0.019 degree in the tangential direction could be achieved by a transverse mechanism in the rotating frame, which was driven by two computer-controlled step motors for radial and tangential traverses. A complete description on the calibration and the reduction of the five-hole probe data was given by Treaster and Yocum [12]. Data at four axial locations were acquired: $X=0.7$, 0.80, 0.90, and 1.10. At each axial location, seven radii were traversed in the radial direction from $H=0.75$ to $H=0.97$. At each radius, about 54 points were traversed tangentially from

Table 3 Estimated data accuracy

Relative total pressure	< 0.33%
Relative static pressure	< 0.27%
Total relative velocity	< 0.80%
Primary flow angle (degree)	+/- 1.12
Radial flow angle (degree)	+/- 2.05

the suction surface to the pressure surface. Beyond $H>0.97$, no data was acquired because the probe might make contact with the casing wall. The total pressure loss, the total pressure drop, and three velocity components (W_x, W_θ, W_r) were derived from the five-hole probe data. The relative accuracy related to the local mean values of the data is summarized in Table 3. The accuracy for the total and static pressure are based on the local dynamic pressure.

Results and Discussion

The effects of the tip clearance on the pressure distribution, the blade loading, the total pressure drop, and the total pressure loss are discussed below. Emphasis in the discussion is placed on the physics. Comparisons are made with cascade data whenever possible to clarify the effects of rotation.

Boundary Conditions at Rotor Inlet. The passage-averaged flow properties at the rotor inlet are shown in Fig. 2. The data was measured with a miniature five-hole probe by Zaccaria et al. [13]. The flow from upstream nozzles had substantial secondary flow and losses existing in the casing wall region. This is the region of concern for this study. The flow in the outer 2~3 percent of span was overturned, and the viscous layer was confined to about 5 percent of the span.

Pressure Distribution on Blade Surfaces. The pressure coefficients C_p on the suction surface and pressure surface are shown in Figs. 4*a* and 4*b*, respectively. Figure 3 shows the C_p values at mid-span and $H=0.90$ with design values. The design values were from an inviscid, Quasi-3D design code. The experimental data is time-averaged. The pressure coefficient C_p within the passage is presented in Fig. 5.

At mid-span (Fig. 3*a*), the local Reynolds number is high enough so that the design values are in good agreement with the experimental data. At $H=0.90$ (Fig. 3*b*), the flow is still mostly inviscid until mid-chord. But beyond the mid-chord, the experimental data on the suction surface is distinctly lower than the design values. This is due to the passage vortex, which is shown in Fig. 5*b*, and verified by the vorticity distribution (Fig. 1 in Part II).

The contour plots (Fig. 4*a* and 4*b*) integrate the pressure on the blade surfaces with the pressure on the casing wall ($H=1.01$) at the corresponding positions to the blade surfaces. A triangular shape with relatively low pressure dominates the blade surface above $H=0.95$ and beyond $X=0.5$ on the suction surface. This triangular shape is due to the tip clearance flow, and it is the trace of the tip leakage vortex left on the suction surface. According to Graham [2], the pressure distribution on the suction surface near the tip clearance region is very close to the pressure distribution at the mid-span if no tip leakage vortex is actually rolled up. The vorticity distribution (Fig. 1 in Part II) and static pressure distribution within the passage (Fig. 5) also prove from two different aspects that a tip leakage vortex is present. The trace of the tip leakage vortex shows the vortex starts at about mid-chord, develops with the flow as it moves downstream, and increases in size. Only one tip vortex was clearly observed in the present situation.

Similar as the Rankine vortex, the points with the lowest pressure are defined to be the core of the tip vortex in this paper. The vortex has a spanwise angle with the casing wall since the casing wall confines the development of the tip vortex in the outward direction. The angle is about 21 degrees in the present situation, which is higher than the 14 to 15 degrees observed in cascades [3]. The higher angle observed in this study is probably due to the casing wall motion. Some part of the boundary layer on the casing wall is scraped away by the blades, generating inward flow (with possible development of a scraping vortex). This interaction could convect the tip vortex downward. It should be remarked here that the boundary layer thickness at the inlet to the rotor (shown in Fig. 2) was substantial, and the tip clearance region was completely immersed in the three-dimensional casing wall boundary

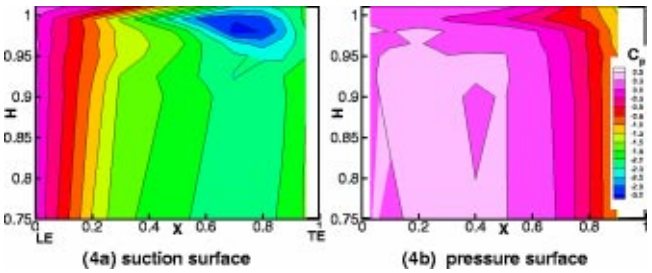

Fig. 4 Static pressure distribution (C_p) on blade surfaces, including corresponding casing wall

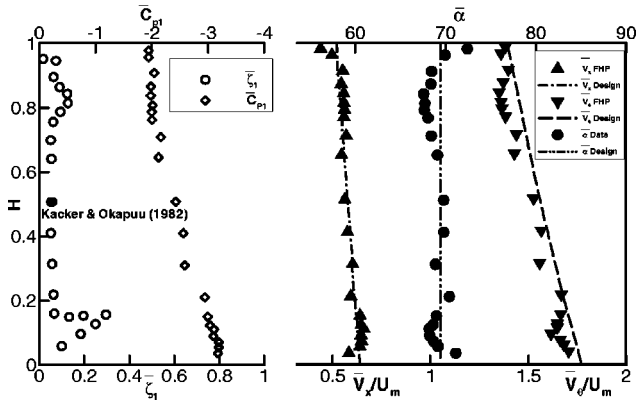

Fig. 2 Inlet properties: $\bar{C}_{pt}$, $\bar{\zeta}_1$, $\bar{V}_x/U_m$, $\bar{V}_\theta/U_m$, $\bar{\alpha}$

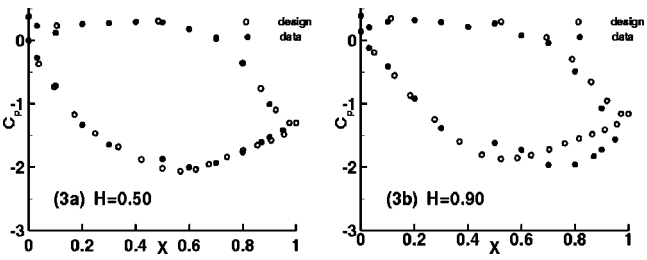

Fig. 3 Blade pressure coefficient (C_p) comparison

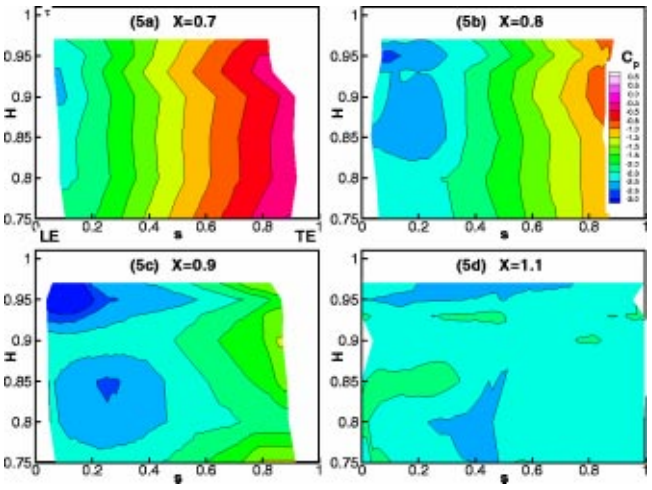

Fig. 5 Static pressure coefficient (C_p) inside rotor passage

layer. This is typical of what most real turbines encounter in practice. Other factors could also result in different angles; for example, the blade loading, the tip clearance height, the inward motion of the tip vortex due to the casing wall motion makes the five-hole probe measurement less significant in the regions very close to the casing wall, for example, in the regions above $H=0.97$. About 5 percent of blade area on the suction surface near the tip is seriously affected by the tip clearance flow. The effect extends to as much as 8 percent near the trailing edge. The minimum C_p value is at 70 percent to 75 percent axial chord from the leading edge and around 2.0 percent span from the blade tip within the region of the triangular shape. The tip vortex starts to detach from the suction surface at the point with the minimum C_p value. The minimum value is about 20 percent lower than its corresponding design value. The pressure on the pressure surface (Fig. 4*b*) is mostly in the design condition except for about 2 percent span at the tip. This 2 percent span undergoes ultra pressure drop. This ultra rapid pressure drop is due to the sharp blade edge near the corner of the pressure surface. The radius of the curvature the leakage flow undergoes as the fluid flows around the sharp edge is very small as pointed out by Bindon [4].

Pressure Distribution Within Passage. The static pressure within the passage was derived from the rotating five-hole probe data. As mentioned earlier, the tip leakage vortex was also indicated by the static pressure distribution within the passage (Fig. 5). At $X=0.7$, the flow is mostly inviscid. The tip vortex is not shown clearly because it is very small and within the region so close to the suction surface that the vortex can not be reached by the five-hole probe (Fig. 5*a*). Furthermore, the tip vortex may not be identified by the probe if the vortex is very small when compared with the probe diameter. The static pressure also indicates the passage vortex close to the suction surface.

At $X=0.8$, the tip vortex is at $H=0.95$. The size of the tip vortex is about 3 percent span in diameter. The upper edge of the vortex is at $H=0.965$, which is different from the tip vortex structure observed from cascade data, where the upper edge is usually at the same level as the blade tip. The difference is primarily due to the interaction of the casing wall and the rotation of the blades as explained earlier. The interaction generates a downward movement of the tip leakage vortex. As explained earlier, the flow field beyond $H=0.97$ can not be measured using the five-hole probe. Fortunately, the downward movement of the tip leakage vortex makes the measurement at the tip regions beyond $H=0.97$ less significant for the study of the tip leakage vortex.

At $X=0.9$, the tip vortex develops rapidly, and its size is much larger than that at $X=0.8$. The region affected by the vortex occupies nearly half the passage in width and approximately 10 percent of span in height. The tip vortex seems to have detached from the suction surface here. In addition to the tip vortex, another low-pressure region was also observed at $s=0.25$ and $H=0.85$. This low-pressure region is caused by the secondary flow and possibly a passage vortex. The low-pressure region is larger in extent than the tip vortex.

The passage vortex is located at a much lower spanwise position than the tip vortex until $X=0.9$, indicating weak interaction between these two vortices. Beyond $X=0.9$, however, the interaction between the vortices becomes strong. At $X=1.1$, the static pressure distribution indicates intense interaction among these two vortices and the blade wake. Both the leakage vortex and secondary flow diffuse rapidly downstream.

Pressure Distribution on Blade Tip and Casing Wall. The tip gaps in actual turbine rotors are usually very small and the rotational speeds of turbines are high (0.97 mm tip gap and 64 m/s relative casing wall speed for the present situation). The pressure measurement on the blade tip surface (Fig. 6) and the casing wall (Fig. 7) is therefore an easy, yet effective, way to investigate the flow inside the gap. The relative rms value to its mean is about 5.5 percent for the pressure on the casing wall. Figure 6 also presents the result from a CFD code, which will be described later.

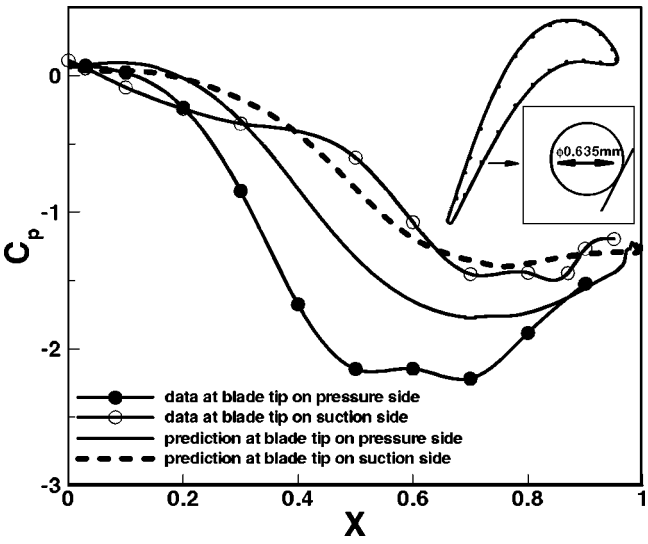

Fig. 6 C_p distribution on blade tip

The pressure at the corner between the pressure surface and the tip is so low that it is even much lower than the pressure at the corner of the corresponding suction surface (Fig. 6). The same phenomenon was found in cascade as well [3]. The ultra low pressure at the corner between the pressure surface and the tip is due to the sharp radius of the curvature the leakage flow undergoes. The sharp radius of the leakage flow could result in a converging-diverging flow path inside the tip gap. This will be discussed in more details later in the part concerning the static pressure on the casing wall. The converging-diverging flow path then suggests the possible existence of a separation bubble at the

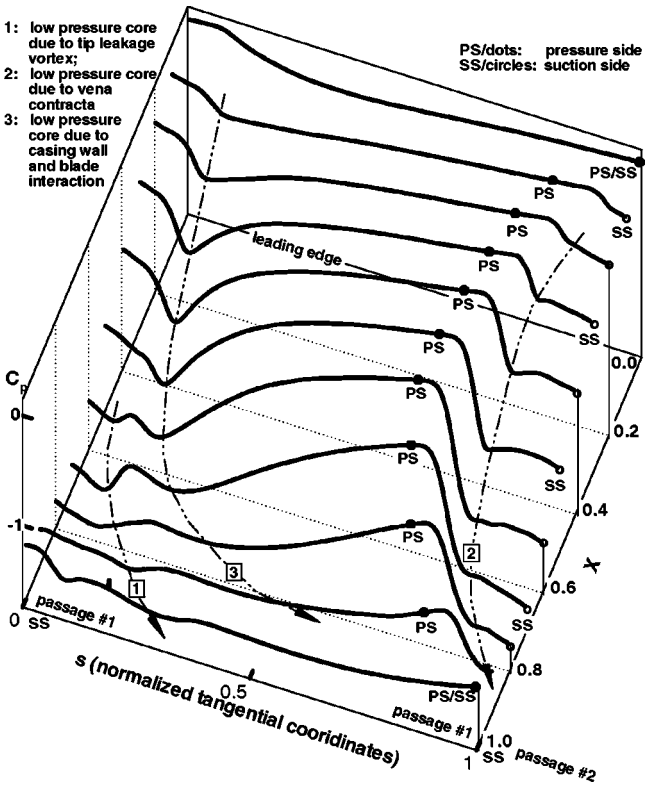

Fig. 7 Static pressure coefficient C_p on casing wall

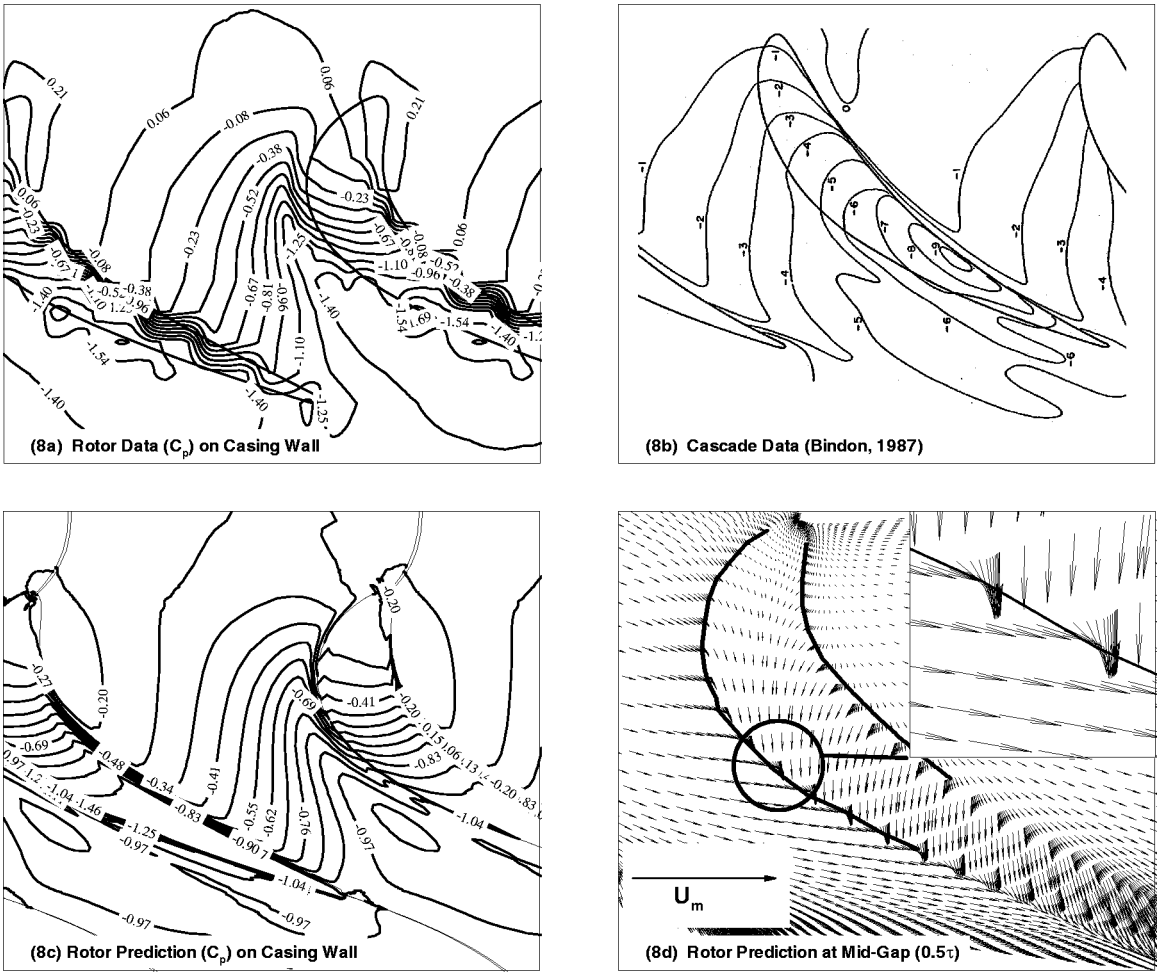

Fig. 8 Effects of moving wall

edge near the pressure surface. This has been observed in cascades [1].

Figure 7 shows the pressure distribution on the casing wall at 11 axial locations: $X=0.0$, 0.1, to 1.0. The leading edge is $X=0.0$, and the trailing edge is at $X=1.0$. The tangential coordinate was normalized with the local blade spacing. The plot for each axial location shows the data from the suction surface ($s=0$ and marked ''SS''), though the passage, to the pressure side (marked with ''PS'' and dots), through the blade tip, and to the suction side ($s=1$ and marked ''SS'') of another neighbor passage. Three low-pressure cores were found on the casing wall (Fig. 7). They are marked as ''1,'' ''2,'' and ''3,'' respectively. The low-pressure core ''1'' is the trace of the tip vortex left on the casing wall. The vortex starts at about mid-chord, as was shown by the pressure distribution on the suction surface (Fig. 4*a*). The pressure on the casing wall due to the tip leakage vortex becomes weaker beyond $X=0.7$ due to the inward movement of the vortex. The low-pressure core ''2'' might be at the converging-diverging location as suggested in the preceding text of this paper. The sharp pressure change from the pressure surface (''PS'' in Fig. 7) to the core ''2'' is caused by the converging of the path of the tip leakage flow.

The low-pressure core ''3'' is due to the interaction of the tip clearance flow and the movement of the casing wall. To clarify the moving wall effect, Fig. 8*a*[1] shows again the casing wall pressure distribution in contour plot compared with the cascade data (Fig. 8*b*, tip clearance height was 1 percent chord), which is typical for cascades. No low pressure core similar to core ''3'' was observed at the corresponding position in cascade. Instead, the cascade shows a rather smooth pressure distribution on the casing wall across this region.

The difference of the casing wall pressure in rotor and cascades can be explained on the basis of the velocity vectors at the mid-height of tip gap shown in Fig. 8*d*. These vectors were the result of a numerical simulation using a Navier-Stokes solving CFD code described by Luo et al. [15], but the present case used more grid lines (78 grid lines) in the spanwise direction and an algebraic Reynolds stress turbulence model. The casing wall pressure from the simulation is shown in Fig. 8*c*, and is in good agreement with the data (Fig. 8*a*). The predicted velocity field at the mid-height (Fig. 8*d*) indicates the flow is complicated near both the pressure and suction side of the tip gap. Near the tip at the suction side, the boundary layer on the casing wall is predominately tangential (relative to blade) in direction, and merges with the gap flow. The gap flow tends to move down the suction surface as it exits. The blade scrapes the casing boundary layer flow, which then moves downward near the suction surface. Therefore, these counter rotation flow fields result in low pressure (marked with ''3'' in Fig. 7). In contrast, the flow near the exit in cascades is much smoother since there is no wall motion. Therefore, there is no opposing flow near the casing wall and the pressure distribution from the suction surface to the pressure surface is very smooth. This is one of the major differences. The low-pressure

[1]The ''wave shape'' near the pressure side was generated from plotting software due to large length ratio of measurement grid in axial and tangential direction. It is not physics. There is no such ''wave shape'' in original data Fig. 7

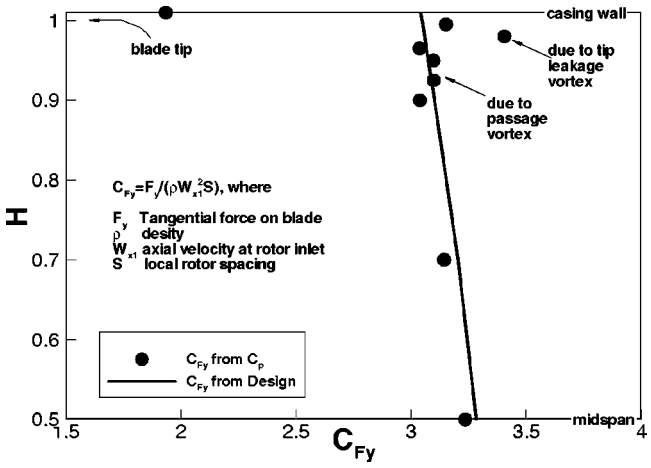

Fig. 9 Tangential force coefficient (C_{Fy}) along blade height

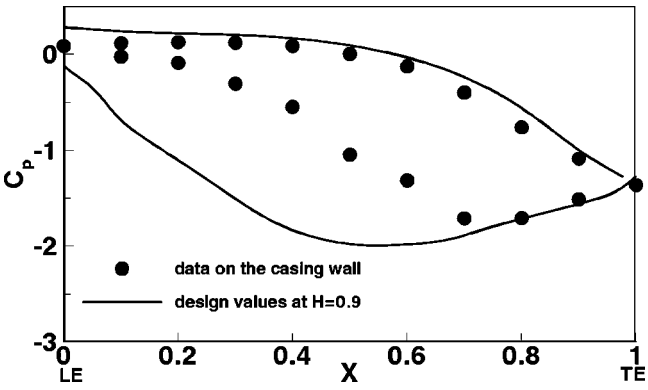

Fig. 10 Pressure coefficients on the casing wall (at the corresponding positions to the pressure surface and suction surface)

core ''3'' may tend to induce more tip leakage flow and cause more losses since it tends to increase the pressure difference across the tip gap.

The tangential position of the low-pressure core ''3'' does not change much from the leading edge until the mid-chord. It lies at about 10 percent of the local blade spacing from the suction surface. Beyond the mid-chord, the core ''3'' starts to deviate away from the suction surface due to the onset of the leakage vortex. The leakage vortex has a blockage effect on the passage flow, since the axial velocity within the leakage vortex is lower than that outside the vortex.

Blade Loading. It has been pointed out in the foregoing text that the tip clearance flow and vortex affect the pressure distribution on the blade surfaces near the tip region. In turbines, the tangential force per unit blade height (F_y) is directly proportional to power output per blade height. The F_y can be calculated by integrating the blade static pressure over the whole blade chord with unit height and then projecting the integration along tangential direction. The tangential force coefficient C_{Fy} is calculated by the formula: $C_{Fy}=F_y/(\rho W_{x1}{}^2 S)$, where S is the local blade spacing. The results are shown in Fig. 9 with the design values, which were calculated from blade geometry. The difference between the data and design values indicates the blade force defect due to viscous effects and the tip clearance.

Near the mid-span, the viscous effects on the tangential force are almost negligible (Fig. 9). In the region near $H=0.92$, the flow is dominated by the passage vortex, the tangential force varies slightly. The measured loading coefficient at some height is larger than the design values, and is smaller than the design values at another height. This variation is due to the passage vortex, which causes the flow to be overturned near the upper half of the passage vortex, and underturned near the lower half of the passage vortex.

As observed in Fig. 4*a*, the tip vortex results in a low-pressure region on the suction surface. The lowered pressure increases the blade loading near the tip since the tip clearance flow has little effect on the flow on the pressure surface. The blade loading is increased nearly 5 percent with respect to the design values. Near and above the upper half of the tip vortex, the tangential force coefficient decreases again. The upper half of the tip vortex decreases the flow turning angle. At the height very close to the blade tip, the pressure on the pressure side tends to decrease rapidly, and the pressure on the suction side tends to restore to the corresponding design values from a low pressure due to the leakage vortex. Both of these changes in pressure distributions on blade surfaces act to decrease the blade loading coefficient dramatically near the blade tip.

The last data point represents the effective tangential force coefficient on the casing wall. The effective tangential force is derived from the pressure distribution measured on the casing wall (Fig. 10). The decrease is substantial (40 percent decrease from the design value) and represents the effect of the viscous layers on the casing. However, the loading coefficient on the casing wall is still considerable. The low pressure core ''3'' (Fig. 7) may have a small contribution to the considerable value of the blade loading coefficient on the casing wall. Yaras et al. [5] also reported that pressure difference on the casing wall was comparable with the pressure difference on blade in cascades.

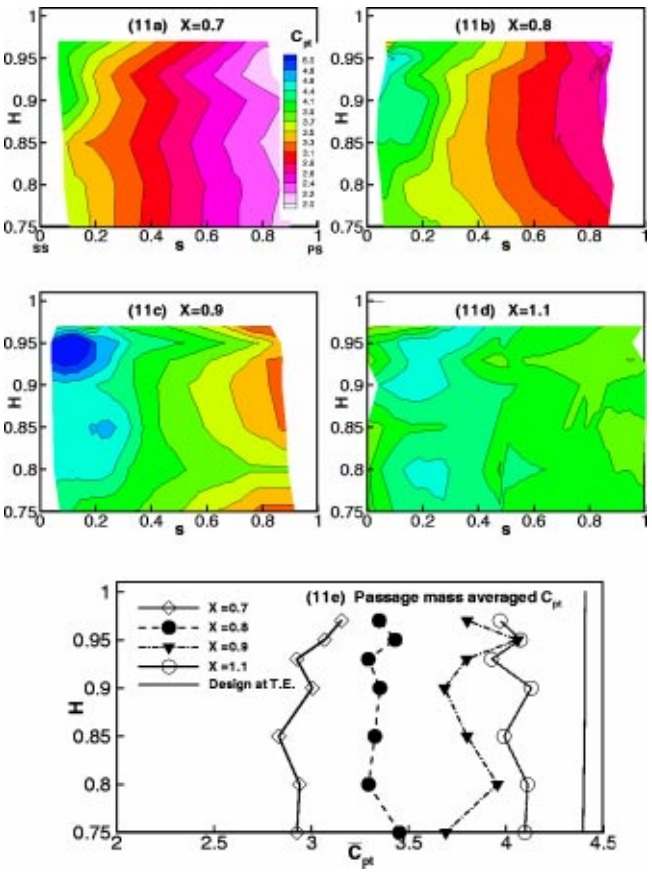

Fig. 11 Development of total pressure drop coefficient (C_{pt})

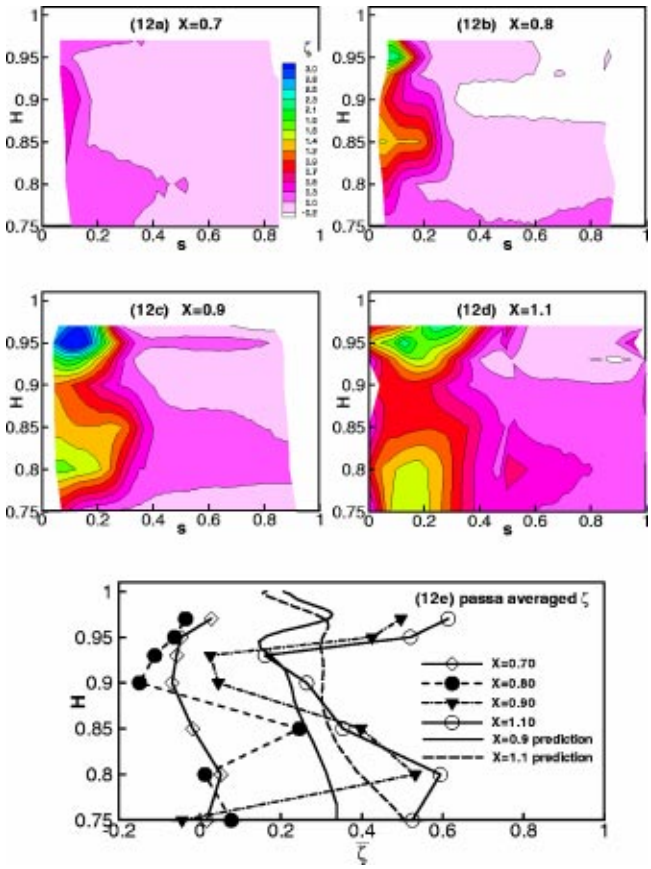

Fig. 12 Development of total pressure loss coefficient (ζ)

Development of Total Pressure Drop. Figure 11*a–d* shows the total pressure drop coefficients C_{pt} in contour plots at various axial locations. The C_{pt} is based on the total pressure in the absolute frame.

The flow is mostly main stream within the measured region at $X=0.7$. The passage vortex causes a higher total pressure drop in the region at $H=0.90$. As the flow moves downstream to $X=0.8$ and 0.9, the passage vortex spreads as it entrains low velocity fluid from the boundary layer on the suction surface.

A high pressure drop region due to the tip leakage vortex also spreads out substantially as the flow moves downstream. At $X=0.9$ chord, the total pressure drop varies rapidly in the tip vortex region as the tip leakage vortex entrains low momentum fluid from the leakage flow and from the boundary layers on the blade and casing wall.

Downstream of the blade at $X=1.1$, the pressure drop becomes uniform as the secondary and leakage flows diffuse and dissipate.

It should be mentioned here that the higher total pressure drop in the leakage vortex and secondary vortex regions is achieved through viscous and turbulent dissipation, and associated with this is the higher losses in total pressure and lower efficiency. The passage mass-averaged values of C_{pt} are also plotted in Fig. 11*e*. As indicated earlier, the tip clearance region (near 95 percent span) and secondary flow region (near 80 percent span), show a higher pressure drop. The measured pressure drop near the trailing edge is generally lower than the design values due to viscous, leakage flow, and secondary flow losses.

Development of Total Pressure Loss. Figure 12 shows the distribution of the total pressure loss coefficient (ζ). Figure 12*e* is the total pressure loss coefficients mass-averaged circumferentially.

At $X=0.7$, the small loss region observed near the blade tip suction corner is mainly due to the blade motion. These losses are probably also due, in a small part, to the tip clearance flow close to the blade surface. The tip clearance flow losses are very small at $X=0.7$. Higher losses from the passage vortex are also seen around $H=0.90$ as it interacts with the blade boundary layer fluid.

At $X=0.8$, the contour plot of the loss coefficient shows the effects of the secondary flows from $H=0.80$ and 0.90 on the suction side. Large losses are observed in this area, and are caused by the mixing of the passage vortex with the main flow. The vortex entrains the low momentum fluid from the blade boundary layer causing it to mix further away from the blade resulting in much higher total pressure losses in the vortex region. The losses then decrease around $H=0.90$ as the effects of the secondary flow decay. The relative total pressure losses at $H=0.90$ return to the previous values that they were in the boundary layer flow unaffected by the secondary flow. Figure 11 also shows an increase in the total pressure drop due to the passage vortex at $H=0.85$. In moving towards the tip, $H=0.93$ through $H=0.97$, the contours show substantially larger losses due to complex interactions between the casing boundary layer and tip clearance flow. The losses due to the leakage flow at $X=0.8$ around $H=0.95$ increases dramatically compared to those at $X=0.7$. The highest relative total pressure losses were observed in the region of the tip leakage vortex at $H=0.95$ and $H=0.97$. The losses here are nearly twice as high as the losses observed near the secondary passage vortex region at $H=0.85$, indicating a relatively stronger leakage flow in the tip region. The tip clearance flow acts to sweep the low momentum fluid from the casing wall to the suction side. It can be seen that the tip leakage has a major impact on the flow near the blade tip. This impact is shown to be stronger than that of the passage vortex. At $X=0.8$, the losses due to the passage and tip leakage vortices are clearly separated. The losses due to the passage vortex occupy about 10 percent span (from $H=0.75$ to 0.90), and about 25 percent blade spacing. The tip leakage losses occupy the outer 7 percent span and about 20 percent blade spacing.

At $X=0.9$, the losses due to these two vortices become dramatically larger than those at $X=0.8$ and occupy larger regions in the blade passage. The passage vortex losses occupy approximately 15 percent span and about 28 percent blade spacing. The pressure loss due to the tip clearance flow increases significantly and spreads out into the passage. The tip leakage vortex losses occupy the last 9 percent span of the blade and about 25 percent blade spacing. The losses from the tip leakage and passage vortices are moving closer together and are beginning to merge. This location is where the tip leakage vortex is strongest, and it is observed that the tip leakage vortex causes significantly higher losses than the passage vortex at this location.

The dramatic increase in total pressure loss in the last 20 percent blade chord compares well with the results for a cascade presented by Bindon [7]. Bindon found that the mixing losses from the leakage flow in the rotor passage start to rise significantly after $X=0.8$, and the losses increase about eight times over the last 20 percent of the blade chord. Part II of this paper will show that the losses due to the leakage flow are primarily mixing losses showing agreement with Bindon [7].

Downstream of the blade, the loss contour at $X=1.1$ shows the losses from the two vortices spreading out and weakening. The losses from the tip leakage vortex diffuses quickly after $X=0.9$ due to the decay of the vortex and interactions of the leakage vortex with blade wake, casing boundary layer, and the counter-rotation passage vortex. Also, the pressure difference across the blade tip, which drives the tip clearance flow, becomes insignificant after $X=0.9$, interrupting the development of the vortex and allowing it to weaken. The losses from the passage vortex appear to increase slightly downstream of the blade trailing edge. Mixing of the flow downstream of the blade and turbulence mixing could cause this. The losses at $H=0.90$ increase downstream of the blade as the tip leakage vortex begins to interact with the counter-rotating passage vortex.

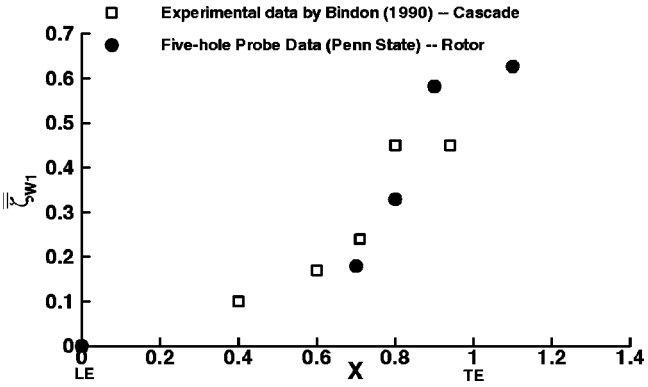

Fig. 13 Area integrated mass averaged loss coefficient

It is seen that the secondary flow vortices account for much of the losses in the blade passage (Fig. 12*e*). Up to $H=0.70$, the losses are mainly due to the profile boundary layer and wakes. Examining the losses in the wake region at $H=0.75$ through $H=0.85$, the relative total pressure losses are high due to the presence of the passage vortex. The losses measured at $X=1.1$ include the losses due to the blade wake due to turbulent dissipation, as well as losses from the mixing and dissipation of the passage vortex.

The losses decrease around $H=0.90$ as the effects of the passage vortex near $H=0.80$ decay. The losses in this region are caused by the turbulent dissipation from the boundary layer and wake alone. In the tip region from $H=0.95$ to $H=0.97$, the losses are much higher due primarily to the tip leakage vortex. The contributions to the losses include the turbulent dissipation of the blade boundary layer and wake, turbulent mixing and dissipation of the tip leakage vortex, dissipation in the casing boundary layer, and the interaction of the vortex with the casing boundary layer.

As the flow moves downstream, the losses from the tip leakage vortex and passage vortex increase. The vortices also spread out as they move downstream. The losses at $H=0.90$ increase at $X=1.1$ as the tip clearance vortex and passage vortex begin to interact.

The development of the loss within the passage is indicated by the mass averaged loss coefficient $\bar{\bar{\zeta}}_{w1}$ in Fig. 13. The mass averaged loss coefficient was normalized using inlet dynamic pressure. A comparison is made between the measured data for the rotor presented in this paper and the measured data from a cascade [16]. The measured data for both the cascade and the rotor losses were only integrated over the last 25 percent of the blade at the tip and did not include the effects of blade and end wall boundary layer. These layers are relatively thin, so they do not significantly affect the value of the integrated losses. So Fig. 13 shows the development of the tip clearance losses as the flow moves downstream in the blade passage. Both the measured cascade and rotor data show a similar trend where the losses rise sharply in the last 20 percent of the chord. The losses are higher in the rotor (beyond $X=0.8$) due to larger flow turning and the relative motion between the rotor and casing.

Conclusion

Some of the important conclusions based on the measurements reported in this paper are as follows:

1 The tip clearance flow originates near the mid-chord on the suction surface, interacts with the main stream, and rolls up into a leakage vortex. Beyond $X=0.9$, the diffusion effect dominates the development of the vortex. The vortex affects the flow fields up to about 10 percent span near the end wall region beyond the mid-chord. At radial locations below 10 percent span from the blade tip, the flow field is primarily inviscid except for the presence of a passage vortex.

2 The tip vortex core moves inward in the spanwise direction at an angle of about 21 degrees with the blade tip surface, This angle is much larger than that observed in turbine cascades, probably due to the casing wall movement.

3 The movement of the casing wall in turbine rotors has significant effect on the flow field near the tip corner of the casing wall and the suction side. The casing wall boundary layer and the relative motion oppose the tip clearance flow near the suction side. These two streams interact and form a low-pressure region and a possible scraping vortex. This low pressure region may increase the flow velocity of the tip leakage. This is not observed in turbine cascades due to the absence of relative wall motion.

4 The pressure near the corner of the pressure surface is very low due to the sharp radius of the curvature the leakage flow undergoes as observed in cascades. A converging-diverging flow path inside the tip gap probably exists based on the pressure distribution on the casing wall.

5 The tip leakage vortex has no significant effect on the blade loading near the tip clearance region. The local tangential force coefficient increases slightly in the region where the tip leakage vortex core is located.

6 The interaction between the tip vortex and passage vortex is weak and these two vortices are distant until about $X=0.9$. Beyond $X=0.9$, these two vortices tend to merge together and interact strongly causing appreciable loss.

7 A high total pressure loss coefficient is observed in the region of the tip leakage vortex between $H=0.95$ to $H=0.97$. The loss coefficient here is nearly twice as high as the loss coefficient observed near the secondary passage vortex region at $H=0.80$. But the loss region is substantially wider in the passage vortex region, and the tip clearance losses are confined to a small region near the tip.

The work presented in this paper is applicable to reduce the effects of the tip clearance flow in axial turbine rotors. One important aspect of the tip leakage vortex needing more study is the unsteady behavior, including the effects of the upstream nozzles.

Acknowledgments

This work was sponsored by the U.S. Army Research Office under the Grant DAAH04-95-1-0179 with Dr. T. Doligalski as the technical monitor. The second author was supported by the U.S. Army Research Office AASERT Grant DAAG55-97-1-0201, with Dr. T. Doligalski as the technical monitor.

Nomenclature

C_x = Axial chord length
C_{Fy} = Tangential force coefficient $=F_y/(\rho W_{x1}{}^2 S)$
C_p = Pressure coefficient on rotor blade surface $=(P-\bar{P}_1)/(0.5\rho U_m^2)$
$\bar{C}_{p1}$ = Pressure coefficient at nozzle exit $=(\bar{P}_1-\bar{P}_{t0})/(0.5\rho U_m^2)$
C_{pt} = Total pressure drop coefficient $=(\bar{P}_{t1}-P_t)/(0.5\rho U_m^2)$
$\bar{C}_{pt}$ = Pitchwise mass-averaged C_{pt} over passage
F_y = Force on rotor in tangential direction per unit height
H = Relative spanwise coordinate (0 at hub, 1 at tip)
P = Static pressure
P_t = Total pressure in absolute frame
P_{tr} = Total pressure in rotation frame
S = Local blade spacing
U_m = Blade rotation speed at mid-span
V = Absolute velocity
W = Relative velocity in rotation frame
X = Axial coordinate normalized with axial chord C_x

s = Pitchwise coordinate normalized with local blade spacing (0 suction surface, 1 pressure surface)

$\overline{\alpha}$ = Pitchwise mass-averaged absolute flow angle at nozzle exit

ρ = Density of fluid

τ = Tip clearance height

ζ = Total pressure loss coefficient $=(\overline{P}_{tr1}-P_{tr})/(0.5\rho U_m^2)$

$\overline{\zeta}$ = Pitchwise mass-averaged total pressure loss coefficient $=(\overline{P}_{tr1}-\overline{P}_{tr})/(0.5\rho U_m^2)$

$\overline{\zeta}_1$ = Pitchwise mass-averaged total pressure loss coefficient at the exit of nozzle $=(\overline{P}_{t0}-\overline{P}_{t1})/(0.5\rho U_m^2)$

$\bar{\bar{\zeta}}_{W1}$ = Mass-averaged and passage-averaged (from pressure surface to suction surface, and from $H=0.75$ to 0.97) total pressure loss coefficient normalized with respect to the rotor inlet relative dynamic pressure $0.5\rho W_1^2$

Superscript

$\overline{\ }$ = Pitchwise mass-averaged value. For example:

$$\overline{C}_{pt}=\left(\int_{\theta_{ps}}^{\theta_{ss}} C_{pt}\rho W_x r\,d\theta\right)\Big/\left(\int_{\theta_{ps}}^{\theta_{ss}} \rho W_x r\,d\theta\right)$$

Subscript

0,1,2 = Nozzle inlet, rotor inlet, and rotor outlet, respectively

m = Midspan

r,θ,x = Components in radial, tangential, and axial directions, respectively

References

[1] Sjolander, S. A., 1997, ''Overview of Tip-Clearance Effects in Axial Turbines,'' VKI Lecture Series 1997-01, ''*Secondary and Tip-Clearance Flows in Axial Turbines*,'' Directed by Sieverding, C.H., the Von Karman Institute for Fluid Dynamics, Belgium.

[2] Graham, J. A. H., 1986, ''Investigation of a Tip Clearance Cascade in a Water Analogy Rig,'' ASME J. Eng. Gas Turbines Power, **108**, pp. 38–46.

[3] Sjolander, S. A., and Amrud, K. K., 1987, ''Effects of Tip Clearance on Blade Loading in a Planar Cascade of Turbine Blades,'' ASME J. Turbomach., **109**, pp. 237–244.

[4] Bindon, J. P., 1987, ''Pressure Distributions in the Tip Clearance Region of an Unshrouded Axial Turbine as Affecting the Problem of Tip Burnout,'' ASME Paper No. 87-GT-230.

[5] Yaras, M., Zhu, Y., and Sjolander, S. A., 1989, ''Flow Field in the Tip Gap of a Planar Cascade of Turbine Blades,'' ASME J. Turbomach., **111**, pp. 276–293.

[6] Yamamoto, A., Matsunuma, T., Ikeuchi, K., and Outa, E., 1994, ''Unsteady Endwall/Tip-Clearance Flows and Losses due to Turbine Rotor-Stator Interaction,'' ASME Paper No. 94-GT-461.

[7] Bindon, J. P., 1989, ''The Measurement and Formation of Tip Clearance Loss,'' ASME J. Turbomach., **111**, pp. 257–263.

[8] Yaras, M., and Sjolander, S. A., 1989, ''Losses in the Tip-Leakage Flow of a Planar Cascade of Turbine Blades,'' AGARD-CP-469, ''*Secondary Flows in Turbomachines*,'' Paper 20.

[9] Yamamoto, A., Tominaga, J., Matsunuma, T., and Outa, E., 1994, ''Detailed Measurements of Three-Dimensional Flows and Losses Inside an Axial Flow Turbine Rotor,'' ASME Paper No. 94-GT-348.

[10] Peter, D. W., and Moore, J., 1995, ''Tip Leakage Loss Development in a Linear Turbine Cascade,'' AGARD-CP-571, ''*Loss Mechanisms and Unsteady Flows in Turbomachines*,'' Paper 12.

[11] Lakshminarayana, B., Camci, C., Halliwell, I., and Zaccaria, M., 1996, ''Design and Development of a Turbine Research Facility to Study Rotor-Stator Interaction Effects,'' International Journal of Turbo and Jet Engines, **13**, pp. 155–172.

[12] Treaster, A., and Yocum, A. M., 1979, ''The Calibration and Application of Five-Hole Probes,'' ISA Trans., **18**, pp. 23–34.

[13] Zaccaria, M., and Lakshminarayana, B., 1995, ''Investigation of Three Dimensional Flow Field at the Exit of a Turbine Nozzle,'' J. Propul. Power, **11**, No. 1, pp. 55–63.

[14] Kacker, S. C., and Okapuu, U., 1982, ''A Mean Line Prediction Method for Axial Flow Turbine Efficiency,'' ASME J. Eng. Gas Turbines Power, **104**, pp. 111–119.

[15] Luo, J., Lakshminarayana, B., 1997, ''Three-Dimensional Navier-Stokes Analysis of Turbine Rotor and Tip-Leakage Flowfield,'' ASME Paper No. 97-GT-421.

[16] Bindon, J. P., 1990, Private Communication.

Tip Clearance Effects in a Turbine Rotor: Part II—Velocity Field and Flow Physics

Andrew A. McCarter
Graduate Assistant

Xinwen Xiao
Graduate Assistant

Budugur Lakshminarayana
Evan Pugh Professor and Director
e-mail: b1laer@engr.psu.edu

Center for Gas Turbines and Power,
Pennsylvania State University,
153-J Hammond Bldg.
University Park, PA 16802

A comprehensive experimental investigation was undertaken to explore the flow field in the tip clearance region of a turbine rotor to understand the physics of tip leakage flow. Specifically the paper looks at its origin, nature, development, interaction with the secondary flow, and its effects on performance. The experimental study was based on data obtained using a rotating five-hole probe, Laser Doppler Velocimeter, high-response pressure probes on the casing, and static pressure taps on the rotor blade surfaces. The first part of the paper deals with the pressure field and losses. Part II presents and interprets the vorticity, velocity, and turbulence fields at several axial locations. The data provided here indicates that the tip leakage vortex originates in the last half chord. The leakage vortex is confined close to the suction surface corner near the blade tip by the relative motion of the blade and the casing, and by the secondary flow in the tip region. The tip leakage flow clings to the blade suction surface until midchord then lifts off of the suction surface to form a vortex in the last 20 percent of the blade chord. The relative motion between blades and casing leads to the development of a scraping vortex that, along with the secondary flow, reduces the propagation of the tip leakage flow into the mainflow. The rotational effects and coriolis forces modify the turbulence structure in the tip leakage flow and secondary flow as compared to cascades.
[DOI: 10.1115/1.1368365]

Introduction

This paper is Part II of a two-part paper on the investigation of the pressure and velocity flow fields in the tip region of a 1-1/2 stage turbine rotor. The pressure data acquired on the blade surface, casing, and inside the rotor passage are presented and interpreted in Part I of this paper [1]. The flow losses are also covered in Part I. This paper deals with the velocity field and flow physics in the tip region of the turbine rotor based on the data acquired using a rotating five-hole probe and Laser Doppler Velocimeter (LDV) system.

Very little information is available in the open literature on the development of tip leakage flow inside the blade passages of turbine rotors. Most of the current knowledge on the development and physics of tip leakage flows in turbines has come from cascade testing. There has been no systematic investigation of tip clearance flow field development in rotating turbine rotors. This is the objective of the current research. It is anticipated that leakage flows and vortices in a rotor will be substantially different from those in a cascade due to the effects of centripetal and corriolis forces as well as the relative motion between the blade tips and endwall.

In studies by Yaras and Sjolander [2,3] and by Graham [4] the relative motion between the blade and endwall was simulated in a cascade using a moving belt. Their work identified the formation of the scraping vortex and discussed significant changes in the structure of the tip leakage and passage vortices due to their interaction with the scraping vortex. They also found a reduction in the leakage mass flow through the gap in a turbine due to the opposing relative motion. Yamamoto et al. [5,6] studied the development of loss mechanisms in turbine rotors and found similar loss generation processes in rotors and stators. Recent investigations in a compressor rotor by Lakshminarayana et al. [7] and Stauter [8] suggest that the leakage flow diffuses before it has had a chance to roll up into a discrete vortex. Morphis and Bindon [9] compared results of the losses due to tip leakage flows downstream of a cascade and rotor. They found the secondary flows behave differently in a rotor than in a cascade. The leakage flow behaved more like a flat wall jet in a rotor rather than the tip leakage vortex observed in the cascade. These results have not been reproduced in other experiments. It is anticipated that the data obtained inside the rotor passage will be valuable in defining the physics of the tip leakage flow such as its nature, development, interactions with secondary flows, and its effects on the main flow. The data will be valuable in assessing computer codes for their ability to predict this complex flow field. The flow physics derived from the collected data will also be used to design blades that reduce the effects of tip clearance flows.

Experimental Facility and Instrumentation

This research was performed using the Axial Flow Turbine Research Facility at the Pennsylvania State University. This facility represents the features of a current or near-future high-pressure turbine stage. The rotor tip radius is 0.4583 meters, the hub to tip ratio is 0.7269, and the tip axial chord (C_x) is 0.088 meters. The facility operates at 1300 rpm. The rotor tip clearance is 0.98 mm. A description of the facility, instrumentation, and rotating five-hole probe, is described in Part I of this paper and in Lakshminarayana et al. [10]. The LDV system is described in this paper.

The time-averaged velocity and pressure fields in the outer 25 percent of the blade span were measured using a rotating five-hole probe with a 1.67 mm tip diameter. This allowed a study of the tip leakage flow and passage vortex. Measurements were taken at 7 radial locations at H=0.75, 0.80, 0.85, 0.90, 0.93, 0.95, and 0.97.

Approximately 54 data points were taken in the tangential direction (blade-to-blade) at each radial location. All five-hole probe data was measured between the same two rotor blades with a tip clearance of 0.98 mm. All measurements were taken with the turbine operating at peak conditions.

The instantaneous velocity fields in the last 20 percent of the blade near the tip clearance region were also acquired using a three-dimensional Laser Doppler Velocimeter (LDV). This region includes the tip leakage vortex, and most of the upper passage

Contributed by the International Gas Turbine Institute and presented at the 45th International Gas Turbine and Aeroengine Congress and Exhibition, Munich, Germany, May 8–11, 2000. Manuscript received by the International Gas Turbine Institute February 2000. Paper No. 2000-GT-477. Review Chair: D. Ballal.

vortex. Eight radial measurement stations were exponentially distributed along the outer 20 percent of the span at H=0.80, 0.846, 0.883, 0.913, 0.936, 0.955, 0.970, and 0.983, respectively. The LDV data provides turbulence intensities and shear stresses along the intrinsic coordinate system: stream wise ''s,'' binormal wise ''n,'' and radial wise ''r.'' Local total relative velocity is used to normalize these turbulence intensities and shear stresses. Ristic et al. [11] has described the data processing methods. The accuracy of the LDV turbulence intensity data is 1.5 percent.

LDV System. The LDV system is a three-color crossbeam system (TSI model 9100-12). The light source is a 7-W argon-ion laser operating in multiline mode. The laser beams enter the flow field through flat glass window 1-1/2 inches high on the turbine casing. The blue and green light beams are introduced into the flow field in one optical rail to sample the axial and tangential components of velocity. The violet beam is arranged in another optical rail at an angle of 27.8 degrees from the perpendicular to measure the radial component. Frequency shifting of 40 MHz is used to reduce the fringe bias and to solve the directional ambiguity. Shifting is accomplished by passing one of the two crossing beams through a Bragg cell. The flow field is seeded with propylene glycol particles generated by a six-jet atomizer. The particles have a nominal mean size of about 0.6 μm.

A Dostek model 1400 A personal computer based system records the three velocity component data along with the rotor orientation from a shaft encoder (6000 pulses per revolution, clocking 1 pulse per revolution triggering). All measurements are acquired with the facility operating at peak efficiency. The data reduction is accomplished by ensemble averaging according to the recorded rotor orientation. The entire rotor is discretized into 1450 bins (windows) (50 per blade passage) and the corresponding measurements are averaged over the individual bins to yield the ensemble-averaged velocity.

The intrinsic coordinate system (s, n, and r) is used to derive the turbulence intensities and stresses. This provides valuable information on the stresses in the streamwise and radial directions. The s coordinate is aligned with the design flow angle.

Experimental Results

The secondary flow vectors provide valuable insight into the nature of leakage and secondary flows. The secondary flow vectors were derived using Eq. 1. The projection of this vector in the r-θ plane are shown in Fig. 1 for X=0.7, 0.8, 0.9, and 1.10.

$$\vec{W}_{\text{sec}} = (\vec{W})_{measured} - (\vec{W})_{design} \tag{1}$$

The axial component of vorticity was calculated from the measured five-hole probe data using the velocity gradients in the radial and tangential directions. The axial vorticity was calculated using Eq. 2.

$$\frac{\omega_x}{\Omega} = \left[\frac{I}{r} \frac{\partial (r W_\theta / U_m)}{\partial r} - \frac{\partial (W_r / U_m)}{r \partial \theta} \right] r_m \tag{2}$$

The five-hole probe measurement grid is very coarse in the axial direction; hence the strength of the total secondary vorticity cannot be derived from this data. The data was interpolated at 6 radial locations in between the measured 7 radial locations in order to make the measurement grid fine enough in both the tangential and radial direction (50 points by 13 points, respectively) to accurately derive the axial vorticity component. The axial vorticity component is a good measure of the total secondary vorticity; hence it is plotted and interpreted in this section. The contour plots of axial vorticity are shown in Fig. 1. Positive values represent counter-clockwise rotation.

The vorticity in the main flow is very small. Along the suction side, the flow field is very complex due to interactions of the leakage flow, secondary flow, and blade motion. In Fig. 1, the clockwise (negative) scraping vortex (labeled S.V.), counter-clockwise (positive) tip-leakage vortex (labeled T.L.), and clockwise (negative) passage vortex (labeled P.V.) are identified. The centers of these vortices are marked with circles in Fig. 1. The same coordinates are marked in subsequent figures for reference.

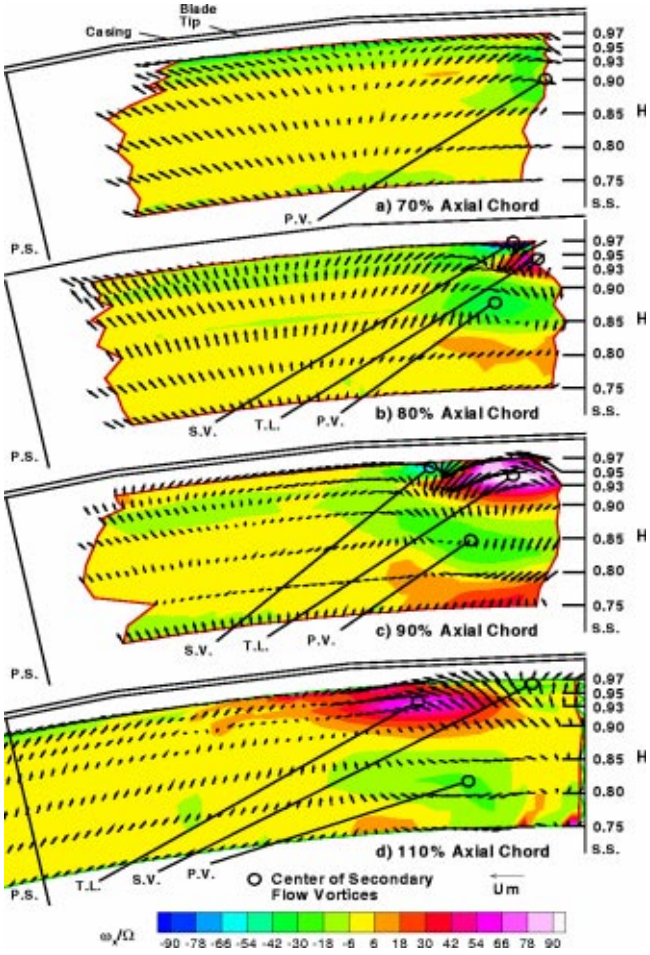

Fig. 1 Relative secondary velocity vectors (W_{sec}) with axial vorticity (ω_x/Ω) in background

Contour plots of the loss coefficient, total relative velocity, axial velocity, relative tangential velocity, and relative primary flow angle derived from the five-hole probe, are presented in Figs. 2, 3, 4, 5, and 6, respectively. The velocity profiles show that the flow is predominantly inviscid away from the suction surface.

Passage Vortex. The passage vortex displays a clockwise flow and occupies a large part of the passage. Data at 80 percent, 90 percent and 110 percent axial chord shows an inward flow along the blade suction surface from H=0.75 to H=0.90 (Fig. 1). This inward flow occurs as the low velocity fluid in the blade boundary layer is entrained into the passage vortex where it is mixed with flow further out in the passage. The mixing of this low velocity fluid is responsible for much of the losses associated with the passage vortex presented in Fig. 2.

In Fig. 1(*a*) the major feature observed at 70 percent chord is the presence of the passage vortex which is already well developed and is centered at 91 percent span. Compared to the main passage flow, the flow field at 70 percent chord near the suction surface corner has higher relative tangential velocity (Fig. 5), flow over turning (Fig. 6), and lower axial velocity (Fig. 4). The secondary flows act as a blockage to the mainstream flow resulting in higher axial velocities in the region around H=0.85 away from the suction surface.

As the passage vortex moves downstream to 80 percent chord the vorticity has increased substantially and its influence spreads

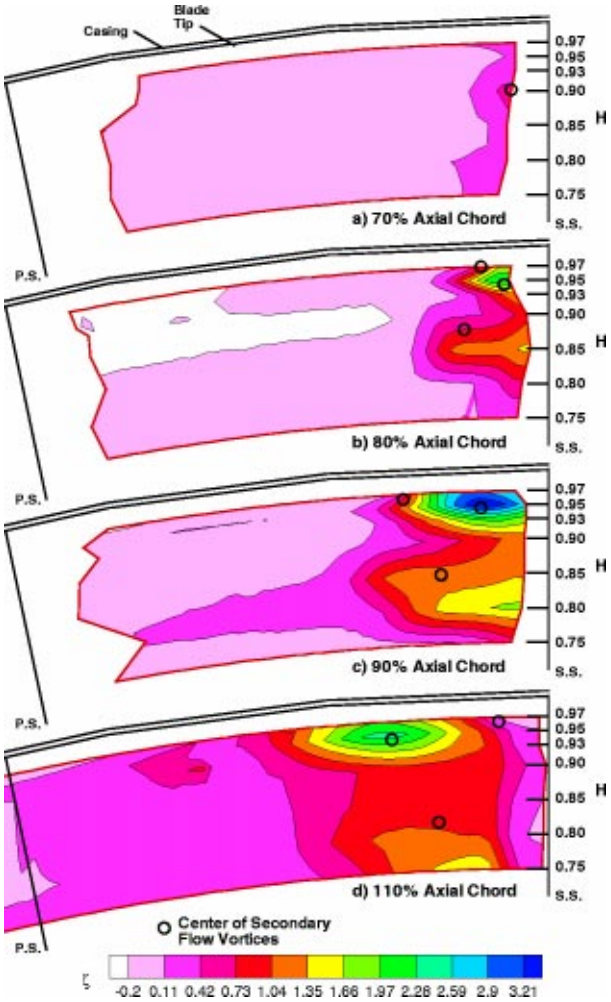

Fig. 2 Loss coefficient (ζ) in rotor passage

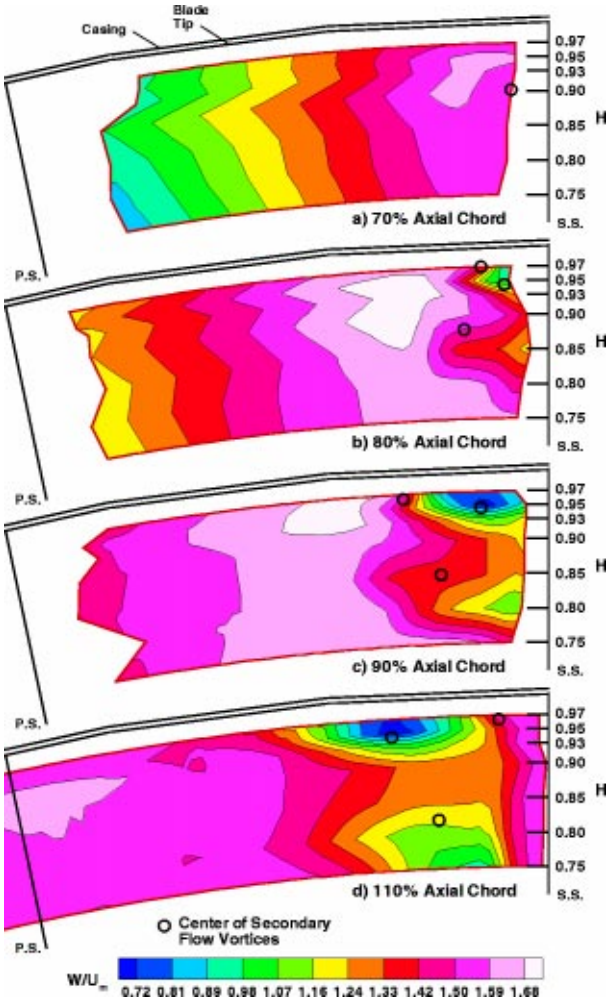

Fig. 3 Relative total velocity (W/U_m) in rotor passage

out to 85 percent span. This secondary vortex is confined to about 20 percent of the passage from the suction surface due to blade motion. This feature is substantially different from flows observed in cascades. The leakage flow begins to develop at 80 percent chord and interacts with the passage vortex pushing it inwards along the span. At 80 percent chord, the leakage vortex and the secondary vortex introduce a more dramatic blockage effect to the main flow than observed upstream. This results in substantial acceleration of W and W_x in the region of H=0.80 to 0.95 and about 20 percent blade spacing away from the blade suction surface. The secondary flow and the associated mixing with the blade boundary layer causes substantial dissipation of kinetic energy, resulting in decreased relative velocity, and losses in this region (Fig. 2). The secondary flow area shows the reduced tangential velocity and higher radial velocity (caused by the vorticity) near the suction surface (Figs. 5 and 1). The tangential velocity variations then decrease around H=0.90 as the effects of the secondary flow decays.

At 90 percent chord the secondary flow shows substantial growth and influences a much larger region. This is evident from substantial overturning (Fig. 6), and decreased axial velocity (Fig. 4). The relative tangential velocity contours (Fig. 5) clearly show the overturning (top leg) and underturning (bottom leg) effects of the secondary flow in the region from H=0.80 to 0.97.

There is a patch of positive vorticity, which appears below the secondary flow region (Fig. 1). This is due to the interaction of the secondary flow with the mainstream and results from entrainment of flow from the lower radii. One of the interesting features is the secondary flow-wake interaction region that appears near the suction surface at H=0.75. This vortex is in the opposite direction of the passage vortex. The numerical simulation of Ho and Lakshminarayana [12] clearly identifies the presence and causes of the secondary flow-wake interaction vortex.

There is no evidence of a Rankine type vortex structure in the passage vortex. The flow angle shows overturning in most of the secondary flow regions with reduced axial, relative tangential, and secondary flow region (Fig. 4) seems to indicate that the vorticity is distributed and has not rolled up into a strong Rankine vortex.

Scraping Vortex. In the tip region, Fig. 1 shows the scraping vortex as the area of negative vorticity located above the tip leakage vortex at H=0.97. The axial vorticity due to this vortex is apparent and is confined to a thin region near the blade tip. At 80 percent chord the formation of the scraping vortex (marked S.V.) is first observed. At 90 percent chord the scraping vortex is still present, but its extent is reduced due to the presence of and interaction with the leakage flow.

In the region very close to the casing, the flow is directed towards the suction surface by the relative motion between the blade and casing. The effects of the relative motion between the blade and the casing are evident from the low axial velocity (Fig. 4) and overturning (Fig. 6) observed near the blade tip. Beyond 70 percent chord, this flow due to the relative motion interacts strongly with the tip leakage vortex, which is in the opposite direction. The mixing of these two flows results in the formation of the scraping vortex which reduces the leakage flow and confines the vortex to the tip region of the suction surface. The interaction of these two

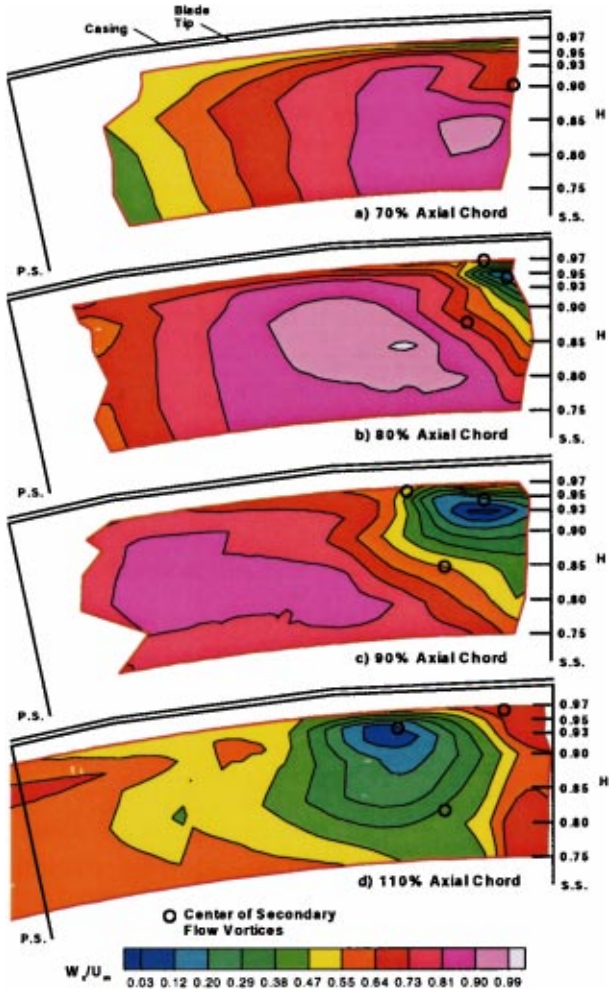

Fig. 4 Axial velocity (W_x/U_m) in rotor passage

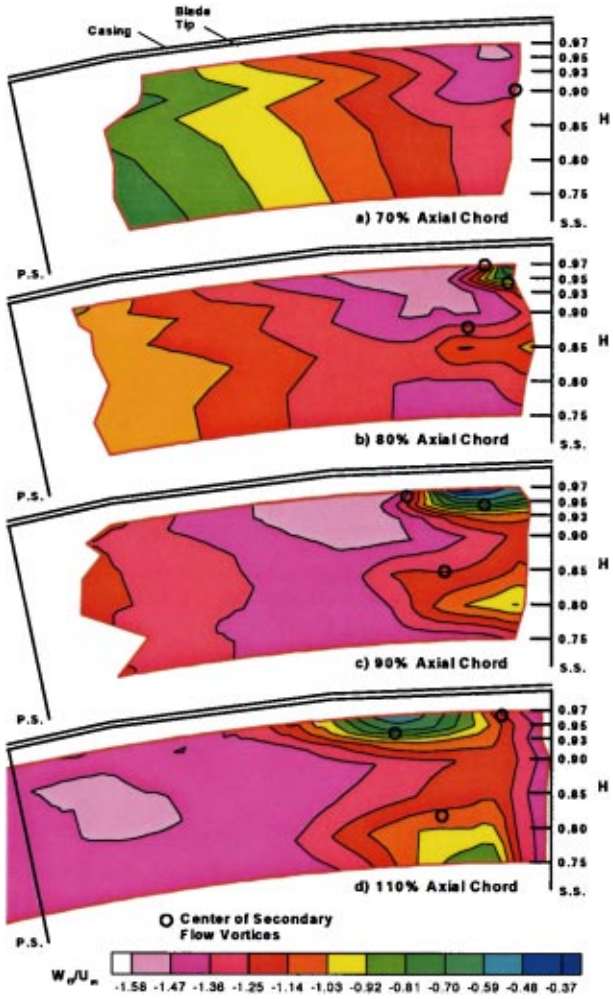

Fig. 5 Relative tangential velocity (W_θ/U_m) in rotor passage

vortices can be seen in the casing pressure distribution shown in Fig. 7 of Part I of this paper. The presence of the blade motion results in a low-pressure vortex region at the exit of the gap very near the suction surface (core 3 in Fig. 7, Part I). It is thought that this low-pressure core may be caused by the scraping vortex although this cannot be proven from the data. The reaction of this low pressure core with the leakage flow (core 1 of Fig. 7, Part I) can be seen as the scraping vortex (core 3) is pushed away from the suction surface by the formation of the tip leakage vortex beyond 70 percent chord. The leakage vortex seems to keep this scraping vortex confined to a relatively small area. The formation of the scraping vortex is perhaps one of the major differences between the cascade (with no relative wall motion) and rotor tip leakage flows.

Leakage Vortex. Flow in the mainstream close to the pressure surface (Fig. 1) is moving towards the pressure surface tip gap (70 percent and 80 percent axial chord) driven by the pressure gradient across the blade tip. This flow feeds the tip-leakage flow, which can be seen close to the suction surface at 80 percent and 90 percent chord. At 70 percent chord, Fig. 1(*a*), the leakage flow is not detected. Bindon [13] also found the leakage flow and the mixing losses to be negligible upstream of 80 percent chord. In the current experiments the five-hole probe could not be traversed beyond 97 percent span due to safety considerations. At 70 percent chord, the leakage flow may be confined close to the blade tip beyond 98 percent span. Therefore the tip leakage flow may have been missed.

At 80 percent chord the plots show the leakage vorticity centered on H=0.95. The data shows the strong interaction between the leakage flow from the tip gap and the main flow. There is also a very sharp change in the relative tangential velocity around the edge of the tip leakage vortex caused by interactions of the tip-leakage flow with the mainstream. The leakage flow changes direction to that of the mainflow very quickly. The mixing of these two flows is responsible for the areas of highest losses in the tip region, which is shown in Fig. 2. Bindon [13] found similar results in the losses from cascades and suggested that almost half of total tip clearance losses are due to the interaction of leakage flow with the mainstream flow. The leakage vortex region is intense with very low relative velocities (Fig. 3), extremely low axial velocities (Fig. 4), and substantial flow underturning (Fig. 6). The tip leakage vortex area shows the reduced tangential velocity and higher radial velocity caused by the vortex (Fig. 1). Figure 1 shows that the tip leakage flow entrains fluid from the blade and casing boundary layer, which mixes with the main flow.

The leakage vortex at 80 percent chord is still confined to the suction surface corner at 95 percent span (marked T.L. in Fig. 1) due to interactions with the counter rotating secondary flow and the relative motion between the casing and the blade. Compared to the tip-leakage vortex found in many cascades [13], the tip-leakage flow in the turbine rotor stays more confined to the suction surface corner and nearer to the casing.

The tip-leakage flow region has low stagnation and static pressure (Fig. 2 of Part II and Fig. 5 of Part I). This acts to sweep the low momentum fluid from the casing wall to the suction side. The

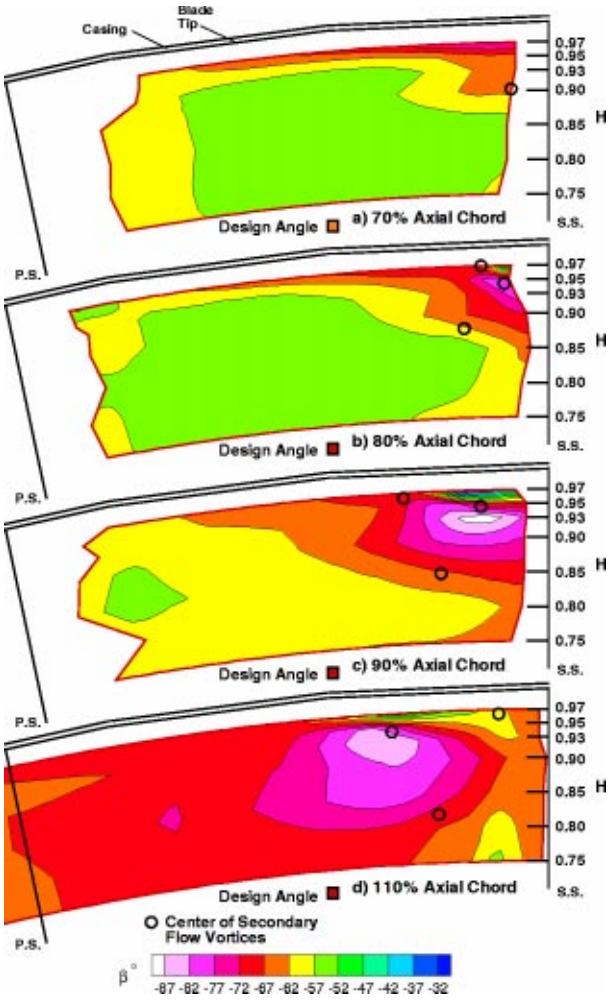

Fig. 6 Relative primary flow angle (β) in rotor passage

entrainment of the fluid by the tip vortex can be seen in the plot of relative tangential velocity as the area of high tangential velocity above the tip-leakage vortex. This area of high tangential velocity shows fluid moving into the vortex from the surrounding flow. Larger losses and static pressure in this region are observed (Fig. 2 of Part II and Fig. 5 of Part I). The leakage and secondary flow and the associated mixing with the blade boundary layer causes substantial dissipation of kinetic energy, resulting in decreased relative velocity.

The leakage vortex intensity and size increases substantially at 90 percent chord. A strong leakage vortex region is present from H=0.93 to 0.97 covering approximately 20 percent of the blade passage tangentially. It is interesting to note that the radial velocities (Fig. 1) and the flow into the gap region near the pressure surface have been reduced dramatically as compared to 80 percent chord.

Leakage Flow and Vortex Development. At 70 percent chord, the leakage flow clings closely to the endwall and suction surface and suddenly rolls up forming the leakage vortex, which lifts off the suction surface to move out into the passage at 80 percent chord. Between 80 percent and 90 percent, chord, the distance of the vortex center from the suction surface nearly doubles. The same rolling up and lift off between 80 percent and 90 percent was observed in cascade testing by Bindon and Morphis [14]. The leakage vortex follows a trajectory at an angle of 9 degrees with the blade tip moving inwards towards the hub as flow progresses downstream. As the tip-leakage flow progresses

Table 1 Design values of relative primary flow angle (β) at several measurement locations

X	H=0.75	H=0.80	H=0.85	H=0.90	H=0.95
0.70	-62.64	-62.86	-63.10	-63.32	-63.32
0.80	-66.26	-66.39	-66.52	-66.65	-66.81
0.90	-68.10	-68.26	-68.46	-68.65	-68.65
1.10	-68.58	-68.85	-69.13	-69.41	-69.54

downstream inside the rotor passage, its effect increases dramatically, and it extends further out from the suction surface into the main core flow region.

The formation of the tip leakage flow and vortex at 80 percent chord is consistent with the blade pressure distribution shown in Figs. 3 and 4 of Part I of this paper. These figures show the blade suction peaks located close to 80 percent chord near the tip region. It should be remarked here that the design suction peak (Fig. 3, Part I) is located close to 60 percent chord. The leakage flow in the gap tends to move towards the lowest pressure. Hence, most of the leakage flow is expected to exit the gap at the suction peak beyond 70 percent chord. From the five-hole probe data, the inception point of the leakage vortex seems to originate beyond the 70 percent chordwise location. Therefore, the formation of the tip leakage vortex, its location, and its strength is very much dependent on the design pressure distribution and the blade profile.

The design value of blade primary flow angles at exit is shown in Table 1. As Fig. 6 demonstrates, in the core flow region the measured flow angle is slightly less than the design. From the primary flow angle, the effects of the tip-leakage vortex can be easily seen. The leakage flow and the mainflow are at widely differing angles and tend to roll up into a vortex. At 80 percent chord, (Fig. 6), the flow around H=0.93 is highly overturned and at H=0.97 the flow becomes highly underturned due to the leakage flow vortex. The change in flow angle across the tip leakage vortex at 80 percent chord is about 27 degrees. A similar over and under turning due to the leakage flow is observed at 90 percent chord (Fig. 6) with an angle change of 45 degrees across the vortex. At 90 percent chord the design angle is −68.65°. The measured data shows a maximum underturning of 37° and overturning of 20°. The radial velocity (Fig. 1) in this region also shows the high outward velocity on the suction side and inward flow on the opposite side of the vortex (away from the suction surface) associated with the tip-leakage vortex. This shows a vortex in this region moving counterclockwise.

At 90 percent chord, H=0.93, the axial velocity (Fig. 4) shows nearly reversed flow; an indication of a strong leakage vortex. The presence of underturning in the region of H=0.95 to 0.97 and overturning immediately below this radius is another strong evidence for the presence of a leakage vortex with a strong core. While it is difficult to define the exact structure of the vortex, there is strong evidence for the formation of a tip leakage vortex. The secondary flow vectors do not show a completely rotating vortex in the tip leakage flow. A secondary flow structure similar to the one observed in this study was found in numerical simulations of tip leakage flows by Tallman and Lakshminarayana [15]. Their more comprehensive model of the tip leakage physics found the tip leakage flow behaves as a plume of sheet vorticity leaving the tip gap and rolling up into a distinct vortex. It is felt that the similarities between the data in the two studies indicate that much of the vorticity observed in the current study is generated as sheet vorticity in the tip gap.

Mass Averaged Properties. The tangentially mass-averaged primary flow angle (β) was derived using Eq. 3. The tangentially mass-averaged primary flow angle at each radius is given in Fig. 7.

$$\overline{\beta} = arctan(\overline{W}_x / \overline{W}_\theta) \tag{3}$$

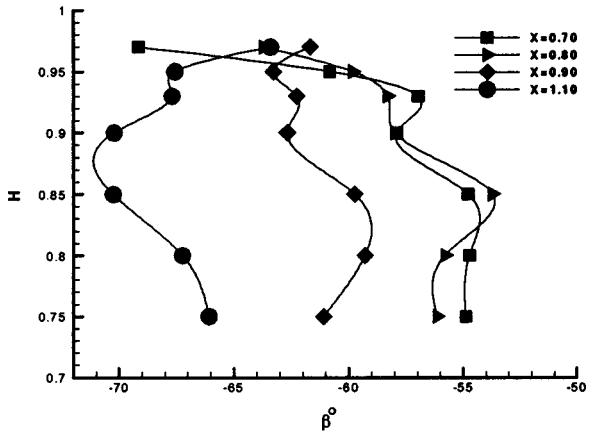

Fig. 7 Mass averaged relative primary flow angle

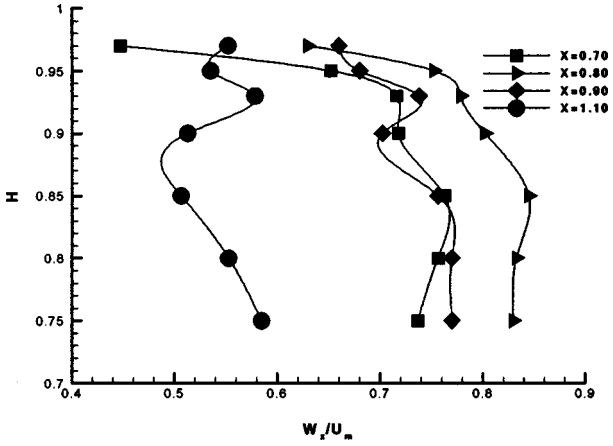

Fig. 8 Mass averaged axial velocity

At 70 percent and 80 percent chord, the flow is overturned at H=0.97 (see Table 1). The leakage flow is still relatively small at these locations and flow is overturned due to the secondary flow. The over and under turning due to the passage vortex between H=0.93 and H=0.85 are also visible. At 90 percent chord, the leakage flow is more dominant and causes underturning at H=0.97 and overturning at H=0.95, which is typical of a tip leakage vortex. The passage vortex results in the underturning at H=0.85 and H=0.80. At 110 percent chord, H=0.97, the flow is underturned due to the leakage flow. Because the passage vortex moves closer to the hub at 110 percent chord, the underturning due to the passage vortex also moves closer to the hub and is not fully captured in this data.

Figure 8 shows the mass-averaged values of the axial velocity. Velocity near the casing is lowest at 70 percent axial chord due to the casing boundary layer. The increase in the axial velocity at H=0.85 (80 percent to 110 percent chord) is due to the acceleration of the flow around the passage vortex and its associated blockage. There is a slight drop in the axial velocity at H=0.95 due to the tip leakage vortex. At 90 percent chord, the axial velocities are much lower in the tip region than at 80 percent chord as the effects of the tip leakage and passage vortices become more dominant in the flow. At 110 percent chord the axial velocity reduces substantially from 80 percent to 97 percent span due to the increased extent of the tip leakage and the secondary flow regions and their interaction.

Interaction and Decay of Secondary Flows

Both the vorticity and the losses from the tip leakage vortex core (Figs. 1 and 2) increase by about 35 percent between 80 percent and 90 percent chord. The vorticity from the passage vortex core decreases by about 30 percent from 80 percent to 90 percent chord. The leakage flow appears to entrain more fluid than the passage vortex as it progresses downstream leading to the weakening of the passage vortex at X=0.90. A similar trend is seen in the computation results presented by Chernobrovkin [16]. The computational results show that the percentage of the leakage flow entrained in the tip-leakage vortex increases from 80 percent chord to the trailing edge. As the flow progresses downstream of the blade at X=1.10 (27 percent axial chord from the trailing edge along the relative streamwise direction), the flow in the mainstream becomes more uniform, with considerable mixing of the wake and secondary flows (Figs. 1, 4, 5). The data shows diffusion and spreading of the leakage and secondary flow/vortex regions.

The leakage and secondary flow and the associated vortices are fairly distinctive and do not interact directly until the flow leaves the trailing edge. Beyond the trailing edge, The passage vortex and leakage vortex begin to interact. The interactions of these flows (leakage flow, casing boundary layer, rotor wakes, and secondary flow) cause diffusion of the leakage and the secondary vorticity.

The maximum vorticity value in the tip leakage vortex drops by about 37 percent from 90 percent chord to 110 percent chord. The passage vortex dissipates more slowly loosing about 23 percent of its maximum vorticity value between 90 percent and 110 percent chord. The secondary flow prevents movement of the leakage vortex hence its effect is still confined to the tip region and the vorticity is now smeared along the passage (approximately 40 percent of the blade spacing) with large decreases in the axial, relative tangential, and relative total velocities in this region. The absence of a flow overturning region near the leakage vortex seems to indicate either the break up of the vortex or substantial vortex dissipation caused by intense mixing of suction surface boundary layer (outward flow), casing wall boundary layer, secondary flow, and the rotor wake. Some of these features (outward flow in blade boundary layers, and relative motion between blade and casing) are not present in a cascade. Thus these features of the flow may lead to a more rapid decay or breakdown of the vortex structure (Fig. 1) than observed in cascades.

Figure 9 shows the area mass-averaged values of the positive values of vorticity due to leakage flow at each axial location normalized by the two-dimensional value of the circulation at the blade tip. Since the tip leakage flow is responsible for the majority of the positive vorticity in the tip region, information about the amount of vorticity shed by the tip leakage vortex is provided in Fig. 9. At 70 percent chord, there is little visible vorticity from the tip leakage vortex and the positive vorticity, most of which comes from the main flow, is very low. Beyond 80 percent chord, the vorticity due to leakage flow increases dramatically as the tip leakage flow develops and becomes stronger. The vorticity continues to increase downstream of the trailing edge. Approximately 55 percent of the vorticity downstream of the blade can be attributed to the leakage flow.

Turbulence Intensity and Shear Stress

An understanding of the turbulence field is essential in assessing the sources and magnitude of losses and its influence on the mean flow field. Figure 10(*a*) shows the streamwise turbulence intensity component (T_s) at 80 percent, 90 percent, and 1.01 percent chord. The flow field near the pressure side is not investigated due to the shadow of the turbine blade on the optical laser and these regions are marked as ''Blade Shadow Region.'' Measurements were also not obtained in the blank region close to the suction surface. This area comprises the boundary layer on the blade surface and sufficient LDV seeding rates could not be sustained in this region.

Four regions of high turbulence intensities can be identified from the plot. The highest turbulence intensity occurs in the leak-

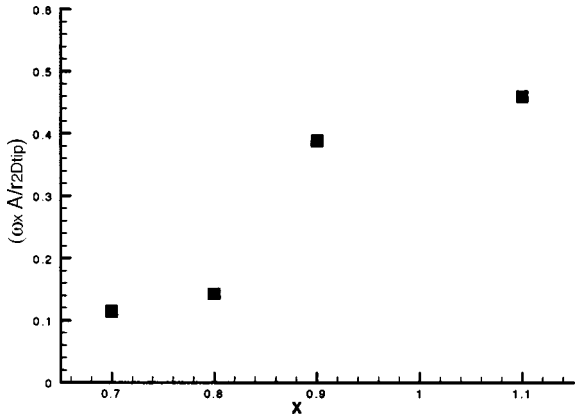

Fig. 9 Area mass averaged vorticity shed by the tip leakage vortex

age vortex region (about 10 percent), followed by the secondary flow region (7∼9 percent), casing wall region (5∼6 percent), and the wake. The extent of these regions is very similar to the extent of vorticity (Fig. 1), and the extent of loss described in Fig. 2. The value of T_s increases substantially from 80 percent to 90 percent due to the growth of the vortex and secondary flow regions. From 90 percent to 101 percent (1 percent downstream of the trailing edge), diffusion of the leakage vortex and the secondary flow results in higher turbulence intensity over a larger area. The high turbulence intensity region at 101 percent chord extends to almost half of the passage from H=0.80 to 0.98. This is consistent with the intense mixing associated with the interaction of the leakage vortex, secondary vortex, wake and casing boundary layer described earlier. The adverse pressure gradient in the flow which exists beyond mid-chord, shown in the Part I of this paper (Figs. 3 and 4), rapidly increases the blade boundary thickness, resulting in a thick wake. The tip vortex and the passage vortex generate extra shear stresses besides those produced by the boundary layer. These shear stresses interact three dimensionally to dramatically increase the production of the turbulent kinetic energy and also the turbulence intensity. The tip leakage vortex is small but very strong; therefore, the shear stress caused by the tip vortex is much stronger than that caused by the passage vortex and the blade boundary layer. This is the reason that the strongest turbulence intensity lies in tip vortex region.

Among the three turbulence intensity components T_s, T_n, and T_r (Figs. 10(*a*)–(*c*)), the stream wise component T_s and the component in the binormal direction T_n are about equal, but the radial component T_r is much higher. This situation is not the same as found in a cascade, where the streamwise turbulence intensity component (T_s) is the highest. This situation arises from the effects of rotation on turbulence [17]. In a turbine rotor, the centrifugal and corriolis forces modify the structure of the turbulence by transferring the turbulent kinetic energy from the streamwise and binormal direction to the radial direction. This results in a much higher value of the radial component of the turbulence intensity [18]. The transfer of the turbulent kinetic energy is especially strong near the end wall at 90 percent chord, and flow probably stalls. Another consequence of the redistribution of the turbulent kinetic energy among different directions is that the turbulence field is anisotropic. The turbulence modeling based on isotropic turbulence (e.g., two-equation models) would be inaccurate near the end wall, leakage vortex, secondary flow, and the blade boundary layer region near the suction side. Full Reynolds stress turbulence model may capture the anisotropy and the rotation effects, but one or two equation models based on isotropic turbulence assumption would not capture the redistribution due to rotation. The location of the high turbulence intensity region and

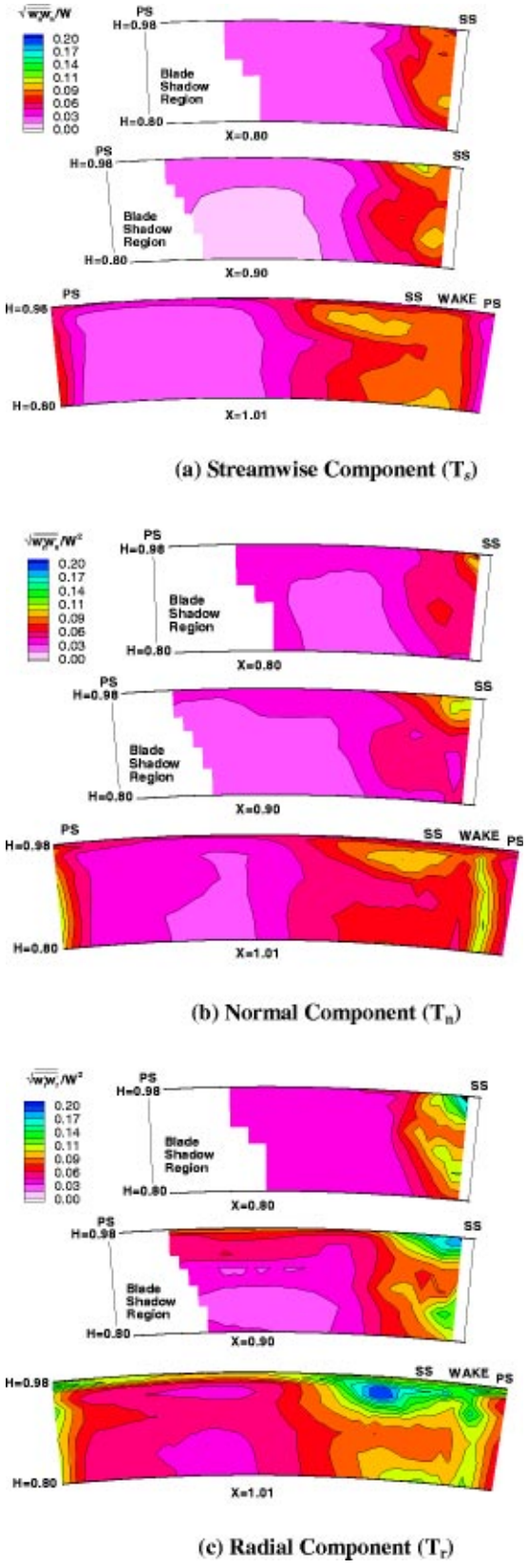

Fig. 10 Turbulence intensities in (s, n, r) coordinate

high loss region (Fig. 2) is almost the same indicating that strong mixing of the tip vortex with the main stream produces high turbulence intensity and causes high flow losses.

The turbulence shear stresses in the streamwise direction (τ_{sn}) and radial direction (τ_{nr}) are plotted in Figs. 11(*a*)–(*b*) respec-

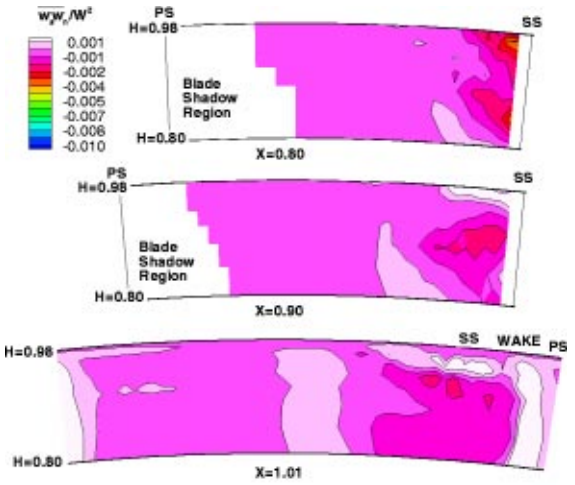

(a) Streamwise Component (τ_{sn})

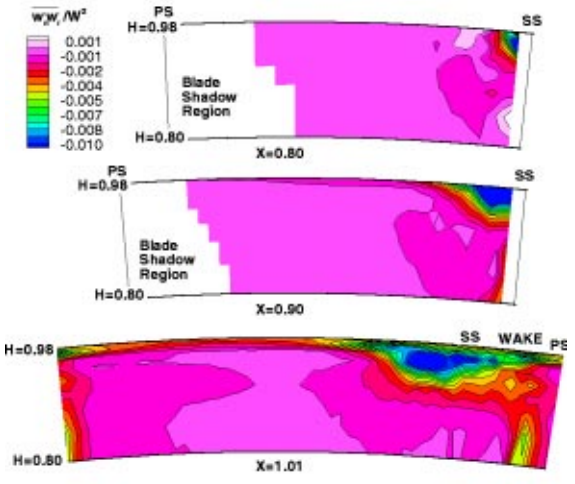

(b) Radial Component (τ_{nr})

Fig. 11 Shear stresses in the streamwise and radial directions

tively. These plots show the anisotropy in the turbulence field. The maximum τ_{sn} normalized by local total velocity square (W^2) in the leakage vortex is -0.003 (the streamwise direction is positive ''s,'' the normal direction is positive from the suction surface to the pressure surface, and the radial inward direction is positive ''r''). In the secondary flow region the maximum τ_{sn} is about -0.003. The corresponding values for τ_{nr} in the tip clearance and passage vortex regions are -0.015 and -0.001, respectively. It is clear that the radial stress in the leakage flow is much higher than the streamwise stress, it is the same order of magnitude as streamwise stress in the secondary flow region. This is caused by the rotation and curvature effects (swirling flow in the vortex) on turbulence. It is evident that for such flows the eddy viscosity models fail to capture the turbulence field.

Nature of Tip Clearance Flow and Conclusions

The formation of the tip leakage vortex, its location and strength is very much dependent on the design pressure distribution and the blade profile. The leakage flow prior to 80 percent chord is relatively weak and clings to the blade suction surface. Little interaction with the mainstream flow can be seen in the passage around 70 percent chord. The tip-leakage flow in the turbine rotor begins to exit the tip gap beyond 70 percent chord, at the location of the suction peak on the suction surface. As the flow progresses downstream, the leakage flow strengthens dramatically at 80 percent chord and penetrates further out into the passage both tangentially and radially. This is the point where the pressure on the suction surface is the lowest and the pressure difference across the tip is maximum. The leakage flow begins to interact strongly with the mainflow resulting in high mixing losses. When the leakage flow interacts with the mainflow, they are at widely differing angles, and the leakage flow rolls up into a vortex close to the suction surface of the blade tip. The resulting interaction region has very low velocities and stagnation pressures. This low-pressure region entrains fluid from the surrounding areas and interacts with the passage vortex in the tip region. The relative motion between the rotor blade and the casing wall causes a flow towards the suction surface in the region close to the casing. This induces resistance to the leakage vortex and tends to confine the leakage vortex to a region very close to the suction surface of the rotor blade. The leakage flow in the present paper stays confined closer to the blade than indicated by the data obtained from cascade studies. The area where the leakage flow rolls up into a vortex remains a relatively small area close to the blade.

The leakage vortex continues to strengthen as it moves downstream. At 90 percent chord, the interaction region moves further out into the passage and the vorticity and turbulence intensity both increase dramatically. The tip leakage flow also begins to interact with the passage vortex in the tip region and pushes the passage vortex further out in the blade passage. In the present study, the highest losses were caused by the tip leakage vortex at 90 percent chord. The losses due to the leakage flow were approximately 25 percent higher than the losses due to the passage vortex. The leakage flow is a much more dominant flow disturbance in the tip region. The shear stress caused by the tip vortex is much stronger than that caused by the passage vortex and the blade boundary layer. This is the reason that the strongest turbulence intensity lies in tip vortex region. As the flow moves downstream from the blade trailing edge, the tip leakage vortex spreads out into the passage. In a cascade study, Bindon [13] observed results similar to those described above. He observed the strengthening of the leakage flow in the last 20 percent of the blade chord. Yamamoto [19] found a similar trend in his cascade tests where the leakage flow forms a large vortex at the rear part of the blade tip. Bindon also suggested that the leakage effects would dissipate much more slowly downstream of the blade than the effects observed in the present paper. Downstream of the blade, the effects from the leakage vortex disappear quicker than the effects from the passage vortex.

There are differences in the turbulence structure observed in rotor and cascade flows. In cascades, the streamwise turbulence intensity component is the highest. In rotor flows, the effects of rotation and corriolis forces transfer turbulent kinetic energy to the radial direction. This modifies the structure of the turbulence making the turbulence field anisotropic.

Acknowledgments

This work was sponsored by the U.S. Army Research Office under the Grant DAAH04-95-1-0179 with Dr. T. Doligalski as the technical monitor. The senior author was supported by the U.S. Army Research Office AASERT Grant DAAG55-97-1-0201, with Dr. T. Doligalski as the technical monitor.

Nomenclature

A = Area over which measurements were taken in rotor passage
C_x = Rotor blade axial chord at blade tip
H = Distance from the hub normalized by blade height
P_{tr} = Total pressure in the relative frame
PS = Pressure surface
r = Radius

r_m = Radius at mid-span
S = Rotor blade spacing
SS = Suction Surface
T = Turbulence intensity $=\sqrt{w'^2}/W$
U_m = Blade speed at mid-span
V = Absolute total velocity
w_s', w_n', w_r' = Fluctuating relative velocity in streamwise, principal normal, and radial directions
W = Relative total velocity
W_x, W_θ, W_r = Axial, relative tangential, and radial velocities in relative frame
W_{sec} = Secondary relative velocity (Eq. (1))
X = Axial distance measured from the leading edge normalized by C_x

Greek

β = Relative flow angle measured from the axial direction
Γ_{2Dtip} = Circulation at blade tip $=SW_{x1}(tan\ \beta_1 - tan\ \beta_2)$
γ = Flow angle measured in the radial direction
ρ = Air density
τ_{ij} = Shear stress (e.g., τ_{sn} is the streamwise shear stress)
θ = Angle in tangential direction
ω_x = Axial vorticity (Eq. (2))
ζ = Total pressure loss coefficient $=(\overline{P}_{tr\,1} - P_{tr})/0.5\rho U_m^2$
Ω = Rotor angular velocity

Subscript

0, 1, 2 = Nozzle inlet, rotor inlet, rotor exit, respectively
s,n,r = Streamwise, principal normal, and radial directions, respectively
x, θ, r = Axial, tangential, and radial directions, respectively

Superscript

Passage averaged value

References

[1] Xiao, X., McCarter, A., and Lakshminarayana, B., 2000, ''Tip Clearance Effects in a Turbine Rotor Part I: Pressure Fields and Losses,'' ASME J. Turbomach., **123**, pp. 296–304.
[2] Yaras, M. I., and Sjolander, S. A., 1992, ''Effects of Simulated Rotation on Tip Leakage in a Planar Cascade of Turbine Blades—Part I: Tip Gap Flow,'' ASME J. Turbomach., **114**, July, pp. 652–659.
[3] Yaras, M. I., and Sjolander, S. A., 1992, ''Effects of Simulated Rotation on Tip Leakage in a Planar Cascade of Turbine Blades: Part II—Downstream Flow Field and Blade Loading,'' ASME J. Turbomach., **114**, July, pp. 660–667.
[4] Graham, J. A. H., 1986, ''Investigation of a Tip Clearance Cascade in a Water Analogy Rig,'' ASME J. Turbomach., **108**, Jan., pp. 38–46.
[5] Yamamoto, A., Tominaga, J., Matsuunuma, T., and Outa, E., 1994, ''Detailed Measurements of Three-Dimensional Flows and Losses Inside an Axial Flow Turbine Rotor,'' ASME Paper No. 94-GT-348.
[6] Yamamoto, A., Matsuunuma, T., and Outa, E., 1994, ''Unsteady Endwall/Tip-Clearance Flows and Losses Due to Turbine Rotor-Stator Interaction,'' ASME Paper No. 94-GT-461.
[7] Lakshminarayana, B., Zaccaria, M., and Marathe, B., 1995, ''Structure of Tip Clearance Flow in Axial Compressors,'' ASME J. Turbomach., **117**, pp. 336–347.
[8] Stauter, R. C., 1992, ''Measurement of the Three Dimensional Tip Region Flow Field in an Axial Compressor,'' ASME Paper No. 92-GT-211.
[9] Morphis, G., and Bindon, J. P., 1994, ''The Performance of a Low Speed One and a Half Stage Axial Turbine With Varying Rotor Tip Clearance and Tip Gap Geometry,'' ASME Paper No. 94-GT-481.
[10] Lakshminarayana, B., Camci, C., Halliwell, I., Zaccaria, M., 1996, ''Design and Development of a Turbine Research Facility to Study Rotor-Stator Interaction Effects,'' International Journal of Turbo and Jet Engines, **13**, pp. 155–172.
[11] Ristic, D., Lakshminarayana, B., and Chu, S., 1999, ''Three-Dimensional Flow Field Downstream of an Axial Flow Turbine Rotor,'' J. Propul. Power **15**, No. 2, March-April.
[12] Ho, Y., and Lakshminarayana, B., 1996, ''Computational Modeling of Three Dimensional Endwall Flow Through a Turbine Rotor With Strong Secondary Flows,'' ASME J. Turbomach., **118**, pp. 250–261.
[13] Bindon, J., 1989, ''The Measurement and Formation of Tip Clearance Loss,'' ASME J. Turbomach., **111**, pp. 257–263.
[14] Bindon, J. P., and Morphis, G., 1990, ''The Development of Axial Turbine Leakage Loss for Two Profiles Tip Geometries Using Linear Cascade Data,'' ASME Paper No. 90-GT-152.
[15] Tallman, J., and Lakshminarayana, B., 2000, ''Numerical Simulation of Tip Leakage Flows in Axial Flow Turbines, With Emphasis on Flow Physics—Part II: Effect of Outer Casing Relative Motion,'' J. Turbomach., **123**, pp. 324–333.
[16] Chernobrovkin, A., 1999, ''Numerical Simulation of Complex Turbomachinery Flow,'' Ph.D. Thesis, Pennsylvania State University.
[17] Anand, A. K., and Lakshminarayana, B., 1978, ''An Experimental Study of Three-Dimensional Turbulent Boundary Layer and Turbulence Characteristics Inside a Turbomachinery Rotor Passage,'' ASME J. Eng. Power, **100**, No. 4, October.
[18] Lakshminarayana, B., 1996, *Fluid Mechanics and Heat Transfer of Turbomachinery*, Chapter 5, John Wiley & Sons, Inc., New York.
[19] Yamamoto, A., 1988, ''Endwall Flow/Loss Mechanisms in a Linear Turbine Cascade With Blade Tip Clearance,'' ASME J. Turbomach., **111**, pp. 264–275.

Numerical Simulation of Tip Leakage Flows in Axial Flow Turbines, With Emphasis on Flow Physics: Part I—Effect of Tip Clearance Height

J. Tallman
Graduate Research Assistant
e-mail: jat@turbo3.aero.psu.edu

B. Lakshminarayana
Evan Pugh Professor and Director
e-mail: bllaer@engr.psu.edu

Center for Gas Turbine and Power,
Pennsylvania State University,
153-J Hammond Bldg.,
University Park, PA 16802

A pressure-correction based, 3D Navier-Stokes CFD code was used to simulate the effects of turbine parameters on the tip leakage flow and vortex in a linear turbine cascade to understand the detailed flow physics. A baseline case simulation of a cascade was first conducted in order to validate the numerical procedure with experimental measurements. The effects of realistic tip clearance spacing, inlet conditions, and relative endwall motion were then sequentially simulated, while maintaining previously modified parameters. With each additional simulation, a detailed comparison of the leakage flow's direction, pressure gradient, and mass flow, as well as the leakage vortex and its roll-up, size, losses, location, and interaction with other flow features, was conducted. Part I of this two-part paper focuses on the effect of reduced tip clearance height on the leakage flow and vortex. Reduced tip clearance results in less mass flow through the gap, a smaller leakage vortex, and less aerothermal losses in both the gap and the vortex. The shearing of the leakage jet and passage flow to which leakage vortex roll-up is usually attributed to is not observed in any of the simulations. Alternative explanations of the leakage vortex's roll-up are presented. Additional secondary flows that are seen near the casing are also discussed.
[DOI: 10.1115/1.1368881]

Introduction

The tip leakage flow is one of the most prevalent and influential features of the flow through turbomachine rotors. Along with its associated vortex, this flow is detrimental to turbomachine performance for multiple reasons. The most significant effects of the tip leakage flow and vortex are the blockage of the passage flow, downstream unsteadiness in the relative frame of reference, complexities in blade heat transfer, and aerothermal losses associated with resulting secondary flows.

In addition, the tip leakage flow is a phenomenon that is difficult to either predict or measure in most turbomachines. This is particularly true in axial turbines, where the relative motion of the outer casing is opposed to the leakage flow, heat transfer effects are of greater concern, and both the blade thickness and flow turning are of large values when compared to other types of turbomachines.

The general objective of this research is a solid, physical understanding of the leakage flow, leakage vortex, and additional secondary flows present in the near-casing region of axial flow turbines. This understanding includes the mechanisms responsible for these secondary flows, as well as their interdependence and interaction with one another. In other to accomplish this objective, the turbine flow field must be analyzed in great detail and in three dimensions. Therefore, numerical simulation is necessary. Ultimately, this study is aimed at reducing the tip leakage flow and vortex, as well as their ill effects, discussed earlier. An overview of the four simulations presented in this two-part paper is given in Table 1.

The specific objective of Part 1 in this two-part series paper is to study the effect of the tip clearance height on the leakage flow, vortex, and associated secondary flows. A linear turbine cascade originally studied by Bindon and Morphis [1,2] is simulated with no relative wall motion, a tip clearance height of 2.5 percent span, and an inlet velocity profile similar to what was used in Bindon's experimental studies. An overview of the experimental case is given in Table 2. The results of the first simulation are then presented in direct comparison to a second simulation with a tip clearance height of 1.0 percent. This clearance is more representative of a real turbine.

An extensive review of both experimental and numerical studies of tip leakage flow in axial flow turbines can be found in the lecture series by Sjolander [3]. A review of early numerical simulation studies of turbomachines is given in the text by Lakshminarayana [4]. A brief review of more recent CFD tip leakage flow studies that are relevant to this paper is given here for completeness.

Wantanabe, et al. [5] computed the flow through both a stationary turbine cascade and a rotating turbine using compressible Navier-Stokes solver. The cascade showed a large leakage vortex that began to roll up at around 30 percent axial chord and appeared to pull away from the suction surface. For the rotating turbine, roll-up occurred at about 40 percent axial chord and the vortex remained close to the suction surface. Liu and Bozzola [6] solved for the incompressible flow through a turbine cascade with and without outer casing relative motion. The movement of the wall was found to greatly enhance the passage vortex and reduce the leakage vortex. Staubach et al. [7] used a multiblock Navier-Stokes code to predict the effect of different blade stacking patterns on the tip leakage flow. Blade stacking patterns that are bowed, swept, and reduced in turning near the tip all showed a reduction in the leakage vortex and its negative effects. Most recently, Chernobrovkin [8] computed the flow through a turbine with moderate turning and complex blade geometry. The leakage vortex was found to begin at an axial location of 50 percent chord and remain adjacent to the suction surface of the blade. In general,

Contributed by the International Gas Turbine Institute and presented at the 45th International Gas Turbine and Aeroengine Congress and Exhibition, Munich, Germany, May 8–11, 2000. Manuscript received by the International Gas Turbine Institute February 2000. Paper No. 2000-GT-514. Review Chair: D. Ballal.

Table 1 Research overview

Case	Paper	τ	Inlet Conditions	Relative Wall Motion	Case Compared With
1	Part 1	2.5 % Span	Original	0.0 m/s	Experiment
2	Part 1	1.0 % Span	Original	0.0 m/s	1
3	Part 2	1.0 % Span	Calculated	0.0 m/s	2
4	Part 2	1.0 % Span	Calculated	31.0 m/s	3

the prediction agreed well with Laser Doppler Velocimeter measurements of the flow. It should also be noted that Kind et al. [9] discusses the importance of vorticity convection out of the gap to the roll-up structure of the leakage vortex.

Numerical Technique

The full Reynolds averaged Navier-Stokes equations are employed in this research to model the flow through a turbine cascade. The computer code used in this study uses a semi-implicit pressure-correction method to iteratively solve conservation equations for mass, momentum, and turbulence quantities. A standard k-ε model with near wall damping terms due to Chien [10] is used for turbulence closure. Because the method uses a non-staggered grid, additional 2nd and 4th order artificial dissipation terms are added to these equations to aid in smoothing out errors and to prevent numerical oscillations of the centrally differenced pressure equation. In the final solution, these terms are made as small as stability will allow. The complete derivation of the numerical method used in this research can be found in the paper by Basson and Lakshminarayana [11] and in the thesis by Tallman [12].

The two-dimensional embedded H grid used in this study is shown in Fig. 1. The 3D grid is created by simply stacking up the grid in Fig. 1. The stacking near the hub, casing, and tip was close enough to give approximate y+ values in the single digits. Grid points were heavily clustered near the tip, with 28 spanwise grid points in the gap and 60 spanwise grid points within six gap heights of the tip. A total of 103 and 161 grid points were used in the spanwise and axial directions, respectively. In the tangential direction, 50 and 26 grid points were used across the inner and embedded regions, respectively. The inlet and exit of the computational domain (not shown if Fig. 1) are situated one and two axial chord lengths upstream and downstream of the blade, respectively. The Cartesian coordinate system used throughout this paper is also shown in Fig. 1. Coordinates X, Y, and Z correspond to the axial, tangential, and spanwise directions, respectively.

A thorough validation of the numerical procedure's ability to resolve turbomachinery flows has been previously carried out by Basson and Lakshminarayana [11]. In this validation study, a simulation of Case 1, described in Table 1, was performed using a less-refined grid. The results were then compared to experimental

Table 2 Turbine cascade design geometry

Chord Length = Span Length	0.186 m
Pitch Length	0.1323 m
Inlet Camber Angle	0.0°
Exit Camber Angle	68.0°
Tip Gap Height	2.5% Chord
Inlet Flow Velocity	13.82 m/s
Inlet Boundary Layer Thickness	10% Span
Inlet Turbulence Intensity	2% Inlet Velocity
Working Fluid	Air

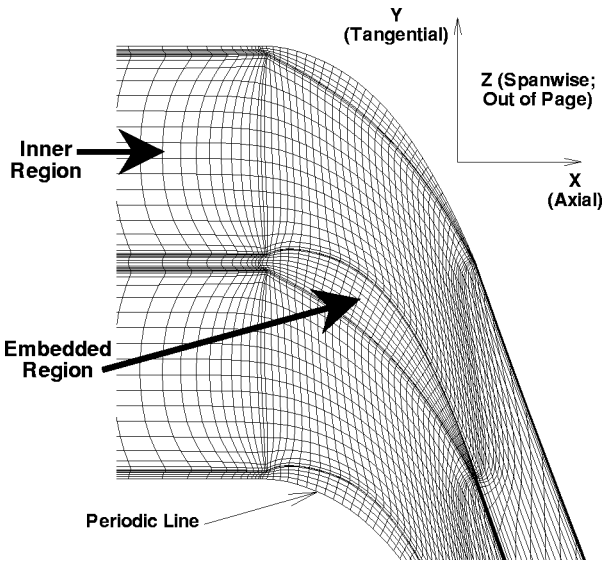

Fig. 1 Grid (every other gridline shown)

data by Bindon and Morphis [1,2]. For completeness, the simulation of Case 1 (Table 1) in this current study was also compared to the data of Bindon and Morphis, in order to ensure solution validity and grid independence. Both validation comparisons found that the solver was capable of predicting complex, three-dimensional flow features inside turbines to an extent equal to or above what is currently capable in the field of CFD. For the sake of brevity, validation results are not presented in this paper. The reader is encouraged to refer to the paper by Basson and Lakshminarayana [11] and chapter 2 of the thesis by Tallman [12] for verification of the code's validity. At the time of this paper's publication, chapter 2 is available on the World Wide Web at http://navier.aero.psu.edu/~jat.

Flow Physics and the Effect of Tip Clearance Height

The results of two numerical simulations of the 3D turbine blade described earlier are presented here. The tip clearance heights in the two cases are 2.5 percent and 1.0 percent of the blade span, or 4.65 and 1.86 mm, respectively. All other parameters of the two computations are identical. Relative motion of the outer casing is not included in these two cases. Casing relative motion is included in Part 2 of this paper. The two cases are referred to as the ''2.5 percent case'' and ''1.0 percent case'' throughout Part 1. Note that in descriptions of the flow field, the generic term ''Secondary Flow'' is used to represent any deviation from the 2D-inviscid design conditions, and should not be misinterpreted as the term ''Passage Vortex.''

Flow Particle Traces in the Tip Clearance Region. A Lagrangian method of following fluid particles through the flow field was developed for this research. Points on the particle traces are located on grid cell faces. At each point, the velocity vector is interpolated from the nodes of the adjacent grid points, and followed until it intersects another cell face. The velocity vector is again interpolated and the process is repeated until the pathline exits the passage. Besides the velocity components, static and total pressures are also interpolated along the particle traces, and these values are used for loss predictions presented later in the paper.

Figure 2 shows particle traces released from the passage inlet at increasing spanwise locations, corresponding to parts (*a*) through (*c*). Spanwise locations are labeled as a percentage of the total blade span, with 100 percent representing the blade tip. The 1.0 percent and 2.5 percent clearance cases are presented together for

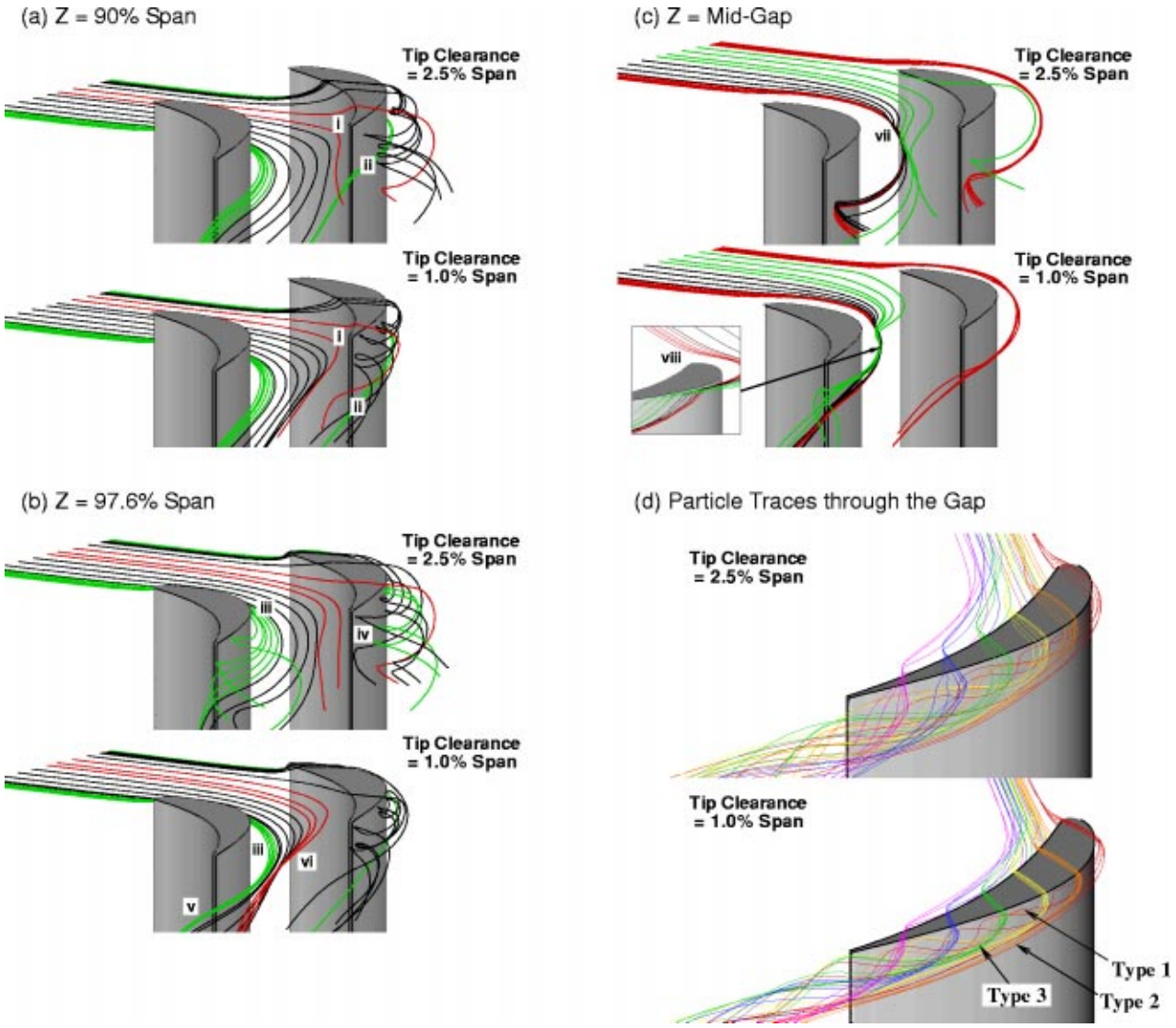

Fig. 2 Fluid pathlines through the turbine

direct comparison. In addition, Roman numeral indicators are used in the text to reference certain flow locations in Fig. 2.

Figure 2(*a*) shows fluid pathlines that are released upstream from a spanwise location of 90 percent span. The leakage vortex is removed from the blade suction surface in the 2.5 percent case but remains adjacent in the 1.0 percent case. The size of the leakage vortex is clearly larger for the 2.5 percent case, due to the greater mass flow through the gap.

Figure 2(*a*) also shows that the fluid pathlines near the pressure surface are being entrained into the mid-chord region of the gap for both cases. This entrainment is driven by a spanwise pressure gradient due to the unloading of the blade at the tip. These paths then exit the gap and wrap around a leakage vortex core that results from the leakage flow further upstream. As the passage flow is entrained into the gap, it acquires a secondary component of velocity directed towards the pressure surface and towards the blade tip. This secondary flow from the passage towards the gap region is referred to as the ''Gap Entrainment Secondary Flow'' throughout this paper. The fluid does not necessarily have to enter the gap to be considered part of the gap entrainment secondary flow. Therefore, the fluid pathlines labeled (i) in Fig. 2(*a*) are also subjected to gap entrainment secondary flow. Once the gap entrainment secondary flow enters the gap region, it is then referred to as the ''leakage flow.''

A close inspection of the suction surface in both cases of Fig. 2(*a*) shows that the leakage vortex acts as a blockage to the passage flow (Fig. 2(*a*), Lab. ii). The passage flow near the suction surface is forced underneath and to the side of the leakage vortex, resulting in an additional secondary flow. This secondary flow is referred to as the ''Blockage Secondary Flow'' throughout the paper. For the fluid pathlines in Fig. 2(*a*), both cases show the blockage secondary flow is directed towards the negative spanwise direction. The fluid pathlines labeled ii in Fig. 2(*a*) illustrate this. In both cases, these pathlines are closer to the blade tip at the leading edge of the blade than at the trailing edge.

Particle traces released from a spanwise location of 97.6 percent span are shown in Fig. 2(*b*). Near the pressure side of the passage, the gap entrainment secondary flow carries fluid into the gap at locations from the leading edge to about 80 percent axial chord for both cases. The blockage secondary flow now forces fluid below and to the side of the leakage vortex in both cases (Fig. 2(*b*), Lab. iii). These fluid pathlines are then entrained around the outside of the leakage vortex, but to different extents in the two cases. In the 2.5 percent case, the leakage vortex is more detached from the suction surface of the blade, so the blocked passage fluid is entrained around the vortex from between the suction surface and the vortex (Fig. 2(*b*), Lab. iv). For the 1.0 percent case, the entrainment around the leakage vortex does not

occur until downstream of the trailing edge, since the vortex is situated closer to the suction surface (Fig. 2(*b*), Lab. v).

In addition, the fluid pathlines in Fig. 2(*b*) for the 1.0 percent case have begun to show the presence of an additional secondary flow. At the outer casing, fluid is transported from the pressure side of the passage towards the suction side of the passage (Fig. 2(*b*), Lab. vi). In two dimensions, this secondary flow appears to be the boundary layer portion of a passage vortex. The passage vortex effect is likely present to some extent, but is not the only cause of this additional secondary flow. The gap entrainment secondary flow in Fig. 2(*a*) acts as an obstruction to the flow through the passage in Fig. 2(*b*). Therefore, the secondary flow in question is due to a combination of both effects. This secondary flow is referred to as the ''Near-Casing Secondary Flow'' throughout the paper.

Figure 2(*c*) shows fluid pathlines originating from midway between the tip and the outer casing. The near-casing secondary flow is most clearly illustrated in Fig. 2(*c*) for both cases. The near-casing secondary flow carries near-casing fluid towards the leakage vortex (Fig. 2(*c*), Lab. vii). The fluid is then forced below the leakage vortex, where it follows the blockage secondary flow along the bottom of the leakage vortex (Fig. 2(*c*), Lab. viii). In the 2.5 percent case, the passage flow pathlines in question are entrained around the leakage vortex as a group. As with parts (a) and (b) of Fig. 2, the greater entrainment around the leakage vortex in the 2.5 percent case is due to the further detachment of the leakage vortex form the suction surface in that case.

Figure 2(*d*) shows fluid pathlines that pass through the gap at various axial and spanwise locations for both the 2.5 percent and 1.0 percent cases. In Fig. 2(*d*), fluid pathlines are colored in the order of the rainbow to correspond with their axial location in the gap. For example, the red pathlines pass through the gap closest to the leading edge and the violet pathlines pass through the gap closest to the trailing edge. The following discussion uses Fig. 2(*d*) to explain the leakage vortex flow physics that are observed.

A common explanation of the roll-up of the leakage vortex is that the passage flow and leakage jet shear across each other, creating a helical type of roll-up (see Lakshminarayana, 1996, p. 341). A shearing explanation of the roll-up is incorrect for the two cases presented here. This can be seen by visually superimposing the 1.0 percent case leakage vortex in Fig. 2(*d*) into its corresponding passage in Fig. 2(*b*). In Fig. 2(*b*), the passage flow near Lab. iii passes near to the tip and leading edge but does not become entangled in the inner core of the leakage vortex. Instead, this fluid is carried below and outside of the leakage vortex by the blockage secondary flow. Only downstream of the blade does this fluid begin to entrain around the outside of the leakage vortex. A similar analysis of the 2.5 percent case shows characteristics both similar to and different from the 1.0 percent case. As with the 1.0 percent case, the passage flow near Lab. iii is forced below and to the outside of the leakage vortex in the region of the vortex's initial roll-up. In the 2.5 percent case, however, some of this obstructed passage flow is entrained around the leakage vortex upstream of the trailing edge. In both cases, fluid pathlines inside the core of the leakage vortex that did not pass through the gap could not be generated. Therefore, alternative explanations of the initial roll-up of the leakage vortex's inner core need to be considered. One such explanation involves the convection of vorticity from inside of the gap into the leakage vortex. This idea will be discussed further after the structure of the leakage vortex in Fig. 2(*d*) has been analyzed.

A close analysis of the 1.0 percent case in Fig. 2(*d*) shows three distinct types of fluid pathlines, corresponding to three different types of leakage vortex roll-up. Representative fluid pathlines for each of the three types of roll-up are labeled in Fig. 2(*d*).

The first type of roll-up (type 1) is exhibited by the red, orange, and possibly yellow fluid pathlines that cross the gap at its upstream half and near to the blade tip. The fluid of these pathlines forms the innermost core of the leakage vortex. The innermost core appears to first roll into a vortex at approximately 30 percent axial chord. The fluid pathlines that make up the inner core are rotational before they exit the gap, due to their shearing on the blade tip. Furthermore, Fig. 2(*d*) shows that the direction of this rotation would be nearly the same as that of the leakage vortex. Therefore, the initial rotation of the type 1 fluid pathlines appears to aid in the roll-up of the leakage vortex core.

In contrast, the second type of roll-up (type 2) occurs in fluid pathlines that cross the gap at its upstream half and near to the outer casing. This fluid is also rotational, due to its shearing on the outer casing. The direction of this rotation will be roughly opposite to that of the tip leakage vortex, meaning that these fluid pathlines will resist rolling into the leakage vortex. This trend can be seen in the 1.0 percent case of Fig. 2(*d*). The red, orange, and possibly yellow fluid pathlines from near the casing avoid rolling around the leakage vortex and instead appear to travel through the passage slightly below and outside the leakage vortex. These fluid pathlines are gradually entrained around the outside of the leakage vortex downstream of the trailing edge, but do not roll up inside the passage.

The third type of roll-up (type 3) consists of fluid that exits the gap from its downstream half. These are the green, blue, and violet fluid pathlines in Fig. 2(*d*). The type 3 pathlines tend to wrap around the leakage vortex as a group, rather than divide based on their proximity to the blade tip or outer casing. This would indicate that vorticity convection from the gap's downstream half is less influential to the structure of the leakage vortex. One possible reason for this is that these fluid pathlines wrap around an existing vortex core and do not have to roll up on their own. A second reason is that the leakage flow through the gap has taken a direction less normal to the direction of the leakage vortex's rotation. Therefore, less of the leakage flow's vorticity will be in a direction that will enhance or deter roll-up. A close inspection of these fluid pathlines shows that, in general, the leakage flow closest to the blade tip wraps around the leakage vortex the fastest. This indicates that minor effects of vorticity convection are still present.

The addition of the type 3 fluid pathlines to the leakage vortex does not appear to be a case of layer stacking, as one might suspect. That is, the green, blue, and violet layers do not situate themselves at successively increasing radii from the center of the leakage vortex. Instead, the fluid pathlines fall together in a candy cane type of pattern, with green, blue, and violet fluid pathlines all at roughly the same radius. Also, the type three fluid pathlines appear to roll around the leakage vortex inside of the type two fluid pathlines, causing the type two fluid pathlines to be further obstructed.

The distinctions between the three regions of the leakage flow are more clearly identified in the 1.0 percent case than in the 2.5 percent case. The yellow fluid pathlines that pass through the gap near the mid-chord location illustrate this point the clearest. In the 1.0 percent case, the yellow fluid pathlines that cross the gap near the blade tip exhibit roll-up behavior somewhere between types 1 and 3, while the fluid pathlines that cross the gap near the outer casing roll-up with type 2 characteristics. In the 2.5 percent case, it is more difficult to define the yellow fluid pathlines' roll-up as a type one, two, or three.

The clearer division between the regions of the leakage vortex in the 1.0 percent case provides further evidence that vorticity transport from the gap, due to the casing and tip boundary layers, plays an appreciable roll in the structure of the leakage vortex. In the 1.0 percent case, a larger percentage of the leakage flow through the gap can expect to be sheared by either the blade tip or the outer casing, due to the smaller gap height. Therefore, the fluid will likely be either positively rotational or negatively rotational, explaining the sharp contrast in the yellow fluid pathlines' behavior. In the 2.5 percent case, more of the leakage flow can expect to pass through the gap without influence from the blade tip or outer casing. Therefore, more of the leakage flow should be less rota-

tional. If the vorticity transport from the gap affects the leakage vortex roll-up, then the less rotational leakage flow pathlines in the 2.5 percent case should show similar roll-up characteristics, regardless of the spanwise location that the leakage flow exited the gap. The yellow pathlines in the 2.5 percent case exhibit this trend.

While the roll-up of the leakage vortex in the 1.0 percent case appears to be due to vorticity convection, the 2.5 percent case shows evidence that the classical leakage jet/passage flow shearing explanation of vortex roll-up is not entirely false. For the 2.5 percent case, Fig. 2(*b*) shows that the passage flow near Lab. iii does not enter the innermost core of the leakage vortex, but does entrain around the leakage vortex inside the passage. This entrainment is due to the leakage vortex's detachment from the suction surface of the blade, which is due to the greater leakage jet mass flow and inertia in the larger tip clearance case. It is reasonable to expect that increases in the tip clearance height will cause the leakage vortex to detach from the blade at locations increasingly near to the leading edge. This would then lead to passage fluid entrainment at locations further upstream, as well as a greater degree of passage fluid entrainment in general. The wrapping of the passage fluid and leakage vortex around each other would then resemble the classical explanation of leakage vortex roll-up. Furthermore, since turbines with larger tip clearance cases are easier to experiment with, the classical explanation of the leakage vortex is based on intuition and observations made in these higher leakage flow Reynolds number cases. Therefore, vorticity convection from the gap appears responsible for leakage vortex roll-up in small tip clearance cases, while leakage jet/passage flow shearing appears responsible in large tip clearance cases. For tip clearance heights between the two extremes, such as the 2.5 percent case, leakage vortex roll-up is most likely due to a combination of the two effects.

It is reasonable to expect that the vorticity in the leakage flow is generated inside the gap. The equations of motion can be written to show that vorticity is generated at a wall and in the presence of a pressure gradient. This is the scenario present in the gap region. The pressure drop across the gap region is such that it produces negative vorticity at the blade tip and positive vorticity at the outer casing. The production of vorticity in the gap is shown in Fig. 3. Figure 3 shows the flow through the gap for the 1.0 percent case. The plane in Fig. 3 follows the orange pathlines in Fig. 2(*d*) as they pass through the gap. Contours in Fig. 3 are of nondimensional vorticity normal to the plane, which Fig. 2(*d*) shows to be the direction corresponding to the leakage vortex's rotation. Figures 3(*a*) and 3(*b*) correspond to the inlet and exit of the gap, respectively. Note that the right side (exit) of Part (*a*) does not correspond to the left side (inlet) of Part (*b*).

Figure 3(*a*) shows the gap entrainment secondary flow carrying passage fluid into the gap region. The entrained fluid is irrotational outside of the gap inlet. A large region of negative vorticity is generated as the flow enters the gap, although no recirculation bubble was found along the pressure side corner of the blade. Downstream of the inlet, Fig. 3(*a*) shows a symmetric velocity profile, with equally sized regions of negative vorticity (blue) on the blade tip and positive vorticity (red) on the outer casing. The thickness of the two regions corresponds to the amount of vorticity in the leakage flow. A close comparison of Fig. 3(*a*) and Fig. 3(*b*) shows that both thicknesses increase by about 60 percent as the leakage flow travels through the gap, indicating vorticity production. Upon exiting the gap, the leakage fluid from near the blade tip is no longer confined by the channel, and wraps around itself, forming the leakage vortex core.

Another intriguing feature of the tip leakage flow is that its direction through the gap is dependent on spanwise location. This is true for both cases, and particularly true for the leakage flow near the trailing edge. Near to the tip, the leakage flow follows a path that is closer in direction to the blade's camber line. This is attributed to different types of gap entrainment secondary flow, which can be seen in Fig. 4 and are discussed in the following paragraphs.

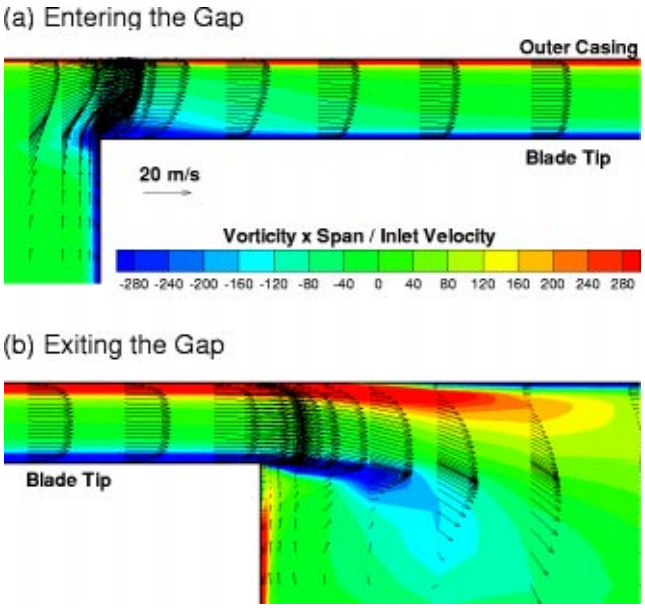

Fig. 3 Leakage flow through the gap (1.0 percent case)

Figure 4 shows the origins of the fluid pathlines in Fig. 2(*d*) upstream of the gap. The periodic labels indicate the tangential location of the leading edge of the blade. The greater mass flow through the gap observed in the 2.5 percent case is shown in Fig. 4 as a greater upstream area corresponding to the eventual leakage flow mass. Upstream of the gap, the fluid pathlines each require a certain degree of turning in either the spanwise or tangential directions in order to reach the gap. At gap locations further downstream, the leakage flow is supplied by fluid pathlines originating at upstream locations increasingly further away from the gap in either the tangential or spanwise direction. This is shown for both cases in Fig. 4 by the clear rainbow pattern of originating locations.

Following the violet pathlines, the flow through the gap near the outer casing has been turned in the tangential direction in order to pass through the gap. The final direction of this fluid through the gap is dependent on the pressure field at the inlet and exit to the gap. According to Fig. 4, the fluid turning takes place over a large, smooth radius. On the other hand, the flow through the gap near the blade tip requires more severe spanwise movement, since the particles originate further from the gap in the spanwise direction. The adjacency to the blade does not allow these fluid pathlines to turn pitchwise in a manner similar to that of the fluid passing near the outer casing. Therefore, the larger turning radius that the near-casing fluid pathline was subjected to

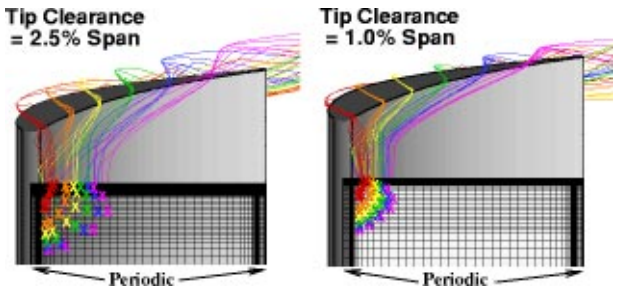

Fig. 4 Leakage fluid upstream of the blade

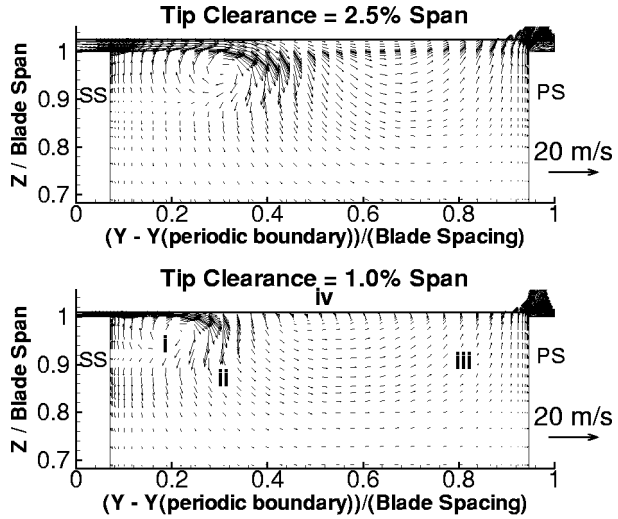

Fig. 5 Secondary velocity vectors in the y-z plane at X=90 percent axial chord

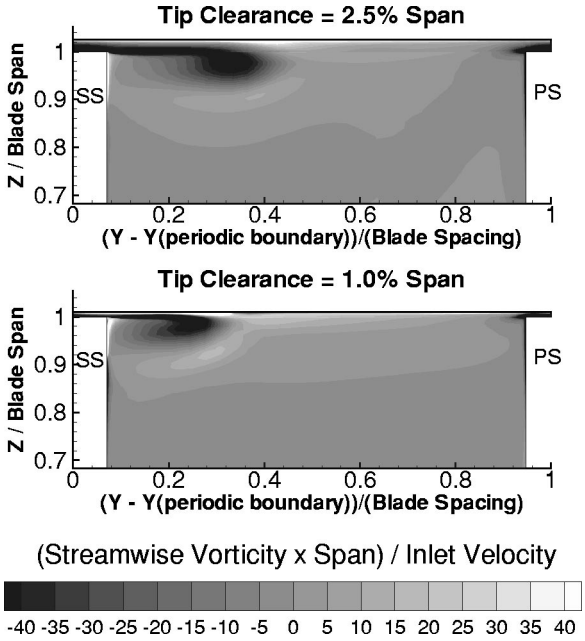

Fig. 6 Secondary vorticity contours in the y-z plane at X=90 percent axial chord

is never available to the fluid pathline that passes near to the blade tip. This results in the varying direction of the tip leakage flow.

Y-Z Plane Flow Description and Comparison. In this section, the secondary velocity, streamwise vorticity, and total pressure are presented in the y-z plane at 90 percent axial chord. y is measured from the periodic line as a percentage of the blade spacing and z is measured from the hub as a percentage of the blade span. Secondary velocity vectors are a combination of two velocities: w and v_s. w is the velocity component in the spanwise direction. v_s is found from decomposing the total velocity in the x-y plane into a 2D streamwise and secondary component, the latter of which being v_s. Non-dimensionalized streamwise vorticity is calculated using the following equation:

$$\omega_{\text{secondary}} = \left[\frac{\partial \nu_n}{\partial z} - \frac{\partial w}{\partial n}\right] \cdot \left(\frac{\text{Blade Span}}{\text{Inlet Velocity}}\right) \quad (1)$$

Total pressure is presented as the percentage remaining of the inlet total pressure. This is a gauge total pressure, based on a static pressure of zero at the exit of the computational domain. For all figures, the two cases are presented together for direct comparison.

Figure 5 shows the secondary velocity vectors projected into the y-z plane at 90 percent axial chord. In both cases, the rolled-up leakage vortex is clearly visible near the suction side of the gap. The leakage vortex is labeled (i) for the 1.0 percent case in Fig. 5. The leakage vortex is seen to extend across about 1/3 of the blade spacing in the 1.0 percent case and almost 1/2 the blade spacing in the 2.5 percent case. In both cases, the leakage vortex influences the 20 percent of the blade span closest to the casing. From Fig. 5, it is apparent that reducing the tip clearance height results in less mass flow through the gap and a smaller leakage vortex.

To the right of the leakage vortex, the vectors in the 1.0 percent case appear to indicate a vortex rotating in the counterclockwise direction. Figure 2 indicates that this is not the case, however. Instead, the vectors are indicative of three different secondary flows: the blockage secondary flow, the gap entrainment secondary flow, and the near-casing secondary flow. These flows are labeled ii, iii, and iv, respectively, in the 1.0 percent case of Fig. 5. These flows are separate entities and not one continual secondary flow. The same explanation holds true for the 2.5 percent case, although the near-casing secondary flow is not noticeable. Figure 5 does not show any near-casing secondary flow, but Fig. 2(*c*) indicates that one is indeed present. The absence of the near-casing secondary flow from Fig. 5 is due to the blockage secondary flow around the larger leakage vortex in the 2.5 percent case. The two secondary flows both act on the fluid near the outer casing, and act to cancel each other out.

Secondary vorticity contours in the Y-Z plane at 90 percent axial chord are shown in Fig. 6. The leakage vortex can be seen in both cases as the dark region of highly negative vorticity. This region extends from inside the gap as a plume, which then rolls around the leakage vortex. The overall size of the region of negative vorticity is similar for the two cases, but the degree of detachment from the blade is greater in the 2.5 percent case. A region of high positive vorticity is situated along the outer casing. To the left of the center of the leakage vortex, this region is due to the leakage flow's boundary layer on the outer casing. Midway between the two blades, the region is due to the near-casing secondary flow. Above and slightly to the right of the leakage vortex's center, the region is due to the turning of the near-casing secondary flow around the leakage vortex.

Both cases in Fig. 6 also show a region of positive vorticity below and to the right of the leakage vortex. The magnitude of the vorticity in this region is considerably less than that in the tip leakage vortex. The region is in the vicinity of the blockage secondary flow, and is the result of two mechanisms. First, the near casing secondary flow is turned around the leakage vortex, as can be seen in Fig. 2(*c*), Lab. viii. In the process, the obstructed fluid is made to rotate positively. The turned near-casing secondary flow is then carried downstream, as Fig. 2(*c*) also indicates, and is seen as the region being discussed. Second, Fig. 2(*d*) shows that the fluid pathlines labeled ''type 2'' are present in the region being considered. As discussed earlier, the fluid following these pathlines carries positive vorticity with it. Both of these two causes are less severe in the 2.5 percent case, resulting in the lower levels of positive vorticity in the region under consideration.

Total pressure contours in the Y-Z plane at 90 percent axial chord are shown in Fig. 7. The lowest total pressure region is associated with the leakage vortex and the entrainment of fluid around it. Although the high loss region associated with the tip leakage flow is larger in size in the 2.5 percent case, the 1.0 percent case does show lower total pressure values overall in the leakage vortex. The total pressure in the leakage vortex core is less than that inside the gap in both cases. This indicates that

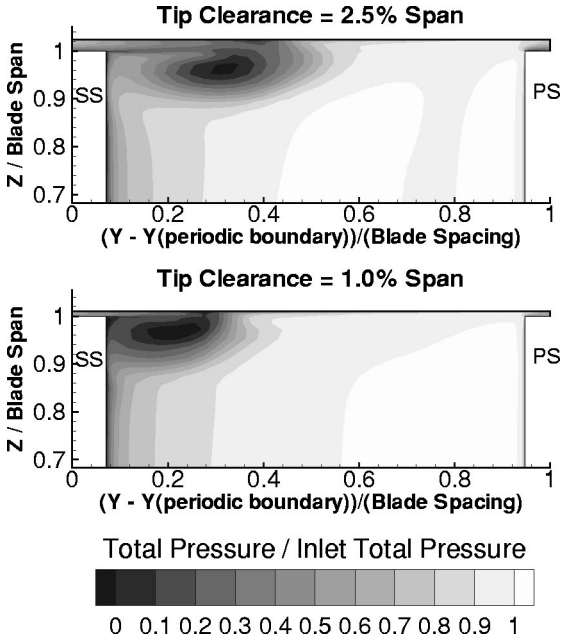

Fig. 7 Total pressure contours in the Y-Z plane at X=90 percent axial chord

losses are occurring inside the leakage vortex and not simply being convected in from the gap or from upstream. Also, the leakage vortex in both cases entrains fluid of higher total pressure around the leakage vortex near the blade suction surface. This can be seen from the plume of higher total pressure fluid below and to the left of the leakage vortex core. Because the leakage vortex in the 2.5 percent case is further removed from the surface, the entrained fluid makes its way further around the leakage vortex.

Blade-to-Blade Pressure Distribution and Velocity Field

The pressure distribution in the blade-to-blade plane at the blade tip is presented in Fig. 8. Pressure is presented as a pressure coefficient, defined below.

$$C_p = \frac{P_{\text{inlet}} - P_{\text{local}}}{Q_{\text{inlet}}} \quad \text{where} \quad Q_{\text{inlet}} = \frac{1}{2}\rho V_{\text{inlet}}^2 \tag{2}$$

The path of the leakage vortex is seen as a region of low pressure propagating from the downstream half of the blade in both cases. Figure 8 shows that the leakage vortex's low-pressure region is larger and oriented less parallel to the suction surface in the 2.5 percent case than in the 1.0 percent case. These features agree with the size and positioning of the vortex observed in Fig. 2. The 1.0 percent case exhibits a second low-pressure region, associated with the tight turning of the near-casing secondary flow around the obstructive leakage vortex. The near-casing secondary flow is not as severe and situated further from the blade tip in the 2.5 percent case, explaining its absence from Fig. 8.

The unloading of the blade pressure surface near the tip can be seen in Fig. 8. For both cases, the pressure distribution away from the gap region does not differ significantly from the data at the blade mid-span (not shown). Near to the pressure surface, however, the pressure at the tip decreases with proximity to the gap region. This decrease in pressure is associated with the gap entrainment secondary flow, and extends further out from the gap region in the 2.5 percent case. As the leakage flow enters the gap it separates over the corner formed by the pressure surface and the blade tip. This can be seen in Fig. 3(*a*). The rise in pressure in the direction of the leakage flow seen inside the gap in Fig. 8 is associated with the diffusing of the leakage flow beyond this separation region.

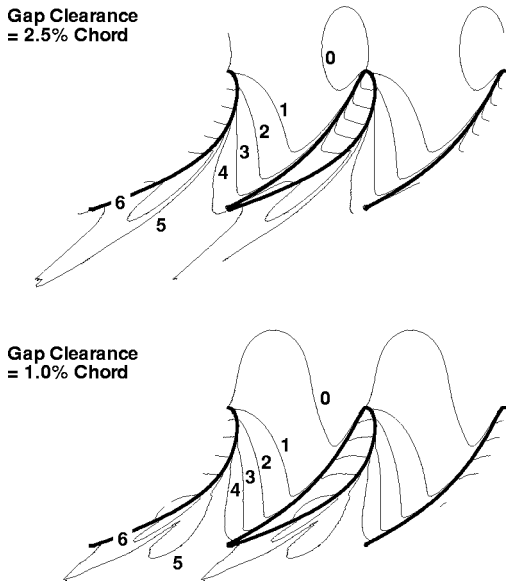

Fig. 8 Static pressure coefficient (Cp) contours in the blade-to-blade plane: Z=Blade tip

The pressure field in Fig. 8 also provides another possible mechanism for the roll-up of the leakage vortex's inner core. The pressure distribution in the passage near the suction surface side of the gap exhibits a largely positive gradient in the y direction. Therefore, the leakage flow, while driven by a pressure drop across the gap, exits at the suction side of the gap and quickly encounters an unfavorable pressure gradient. Rather than fight against the increasing pressure, the leakage flow turns towards the negative spanwise direction. This mechanism may also play a part in the roll-up of the leakage vortex

Velocity vectors in the blade-to-blade plane are presented at two spanwise locations in Fig. 9. Along the interface of the leakage and passage flows, a line has been added to indicate their division. Figure 9(*a*) shows velocity vectors in the blade-to-blade plane at a spanwise location half way between the blade tip and the outer casing. The flow through the gap is very similar in magnitude and direction for the two clearances. The direction of the leakage flow indicates that the flow is not driven by the pressure difference between the pressure and suction surfaces at a given axial location. Commonly, this pressure difference is used in the modeling of the leakage velocity. Instead, leakage fluid that enters the gap near the leading edge will direct itself both tangentially and axially across the gap, as it sees lower pressure values in that direction. The leakage fluid that enters the gap further downstream of the leading edge follows a similar trend, but is also obstructed by the upstream leakage fluid. For this cascade, the minimum pressure on the suction surface is located at approximately 75 percent axial chord.

The leakage flow from the gap begins to obstruct the passage flow very near the blade leading edge in both cases. The severity of the underturning of the flow between the blade suction surface and the sketched interface line is roughly the same for the two cases. The size of the underturned region at the passage exit is roughly half of the blade spacing in the 2.5 percent case, compared to only about a third of the blade spacing in the 1.0 percent case. The greater gap entrainment secondary flow in the 2.5 percent case can also be seen in Fig. 9(*a*). Vectors in the passage near the pressure surface are more severely underturned in the 2.5 percent case.

Figure 9(*b*) shows the velocity vectors in the blade-to-blade plane at a spanwise location of 91 percent span from the hub. This spanwise location corresponds roughly to the bottom of the leakage vortex in both cases. The overturning of the flow can be seen

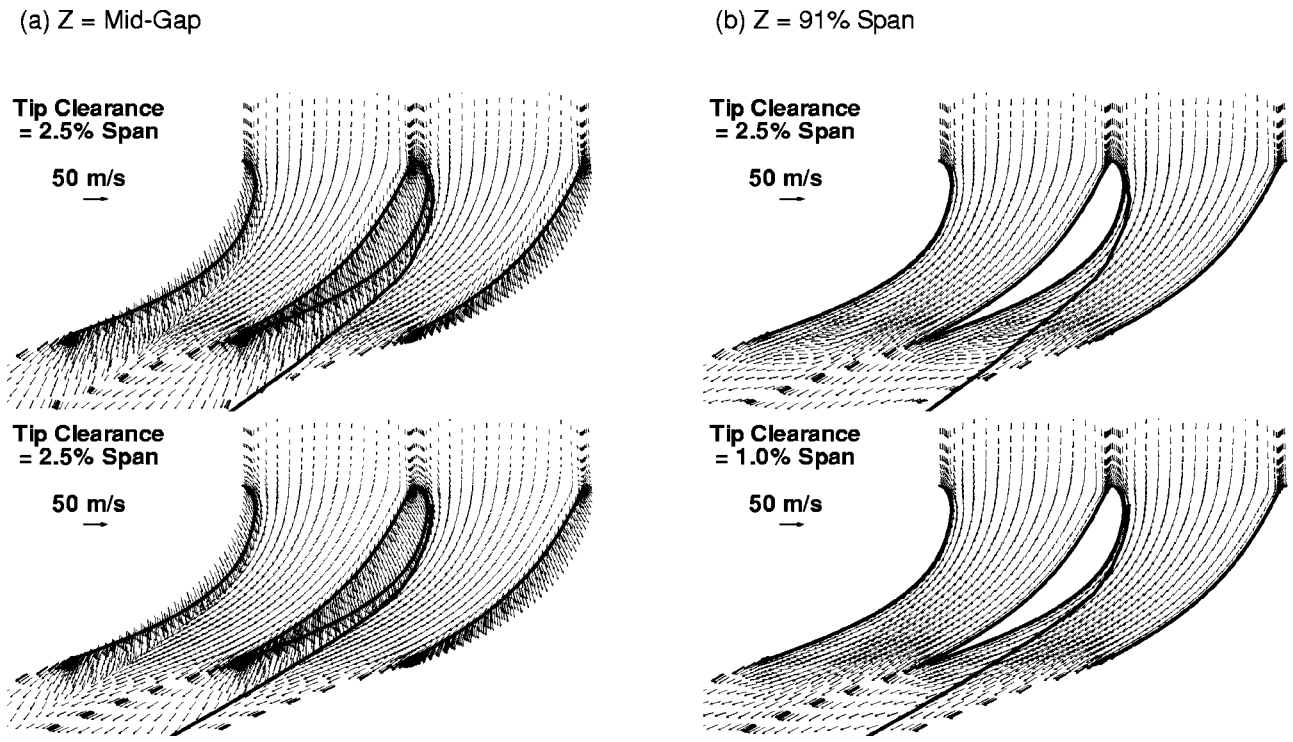

Fig. 9 Velocity vectors in the blade-to-blade plane

in the region between the suction surface and the intersection line for both cases. In the 1.0 percent case, overturning takes place throughout this region. In the 2.5 percent case, however, overturning is limited to the flow adjacent to the intersection line, indicating the vortex's detachment from the blade

Passage Averaged and Global Properties

This section compares the overall performance of the two cases in more quantifiable terms. Loss coefficient and mass flow through the gap are computed and compared. In addition, the particle tracing method used in Figs. 2 and 4 is used for some additional loss predictions.

The total mass flow into and out of the gap was integrated for both cases. In Fig. 10, the aggregate mass through the gap is plotted versus axial distance for both the pressure and suction sides of the gap. The division between the two sides of the gap is set at the intersection of the gap boundary and the periodic line, shown in Fig. 1. The total mass flow through the gap is 0.0213 kg/s in the 2.5 percent case and 0.0079 kg/s in the 1.0 percent case, compared to inlet mass flow values of 0.3414 kg/s and 0.3364 kg/s, respectively. In both cases, the mass flow out of the suction side lags behind the mass flow into the pressure side through the entire passage. This is because the leakage flow does not travel in a purely tangential direction across the gap. The negative mass flows near the leading edge for the suction side of the gap indicates mass entering the gap rather than exiting. Both cases show agreement at the trailing edge, indicating that mass flow is conserved through the tip leakage flow.

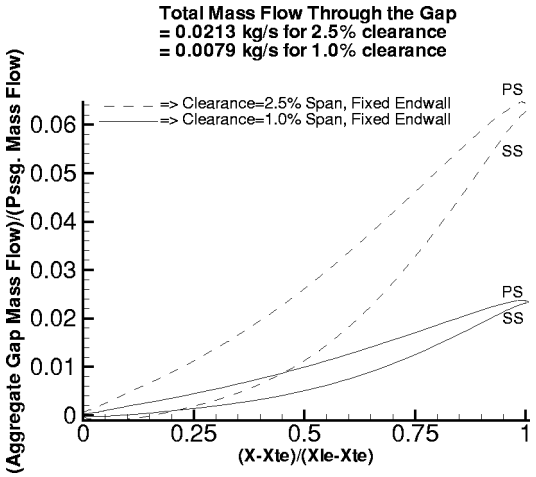

Fig. 10 Aggregate mass flow through the gap

Losses are presented as a loss coefficient, defined as follows:

$$\lambda = \text{Loss Coefficient} = \frac{Po_{\text{inlet}} - Po_{\text{local}}}{Q_{\text{inlet}}} \tag{3}$$

Passage-averaged loss coefficient values (mass averaged in the y-z plane) are compared for the two cases in Fig. 11. Values remain almost constant up until the leading edge. At 10 percent axial chord, the loss coefficient in the 2.5 percent case begins to exceed that of the 1.0 percent case. The rate of increase of the loss coefficient in the axial direction is also greater in the 2.5 percent case. By the trailing edge of the blade, the loss coefficient is roughly 30 percent higher in the 2.5 percent case.

The experimental data due to Bindon [1] for the 2.5 percent case is also shown in Fig. 11. In general, Bindon found slightly lower loss coefficient values throughout the passage. The difference between the measured and predicted values is attributed to two different causes. First, the artificial dissipation terms required for the numerical solution should act to overpredict the losses in the passage. Second, the loss measurements by Bindon did not include losses near the blade surface, where the boundary layer is present. Near the leading edge, these boundary layer losses are responsible for a larger percentage of the passage-averaged losses, and measured values should be less than predicted values.

The loss coefficient at the plane of the blade's mid-span location is also shown in Fig. 11. Analysis of total pressure values near the hub shows negligible losses due to the hub boundary

layer and passage vortex. This is somewhat expected, since the turning of the blade is only 68 degrees. Therefore, the difference between the passage loss distribution and the midspan loss distribution closely represents the losses due to tip clearance effects. At the trailing edge, Fig. 11 shows that the differences between the passage averaged loss coefficients and the 2D profile loss coefficient are 0.24 and 0.10 for the 2.5 percent and 1.0 percent cases, respectively. For these two cases, the ratio of the losses in the endwall region ($\lambda - \lambda_{2D}$) to the nondimensionalized tip clearance height is close to 10 for both cases. This indicates that endwall losses are proportional to the tip clearance height. The endwall region accounts for almost a half of the passage's losses in the 2.5 percent case and a third of the passage's losses in the 1.0 percent case.

In addition to the passage averaged losses shown in Fig. 11, the Lagrangian method used to create Figs. 2 and 4 was also used to predict losses specific to the tip leakage flow and the freestream. The loss coefficient is defined in Eq. 4. Equation 4 also shows how the loss coefficient can be divided into the sum of coefficients, which correspond to different parts of the total flow field.

$$\lambda_{\text{total}} = \frac{P_{o,\ \text{in(mass average)}d} - P_{o,\ \text{out(mass average)}d}}{Q_{\text{in}}} = \frac{m_{\text{leakage}}}{m_{\text{total}}}\left(\frac{P_{o,\ \text{in}} - P_{o,\ \text{out}}}{Q_{\text{in}}}\right)_{\substack{\text{leakage fluid}\\ \text{(mass average)}d}} + \frac{m_{\text{passage}}}{m_{\text{total}}}\left(\frac{P_{o,\ \text{in}} - P_{o,\ \text{out}}}{Q_{\text{in}}}\right)_{\substack{\text{passage fluid}\\ \text{(mass average)}d}}$$

$$= \frac{m_{\text{leakage}}}{m_{\text{total}}}\lambda_{\text{leakage}} + \frac{m_{\text{passage}}}{m_{\text{total}}}\lambda_{\text{passage}}$$

and

$$\lambda_{\text{leakage}} = \left(\frac{P_{o,\ \text{in}} - P_{o,\ \text{gap inlet}}}{Q_{\text{in}}}\right) + \left(\frac{P_{o,\ \text{gap inlet}} - P_{o,\ \text{gap exit}}}{Q_{\text{in}}}\right) + \left(\frac{P_{o,\ \text{gap exit}} - P_{o,\ \text{out}}}{Q_{\text{in}}}\right) = \lambda_{\text{inlet to gap}} + \lambda_{\text{across gap}} + \lambda_{\text{gap to exit}} \quad (4)$$

The Lagrangian method involved following fluid pathlines from every grid point at the inlet of the passage, monitoring whether or not each particle passed through the gap, and mass averaging the total pressure over each of the two sets of particles: those passing through the gap and those passing through the passage. The mass flow along each pathline is found from the normal velocity and grid cell volume at the pathline's origin, as well as the density of air. The method then assumes that each pathline neither gains nor looses mass as it travels through the passage. This assumption becomes more valid with an increasing number of pathlines.

A total of 7,650 pathlines were used in the following computations. Values computed from this Lagrangian method are compared below with values found by direct integration in order to validate the method. The Lagrangian method found the mass flow rate through the gap to be 0.0217 kg/s for the 2.5 percent case and 0.0083 kg/s for the 1.0 percent case, compared with integrated values of 0.0213 and 0.0079 kg/s, respectively. Also, the values of the total passage loss coefficient at 120 percent axial chord were found by the Lagrangian method were 0.568 for the 2.5 percent case and 0.444 for the 1.0 percent case. These values compare favorably with the values found from direct integration, which are 0.615 and 0.481.

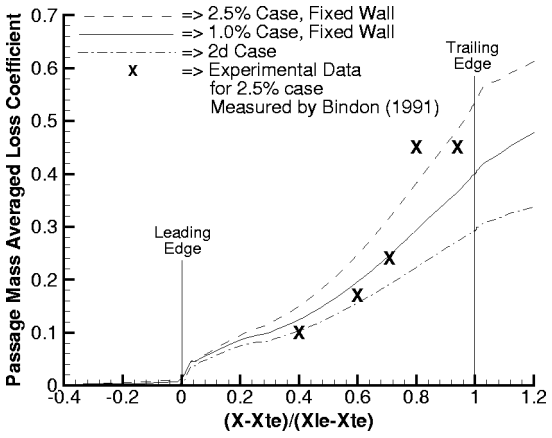

Fig. 11 Passage averaged loss coefficient values through the passage

Table 3 presents the components of the passage loss coefficient as calculated by the Lagrangian method. In Table 3, the term ''Average Local Value'' refers to the average total pressure loss in a particular region of the flow, such as the flow through the gap. The term ''Mass Averaged Value'' is equal to the average local value times the ratio of the mass flow through the particular region to the total mass flow through the cascade. Therefore, the flow through the passage will have a lower average local value of its loss coefficient than the flow through the gap, but a much higher mass averaged value, since much more mass passes through the passage than through the gap. The exit referred to in Table 3 is at 120 percent axial chord.

Comparing the average local values, the 1.0 percent case exhibits higher losses inside the gap than the 2.5 percent case. This is somewhat expected, since the flow in the center of the larger gap is more likely to be inviscid. The passage in the 2.5 percent case shows higher losses, due to the larger leakage vortex and its greater effect on the passage flow. At the same time, the losses from the leakage flow downstream of the gap exit are negative in the 1.0 percent case, indicating that the leakage flow is gaining energy from the passage.

When considering the mass averaged values of the loss coefficient, the losses in the passage account for the greatest percentage of the total losses in the passage. This is because the mass flow through the passage is significantly higher than the mass flow

Table 3 Loss coefficient components computed by a Lagrangian method

Region	λ total	λ inlet to gap	λ across gap	λ gap to exit	λ passage
2.5% Case, Average Local Values		1.322	1.628	0.338	0.418
1.0% Case, Average Local Values		1.415	2.211	-0.523	0.389
2.5% Case, Mass Averaged Values	0.568	0.069 (12.1%)	0.085 (15.0%)	0.018 (3.2%)	0.396 (69.7%)
1.0% Case, Mass Averaged Values	0.444	0.029 (6.5%)	0.045 (10.2%)	-0.011 (-2.4%)	0.381 (85.7%)

through the gap. The percentage of the total losses occurring in the passage flow is as high as 85.7 percent in the 1.0 percent case, where the mass flow through the gap is only 2 percent of the total mass into the passage. For the 2.5 percent case, these two percentage values are 69.7 percent and 5.2 percent, respectively. Of course, this method does not take into account the effect of the leakage flow on the losses in the passage, but it still presents insight into sources in the turbine losses.

Conclusion

A pressure-correction based, three-dimensional, Navier-Stokes CFD code has been used to simulate and study the effects tip clearance height and the associated flow physics in a linear turbine cascade. Simulations were carried out using a grid similar to a typical embedded H-type grid, but with improved skewness and cell aspect ratios in the leading and trailing edge regions. The simulation of a turbine cascade was carried out at tip clearance heights of 2.5 percent and 1.0 percent of the blade's span. The results of the two simulations were then compared directly.

Major conclusions that were common to both of the first two simulations are listed and discussed below.

1 The inner core of the leakage vortex is composed entirely of fluid that passed through the tip clearance gap. This indicates that leakage jet/freestream flow shearing is not responsible for the initial roll-up of the leakage vortex. An alternative explanation of leakage vortex roll-up, involving the convection of vorticity from the gap region and the adverse pressure gradient in the direction of the leakage jet, is proposed.

2 The core of the leakage vortex is composed of fluid that passes through the gap from the leading edge and midchord regions and near to the blade tip. Vortex roll-up begins at between 30 percent and 40 percent of the axial distance from the leading edge. The leakage flow through the gap from leading edge to mid-chord and near to the outer casing resists wrapping around the leakage vortex core, possibly due to its opposing vorticity from its shearing on the outer casing.

3 Three major secondary flows are also present in the passage. A gap entrainment secondary flow acts to carry fluid towards the pressure side of the gap region. The leakage vortex acts to obstruct the passage flow near the suction surface, resulting in the blockage secondary flow. A near-casing secondary flow toward the suction side of the blade is also present, which two different mechanisms contribute toward.

Major conclusions pertaining to the effect of reduced tip clearance height are listed and discussed below.

1 The leakage vortex in the 2.5 percent case is noticeably larger than that in the 1.0 percent case. At the passage exit, the leakage vortex flow/vortex occupies roughly half of the blade spacing near the casing in the 2.5 percent case, compared with roughly a third of the blade spacing in the 1.0 percent case.

2 The mass flow through the gap is larger for the 2.5 percent case, with a value of 6.2 percent of the passage mass flow rate, compared to only 2.3 percent of the passage mass flow rate in the 1.0 percent case.

3 The leakage vortex in the 2.5 percent case is further detached from the blade than the leakage vortex in the 1.0 percent case. This allows for greater entrainment of the passage flow around the leakage vortex.

4 The results indicate that vorticity convection from the gap is most responsible for the roll-up of the leakage vortex in cases with smaller tip clearances, such as the 1.0 percent case. Interpreting the differences between the two cases leads to the conclusion that a leakage jet/freestream flow interaction is responsible for the roll-up of the leakage vortex in cases with larger tip clearances.

5 In general, the gap entrainment secondary flow and blockage secondary flow are more severe in the 2.5 percent clearance case, while the near-casing secondary flow is more severe in the 1.0 percent case.

6 The reduction in tip clearance height leads to a reduction in the passage-averaged loss coefficient at the passage exit from 0.525 to 0.395.

7 A Lagrangian method of calculating losses was developed, which shows that the mass flow passing through the gap accounts for 30.3 percent of the total losses in the 2.5 percent clearance case, compared to only 14.3 percent of the total losses in the 1.0 percent clearance case.

Acknowledgments

This research was supported by the Office of Naval Research (U.S. Navy) through their AASERT program (N 00014-94-1-0839), with J. Fein as the technical monitor. It was also partially supported by Army Research Office (U.S. Army) through the AASERT program (DAAG 55-97-1-0201) with T. Doligalski as the technical monitor.

Nomenclature

Cp	=	static pressure coefficient, $(p_{in}-p)/Q_{in}$
m	=	mass flow rate
n	=	direction normal to the 2D streamwise direction in the blade-to-blade plane
P	=	static pressure
P_o	=	total pressure
Q_{in}	=	inlet dynamic pressure
u, v, w	=	mean velocity components in the x, y, z directions
V	=	total velocity
v_n	=	secondary velocity in the n direction
x, y, z	=	Cartesian coordinates (see Fig. 1)
y+	=	non-dimensional turbulence wall function,
λ	=	loss coefficient, $(p_{oin}-p_o)/Q_{in}$
μ	=	kinematic viscosity
τ	=	tip clearance height/blade span
$\omega_{secondary}$	=	secondary vorticity

References

[1] Bindon, J. P., 1991, private communication.

[2] Bindon, J. P., and Morphis, G., 1992, ''The Development of Axial Turbine Leakage Loss for Two Profiled Tip Geometries Using Linear Cascade Data,'' ASME J. Turbomach., **114**, No. 1, Jan., pp. 198–203.

[3] Sjolander, S. A., 1997, ''Secondary and Tip-Clearance Flows in Axial Turbines: Physics of Tip-Clearance Flows—I,'' von Karman Institute for Fluid Dynamics, Lecture Series 1997–01.

[4] Lakshminarayana, B., 1996, *Fluid Dynamics and Heat Transfer of Turbomachinery*, John Wiley & Sons, Inc.

[5] Wantanabe, T., Nozaki, O., Kikuchi, K., and Tamura, A., 1991, ''Numerical Simulation of the Flow Through Cascades With Tip Clearance,'' ASME FED-120, ''Numerical Simulations in Turbomachinery.''

[6] Liu, J. S., and Bozzola, R., 1993, ''Three-Dimensional Navier-Stokes Analysis of the Tip Clearance Flow in Linear Turbine Cascades,'' AIAA J., **31**, No. 11, pp. 2068–2074.

[7] Staubach, J. B., Sharma, O. P., and Stetson, G. M., 1996, ''Reduction of Tip Clearance Losses Through 3-D Airfoil Designs,'' Proc. R. ASME/IGTI Conference, Singapore.

[8] Chernobrovkin, A., 1999, ''Numerical Simulation of Complex Turbomachinery Flows,'' Ph.D. Thesis, The Pennsylvania State University.

[9] Kind, R. J., Sjolander, S. A., and Yaras, M. I., 1995, ''Retained Lift: Theoretical Difficulties With the Concept and an Alternative Explanation of Observations,'' ASME J. Turbomach., **117**, pp. 485–497.

[10] Chien, K.-Y., 1982, ''Predictions of Channel and Boundary-Layer Flows With a Low-Reynolds-Number Turbulence Model,'' AIAA J., **20**, No. 1, pp. 33–38.

[11] Basson, A. H., and Lakshminarayana, B., 1995, ''Numerical Simulation of Tip Clearance Effects in Turbomachinery,'' ASME J. Turbomach., **109**, No. 4, pp. 545–549.

[12] Tallman, J. A., 1999, ''Simulation of Tip Leakage Flows in a Turbine Rotor Using Computational Fluid Dynamics,'' MS Thesis in Mechanical Engineering, The Pennsylvania State University, available at http://navier.aero.psu-edu/~jat.

Numerical Simulation of Tip Leakage Flows in Axial Flow Turbines, With Emphasis on Flow Physics: Part II—Effect of Outer Casing Relative Motion

J. Tallman
Graduate Research Assistant
e-mail: jat@turbo3.aero.psu.edu

B. Lakshminarayana
Evan Pugh Professor and Director
e-mail: bllaer@engr.psu.edu

Center for Gas Turbine and Power,
Pennsylvania State University,
153-J Hammond Bldg.,
University Park, PA 16802

A pressure-correction based, 3D Navier-Stokes CFD code was used to simulate the effects of turbine parameters on the tip leakage flow and vortex in a linear turbine cascade to understand the detailed flow physics. A baseline case simulation of a cascade was first conducted in order to validate the numerical procedure with experimental measurements. The effects of realistic tip clearance spacing, inlet conditions, and relative endwall motion were then sequentially simulated, while maintaining previously modified parameters. With each additional simulation, a detailed comparison of the leakage flow's direction, pressure gradient, and mass flow, as well as the leakage vortex and its roll-up, size, losses, location, and interaction with other flow features, was conducted. Part II of this two-part paper series focuses on the effect of relative motion of the outer casing on the leakage flow and vortex development. Casing relative motion results in less mass flow through the gap and a smaller leakage vortex. The structure of the aerothermal losses in the passage change dramatically when the outer casing motion was incorporated, but the total losses in the passage remained very similar. Additional secondary flows that are seen near the casing are also discussed. [DOI: 10.1115/1.1369113]

Introduction

Numerical simulation results for a linear turbine cascade were presented in Part I of this two-part paper. These simulations were carried out using a pressure-correction based, 3D Navier-Stokes CFD code. Two cases were simulated, which were identical except for the tip clearance spacing. These simulations provided valuable insight into the secondary flow features present in an axial flow turbine, most notably the leakage flow and vortex. Still, the results presented in Part I are not representative of a true turbine because the relative motion between the blade and the outer casing was not included in the simulations. In a reference frame that is moving with the turbine blade, the outer casing can be seen to move over the top of the blade from suction side to pressure side. This direction is opposite the direction of the leakage flow. Therefore, the outer casing motion and its subsequent shearing on the leakage fluid acts to reduce the leakage flow through the gap and, thus the size of the leakage vortex. Also, the outer casing motion acts to enhance the near-casing secondary flow, which was identified and defined in Part I.

Part II of this two-part paper focuses on the effect of the relative motion of the outer casing on the leakage flow, leakage vortex, and additional secondary flows in axial flow turbines. The reduced tip clearance case (1.0 percent case) presented in Part I was repeated using inlet conditions more representative of a real turbine. The case was then simulated once more with casing relative motion included. Information on the case geometry, operating conditions, and simulation technique are given in Part I.

Modification of the Inlet Conditions

In order to simulate the relative motion of the outer casing, the inlet velocity profile near the outer casing must include a boundary layer with velocity components in both the axial and tangential directions. At the outer casing the velocity must have the value of the outer casing (relative to the blade) and must be in the negative tangential direction. Away from the casing, the velocity must have a magnitude and direction corresponding to the design conditions of the blade. The blade being studied is that of a cascade, however, and the inlet profile used for the simulations in Part I of this paper is based on the boundary layer thickness and turbulence quantities measured by Bindon [1,2], which did not include casing relative motion.

A new inlet velocity profile was computed by simulating a turbine nozzle, using the same cascade with no tip clearance and no casing motion relative to the blade. The axial and tangential components of the flow at the nozzle exit were then used as the inlet conditions to the simulated rotor. This concept is illustrated in Fig. 1. For this study, the casing's speed relative to the blade is 31.0 m/s. The spanwise component of the inlet profile is assumed to be zero everywhere. Because it is taken from a simulated nozzle, the new inlet conditions should better match the conditions inside a real turbine rotor.

The original and computed inlet profiles and turbulence properties are shown in Fig. 2. Note that the Z direction refers to the spanwise direction. The most noticeable change to the inlet profile is the thickness of the outer casing's boundary layer, which is roughly a tenth of that in the original profile. For the moving wall case, the reduced tangential component of velocity in the boundary layer results in a negative incidence angle at the leading edge of the gap. Such a situation makes numerical simulation of the flow in the gap more difficult. The computed boundary layer and its smaller thickness result in a reduction of this ill effect.

The inlet freestream turbulence intensity has increased from 2 percent in the original inlet profile to roughly 11 percent in the computed inlet profile. The higher turbulence intensity is more likely similar to a real turbine, where combustors and flow unsteadiness are present. Also, the turbulence intensity is nondimensionalized with the inlet relative velocity to the blade, or

Contributed by the International Gas Turbine Institute and presented at the 45th International Gas Turbine and Aeroengine Congress and Exhibition, Munich, Germany, May 8–11, 2000. Manuscript received by the International Gas Turbine Institute February 2000. Paper No. 2000-GT-516. Review Chair: D. Ballal.

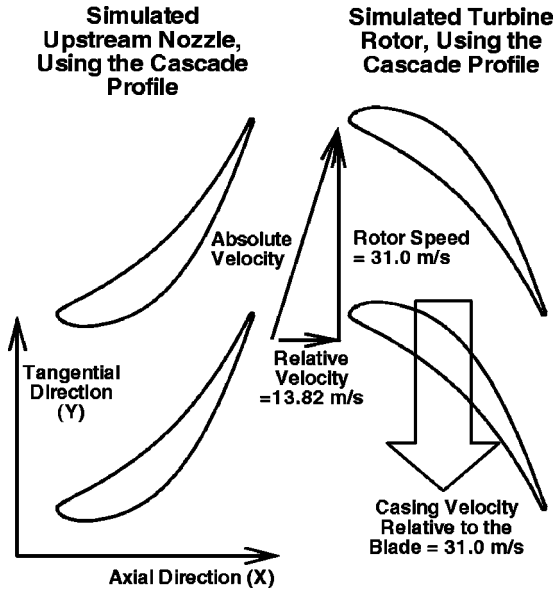

Fig. 1 Rotor inlet conditions from a simulated nozzle upstream

13.82 m/s. Using the total velocity in the absolute frame of reference would result in a turbulence intensity closer to five percent. The turbine rotor sees higher turbulence intensity in the relative frame of reference. Inlet turbulence length scales differ negligibly between the two cases.

For completeness, the flow through the cascade was computed with no relative casing motion, tip clearance of 1.0 percent span, and the computed inlet profile with its tangential component set to zero. This fixed wall simulation was compared directly with the 1.0 percent case in Part I and only a negligible difference between the two flows was observed. Velocity magnitudes and directions near the leading edge of the gap region were very similar for the two cases. This similarity is attributed to the placement of the passage inlet almost a full axial chord length upstream of the leading edge. In the steady solution, the flow near the leading edge is influenced to a greater extent by the downstream disturbance of the blade than by the far upstream disturbance of the change in inlet conditions. An overview of the comparison of these two cases is given in the thesis by Tallman [3].

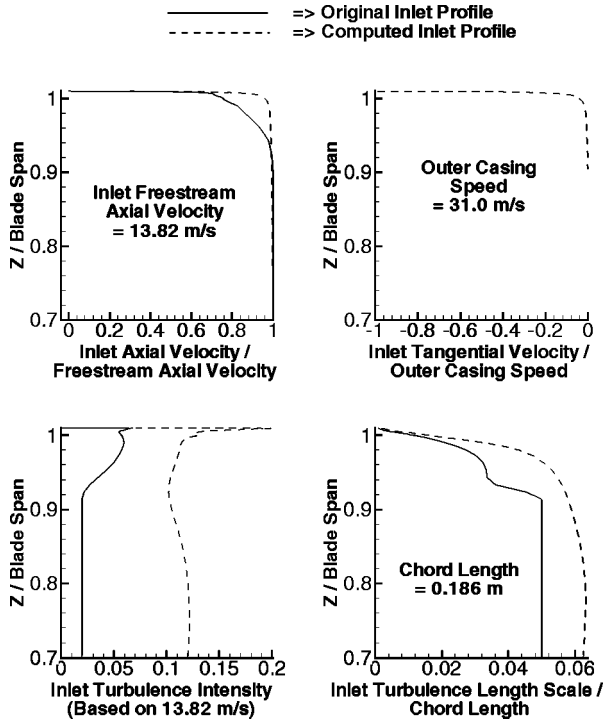

Fig. 2 Inlet velocity and turbulence profile comparison

Flow Physics and the Effect of Outer Casing Relative Motion

The results of two numerical simulations of the 3D-turbine blade described earlier are presented and interpreted here. The relative motion of the outer casing is included in the second simulation. All other parameters of the two computations were identical. The tip clearance height was 1.0 percent of the blade span for both of the cases. The two cases are referred to as the ''fixed wall'' and ''moving wall'' cases throughout this paper.

Flow Particle Traces in the Tip Clearance Region. Figure 3(*a*) shows flow pathlines that pass through the gap for both the fixed wall and moving wall cases. At each of six axial locations, six fluid pathlines are shown, equally spaced throughout the gap in the spanwise direction. The fluid pathlines are colored in the order of the rainbow to correspond with their axial location in the gap. For example, the red pathlines pass through the gap closest to the leading edge and the violet pathlines pass through the gap closest to the trailing edge.

The gap entrainment secondary flow, which was defined for fixed wall cases in Part I of this paper, is also visible in the moving wall case, and is labeled i in both cases of Fig. 3(*a*). The gap entrainment secondary flow is illustrated by the course of the fluid pathlines upstream of the blade in Fig. 3(*a*), and appears similar for the fixed and moving wall cases. Less mass is entrained into the gap near the outer casing in the moving wall case, due to the obstruction of the outer casing's shear layer.

The flow through the gap is noticeably different for the two cases in Fig. 3(*a*). In the fixed wall case, Fig. 3(*a*) shows 36 fluid pathlines, which enter the pressure side of the gap at evenly spaced locations. 36 fluid pathlines of similar origins were generated for the moving wall case, but only about half of them are seen in Fig. 3(*a*). The fluid pathlines that are not seen in the moving wall case of Fig. 3(*a*) are captured by the casing's shear layer and exit out of the pressure side of the gap in a nearly tangential direction. These fluid pathlines are represented by a single fluid pathline labeled ii and act to reduce the tip clearance space available for the leakage flow.

Inside the gap, the obstruction of the leakage flow by the moving casing's shear layer is most severe near the blade leading edge. This is apparent from the absence of red fluid pathlines from the gap in the moving wall case of Fig. 3(*a*), and has two parts to its explanation. First, the outer casing's motion is more directly opposed to the leakage flow near the leading edge. Second, the pressure drop across the gap, which drives the leakage flow, is not yet established.

A comparison of the two cases in Fig. 3(*a*) shows that the leakage flow through the gap is more toward the axial direction in the moving wall case. The shear layer on the moving wall not only reduces the leakage mass flow through the gap, but also obstructs the leakage flow, forcing it to exit the gap at locations further downstream. This effect is observed throughout the gap, but is most severe at axial locations closer to the leading edge. Conversely, the violet fluid pathlines that cross the gap near the trailing edge are quite similar for the two cases.

Figure 3(*a*) also shows that the relative motion of the casing has a substantial effect on the behavior of the leakage flow after it exits the gap. In the fixed wall case, the leakage flow pathlines exit the gap in one of three different manners, one of which forms the inner core of the leakage vortex beginning within about 30 percent to 40 percent axial chord of the blade leading edge. These

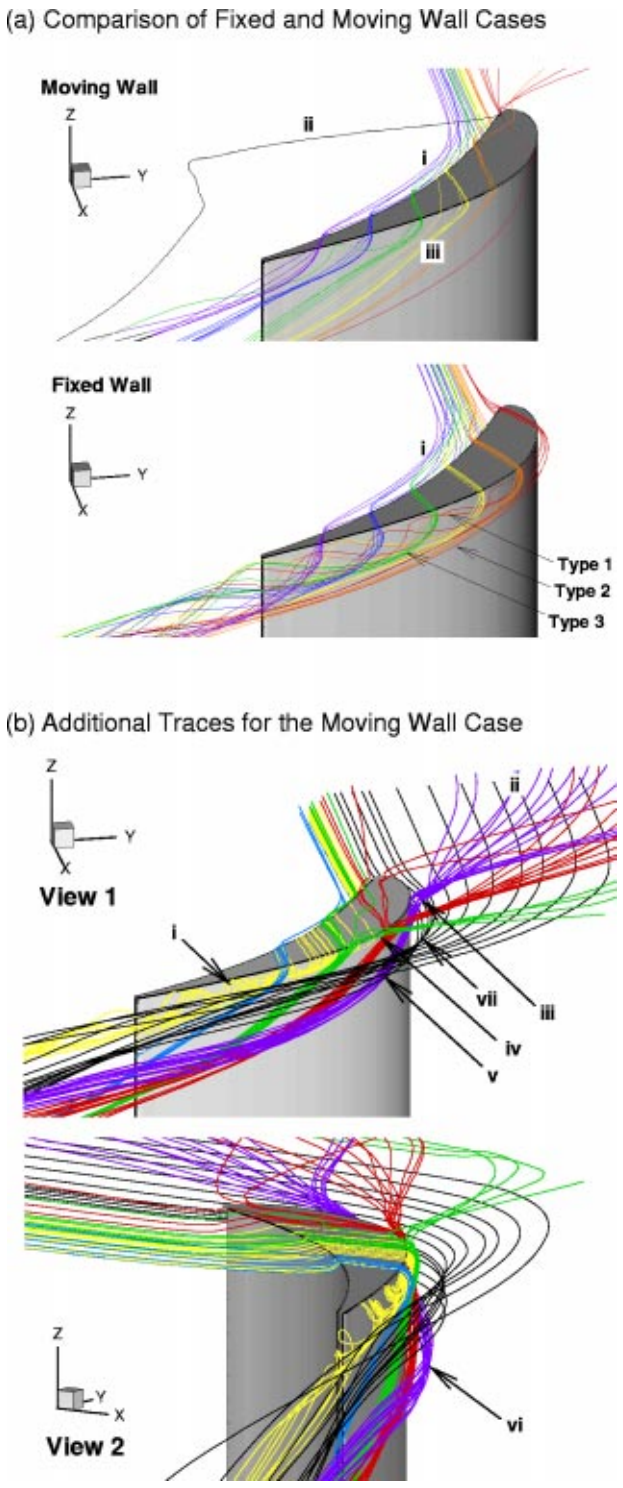

Fig. 3 Particle traces through the passage and gap

three types of leakage flow pathlines are labeled in Fig. 3(*a*), and were previously defined and discussed in Part I of this paper. Figure 3(*a*) shows that in the moving wall case, most of the leakage flow exiting the gap on the suction side does not find its way into the leakage vortex. Instead, the exiting leakage flow travels toward the bottom of the passage and joins together with the passage flow (Fig. 3(*a*), Lab. iii). Only the violet fluid pathlines and one green fluid pathline appear to be entraining around the outside of a leakage vortex core.

Figure 3(*b*) shows a different set of fluid pathlines for the moving wall case than those that are compared in Fig. 3(*a*). In order to illustrate their three-dimensionality, these fluid paths are shown from two different views. Three different secondary flows and their influences are illustrated for the moving wall case by the fluid pathlines in Fig. 3(*b*). These secondary flows are the leakage vortex, the near-casing secondary flow, and the blockage secondary flow. The near-casing secondary flow and blockage secondary flow were defined in Part I of this paper.

Leakage Vortex: The yellow flow pathlines in Fig. 3(*b*) show that a leakage vortex is definitely present in the moving wall case. This leakage vortex is labeled i, and its size is roughly a third of that of the leakage vortex in the fixed wall case, shown in Fig. 3(*a*). The leakage vortex in the moving wall case remains adjacent to the blade suction surface and follows its curvature. This is due to both the reduced mass flow through the gap and the tangential velocity component of the casing shear layer, which acts to hold the leakage vortex against the suction surface.

Figure 3(*b*) shows that the inner core of the leakage vortex in the moving wall case begins to roll-up at about 50 percent axial chord. An extensive flow pathline analysis found that the leakage vortex is composed entirely of fluid that passes through the gap. As is with the fixed wall case, the lack of passage fluid inside the leakage vortex core tends to indicate that leakage jet/passage flow shearing is not responsible for the initial roll-up of the leakage vortex. An alternative explanation for the roll-up of the leakage vortex was proposed for the fixed wall case in Part I of this paper. This explanation pointed to the convection of vorticity from the gap as the primary mechanism for the roll-up of the leakage vortex.

For the fixed wall case, part I of this paper showed that fluid passing through the gap region near to the blade tip was rotational, due to its shearing by the tip. This rotation was in a direction similar to that of the leakage vortex. In contrast, fluid passing through the gap region near to the outer casing was seen to be rotational in a direction opposite to that of the leakage vortex. Upon exiting the gap, the fluid that passed near the tip would roll into the leakage vortex, while the fluid that passed near the casing would not. Figure 3(*b*) shows similar trends in the roll-up of the leakage vortex in the moving wall case. As mentioned earlier, the outer casing's shear layer acts to reduce the amount of gap space available to the leakage flow. This will then lead to a reduction in the leakage flow's boundary layer thickness on the blade tip. Therefore, less of the leakage fluid will convect negative vorticity out of the gap, and a smaller leakage vortex should result. Figure 3(*b*) shows that the size of the leakage vortex agrees with this expectation. In addition, because of the reduced boundary layer thickness on the blade tip, the fluid that does roll into a leakage vortex should pass through the gap very near to the blade tip. Close examination of Fig. 3(*b*) shows this as well. The leakage vortex is composed entirely of leakage fluid that crosses the gap within the 10 percent of the clearance height nearest to the blade tip.

Near-Casing Secondary Flow: The near-casing secondary flow was defined in Part I of this paper for the fixed wall case. In the moving wall case, the motion of the outer casing acts to enhance the near-casing secondary flow and to increase its influence on the overall flow field. The influence of the near-casing secondary flow is explained for the moving wall case by comparing the violet and black fluid pathlines.

Far upstream of the blade, the violet fluid pathlines are situated closer to the outer casing than the black fluid pathlines (Fig. 3(*b*), Lab. ii). At this location, both the violet and the black fluid pathlines are well separated from one another in the tangential direction. As the fluid pathlines travel toward the passage, however, the near-casing secondary flow causes the violet fluid pathlines to deviate from the 2D streamwise course exhibited by the black fluid pathlines. The violet fluid pathlines accumulate together at the suction side of the passage (Fig. 3(*b*), Lab. iii). The leakage fluid (Fig. 3(*a*), Lab. iii) and the accumulated near-casing second-

ary flow fluid further downstream (Fig. 3(*b*), Lab. iv) then act as an obstruction to the cluster of violet fluid pathlines. The violet fluid pathlines (Fig. 3(*b*), Lab. v) are forced underneath both the leakage vortex and the leakage fluid that did not roll into the leakage vortex.

For the moving wall case, Fig. 3(*b*) shows that the region underneath the leakage vortex is composed of fluid that is rotational in a direction opposite to the leakage vortex. The collection of violet fluid pathlines (Fig. 3(*b*), Lab. v & vi) illustrates this most clearly. The two views show that these pathlines rotate positively over the top of the cluster of red pathlines (Fig. 3(*b*), Lab. iv). The violet, red, and green fluid pathlines indicate that the fluid in this region originated near the outer casing. Therefore, positive vorticity from the enhanced near-casing secondary flow is carried downstream to the region below the leakage vortex. Additionally, leakage fluid from the region of the gap near to the casing also carries positive vorticity into this region. This is shown in Fig. 3(*a*) by the fluid pathlines near Lab. iii.

Blockage Secondary Flow: The blockage secondary flow that was defined for the fixed wall case in Part I of this paper is also present in the moving wall case. Figure 3(*b*), Lab. vii shows that near the blade's leading edge and tip, the black fluid pathlines are obstructed around the leakage flow (Fig. 3(*a*), Lab. iii) and the accumulated near-casing secondary flow (Fig. 3(*b*), Lab. iii). This differs from the fixed wall case, where the leakage vortex acted as the obstruction directly. This was shown in Part I of this paper.

y-z Plane Flow Description and Comparison: The secondary velocity, streamwise vorticity, and total pressure are presented here in (*y-z*) planes located at 40 percent and 90 percent axial chord. In Figs. 4 and 5, Parts *a*, *b*, and *c* show secondary velocity vectors, contours of streamwise vorticity, and contours of total pressure, respectively. Secondary velocity and streamwise vorticity are defined in Part I of this two-part paper.

In the moving wall case, total pressure values are no longer normalized directly by the inlet total pressure. Instead, the inlet total pressure first is increased by a quantity based on the integrated work done on the passage fluid by the moving wall. The amount of increase will therefore depend on the axial location of the plane. This new total pressure is more representative of the energy made available to the passage up to a particular axial location, and is used for normalization. The work done on the entire computational domain by the casing motion results in a pressure increase of around 15 Pascals, or about 2 percent of the pressure drop through the flow.

$X=40$ Percent Axial Chord From the Leading Edge: Figure 4(*a*) shows secondary velocity vectors at 40 percent axial chord. The structure of the flow near the outer casing is modified dramatically when casing relative motion is simulated. The leakage jet no longer penetrates into the passage, but instead is forced toward the hub right at the suction surface. This is due to the interaction between the leakage jet and the near-casing secondary flow. A closer analysis of Fig. 4(*a*) for the moving wall case showed no signs of leakage vortex roll-up, like that which is seen near the casing-suction surface corner in the fixed wall case.

The three additional secondary flows that were defined in Part I of this paper are also visible in Fig. 4(*a*). In the moving wall case, the near-casing secondary flow, gap entrainment secondary flow, and blockage secondary flow are labeled i, ii, and iii, respectively. The near-casing secondary flow has been greatly enhanced by the motion of the casing. The fluid pathlines in Fig. 3(*b*) (Lab. iii) show that this flow joins with the leakage flow near the blade's suction surface and the two flows travel together to the area below the leakage vortex {Fig. 4(*a*), label iv}. The passage flow near the suction side of the blade is then obstructed around the flow labeled iv, resulting in the blockage secondary flow. At the pressure side of the passage, the gap entrainment secondary flow is similar for the fixed and moving wall cases. The magnitudes of these secondary vectors are, in general, slightly larger for the fixed wall case, indicating a greater mass flow through the gap.

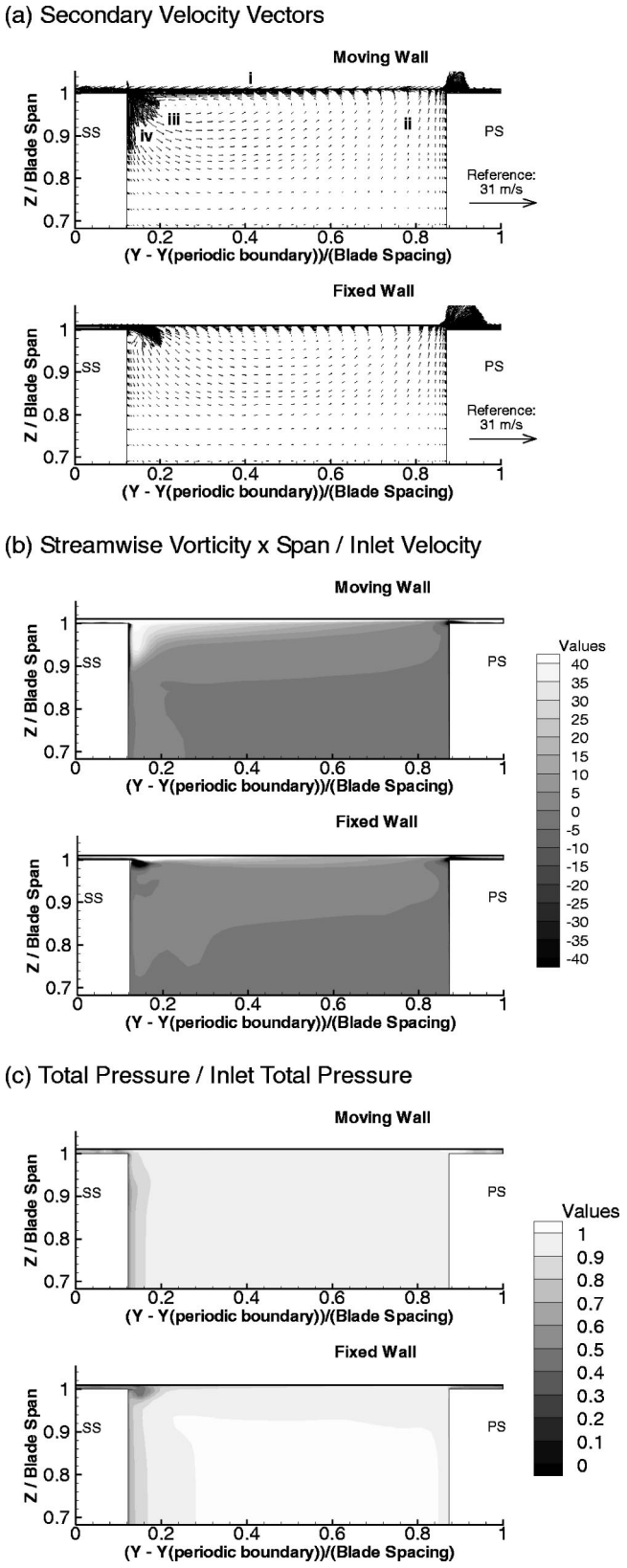

Fig. 4 ***y-z*** **plane at** $x=40$ **percent axial chord**

Figure 4(*b*) compares the streamwise vorticity field at 40 percent axial chord for the two cases. A large region of positive vorticity is present in the moving wall case just to the right of the blade's suction surface. Comparing Parts (*a*) and (*b*) of Fig. 4 shows that most of this region is associated with the interaction of

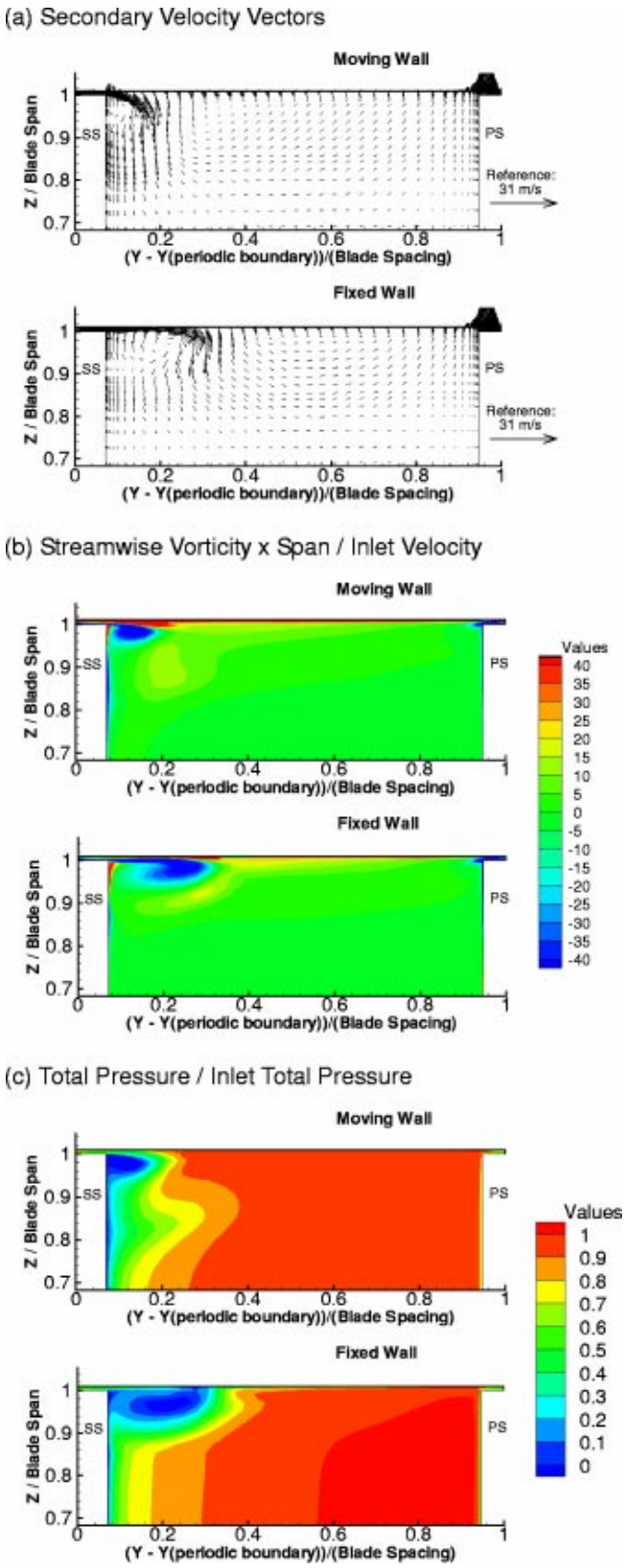

Fig. 5 *y-z* **plane at** $x=90$ **percent axial chord**

the near-casing secondary flow and the leakage jet. A similar situation is present in the fixed wall case. Without casing motion to enhance the near-casing secondary flow, the region of positive vorticity is less severe. The region of negative vorticity near the suction side of the passage is associated with the leakage flow roll-up and is hardly present in the moving wall case. This is expected, since Fig. 3(*b*) showed that the leakage vortex does not show noticeable size until further downstream. In both cases, the region of negative vorticity inside the gap and near the pressure surface is associated with the separation of the entrained leakage flow over the pressure surface corner of the blade. This region is smaller in the moving wall case, due to the lesser gap space made available to the leakage flow.

Total pressure contours at 40 percent axial chord are shown in Fig. 4(*c*). Across the entire passage, total pressure values are slightly lower in the moving wall case. A region of lower total pressure associated with the rolling-up leakage flow is seen in the fixed wall case, but not in the moving wall case, as is expected.

$x=90$ Percent Axial Chord From the Leading Edge: The flow at 90 percent axial chord is illustrated in Figs. 5(*a*) through 5(*c*). In all parts of Fig. 5, outer casing relative motion is seen to greatly reduce the size and, thus, disturbance of the leakage vortex. The secondary velocity vectors in Fig. 5(*a*) show that the leakage vortex has rolled up in both cases. The leakage vortex in the fixed wall case extends across about 20 percent of the blade spacing and about 10 percent of the blade span, and occupies roughly three times the space as its moving wall counterpart. The spanwise secondary flow beneath the leakage vortex is about twice as large in magnitude in the moving wall case. This secondary flow corresponds to the fluid pathlines labeled iii in Fig. 3(*a*). The gap entrainment secondary flow is very similar in magnitude and direction for the two cases, indicating similar mass entrainment into the downstream half of the gap. The violet fluid pathlines in Fig. 3(*a*) also indicated this trend.

Secondary vorticity contours are shown at 90 percent axial chord in Fig. 5(*b*). In both cases, two regions of positive vorticity sandwich the region of negative vorticity associated with the leakage vortex. These two regions of positive vorticity have similar explanations in both cases. Comparison with Fig. 5(*a*) indicates that the region of positive vorticity immediately above the leakage vortex is primarily due to the convection of positively rotating fluid from the gap by the leakage flow. In addition, the turning of the near-casing secondary flow around the obstructing leakage vortex also contributes to the vorticity in this region. Figure 4(*b*) shows that this contribution is more severe at locations further upstream, where the near-casing secondary flow is more severe.

The region of positive vorticity below the leakage vortex acquired its rotation further upstream. For the moving wall case, fluid pathlines in Fig. 3(*a*) (Lab. iii) and in Fig. 3(*b*) (Labs. ii–v) all show that positively rotating fluid from near the outer casing upstream is carried into the region below the leakage vortex further downstream. For the fixed wall case, the Type Two fluid pathlines shown in Fig. 3(*a*) carry positively rotating leakage fluid from the casing to the region below and to the right of the leakage vortex. In addition, fluid pathlines in Fig. 2(*c*) of Part I of this paper show that in the fixed wall case, positively rotating fluid from the near-casing secondary flow also ends up in this region. In both cases, these positive vorticity contours next to the leakage vortex are typically mistaken for a passage vortex. The fluid pathlines shown in this paper indicate that this is not the case.

Total pressure contours at 90 percent axial chord are shown in Fig. 5(*c*). In both cases, the region of lowest total pressure is associated with the leakage vortex. This region contains total pressure values between 0 percent and 50 percent of the inlet total pressure, and is roughly three times larger in the fixed wall case. This indicates that the casing motion causes a reduction of the losses associated directly with the leakage vortex. Although this sounds good at first, Fig. 5(*c*) also shows that the motion of the casing results in an increase in the losses that are indirectly associated with the leakage vortex. A second region of low total pressure is noticeable below the leakage flow in the moving wall case. Comparing Figs. 5(*a*) and 5(*c*) shows that this region of high losses is associated with two different secondary flows. Directly

underneath the leakage vortex, the secondary flow towards the mid-span region of the passage is composed of leakage fluid that did not roll into the leakage vortex (Fig. 3(*a*), Lab. iii). The secondary flow below and to the right of the leakage vortex is made up of fluid that originated near the outer casing and was turned toward the bottom of the passage by the obstruction of the blade (Fig. 3(*b*), Lab. v). For the two cases, similar losses are indicated in the pressure side of the passage and within the boundary layers on the blade surface.

Blade-to-Blade Pressure Distribution and Velocity Field

Velocity vectors in the blade-to-blade plane are presented at two spanwise locations in Fig. 6. Along the interface of the leakage jet and passage flow, a line has been added to indicate the extent of the influence of the leakage vortex. For clarity, only 1/4 of the computed grid points in the plane are shown. Figure 6(*a*) shows velocity vectors in the blade-to-blade plane at a spanwise location half way between the blade tip and the outer casing. In the moving wall case, the skewed casing shear layer is visible upstream of the blade, indicated by the large flow angle away from the axial direction. The magnitude of this flow angle increases with proximity to the moving casing, where the flow is purely tangential. The overturning of the flow upstream of the blade continues downstream along the suction side of the passage. Here, the shearing of the outer casing forces the passage flow towards the suction surface of the blade, resulting in the enhanced near-casing secondary flow discussed earlier. This acts to hold the leakage vortex and flow against the suction surface. In the fixed wall case, the flow at the same location is primarily in the 2D-streamwise direction.

Across the passage near the pressure surface, Fig. 6(*a*) shows that the entrainment of fluid into the gap results in an underturning of the flow. In the leading edge region of the gap, the entrainment of fluid into the gap is more apparent in the fixed wall case than in the moving wall case. This is a direct result of the skewed boundary layer on the casing. In the fixed wall case, the potential interaction between the blade and the approaching axial flow sets up a slightly positive incidence angle on the blade. This is visible in the fixed wall case of Fig. 6(*a*). Therefore at the leading edge, the flow into the gap is already in a direction similar to that of the leakage jet. In the moving wall case, the tangential component of velocity in the casing's shear layer results in negative incidence and causes fluid to enter the gap region through the suction surface side. Meanwhile, the pressure drop across the gap associated with the blade loading tends to drive the leakage flow out of the gap through the suction surface side. In Fig. 6(*a*), the absence of a net leakage flow through the gap near the leading edge indicates that the two mechanisms are about equal in strength at this location. The flow then exits the gap at the suction surface side further downstream, and appears to merge together with the passage flow near the outer casing. This occurs at an axial location of about 40 percent to 50 percent axial chord.

From the mid-chord to the trailing edge of the gap region, Fig. 6(*a*) shows that the leakage flow is very similar for the two cases, both in magnitude and direction. Entrainment into the gap is also very similar for the two cases. In this region, the passage flow direction is more aligned with the direction of motion of the outer casing. Therefore, the effects of relative motion between the casing and the blade should be reduced. These effects are still present, however, and can be seen in the slight overturning of the main passage flow at the trailing edge plane. In the moving wall case, the region of influence of the leakage vortex flow on the main passage flow extends across roughly 10 percent of the blade spacing at the trailing edge. This compares to about 25 percent in the fixed wall case. At an axial location of about 20 percent axial chord downstream of the trailing edge, much of the underturning associated with the leakage flow has disappeared for the moving wall case.

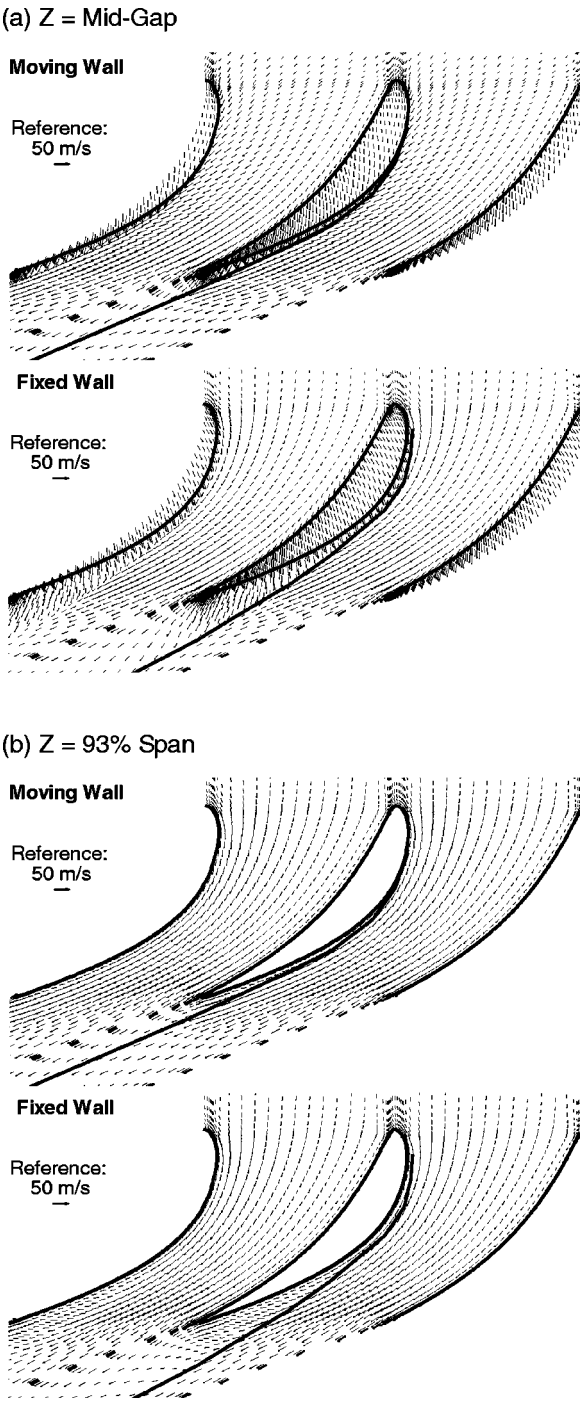

Fig. 6 Velocity vectors in the blade-to-blade plane

The velocity vectors at a spanwise location of 93 percent of the blade span are shown in Fig. 6(*b*). The angle of incidence on the blade is very similar for the moving wall and the fixed wall cases. This indicates that the spanwise location is below the region affected by the casing shear layer. Overturning can be seen to the left of the sketched dividing line in both cases in Fig. 6(*b*). In the fixed wall case, the overturning is associated with the roll-up of the leakage vortex flow. In the moving wall case, the overturning is associated with the interaction region between the underside of the leakage vortex and the region of positive vorticity below the leakage vortex.

The pressure distribution in the blade-to-blade plane at the blade tip is shown in Fig. 7. The pressure coefficient (Cp) is

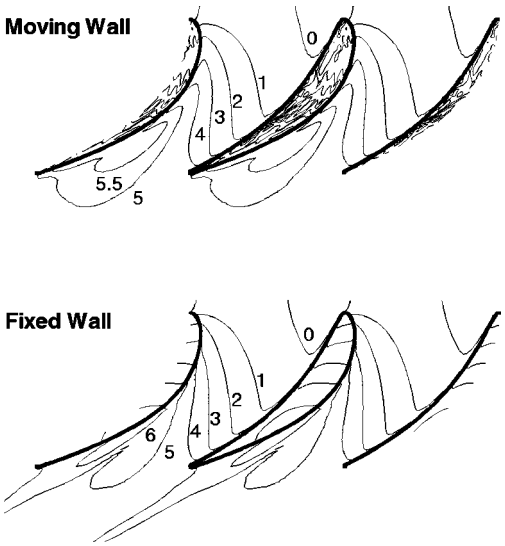

Fig. 7 Static pressure coefficient (Cp) contours in the blade-to-blade plane at the blade tip

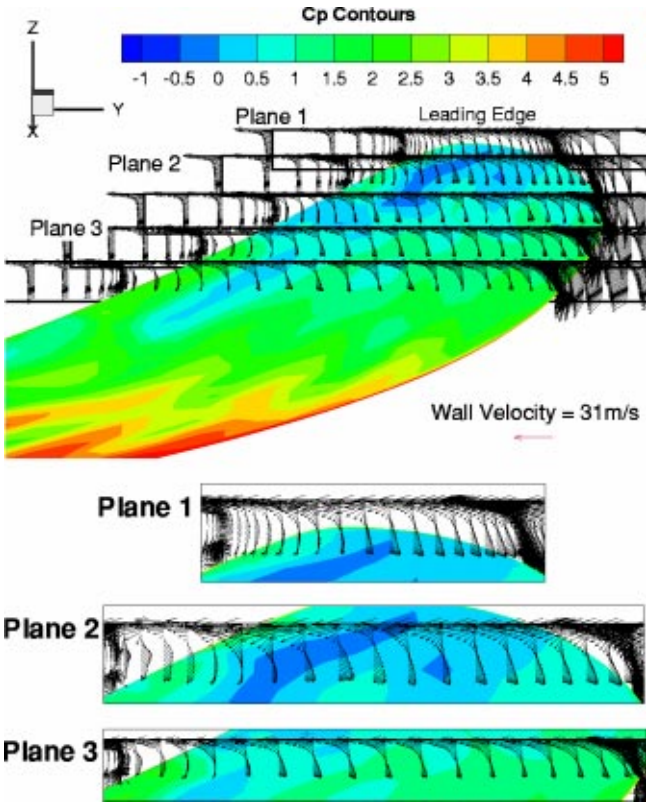

Fig. 8 Velocity in the gap and pressure (Cp) on the blade

defined in Eq. (1) of Part I as the difference between the inlet and local static pressure values, non-dimensionalized by the inlet dynamic pressure. In the moving wall case, a low-pressure trough is visible, which extends through the entire passage and is situated near to the suction surface. This low-pressure region is associated with the turning of the near-casing secondary flow downward along the spanwise direction. This is one of the significant differences between the moving wall and fixed wall cases. To the left of this trough, the portion of the $Cp>5.5$ contour adjacent to the blade is associated with the leakage vortex. In the fixed wall case, the innermost region of the leakage vortex is associated with the $Cp>6$ contour. Downstream, as the vortex decays, the region of the $Cp>5$ contour that extends out of the figure represents the leakage vortex. The unloading of the blade at the pressure side of the gap is similar for the two cases.

The most discerning feature of the pressure distribution in the moving wall case is the non-smooth distribution inside the tip gap region. A more extensive analysis has shown that pressure inside the gap is very much independent of the spanwise direction, so Fig. 7 is representative for the entire gap region. Elongated regions of high pressure are present and aligned with the blade's camber direction. In the global picture, however, there is still an unloading of the blade that is present, which drives the leakage flow through the gap. The pressure distribution inside the gap in the moving wall case has been the focus of a great deal of attention in this study.

Numerous attempts to smooth the pressure field in the gap region have been tried unsuccessfully, including modified boundary conditions, modified inlet conditions, laminar solutions, coarser grids, and incremental solutions where the wall speed was stepped up from zero to full speed. A review of literature failed to produce any experimental or numerical studies that presented the pressure distribution inside the leakage gap for a turbine with similar characteristics as the one in this study. Pressure distributions in the gap region have been observed experimentally and predicted numerically for the 3D turbine at Penn State University. Both of these studies show the distribution of pressure in the gap region to contain similar figures of high and low pressure, but not to the extent of the severity of what has been predicted in this study. The simulation of the Penn State turbine used a numerical technique entirely different from the one used in this research.

Figure 8 (shown earlier in color) shows both the pressure distribution on the blade tip and three-dimensional velocity vectors in the y-z plane at various locations inside the gap, and offers a closer view of the flow region of concern. The main view of the flow through the leading edge region of the gap is supplemented with three zoomed views of specific y-z planes of the flow. The complexities of the flow inside the gap are quite apparent.

Plane 1 of Fig. 8 shows the velocity field very near to the leading edge of the blade. The conflicting nature of the leakage and casing shear layer flows, discussed earlier in reference to Fig. 6(*a*), can be seen inside the gap in Plane 1. The shear layer acts to reduce the amount of gap space available to the leakage flow. Near the suction surface side of the passage, the near-casing secondary flow results in accumulating flow at the suction side of the gap, with a direction opposed to the leakage flow. At the gap boundary, most of this fluid encounters an adverse pressure gradient and is forced toward the inner hub in a manner exhibited by the violet fluid pathlines in Fig. 3(*b*) (Lab. iii). Inside the gap, the flow, on average, moves in the axial direction, with the flow near the casing directed more towards the pressure side of the gap and the flow near the tip directed more towards the suction side of the gap.

Plane 2 of Fig. 8 shows the three-dimensional velocity vectors at an axial location roughly 10 percent axial chord downstream of the leading edge. A long finger of high pressure (low Cp) is present, which runs roughly parallel to the blade's pressure side from the blade leading edge to about 10 percent axial chord. The velocity vectors situated inside this region and near to the blade tip are almost completely in the axial direction (out of the page and slightly toward the page bottom). On either side of the high-pressure finger, the velocity vectors point more towards the suction side of the gap. A similar trend can be seen in Plane 3, which shows the three-dimensional velocity vectors approximately 20 percent axial chord downstream of the leading edge. Once again, the regions of higher pressure correspond to a flow more toward the axial direction. The pressure and velocity fields therefore appear to be coupled together.

The only physical explanation for the non-smooth pressure dis-

tribution inside the gap region is that flows of opposing directions are colliding and turning each other. An example of this can be seen in the high-pressure region in Plane 2 of Fig. 8, near to and aligned with the pressure side of the gap. This region appears to be the result of the leakage flow and casing boundary layer flow merging together. Both flows act to turn each other towards the axial direction, as can be seen in Fig. 6(*a*). The fluid closest to the interface of the two flows will turn over a radius larger than the fluid further from the interface. Thus, the interface region will require higher pressure to support the centripetal acceleration. This situation is analogous to a point of tangency between two adjacent vortices rotating in opposite directions, where the vortices are in solid body rotation. The two red fluid pathlines through the gap and nearest to the leading edge of the blade in Fig. 3(*b*) show signs of the turning discussed above, and are located in roughly the same gap location as the high-pressure region.

The conclusion of the authors is that the non-smoothness in the gap region's pressure distribution is physical, at least in some part. The complex interactions of opposing flows (casing wall boundary layer and leakage flow) result in large curvature changes in the streamlines through the gap, which results in the alternating high and low pressure regions seen in Fig. 8. Both computational and experimental studies have showed similar pressure distributions in the gap region for axial flow turbines, but to a less severe extent. Also, the grid within the gap region is sufficiently refined to resolve fine flow details (88 in x, 21 in y, and 28 in z). Furthermore, the mass flow through the gap was found to be 5.3 g/s through the gap's pressure surface boundary and 5.6 g/s through the gap's suction surface boundary, indicating that mass is conserved fairly well through the gap. Still, the predicted flow inside the gap cannot be accepted as purely physical without additional evidence. Further studies of less complicated, Couette flow-type geometry are necessary to completely resolve the issue.

Passage Averaged and Global Properties

The overall performance of the fixed wall and moving wall cases are compared in this section in more quantifiable terms. Mass flow through the gap and loss coefficient are computed and compared. Some difficulties were encountered in the particle trace method that was used in Part I for predicting losses. The assumption that all of the leakage flow ends up inside the leakage vortex is no longer valid for the moving wall case, as shown in Fig. 3(*a*). Therefore, it was no longer feasible to easily determine whether or not the fluid pathlines were part of the leakage vortex. Therefore, this method of predicting losses was not used for the moving wall case.

Figure 9 shows the aggregate mass flow through the gap for the fixed and moving wall cases. The absolute value of the mass flow was 5.4 g/s, or 1.3 percent of the total passage flow, compared with 7.9 g/s, or 2.3 percent, in the fixed wall case. This indicates a substantial reduction in the leakage flow through the gap due to the outer casing's relative motion. The reduction is due to the blockage of the leakage flow by the casing shear layer. In the moving wall case, the aggregate mass flow through the suction side of the gap remains negative through the upstream half of the passage. This indicates that at the suction side of the gap, the outer casing's shear layer is adding more mass into the gap region than the leakage flow is removing. Similarly, on the pressure side of the gap, the positive values of the aggregate mass flow indicate more mass addition by the leakage flow than mass subtraction by the casing's shear layer. The net flow through the gap is then roughly zero, and the velocity vectors shown in Fig. 6(*a*) prove this to be true in the region of the gap near the leading edge.

Figure 10 shows the passage-averaged loss coefficient's variation through the passage for the fixed and moving wall case. The loss coefficient is defined in Part I of this two-part paper as the difference between the inlet and local passage-averaged total pressure, non-dimensionalized by the inlet velocity dynamic pressure. Two different curves are shown for the moving wall case. The

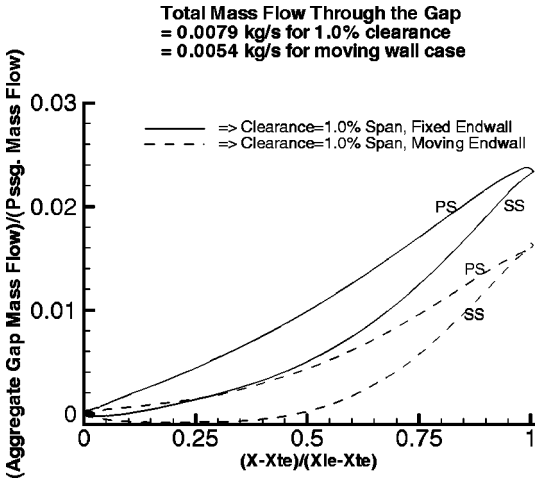

Fig. 9 Aggregate mass flow through the gap

dotted curve uses the inlet passage-averaged total pressure as the referencing value. This referencing value is somewhat incorrect, however. Consider a control volume analysis of the passage in the blade's frame of reference, where the flow enters at the inlet of the computational domain, exits through a y-z plane at some arbitrary axial location, is bounded on the top and bottom by walls, and is periodic on the sides. The motion of the outer casing will do work on the passage fluid inside the control volume at a rate equal to the shear stress on the casing times the wall speed. This work results in an additional amount of energy made available to the flow at the control volume exit. Therefore, using the inlet passage-averaged total pressure as a reference point for the loss coefficient does not represent the losses in the flow.

The dash-dotted curve in Fig. 10 is also for the moving wall case, and uses the inlet passage-averaged total pressure plus an additional pressure as the reference value. This additional pressure is representative of the integrated work that has been done on the fluid by the moving wall. At locations further downstream, the outer casing has done an increasing amount of work on the fluid. Mathematically, this means an increase in the reference value of total pressure and a higher loss coefficient. Physically, the casing motion has added energy to the fluid, and because this energy is not present in the total available energy at some arbitrary y-z plane, it must have been dissipated away. These hidden losses exist upstream of the blade as well, and result in a loss coefficient value of about 0.05 slightly upstream of the leading edge. Losses upstream of the blade due to the casing's shear layer have been subtracted from the dash-dotted curve in Fig. 10, so that losses

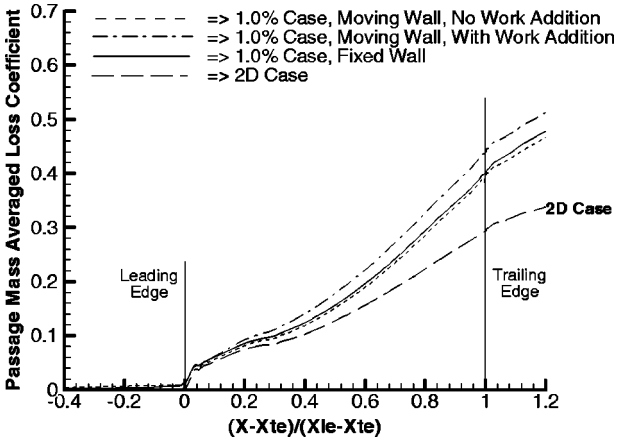

Fig. 10 Passage-averaged loss coefficient

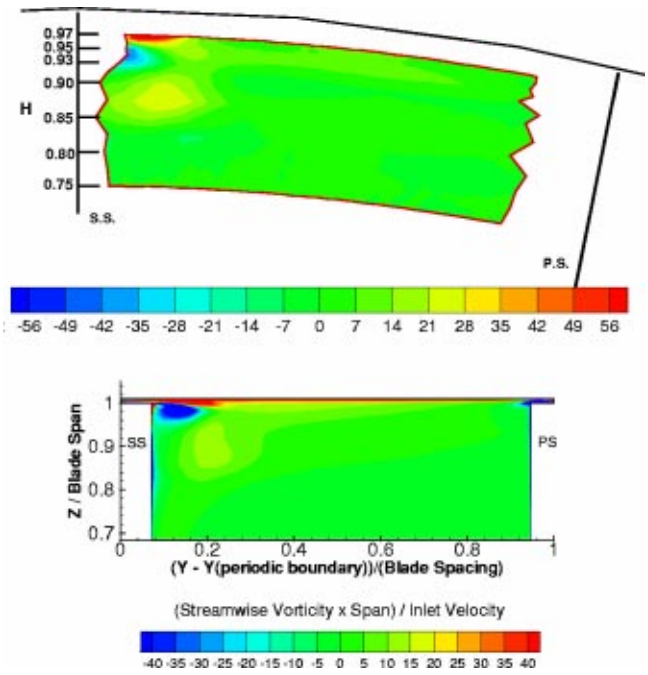

Fig. 11 Streamwise vorticity contours for a measured and numerically simulated turbine

inside and downstream of the passage can be compared directly for the two cases.

The moving-wall case shows slightly higher overall losses through the passage. At 120 percent axial chord, the loss coefficient values are 0.481 for the fixed wall case and 0.502 for the moving wall case. Without including the losses due directly to the casing shear layer, the loss curves for the two cases are very similar. This tends to indicate that the relative motion of the outer casing has very little effect on the total loss field, but Fig. 5(*c*) shows otherwise. Instead, the addition of casing relative motion indirectly results in a decrease in the losses associated with the leakage vortex and an increase in the losses associated with the near-casing secondary flow and its interaction with the blade (Fig. 5(*c*)). For this particular case, the two effects are roughly the same throughout the passage, resulting in the similarity of the two curves. The addition of the losses associated with the work done by the outer casing then result in the higher total losses in the moving wall case. These additional losses are about 7 percent of the total losses for the moving wall case. The similarity of the loss curves in Fig. 10 should not be construed as identical losses. The flow fields and loss mechanisms in the two cases are entirely different.

Qualitative Comparison With Experiment

Real Turbine Similarity: Numerical solutions of turbomachinery flows will remain approximate as long as empirical models are used to represent the effects of turbulence. At the same time, current measurement technologies are far from being able to produce the detailed description of the flow field presented in this paper. Therefore, it is not possible to fully validate the three-dimensional flow results and physics that have been discussed in this paper. Still, the validity of the hypotheses presented in this paper can be improved with a simple comparison with experimental results.

Figure 11 (shown earlier in color) shows secondary vorticity contours for two different turbine cases. The lower case is the simulated turbine from the current study (moving wall case) and is the same as is shown in Fig. 5(*b*). The upper case was measured with a five-hole probe in a rotating turbine rig at Penn State University by McCarter et al. [4]. This turbine operates at similar tip clearance, inlet, turning, and operating conditions as the one simulated in this paper, but is a three-dimensional blade design completely different from the cascade studied in this paper. Additionally, rotational effects are present in this experimental case, which are not accounted for in a cascade study.

The physical size of the five-hole probe prohibits the measurement of the flow very near solid boundaries for the measured case in Fig. 11. Still, the vorticity field in the passage is quite similar for the two different cases. Both cases in Fig. 11 show a region of negative vorticity associated with the leakage vortex sandwiched between two regions of positive vorticity. The lower of these two positively rotational regions is commonly interpreted as a passage vortex. The sizes, locations, and magnitudes of the various regions of vorticity are also quite similar for the two cases. If 2D pictures of the flow field are similar for the two cases, then it is reasonable to expect 3D pictures to be similar as well. Therefore, the agreement of the two cases in Fig. 11 adds validity to the simulated results and their interpretation presented in this paper. Also, the agreement in the two flow fields confirms that these interpretations are common among low-speed turbine rotors.

Conclusion

A turbine rotor was simulated numerically by including outer casing relative motion to a turbine cascade with a tip clearance height of 1.0 percent span. The computed flow field was then compared to the simulated flow field for the turbine cascade without outer casing relative motion. The addition of outer casing relative motion resulted in a decrease in the mass flow through the gap from 2.3 percent to 1.3 percent of the passage mass flow. The relative motion of the casing increased the passage averaged loss coefficient slightly, from 0.481 to 0.502 at 120 percent axial chord. Close examination of the total pressure in the passage, however, indicated that the sources of the losses being incurred in the two cases were quite different.

The major effects of casing relative motion on the turbine flow field are as follows:

1 Relative wall motion acted to strongly enhance the near-casing secondary flow. This was particularly true from the leading edge to the mid-chord of the passage, where the direction of motion of the casing is nearly normal to the primary flow.

2 In the region of the gap from the leading edge to the mid-chord, the moving casing's shear layer obstructed the leakage flow. Therefore, the majority of the leakage flow exited the gap from the downstream half of the gap.

3 In the fixed wall simulation, almost all of the leakage flow was eventually entrained around the leakage vortex. With the moving wall simulation, much of the leakage flow traveled around and underneath the leakage vortex, where it developed a strong secondary flow in the spanwise direction.

4 The size of the leakage vortex in the moving wall case was roughly one third of the size of its fixed wall case counterpart. Vortex roll-up occurred further downstream in the moving wall case.

5 As with the fixed wall case, an extensive Lagrangian analysis of the leakage vortex in the moving wall case revealed that all of the fluid inside the leakage vortex came from the leakage flow and not from the passage flow. The convection of vorticity from the gap offers an alternative explanation of the roll-up of the leakage vortex.

6 In the moving wall case, the losses associated with the leakage vortex and the losses associated with additional secondary flows were similar in magnitude. In the fixed wall case, the leakage vortex losses dominated the total losses in the passage.

7 The pressure field inside the gap was non-smooth in its distribution for the moving wall case. After much consideration, it is the authors' opinion that the non-smoothness in the pressure dis-

tribution is in some part physically representative of a real turbine. Overall, mass was conserved in the leakage flow through the gap.

Acknowledgments

This research was supported by the Office of Naval Research (U.S. Navy) through their AASERT program (N 00014-94-1-0839), with J. Fein as the technical monitor. It was also partially supported by Army Research Office (ARO) through the AASERT program (DAAG 55-97-1-0201) with T. Doligalski as the technical monitor.

References

[1] Bindon, J. P., 1991, private communication.
[2] Bindon, J. P., and Morphis, G., 1992, ''The Development of Axial Turbine Leakage Loss for Two Profiled Tip Geometries Using Linear Cascade Data,'' ASME J. Turbomach., **114**, No. 1, pp. 198–203.
[3] Tallman, J. A., 1999, ''Simulation of Tip Leakage Flows in a Turbine Rotor Using Computational Fluid Dynamics,'' MS Thesis, The Pennsylvania State University.
[4] McCarter, A., Xiao, X., Lakshminarayana, B., 2000, ''Tip Clearance Effects in a Turbine Rotor: Part 2—Velocity Field and Flow Physics,'' ASME J. Turbomach., **123**, pp. 306–313.

The Control of Shroud Leakage Flows to Reduce Aerodynamic Losses in a Low Aspect Ratio, Shrouded Axial Flow Turbine

A. M. Wallis
Siemens Power Generation U.K. Ltd,
C. A. Parsons Works,
Newcastle Upon Tyne,
United Kingdom

J. D. Denton

A. A. J. Demargne

Whittle Laboratory,
Cambridge University,
Cambridge,
United Kingdom

The losses generated by fluid leaking across the shrouds of turbine blade rows are known to form a significant proportion of the overall loss generated in low aspect ratio turbines. The use of shrouds to encase the tips of turbine blades has encouraged the development of many innovative sealing arrangements, all of which are intended to reduce the quantity of fluid (the leakage fraction) leaking across the shroud. Modern sealing arrangements have reduced leakage fractions considerably, meaning that further improvements can only be obtained by controlling the leakage flow in such a way so as to minimize the aerodynamic losses incurred by the extraction and re-injection of the leakage flow into the mainstream. There are few published experimental investigations on the interaction between mainstream and leakage flows to provide guidance on the best means of managing the leakage flows to do this. This paper describes the development and testing of a strategy to turn the fluid leaking over shrouded turbine rotor blade rows with the aim of reducing the aerodynamic losses associated with its re-injection into the mainstream flow. The intent was to extract work from the leakage flow in the process. A four stage research turbine was used to test in detail the sealing design resulting from this strategy. A reduction in brake efficiency of 3.5 percent was measured. Further investigation suggested that much of the increase in loss could be attributed to the presence of axial gaps upstream and downstream of the shroud cavity which facilitated the periodic ingress and egress of mainstream fluid into the shroud cavity under the influence of the rotor potential field. This process was exacerbated by reductions in the leakage fraction.
[DOI: 10.1115/1.1354143]

Introduction

General models of the passage of leakage fluid through a rotor shroud cavity and its interaction with the main flow are discussed by several authors [1–3] enabling a picture of the underlying loss mechanisms to be constructed.

A simple leakage flow path is considered, with the shroud being sealed by a single fin attached to the casing (Fig. 1). The leakage fluid has its origin at the casing end of the previous row of stator blades [4], and is sucked into the clearance space above the shroud under the action of the pressure difference across the rotor blade. The presence of the fin causes the fluid to contract into a jet. Most of the kinetic energy associated with the meridional velocity of the leakage flow is dissipated as the fluid expands in the turbulent mixing zone downstream of the fin. Although the expansion process has minimized the meridional velocity of the flow, it may still retain a large amount of the tangential momentum given to it by the stator blades. Thus, when the leakage flow re-enters the main stream flow, which has by now been turned by the rotor blades, more energy is dissipated as the two flows, with different tangential velocities, mix. The mixed out flow angle will differ from design intent and since it is likely that the leakage flow will interact with the boundary layer flow in the endwall region, secondary flow structures will be altered. Thus incidence and secondary losses will change in the downstream blade row. Neglecting windage, four entropy generating mechanisms can be identified in this process. These are due to fluid entering the shroud cavity; mixing in the clearance downstream of each fin; mixing with the mainstream flow and non-ideal incidence onto the following blade row. Similar losses are generated when fluid leaks across stator shrouds. Of these four mechanisms, mixing in the clearance space is essential for the effective performance of the seal since it reduces the leakage fraction. The losses generated at the inlet to the shroud cavity may also reduce the leakage fraction and it can be speculated that the removal of the boundary layer at the rotor leading edge could be of benefit in hindering the development of casing secondary flows in the rotor blade. Hence, the most obvious strategy for reducing the aerodynamic losses associated with the leakage flows is to try to minimize the entropy generated when the leakage flow re-enters the main flow. Denton [5] developed a simple model to estimate the magnitude of this

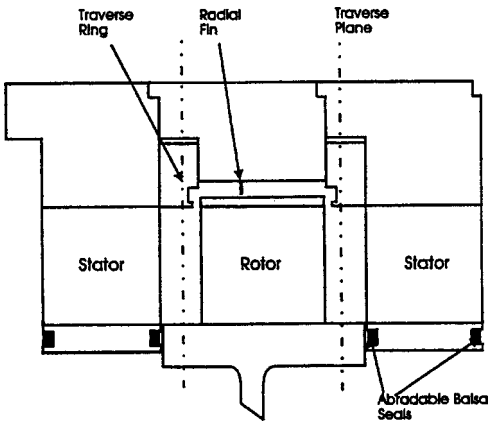

Fig. 1 The shroud sealing arrangement

Contributed by the International Gas Turbine Institute and presented at the 45th International Gas Turbine and Aeroengine Congress and Exhibition, Munich, Germany, May 8–11, 2000. Manuscript received by the International Gas Turbine Institute February 2000. Paper No. 2000-GT-475. Review Chair: D. Ballal.

loss. Equation (1) taken from his theory suggests that it is possible to eliminate a proportion of the loss generated by the shroud leakage flow by re-introducing it into the main flow with the same value of tangential velocity as the mainstream flow. This would also reduce the deviation of the mixed-out flow angle from the design intent.

$$\frac{T\Delta s}{0.5V_2^2} = 2\frac{\dot{m}_L}{\dot{m}}\left(1 - \frac{V_{tL}}{V_{t2}}\sin^2\beta_2\right) \quad (1)$$

In order to achieve this, the leakage flow must be turned. By locating a ''turning device'' on the rotor shroud, the required change in tangential velocity can be achieved by extracting useful work from the leakage flow, thus increasing the power output of the machine.

The Model Turbine and Experimental Methods

A four stage, low aspect ratio, model air turbine was used as the vehicle to test the strategy (Fig. 2). It was designed to be typical of the first few stages of a large high pressure steam turbine. Basic geometric and operational parameters are listed in Table 1. Both rotor and stator blade rows were shrouded, with the original sealing arrangement comprising two axial abradable balsa seals forming an axial clearance of approximately 0.4 mm with the shroud. The shroud formed a radial clearance of 0.5 mm with the casing [6]. The arrangement was intended to reduce the leakage fraction to negligible levels but as it is unrepresentative of normal turbine designs it was necessary to modify the rotor shrouds.

The modified rotor sealing arrangement comprised a 4 mm thick shroud forming a clearance with the casing of 10.5 mm. A single radial fin formed of 1 mm thick aluminum angle (section) was fitted onto the casing at 33 percent axial chord, forming a nominal clearance of 0.5 mm with the rotor shroud. The axial balsa wood seals were removed and the bottom lip of each seal housing machined back to form an axial clearance of 5.45 mm with the edge of the rotor shroud (Fig. 1). Axial gaps of this magnitude or more are common in steam turbines. Thus the radial seal formed the only significant constriction within the leakage flow path. The stator sealing geometry was not changed. The use of only one radial fin was a simplification in comparison to commercial sealing designs, but it was hoped that an understanding of the flow behavior behind this fin would be a first step towards understanding the flows found in more complicated geometries.

An experimental test program was devised using pneumatic probes to study the time-mean properties of both the leakage flow within the modified rotor shroud cavity and the main flow downstream of the rotor trailing edge after the re-injection of the leakage flow, and then to use this information to develop a prototype turning device to turn the leakage flow above the rotor shroud of the third stage. By repeating the tests with the turning device installed on the rotor shroud, the influence of the turning device on the turbine flow field could be assessed and, if necessary, the device modified and retested. The measurement of brake performance characteristics determined overall performance changes.

Table 1 Turbine geometrical and operational parameters

Stator Blade No.	33	Mean Reaction	50.0%
Rotor Blade No.	30	Stage Number	4
Midheight Pitch to Chord Ratio	0.9	Blade Height (h)	75.0 mm
Aspect Ratio (h/c_{rotor})	0.7	Hub to Tip Ratio	0.85
Inlet Axial Velocity, Vax (m/s)	11.6	Rotational Speed	640.0 rpm
Inter Blade Row Spacing	25.0 mm	Flow Coefficient	0..384
Reynolds No., Re_{stator}	2.0×10^5	Stage Loading, $\Delta h_o/U^2$	1.0

Special provision was made to traverse radially across the shroud cavity at six axial locations. Owing to the restricted amount of space in the axial direction, the traverse points downstream of the seal were offset circumferentially from one another within 3 percent of the turbine circumference, slightly less than one stator pitch (Fig. 3). Significant circumferential differences in conditions in the clearance space were not expected. A three hole cobra probe with a head thickness of 0.75 mm was chosen to measure the flow field here. The probe was traversed manually across the cavity using a simple screw-in traverse mount and rotated manually into the flow direction to measure total pressure and yaw angle. Static pressure was measured from tappings on the casing wall. It was assumed to be constant across the depth of the shroud cavity. Since the probe could not measure radial velocity components, the distance between the probe head and stem was made as large as possible to reduce the influence of pitch on the probe readings. This was considered acceptable since, for the purposes of the turning device development, the jet issuing from under the seal was of principal interest. Here radial components of the flow are negligible.

The time-mean properties of the mainstream flow were measured by performing full-span area traverses at an axial distance of 15 percent rotor axial chord downstream of the rotor 3 trailing edge using a four hole probe, with the flow field being mapped in greatest detail in the vicinity of the casing. The four hole probe was of similar construction to the three hole probe, with the fourth hole located under the central hole. Thus the pitch angle of the flow could be measured without inhibiting access to the casing endwall.

The measurements described in this section were made for every leakage flow path configuration tested in the model turbine. Other measurements made in the course of development are detailed in the text as appropriate.

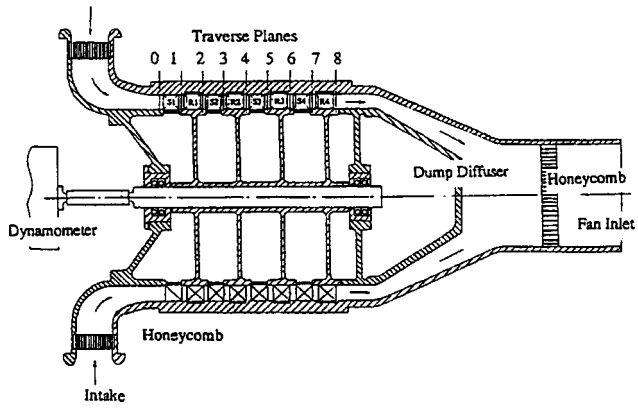

Fig. 2 Schematic of model turbine

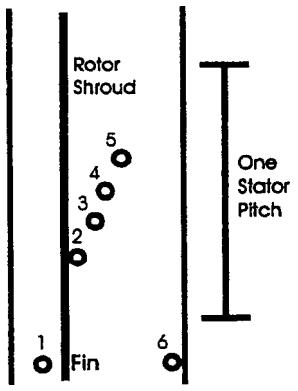

Fig. 3 Traverse locations in shroud cavity

Presentation of Data. The velocities derived from probe measurements in both the shroud cavity and the annulus are nondimensionalized by blade tip speed. Flow quantities measured in the radial line traverses across the shroud cavity are presented directly, whilst the area traverse measurements are presented as pitchwise averages across the blade span. Estimates of the total mass and angular momentum were made at each traverse station in the shroud cavity by assuming that the flow quantity at each radial traverse point was representative of the flow around the entire circumference. An integration was then performed across the shroud cavity (r_{sh} and r_c are the radii at the shroud and the casing of the cavity, respectively).

$$\dot{m} = \int_{r_{sh}}^{r_c} 2\pi r \rho V_{ax} dr \tag{2}$$

$$\vec{r}\dot{m}_L \vec{V}_t = \int_{r_{sh}}^{r_c} 2\pi r^2 \rho V_{ax} V_t dr \tag{3}$$

Given the high uncertainty associated with these quantities, they were only intended to give a rough approximation of the flow field properties. The mass flow rate through the turbine annulus was estimated in a similar manner, by assuming that the flow through each blade passage in a row was identical.

In total, four sealing arrangements were tested. The first was the datum configuration (with no turning device installed).

The Performance of the Datum Configuration

The performance characteristics of all four configurations tested are shown in Fig. 4. The brake efficiency of the datum configuration at the design operating point was measured to be 84.5 percent.

Figure 5 (upper diagram) shows the variation in axial velocity within the shroud cavity at stations 1 to 6. These profiles were integrated to give an indication of the mass leakage fraction. The mean of these integrals was 1.8 percent with a variation shown in Table 2. A proportion of the station to station variation was attributed to a small circumferential variation in fin clearance that was known to occur during operation. The flow upstream of the fin (station 1) was located near to the casing, with slight negative axial velocities occurring at the shroud surface. This indicated that the leakage flow, which would enter the shroud cavity almost radially, was being turned—first by the casing into the axial direction, and then by the upstream face of the fin—so that it flowed radially inwards (see Fig. 6). Thus a slow moving recirculatory

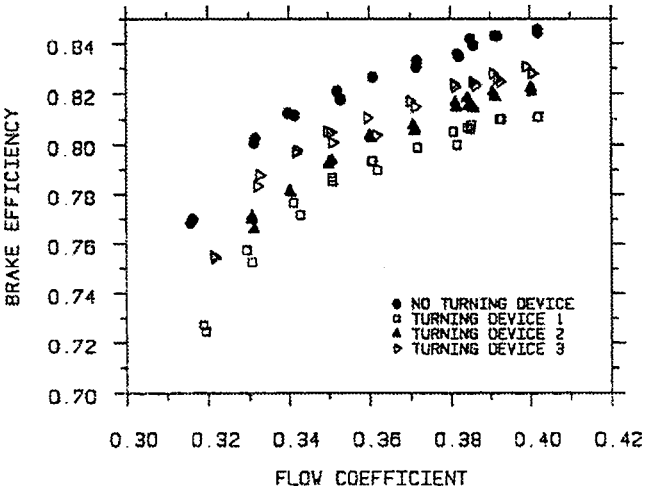

Fig. 4 Turbine performance characteristics for turning device configurations

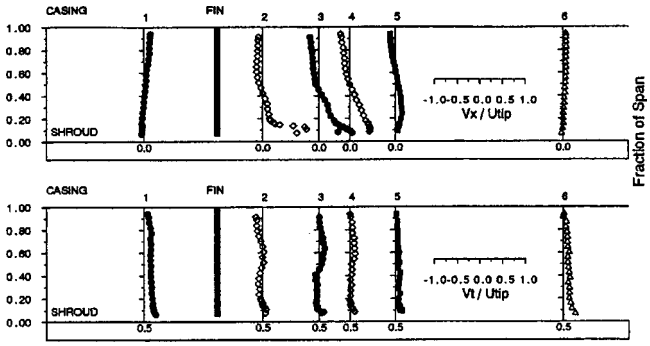

Fig. 5 Datum configuration: Velocity profiles in the cavity

flow was forming upstream of the fin. This agreed with the test results of Denton and Johnson [4] on a similar sealing geometry.

Downstream of the fin (station 2), the flow contracted into a jet, which moved along the shroud surface, expanding and slowly mixing out (station 3–5). By station 6, near the exit gap of the shroud cavity, the axial velocity profile was almost zero, with slight negative velocities at the shroud and positive velocities at the casing. This was surprising as the converse was expected.

In the casing region, the flow was moving with low velocity upstream at all stations except station 6. The implication of this was that two counter-rotating regions of flow existed downstream of the fin (Fig. 6), although the exact flow pattern was uncertain.

The variation in absolute tangential velocity along the shroud is shown in the lower diagram of Fig. 5. The magnitude of tangential velocity at station 1 corresponded to the values measured upstream of the rotor blade row in the casing region, suggesting that the leakage flow was being sucked into the cavity out of this region.

The estimated mass-averaged angular momentum of the leakage flow is listed for each traverse station in Table 2. Apart from a slight increase in momentum due to windage on the shroud, and a small loss in the casing region due to skin friction, it was expected that the total absolute tangential momentum of the leakage flow would not vary across the fin. The total change in angular momentum between stations 1 and 6 supported this assumption. However, between these points, it appeared to increase across the fin and then decrease as the flow mixed out. It was conceivable that these discrepancies were only reflecting measurement uncertainties. Figure 7*a* shows the radial variation in the pitchwise, mass-averaged absolute tangential velocity measured downstream of rotor 3. The measurements displayed a rapid increase in tangential velocity near the casing which was greater than that which was expected to be caused by secondary flow features within this blade. This was attributed to the mixing of the mainstream flow (which was designed to have almost zero angular momentum) with the leakage flow (which still possessed some positive angular momentum) upstream of the traverse plane. The fluid in the casing

Table 2 Datum configuration: Estimate of leakage fraction and angular momentum along the shroud

Station No.	1	2	3	4	5	6
Leakage Fraction	1.66%	2.04%	2.05%	2.13%	1.19%	1.73%
Ang Mntm. kgm^2s^{-2}	0.87	1.77	2.19	2.09	1.03	0.60

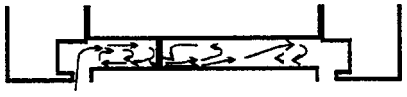

Fig. 6 Possible flow structures downstream of the fin

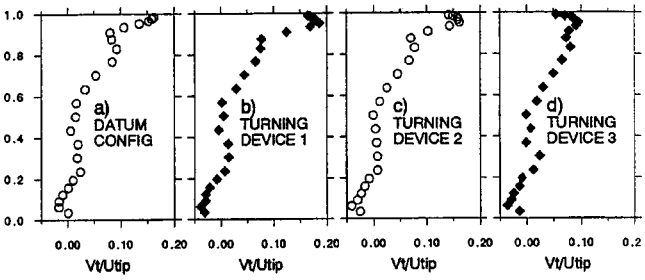

Fig. 7 Rotor 3 exit: Radial variation in tangential velocity

region was associated with a large deficit in total pressure (not presented). This was attributed partly to the loss generated by the secondary flow but also to the losses associated with the mixing. The combination of a relatively high absolute tangential velocity with a low axial velocity meant that the incidence angle onto the next blade row increased to over −30 degrees in the outer 10 percent of the blade.

The Development of a Turning Device

The turning device took the form of a row of tiny ''bladelets'' fixed onto the rotor shroud immediately downstream of the radial fin to capture the kinetic energy contained within the leakage jet (Fig. 8). The bladelets were developed on a stationary linear model of the shroud cavity. Since the turbine was dismantled by sliding the moving components along the rotor shaft, it was impossible to locate any component on the rotor shroud surface at a radius greater than the inner radius of the fin. The shroud surface between the leading edge of the blade and 14 mm downstream of the fin was therefore built up with 3.2 mm thick aluminum sheet to produce a stepped shroud surface. The fin was machined back to accommodate this change (whilst maintaining the radial clearance) and the chosen turning device shape was then pressed into the aluminum downstream of the fin, providing an interface between the shroud surface upstream and downstream of the fin (Fig. 9). The endwall in the bladelet inlet region was convex, encouraging the jet to move radially inwards into the device by means of the Coanda effect. The bladelets were designed to match the jet inlet angle which had been measured to be −20.0 degrees in the datum configuration. The loading was provided by using the pressure surface to slow the jet, whilst maintaining the jet velocity on the suction surface. The positioning of a second fin above the bladelets at 66 percent axial chord ensured a minimum of flow spillage over the open end of the bladelet, with only a slight reduction in leakage fraction. One of the passages on the stationary model was fitted with static pressure trappings from which it was estimated that an increase in power output of 1.0 percent would be achieved by fitting the turning device to all four stages of the turbine. Thus, an increase in power output of 0.25 percent was expected for the model turbine with the turning devices fitted onto rotor 3 only. Such a small increase could not be directly

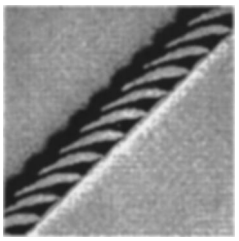

Fig. 8 The turning device

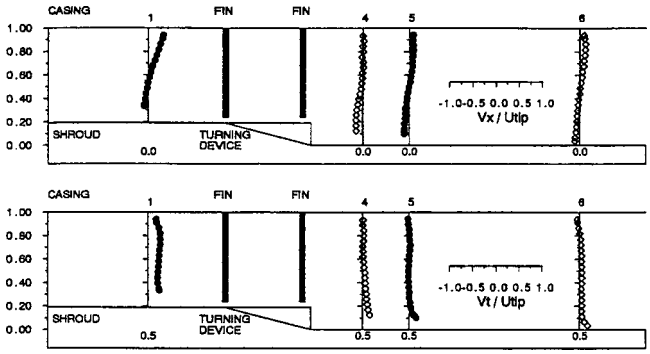

Fig. 9 Configuration 1: Velocity profiles in the cavity

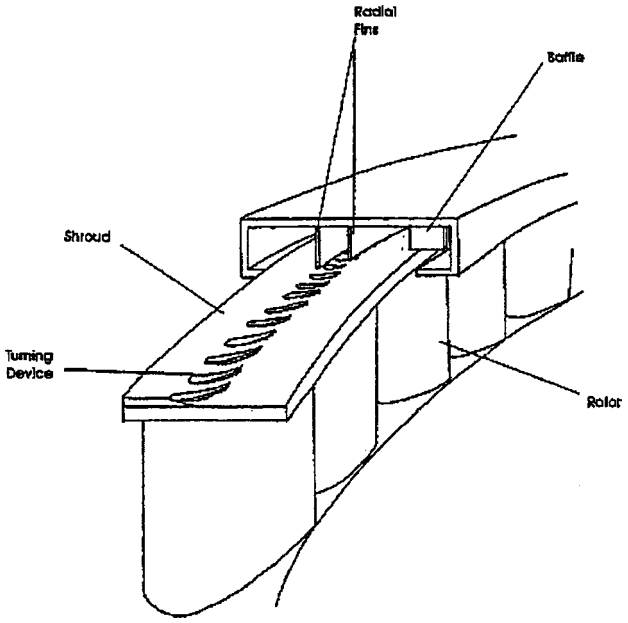

Fig. 10 Schematic of the shroud sealing arrangement (third configuration)

measured. Instead the pneumatic probe measurements would be used to indicate alterations in angular momentum and regions of reduced loss.

Figure 10 indicates the general arrangement of the sealing configuration above rotor 3. It should be noted that the baffles were only attached prior to the testing of the third configuration.

The First Turning Device Configuration

At the design operating conditions, a brake efficiency of 81.0 percent, was measured (Fig. 4). This was a decrease of 3.5 percentage points compared to the datum configuration. Despite the unexpected drop in performance, examination of the change in tangential velocity across the turning device suggested that it was turning the flow (Fig. 9, lower diagram). However, since the variation in the calculated leakage fraction along the shroud was very large (over 4.5 percent compared to under 1.0 percent in the datum case) with a mean value of 0.08 percent any estimation in the reduction of angular momentum across the device was meaningless. This variation was too large to be attributed to circumferential variations in fin clearances suggesting that either the leakage flow was actually circumferentially nonuniform or that the experimental measurements were inaccurate.

Examination of the axial velocity profiles (Fig. 9, upper diagram) indicated that the latter possibility could not entirely be ruled out. Reverse flow was observed on the shroud downstream

of the turning device. A very tiny amount of ''positive'' flow (i.e., flow moving downstream) was observed in the casing region of the cavity. It was speculated that either the leakage flow was emerging early from the turning device immediately downstream of the second fin and being flung radially outwards to the casing wall, or that it had reduced to almost zero. Since the probe could not detect radial velocity components it was impossible to deduce exactly what was happening.

Nevertheless, the presence of the turning device influenced the mainstream flow downstream of rotor 3, especially in the vicinity of the casing [Fig. 7(*b*)]. The tangential velocity increased from midspan up to approximately 97 percent span and then decreased towards the casing. Rather than reducing the mixed-out tangential velocity in the casing region as intended, the presence of the turning device had actually increased it slightly. This corresponded to a lower measured axial velocity, the net effect being an increase in yaw angle in the casing region, increasing the negative incidence onto the following stator blade row, and probably the secondary flows generated here too.

The magnitude of the drop in turbine performance was puzzling, especially as the blade section was known to be extremely tolerant to incidence. The turning device was not performing as expected. The axial position of the fins was therefore adjusted in an attempt to channel the leakage jet through the entire bladelet channel. Swash on the rotor 3 disc meant that the first fin was not positioned directly over the leading edge of the turning device throughout an entire revolution of the turbine. It was therefore moved downstream so that it would always be above the turning device. The second fin was moved downstream to the trailing edge of the turning device to keep the leakage flow close to the shroud surface in the cavity downstream of the turning device. These modifications formed the second turning device arrangement to be tested on the model turbine.

The Second Turning Device Configuration

The repositioning of the fins on rotor 3 increased the brake efficiency by 1 percent compared to the first turning device arrangement (Fig. 4), but there was still a difference of two percentage points between the brake efficiency of the second turning device and that of the datum.

The variation in axial velocity profile along the seal (Fig. 11, upper diagram) showed evidence of a small jet forming downstream of the turning device (station 4). Positive axial velocities were maintained along the shroud surface right up to station 6. Greater continuity between the values of net mass flowrate at each station was observed, but the net flowrate measured at stations 4 and 5 was almost zero. At station 6 this increased to 0.4 percent of the total mass flowrate passing through the turbine. The change in the net angular momentum across the turning device was equivalent to 0.23 percent of the power output of the machine (roughly as expected) but downstream of this the integrated value of angular momentum at station 5 was smaller than that at station 6.

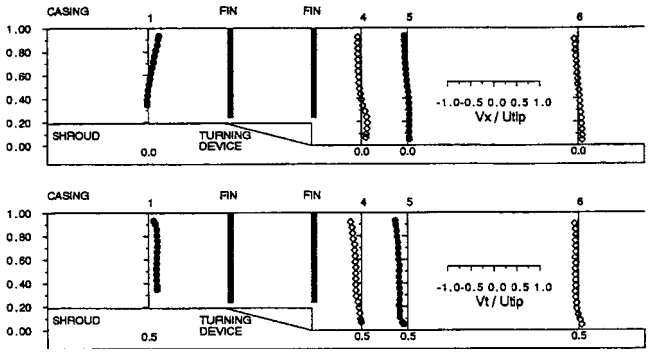

Fig. 11 Configuration 2: Velocity profiles in the cavity

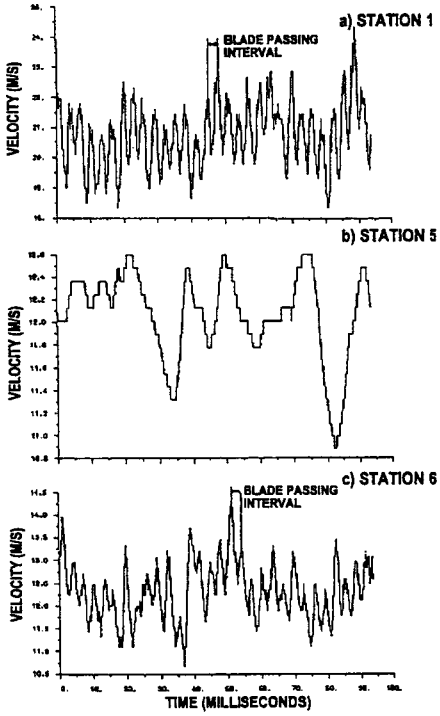

Fig. 12 Configuration 2. Hot-wire traces in the shroud cavity

When compared to the first turning device configuration, the pitchwise averaged absolute tangential velocity [Fig. 7(*c*)] had reduced in the casing region, although the levels were still not as low as those seen in the datum configuration. This reduced the high level of negative incidence onto the following blade row.

The repositioning of the fins was partially successful, but the fact that mass continuity was still not conserved suggested that the behavior of the leakage flow in the shroud cavity was not as straightforward as had been initially supposed. The three-hole probe only measured the time-mean flow. It was not known how it would respond to any temporal fluctuations in the flow field. A hot-wire can detect these fluctuations. The line traverses were therefore repeated at stations 1, 5, and 6 using a straight hot-wire probe. The hot-wire was traversed across the shroud cavity in an identical manner to the three-hole probe. It was nulled approximately into the flow at every traverse point by rotating the hot-wire until a minimum voltage was recorded by the measuring equipment and then rotating the probe stem back by 90°. 938 samples were taken at 100 microsecond intervals in one rotor revolution and ensembled using an ensemble size of 150. The time-mean ensemble-averaged velocity profiles (not presented) agreed well with those obtained using the three hole probe. The variation in ensembled velocity over one rotor revolution is plotted for stations 1, 5, and 6 in Fig. 12. These measurements were made near to the casing, although similar distributions were also observed closer to the shroud.

The fluctuation in velocity over one rotor revolution at station 5 appeared to be random and, given the proximity of the turning device, was presumably caused by non-uniformities in the fin clearance. In contrast, the velocity fluctuations at stations 1 and 6 were of a higher frequency of ~30 cycles per revolution. This corresponded to the number of rotor blades, indicating that the rotor blade rotation was influencing the flow at the axial extremities of the cavity. Upstream of the fin, the strong potential field upstream of the blade could be expected to induce the air to pulse up into the shroud cavity when it stagnated at the leading edge of the blade. This periodicity was immediately damped out downstream of the fin and so the cause of the fluctuations at station 6 could only be attributed to the influence of the potential flowfield

downstream of the blade row. Two possible mechanisms were proposed. Either the mainstream flow was providing a temporally varying resistance to the egress of the leakage fluid from the cavity, or it was itself periodically ingressing into the shroud cavity downstream of the fin. It was speculated that the likelihood of mainstream flow ingress into the shroud cavity would increase with reductions in the leakage fraction and would be a large source of entropy generation. Since the hot-wire could not detect flow reversals, the possibility that both mechanisms were occurring was not discounted. Nevertheless, the direct ingress of mainstream fluid provided a possible explanation for the regions of reverse flow seen in the axial velocity profiles of the first turning device arrangement where the leakage fraction was thought to be very low, and would provide a further explanation for the poor performance of this configuration.

The Third Turning Device Configuration

The experimental results indicated that the potential increase in power output generated by turning the leakage flow was being offset by a decreased effectiveness of that flow in preventing mainstream fluid from entering the shroud cavity. An energetic leakage flow in the vicinity of the shroud surface at the trailing edge would effectively ''seal'' the cavity from the downstream flow. The sealing arrangement was located near to the upstream edge of the shroud. This enabled leakage flow to fully mix out before leaving the shroud cavity, dispersing the energy in the leakage jet over the entire depth of the cavity. Moving the sealing arrangement towards the downstream end of the cavity would have improved its ''sealing'' ability. However, there was no time to do this in the experimental program. Instead, a series of baffles was fixed onto the casing wall at the exit of the shroud cavity. These were formed from flat plates, fixed to the casing and aligned to the machine axis (Fig. 10). It was intended that these would turn the leakage flow into the axial direction immediately before reentry into the main flow and impede the progress of the mainstream flow entering the shroud cavity from downstream.

The addition of the baffles increased the brake efficiency by almost 2 percent compared to the first turning device arrangement (Fig. 4), although the datum configuration still displayed the greatest efficiency.

Axial velocity profiles measured in the shroud cavity are presented in Fig. 13 (upper diagram). The jet appeared to be stronger in the presence of the downstream baffles than it had without them. The variation in angular momentum, downstream of the fin had reduced. The net change in angular momentum across this turning device configuration was equivalent to 0.21 percent of the power output of the machine.

Downstream of rotor 3, significant differences to the pitchwise-averaged flowfield were seen in the casing region. In particular, the absolute yaw angle had been reduced by almost 20 degrees compared to the datum configuration. This was produced by a marked decrease in tangential velocity in this region [Fig. 7(*d*)],

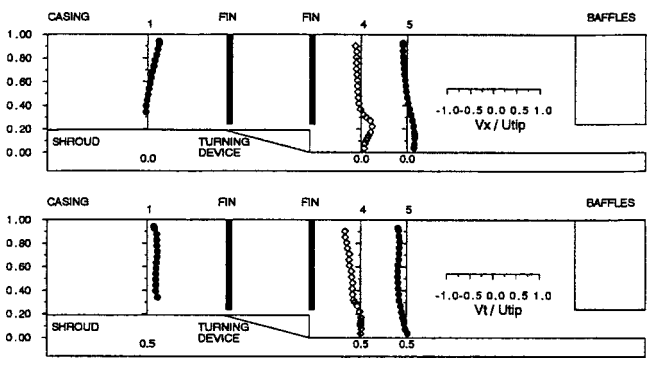

Fig. 13 Configuration 3: Velocity profiles in the cavity

coupled with a slight increase in axial velocity. The baffles were obviously straightening the leakage flow and the ingested flow, effectively reducing the angle of negative incidence onto the following blade row (stator 4) in the casing region. Area traverses downstream of stator 4, made during the tests of the second and third turning device configurations, (not shown) revealed that this more axially aligned flow reduced the negative skew in the casing boundary layer at the inlet to the following stator blade row. This in turn reduced the spanwise extent of the casing secondary flow of this blade row as well as the overturning in the immediate vicinity of the casing endwall.

CFD Modeling

The investigation of the flow through the shroud cavity indicated that the flow in this particular sealing arrangement was strongly influenced by temporal variations in the potential field of the main flow. As an aid to understanding this interaction more fully, the outer 60 percent of the rotor blade and the datum shroud sealing arrangement were modeled in a NEWT calculation. NEWT is a three-dimensional, steady, unstructured, finite-volume, Navier-Stokes solver with solution-adaptive mesh refinement. Turbulence is modeled via a standard k-ε model together with Lam-Bremhorst low Reynold's number corrections to handle the approach to distant walls smoothly. Further details of the numerical procedure can be found in [3]. An experimentally measured radial stagnation pressure profile was specified at inlet, together with stagnation temperature and three inflow angles. The exit boundary condition specified a static pressure and was of a non-reflecting type. Periodicity was enforced on the sides of the domain, and viscous wall boundary conditions were applied to all solid surfaces. In order to accelerate convergence, the calculation was run at a slightly elevated Mach number. The computational domain extended 40 percent of axial chord upstream and downstream of the shroud gaps and one blade pitch circumferentially. The ''part'' rotor was modelled as an isolated blade row, although it was acknowledged that the adjacent stator blade rows would influence the shroud cavity flow in an unsteady manner. The mesh, an unstructured tetrahedral mesh, was refined selectively as the calculation progressed. Although overall grid independence was not reached, local refinement of regions of interest (gaps, fin, jet) was carried out until no significant change in flow features or properties was observed in these regions. The refined mesh of the final calculation contained 700,000 cells and 140,000 nodes. Simulations were run until a four-order of magnitude decrease was obtained on the maximum residue, and these residues, as well as mass flow and minimum pressure, no longer changed with iterations.

The objective of the calculation was to gain some insight into the flowfield in the vicinity of the inlet and exit axial gaps to the shroud cavity. No experimental data had been taken in these regions, but it was evident from measurements made within the shroud cavity that they were influencing the leakage flow field. Since the NEWT calculation was performed in the frame of reference of the moving rotor blade, details of any periodically varying flow features could be examined. Figure 14 is a view of the computational domain looking obliquely inwards onto the shroud surface with the pressure surface to the front of the figure. The leading edge of the blade is at the right-hand side so that the blade passage flow is moving from right to left. A selection of streamlines at the principal regions of interest is shown. These streamlines show the movement of the leakage fluid relative to the moving blade, with the double headed arrows indicating the direction of motion. The vector plots, shown as insets in Fig. 14, are intended to assist in the interpretation of the streamline motion.

Flow in the Inlet Gap. The mainstream fluid approached the rotor blade row at negative incidence. In the vicinity of the stagnation point on the leading edge it was deflected upwards into the shroud cavity (inset A). Some of the fluid moved along the cavity in the downstream direction, but a proportion of it remained in the

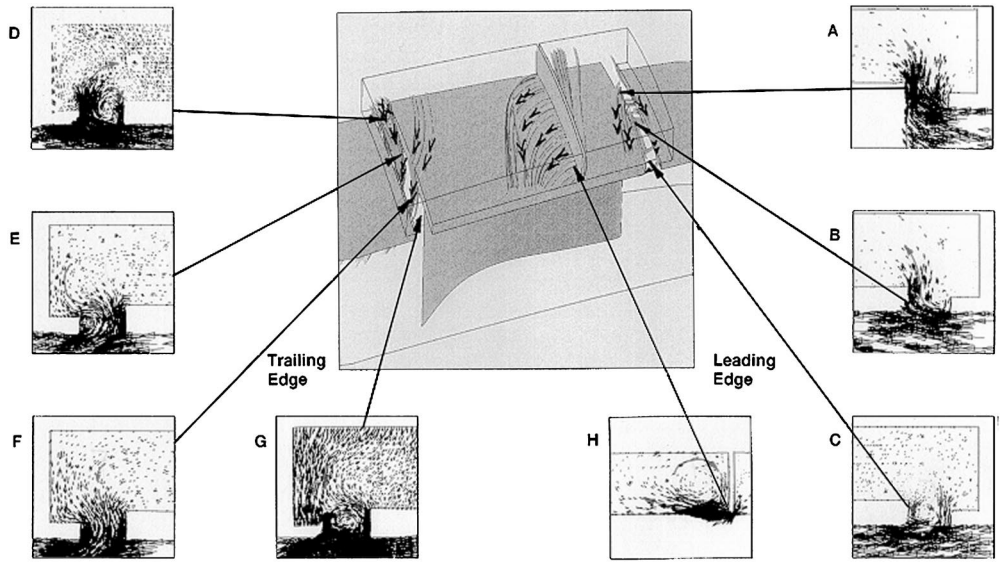

Fig. 14 Flow structures shroud cavity region

gap, developing into a vortical motion within the gap. The development of this structure is illustrated in insets A through to C. Inset C shows a position close to the casing mid-pitch position. Here the static pressure was lower than that in the leading edge region, enabling some of the fluid in the gap to re-enter the main blade passage, causing a mixing loss in the mainstream flow.

The Fin. The leakage fluid was sucked into the fin clearance from the casing region upstream of the fin. As the energy in the jet downstream of the fin dissipated, the fluid slowed and moved radially outwards. The curve of the streamlines indicated the deceleration of the jet relative to the surface of the shroud, causing the fluid to ''wrap'' around the circumference of the machine as it progressed towards the exit of the cavity. Inset H illustrates the circulatory motion that developed immediately downstream of the fin.

Flow in the Exit Gap. The calculation indicated that the ingress of fluid into the exit gap appeared to be associated with the blade pressure field, with the greatest net inflow close to the pressure surface of the blade (inset D). The net inflow slowly diminished as the suction surface was approached, (inset E), until eventually there was a switch to a net outflow of fluid. Close to the suction surface (inset F) where pressures are lower, the mainstream fluid re-entered the main passage. In this way a vortical structure developed in the axial gap. Its presence prevented the leakage flow from exiting the shroud cavity in a circumferentially uniform manner. Instead it was deflected within the cavity towards the suction side of the trailing edge where it then re-entered the main annulus. In this geometry, the flow direction in the casing region of the annulus downstream of the rotor blade row was therefore determined by the circumferential circulation of the flow in the axial exit gap of the shroud cavity, rather than by the initial angular momentum of the flow passing under the fin.

The calculation was a first attempt to study the flow structures in a shroud cavity and project time constraints did not permit its further refinement. However, it did confirm the periodic ingress and egress of fluid into the axial gaps both upstream and downstream of the shroud cavity. Similar vortical structures have been observed in seal cavities under compressor stators [7] where the extent to which they filled the axial gaps was observed to depend upon the leakage fraction passing through the seal. The NEWT calculation only modelled the datum configuration, but the hot-wire measurements suggested that these vortical structures existed in all the test configurations, with their magnitude dependent upon the condition of the leakage flow downstream of the turning device.

Re-Interpretation of Experimental Results

With the insight gained from the NEWT calculation the experimental results were reassessed. At the outset of the tests it had been assumed that all the flow entering the shroud cavity upstream of the fin would pass under the fin and leave the cavity at the exit gap. The calculation indicated that a quantity of the fluid in the shroud cavity was not actually passing under the fin, but was leaving the cavity via the gap by which it entered. This explained the discrepancies in the measured leakage fraction and angular momentum measured in all configurations, which had originally been entirely attributed to circumferential non-uniformities in the sealing geometry. In the datum configuration, up to 0.38 percent of the total mass flow through the turbine may have been moving into and out of the cavity upstream of the fin without passing under it. The NEWT calculation indicated that it would pass into the rotor blade row at high negative incidence. This would influence the blade loading in the casing region. At the exit gap of the shroud cavity, this quantity could have been as much as 0.88 percent of the total mass flow. This would cause the following blade row to also run off-design in the casing region. The first turning device configuration had reduced the mass flow rate passing through it to almost zero. Thus it might be expected that this pulsation of mainstream flow in and out of the axial gaps would be increased. It is suggested that this phenomenon contributed to the 3.5 percent reduction in brake efficiency observed between the datum configuration and that of the first turning device.

Both the second and the third turning device configurations allowed leakage fluid to pass through them, with the presence of the baffles enhancing the strength of the jet in the third configuration. It was possible that the baffles were preventing the formation of the vortical structures in the exit gap. This was deduced from the large reduction in absolute yaw angle measured in the casing region downstream of rotor 3.

Conclusions

The intent of this study was to investigate whether a reduction in the tangential velocity of the leakage flow would reduce the magnitude of downstream leakage losses and improve incidence

onto following bladerows. The success of the baffles showed that this is possible (Fig. 7). However, the poor performance of the turning devices clearly demonstrated the importance of understanding the unsteady, three-dimensional flow phenomenon occuring in the shroud region prior to developing new methods of managing the leakage flows.

An unexpected result of the investigation was to reveal the penalties incurred by directly exposing large labyrinth sealing cavities to the mainstream flow in instances where the leakage fraction is small. Large axial gaps at the shroud inlet and exit encourage fluid from the mainstream to spiral around the regions upstream and downstream of the fin rather than passing under the fin. The leakage jet measured in the datum configuration appeared to have been acting as a kind of air curtain, preventing fluid from downstream of the blade row from ingressing too far into the shroud cavity. The bladelets removed that ''curtain'' on the shroud surface, allowing the mainstream flow to penetrate further into the cavity and then re-enter the main annulus as a highly swirling flow, increasing turbine losses. The installation of baffles in the downstream axial gap improved the machine performance by aligning the leakage flow to the main flow direction before it left the cavity.

Acknowledgments

The work described in this paper was financially supported by Parsons Power Generation Systems Ltd. (now Siemens Power Generation UK) and the Engineering and Physical Science Research Council of the United Kingdom. The advice of Professor W. N. Dawes in the use of his code and the technical assistance of N. Hooper of the Whittle Laboratory are gratefully acknowledged.

Nomenclature

c = true chord
h = blade height
h_0 = total enthalpy
$\dot{m}$ = mass flowrate
r = radius
Re = Reynolds number based on stator chord and exit velocity
s = specific entropy
T = temperature
U = blade speed
V = absolute velocity
W = relative velocity
β = relative circumferential flow angle
ρ = density

Subscripts

2 = exit from blade row
c = casing
L = leakage
sh, = shroud
tip = blade tip
ax, t = axial, tangential components of direction

References

[1] Jefferson, J. L., 1954, ''Some Practical Effects of Tip Clearance in Turbine Blading,'' *NE Coast Inst. of Engineers and Shipbuilders*.
[2] Traupel, W., 1966, *Thermische Turbomaschinen*, Springer-Verlag, Berlin.
[3] Dawes, W. N., 1993, ''The Practical Application of Solution-Adaption to the Numerical Simulation of Complex Turbomachinery Problems,'' Prog. Aerospace Sci., Pergamon Press Ltd., **29**, pp. 221–269.
[4] Denton, J. D., and Johnson, C. G., 1976, ''An Experimental Study of the Tip Leakage Flow Around Shrouded Turbine Blades,'' CEGB Report No R/M/N848, Marchwood Engineering Laboratories.
[5] Denton, J. D., 1993, ''Loss Mechanisms in Turbomachines,'' ASME Paper No. 93-GT-435.
[6] Wallis, A. M., and Denton, J. D., 1998, ''Comparison of Design Intent and Experimental Measurements in a Low Aspect Ratio Axial Flow Turbine With Three-Dimensional Blading,'' ASME Paper No. 98-GT-516.
[7] Heidegger, N. J., Hall, E. J., and Delaney, R. A., 1996, ''Parameterized Study of High-Speed Compressor Seal Cavity Flow,'' AIAA Paper No. 96-2807, *32nd AIAA/ASME/SAE/ASEE Joint Propulsion Conference and Exhibition*.

Flow Interaction From the Exit Cavity of an Axial Turbine Blade Row Labyrinth Seal

A. Pfau

M. Treiber

M. Sell[1]

G. Gyarmathy[2]

Turbomachinery Laboratory,
Institute of Energy Technology,
Swiss Federal Institute of Technology,
8092 Zurich, Switzerland

The structure of labyrinth cavity flow has been experimentally investigated in a three fin axial turbine labyrinth seal (four cavities). The geometry corresponds to a generic steam turbine rotor shroud. The relative wall motion has not been modeled. The measurements were made with specially developed low-blockage pneumatic probes and extensive wall pressure mapping. Instead of the classical picture of a circumferentially uniform leakage sheet exiting from the last labyrinth clearance, entering the channel, and uniformly spreading over the downstream channel wall, the results reveal uneven flow and the existence of high circumferential velocity within the entire exit cavity. The circumferential momentum is brought into the cavity by swirling fluid from the main channel. This fluid penetrates the cavity and breaks up the leakage sheet into individual jets spaced according to the blade passages. This gives rise to strong local cross flows that may also considerably disturb the performance of a downstream blade row.
[DOI: 10.1115/1.1368124]

1 Introduction

Labyrinth seals placed on shrouded blades are a standard method of reducing the efficiency penalties, as compared to free ended blades. The loss of stage efficiency resulting from the use of labyrinth seals is proportional to the leakage mass flow. The leakage flow itself is directly proportional to the radial clearance width and inversely proportional to the square root of the row pressure drop and the number of fins (see for example Traupel [1]). Additional loss may occur due to interactions caused by the leakage stream re-introduced into the main duct flow.

Much research activity has been dedicated to the improvement of blade row aerodynamics by investigating secondary flows in general (for example Sieverding [2]) or tip clearance affected secondary flows (for example Moore et al. [3], Heyes et al. [4], Sell et al. [5]). Labyrinth flow research has been based mainly on internal labyrinth studies aimed at the understanding and optimization of the labyrinth discharge coefficient (Egli [6], Rhode et al. [7], Takenaga et al. [8]). Worn labyrinth seals [9] and windage heating (Millward et al. [10]) are examples of related research topics. Seals in hydraulic machinery may give rise to rotor dynamic excitation and are still receiving considerable attention (Florjancic [11], Graf [12], Amoser [13], Spirig [14]).

However, beyond such studies little information is available in the open literature concerning the details of the flow physics arising from the combination of blade row aerodynamics and labyrinth flows. Notable is an early paper, Denton and Johnson [15], that presented two-dimensional experimental data for the flow over a shrouded model steam turbine.

This paper extends the research base by combining a labyrinth seal with a turbine blade row. In particular the aim of the work is to investigate the nature of the mixing of the labyrinth leakage flow and the main core flow, with the objective of identifying the flow processes responsible for disturbances in the flow entering the next blade row.

2 Test Case

The test case concerns the flow through a shrouded single blade row and its labyrinth in an annular channel. The blade form, shown in Fig. 1, is that of a moderately loaded turbine profile typically used in 50 percent reaction stages, which has an axial inlet flow and a nominal 68 deg of turning at mid span. The blading is prismatic, with the leading edge aligned radially. The blade stagger angle is 54.5 deg relative to the tangential direction.

The labyrinth chosen for this study (Fig. 2) is a simple three step labyrinth with equidistant fins placed within a rectangular casing groove. The labyrinth was designed using simple empirical correlations [1] with the aim of a labyrinth throughflow of 1 percent of the main passage massflow. This resulted, for three fins, in a fin gap of 1 mm, giving a ratio of fin gap to blade height (j/h) of 1.1 percent.

The fins, through constraints of fabrication, have blunt edges of 1 mm thickness. This gives a gap width to seal thickness ratio j/b of 1. This ratio does not yield an optimum discharge coefficient (see Trutnovsky and Komotori [16]) but is considered to be small enough not to play a significant role in framing the overall flow dynamics.

2.1 Test Stand and Experimental Methodology. The experiments were performed within an annular cascade facility (Sell et al. [17,18]) at constant flow conditions. For the measurements presented here a nominal exit Mach number at midspan of 0.33 was used. The test stand operates at quasi-atmospheric exit pressure and temperature. The most important geometrical features of the test rig are collated in Table 1.

The experimental procedure exploits a design feature of the test stand, which is explained more fully in Sell et al. [18]. In the rig, it is possible to circumferentially displace the blading relative to

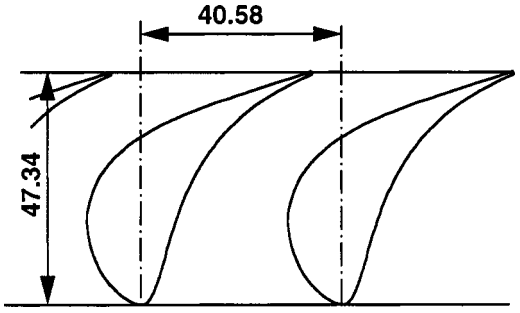

Fig. 1 Blade form and dimensions (hub)

[1]Currently at ALSTOM Power AG, 5401 Baden, Switzerland.

[2]Current position: Consul general for Hungary, Munich, Germany.

Contributed by the International Gas Turbine Institute and presented at the 45th International Gas Turbine and Aeroengine Congress and Exhibition, Munich, Germany, May 8–11, 2000. Manuscript received by the International Gas Turbine Institute February 2000. Paper No. 2000-GT-481. Review Chair: D. Ballal.

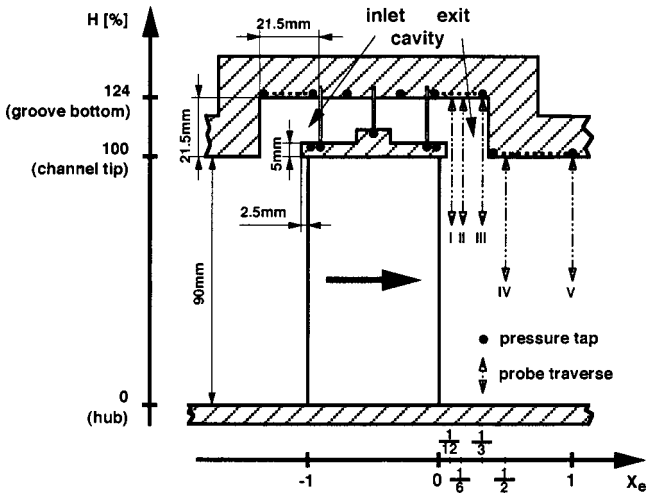

Fig. 2 Test cascade geometry and measurement position

the fixed outer casing. This system has a number of advantages, one of which is that the measurement systems (static pressure taps, flow field probes etc.) remain at fixed positions in the casing. Thus with small incremental steps in the blade position highly resolved flow field measurements can be made.

To study labyrinth flow interaction the approach was taken that the shroud itself was fastened to the outer casing, with the blades being snugly positioned under the fixed shroud. Thus, mechanically the shroud and the blading were independent of each other. This approach is permissible under the condition that the gap between the blade and the fixed shroud is so small that it is aerodynamically closed. Due to careful attention to manufacture and assembly, it was ascertained that the gap from the shroud to the blade tip was in the range 0.01 . . . 0.02 mm, and thus effectively closed.

Results were taken in two blade passages. Investigation of the static pressure and flow field in seven neighboring blade passages indicated that repeatable, periodic flow existed.

2.2 Experimental Tools. All the experimental results presented in this paper are pneumatic data and comprise static pressure taps on the casing and shroud together with flow field data gathered in tangential planes downstream of the blade trailing edge using radially traversed multiple hole probes.

Wall pressure taps of 0.3 mm diameter were provided at 9 axial positions within each of the inlet cavity, the exit cavity and the downstream part of the casing. The locations of pressure taps are indicated in Fig. 2. Typically casing pressure fields comprising 580 discrete points within 2.2 pitches were measured.

Flow field quantities were measured in 5 cross sectional planes located at 1/12, 1/6, 1/3, 1/2 and 1 axial chord downstream of the blade trailing edge as shown in Fig. 2. Note that the first three measurement planes are located within the exit cavity of the labyrinth, and the last two downstream of the labyrinth groove. Each plane was typically traversed with 460 points, in unstructured measurement grids covering 1.4 pitches in the circumferential direction.

Two probe types were used to gather the flow field data: First, a small head diameter (0.9 mm) five hole cobra-probe, and second, a virtual four hole needle probe. A virtual four hole needle probe is an arrangement whereby two separate probes are used sequentially in the same location in order to determine the full three dimensional flow field data. The first probe is a normal lateral-tap needle probe, based upon a 0.5 mm steel tube. This probe is used to simulate a three hole yaw probe, by measuring sequentially at three probe rotational positions each separated by 49 deg. A fourth pressure is then derived by measuring in the same location with a needle pitch probe with a hole bored into a canted tip. With the two probes a priori calibrated in a free jet test stand, it is possible to derive the full three dimensional flow field information.

Within the last cavity of the labyrinth the local yaw angle may grossly differ from the nominal exit flow angle, therefore the virtual four hole probe was used in a flow nulling mode. Because of the time-consuming sequential nature of the flow measurements taken with the virtual four hole probe, it is important to reduce the number of interim probe measurements required to reach the probe null positions. This is done by the use of an efficient fuzzy logic algorithm (Biswas [19]) which can typically find the unknown main flow yaw angle to 0.5 deg accuracy in three steps or less.

For the results shown here, accuracy in flow exit angles for the five hole probe of better than ± 0.2 deg have typically been achieved at the nominal exit Mach number (Treiber et al. [20]). In the exit cavity, the flow accuracies degrade with a typical accuracy of ± 1 deg in both yaw and pitch angle for the virtual four hole probe.

2.3 Test Case Restrictions. Several factors in the experimental arrangement require comment. Firstly, the incoming flow is free of any periodic unsteadiness such as wakes or secondary vortices as would be the case for a rotor blade row within a turbine. Secondly, the use of stationary blades, shroud and casing (absence of relative endwall motion) certainly alters the flow within the labyrinth cavities in comparison to that seen in true systems, so for example local flow directions close to the endwalls may be falsified. Thirdly, the absence of a downstream blade row moving relatively to the rotor fails to produce realistic unsteady exit flow conditions.

Nevertheless, many essential geometric features are modelled. In particular the interaction of the labyrinth leakage flow, the blade exit swirl and the main-flow secondary flow structure are representative for real configurations. (A major modification of the test rig would have been required for the study of these flows under fully realistic conditions.)

A further factor requiring comment is that the inlet boundary layer at the outer casing is relatively thick (see Table 2). A part, or all, of the flow entering a labyrinth system consists of the boundary layer material, with low momentum and stagnation pressure compared to the core flow. In this case it may be therefore expected that low energy fluid is over represented in the labyrinth flow.

Table 1 Test stand parameters

Tip Radius	r	400	[mm]
Blade Height	h	90	[mm]
Blade Count	n	48	[−]
Axial Chord Length	s	47.34	[mm]
Tip-Hub Ratio	Y	1.29	[−]

Table 2 Casing boundary layer conditions at inlet

	δ_1	δ_2	δ_3	H_{12}	H_{32}	$\mathrm{Re}_{\delta 2}$
Hub	0.8	0.6	1.1	1.27	1.79	2040
Tip	1.1	0.9	1.6	1.27	1.80	3010

3 Experimental Results

3.1 System Characteristics. This chapter presents the system behavior in terms of thermodynamic state determined by pressure measurements at all characteristic locations. Further, the actual leakage mass flow is determined and a mass flow ratio given.

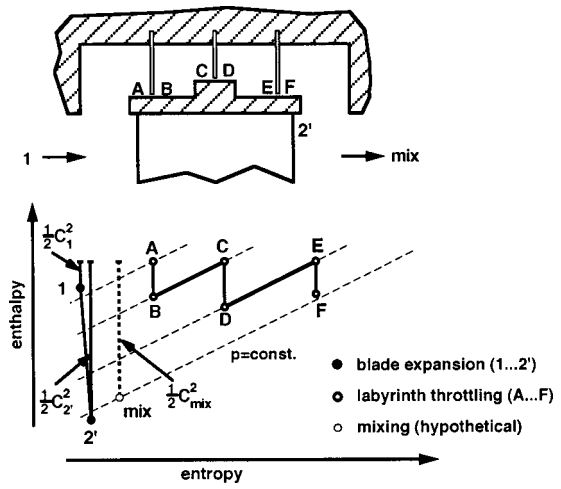

Fig. 3 h-s-diagram of blade labyrinth system

The enthalpy-entropy diagram in Fig. 3 describes in a simplified, schematic manner the overall thermodynamic behavior of the labyrinth flow. Numbers within the diagram indicate the location of pressure measurements shown in the labyrinth sketch. The corresponding static pressure levels are summarized in Table 3 in which the values are derived by pitch averaging the pressure measurements.

The pressure drop over the blading results from its acceleration and turning characteristic. The starting state 1 of the expansion curve is the inlet static pressure ($C_p = 0.15$) and the inlet dynamic head $c_1^2/2$ measured upstream of the entire system. The expansion ends at a far lower static pressure (state 2′). An evaluation radius $H = 80$ percent was chosen which is close to the tip but not yet affected by the labyrinth exit cavity.

The throttling curve of the flow through the labyrinth seal is also shown in Fig. 3. The inlet and exit chamber pressure determines the driving pressure difference across the labyrinth. The effective pressure difference can be measured shortly before the first (state A) and after the last (state F) seal. Assuming that the fluid is completely stagnating in front of the first fin there the wall pressure corresponds to the total pressure of the labyrinth flow. The starting point of the leakage expansion curve shows a lower total pressure than the main core flow due to the presence of incoming boundary layer fluid within the inlet cavity. The labyrinth flow itself is assumed to be ideal which means isentropic acceleration in the gap and complete mixing within the cavities (state BC and DE) so carry over effects can be neglected. The static pressure drop shortly after the third seal completes the effective pressure difference.

Differing thermodynamic states result at the end of both expansion curves (state 2′ vs. F). A slight static pressure difference is left over. Within and downstream of the exit cavity both mass flows are mixed again. The mixing of a small mass flow of high entropy (state F) with a large mass flow of low loss (state 2′) leads to a thermodynamic state with some entropy increase in comparison to state 2′. Assuming constant total enthalpy the dynamic head of the mixed flow is reduced due to the mixing induced static pressure increase. Consequently the total pressure is decreasing. The dashed line within the h-s diagram of Fig. 3 indicates a hypothetical resulting mixing condition.

Table 3 System pressures (C_p)

1 tot	1	2′	2ref	A	BC	DE	F
0	0.155	0.977	1	0.202	0.419	0.698	0.899

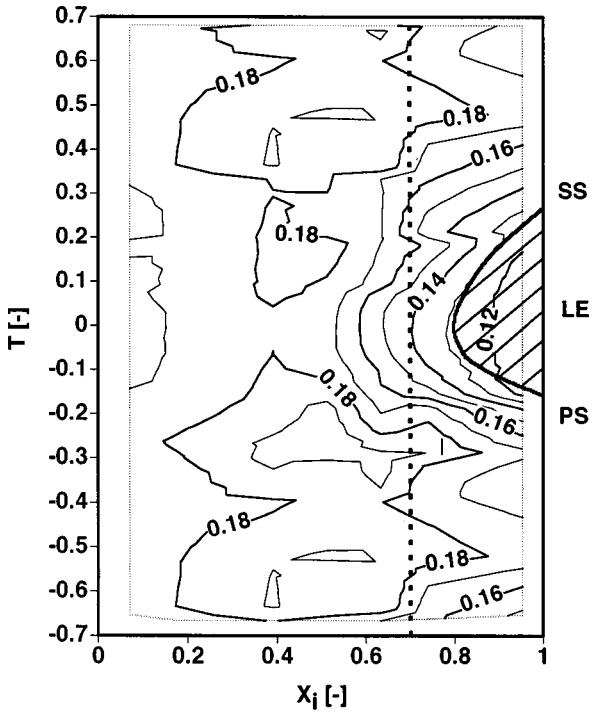

Fig. 4 Inlet cavity wall pressure distribution (C_p), Δcontour =0.1. The dash lines represent the location of the shroud leading edge.

The leakage mass flow of the labyrinth seal can now be estimated by the use of generic models, e.g. that of Traupel [1]. The mass flow over the fin depends on the seal gap cross section, the number of seals and the discharge coefficient of the specific labyrinth geometry. Equation 1 shows the estimation of mass flow according to Traupel where e is an empirical discharge function which already includes the established $1/(\sqrt{n_f})$ dependency upon the number of seals, the pressure ratio and the discharge coefficient of a stepped labyrinth geometry. With $e = 0.13$ (pressure ratio=0.95, $n_f = 3$), a density of 1.18 kg/m^3 and a measured inlet pressure of $C_{ps} = 0.202$ the leakage mass flow is 2.3 g/s per pitch. This is approximately 1.2 percent of the main mass flow.

$$\dot{m} = eS\sqrt{p_A \rho_A} \tag{1}$$

3.2 Inlet Cavity Flow. The casing-wall static pressure measurements in the inlet labyrinth cavity are shown in Fig. 4. The highest pressure in the cavity ($C_{pw} \approx 0.12$) is seen to exist at the circumferential position aligned with the leading edge. Consequently, the leading edge circumferentially modulates the static pressure field in the entire inlet cavity.

The cavity flow is fed by low momentum flow from the tip boundary layer. Fluid enters the groove mainly within the fore field of the leading edge. In the cavity it is deflected either to the right or to the left. Thus, a periodic cell structure of highly three dimensional vortices is created. These conclusions are supported by the preliminary numerical simulations presented in the Appendix.

3.3 Wall Pressure in Labyrinth. As shown in the previous section the inlet cavity has highly three-dimensional flow structures that result in pressure variations in the circumferential direction. This pressure field has a direct impact on the flow through the first and the following seal gaps. To measure this influence static pressure taps were placed on the shroud opposite the edge of each fin. Since the fins are 1 mm thick, and the tips are rectangular, the pressure measured there does not reach the static pressure of the fully expanded jet, as described by Egli [6]. The resulting

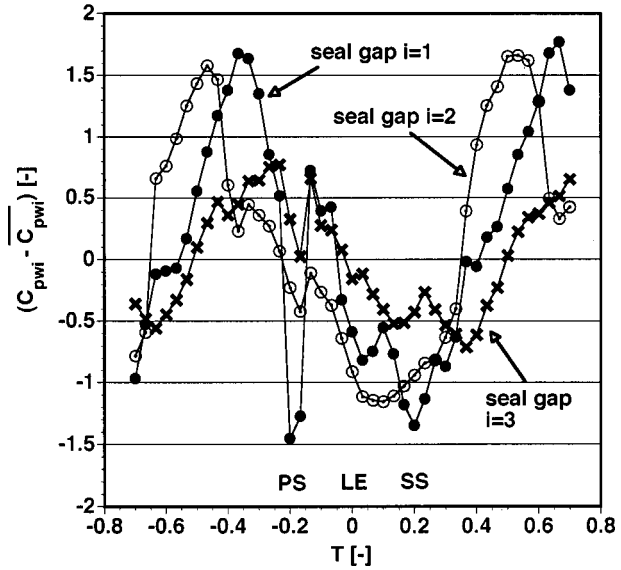

Fig. 5 Relative pressure distribution within the seal gap

pressure level under the fin lies between the pressure levels of the preceding and succeeding labyrinth cavity as evaluated in 3.1. Pitch averaging of these measurements yields the following results.

$$\overline{C_{pw1}} = 0.316$$

$$\overline{C_{pw2}} = 0.584$$

$$\overline{C_{pw3}} = 0.808$$

Figure 5 shows the deviation of the measured gap static pressures from these averages. Within gap 1 C_p varies strongly in the circumferential direction having a maximum range of ± 1.5. Overall, a profile is seen possessing lower values of C_p (high pressure) near the leading edge position and higher near mid passage. In fact the high pressure coincides with the effective blade stagnation point which is shifted slightly to the suction side (Treiber [21]). However, locally a sharp negative spike is seen on the pressure side (at a location of $T = -0.2$), with the minimum seal pressure approximately that seen on the suction side. Under the second fin the pressure amplitude remained virtually unchanged. Again, on the pressure side a spike is seen with the minimum pressures at the same circumferential location as the first fin. The magnitude of the spike is reduced strongly in comparison to the level seen under the first fin at the same location. Under the third seal position the variations have a range of ± 0.8, only. Again, a weak spike in the distribution on the pressure side is seen.

From these results it can be inferred that the three dimensionality seen in the first labyrinth induces three dimensionality in the subsequent chambers, but the three dimensional character of the labyrinth flow is attenuating due to the mixing processes within the chambers.

In the absence of complete internal flow field data from the first cavity conclusive interpretation of the spike remains impossible. However, it could be hypothesized that the spike indicates a division plane of the periodic three dimensional vortex cells mentioned in the previous section. The periodicity is induced by the leading edge pressure field and remains unchanged within the stationary labyrinth cavities.

3.4 Exit Cavity and Downstream Flow

Total Pressure Loss in the Exit Traverses. Figure 6 shows total pressure loss contours for the three measurement planes within the exit labyrinth. A radial height of 100 percent corresponds to the channel tip, and 124 percent corresponds to the labyrinth groove bottom. In Fig. 6 and subsequent figures, a small gap appears between the solid boundary and the measurements. This gap represents the area where wall proximity effects degrade excessively the experimental accuracy of the probe surveys.

In the first measurement plane 6(a), 1/12 axial chord downstream of the trailing edge, the loss patterns divide up into three distinct areas. Below $H = 97$ percent the main flow is substantially undisturbed by the presence of the labyrinth. The loss pattern is very typical for a turbine blade without tip clearance, showing a radial blade wake which is situated between low loss, uniform core flow regions.

The wake loss peak at 89 percent radial height is due to secondary flows within the blade channel (Sieverding [2]). Although not shown here, results obtained with the same blade in the case of smooth casing wall (no labyrinth, zero tip clearance) show higher loss at the peak (Treiber [21]). This shows that by sucking away part of the incoming boundary layer through the inlet cavity as in the present case less low momentum fluid is left over to roll up and form the secondary loss core.

A distinct area of very high loss, corresponding to the labyrinth leakage flow, is seen between $H = 103$ percent and the wall. Here up to 91 percent of the exit dynamic head has been lost. The

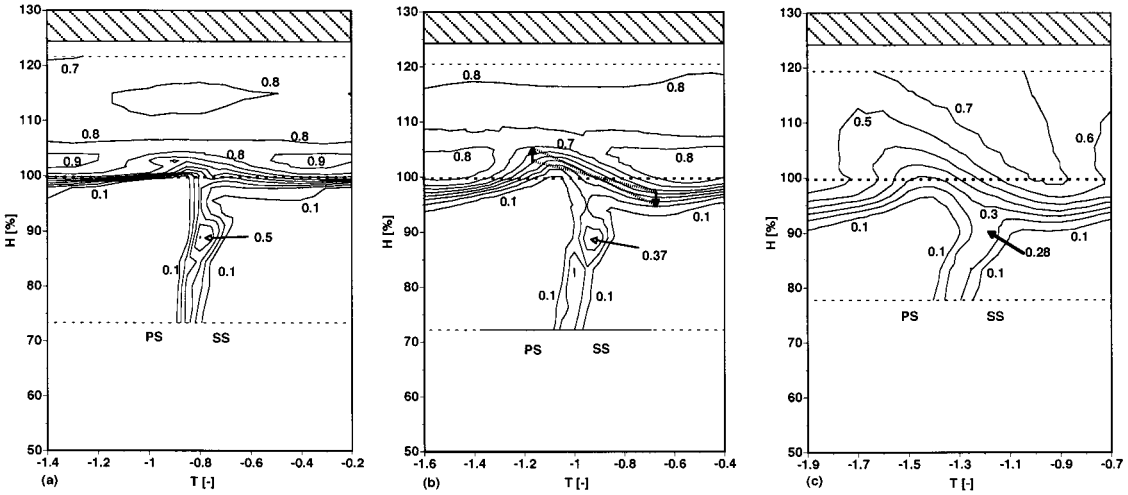

Fig. 6 Total pressure loss (ΔC_p^0) downstream of the trailing edge (*a*) 1/12, (*b*) 1/6, (*c*) 1/3 axial chord, Δcontour =0.1

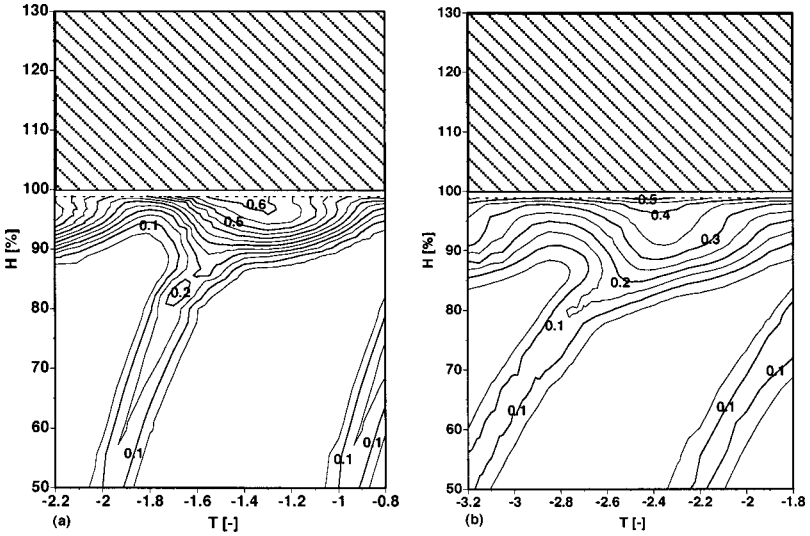

Fig. 7 Total pressure loss (ΔC_p^0) downstream of the trailing edge (*a*) 1/2, (*b*) 1 axial chord, Δcontour=0.05

distribution is periodic and an average total pressure loss of 85 percent can be deduced. Further detail of the flow in this region is revealed by the velocity contours, discussed in the following section.

These flow regions of differing loss levels are linked together by a third flow region between 97 percent and 103 percent radius which can be called the mixing sheet zone. Within this region steep loss gradients are observed as the high loss labyrinth flow starts to mix with the low loss channel flow. The gradients of pressure loss are not constant across one pitch. On the pressure side of the wake the contour lines are pushed together with the radial gradient reaching a maximum of 0.25/percent radial height. On the suction side of the wake the same absolute difference in total pressure loss is crossed in about thrice the radial extent.

At the second measurement plane within the cavity, 6(*b*), the flow patterns are not substantially different to 6(*a*). The wake has moved circumferentially from $T=-0.8$ to -1. The secondary loss peak retains its position relative to the wake center line and in absolute radial height. However, it has lost some of its strength due to the mixing process.

In contrast, there are significant changes in the structure of the mixing sheet. Note that the pressure loss gradient is now nearly constant across the sheet. For a better understanding of the flow motion, one should focus upon the contour lines 0.7 and 0.2, representing the cavity flow and main flow respectively. The mixing sheet has an ''*s*''-type form with the center of the ''*s*'' corresponding to the point where the wake intersects with the mixing sheet (at a radial position of 100 percent and a circumferential position of -0.95). Notice that the intersection point of the wake with the mixing sheet is co-incident with the center of rotation of the mixing sheet. This turning motion is depicted in the figure with the dashed lines and arrows.

The third traverse, 6(*c*), shows more marked changes, particularly for the labyrinth flow material. The primary reason for this is that the third measurement plane is much closer to the cavity face wall. Consider first the main flow region. The loss core is more blurred and has moved fractionally down into the passage, but structurally no major changes are apparent. In contrast, the distinction between the mixing sheet and the cavity flow is no longer obvious. The pressure gradients are attenuated. The ''*s*''-type structure is visible but the *s*-bends of contour have elongated in the circumferential direction resulting in a phase shift of nearly half a pitch into negative tangential direction.

Consider the flow downstream of the labyrinth groove, Fig. 7. At 1/2 axial chord 7(*a*) the maximum total pressure loss seen is 0.65. High loss fluid, whose origins are the flow through the labyrinth, has gathered on the suction side of the wake center line. The high loss layer has an average thickness of 10 percent of the radial height.

The secondary loss core has been displaced from the end wall reaching a radial height of $H=83$ percent. It has lost much of its strength (with a peak of 0.21) and is apparently merging with the loss layers at the wall.

Further downstream 7(*b*) mixing reduces further the peak total pressure loss. A movement of the high loss region, relative to the wake center line, is seen. The loss layer at the wall now reaches down an average thickness of 14 percent of channel height. This is due to both mixing within the loss layer and the presence of the blade generated exit radial pressure gradient. As a consequence of the mixing process there is no identifiable loss core associated only with the blade secondary flows.

Velocity Distributions in the Exit Plane. Figure 8 presents the normalized axial and circumferential velocity components at the first measurement plane. In comparison to the pressure loss distributions, three additional regions within the cavity flow are observable.

From the groove bottom down to a radius of $H=108$ percent the flow is characterized by a radially stratified axial velocity distribution with no axial velocity at a radial height of $H=114$ percent. Taking into account that this region has a rather uniform tangential velocity around -0.35 (see Fig. 8(*b*)) it can be postulated that this structure corresponds to a ring vortex with a high circumferential velocity.

Crossing the shroud perimeter height at $H=106$ percent a discontinuity in axial velocity component can be observed between $T=-1.3$ and $T=-0.6$. Corresponding to the pressure side corner of the passage the contour lines of 0.3 are divided and form a very narrow sheet of higher axial velocity of up to 0.31. Within these regions a relatively low tangential velocity of about -0.21 is seen. Obviously, the fluid in this sheet originates directly from the jet leaking out of the last fin gap.

The third identifiable zone is a recirculation zone cut by the measurement plane downstream of the shroud lip. A recirculation zone is characterized by two vortices with upstream flow in its center where the center velocity component is of the same magnitude as the component at the limit of the recirculation zone but with opposite sign. This can be observed at $H=103$ percent and

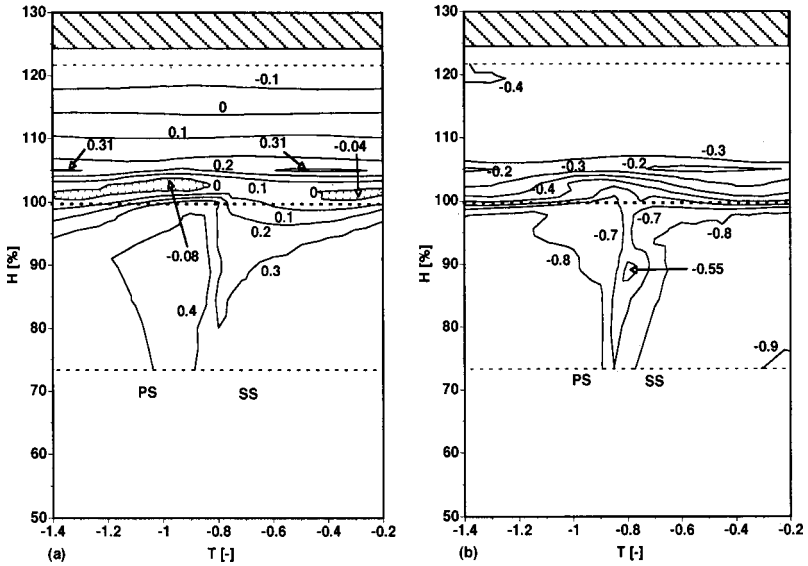

Fig. 8 Velocity components 1/12 axial chord downstream of the trailing edge normalized with c_0: (*a*) axial velocity, (*b*) circumferential velocity, Δcontour =0.01

−1 circumferential location. Considering a velocity range of ±0.1 a flow ribbon of contour lines can be isolated. Its center line lies on the tangential velocity contours representing −0.4 and is modified by the trailing edge pressure field within a range of radial heights of 103 percent and 101 percent. The geometrical center radius of the shroud back face is at $H=103$ percent. The radial thickness of the ribbon varies between 2.7 percent and 4.2 percent, which equals to 48 percent and 76 percent of shroud thickness.

It can be seen from the tangential velocity that the recirculation zone is circumferentially sheared. A low tangential velocity (−0.3) occurs at the upper limit ($H=104$ percent) and a high velocity (−0.6) is present at the lower border ($H=99$ percent). The center line of the recirculation zone has a constant tangential velocity of −0.4. This is the same order of magnitude as the tangential velocity of the cavity vortex.

The highest radial gradient in tangential velocity component is reached between the pressure side main flow and the recirculation zone (for example position −1/100 percent). There, 0.2 of normalized velocity is passed within only 1 percent of radial height. Tangential shear stress is therefore the main source of mixing and hence total pressure loss production. In Figure 6(*a*) this location is associated with the highest total pressure loss gradient.

At the second measurement plane, Fig. 9 the downstream development of these flow regions can be followed. Here the radial velocity patterns are more interesting than the circumferential ones.

The lateral moving vortex within the cavity is cut at a different radial position relative to the vortex axis. Thus the key characteristics of the vortex remain unchanged: upstream velocity components near the cavity end wall and downstream components near

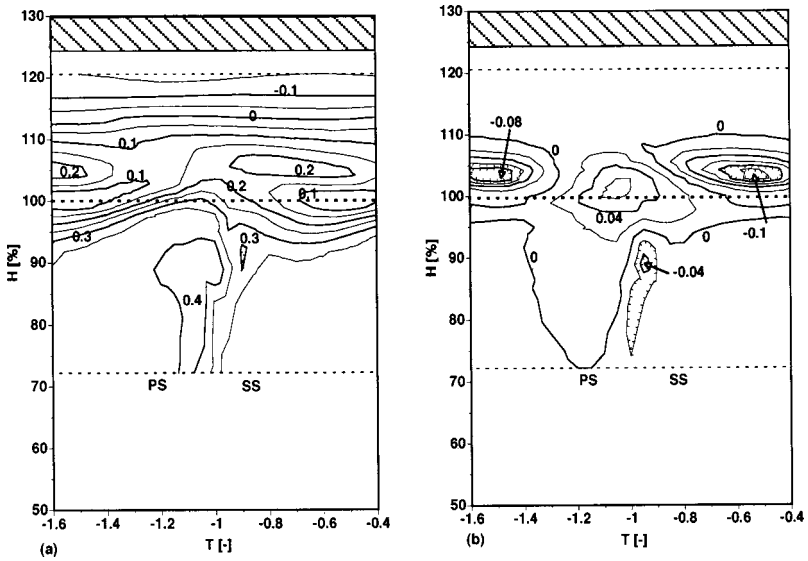

Fig. 9 Velocity components 1/6 axial chord downstream of the trailing edge normalized with c_0: (*a*) axial velocity, Δcontour=0.05, (*b*) radial velocity, Δcontour=0.02

the mid cavity region combined with a high circumferential velocity. Within the main flow the axial velocity distribution has leveled out becoming more homogeneous.

The recirculation zone is no longer present at this axial position. Downstream of the recirculation zone the shroud wake should be found. It is in this case not easy to detect it because inflow from the pressure side and the leakage jet camouflage the traces of the wake. Using the minimum axial velocity as a wake marker the regions at circumferential position $-0.6/-1.55$ and 100 percent radial height can be postulated as a part of the circumferential shroud wake. It is filled up in the near wake region by passage fluid and therefore gets interrupted. On the lower side the wake is again circumferentially sheared, since strong gradients in tangential velocity components are present there.

The leakage jet can be found within the hook like contour at position $-0.75/106$ percent. It now features an axial velocity component of about 0.23. In circumferential direction the fluid has accelerated to approximately -0.28. The jet retains its kinetic energy but is simply bent into negative circumferential direction while it moves slightly out of the cavity. This is due to the corresponding radial velocity component that reaches values down to -0.05 near this region.

The minimum of -0.1 in radial velocity is reached near the shroud wake position (e.g. $-0.5/103$ percent) and corresponds to fluid whose source is the cavity.

From the radial velocity component the inflow jet can easily be detected. It reaches values up to 0.06 and has its origins in the pressure side corner of the wake indicated by the zero radial velocity contour line. Within the wake the radial pressure gradient due to the blade turning is causing the radial migration of low momentum fluid toward the hub.

Exit Casing Pressure Measurements. Detailed wall static pressure measurements from the exit cavity casing wall ($H=124$ percent) and the duct casing wall ($H=100$ percent) downstream of the labyrinth exit are presented in a combined manner in Fig. 10.

The diagram covers two pitches in circumferential direction and one axial chord downstream of the trailing edge. The jump from cavity groove bottom to casing wall occurs at the axial position $X_e=0.37$. This is marked with a dashed vertical line, as is the shroud trailing edge. The oblique dash-dotted lines show the downstream trace of the wake center lines in the channel flow at $H=78$ percent. The solid curves show the direction of the leakage jet flows. At the channel/cavity interface the flow structure will be seen to be circumferentially variable, with zones where the channel fluid penetrates into the cavity and zones, lying in between, where the jet formed by the contraction of the leakage sheet exits into the channel. The arrows indicate the measured local flow direction within the core of the leakage jet. The length of the arrows do not represent a local velocity. Since the diagram is stretched in axial direction the true blade exit angle of 22 deg relative to the tangential is approximately 40 deg within the diagram.

Consider first the pressure contours in the cavity. Periodic high pressure regions (C_p of 0.88) are present at the downstream cavity corner ($X_e=0.33$). The inflow jet (see Fig. 9(*b*)) which has entered the cavity is decelerated in the corner. It is also responsible for the total pressure loss contour shift in Fig. 6(*c*) and therefore transports fluid of relatively low total pressure loss into the cavity.

The blade exit flow yaw angles near the cavity bottom reveal a lining up of the weak pressure maxima of $C_p=0.88$, the lower pressure island of $C_p=0.92$ and the regions of pressure $C_p \geqslant 0.91$ at the upstream cavity corner.

Within the distance from the fin gap to the shroud trailing edge the leakage jet is turned by 25 deg from assumed purely axial flow to 65 deg relative to the tangential axis due to tangential momentum exchange with the inflow jet, shown at the top of Fig. 10 by a weak dotted line. Further downstream the leakage jet is overturning as the small arrows on the jet trace line indicate. This is

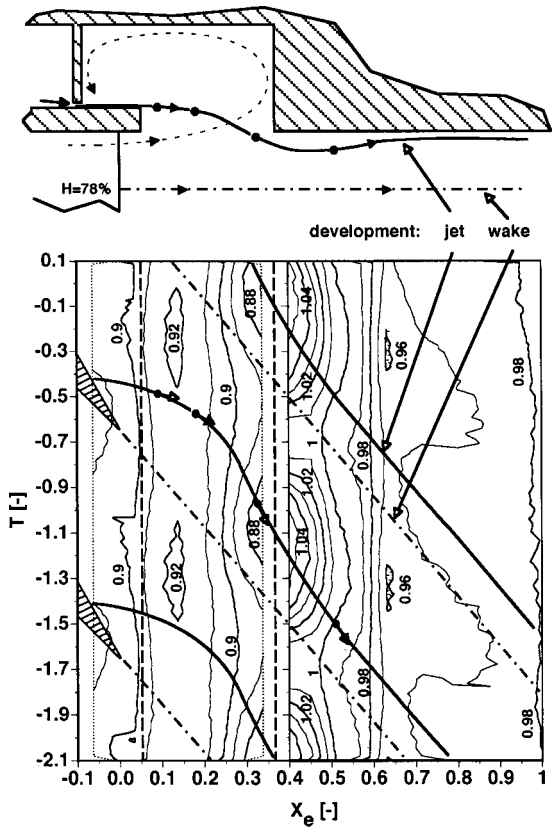

Fig. 10 Wall static pressure measurements (C_p), left on the cavity groove bottom ($H=124$ percent), right on the channel casing wall ($H=100$ percent), Δcontour=0.01. Note that the length scale is axially stretched by a factor of 2.

due to the continued process of tangential momentum exchange from both the main flow and the cavity vortex to the leakage jet.

Downstream of the cavity exit edge the wall pressure exhibits a lower level than in the cavity groove. Obviously dictated by the downstream development of the leakage jet the periodic low pressure regions of $C_p=1.05$ indicate two flow features: Firstly, the net exit mass flow leaves the cavity in one discrete leakage jet per passage. Secondly, it is accelerated and deviated strongly, which will be discussed later.

Entering the main flow region near the exit edge the leakage jet is characterized by strong negative radial velocity components (see Fig. 9(*b*)) and some overturning (see arrows in Fig. 10) in comparison to the main flow direction.

Going further downstream the wall pressure contours show a circumferentially constant series of contours at an axial position of $X_e=0.6$. A minimum local C_p is reached at $X_e=0.65$. Downstream of this position the wall pressure slightly decreases due to the mixing processes in the duct. Overall this region shows less gradients and less pronounced structures.

From this wall pressure description the following can be concluded. Each leakage jet separates from the wall at the exit edge, attaches quickly at $X_e=0.6$ and then adheres to the end wall. This results in a flattening of the jet's cross section until it merges with the neighboring jets. As consequence a high total pressure loss layer of wavy structure is observable (see Fig. 7) which is additionally characterized by overturning flow angles in comparison to the main flow direction.

Secondary Flow Vectors. To complete the presentation of experimental results vector plots of the secondary flow components present within the last two measurement planes are discussed (Figs. 11, 12). A usual definition of the primary flow for the

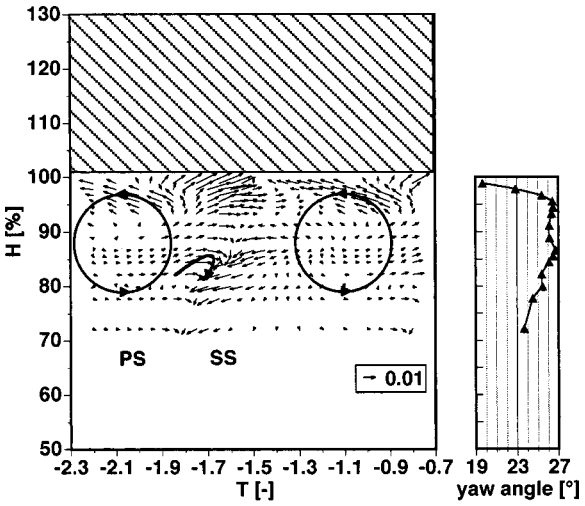

Fig. 11 Secondary flow vectors normalized with c_0, 1/2 axial chord downstream of the trailing edge

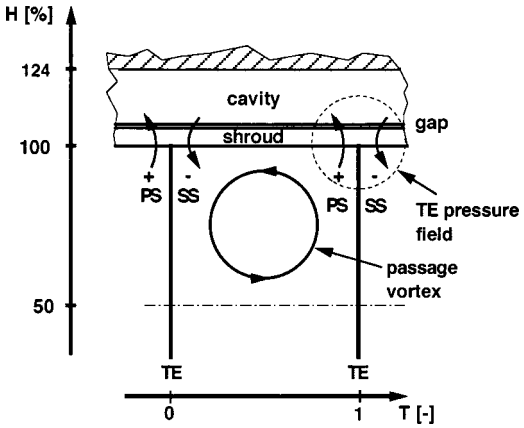

Fig. 13 Sketch of driving mechanisms

purpose of deriving the secondary flow is the Euler solution. However, for this case with the presence of flow that has moved through the labyrinth structure, the Euler solution is not necessarily attractive as a description of the core flow. Instead the core flow has been defined by the pitch averaged exit flow yaw angle, (derived by circumferentially momentum averaging at constant radial height the axial and tangential velocity components). Therefore, as reference the radial distribution of the pitch averaged yaw angle is included on the right hand side of the diagram.

The briefly mentioned overturning of the exit cavity leakage jet (see Fig. 10) is now justified with experimental results presented in Fig. 11. The design exit angle of the blade is 21.8 deg relative to the tangential axis at mid span. In an unaffected flow the yaw angle near the tip wall would increase to ≈24 deg due to lower effective turning of a prismatic blade at higher radial heights. The lowest measured yaw angle is 19.5 deg at $H=98$ percent. This leads to a local overturning of 4.5 deg.

The passage vortex is clearly identifiable. It is one of the major driving mechanisms to the exit cavity and mixing flow. The passage vortex pushes low momentum fluid at the casing wall from the pressure side of a wake across the passage to the center of the neighboring wake. The vortex center is at a radial position of $H=87$ percent in a circumferential distance of 0.46 relative to the wake. On the blade pressure side the vortex fluid is radially sheared and partially deviated into the center of the wake. There, low kinetic energy fluid is radially transported away from the end wall. This mechanism originates from the blade induced radial pressure gradient. The passage vortex supplies the wake root at the end wall with additional fluid. Notice that the cavity outflow sheet ($H>97$ percent) only shows vector arrows pointing to the end wall. This suggests that the already reattached high loss flow is flattened by the main flow.

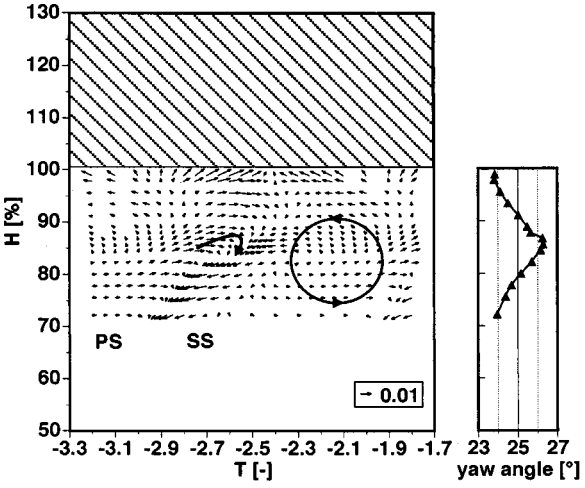

Fig. 12 Secondary flow vectors normalized with c_0, 1 axial chord downstream of the trailing edge

One axial chord downstream at the last measurement plane in principle the same flow structure is present (Fig. 12). The overturning of the near wall flow regions has become≈2 deg. So the loss layer is adjusting to the main flow direction. The passage vortex has shifted the radial position to $H=83$ percent reaching 0.29 pitch circumferential distance to the wake. On the pressure side of the wake the passage vortex side shears the migrating flow within the wake and contributes a smaller part to the wake secondary mass flow.

3.5 Exit Cavity Flow Structure. A summary of the experimental results downstream of the trailing edge will be presented by way of a description of the flow physics incorporating reference to the major driving mechanisms and flow characteristics.

The driving forces were found to be the following:

- periodic trailing edge static pressure field
- passage vortex
- different flow characteristics:
  - cavity flow: low momentum
  - main flow: high momentum.

The first two driving mechanisms are sketched in Fig. 13. Both act in the same sense and enhance each other. The resulting deflection of core and cavity flow is indicated by arrows in Figure 6(*b*). This is also the cause of the deformation of the mixing sheet into a wavy sheet form. Two jets per passage form within the cavity (see also Fig. 9): one entering the cavity on the pressure side of the blade passage the other leaving it on the suction side. The three dimensional paths the jets follow are depicted schematically in Figs. 14, 15.

Figure 14 shows a sketched model view from above the labyrinth and the velocity triangles, which are discussed further down in this section. Due to its low momentum the leakage jet is deflected quickly by the tangential momentum of the remnant of the inflow jet. At the cavity/channel interface both types of jets move parallel to each other. At this point the leakage sheet leaving the clearance gap has completely broken up into a periodic sequence of jets (''leakage jet'').

Getting close to the cavity exit edge the inflow jet crosses the leakage jet at a radial height of about $H=103$ percent and is deflected by the back face of the groove. Downstream of the shroud

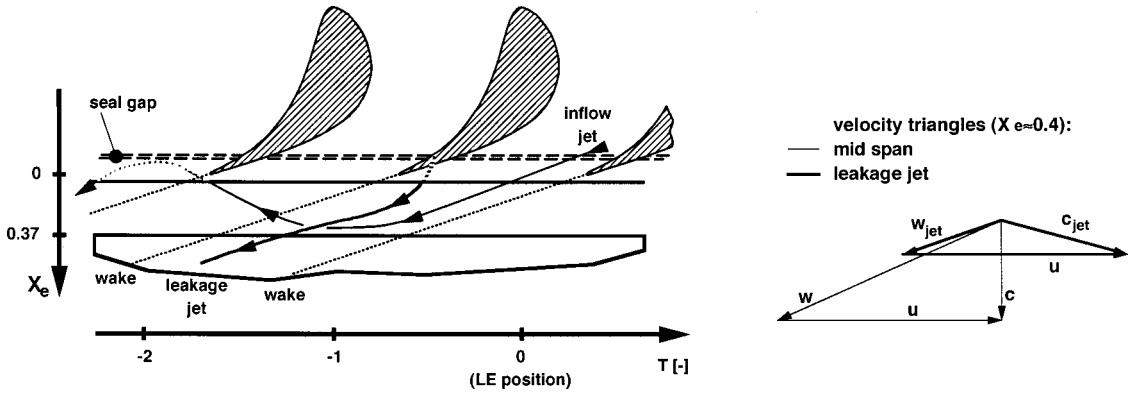

Fig. 14 Sketch of flow effects (top view), velocity triangles at $X_e \approx 0.4$

trailing edge the leakage jet is further deviated into circumferential direction by both the main flow and the cavity ring vortex. Passing the exit edge the leakage jet has slightly ''overturned'' relative to the main flow direction as it can be seen from the velocity triangles given in Fig. 14. Therefore, a succeeding stator blade row would see jets of heavily negative and time-periodic incidence, as shown by the absolute vector, c_{jet}.

Figure 15 explains some additional flow effects: The inflow jet drives the cavity ring vortex and induces its tangential velocity. Behind the shroud a recirculation zone is formed. Here the fluid is kept in circumferential movement by shear stresses. The leakage jet passing the cavity exit edge is pushed against the tip wall where it attaches quickly.

Because of the inflow jets and leakage jets passing each other radially near the cavity/channel interface (see Figs. 14 and 9(*b*)) the mixing sheet bounding the separation zone obtains circumferential waviness. At the cavity exit edge the sheet it is cut periodically into upper bends along the inflow jets and lower bends along the leakage jets. The highly periodic feature of these flows is clearly seen in the total and static pressure fields shown in Figs. 7 and 10, respectively.

3.6 Neglect of Wall Motion. It is useful to speculate at this point about the neglect of wall motion in the experiment. Thinking of the test case as a rotor blade row looked upon in the relative frame of reference, the casing and groove walls should move circumferentially in the negative T direction. This would affect the leakage stream in several ways. Firstly, the fluid entering the upstream cavity would have non-zero circumferential momentum. In the cavities this momentum is likely to be enhanced by wall friction. As a result the leakage sheets issuing from the successive fin clearances have an increasing tangential momentum toward $-T$. In contrast to Fig. 10, the leakage stream does not enter the exit cavity axially and needs less deflection in order to become parallel to the main flow. The periodic structure of the inflow jets and contracted leakage sheet/jets, being caused by the dominant blade-to-blade pressure pattern of the main flow, is maintained however. Therefore wall motion enhances, but does not alter, the exit cavity flow, maintaining its main feature of high circumferential velocity.

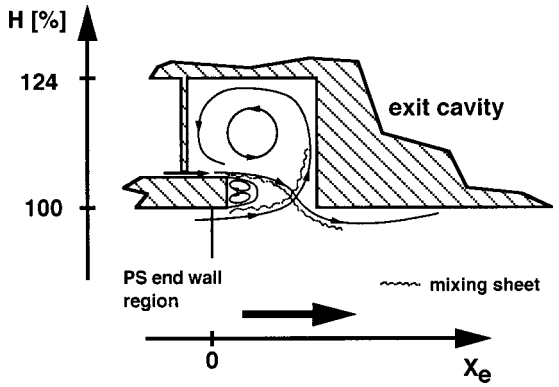

Fig. 15 Sketch of flow effects (side view)

4 Summary and Conclusions

This work has presented detailed measurements made in a stationary blade row labyrinth system and has lead to detailed insights concerning the flow structure in the labyrinth inlet and exit cavities. The inlet cavity flow was found to be highly three dimensional, a consequence of the blunt blade leading edge stagnation effect. This influence of the leading edge attenuates, but remains noticeable in the labyrinth path down to the last sealing fin.

Flow within the exit cavity was found to be dictated by three inherent effects. First, the blade-to-blade structure of the main channel flow creates a periodic static pressure field on the exit cavity wall face, where the high momentum of the oblique outflow from the blade passages is partially deflected into the cavity. This penetration of main flow fluid of high circumferential momentum into the labyrinth leakage flow in the exit cavity creates a complex, three dimensional flow pattern of high circumferential and low axial velocity. Second, this periodicity is enhanced by the secondary flow structure created by the blade passages. Third, the circumferential component is enhanced by shear stresses between the high momentum swirling annular flow and the more nearly axial leakage stream.

An interesting finding is that the fluid leaving the cavity is broken up into distinct oblique jets of low momentum embedded in the channel flow. In real machines, where the cavity is followed by a next blade row, the velocity of this leakage jet relative to the blade is directed against the blade back side (negative incidence) and is likely to cause additional high losses. This problem certainly merits further investigations under realistic conditions.

Acknowledgments

The test facility was built with the financial support of ABB Power generation Ltd. and NEFF. The Swiss National Energy Research foundation. The CFD results presented in Appendix 1 were graciously provided by C. Casciaro. Helpful discussions with J. Schlienger are gratefully acknowledged.

Nomenclature

LE = leading edge
PS = pressure side
SS = suction side
TE = trailing edge

ER = Euler (RMS) radius
C_p = pressure coefficient [−] $C_p = p^0_{1,\mathrm{ref}} - p / p^0_{1,\mathrm{ref}} - p_{2,\mathrm{ref}}$
ΔC^0_p = total pressure loss coefficient [−] $\Delta C^0_p = p^0_{1,\mathrm{ref}} - p^0 / p^0_{1,\mathrm{ref}} - p_{2,\mathrm{ref}}$
H = non-dimensional radius $= (r - r_{\mathrm{hub}})/(r_{\mathrm{tip}} - r_{\mathrm{hub}}) \times 100$ [%]
H_{12} = Shape factor, $H_{12} = \delta_1 / \delta_2$
H_{32} = Shape factor, $H_{32} = \delta_3 / \delta_2$
M = Mach number [−]
Re = Reynolds number [−]
S = cross sectional area of the seal gap [mm^2]
T = pitch position normalized with pitch angle [−]
X_e = axial position downstream of TE normalized with s [−]
X_i = axial position in inlet cavity normalized with cavity width [−]
Y = tip-hub ratio [−]
b = fin thickness [mm]
c = absolute velocity [m/s]
c_0 = nominal duct exit velocity $c_0 = \sqrt{(2(p^0_{1,\mathrm{ref}} - p_{2,\mathrm{ref}}))/\rho_1}$
c_r = radial velocity [m/s]
c_u = tangential velocity [m/s]
c_x = axial velocity [m/s]
e = empirical discharge coefficient (see Eq. (1)) [−]
h = enthalpy [J/kg]
h = blade height [mm]
j = fin clearance [mm]
$\dot{m}$ = mass flow rate [kg/s]
n = blade count [−]
n_f = number of fins [−]
p = static pressure [Pa]
p^0 = total pressure [Pa]
$p^0_{2,\mathrm{ref}}$ = reference total pressure, $\tilde{p}^0_{1,\mathrm{ER}}$ [Pa]
r = radius [mm]
s = axial chord length [mm]
s = entropy [J/kg K]
u = rotational speed [m/s]
w = velocity within relative frame of reference [m/s]
α = yaw angle, from tangential [deg]
δ_1 = displacement thickness [mm] $\int_0^{re}(1 - c_x/c_{xe})dr$
δ_2 = momentum thickness [mm] $\int_0^{re} c_x/c_{xe}(1 - c_x/c_{xe})dr$
δ_3 = kinetic energy thickness [mm] $\int_0^{re} c_x/c_{xe}(1 - (c_x/c_{xe})^2)dr$
ρ = density [kg/m^3]

Subscripts

1 = Inlet
2 = Outlet
1,2,3 = fin number
dyn = dynamic
e = Boundary layer edge
ref = Euler Radius
w = wall

Appendix

Preliminary Presentation of Numerical Simulations. The aim of this appendix is to reinforce, by way of a preliminary presentation of the results from a numerical simulation, some of the comments made concerning the three dimensional nature of the vortex structure in the first cavity (Section 3.2).

A1.1 Methodology. A preliminary numerical simulation of the experimental test case has been performed with the commercial CFD solver, CFX-Tascflow. This is a block-structured finite volume three dimensional Navier-Stokes solver with the Kato-Launder implementation of the k-ε turbulence model. The solver has been extensively validated (Casciaro [1]) for equivalent test cases generated from the same experimental facility, with particular emphasis on physically difficult cases, for example the vortex breakdown present in some unshrouded tip leakage flows (Casciaro et al. [2]). The mesh used has 228.000 nodes in the labyrinth, and 210,000 in the main blade channel, and is considered to be giving, in terms of the flow physics at least, mesh independent results. The boundary conditions employed (pressure and velocity distributions) are always those measured from the experiments. The casing wall was stationary. Therefore, there is confidence in the correctness of flow mechanisms computed and presented below, but in the absence of a fully explored numerical simulation, a deep quantitative interpretation of the numerical results would be inappropriate.

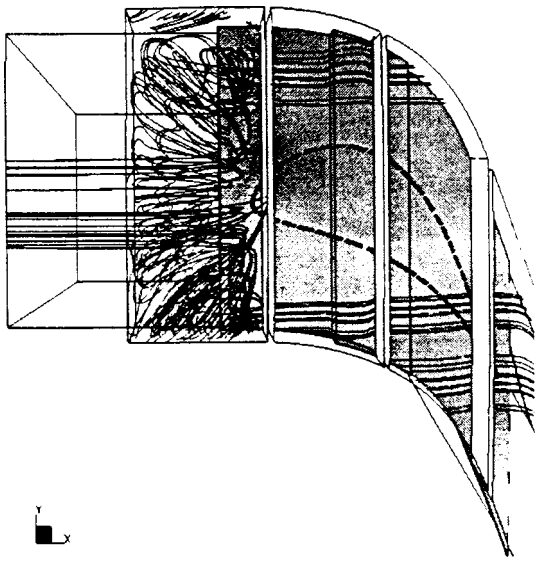

Fig. A1 Streamlines of preliminary CFD calculations: viewed from above into labyrinth cavities

A1.2 Results. In Fig. A1 computed streamlines are shown whose starting points lie within the inlet casing boundary layer. Most streamlines are pushed into the inlet cavity groove where they form a three dimensional vortex which is seen to wrap around the leading edge stagnation fore field. This results in a pitch periodic vortex cell structure divided by an imaginary division plane.

References

[1] Traupel, W., 1966, ''Thermische Strömungsmaschinen,'' Springer-Verlag.
[2] Sieverding, C. H., 1984, ''Recent Progress in the Understanding of Basic Aspects of Secondary Flows in Turbine Passages,'' ASME Paper No. 84-GT-78.
[3] Moore, J., and Tilton, J. S., 1988, ''Tip Leakage Flow in a Linear Turbine Cascade,'' ASME J. Turbomach., **110**, pp 18–26.
[4] Heyes, F. J. G., Hodson, H. P., and Bailey, M., 1992, ''The Effect of Blade Tip Geometry on the Tip Leakage Flow in Axial Turbine Cascades,'' ASME J. Turbomach., **114**, pp. 543–651.
[5] Sell, M., Treiber, M., Casciaro, C., and Gyarmathy, G., 1999, ''Tip Clearance Affected Flow Fields in a Turbine Blade Row,'' Proc. of the Institution of Mechanical Engineers, **201**, Part A, pp. 308–318.
[6] Egli, A., 1935, ''The Leakage of Steam Through Labyrinth Seals,'' Trans. of the ASME, **57**, pp. 115–122.
[7] Rhode, D. L., Johnson, J. W., and Broussard, D. H., 1996, ''Flow Visualization and Leakage Measurements of Stepped Labyrinth Seals; Part I: Annular Groove,'' ASME Paper No. 96-GT-136.
[8] Takenaga, H., Matsuda, T., and Yokota, H., 1998, ''An Experimental Study on Labyrinth Seals for Steam Turbines.'' Proc. 8th International Symposium on Flow Visualisation, Sorrento, Italy.
[9] Zimmerman, H., Kammerer, A., and Wolff, K. H., 1994, ''Performance of Worn Labyrinth Seals,'' ASME Paper No. 94-GT-131.
[10] Millward, J. A., and Edwards, M. F., 1994, ''The Windage Heating of Air Passing Through Labyrinth Seals,'' ASME Paper No. 94-GT-56.
[11] Florjancic, M., 1990, ''Annular Seals of High Centrifugal Pumps: A New Theory and Full Scale Measurements of Rotodynamic Coefficients and Hydraulic Friction Factors,'' ETH Dissertation No. 9087, Zürich, Switzerland.

[12] Graf, K., 1991, ''Spaltströmungsbedingte Kräfte an berührungslosen Dichtungen von hydraulischen und thermischen Turbomaschinen,'' ETH Dissertation No. 9319, Zürich, Switzerland.
[13] Amoser, M., 1995, ''Strömungsfelder und Radialkräfte in Labyrinthdichtungen hydraulischer Strömungsmaschiner,'' ETH Dissertation No. 11150, Zürich, Switzerland.
[14] Spirig, M., 1999, ''Einfluss der Kammerströmung auf die Kräfte im endlich langen Spalt einer Labyrinthdichtung,'' ETH Dissertation No. 13288, Zürich, Switzerland.
[15] Denton, J. D., and Johnson, C. G., 1976, ''An Experimental Study of the Tip Leakage Flow Around Shrouded Turbine Blades,'' CEGB research report CEGB-R/M/N848.
[16] Trutnovsky, K., and Komotori, K., 1981, *Berührungsfreie Dichtungen*, 4th ed., VDI-Verlag, Düsseldorf.
[17] Sell, M., Althaus, P., and Treiber, M., 1996, ''Data Acquisition and Control Within the Zürich Annular Cascade,'' Proceedings XIIIth Symposium on Measuring Techniques for Transonic and Supersonic Flows in Cascades and Turbomachines. Zürich. eds., Gossweiller and Gyarmathy.
[18] Sell, M., Treiber, M., Althaus, P., and Gyarmathy, G., 1997, ''The Design and Construction of a New Test Stand for the Study of Basic Turbine Flow Phenomena,'' Proc. Second European Conference on Turbomachinery, Antwerp, Belgium.
[19] Biswas, R., 1994, ''A Fuzzy Logic Controller to Balance Pneumatic Multi-Hole Probes,'' XIIth Symposium on Measuring Techniques for Transonic and Supersonic Flow in Cascades and Turbomachines, Prague, Czechoslovakia.
[20] Treiber, M., Kupferschmied, P., and Gyarmathy, G., 1998, ''Analysis of Error Propagation Arising From Measurements With a Miniature 5-Hole Probe,'' Proceedings XIVth Symposium on Measuring Techniques for Transonic and Supersonic Flows in Cascades and Turbomachines, Limerick, Ireland.
[21] Treiber, M., 2000, Dissertation, ETH Zürich, Switzerland (in preparation).

K. K. Nielsen[1]
Machinery Dynamics Group,
Ødegaard & Danneskiold-Samsøe A/S,
Copenhagen, Denmark

D. W. Childs
Turbomachinery Laboratory,
Mechanical Engineering Department,
Texas A&M University,
College Station, TX 77843

C. M. Myllerup
Machinery Dynamics Group,
Ødegaard & Danneskiold-Samsøe A/S,
Copenhagen, Denmark

Experimental and Theoretical Comparison of Two Swirl Brake Designs

Experimental and theoretical data are presented for two interchangeable swirl brakes designed in connection with the Space Shuttle Main Engine (SSME) Alternate Turbopump Development (ATD) High-Pressure Fuel Turbopump (HPFTP) program. The experimental data includes rotordynamic data for a extensive variation of test variables. Comparison of the swirl brake performance revealed that a nonaerodynamic swirl brake design proved as efficient and at times better than an aerodynamic design. For this reason a theoretical investigation using computational fluid dynamics (CFD) was recently carried out. This modeling focused on predicting the seal inlet swirl ratio which is the primary swirl brake performance parameter. The nonaerodynamic swirl brake showed superior performance for a variety of test variable conditions. Strong separation vortices within the swirl vanes are the main reason for this finding. [DOI: 10.1115/1.1354140]

Introduction

Fluid induced rotordynamic forces play an important role in modern turbomachinery design. The continued push for more efficient designs and higher power densities necessitates careful rotordynamic design investigations.

For small motion about a centered position, the motion/reaction-force model for an annular gas seal is

$$-\begin{Bmatrix} F_X \\ F_Y \end{Bmatrix} = \begin{bmatrix} K & k \\ -k & K \end{bmatrix} \begin{Bmatrix} X \\ Y \end{Bmatrix} + \begin{bmatrix} C & c \\ -c & C \end{bmatrix} \begin{Bmatrix} \dot{X} \\ \dot{Y} \end{Bmatrix} \tag{1}$$

X and Y denote components of the rotor displacement vector relative to the housing, and F_X and F_Y are components of the reaction vector acting on the rotor. K, k, C, and c, are denoted as the direct stiffness, cross-coupled stiffness, direct damping, and cross-coupled damping coefficients, respectively. Assuming a circular rotor whirl orbit at amplitude A and precessional frequency ω, the radial and tangential force coefficients can be stated

$$-F_r/A = K + c\omega \quad F_\theta/A = k - C\omega \tag{2}$$

By acting in the radial direction K and c would be assumed to primarily influence rotor critical speeds. k and C act in the tangential direction and predominantly influence rotor stability. K and c have only secondary influence on rotor stability for typical gas labyrinth seal applications. Conversely, k can markedly degrade stability, whereas C can markedly improve stability. Seal inlet fluid prerotation in the direction of the rotor rotation, as it occurs naturally in the cavity between the rotor and the stator, is the primary factor influencing the magnitude of the seal cross-coupled stiffness. The use of swirl brakes at the inlet of the seal, first demonstrated by Wachter and Benchert [1], is a well-known way to improve stability by decreasing the fluid swirl velocity or even inverting its direction.

Nielsen [2–4] have addressed swirl brake design and flow structure description. Excessive separation vortices within the swirl brake control the flow and determine the seal inlet swirl velocities.

The geometry considered in this study originates from the Space Shuttle Main Engine (SSME) Alternate Turbopump Development (ATD) for the High-Pressure Fuel Turbopump (HPFTP) undertaken by Pratt and Whitney [5]. Rotordynamic analysis of the ATD-HPFTP indicated a strong sensitivity of the rotordynamic stability to the turbine interstage seal. Further studies showed that the destabilizing forces could be reduced or eliminated by introducing a swirl brake upstream of the seal. To verify the analyses a model of the ATD-HPFTP turbine interstage seal with swirl brake was built and tested at the Turbomachinery Laboratory at Texas A&M University. The tests showed that the aerodynamically designed swirl brake was remarkably effective. The swirl brake ''reduced k markedly and actually yielded a reduction in k with increasing values for $u_{\theta 0}$'' [5], $u_{\theta 0}$ denotes the fluid swirl velocity upstream of the swirl brake. Subsequently, it was decided to test a nonaerodynamic swirl brake design for comparison purposes. The nonaerodynamic swirl brake generally showed superior performance compared to the aerodynamically designed swirl brake. These unexpected findings could not be explained until the present study in which CFD modeling is utilized for prediction of the swirl brake flows.

Experimental Setup

The experimental setup has been discussed in earlier publications [5–8]. The rotor housing is excited horizontally by means of a swept-sine-wave hydraulic shaker. The seal reaction force components due to relative seal motion are measured by means of load cells and then corrected to account for stator acceleration. Simultaneously, the relative motion between stator and rotor is measured. The seal rotordynamic coefficients are then calculated.

The model seal dimensions are illustrated in Fig. 1. The unconventional seal design has a 13 teeth rotor surface and a honeycomb stator surface. Figure 2 shows both swirl brakes investigated. Except for the vane curving, the two swirl brake designs are identical and can be interchanged. The swirl brake designs have 145 vanes with a pitch 3.12 mm at their base radius of 74.2 mm. Each vane is 2.1 mm high and the tip clearance is 0.51 mm. The trailing edge of the vanes is 2.5 mm upstream of the first labyrinth seal tooth.

Experimental Results

Test Variables. The test apparatus facilitates control of four independent variables: supply pressure, pressure ratio, rotor speed, and inlet circumferential velocity. The pressure ratio definition

[1]Attending an industrial Ph.D. study in collaboration with Aalborg University, Denmark.

Contributed by the International Gas Turbine Institute and presented at the 45th International Gas Turbine and Aeroengine Congress and Exhibition, Munich, Germany, May 8–11, 2000. Manuscript received by the International Gas Turbine Institute February 2000. Paper No. 2000-GT-399. Review Chair: D. Ballal.

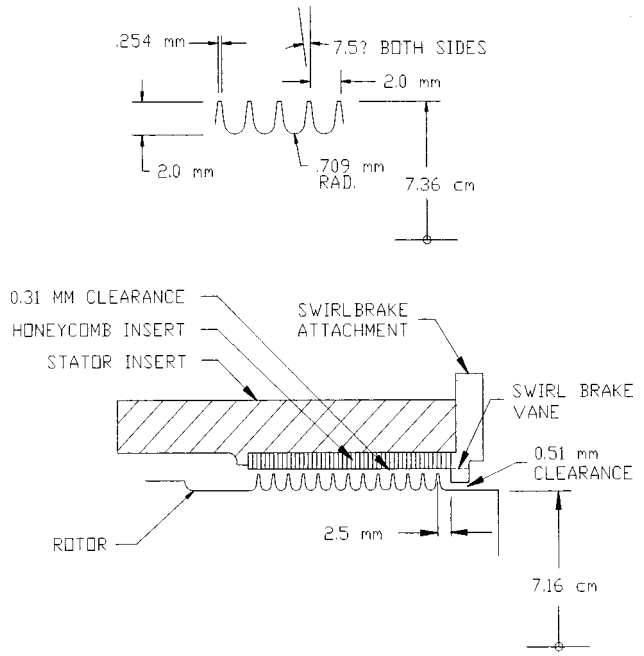

Fig. 1 Model seal dimensions

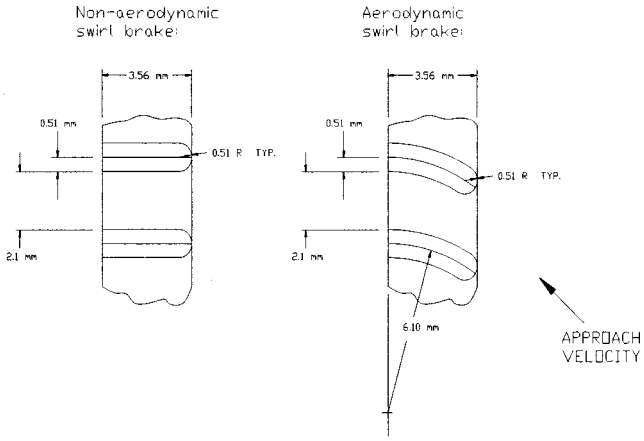

Fig. 2 Both swirl brake designs investigated

employed in this context is the discharge pressure divided by supply pressure. Table 1 lists all independent test variable settings investigated. Only the three middle pressure ratios were investigated for both swirl brake designs. Besides this all combinations of test variable settings were tested.

The variation in inlet circumferential velocity is realized by using different guide vane inserts upstream of the seal and swirl brake. Three different levels are considered. The zero pre-rotation is obtained using straightening vanes.

Table 1 Test points for independent test variables

Supply pressures	Pressure ratios	Rotor speeds	Inlet circumferential velocities
7.9 bar	0.56	5000 rpm	Zero swirl velocity
13.1 bar	0.50	12000 rpm	Intermediate velocity
18.3 bar	0.42	16000 rpm	with rotation
	0.35		High velocity with
	0.30		rotation

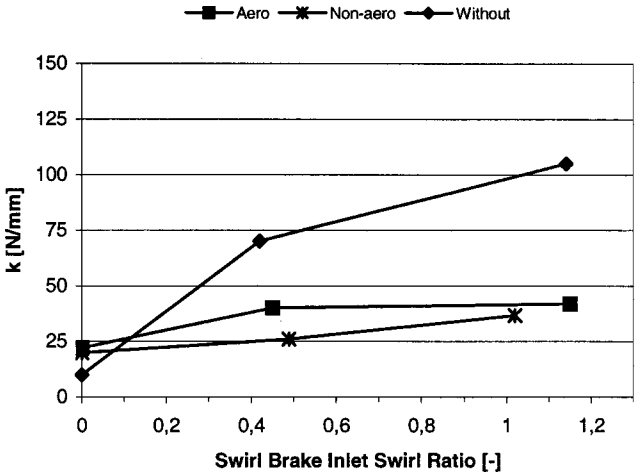

Fig. 3 Cross-coupled stiffness variation with inlet swirl ratio for rotor speed of 5000 rpm

The leakage flow rates were measured for all test points and found to be practically independent of the inclusion of swirl brakes and thus seal inlet swirl. It should be noted in this connection that the pressure drop within the swirl brakes is very small compared to the pressure drop in the seal.

Relative Uncertainty. The method by Holman [9] was used to determine uncertainty in the rotordynamic coefficients. Childs and Ramsey [7] report the uncertainty in force, excitation frequency, and displacement measurements are 0.55 N, 0.0065n Hz, and 0.0013 mm, respectively. The nominal calculated uncertainty in the stiffness coefficients is 6.7 N/mm and 0.014 N s/mm for the damping coefficients. The predicted uncertainties are generally satisfactory in comparison to nominal values for K and k. They are generally unsatisfactory for c and are only satisfactory for C at the highest supply pressure.

Experimental Results. Data for a reservoir pressure of 18.3 bars and a pressure ratio of 0.42 are presented in this paper. Figures 3–5 show the variation of cross-coupled stiffness with inlet swirl ratio for rotor speeds of 5000, 12,000, and 16,000 rpm, respectively. Swirl brake inlet swirl ratio here denotes the swirl ratio of the flow upstream of the swirl brake, if any.

Figures 3–5 clearly demonstrate the strong dependence of the seal cross-coupled stiffness on inlet swirl if no swirl brake is

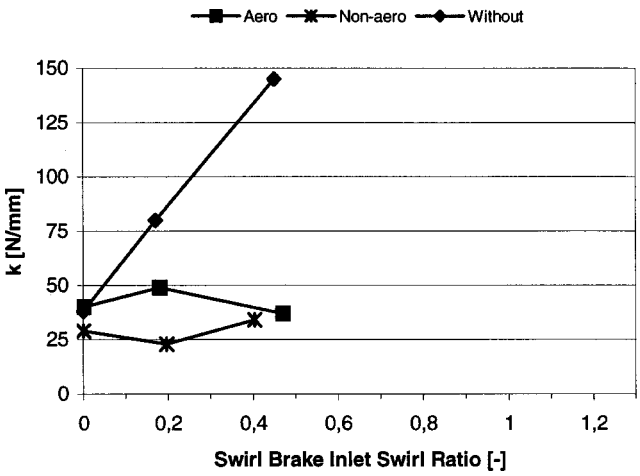

Fig. 4 Cross-coupled stiffness variation with inlet swirl ratio for rotor speed of 12000 rpm

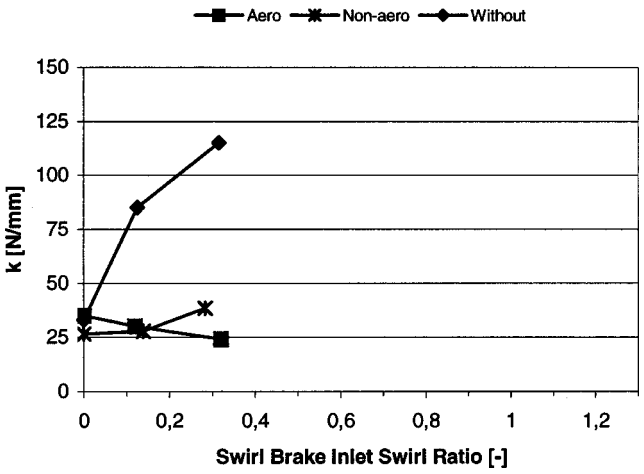

Fig. 5 Cross-coupled stiffness variation with inlet swirl ratio for rotor speed of 16000 rpm

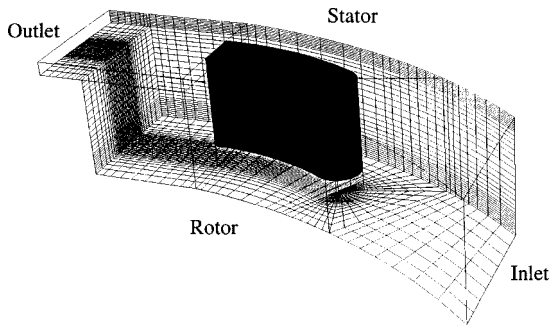

Fig. 6 Computational domain with grid surfaces

applied. For rotordynamic analyses it is normally assumed that the seal cross-coupled stiffness is linearly dependent on the inlet swirl ratio. The data for no swirl brake indicate a similar tendency, although a weakening dependency seems to be present for higher inlet swirl ratios.

Both swirl brakes are seen to be very effective in terms of reducing the cross-coupled stiffness for nonzero preswirl. However, the two swirl brakes differ in their performance characteristic. The nonaerodynamic swirl brake is generally performing slightly better than the aerodynamic swirl brake, especially for intermediate inlet swirl ratios. For high inlet swirl ratios the cross-coupled stiffness for the nonaerodynamic configuration increases with the inlet swirl ratio. The aerodynamic swirl brake shows an opposite trend. The performance of the aerodynamic design improves with increasing inlet swirl ratio.

As stated in the introduction, the finding of equivalent or even improved performance of the nonaerodynamic swirl brake compared to the aerodynamic swirl brake was not expected. To address this issue the current study, encompassing CFD analyses of the swirl brake flows, was undertaken.

Flow Analyses

Flow Solver. The flow simulations presented in this paper have been made with the 3D Navier-Stokes solver CFX-TASCflow from AEA Technology [10]. This is a general purpose CFD code able to deal with complex 3D flows. It includes many features that make it suitable for turbomachinery flows.

The code uses a pressure-based finite volume approach in colocated (*i.e.*, unstaggered) grids. The discretization in the code is strongly conservative. The algebraic multigrid method and the time stepping techniques included in the code to speed up convergence were used in the present study. Likewise, the second order accurate linear profile skew scheme including physical advection correction (PAC) was used. The code facilitates use of body fitted structured multiblock grids.

The code provides three types of k-ε turbulence models. The wall boundary conditions can be handled by using a wall function approach or a two-layer model. The latter facilitates resolving the wall boundary layer with a one-equation model. Nielsen et al. [4] obtained good results using the wall function approach which was also used in the current study together with the standard k-ε turbulence model. Additional information on the flow solver is available in AEA Technology [10].

The swirl brake flow was modeled as being steady and compressible, the latter facilitated through the use of the ideal gas law.

Computational Domain and Boundary Conditions. The circumferential geometrical periodicity of the swirl brakes was used, thereby only modeling one of the 145 vane-to-vane passages. Periodic boundary conditions are imposed on the periodic grid surfaces.

Figure 6 shows the calculation domain for the aerodynamic swirl brake. The vane is given in solid color and the grids on the rotating surface and one of the periodic surfaces are included. The computational domain of the nonaerodynamic swirl brake is straight axial.

The computational domain extends 3.56 mm upstream from the vane leading edge (one chord length of the nonaerodynamic swirl vanes). At the inlet surface of the computational domain, a flow angle equal to the outlet angle of the upstream guide vane is imposed. The total pressure at the inlet is set equal to the reservoir pressure. The leakage flow rate measured is specified. As a consequence the specification of a static pressure at the outlet is not needed.

The outlet section of the computational domain is conveniently modified from the actual geometry. At the top of the first tooth of the labyrinth seal a straight axial section is attached. Compared to a calculation of the entire seal including all twelve labyrinth cavities, a very substantial reduction of calculation time is obtained by this simplification. Additionally, the influence of this simplification on the flow within the swirl brake vanes is negligible.

All wall surfaces in the calculation domain are assumed to be hydraulically smooth. This also encompasses the short section of honeycomb stator surface found between the swirl brake outlet and the first tooth of the labyrinth seal. A grid resolution of the honeycomb cells would require a prohibitive number of calculation cells. A test calculation with increased roughness of the stator between the swirl brake outlet and the seal inlet was carried out, only showing minor influence.

The rotor surface is prescribed a circumferential velocity component, equal to the product of rotor rotational speed and rotor radius. All other surfaces are static.

It is important to note that the tip clearance region between the vane tip and the rotor surface is fully resolved. No simplifying assumptions are made. A correct description of this region is important because of the large tip clearance, amounting to 24 percent of the vane height, and the large vane thickness which is comparable to the vane-to-vane pitch.

The computational domain is partitioned into several blocks, thereby enhancing the grid quality. The grid surfaces included in Fig. 6 illustrate good grid quality, the minimum and maximum grid angles are 38 and 138 degrees, respectively. The grid density is increased in strong gradient regions, such as the tip clearance. When increasing the grid density close to wall surfaces, caution is needed to avoid violation of the y^+ criteria imposed by the use of the wall function approach. y^+ should be in the range 30 to 500 for the first grid point in the flow domain and it is defined by:

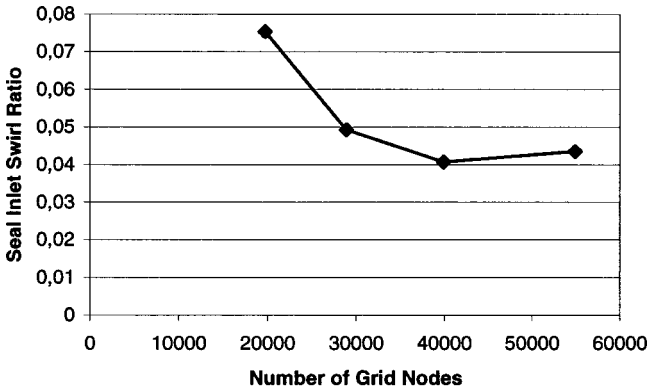

Fig. 7 Dependence of seal inlet swirl ratio on the number of grid nodes

$$y^+ = \frac{\Delta n \sqrt{\rho \tau_w}}{\mu} \tag{3}$$

The total number of grid nodes is 39909. A grid independence investigation was undertaken. An example from this study is shown in Fig. 7.

CFD Results

Seal inlet swirl ratio is a parameter of outmost importance for seal rotordynamic stability. Figures 3–5 clearly illustrate this dependence. As stated previously it is normally assumed for rotordynamic analyses that the seal cross-coupled stiffness is linearly dependent on the seal inlet swirl ratio.

CFD analyses of the swirl brake geometry, as illustrated in Fig. 6 for the aerodynamic swirl brake design, facilitates determination of the seal inlet swirl ratio. Thus the seal inlet swirl ratio is a measure of the swirl brake performance and it is chosen as the parameter of primary interest in this study.

For a reservoir pressure of 18.3 bars and a pressure ratio of 0.42, Figs. 8–10 show the variation of seal inlet swirl ratio with the swirl brake inlet swirl ratio. In this context the seal inlet swirl ratio has been defined as the axial mass flow averaged swirl velocity at the first labyrinth teeth location, nondimensionalized by the rotor surface speed:

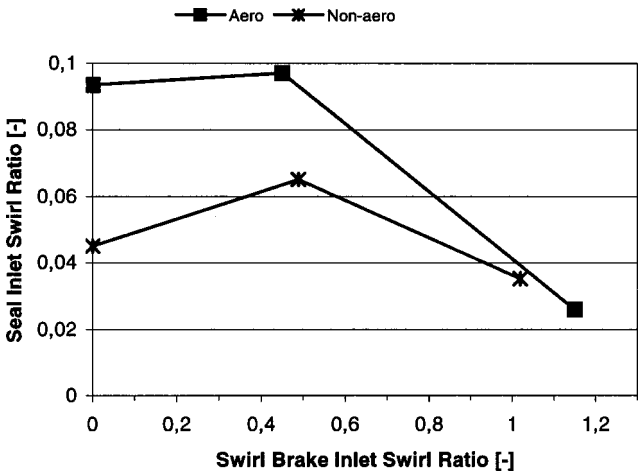

Fig. 8 Seal inlet swirl ratio variation with swirl brake inlet swirl ratio for rotor speed of 5000 rpm

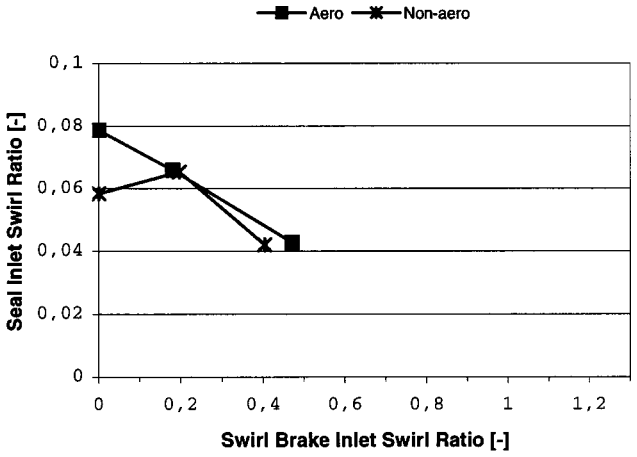

Fig. 9 Seal inlet swirl ratio variation with swirl brake inlet swirl ratio for rotor speed of 12000 rpm

$$\textit{Seal Inlet Swirl Ratio} = \frac{\int_{Rr}^{Rs} \int_{\theta_1}^{\theta_2} u_{\mathrm{ax}} \frac{u_\theta}{Rs\,\omega_{rot}} dA}{\int_{Rr}^{Rs} \int_{\theta_1}^{\theta_2} u_{\mathrm{ax}} dA} \tag{4}$$

θ_2 and θ_1 are the two circumferential endpoints of one periodic domain. Rr and Rs are the rotor and stator radii evaluated at the seal inlet. u_θ and u_{ax} denote fluid circumferential and axial velocity components, respectively.

Both swirl brake designs are very effective and facilitate a seal inlet swirl ratio of less than 0.1 for all flow conditions investigated which for most applications is very satisfactory. Thus the introduction of a swirl brake design similar to the present aerodynamic design at the inlet of the ATD-HPFTP turbine interstage seal proved effective in terms of preventing subsynchronous vibrations.

The aerodynamic swirl brake design shows improving performance with swirl brake inlet swirl ratio, except for low swirl at a rotor speed of 5000 rpm. Comparison of Figs. 5 and 10 reveals similar trends for cross-coupled stiffness and seal inlet swirl ratio at a rotational speed of 16000 rpm. Comparison of trends for Figs. 3 and 8 and Figs. 4 and 9, respectively, does not reveal as good an agreement for lower rotational speeds.

The predicted performance variation for the nonaerodynamic swirl brake is similar for the three rotational speeds: Decreasing performance when increasing swirl brake inlet swirl from no to intermediate swirl. Best performance is predicted for high swirl

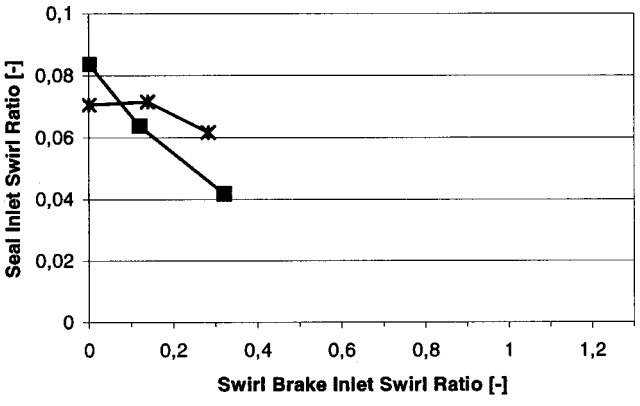

Fig. 10 Seal inlet swirl ratio variation with swirl brake inlet swirl ratio for rotor speed of 16000 rpm

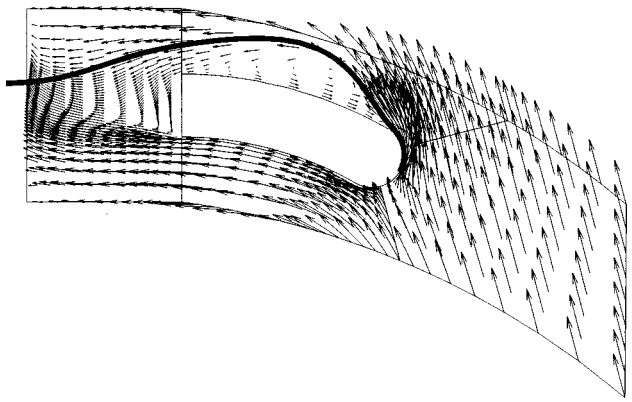

Fig. 11 Vector field for aerodynamic swirl brake design at 42 percent span from stator. Projected streak line originating from vane leading edge included. Seal inlet at left side of plot.

brake inlet swirl. The trends predicted for the nonaerodynamic swirl brake design differ from the measured variation in k.

For rotational speeds of 5000 and 12000 rpm the nonaerodynamic swirl brake design is superior to the aerodynamic design. The aerodynamic swirl brake is only predicted to show better performance for high swirl brake inlet swirl at a rotational speed of 16000 rpm. These findings are in good agreement with Figs. 3–5.

It is important to understand the complex flow field found within the swirl brake vanes as the flow field determines the performance of the swirl brake design. When the swirl brake inlet flow direction differs substantially from the vane angle the flow within the vanes separates. The separation vortices were shown by Nielsen et al. [3] to be very important for the level of seal inlet swirl obtained with a given swirl brake design.

Figure 11 shows the vector field for the aerodynamic swirl brake at 42 percent span from the stator surface. A streak line originating from the vane leading edge at 42 percent span is included. The test variables used for the simulation are: Reservoir pressure: 18.3 bars, Pressure ratio: 0.42, Rotor speed: 12000 rpm, Swirl brake inlet swirl: High. This combination of test variables is equivalent to the high swirl condition of Fig. 9.

Figure 12 is a similar plot for the nonaerodynamic swirl brake. Figures 11 and 12 together with Fig. 13 are included to illustrate the flow structures found in the present swirl brake designs. However, substantial variations in flow field characteristics are found with varying test variables. Figures 11–13 should therefore be considered examples.

Figures 11 and 12 illustrate that excessive separation is present at high inlet swirl for both swirl brake designs. Due to the high incidence angle the flow is unable to remain attached to the vane suction side. The flow detaches and creates a large vortex, referred to as the vane-to-vane vortex by Nielsen et al. [3]. Due to higher

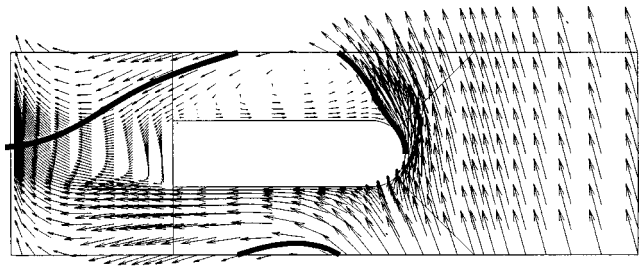

Fig. 12 Vector field for nonaerodynamic swirl brake design at 42 percent span from stator. Projected streak line originating from vane leading edge included. Seal inlet at left side of plot.

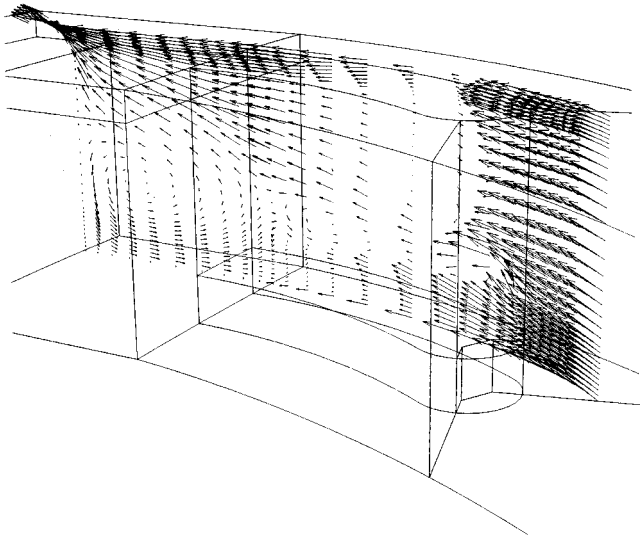

Fig. 13 Rotor to stator vector field for the aerodynamic swirl brake at a pitch of 19 percent from the vane suction side towards the pressure side

incidence the nonaerodynamic swirl brake has the largest vane-to-vane vortex. The strong influence of the vortex is also illustrated by the vane leading edge streak lines. The streak lines are initiated at 42 percent span from the stator at the vane leading edge. The streak lines departure considerably from the 42 percent span plane downstream of the vane leading edge due to strong three-dimensionality of the flow field which causes the projected streak lines not to be aligned with the local flow vectors in the 42 percent span plane.

The vane-to-vane vortex is beneficial in terms of swirl control as it locally generates swirl against the rotor rotation at the vane trailing edge. However, as the seal inlet in the experimental setup is considerably downstream of the vane trailing edge the counter swirl decreases substantially before the flow enters the seal. This is due to the shear stress imposed by the rotor surface and the mixing with the strongly swirling tip clearance flow.

Considering Fig. 9 the nonaerodynamic swirl brake performed slightly better than the aerodynamic swirl brake for the high swirl conditions. However, because of the complexity and the strong three-dimensionality of the flow field, a quantitative conclusion regarding overall seal inlet swirl cannot be drawn from considering Figs. 11 and 12.

The level of three-dimensionality in the swirl brake flow fields can be appreciated by considering Fig. 13. The flow field varies substantially from the rotor to the stator. The significant vane tip clearance, the large flow contraction at the seal inlet and the inherent variation from the rotor to stator are the main reasons. Figure 13 shows that the vane-to-vane vortex extends over the full vane height. Additionally, a vortex structure is identified between the vane trailing edge and the seal inlet. However, due to a substantially different swirl brake and seal configuration, the seal inlet vortex structure in the present study should not be directly compared to the vortex structure identified by Nielsen et al. [3,4].

Conclusion

The experimental and the theoretical data presented in this paper showed that the two interchangeable swirl brake designs considered are effective in terms of reducing the seal inlet swirl and thereby improving rotordynamic stability. The experimental data revealed a very significant decrease in cross-coupled stiffness for both swirl brake designs. The numerical simulations similarly showed low seal inlet swirl levels for all swirl brake inlet swirl levels.

The experimental data showed an equivalent or better performance of the nonaerodynamic swirl brake compared to the aerodynamic swirl brake for most test conditions.

Considering the seal inlet swirl ratio obtained by the two swirl brake designs for identical test conditions confirmed that the nonaerodynamic swirl brake for many cases is superior to the aerodynamic design. Comparing trends between the measured variation of cross-coupled stiffness and predicted variation of seal inlet swirl ratio showed modest agreement.

The vortex flow structures within the vanes responsible for swirl brake performance were identified and compared to previous work. The flow was seen to be strongly three-dimensional.

Although effective, the swirl brake designs considered in this study were not originally optimized for low seal inlet swirl. Guide lines for swirl brake design optimization were presented by Nielsen et al. [3,4].

Acknowledgments

The authors would like to thank Ødegaard & Danneskiold-Samsøe A/S and the Academy of Technical Sciences in Denmark for financial support. The assistance from Professor K. E. Widell, Aalborg University, and Dr. F. Pløger, HV-Turbo A/S, is appreciated.

Nomenclature

C = direct damping
c = cross-coupled damping
K = direct stiffness
k = cross-coupled stiffness
F_X = X direction reaction vector component
F_Y = Y direction reaction vector component
F_r = radial reaction vector component
F_θ = tangential reaction vector component
X = rotor-stator relative displacement component
Y = rotor-stator relative displacement component
ω = whirl orbit precessional frequency
A = whirl orbit amplitude
$u_{\theta 0}$ = fluid swirl velocity upstream of swirl brake
y^+ = nondimensional wall adjacent node distance
τ_w = wall shear stress
ρ = fluid density
Δn = wall adjacent node distance
k = turbulent kinetic energy
μ = dynamic viscosity
u_θ = fluid swirl velocity
u_{ax} = fluid axial velocity
ω_{rot} = rotor rotational speed
Rr = rotor radius at seal inlet
Rs = stator radius at seal inlet
θ_1 = circumferential endpoint of periodic domain
θ_2 = circumferential endpoint of periodic domain

References

[1] Benchert, H., and Wachter, J., 1980, ''Flow Induced Spring Coefficients of Labyrinth Seals for Application in Rotordynamics,'' NASA CP2133, *Proceedings of the workshop: Rotordynamic Instability Problems in High Performance Turbomachinery*, held at Texas A&M University, 12–14 May 1980, pp. 189–212.

[2] Nielsen, K. K., 1997, ''Rotordynamic Impact of Swirl Brakes,'' Diploma Course Report 1997-28, von Karman Institute for Fluid Dynamics, Rhode-St-Genèse, Belgium.

[3] Nielsen, K. K., Van den Braembussche, R. A., and Myllerup, C. M., 1998, ''Optimization of Swirl Brakes by Means of a 3D Navier-Stokes Solver,'' ASME Paper No. 98-GT-328.

[4] Nielsen, K. K., Myllerup, C. M., and Van den Braembussche, R. A., 1999, ''Parametric Study of the Flow in Swirl Brakes by Means of a 3D Navier-Stokes Solver,'' C557/088/99/, Transactions of the Third European Conference on Turbomachinery, pp. 489–498.

[5] Childs, D. W., and Ramsey, C., 1990, ''Seal-Rotordynamic-Coefficient Test Results for a Model SSME ATD-HPFTP Turbine Interstage Seal With and Without a Swirl Brake,'' ASME J. Tribol., **113**, pp. 198–203.

[6] Childs, D. W., Nelson, C. E., Nicks, C., Scharrer, J., Elrod, D., and Hale, K., 1986, ''Theory Versus Experiment for the Rotordynamic Coefficients of Annular Gas Seals: Part 1—Test Facility and Apparatus,'' ASME J. Tribol., **108**, pp. 426–432.

[7] Childs, D. W., Baskharone, E., and Ramsey, C., 1991, ''Test Results for Rotordynamic Coefficients of the SSME HPOTP Turbine Interstage Seal With Two Swirl Brakes,'' ASME J. Tribol., **113**, pp. 577–583.

[8] Griffin, M., Kleynhans, G., Alexander, C., Gansle, A., Pierce, T., and Childs, D. W., 1992, ''Experimental Rotordynamic Coefficient and Static Characteristic Results for a Model SSME ATD-HPFTP Turbine Interstage Seal With and Without a Non-Aerodynamic Swirl Brake,'' TL-SEAL-20-92 #366.

[9] Holman, J. P., 1978, *Experimental Methods for Engineers*, McGraw-Hill, New York, p. 45.

[10] AEA Technology, 1999, CFX-TASCflow User Documentation, Version 2.9.

Mixed Flow Turbines: Inlet and Exit Flow Under Steady and Pulsating Conditions

N. Karamanis

R. F. Martinez-Botas

C. C. Su

Department of Mechanical Engineering,
Imperial College of Science, Technology
and Medicine,
London, England

The performance and detailed flow characteristics of a high pressure ratio mixed flow turbine has been investigated under steady and pulsating flow conditions. The rotor has been designed to have a nominal constant incidence (based on free vortex flow in the volute) and it is for use in an automotive high speed diesel turbocharger. The results indicated a departure from the quasi-steady analysis commonly used in turbocharger turbine design. The pulsations from the engine have been followed through the inlet pipe and around the volute; the pulse has been shown to propagate close to the speed of sound and not according to the bulk flow velocity as stated by some researchers. The flow entering and exiting the blades has been quantified by a laser Doppler velocimetry system. The measurements were performed at a plane 3.0 mm ahead of the rotor leading edge and 9.5 mm behind the rotor trailing edge. The turbine test conditions corresponded to the peak efficiency point at 29,400 and 41,300 rpm. The results were resolved in a blade-to-blade sense to examine in greater detail the nature of the flow at turbocharger representative conditions. A correlation between the combined effects of incidence and exit flow angle with the isentropic efficiency has been shown. The unsteady flow characteristics have been investigated at two flow pulse frequencies, corresponding to internal combustion engine speeds of 1600 and 2400 rpm. Four measurement planes have been investigated: one in the pipe feeding the volute, two in the volute (40 deg and 130 deg downstream of the tongue) and one at the exit of the turbine. The pulse propagation at these planes has been investigated; the effect of the different planes on the evaluation of the unsteady isentropic efficiency is shown to be significant. Overall, the unsteady performance efficiency results indicated a significant departure from the corresponding steady performance, in accordance with the inlet and exit flow measurements.
[DOI: 10.1115/1.1354141]

Introduction

Turbochargers are widely applied in the automotive industry as effective means of achieving engine exhaust energy recovery. A turbocharged engine leads to a better overall system efficiency and a reduction in exhaust emissions compared, at constant power, with a naturally aspirated engine. The approach in the present work is to explore ways of improving the exhaust energy recovery by moving the design turbine operating point to a more favorable location in the corresponding component map. It has been shown previously [1], that a mixed flow turbine can achieve this aim as this design has an additional degree of freedom in the form of the inlet leading edge configuration (see Fig. 1). The corresponding change to the turbine map takes the form of a peak efficiency at an increased pressure ratio [or a decreased velocity ratio, (U/C_{is})], thus leading to a more effective recovery of the energy which is concentrated in the regions of high exhaust manifold pressure. The mixed flow turbine geometry maintains the requirement of radially directed material fibres, necessary to achieve the desired levels of stress in the material.

The turbine inlet flow is normally considered to be uninfluenced by the blade passing, if the measuring location is taken sufficiently upstream this is generally the case. In a small machine such as the one tested here the influence of the rotor passing can be much more significant. This paper will investigate the precise effect of the rotor on the flow and its upstream extent. This is particularly important if computational fluid dynamics (CFD) is to be used for the rotor design. On the other hand, in order to study the flow in the downstream region of the rotor it is essential to take blade-to-blade measurements so as to capture the main flow structures and as a means to validate the CFD results.

Furthermore, the flow conditions encountered by turbocharger turbines are of a highly pulsating nature. It is thus necessary to measure all the turbine performance parameters (inlet pressure, mass flow rate, rotational speed, and torque) as a function of time; similarly if a clear understanding of the flow features is required, it is necessary to measure the flow velocities as a function of time as well. This later requirement imposes difficulties as the data rate to capture the passing of the blade and the pulsation of the main flow is very low.

Given the lack of experimental data on the flow behavior of mixed-flow turbines, the aim of the present study is to observe—using a three-dimensional LDV system—the periodicity of the flow characteristics of the mixed-flow turbine in question:

(a) with the rotor revolution (blade-to-blade resolution).
(b) with the pulsating frequency.

This study will allow an improved understanding of the complicated rotor flow field, and its correlation with inlet incidence, exit swirl and kinetic energy loss.

Literature Survey

Mixed-flow type of rotor design has been investigated both experimentally and theoretically for a number of years; most of these studies have focused on the design, manufacture, and performance evaluation under steady and pulsating flow conditions [1–6], whereas the information of the velocity distribution in this type of rotor is rare. Arcoumanis et al. [7] presented circumferentially averaged exit LDV measurements on mixed-flow turbines;

Contributed by the International Gas Turbine Institute and presented at the 45th International Gas Turbine and Aeroengine Congress and Exhibition, Munich, Germany, May 8–11, 2000. Manuscript received by the International Gas Turbine Institute February 2000. Paper No. 2000-GT-470. Review Chair: D. Ballal.

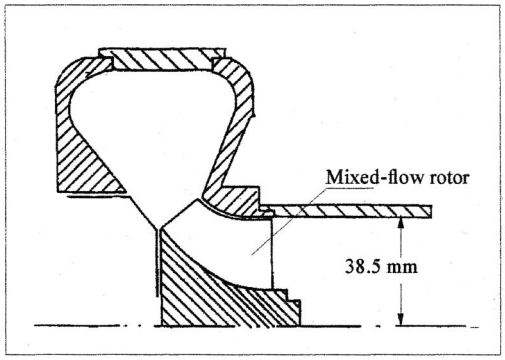

(1a)

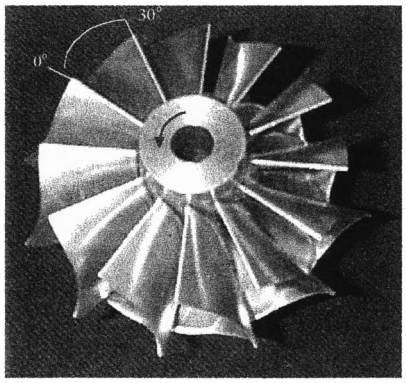

(1b)

Fig. 1 (*a*) Schematic and (*b*) photograph of the mixed flow turbine rotor *B*

this approach does not reveal the detailed nature of the exit flow, hence it is difficult to point out specific areas of design improvement.

There is some experimental work regarding the flow field development under steady flow conditions resolved in a blade-to-blade sense, however limited only to radial inflow turbines. Murugan et al. [17] performed a three-dimensional flow field investigation in the exit region of a radial-inflow turbine using a LDV system at the well off design speed of 1,000 rpm. The flow velocities were measured at three cross-sectional planes of 2.54, 7.62, and 15.24 mm downstream of the rotor exit. The tangential velocities at the three cross sections showed that the degree of swirl was higher near the tip region and the levels of the tangential velocities reduced in the downstream direction. The radial velocities showed that there was a general radially inward movement of the flow due to the loss of centrifugal force as the flow left the rotor. At the furthest downstream cross-section, it was noted that there were some slightly outward radial velocities along the mid-passage near the rotor hub due to the wake behind the hub-end. The axial velocities were higher along the suction surface than those along the pressure surface at the first cross section, then the velocity became mostly uniform at down stream cross sections.

Benisek [8], presented laser measurements based on a L2F system at the inlet and exit of a 110 mm radial inflow turbine rotor. His attempts to investigate the flow inside the blade proved the difficulty of such a task at high speeds of rotation (42,000 rpm), limited results were obtained. Kreuz-Ilhi et al. [9], investigated the inlet flow field of a radial-inflow turbine with a LDA system. The axial and circumferential components of the flow had been measured at two different azimuthal locations, however the most critical radial component is not presented.

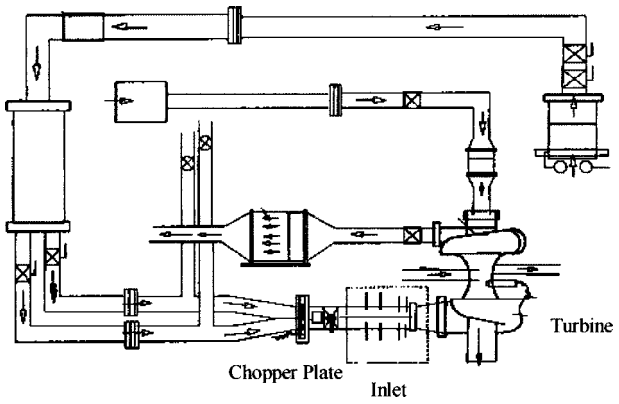

Fig. 2 Turbocharger test rig

The unsteadiness of the flow due to the pulses coming from the engine exhaust has been assessed by a number of authors, however the reported work is limited to radial-in-flow turbines. In particular, Baines and Yeo [10] measured the flow field characteristics at the rotor inlet and exit of a twin-entry vaneless radial-inflow turbine using a L2F velocimeter. The measurements were conducted 3 mm before the blade and at an axial distance of 30 mm downstream of the blade trailing edge. Their results showed the dependence of the flow characteristics to the pulsating frequency, and in particular that even in pulsating conditions the fluid is in dynamic equilibrium, i.e. the turbine is operating in a ''quasi-steady'' fashion.

Experimental System

The turbocharger facility is presented in Fig. 2, it consists of the research turbine, an air supply system, a power absorber in the form of a centrifugal compressor, and a data acquisition system. This system can be also used for a twin-entry turbocharger as it consists of an inner and an outer limb. Upstream of the turbine inlet there is a pulse generator consisting of two counter-rotating chopper plates with specially made cutouts to produce the pulse profile. This type of pulse generator in contrast to a cylindrical-rotor-type [11] has the advantage that the cutouts can be shaped in different forms to provide the required pulse profiles. Both inner and outer limb pulses are in-phase in this investigation.

The turbine rotor tested here is of the mixed-flow type; a schematic diagram illustrating this type of rotor geometry can be seen in Fig. 1. Table 1 gives the test conditions while Table 2 shows the geometric characteristics of the rotor, which has a nominally constant incidence angle (this rotor is name as rotor *B* by Karamanis et al. [12]. The volute feeding the rotor is single-entry, nonsymmetric, and nozzleless.

The steady-state performance was evaluated by means of the energy balance method, where the turbine actual output power is estimated by measuring the power absorbed by the loading device (centrifugal compressor) and the heat discharged to the bearing lubricating oil.

Table 1 Test conditions at 100 percent speed

Parameter	Design	Equivalent
Inlet total temp	923 K	344 K
Mass flow rate	0.414 kg/s	0.678 kg/s
Rotational speed	98,000 rpm	59,828 rpm
Pressure ratio	2.91	2.91
Velocity ratio	0.616	0.616

Table 2 Mixed-flow rotor geometry

Rotor tip mean diameter	83.58 mm
Rotor inlet blade height	18 mm
Number of blades	12
Exducer tip diameter	78.6 mm
Exducer hub diameter	27 mm
Blade angle at exducer root mean	-52^0

The unsteady performance can be carried out by evaluating the following equation:

$$(\eta_{t\text{-}s})_{\text{unsteady}} = \frac{(\dot{W}_T)_{\text{inst}}}{\left(\dot{m}_{\text{inst}} \times \frac{C_{\text{is}}^2}{2}\right)}, \tag{1}$$

where C_{is} is the isentropic expansion velocity at any instant of time during the pulse cycle is defined according to the following equation (variable properties have been taken into account as seen by the integral of the C_p over the temperature range),

$$C_{\text{is}} = \sqrt{2\left[\int_3^1 c_{p,T}\,dT + \frac{1}{2}U_1^2\right]} \tag{2}$$

and

$$(\dot{W}_T)_{\text{inst}} = \tau_{\text{inst}} \times \omega_{\text{inst}}. \tag{3}$$

Hence the following quantities must be measured: (*a*) time-averaged turbine inlet temperature, (*b*) turbine inlet and exit instantaneous pressure, (*c*) instantaneous mass flow rate, (*d*) instantaneous speed, (*e*) time-averaged turbo-shaft speed, (*f*) polar moment of inertia of rotating components, and (*g*) pulse frequency.

The laser Doppler velocimetry system used in this investigation comprised of an Argon-ion laser (Spectra Physics) operating at a wavelength of 0.514 μm and power of up to 1 W, an optical unit dividing the laser beam into two of equal intensity and bringing the two beams to an intersection volume, a photomultiplier, and a frequency counter (TSI model 1995) interfaced to a microcomputer. The intersection volume was approximately 1160 μm in length and 64.0 μm in diameter, with a fringe spacing of 4.65 μm. It should be emphasized that the measured parameters are correlated to the rotor blade rotation, to observe any periodic nature of the flow. Therefore, the results presented here are blade-to-blade quantities with an angular resolution of 1 deg. Similarly, the pulsating flow measurements have been referenced to the pulse generator plate rotation (0 deg–360 deg) with one degree resolution. The digital output of the frequency counter was fed into a microcomputer via a DOSTEK DMA interface card and a sample of 40,000 data was recorded over many turbine rotations and then resolved to nearly 1000 data per degree.

In order to measure the flow at the rotor inlet three optical windows have been installed in the volute, located at 72 deg, 130 deg and 157 deg from the volute tongue [Fig. 3(a)]. The measuring plane is parallel to the blade span at 3 mm before the leading edge. At the rotor exit, a plexiglas tube was added and the radial distribution of the axial and tangential velocities was measured at a distance of 9.5 mm from the blade trailing edge, as shown in Fig. 3(b). Both in the inlet and exit measurement locations, the orientation of the LDV receiving optics was at a near-forward scattering angle of 60 deg to the optical axis.

A possible source of uncertainty in LDV measurements is the size of the seeding droplets and their ability to follow the flow fluctuations. Silicone oil droplets were generated by an air-blast atomizer and added to the flow in the divergent section upstream of the volute. The atomizer has been shown to produce droplets with Sauter mean diameter d_p of up to 2 μm which corresponds to a maximum effective Stokes number of 0.1. This implies that the droplets, on average, follow the flow fluctuations although occasional larger droplets may occur, giving rise to an uncertainty due to their size which can be considered to be negligible. Other uncertainties such as those due to velocity gradients were minimized by aligning the smaller measuring volume across the velocity gradient and collecting the light off the optical axis. The statistical uncertainty was estimated to be less than 1.8 percent and 4.4 percent with a 95 percent confidence level, in the mean and rms value of the velocity, respectively. The maximum counting ambiguity of the TSI counter having a clock frequency of 1000 MHz was 1.1 percent of the Doppler frequency shift. The whole optical system was mounted on a three-dimensional traversing mechanism with a positional uncertainty of 0.025 mm.

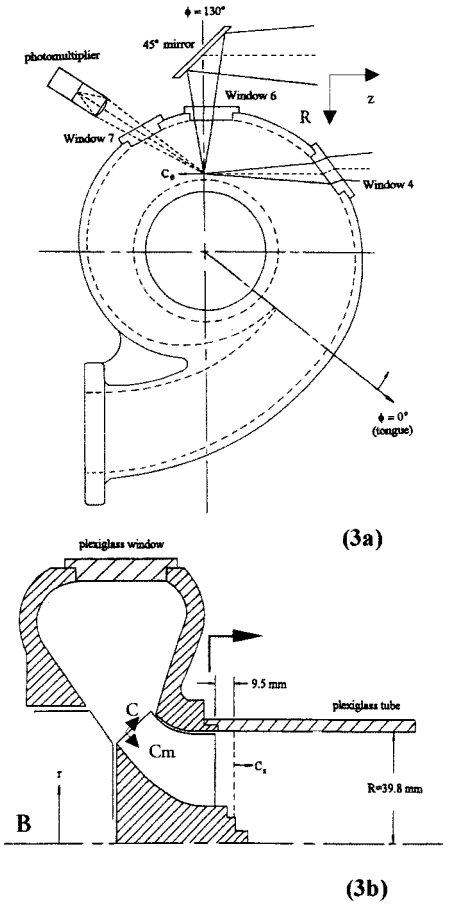

Fig. 3 Velocity measurements (LDV) setup: (*a*) inlet and (*b*) exit arrangement

Results and Discussion

Steady Flow Performance. The steady-state performance of the mixed flow rotor was investigated at five different rotational speeds, covering a range from 50 to 90 percent equivalent design speeds. The total-to-static efficiency and the swallowing capacity are shown in Fig. 4.

The total-to-static efficiency increases with rotational speed up to the 70 percent condition, after which it remains nearly constant. The total-to-static peak efficiency value (0.72 at 90 percent speed) occurs at a velocity ratio (U/C_{is}) around 0.62; this is in contrast to the well known result, for radial in-flow turbines, where the peak efficiency occurs at a 0.7 velocity ratio [13]. As explained previously, this change in velocity ratio at peak efficiency has implications on the level of exhaust gas energy recovery than can be

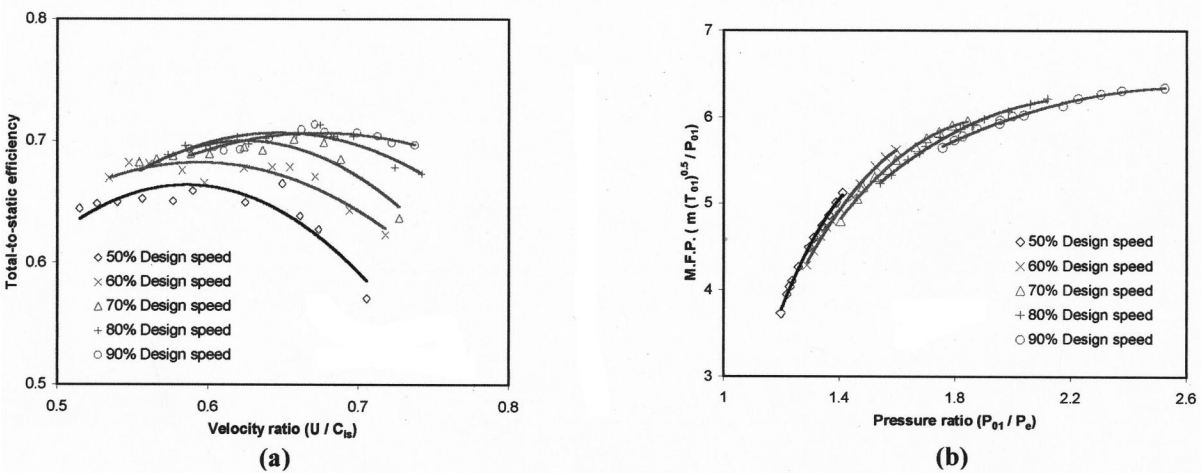

Fig. 4 Steady performance (*a*) total-static efficiency vs. (*b*) swallowing capacity of mixed flow rotor *B*

attained; this need is made all the more important given recent advances in automotive diesel engines as explained below.

The high air-fuel ratios required for reduced fuel consumption and exhaust emissions, together with the use of an intercooler, result in lower exhaust temperatures and hence, lower energy and higher density of the engine exhaust stream. Sufficient power, however, must be extracted by the turbine from this low-energy exhaust to drive the compressor at high boost pressures. This can only be achieved by a smaller turbine running at high rotational speeds: the turbine speed is limited, however, by stresses and hence a large expansion ratio (or high C_{is}) is required, which corresponds to low velocity ratios. Furthermore, the size and volume of the exhaust manifold are limited by the need for high power-to-weight ratios. This implies that the exhaust pulses are largely undamped at the turbine inlet and the flow conditions through the rotor are highly pulsating, with much of the kinetic energy in the exhaust available at higher manifold pressures. Since the rotor tip speed during the pulse cycle remains almost constant, it is desirable to achieve maximum turbine efficiency at low velocity ratios (U/C_{is}). These important requirements are better met by the currently proposed mixed-flow turbine, rather than a typical radial-inflow rotor.

Steady Flow Velocity Measurements. In order to understand the fluid dynamic processes in mixed-flow turbines, the detailed inlet and exit flow velocity field was measured with a LDV system under steady flow conditions, as explained in the Experimental Setup section.

Turbine Inlet Flow. Velocity measurements at the inlet of the rotor were conducted in a plane 3 mm upstream from to the rotor leading edge, this plane is located 130 deg from the volute tongue. In order to get the relevant quantities to the rotor at inlet, the axial and radial measured components were transformed to the meridional (normal to the blade leading edge, C_m) and a spanwise (parallel to the blade leading edge, C_s) component. The inlet velocity triangle was thus obtained. Similarly, the axial and tangential velocity components at a plane 9.5 mm from the trailing edge were measured. The test conditions corresponded to the peak efficiency point at 50 and 70 percent equivalent design speeds, corresponding to 29,400 and 41,300 rpm (see Table 3). Given that there was no appreciable efficiency increase beyond the 70 percent design speed point, it was decided to limit the LDV data to this maximum speed. Further investigation beyond this speed should be carried out in the future so as to identify the reasons for the constancy of the efficiency beyond 70 percent speed.

The flow velocity magnitude entering the rotor is significantly affected by the presence of the rotor, a blade to blade correlation can be seen in Fig. 5. Note that in this figure the yellow dots correspond to the location of the blade leading edge, the meridional component is normal to this plane, while the vertical axis is the span distance. In this figure there is also visible a departure from free-vortex flow that is commonly assumed in volute design. Indeed in a free vortex flow, the mixed flow rotor would have zero span-wise component of velocity, a constant meridional component of velocity and a tangential component of velocity decreasing from hub to shroud but constant in the blade-to-blade direction. It is clear that none of these trends are followed in the present flow.

The span component of velocity is small at the lower speed of rotation (50 percent) but it shows a significant peak behind the blade for the higher rotational speed. The meridional component of velocity shows a depression in the mid passage close to the shroud and a very significant acceleration towards the hub; the former effect can be explained by the blockage that the rotor imposes on the flow while the latter effect can only be explained by the poor guidance of the flow by the hub side of the volute wall (Fig. 3). The tangential component of velocity generally decreases from hub to shroud but a peak can be seen close to the blade. It is clear that as the rotor imposes a blockage to the meridional flow, the tangential component increases locally in magnitude to maintain the same flow rate. This effect can also be seen in the increase in flow angle just where the blade is as shown in Fig. 6.

The actual incidence angle ''seen'' by the rotor is plotted in Fig. 6. The incidence at the lower rotor speed is mostly positive reaching values as high as 70 deg at the blade location; a very detrimental aerodynamic performance can be inferred, this agrees with the performance results. The incidence variation for the higher rotational speed is far from uniform. The angle of incidence tends to the negative as the speed of rotation increases; in a radial rotor one would expect a negative angle of incidence at peak efficiency design speed. It is important to note that the volute

Table 3 LDV test conditions

Parameter	50% speed	70% speed
Total–to–static efficiency	0.665	0.701
Velocity ratio	0.59	0.63
Pressure ratio	1.295	1.588
Mass flow parameter (Kg/s (K)$^{0.5}$/bar)	4.493	5.482
Temperature (K)	344	344

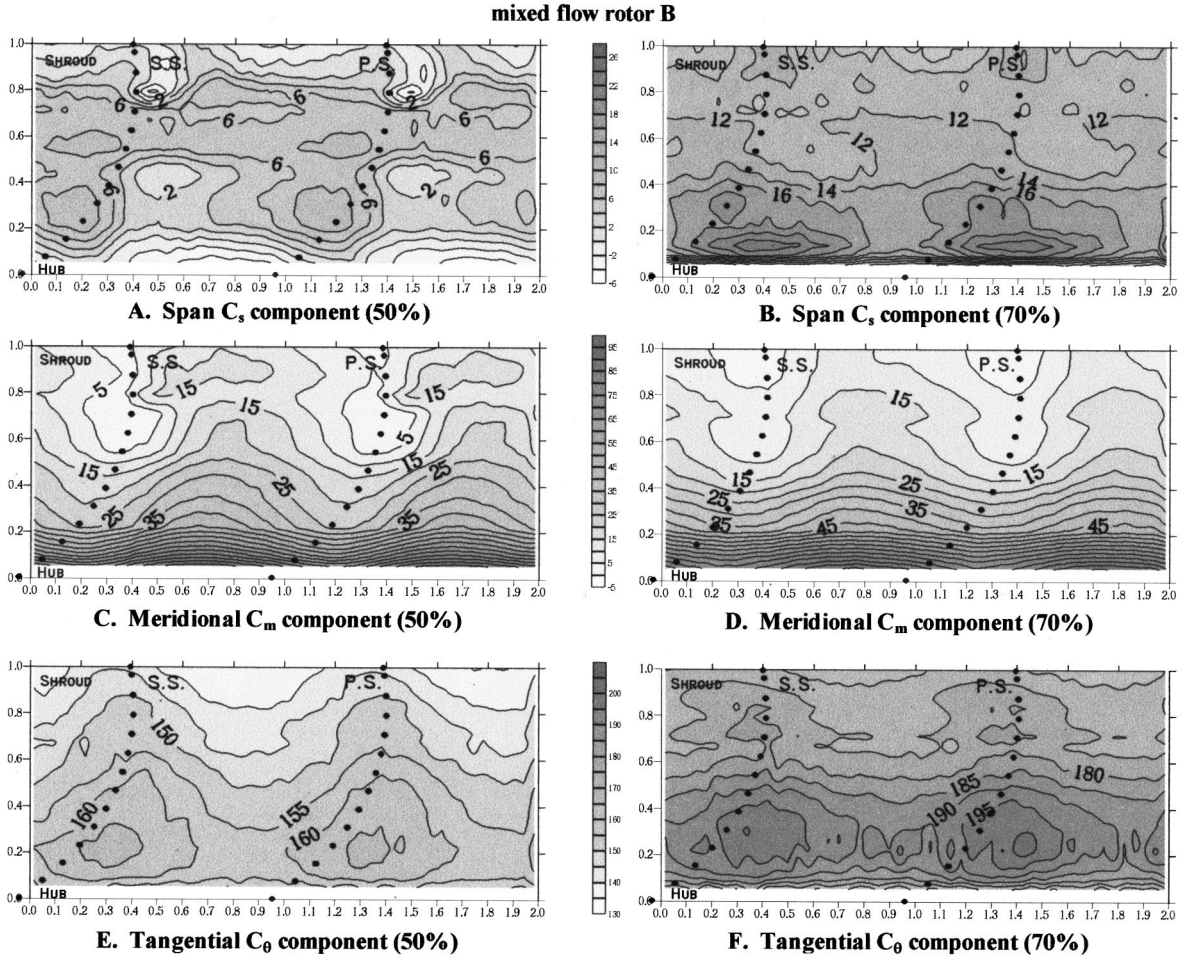

Fig. 5 Mean velocity (m/s) contours at the inlet of rotor *B*, 3 mm before blade leading edge (130 deg), for 50 vs. 70 percent design speeds

used in this present investigation was modified from a commercial volute meant for a radial turbine. The flow is not well guided from mid-span to shroud; note the sharp corner close to tip of the blade at inlet (Fig. 3).

Turbine Exit Flow. The exit axial and tangential mean and rms velocities at the measuring plane of $x = 9.5$ mm from the blade trailing edge were measured, these are resolved in a blade-to-blade sense in order to explore in detail the exit flow field characteristics which covers one rotor blade passage. The axial and tangential mean velocities are presented as contour plots, as shown in Figs. 7 and 8, respectively. These figures show that the flow pattern of each velocity component is similar at both rotational speeds, and that the velocity gradient becomes larger at higher rotational speed. It is also found that the axial and tangential velocities vary with radius and angular position which indicates a nonuniform flow behavior in the rotor exit region.

The axial mean velocities (Fig. 7) are higher along the suction surface than those along the pressure surface. It is also evident that the minimum axial velocity is in the region close to the exit duct wall (shroud), this is due to the tip clearance flow penetrating into the blade passage along the pressure surface and mixing with the main flow. The interaction of the tip clearance flow and the main flow explains the high axial rms velocity in this region Arcoumanis et al. [3]. There is also a high axial velocity region near the center of the exit cross section extending to the hub region, suggesting that the flow in this region is less affected by the tip clearance flow. The axial velocity results of the mixed-flow turbine rotor is in broad agreement with the results obtained by Murugan et al. [14] at the exit of a radial-inflow turbine rotor.

Figure 8 displays the contours of the tangential mean velocity. It exhibits that the tangential velocities of the fluid leaving the rotor exit are higher along the pressure surface as compared to those near the suction surface. This can be attributed to the pressure field acting between the pressure and suction surfaces, which drives the flow to come into equilibrium behind the blade trailing edge. In addition, the tangential velocity is generally higher in the upper region of the exit cross section, showing two peaks, one of which is near the pressure surface in the mid-span region due to the pressure field acting as mentioned above, and the other is near the exit duct wall which may be due to the tip clearance flow. It is interesting to note that the regions with high tangential velocities correspond to the regions with lower axial velocities. The higher tangential velocities indicate that the exit kinetic energy losses are higher along the pressure surface and in the upper region of the exit cross section. The turbine specific power output extracted from the fluid is calculated by knowing the velocity triangles at the rotor inlet and exit which leads to the fact that the high tangential velocity at the rotor exit significantly reduces the specific power output due to the increased exit kinetic energy losses, as explained by the Euler turbomachinery equation.

The exit absolute flow angles are obtained from the exit velocity triangle and the resulted contours are shown in Fig. 9. The absolute flow angle is an indication of the level of swirl in the flow and the positive values imply a swirling flow in the direction

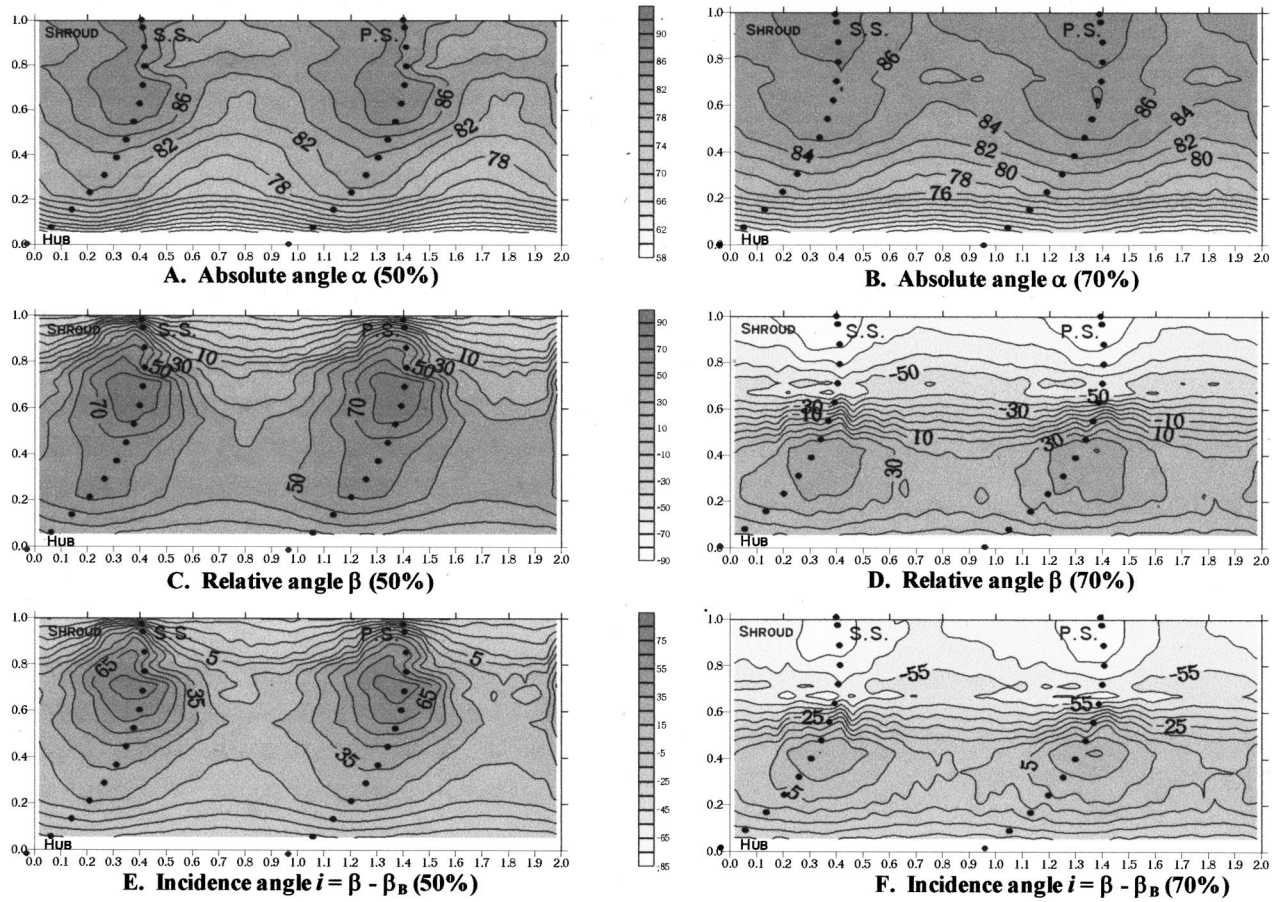

Fig. 6 Flow angle (degrees) contours at the inlet of rotor *B*, 3 mm before the blade leading edge (130 deg), for 50 vs. 70 percent design speed

of rotor rotation. It is found that the exit flow has a region of smaller absolute flow angle (lower level of swirl) which is in the lower part of the exit cross section above the rotor hub. The flow also exhibits a higher level of swirl in the regions near the mid-span pressure surface and exit duct wall. This feature is consistent with the pattern of the tangential mean velocities. It is also noted that the absolute flow angle is reduced with increasing rotational speed which implies that the level of swirl is smaller at higher rotational speed. This characteristic is in agreement with the steady flow performance test results that the turbine total-to-static efficiency is higher at higher rotational speeds.

The deviation angle is an indication of the level of flow guidance at the rotor exit. The closer the deviation angle is to zero, the smaller the departure of flow from the blade is. Large positive

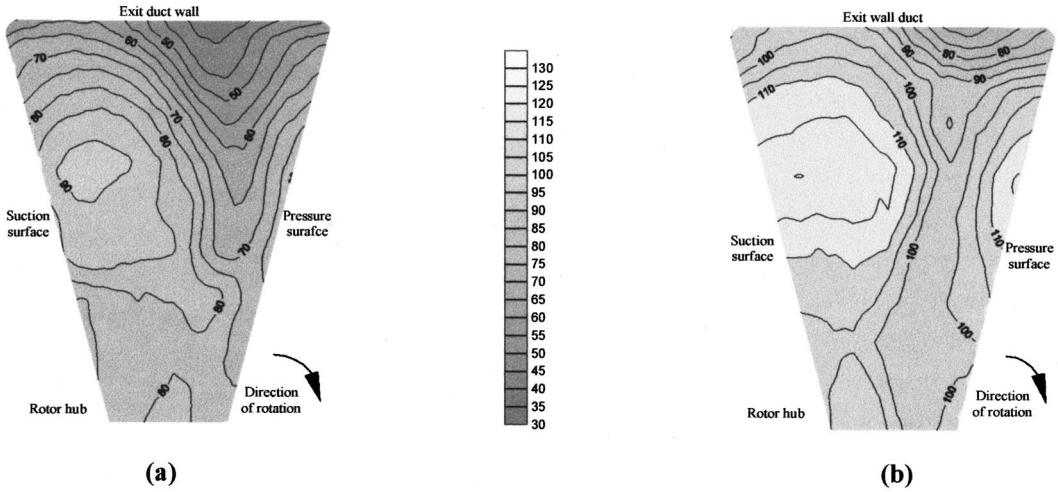

Fig. 7 Axial component of velocity C_m at peak $\eta_{t\text{-}s}$ for rotor *B* at (*a*) 50 percent and (*b*) 70 percent design speed, 9.5 mm after the blade's trailing edge

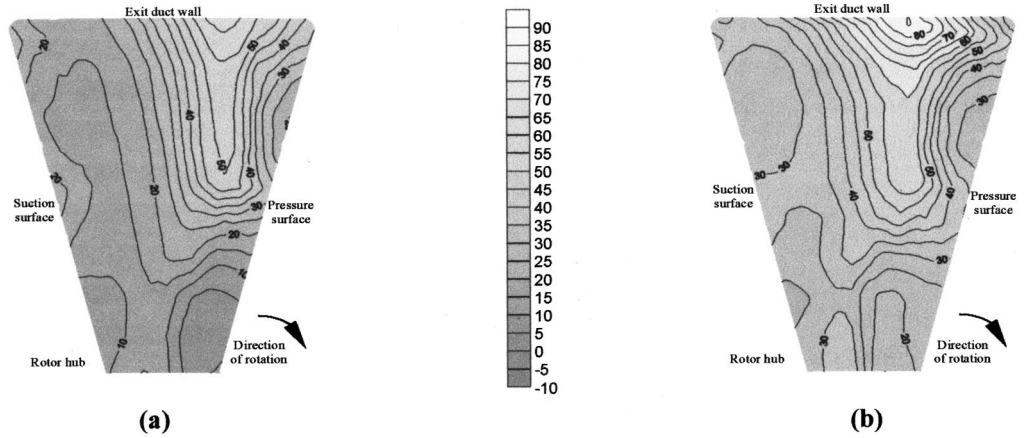

Fig. 8 Tangential component of velocity C_m at peak $\eta_{t\text{-}s}$ for rotor *B* at (*a*) 50 percent and (*b*) 70 percent design speed, 9.5 mm after the blade's trailing edge

values of the deviation angle imply an underturned flow which may have been caused by a flow separation on the suction surface. Negative values of the deviation angle imply an overturned flow which may have been caused by a flow separation on the pressure surface. The contours of the deviation angle are shown in Fig. 10. It is noted that the flow is overturning at rotor exit for most regions. A more uniform distribution of deviation angle is developed as the rotational speed increases from the 50 percent to the 70 percent equivalent design speed. This demonstrates that the flow is better guided at higher rotational speeds. The actual value of the deviation angle are very high and lead to the conclusion that the rotor is not guiding the flow properly in the exducer region; a longer rotor would have reduced the levels of deviation to a more acceptable value despite the accompanying increase in frictional loss due to the increased wetted flow area.

Unsteady Flow Performance. In order to improve the understanding of the behavior of mixed-flow turbines under real engine operating conditions which are of a pulsating nature rather than steady flow conditions, the unsteady flow performance tests were performed. The unsteady flow performance tests were carried out at the peak efficiency point of 50 and 70 percent equivalent design speed that corresponds to 29400 rpm and 41300 rpm, respectively. In addition, two air pulse frequencies of 40 Hz and 60 Hz were used to simulate the pressure pulse of the engine exhaust gas. The pulse frequencies are produced by the pulse generator and are equivalent to the engine speeds of 1600 rpm and 2400 rpm, respectively, based on a four-stroke, six-cylinder diesel engine with a single-entry turbine.

As mentioned in the Experimental System section, the evaluation of the unsteady flow performance, the instantaneous turbine inlet static pressure, mass flow rate, and rotational speed were measured during the pulse cycle. These are shown in Figs. 11–13. The mass flow parameter is plotted against the pressure ratio in Fig. 14 for one particular test condition. As can be seen in this figure, the instantaneous mass flow parameter circles around the steady parameter; the reason for this behavior is that the turbine/volute acts as a finite volume, so as the pulse generator is opened it takes a certain amount of time to fill up the volume while when the plate is closing it does not have enough time to empty.

It is worth noting that the instantaneous turbine inlet temperature was not recorded during the unsteady flow performance tests, a shielded *E*-type thermocouple was used to give the time-averaged temperature instead. Hence, in order to obtain all instantaneous physical quantities at the turbine inlet, an assumption must be made regarding the variation of the turbine inlet temperature. Two approaches are possible and have been used by a number of researchers: One is to assume that the turbine inlet total temperature remains constant during the pulse cycle, as a result, the time-averaged temperature was used to calculate the turbine unsteady flow performance and this approach was followed by

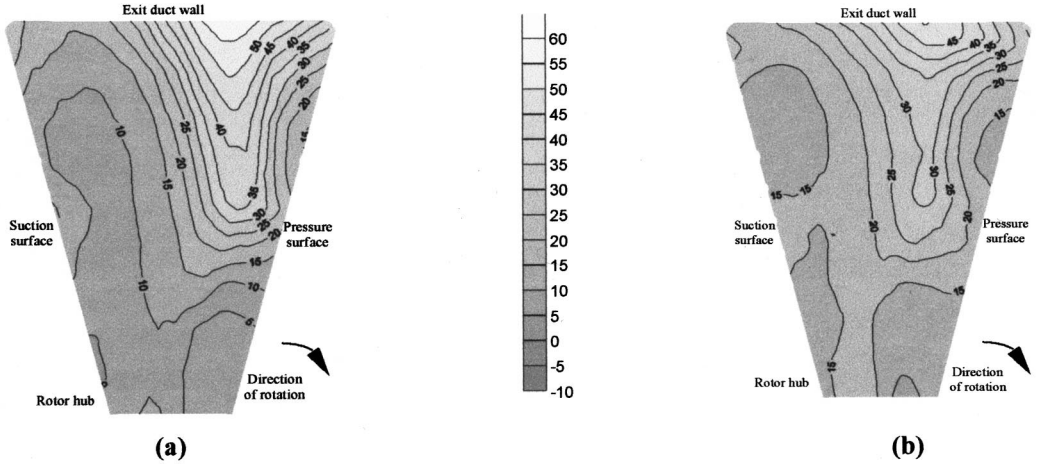

Fig. 9 Absolute flow angle (degrees) at peak $\eta_{t\text{-}s}$ for rotor *B* at (*a*) 50 percent and (*b*) 70 percent design speed, 9.5 mm after the blade's trailing edge

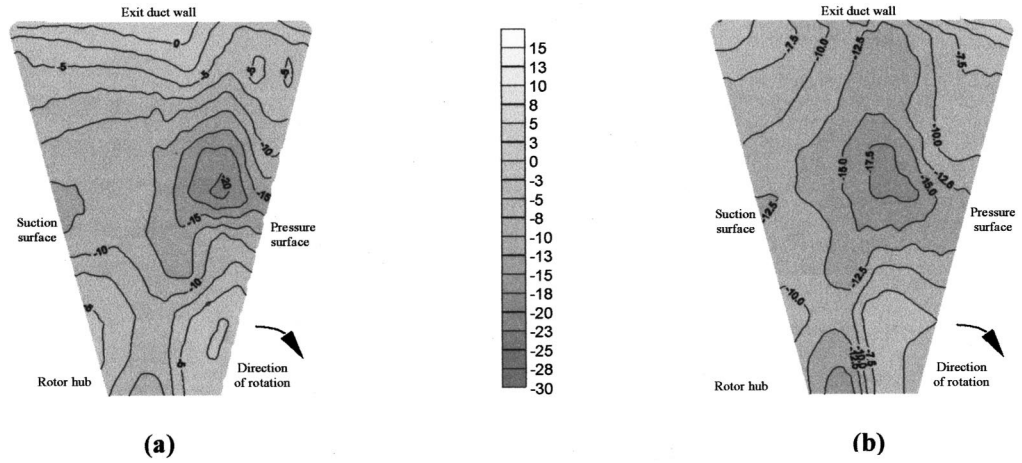

Fig. 10 Deviation angle (degrees) at peak $\eta_{t\text{-}s}$ for rotor *B* at (*a*) 50 percent and (*b*) 70 percent design speed, 9.5 mm after the blade's trailing edge

Kosuge et al. [15], Dale and Watson [13], Dale et al. [16], Winterbone et al. [11], Baines et al. [17], and Arcoumanis et al. [1]. The other approach is that if an accurate time-averaged temperature is known, then an approximate value for the instantaneous temperature can be calculated by assuming an isentropic relationship between temperature and pressure, that is

$$\frac{T_{\text{inst}}}{T} = \left(\frac{P_{\text{inst}}}{P}\right)^{\gamma-1/\gamma} \tag{4}$$

This approach was used by Mollenhauer [18], Benson [19], Capobianco et al. [20], and Chen et al. [4]. Mollenhauer [18] pointed out that the instantaneous exhaust gas energy obtained

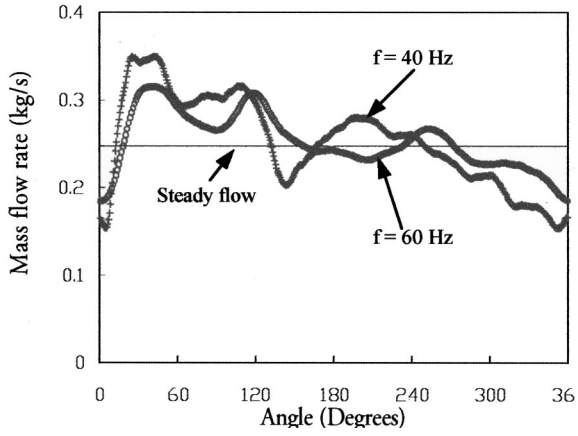

Fig. 11 Instantaneous mass flow rate at the peak $\eta_{t\text{-}s}$ of 70 percent design speed under pulsating conditions

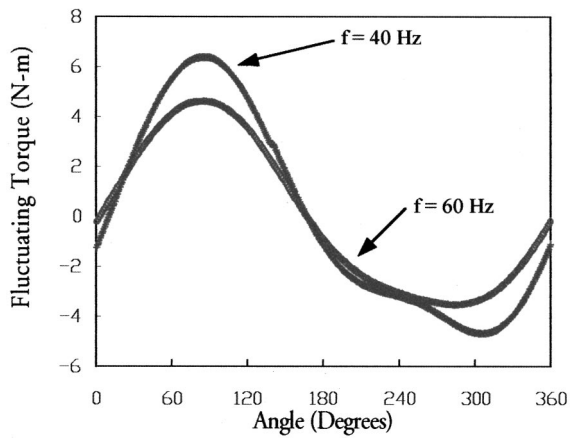

Fig. 13 Instantaneous torque at the peak $\eta_{t\text{-}s}$ of 70 percent design speed under pulsating conditions

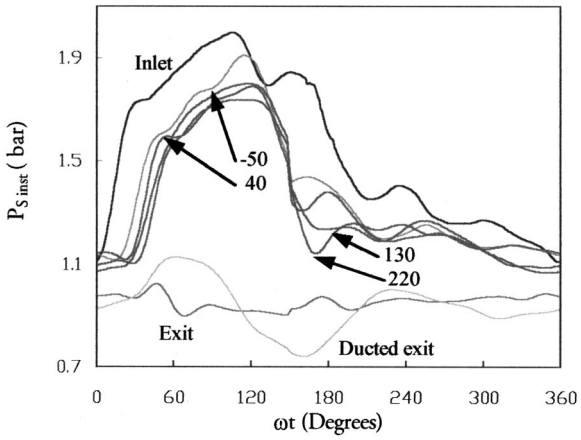

Fig. 12 Instantaneous static pressure at the peak $\eta_{t\text{-}s}$ of 70 percent design speed under pulsating conditions

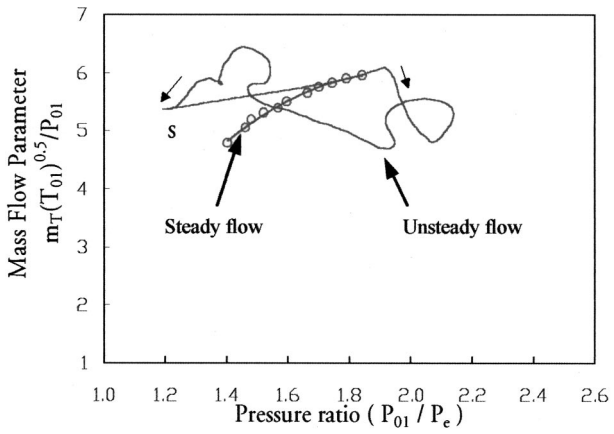

Fig. 14 Instantaneous swallowing capacity at the peak $\eta_{t\text{-}s}$ of 70 percent design speed at 40 Hz pulsating flow

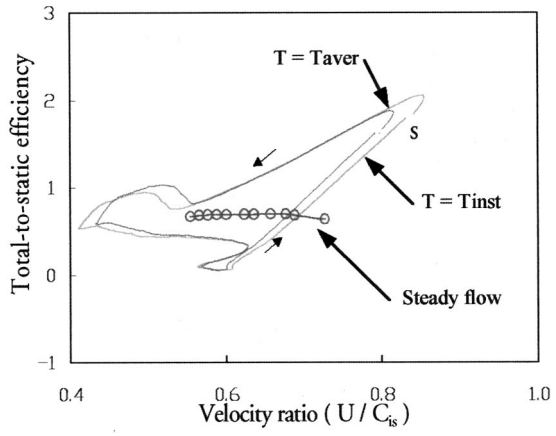

Fig. 15 Instantaneous total-to-static efficiency vs. velocity ratio of rotor *B* for 70 percent peak $\eta_{t\text{-}s}$ at pulsating flow 60 Hz; comparison of the treatment of the unsteady inlet temperature

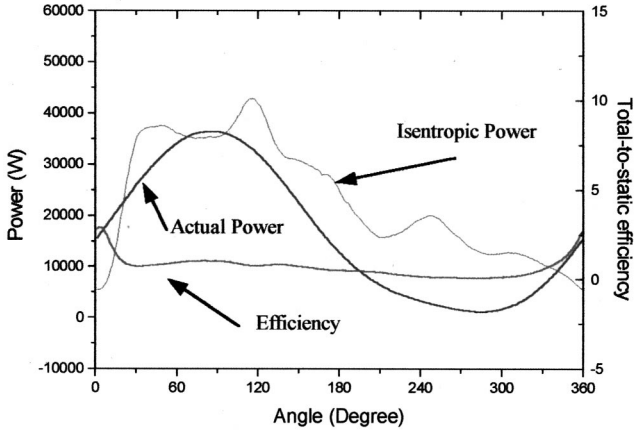

Fig. 16 Instantaneous actual vs. isentropic work at the peak $\eta_{t\text{-}s}$ of 70 percent design speed at 40 Hz pulsating flow

from the calculated instantaneous temperature [Eq. (4)] has small deviation from the true one obtained from the measured instantaneous temperature for which the mean error was only 1.3 percent in his tests. In the present paper both approaches are compared in Fig. 15 for one operating flow condition.

Another important point that should be noted in the unsteady flow performance calculation is that all the physical quantities used in Eq. (1) must be measured simultaneously at the same location in order to obtain a representative performance map. However, in the present test facility the inlet static pressure and mass flow rate, which are used to calculate the instantaneous turbine isentropic power, are measured at the turbine inlet, while the instantaneous rotational speed, from which the instantaneous torque and turbine actual power are deduced, is measured at the impeller shaft. Under steady flow conditions this is of no consequence, but when the unsteady flow performance is measured, it is important to recognize that at any instant in time the torque generated by the rotor is a function of the state of the fluid within the rotor passages rather than that of the fluid measured at the turbine inlet, which corresponds to an earlier time. It is, therefore, necessary to shift the torque signal forward in time in order to achieve the appropriate equivalent flow conditions.

In order to fulfill the correction of the time lag mentioned above, two approaches have been adopted by researchers. One is based on the time calculated using the bulk flow travel time, which was first proposed by Winterbone et al. [21] followed by Hajilouy-Benisi and Baines [22] and Baines et al. [17]. The other approach is to take the sonic speed travel time as suggested by Dale and Watson [13] which assumes that the traveling time corresponds to the propagation time of a pressure wave from the measuring plane to the turbine rotor passage. The present authors measured the static pressure development from the inlet measuring plane to the rotor inlet. The instantaneous pressure is measured at various locations: 250 mm upstream the volute inlet (where the measuring plane is located, indicated ''inlet'' in Fig. 2), −50 deg upstream of the tongue, 40 deg, 130 deg, and 220 deg downstream the tongue plane, see Fig. 12. From this figure the only appropriate time to shift the signal is given by the sonic travel time. This is in accordance with Arcoumanis et al. [1]. This discussion of the travel time is of the utter most importance in order not to present unrealistic unsteady efficiencies.

Figure 16 shows the performance parameters for one testing condition (70 percent and 40 Hz) as a sample of the data. Three quantities are plotted: isentropic power, actual power and isentropic efficiency, all these as a function of pulse generator angle (this angle can be viewed as equivalent to time). It is worth noting that the values of the unsteady efficiency in some regions are in excess of unity. The isentropic power follows the trace of inlet static pressure since it is calculated from the instantaneous inlet pressure and mass flow rate; the turbine actual power follows the trace of the fluctuating torque. These signals have been shifted according to the sonic travel time as explained previously. Before the pulse generator goes into its open position, the inlet pressure and mass flow rate reach their lowest values and result in a minimum isentropic power. At the same time, the actual power in this initial stage of the pulse is higher than the isentropic power due to the effect of the rotational inertia of the turbine compressor assembly which causes the rotor to act as a flywheel. As a result, the isentropic efficiency becomes greater than unity during this short period. A similar behavior has been observed by Winterbone et al. [11,21] and Baines et al. [17] in their studies of the radial-inflow turbines. Had the bulk travel time been used to shift the signal, the isentropic efficiency would have been greater than one for most of the pulsating period.

The traces of the instantaneous total-to-static efficiency are shown in Fig. 17 as a function of velocity ratio for all pulsating flow conditions, they are compared with the corresponding steady flow efficiency curves. Included for comparison are two exhaust conditions, one referred to as atmospheric expansion ($P_{ex}=P_{atm}$, that is, the exhaust surrounding pressure) and the second referred to as instantaneous pressure expansion ($P_{ex}=P_{atm}$, that is, the actual exit static pressure as a function of time measured at the wall 9.5 mm from the trailing edge). It is evident that the unsteady efficiency curves deviate from the steady flow values. The range of the velocity ratio and the total-to-static efficiency is reduced as the pulse frequency is increased. Hence, the enclosed area by the loop is reduced with the increasing pulse frequency. The effect of the two possible exhaust conditions is very significant; previous authors on radial turbines have not considered the fluctuation of exhaust pressure and have therefore arrived at unrealistic expansion ratios of the turbine. The use of the instantaneous pressure leads to a reduction of the regions of efficiency greater than unity as compared to a constant atmospheric pressure expansion.

In order to arrive at a single value of efficiency independent of the time shift, the results have been cycle averaged over a complete pulse cycle. The definition of this average efficiency is given by the following equation:

$$\eta_{t-s,\mathrm{av}}=\frac{\int_0^{\phi}\dot{W}_{\mathrm{inst}}\,dt}{\int_0^{\phi}\dot{W}_{\mathrm{isent}}\,dt}. \tag{5}$$

This equation considers the energy transfer in a complete pulse, but without indicating the regions of the pulse where the conversion of available work into actual work has been effective or

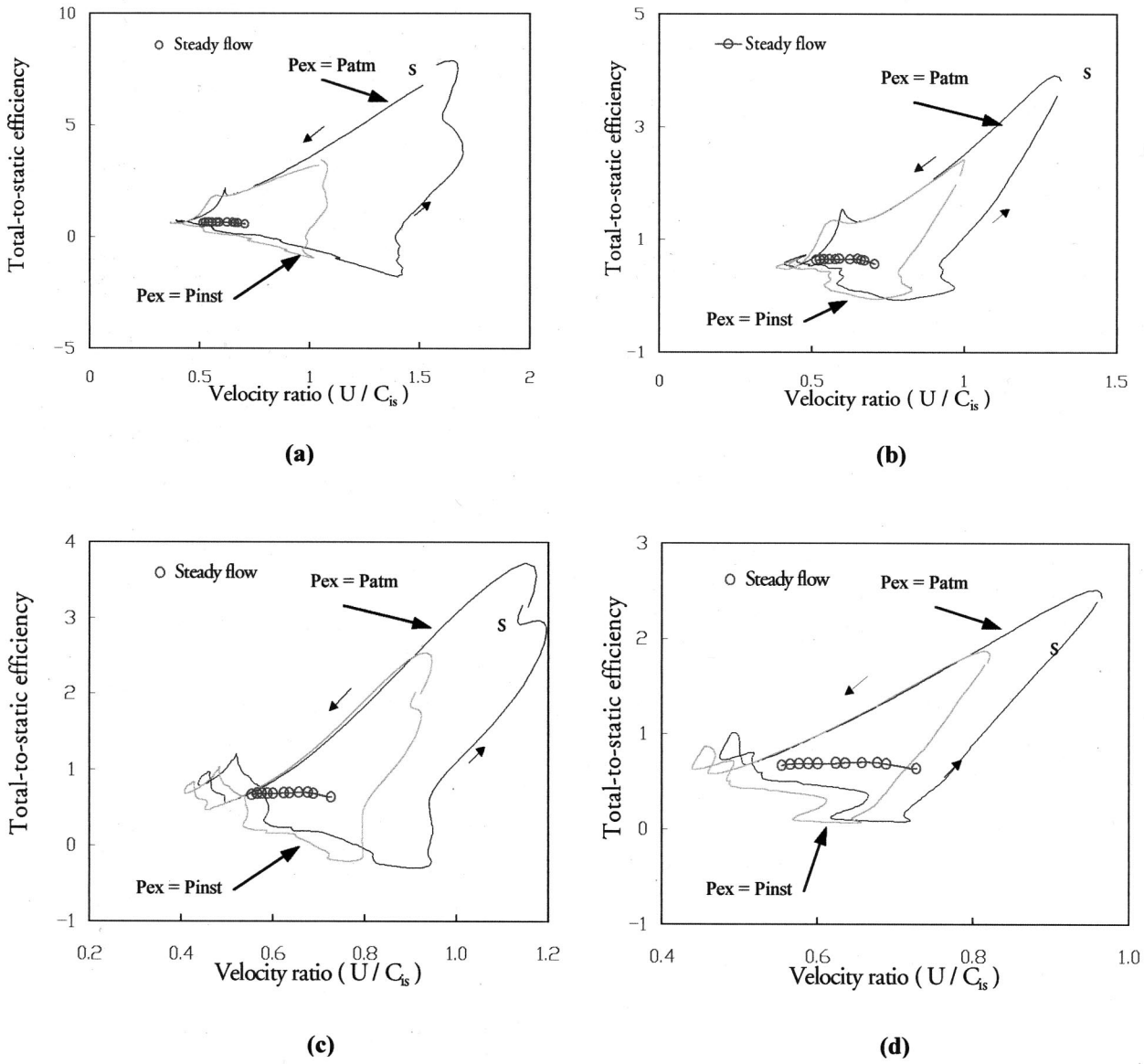

Fig. 17 Instantaneous total-to-static efficiency vs. velocity ratio of rotor *B* at atmospheric expansion and $T_{01}=T_{inst}$ under pulsating conditions at peak $\eta_{t\text{-}s}$ of 50 percent design speed (*a*) 40 Hz, (*b*) 60 Hz, and 70 percent (*c*) 40 Hz and (*d*) 60 Hz

ineffective; the answer to this question lies in the proper analysis of the unsteady efficiency as explained above. The integrated results are given in Table 4. It is clear that the cycle-averaged efficiency is always lower than the corresponding steady-state peak efficiency, this is to be expected given that during the pulse the turbine will be covering a large range of flow conditions and hence regions of low efficiency are expected. It is worth noting the lower speed condition results in a much lower cycle efficiency, the flow is thus highly disturbed by the pulse, this fact will be explained in the following section where large changes in incidence are shown.

Pulsating Flow Velocity Measurements. The velocity measurements presented previously refer to steady flow conditions, that is, the pulsating plate was not in operation. The investigation of the unsteadiness of the flow field with pulsating frequency was also conducted, but limited to one location: mid-span at the inlet of the rotor at 3 mm before the blade, at a cross-sectional plane 130 deg of azimuth downstream of the tongue. The frequency was set at 40 Hz at 50 percent equivalent design speed. Similar to the steady case the three velocity components were resolved to the meridional, spanwise and tangential directions.

In a similar way, the axial and tangential velocity components at the exit of the rotor were obtained at the root mean square radius ($r/R=0.75$) at an axial plane of $x=9.5$ mm from the trail-

Table 4 Unsteady cycle average efficiency

Condition	Steady	Unsteady
50% and 40 Hz	0.69	0.44
50% and 60 Hz	0.69	0.57
70% and 40 Hz	0.74	0.66
70% and 60 Hz	0.74	0.70

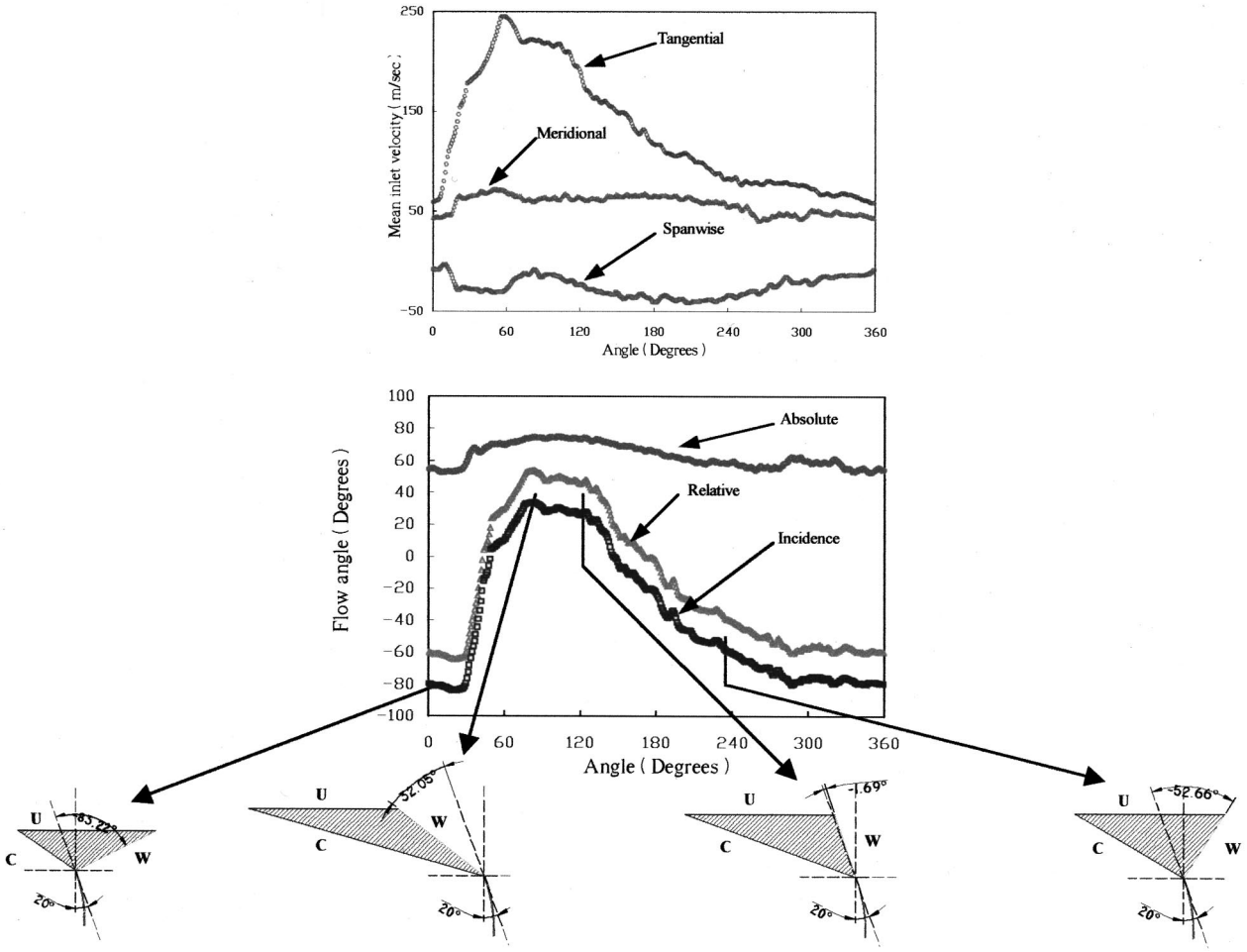

Fig. 18 Pulsating flow characteristics at the inlet of the turbine rotor

ing edge of the blades. In both inlet and exit measurements the results are resolved with the pulse generator rotation. All values are shifted back to the chopper plate location based on the sonic velocity assumption as described earlier.

The magnitude of the absolute velocity vector at inlet changes significantly during the pulse period, see Fig. 18. It peaks at the fully open pulse generator position, and it reaches its lowest value at the close position where it remains until the plate is again opened (note the close correlation with the pressure traces presented in Fig. 12). Given that the blade velocity U is relatively constant during the pulse period, the relative velocity vector follows a similar pattern. In consequence the turbine should be optimized to extract maximum energy at the peak condition. Figure 18 also shows the variation of the flow angles and incidence. As it can be seen there are wild variations of incidence during the pulse, going from -80 deg to $+40$ deg.

At the rotor exit similar results can be observed. The axial velocity C_m, exhibits a similar pattern as described earlier with a peak at the fully open position of the chopper plate when the mass flow rate is maximum. As expected the deviation of the flow at this point reaches its minimum value meaning that the flow is well guided by the blades.

The velocity triangles at the fully close, and fully open positions, are presented in Fig. 19. It is very clear that the flow deviates from its optimum design point at the former whilst it meets the designer's specifications at the latter condition. These results will help to understand the unsteady fluid dynamic processes under pulsating flow conditions.

Conclusions

This paper has brought together steady and pulsating performance with detailed flow measurements in a turbocharger turbine. The insights on the fluid dynamic nature of such an adverse flow will help the designer to choose the correct operating point for the steady calculations carried out during the evaluation of a new turbocharger turbine. The data presented here can also serve as a validating test case to CFD.

LDV blade-to-blade measurements reveal a complex flow pattern at both the inlet and the exit of the rotor. The flow entering the rotor is significantly higher at the mid-passage between the pressure and suction surfaces of the blade, in comparison to that on the blade tip. This is a clear indication that the blade tip is acting as a blockage to the flow, therefore, even though the measuring plane is at 3 mm before the blade tip the flow is significantly affected by the passing blade.

At the rotor exit wherever the axial component is relatively high the tangential component remains low. The tangential velocities exiting close to the pressure surface are higher compared to those near the suction surface, which should be attributed to the pressure field acting between the pressure and suction surfaces, which drives the flow to come into equilibrium behind the trailing edge of the blade. A region of minimum axial velocity is a clear evidence of the presence of the tip clearance flow.

The flow at both the inlet and exit of the rotor deviated from its optimum design requirements under pulsating conditions. The optimum point is reached at the maximum mass-flow rate hence at

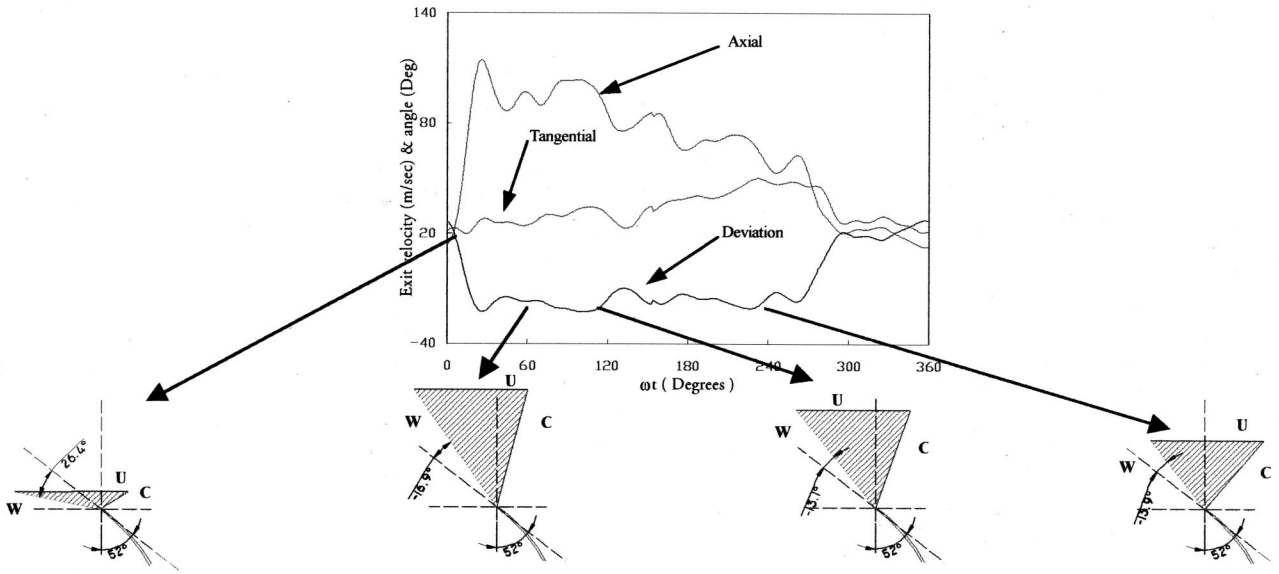

Fig. 19 Pulsating flow characteristics at the exit of the turbine rotor

the pressure peak. This is equivalent to a fully open exhaust valve position. The flow fails however to meet those requirements when the pressure is minimum equivalent to a fully close exhaust valve condition.

The instantaneous total-to-static efficiency trace under pulsating conditions deviated significantly from the steady results. This should be attributed to the previous remark and the dependence of the flow to the pulse frequency.

Acknowledgments

The authors would like to thank the Engineering and Physical Sciences Research Council for providing Grant GR/K77426 and Holset Engineering Company Limited for technical support and useful discussions.

Nomenclature

C_{is} = isentropic expansion velocity
C_p = specific heat capacity at constant pressure
C = absolute flow velocity
d_s = sauter mean diameter
f = pulse frequency
i = inlet flow incidence
M.P. = mass flow parameter $=\dot{m}(T_{01})^{0.5}/P_{01}$
I = polar moment of inertia
$\dot{m}$ = mass flow rate
N = rotational speed
P = pressure
t = time
T = temperature
U = blade tip speed; air velocity
W = relative flow velocity
$\dot{W}$ = power
α = absolute flow angle
β = relative angle
δ = exit flow deviation
γ = ratio of specific heat capacities
η = efficiency
ϕ = air pulse period
ω = rotational speed
τ = torque

Subscripts

0 = total or stagnation value
1 = turbine inlet
2 = rotor inlet
3 = turbine exit
act = actual quantity
atm = atmospheric
aver = cycle-averaged
B = blade
ex = turbine exit
isent = isentropic
inst = instantaneous
m = meridional component (perpendicular to rotor leading edge)
s = static; span velocity (parallel to rotor leading edge)
T = turbine
t-s = total-to-static
θ = tangential component

References

[1] Arcoumanis, C., Hakeem, I., Khezzar, L., Martinez-Botas, R. F., and Baines, N. C., 1995, ''Performance of a Mixed Flow Turbocharger Turbine Under Pulsating Flow Conditions,'' ASME Paper No. 95-GT-210.
[2] Abidat, M., Chen, H., Baines, N. C., and Firth, M. R., 1992, ''Design of a Highly Loaded Mixed Flow Turbine,'' Proc. Inst. Mech. Eng., J. Power Energy, **206**, pp. 95–107.
[3] Baines, N. C., Wallace, F. J., and Whitfield, A., 1978, ''Computer Aided Design of Mixed Flow Turbines for Turbocharger,'' ASME Paper No. 78-GT-191.
[4] Chen, H., Hakeem, I., and Martinez-Botas, R. F., 1996, ''Modelling of a Turbocharger Turbine Under Pulsating Inlet Conditions,'' Proc. Inst. Mech. Eng., Part A: J. Power Energy, **210**, pp. 397–408.
[5] Chou, C., and Gibbs, C. A., 1989, ''The Design and Testing of a Mixed-Flow Turbine for Turbochargers,'' SAE Paper No. 890644.
[6] Wallace, F. J., and Pasha, S. G. A., 1972, ''Design, Construction and Testing of a Mixed-Flow Turbine,'' *The 2nd International JSME Symposium, Fluid Machinery and Fluids*, Tokyo.
[7] Arcoumanis, C., Martinez-Botas, R. F., Nouri, J. M., and Su, C. C., 1997, ''Performance and Exit Flow Characteristics of Mixed Flow Turbines,'' Int. J. Rotating Mach., **3**, No. 4, pp. 277–293.
[8] Benisek, E., 1998, ''Experimental and Analytical Investigation of the Flow Field of a Turbocharger Turbine,'' IMechE, Paper No. C554/027/98.
[9] Kreuz-Ilhi, T., Filsinger, D., Schulz, A., and Wittig, S., 1999, ''Numerical and Experimental Study on the Unsteady Flow Field and Vibration of Radial Inflow Turbines,'' ASME Paper No. 99-GT-341.
[10] Baines, N. C., and Yeo, J. H., 1991, ''Flow in a Radial Turbine Under Equal and Partial Admission,'' IMechE Paper No. C423/002.

[11] Winterbone, D. E., Nikpour, B., and Alexander, G. L., 1990, ''Measurement of the Performance of a Radial Inflow Turbine in Conditional Steady and Unsteady Flow,'' IMechE Paper No. C405/015.
[12] Karamanis, N., Martinez-Botas, R. F., and Su, C. C., 1999, ''Detailed Flow Measurements at the Exit of a Mixed Flow Turbine,'' ASME Paper No. 99-GT-342.
[13] Dale, A., and Watson, N., 1986, ''Vaneless Radial Turbocharger Turbine Performance,'' IMechE Paper C110/86.
[14] Murugan, D. M., Tabakoff, W., and Hamed, A., 1996, ''Three-Dimensional Flow Field Measurements Using LDV in the Exit Region of a Radial Inflow Turbine,'' Exp. Fluids, **20**.
[15] Kosuge, H., Yamanaka, N., Ariga, I., and Watanabe, I., 1976, ''Performance of Radial Flow Turbines Under Pulsating Flow Conditions,'' ASME J. Eng. Power, **98** pp. 53–59.
[16] Dale, A., Watson, N., and Cole, A. C., 1988, ''The Development of a Turbocharger Turbine Test Facility,'' IMechE, Seminar on Experimental Methods in Engine Research and Development.
[17] Baines, N. C., Hajilouy-Benisi, A., and Yeo, J. H., 1994, ''The Pulse Flow Performance and Modelling of Radial Inflow Turbines,'' IMechE Paper No. C405/017.
[18] Mollenhauer, K., 1967, ''Measurement of Instantaneous Gas Temperatures for Determination of the Exhaust Gas Energy of a Supercharged Diesel Engine,'' SAE Paper No. 67929.
[19] Benson, R. S., 1974, ''Non-Steady Flow in a Turbocharger Nozzleless Radial Gas Turbine,'' SAE Paper No. 740739.
[20] Capobianco, M., Garambarotta, A., and Cipolla, G., 1989, ''Influence of the Pulsating Flow Operation on the Turbine Characteristics of a Small Internal Combustion Engine Turbocharger,'' IMechE Paper No. C372/019.
[21] Winterbone, D. E., Nikpour, B., and Frost, H., 1991, ''A Contribution to the Understanding of Turbocharger Turbine Performance in Pulsating Flow,'' IMechE Paper No. C433/011.
[22] Hajilouy-Benisi, A., and Baines, N. C., 1992, ''Small High Speed Radial Inflow Turbine,'' Int. Conf. Eng. Appl. Mech..

Some Aspects of Modeling Compressor Behavior in Gas Turbine Performance Calculations

Claus Riegler
Michael Bauer
Joachim Kurzke

Engine Performance Department,
MTU München GmbH,
DaimlerChrysler Aerospace,
80995 München, Germany

Performance calculation procedures for gas turbine engines are usually based on the performance characteristics of the engine components, and especially the turbo components are of major interest. In this paper methods of modelling compressors in gas turbine performance calculations are discussed. The basic methodologies based on Mach number similarity are summarized briefly including some second order effects. Under extreme engine partload conditions, as for example subidle or windmilling, the operating points in the compressor map are located in a region which is usually not covered by rig tests. In addition the parameters usually used in compressor maps are no longer appropriate. For these operating conditions a method is presented to extrapolate compressor maps towards very low spool speed down to the locked rotor. Instead of the efficiency more appropriate parameters as for example specific work or specific torque are suggested. A compressor map prepared with the proposed methods is presented and discussed. As another relevant topic the performance modelling of fans for low bypass ratio turbofans is covered. Due to the flow splitter downstream of such a fan the core and bypass stream may be throttled independently during engine operation and bypass ratio becomes a third independent parameter in the map. Because testing a fan on the rig for various bypass ratios is a very costly task, a simplified method has been developed which accounts for the effects of bypass ratio. [DOI: 10.1115/1.1368123]

1 Introduction

In most performance calculation programs the off-design behavior of compressors is modelled with the help of so-called maps or characteristics, which present the correlations between the main compressor performance parameters. The maps have to cover physical aspects, as for example to describe all the relevant physical phenomena with a sufficient accuracy, as well as numerical requirements, as for example to allow unambiguously interpolating the data. The physical aspects may be split into first order effects being dominant for the off-design behavior of compressors, and second order effects which are relevant as well but usually have a minor effect on the overall performance of the gas turbine being simulated. Usually the maps are based on compressor rig tests or on calculations with sophisticated computer codes.

The basic modelling methodology is generally well-known and used widespread. It is therefore described very briefly and the reader is referred to the literature for details. However, there are some issues which still cause some uncertainties in performance calculations. Two of them,

- the compressor behavior in extreme partload and
- the behavior of a fan with a splitter downstream,

will be covered in this paper to some detail.

2 Basic Methodology

2.1 Compressors With Fixed Geometry

2.1.1 Map Representation Including First Order Effects. The parameters used in compressor maps are based on Mach number similarity to reach general validity of the map for various inlet conditions in terms of pressure, temperature and working fluid composition (gas constant), see for example [1] for a detailed description. Hence to describe unambiguously an operating point in a compressor map—and also to set unambiguously an operating point on a test rig—two independent parameters are necessary to define the rotational Mach number of the blades and the flow Mach number.

The conventional map resulting from this is usually a plot of total pressure ratio versus corrected flow (representing flow Mach number) for lines of constant corrected speed (representing rotational Mach number of the blades). In addition usually lines of constant efficiency are plotted in the same diagram. Storing a compressor map that way incorporates some numerical problems for the use in performance calculation programs because, for example, with given corrected flow and corrected speed pressure ratio is ambiguous in the choking regime of the speed line where the latter is vertical.

To overcome these problems an artificial map parameter is introduced which often is called β [1]. One reasonable way to define the β lines appropriately for interpolation is described in detail in [2]. Despite the fact that β is artificial and has no physical meaning the lines of constant β are usually very close to a constant position of the exit throttle valve, which is used in compressor rig tests to define the flow Mach number, or to a constant exit corrected flow. Hence exit corrected flow could also be used instead of β as a map parameter.

Another approach to store compressor maps for performance calculations is to use the well-known turbomachinery parameters, the flow coefficient φ and the work coefficient ψ. These parameters describe angles in a velocity triangle diagram and therefore have a distinct physical meaning. When using maps with φ, ψ-parameters the exit flow coefficient could be a substitute with a physical meaning for the artificial parameter β.

Besides the information concerning the compressor performance the stability limit in terms of the surge line has to be provided to the performance calculation program. This is usually done by tabulating surge line pressure ratio versus corrected flow, but depending on the stability margin definition used tabulation of surge pressure ratio and surge mass flow versus corrected speed might be more appropriate.

Contributed by the International Gas Turbine Institute and presented at the 45th International Gas Turbine and Aeroengine Congress and Exhibition, Munich, Germany, May 8–11 2000. Manuscript received by the International Gas Turbine Institute February 2000. Paper No. 2000-GT-574. Review Chair: D. Ballal.

2.1.2 Second Order Effects. The maps based on Mach number similarity do not include second order effects. Even though they are not dominant for the compressor behavior, they are relevant for high accuracy gas turbine performance calculations. Second order effects are

- Reynolds numbers lower than the critical values due to small compressor size or low inlet pressure at high altitude,
- changing properties of the working fluid, especially of the isentropic exponent due to varying inlet temperature or gaseous humidity,
- variable inlet flow angles produced by an upstream compressor or by the inlet of a fighter aircraft,
- radial and circumferential inlet pressure distortion produced by an upstream inlet and
- temperature distortion produced by an upstream compressor with pressure distortion at its inlet.

For a detailed description of these issues the reader is referred to the literature [1,3–5].

2.2 Compressors with Variable Geometry. The map representations described so far are valid for fixed geometry compressors. Due to varying operating conditions and for the sake of compressor performance improvement geometry variations take place during compressor operation, which affect the compressor map, too.

2.2.1 Geometry Variations Due to Operating Conditions. Compressor geometry variations due to varying centrifugal forces, as for example blade untwist or tip clearance changes, depend on mechanical spool speed, whereas the Mach number similarity results in corrected speed as a map parameter. Therefore for the same corrected speed, i.e. the same speed line in the map, a different inlet temperature gives a different mechanical speed and hence different blade twist and tip clearances. These effects are usually not dominant but have to be taken into account when high accuracy is required. This is often done by correction terms dependent on inlet temperature which are applied to the map parameters [5].

2.2.2 Variable Geometry to Improve Compressor Behavior. Above all in multistage axial compressors variable geometry is vital for stable operation of the compressor in partload conditions. Especially variable (inlet) guide vanes and variable interstage bleed are used. Both of them affect the performance behavior and hence the map as well as the surge line. They are usually optimized during engine development, among other things by means of a performance model taking these effects into account. Usually the effects of variable geometry are complex, not linear and different in various operating ranges. Therefore the best approach is to use additional independent map parameters to account for variable geometry.

2.3 Map Data. To fill the maps with data either compressor rig tests are performed or sophisticated calculation procedures are used.

Rig tests are appropriate to generate an excellent data base of compressor performance over a wide operating range. On the other hand rig tests are expensive and often the rig hardware is not identical with the in-engine hardware resulting in some second order rig-to-engine effects which have to be taken into account when using a rig map in performance calculations [5]. Usually with regard to low costs rig tests are performed to evaluate the dominant effects on compressor behavior in a rather small operating range only. Afterwards mean values are calculated from the measured data, the results are smoothed and extrapolated [2].

In contrary the whole range of map calculation procedures from midsection methods to todays sophisticated CFD codes are able to produce compressor performance data comparably cheap, with no scatter, absolutely reproducible and over a wide parameter range. But usually the calculations are not accurate enough and hence calibration of the data by comparison with rig data is necessary. Especially for studying second order effects map calculation programs are very useful. They may be even more accurate than rig tests when the effect looked for is in the same order of magnitude as the scatter in the measured data.

3 Compressor Maps for Low Spool Speed

The methods described in chapter 2 to model the compressor behavior are applicable in the normal operating range of a turbo engine. But for simulating extreme partload conditions such as steady-state windmilling, windmilling relights or even starting some parameters used are not appropriate, as for example any kind of efficiency definition. In addition compressor rig data are available typically down to 50 or 60 percent corrected speed only, hence not allowing the simulation of windmilling or starting based on the available data [6].

3.1 Appropriate Map Parameters and Representation. The map parameters corrected speed, corrected flow and pressure ratio are appropriate even under extreme partload conditions. But any efficiency definition is reasonable only as long as pressure ratio is higher than one, i.e. the compressor actually works as a compressor. When the compressor works as a stirrer ($\Pi<1$ and $a/T_t>0$) or as a turbine ($\Pi<1$ and $a/T_t<0$) the efficiency becomes negative, runs towards infinity, changes sign at $a/T_t=0$ and stays larger than one [1]. Especially the infinite values are a big problem for any iterative numerical algorithm as, for example, in performance calculation programs. Instead of efficiency corrected specific work may be used, which is a good idea as long as corrected speed does not become zero. For zero speed, which occurs for example in a transient simulation of engine starting, there is no energy transfer between fluid and rotor and specific work and power are zero by definition. However, the torque, which is not zero for non-zero flow, can not be calculated from specific work.

The parameters φ, ψ and ψ_s are not appropriate for zero speed either because they run towards infinity by definition.

One possible solution to the zero speed problem is the parameter corrected torque

$$\frac{M}{\dot{m}\sqrt{T_t}}=\frac{a/T_t}{n/\sqrt{T_t}}=\psi\cdot\frac{n}{\sqrt{T_t}}, \tag{1}$$

which stays with finite numbers in the whole operating range of a compressor including zero speed, no matter whether the compressor is operating as a compressor, a stirrer or a turbine.

A rather universally applicable map representation is therefore given by

$$\frac{\dot{m}\sqrt{T_t}}{p_t},\quad \Pi_t,\quad \frac{M}{\dot{m}\sqrt{T_t}}=f\left(\frac{n}{\sqrt{T_t}},\beta\right). \tag{2}$$

3.2 Extrapolation Towards Low Spool Speed. As mentioned above, usually there are no measurements available for the low speed range, and therefore this part of the map must be extrapolated.

3.2.1 Theoretical Approach. The extrapolation methods proposed here are based mainly on the flow similarity laws for incompressible flow. Reynolds number effects are neglected. The following items deduced from incompressible similarity laws are helpful for this task.

- The interrelations between the parameters φ, ψ and ψ_s become independent of corrected speed, see [7] for details. Especially for low corrected speed and low φ (i.e. high ψ) the speed lines come close together in any diagram using these parameters.
- In the φ,ψ-diagram the lowest speed lines are nearly straight lines.

• The diagram $\psi - \psi_s = f(\psi)$ is very sensitive to extrapolation errors because it represents the loss characteristics of the compressor blading.

• For very low corrected speed (lower than 1 percent) the φ,ψ-parameters cause some problems because they run towards infinity for zero speed.

• The peak efficiency line, i. e. the line connecting the maximum efficiency values on all speed lines, plotted versus corrected speed or flow becomes horizontal for low speed.

• When plotting corrected torque (see Eq. (1) for definition) versus corrected flow the lower speed lines are nearly parallel straight lines with a negative gradient. The zero speed line in this diagram includes the point (0/0).

3.2.2 Application. For the application of the extrapolation rules a software is recommended which allows to manipulate the compressor map interactively by adjusting the speed lines. Furthermore, the software should be able to produce a large variety of useful diagrams fast and simultaneously on the screen. Of course all the parameters mentioned above should be included in the selection. According to the experience of the authors such an approach is much more appropriate than an automatic mathematical extrapolation algorithm. For the results shown in this paper the publicly available software described in [8] was used.

The extrapolation of a new speed line for low corrected speed is done in three steps.

At first the relationship between corrected flow and pressure ratio is manipulated. To check the result the most important diagram is ψ_s versus φ, in which the low speed lines must come close together. But caution is necessary when variable geometry is used in the speed regime under discussion because it will change the flow/speed relationship.

The second step is manipulating either efficiency, specific work or torque. The efficiency level should be verified with the peak efficiency diagram and the efficiency changes along the speed line should be checked with the help of the diagram $\psi - \psi_s = f(\psi)$. Of course one can use ψ versus φ or φ versus $n/\sqrt{T_t}$ with lines of constant ψ as well.

Because the manipulation of corrected flow, pressure ratio (step one) and efficiency (step two) are completed independently, a third step is necessary to check the results by using a diagram which combines all three parameters, for example corrected torque versus corrected flow.

Due to the general approach using not a mathematical algorithm but a sophisticated drawing tool and some engineering judgement, the results of the extrapolation procedure are not fully reproducible, neither by the same person doing the job twice, nor by two different people meant to do the same job. Nevertheless the approach is thought to be superior compared to a mathematical algorithm due to the inclusion of engineering judgement at the time the job is being done.

Unfortunately demonstrating the proposed method by showing the large variety of used diagrams within this paper would be out of all proportion. Therefore only some results will be shown in the next chapter.

3.2.3 Validation With Test Data. The procedure described above was used to extrapolate the map of a five stage axial compressor towards low speed. The map originates from rig test data covering a corrected speed range down to 30 percent. The 30 percent speed line was left out and the remaining data set with the two lowest speed lines being 40 percent and 64.4 percent was smoothed. Based on the smoothed map the 30 percent speed line was extrapolated by three engineers with various experience in handling compressor maps, using the methodology described above. For the three extrapolated 30 percent speed lines pressure ratio and efficiency are shown versus corrected flow together with the corresponding measured data in Fig. 1.

In addition Fig. 1 shows the 40 percent and 64.4 percent speed lines, the measured data and the smoothed lines, which have been

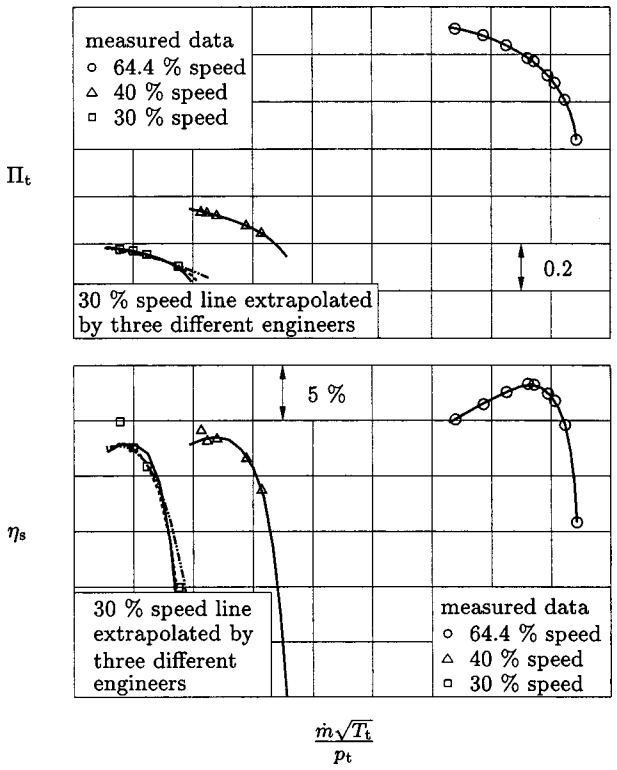

Fig. 1 Extrapolated 30 percent speed lines and measured data

the basis for the extrapolation. All three extrapolated flow/pressure ratio relationships match the measured data very well, the extrapolations matching somewhat worse at higher corrected flow. The extrapolated efficiency values are quite close to the measured data, too, with the exception of the surge point. But looking at the surge point efficiency of both the 30 percent and the 40 percent speed line the conclusion has to be that the measured values are doubtful and the extrapolation results are reasonable. Comparing the measured and the extrapolated data for a given exit corrected flow (and thus a given throttle valve position downstream the compressor) one ends up in maximum deviations between measured and extrapolated inlet corrected flows respectively pressure ratios of about 0.7 percent. Keeping in mind the pure extrapolative nature of the method this result is quite outstanding.

4 Fans for Low Bypass Ratio Turbofans

Compared to axial compressors with one exit station a fan with a splitter downstream delivers compressed working fluid into two exit stations. Thus the fan flow is split into two streams according to the bypass ratio. The flow situation with the split stream line for a nominal bypass ratio as well as the nomenclature used are shown in Fig. 2.

The total inlet corrected mass flow delivered by the fan is usually stored in the way described in chapter 2. The flow split is then calculated from bypass ratio.

4.1 Core and Bypass Stream Temperature and Pressure Rise. Due to the rather low hub-to-tip ratios the circumferential velocities at different radii of the fan blading differ considerably, resulting in very different blade loading at various radii. Moreover in a modern, aerodynamically highly loaded fan the blade tip Mach numbers are transonic resulting in rather high losses at the blade tip. The pressure and temperature rise produced by the fan thus is dependent on radius, which in turn means that the mean values of fan exit pressure and temperature in core and bypass exit

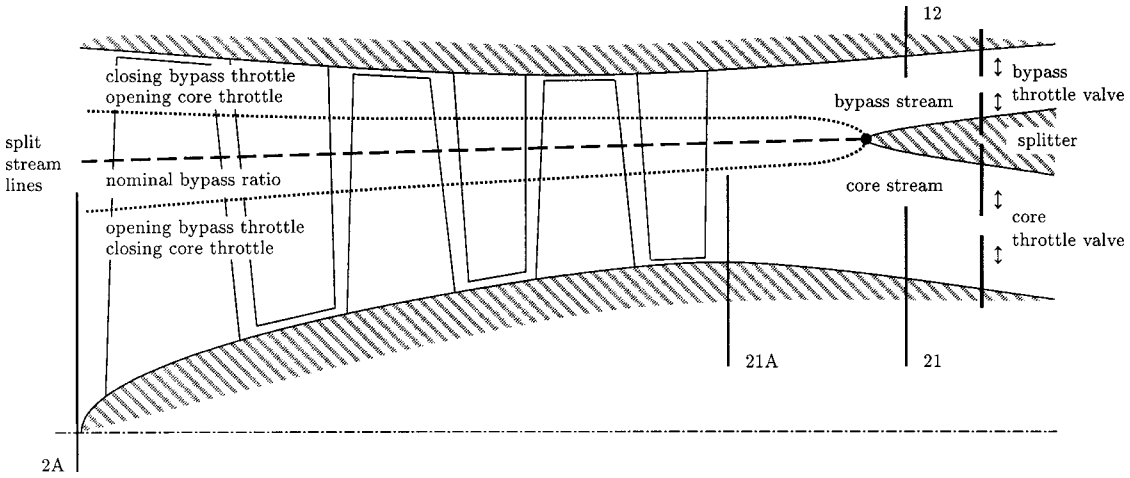

Fig. 2 Fans with splitter downstream and typical split stream lines

stations can differ considerably. Therefore the characteristics of core and bypass stream must be described with two parallel compressor maps separated by the split stream line.

There are two popular ways to do that. One is to store pressure ratio and efficiency of the core stream in a map. To evaluate pressure ratio and efficiency of the bypass stream, profile factors Π_{byp}/Π_{core} and η_{byp}/η_{core} are applied which are stored, for example, dependent on corrected speed and β. This method is presented in some detail in [2]. Another way is to describe the so-called split characteristics of the fan, which means storing

$$\Pi_{core}, \quad \eta_{core}, \quad \Pi_{byp} \quad \text{and} \quad \eta_{byp}=f\left(\frac{n}{\sqrt{T_t}},\beta\right). \tag{3}$$

4.2 Additional Independent Parameter for Bypass Ratio. In the methods described so far two independent map parameters, one of them being β, were used to define a fan operating point. Despite the fact that β is an artificial parameter it may be interpreted as the position of a throttle valve in the compressor exit station. Because a fan delivers the working fluid into two separate exit stations, there are two throttle valves which may be adjusted separately. They can be used to define the mass flows in the core and bypass stream, or in other words, to define the total mass flow at the fan inlet and the bypass ratio independently. When the throttle valves are positioned in such a way that the total mass flow stays constant but the bypass ratio is varied, according to Fig. 2 the split stream line will vary. In consequence the geometry of the two parallel compressors and their characteristics change with bypass ratio, too.

To take into account the influence of bypass ratio on the fan characteristics often a nominal bypass ratio dependent on corrected speed is pre-calculated with a performance calculation model before the fan rig test is carried out. The rig test is then performed with a schedule $\mu_{nom}=f(n/\sqrt{T_t})$ and the fan map is valid for this schedule.

But unfortunately in engine operation there are deviations from the nominal bypass ratio schedule due to power offtake, bleed, engine deterioration and transient manoeuvres. In addition during an engine development program there are changes in detailed engine design and in the variable geometry schedules, as for example nozzle throat area, which influence the bypass ratio.

Thus to reach high accuracy in engine performance calculations the influence of deviations in bypass ratio from the schedule $\mu-\mu_{nom}$ on fan performance has to be taken into account. This can be done by producing several fan maps with $\mu-\mu_{nom}$ as a third independent parameter, which however is very costly in terms of rig testing time, resulting in

$$\begin{aligned}
&\Pi_{core}, \quad \eta_{core}=f\left(\mu-\mu_{nom},\frac{n}{\sqrt{T_t}},\beta\right),\\
&\Pi_{byp}, \quad \eta_{byp}=f\left(\mu-\mu_{nom},\frac{n}{\sqrt{T_t}},\beta\right),\\
&\left(\frac{\dot{m}\sqrt{T_t}}{p_t}\right)_{2A}=f\left(\mu-\mu_{nom},\frac{n}{\sqrt{T_t}},\beta\right).
\end{aligned} \tag{4}$$

Alternatively a correcting algorithm may be applied to calculate approximate values for the fan map in the case of $\mu\neq\mu_{nom}$.

4.3 Approximate Influence of Bypass Ratio

4.3.1 Test Data. To study the influence of bypass ratio variations on fan characteristics rig test data of a three stage low design bypass ratio fan ($\mu_D=0.4$) was analyzed. This fan rig was tested at MTU within the development program of a low bypass turbofan engine. A number of lines of constant corrected speed were produced for a schedule $\mu_{nom}=f(n/\sqrt{T_t})$ and $\mu-\mu_{nom}=0$, 0.2 and 0.4. Total pressure and temperature measurements were performed in stations 2A, 12 and 21 (see Fig. 2) allowing to derive radial total pressure and temperature profiles as well as mean values for all stations. Of course the instrumentation allowed us also to deduce total inlet mass flow and bypass ratio.

4.3.2 Theoretical Approach. With a splitter far downstream the last fan stator row it is obvious that bypass ratio variations, produced by various settings of the core and bypass throttle valves, have no influence on the fan flow field, as long as the inlet corrected flow stays constant. All stream lines within the fan remain unchanged and the adaption for varying bypass ratios takes place downstream the last stator row by a bend of the split stream line towards the leading edge of the splitter, see Fig. 3. Consequently the pressure and temperature profiles in station 21A and thus the mean characteristic of the fan remain unchanged. This is especially true for all Mach number related parameters in station 21A including exit corrected flow $(\dot{m}\sqrt{T_t}/p_t)_{21A}$, and for the surge line. The effect of varying bypass ratio then can be evaluated by using the pressure and temperature profiles of the nominal bypass ratio and calculating the mean values in core and bypass by integrating the radial profiles beginning with the radius on the split stream line which is dependent on the actual bypass ratio.

4.3.3 Validation With Test Data. In the three stage fan rig discussed here the splitter is located two times the chord length of the exit guide vanes downstream of the fan. We now speculate

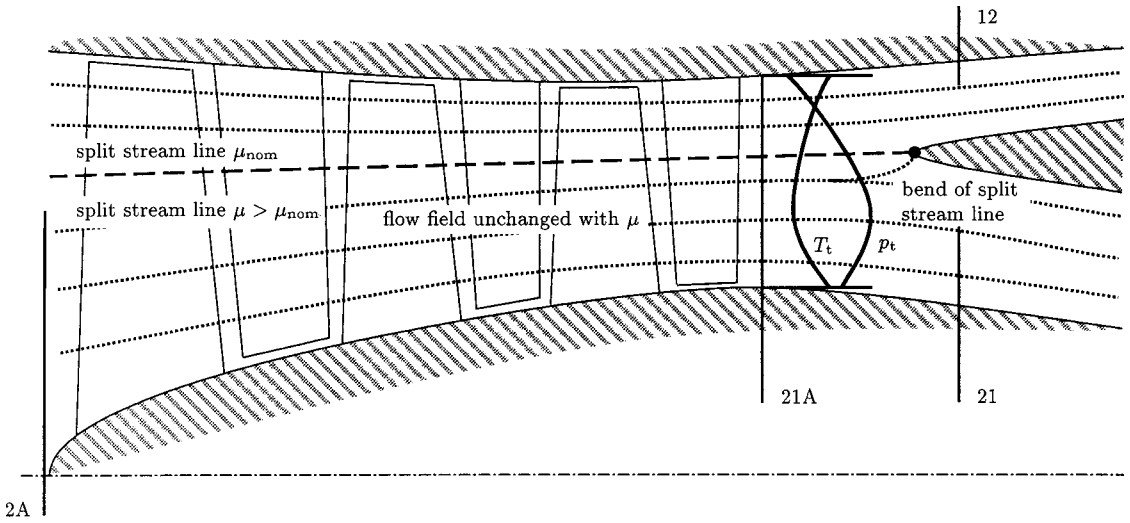

Fig. 3 Stream lines, pressure and temperature profiles in a fan with splitter far downstream the last stator row

that this distance is big enough to assume that bypass ratio variations have no effect on the mean fan characteristics. To validate this assumption Fig. 4 shows the mean characteristic for various corrected speeds and bypass ratios. The variations in mean pressure ratio and mean efficiency with bypass ratio are very small and can not be separated from the scatter within the test data.

4.3.4 Correcting Algorithm. Starting from the theoretical approach and its experimental validation described above a correcting algorithm was developed for calculating fan performance data for $\mu_{new} \neq \mu_{nom}$ based on the map data for $\mu = \mu_{nom}$ only. The operating point under consideration is defined by corrected speed and mean exit corrected flow. Three steps were identified to be necessary:

1 Find the radial pressure and temperature profiles and the radius of the split stream line in station 21A for the given operating point and μ_{nom}.

2 Find the radius of the split stream line for μ_{new}.

3 Integrate the pressure and temperature profiles from the new split stream line radius in station 21A to the inner wall radius to calculate the core parameters and to the outer wall radius to calculate the bypass parameters for μ_{new}.

The steps are discussed in the following and illustrated for the pressure profile in Fig. 5.

Pressure and Temperature Profiles. From the rig test data we concluded that the pressure and temperature profiles can be approximated as parabolic curves versus radius. To determine the coefficients of the parabolas three boundary conditions are necessary. We use the mean values in the core and bypass stream, both of which are measured on the rig and stored in the nominal bypass ratio map. Moreover, the test data show a maximum/minimum value in the pressure/temperature profiles, which is located at a constant radius r_{max}. From this information the parabola coeffi-

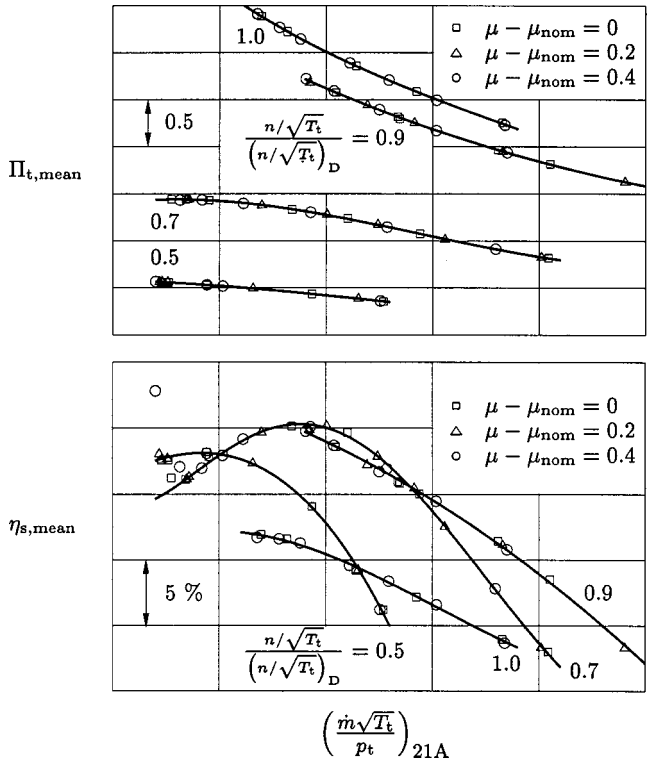

Fig. 4 Mean fan characteristic for various corrected speeds and $\mu - \mu_{nom} = 0$, 0.2 and 0.4

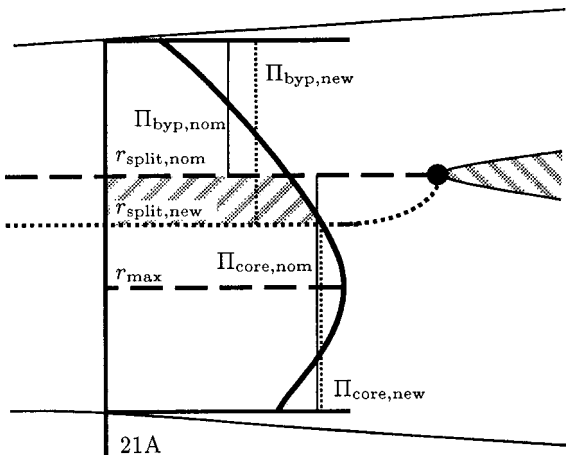

Fig. 5 Correcting algorithm for pressure ratio

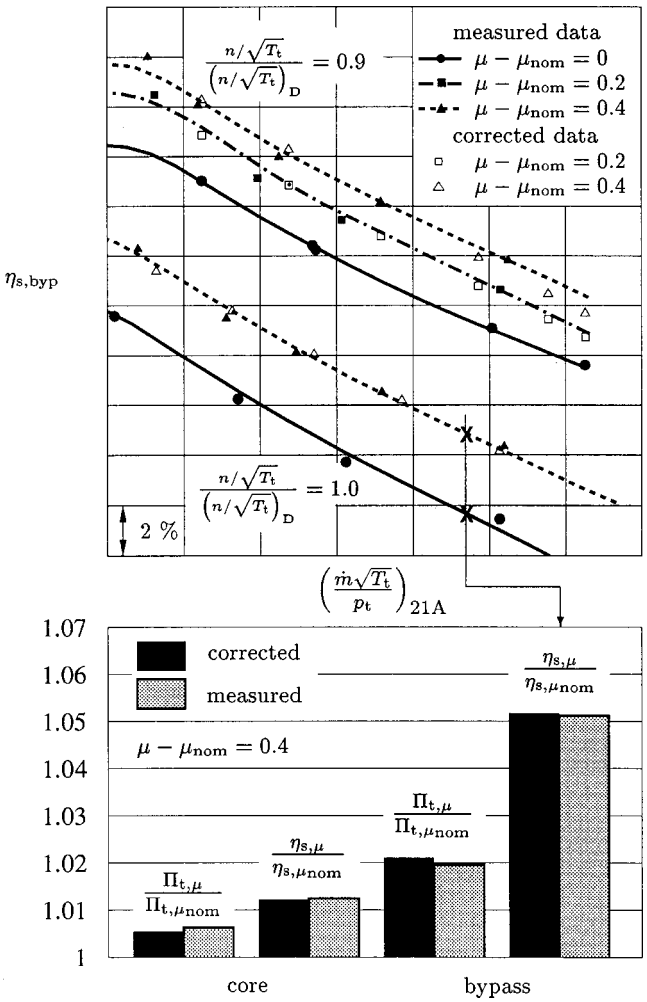

Fig. 6 Comparison of corrected and measured map parameter values

cients and the radius of the split stream line for μ_{nom} can be calculated using basic gas dynamics assuming constant static pressure in station 21A for simplicity.

Split Stream Line for μ_{new}. The radius of the split stream line in station 21A for μ_{new} is calculated from the new bypass ratio based on the pressure and temperature profiles determined in step one. Because the mean characteristic remains constant, the static pressure in station 21A and the total mass flow are the same as for μ_{nom}.

Calculation of the Map Parameters for μ_{new}. The map parameters are calculated in the third step by integrating the pressure and temperature profiles with $r_{split,new}$. This is equivalent to a shift of the hatched part of the pressure profile from core to bypass flow as indicated in Fig. 5.

4.3.5 Accuracy of the Correcting Algorithm. The procedure described was applied to the map of the three stage low bypass ratio fan mentioned above. The map parameters for the nominal bypass ratio were used as a basis and the values for the bypass ratios $\mu - \mu_{nom} = 0.2$ and 0.4 were produced by the correcting procedure, which is equivalent to a variation in bypass ratio of up to about 100 percent. Because for these bypass ratios also rig test data were available it was possible to check the procedure very well. In the upper part of Fig. 6 bypass efficiencies for the 90 percent and the 100 percent speed lines produced by the correcting algorithm are compared to measured data.

In the lower part of Fig. 6 all relevant map parameters produced by the algorithm are compared to the measured data for the operating point marked in the upper part of the figure.

Figure 6 firstly shows that the influence of bypass ratio on the map parameters is not negligible at all. The bypass pressure ratio varies up to about 2 percent while the core pressure ratio variations remain under 1 percent. The bypass efficiency shows variations of up to 5 percent whereas the core efficiency variations again are much smaller. These results, in terms of numbers and trends, depend very much on the pressure and temperature profiles in station 21A and therefore on the fan characteristics. Here for the nominal bypass ratio $\Pi_{t,byp}$ is much lower than $\Pi_{t,core}$ resulting in an increase of $\Pi_{t,byp}$ with $\mu - \mu_{nom} > 0$. In [9] results from an experimental study are presented with opposite trends, but again following the rules described here.

As a second result from Fig. 6 it can be derived that the approximation method works quite reasonable. The trend and the magnitude of the influence is calculated very well under all operating conditions investigated. The largest deviations between calculations and smoothed measured data occur at 90 percent speed in the choking regime and amount to about 0.5 percent in bypass efficiency. This in turn means that about 85 percent of the necessary correction are applied by the correcting algorithm. For lower exit corrected flows the deviations are even much smaller, see the upper part of Fig. 6. The deviations are caused mainly by the approximation of pressure and temperature profiles in station 21A which is not exact, and by the scatter in the measured data themselves due to measurement uncertainties.

Of course these results also confirm the validity of the assumption in chapter 4.3.3 that the mean fan characteristics and the pressure and temperature profiles in station 21A do not depend on bypass ratio.

4.4 Additional Remarks. Some additional aspects should be kept in mind when applying the correction procedure to other fan configurations.

- The correcting algorithm is based on the assumption that the splitter is far downstream the last fan stator, which is not necessarily true. The effect of a splitter close to the last fan stator will be a stronger influence on the fan flow field and hence the approximation will get worse.
- When looking at single stage fans for high bypass turbofan engines the splitter is usually located within the fan stage between rotor and stator row which will result in a stronger interaction between the splitter and the fan flow field.
- When the mean characteristic of the fan is constant the influence of bypass ratio is caused only by the part of mass flow which is shifted from core to bypass when increasing the bypass ratio. For a given percentage change in bypass ratio this part is lower when the nominal bypass ratio is higher. For example a 10 percent increase in bypass ratio causes a 5 percent increase in bypass mass flow when $\mu_{nom} = 1$, whereas for $\mu_{nom} = 10$ the bypass mass flow varies only by 0.8 percent.

5 Conclusions

This paper deals with some special issues of modelling compressor behavior in gas turbine performance calculations.

Based on the standard methodology which is well-known in gas turbine industry, universities and research institutes, the extreme partload regime of compressor operation is covered. The methods discussed for extrapolating compressor maps show reasonable results which are appropriate to be used in gas turbine windmilling and starting calculations. The proposed map representation using corrected torque instead of efficiency allows to calculate gas turbine behavior for these operating conditions. The methods using typical turbomachinery relationships are applicable to turbines, too. For further checks of the extrapolation procedure test results for locked rotor conditions or for zero torque at various speeds would be very helpful.

For low bypass turbofan engine fans with a splitter downstream a method is presented to easily take into account the effect of varying bypass ratio without performing rig tests for a variety of bypass ratios. A correcting algorithm is derived based on a map which is valid for a nominal bypass ratio. Again the accuracy of the results is fully appropriate for gas turbine performance calculations.

Acknowledgments

The authors wish to thank MTU München GmbH for the opportunity to use the company's own data to perform the investigations. Special thanks go to Prof. Dr.-Ing. W. Braig and H. Schulte of the Institut für Luftfahrtantriebe at Universität Stuttgart in Germany for the stimulating discussions about compressor off-design performance in extreme partload.

Nomenclature

a = specific work
$\dot{m}$ = mass flow
M = torque
n = spool speed
p = pressure
r = radius
T = temperature
β = artificial map parameter
η = efficiency
μ = bypass ratio
Π = pressure ratio
φ = flow coefficient, $\varphi=(\dot{m}\sqrt{T_t}/p_t)/(n/\sqrt{T_t})$
ψ = work coefficient, $\psi=a/n^2$

Subscripts

12 = fan bypass exit station downstream splitter
21 = fan core exit station downstream splitter
2A = fan inlet station (mean)
21A = fan exit station (mean)
byp = bypass duct
core = core engine
D = design
max = maximum
mean = mean value
new = new
nom = nominal
s = isentropic
split = split
t = total

References

[1] Walsh, P. P., and Fletcher, P., 1998, *Gas Turbine Performance*, Blackwell Science.
[2] Kurzke, J., 1996, ''How to Get Component Maps for Aircraft Gas Turbine Performance Calculations,'' ASME Paper No. 96-GT-164.
[3] AGARD-PEP WG 24, editor, 1995, *Recommended Practices for the Assessment of the Effects of Atmospheric Water Ingestion on the Performance and Operability of Gas Turbine Engines, AGARD-AR-332*.
[4] Braig, W., and Riegler, C., 1994, ''Berücksichtigung des Einflusses des Isentropenexponenten auf die Kennfelder von Turbinen,'' *Forschung im Ingenieurwesen*.
[5] Kurzke, J., 1992, ''Calculation of Installation Effects Within Performance Computer Programs,'' in: *AGARD-LS-183*, pages 7.1–7.19.
[6] Anderson, B. A., Messih, D., and Plybon, R. C., 1997, ''Engine-Out Performance Characteristics,'' in: *ISABE 97-7216*.
[7] Therkorn, D., and Braig, W., 1994, ''Turbinenkennfelderstellung für kleine Arbeiten und Drehzahlen,'' Z. Flugwiss. Weltraumforsch., **18**, No. 2, pp. 140–144.
[8] Kurzke, J., 1999, ''Smooth C 7.0: Preparing Compressor Maps for Performance Calculations,'' User's Manual.
[9] Tzannatos, E., and Elder, R. L., 1993, ''The Stability of Split Flow Fans,'' Int. Journal of Turbo and Jet Engines, **10**, pp. 235–251.

Steady Performance Measurements of a Turbofan Engine With Inlet Distortions Containing Co- and Counterrotating Swirl From an Intake Diffuser for Hypersonic Flight

Norbert R. Schmid
Dirk C. Leinhos
Leonhard Fottner

Institut für Strahlantriebe,
Universität der Bundeswehr München,
D-85577 Neubiberg, Germany

The influence of distorted inlet flow on the steady and unsteady performance of a turbofan engine, which is a component of an air-breathing combined propulsion system for a hypersonic transport aircraft, is reported in this paper. The performance and stability of this propulsion system depend on the behavior of the turbofan engine. The complex shape of the intake duct causes inhomogeneous flow at the engine inlet plane, where total pressure and swirl distortions are present. The S-bend intakes are installed axisymmetrically left and right into the hypersonic aircraft, generating axisymmetric mirror-inverted flow patterns. Since all turbo engines of the propulsion system have the same direction of rotation, one distortion corresponds to a corotating swirl at the low pressure compressor (LPC) inlet while the mirror-inverted image counterpart represents a counterrotating swirl. Therefore the influence of the distortions on the performance and stability of the 'CO' and 'COUNTER' rotating turbo engine are different. The distortions were generated separately by an appropriate simulator at the inlet plane of a LARZAC 04 engine. The results of low-frequency measurements at different engine planes yield the relative variations of thrust and specific fuel consumption and hence the steady engine performance. High-frequency measurements were used to investigate the different influence of CO and COUNTER inlet distortions on the development of LPC instabilities.
[DOI: 10.1115/1.1343466]

Introduction

In 1990 a collaborative research center was initiated in order to involve German universities strongly in the technology of hypersonic flight [1,2]. A reference concept aircraft HTSM (Hypersonic Transport System Munich) was planned to be equipped with an airbreathing combined propulsion system for operation in turbo as well as in RAM mode. In the range from take-off to a flight Mach number of $M=2.8$ the transport system is powered by the turbo engines. Above this transition Mach number, up to $M=6.8$, the RAM engines are active. One combination of a turbo and a RAM engine uses the same intake and nozzle, respectively. This extended flight envelope makes a variable intake geometry indispensable both in the super- and subsonic sections. Inhomogeneous flow generated by the supersonic part of the intake may cause separation and thus the occurrence of additional secondary flow in the geometrically complex shaped subsonic part of the intake canal leading to vortices and sectorial changes in total pressure and temperature.

Performance and stability of the complete propulsion system are strongly influenced by the interaction between variable intake, intake duct, and engine. For any discrete operating point, the performance of the turbo engine depends on the behavior of the intake duct if the area of the variable nozzle is held constant, while a variation of the engine behavior results in a change of the thrust. The thrust vector varies not only in magnitude but also in direction (Fig. 1) because of a projected Single Expansion Ramp Nozzle (SERN) that leads to a nonaxisymmetric expansion in any case, influencing flight mechanics and flight control. Therefore it is necessary to investigate the steady engine performance with typical inlet distortions generated in the intake diffuser of an engine for hypersonic flight by simulating them at the test engine's inlet plane.

Besides the performance behavior throughout the whole speed range, the safety requirements have to be considered particularly by carrying out investigations near and beyond the surge line of the LPC. A surging LPC may not only cause severe engine damages but the influence on the propulsion system might also be a major hazard to the HTSM.

Detailed measurements inside a scale model intake reveal the existence of an extended three-dimensional flow separation on the top wall of the duct. This combining with complex secondary flows generated by the curved canal lead to highly distorted flow fields at the engine inlet face [3,4]. The results have been derived from the geometry of the *right* intake, while the flow pattern of the *left* intake will be an axisymmetric mirror image. Since all turbo engines of the propulsion system have the same direction of rotation, the influence of the distortions on the performance will differ for engines installed left or right, because corotating swirl will occur for those turbo engines installed on one side and counterrotating swirl for the others, respectively.

In combination with the test engine LARZAC 04, the flow pat-

Contributed by the International Gas Turbine Institute and presented at the 45th International Gas Turbine and Aeroengine Congress and Exhibition, Munich, Germany, May 8–11, 2000. Manuscript received by the International Gas Turbine Institute February 2000. Paper No. 2000-GT-11. Review Chair: D. Ballal.

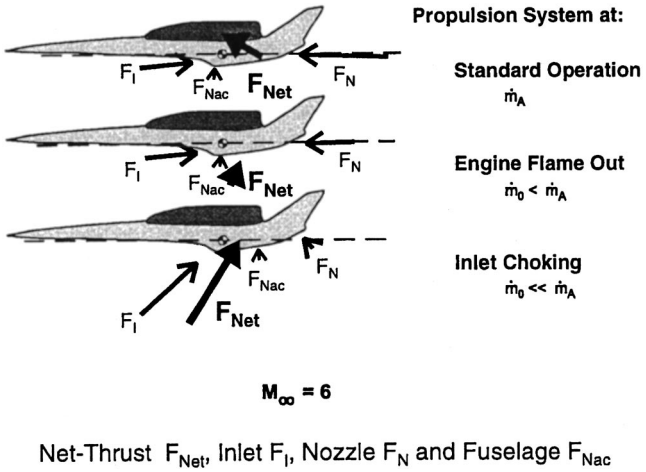

Fig. 1 Variation of the thrust vector

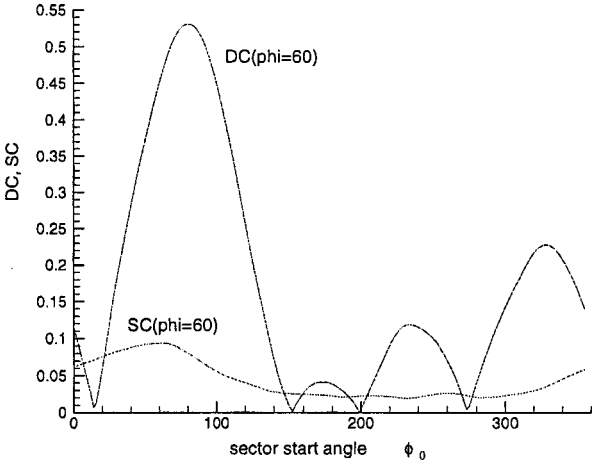

Fig. 3 Measured distortion parameters (model)

tern of the *right* intake duct is corresponding with corotating swirl at the LPC inlet, while the flow pattern of the *left* intake generates a counterrotating distortion. Therefore, one requirement for the simulator was to reproduce distortions of variable intensities and to be adaptable for the simulation of the so-called CO and COUNTER distortions.

Simulator Setup

Distorted Flow Pattern. The subsonic section of the right intake duct was modeled in 1/4-scale. Traverse measurements in the outlet plane show the strong influence of a separation on the canal's top wall. The distribution of local total pressure related to the momentum averaged total pressure in the outlet face (Fig. 2) shows that the main flow is deflected downward, while the upper half is filled with lower energetic fluid caused by the separation. The duct's **S**-bend initiates the formation of a strong bulk swirl as it can be detected in the counterclockwise rotation of the complete flow pattern.

Analyzing the relative cross-velocity vectors (white arrows), the result of the superposition of the two main effects becomes visible. One vortex passes the outlet plane at the 100 deg position, while its former counterpart has been dissolved. Only a weak influence on the main flow can be detected at 140 deg. Representing the right intake canal, the 100 deg vortex is corotating with the LP spool.

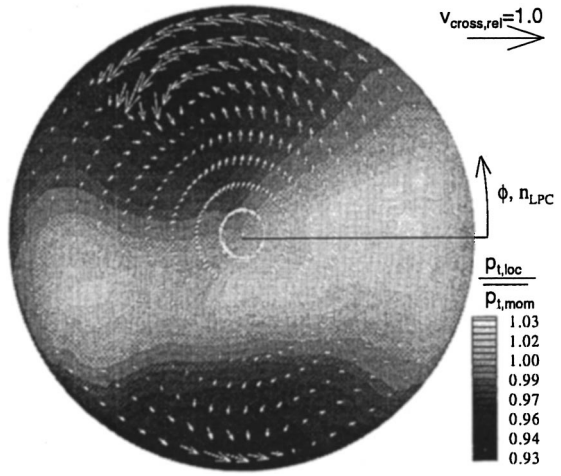

Fig. 2 Measured relative total pressure, cross velocities

In order to make the results comparable with the characteristics of other aircraft inlets and with the designed simulator or in general with aerodynamic interface planes (aip) the more commonly used coefficients *D*istortion *C*oefficient DC (φ) and *S*wirl *C*oefficient [5] were calculated for the sector size $\varphi = 60$ deg at a given position x using:

$$\mathrm{DC}(\varphi,x)\big|_{\varphi_{\mathrm{crit}}} = \frac{|\overline{p_t(x)} - \overline{p_t(\varphi,x)}|_{\max}}{\overline{p_t(x) - p(x)}},$$

$$\mathrm{SC}(\varphi,x)\big|_{\varphi_{\mathrm{crit}}} = \frac{|\overline{v_{\mathrm{cross}}(\varphi,x)}|_{\max}}{v_\infty}$$

Due to the absolute value of the total pressure deviation, areas of total pressure higher or lower than the average value at x both give positive DC(φ) values. When comparing different inlets, the starting position φ_0 of the critical sector with size φ does not have any influence on the engine behavior. But the development of the DC(φ) by variation of φ_0 in the range $0\ \mathrm{deg} < \varphi_0 < 360\ \mathrm{deg}$ is a good reference for designing a simulator. The two coefficients are rather sensitive values, thus a reproduction of a given distribution proves the quality of the simulating device. $\varphi_0 = \varphi_{\mathrm{crit}}$ occurs, where DC(φ) has its maximum. The reference case from the model measurements DC(φ) for the variation of φ_0 shows one significant peak at $\varphi_0 = 80$ deg (Fig. 3) representing the area of maximum total pressure loss at the 110 deg position ($\varphi_0 + \varphi/2$). The following two peaks show the area of deflected main flow $\varphi_0 = 175$ deg and a second area of low total pressure $\varphi_0 = 240$ deg. The last peak at $\varphi_0 = 340$ deg shows the second area of higher energetic flow.

Figure 3 also shows the Swirl Coefficient SC(φ), which is the maximum average circumferential component of crossflow velocity in a sector of size φ nondimensionalized by dividing it by the mean duct velocity at a given position x in the duct. Similar to DC(φ) the circumferential development of SC(φ) can be found by varying φ_0. The reference measurement shows only a single swirl distortion at $\varphi_0 = 70$ deg indicating the one vortex that has been detected in the cross-velocity distribution at the 100 deg position and little cross velocities at $\varphi_0 = 260$ deg. The maximum values are DC(φ) = 0.53 and SC(φ) = 0.10.

Accompanying CFD calculations confirm the experimental results [6].

Simulator Development and Results. The simulator has to reproduce the given CO and COUNTER flow patterns and it has to resist the mechanical loads.

Since a symmetric delta wing under a high angle of attack creates a symmetric pair of counterrotating vortices [7], the approach was to generate the single vortex with a nonsymmetric half

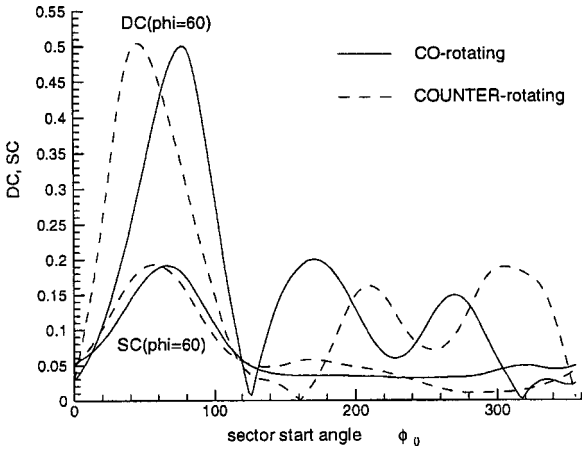

Fig. 4 Distortion parameters delta wing simulator

delta wing with one edge parallel to the main flow and a huge winglet aside this streamwise edge to prevent flow around this edge and hence to avoid a second vortex. The construction has also to meet mechanical requirements such as induced vibrations at the simulator's eigenfrequencies caused by the rotation of the LP and HP spools. Furthermore, aeroelastic problems had to be considered to avoid self-induced vibrations due to positioning the winglet in compressible high-speed flow. These calculations have been performed in-house (mechanical) and by MTU-Munich (aeroelastics) to assure safety [8].

The flow pattern downstream of the simulator is measured with a rake containing eight five-hole probes. The rake can be varied in the radial and circumferential directions in order to capture the complete plane of analysis, which is positioned one intake duct radius upstream of the inlet plane of the test engine. With the delta wing at an angle of attack of 20 deg and two wire gauze elements, best accordance with previous CFD calculations and the reference case was obtained [9]. Different speeds were tested to prove that the given flow pattern is generated over the whole speed range. The results presented herein were obtained at a relative corrected LPC rotor speed of $n_{\theta\mathrm{LPC}}=76$ percent (midspeed range). The distributions of the DC(φ) and SC(φ) coefficients (Fig. 4) show good accordance with the measurements in the model duct (Fig. 3). Number and extension of the distortions match the targets. The maximum DC(φ)=0.50 is only 6 percent off the given reference value of 0.53. The swirl coefficient reaches its maximum at SC(φ)=0.19 at the plane of analysis. As mentioned above, the inlet face of the test turbofan engine is positioned approximately one intake radius downstream of the rake. Vortices are more unstable than total pressure distortions, so it is assumed that the swirl distortions get damped out due to internal friction and reach the engine in the required strength of about SC(φ)=0.10, while the total pressure losses are transported without any appreciable change.

To generate the COUNTER distortion, the simulator was mounted axisymmetrically mirror inverted. In order to prove the symmetric flow pattern and to detect influences of the devices the simulator is mounted, the measurements were repeated. Figure 10 shows the cross-velocity distribution of the COUNTER distortion compared with CO distortion. Most significant is the reversed direction of rotation of the single vortex. Its diameter is again one radius of the intake duct and its position is at the 80 deg position consequently mirror-inverted at the vertical axis. Comparing the CO and COUNTER DC(φ) and SC(φ) distributions one can see that the distortion pattern is mirror inverted (Fig. 4).

CO Distortion. Beginning at $\varphi_0=0$ deg the gradient of the main peak of DC(φ) in the ascending section is slighter than in the descending section. Two more lower peaks are following, while the fourth peak at $\varphi_0=330$ deg leads into the first peak again. The SC(φ) distribution shows one significant peak near the maximum of DC(φ) followed by a slight rising at $\varphi_0=320$ deg being at a 240 deg distance.

Table 1 Distortion parameters

	Model Measurement	CO distortion	COUNTER distortion
$DC(\varphi)_{max}$	0.53	0.50	0.50
$SC(\varphi)_{max}$	0.10	0.19	0.19
peaks DC	4	4	4
peaks SC	1	1	1

COUNTER Distortion. The best way to detect the mirror image character of the distortion is to begin the analysis at $\varphi_0=105$ deg following the direction of descending φ_0. From this point of view, again the gradient of the main peak of DC(φ) in the ascending section is slightly lower than in the descending section, followed by two medium peaks, while the fourth peak again leads into the main peak. In this reversed direction of view the swirl distortion has the same distribution of intensity with a first main peak followed by a slight one being in a 240 deg distance.

Hence the simulator's ability to produce both, the CO and the COUNTER distortion, is proven. Table 1 summarizes the distortion parameters for $n_{\theta\mathrm{LPC}}=76$ percent. Measurements at different speeds confirmed the development of the distortion coefficients over the whole speed range in good accordance with various measurements inside the model intake duct [10]. It can therefore be concluded that the test engine is exposed to the given distortions over the whole speed range and that the CO and COUNTER distortions have the same magnitude.

Experimental Setup

Test Engine. The engine tests were carried out at the institute's ground test facility using the twin-spool turbofan engine LARZAC 04 C5 (Fig. 5). It comprises a two-stage, highly transonic low-pressure compressor, a four-stage high-pressure compressor, an annular combustion chamber, and single-stage high and low-pressure turbines, respectively. The core and bypass flow expand unmixed through separate nozzles, which allows an almost independent throttling of both compressors. Since there are no inlet guide vanes at the LPC, the LARZAC 04 is well suited for a test program with generated inlet distortions typical for hypersonic transport systems.

Throttling Devices. In order to operate the compressors of the test engine away from their equilibrium running line, three

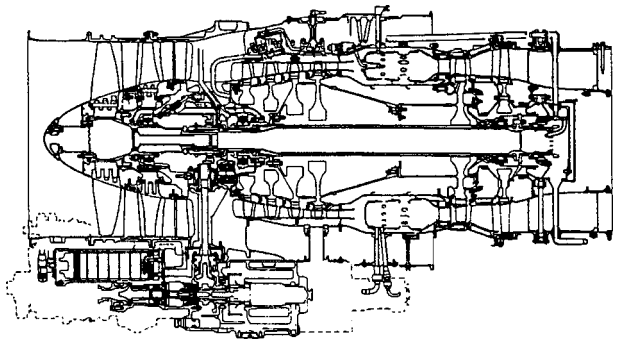

Fig. 5 LARZAC 04 C5 test engine

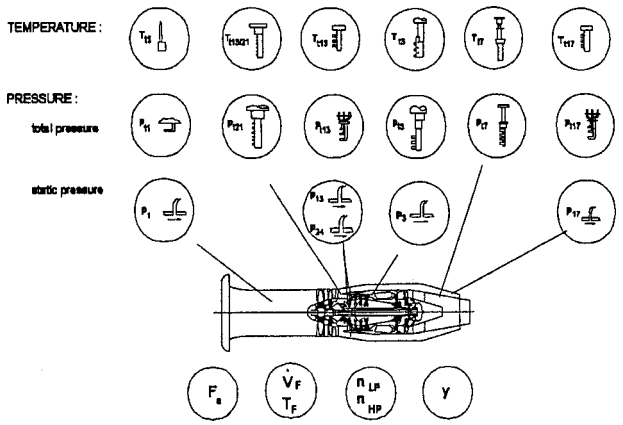

Fig. 6 Positions of the low-frequency instrumentation

independently operating throttling devices are installed at the engine. The LPC is throttled by reducing the bypass nozzle area with an aperture-like device. Details of the controlling of the throttling devices can be found in [11]. For the results presented herein only bypass throttling was performed in order to obtain the LPC characteristic and to examine the development of instabilities.

Instrumentation and Data Acquisition. The test engine is equipped with two different categories of instrumentation that exceed the standard instrumentation of an in-service aero engine by far. A number of thermocouples and wall static pressure probes, total pressure probes, connected with standard pressure transducers, are installed throughout the engine (Fig. 6). They represent the so-called low-frequency instrumentation. They enable calculating mass flows and a detailed gas path analysis for steady and transient operations. Furthermore the rotor shaft speeds, the thrust (F_s), the fuel flow ($\dot{V}_F$) and temperature (T_F), and the humidity (ψ) of the air are measured. The data correction and gas path analysis procedure for deriving compressor maps and running lines is described by [12].

In addition to the conventional pressure probes, a number of high frequency wall static and freestream total pressure probes are installed at various positions throughout the LPC in order to track pressure fluctuations during stall onset. Details of the full high-frequency instrumentation are found in [11].

Experimental Results

LPC Measurements. Since the LPC is directly exposed to the inlet distortions, the engine performance is mainly influenced by the deterioration of the LPC characteristic. In order to obtain the steady LPC characteristic the engine was throttled at constant relative aerodynamic speeds $n_{\theta\mathrm{LPC}}$. Starting from the equilibrium running line the bypass throttle was closed continuously until the LPC became unstable. This procedure led to fully developed rotating stall at all speeds but no surge. The closing speed of the throttle was slow to maintain steady engine conditions. The characteristics for clean inlet flow (gray map, numbers) and for the simulated ''hypersonic'' CO and COUNTER distortions generated by the delta wing simulator (black map, numbers, symbols) are depicted in Fig. 7. The diamond symbols show the points of CO data, the circle symbols represent the COUNTER data. The labeled lines represent speedlines of constant relative aerodynamic speeds. They are measured from the equilibrium running line up to stall, while it is not possible to de-throttle the compressor below the equilibrium running line. Therefore the speedlines have to be extrapolated in a reasonable way using energetic and efficiency considerations. For a better identification, some efficiency lines are neglected.

Pressure Ratio Over Mass Flow. Taking a look at the compressor map, one can see that performance and stability decrease with both distortions. The surge margin decreases significantly with increasing speed. The main influence is the behavior of the simulator, which produces increasing distortions with growing speeds. The swirl distortion changes linearly with inflow velocity while total pressure loss approximately increases with the square of the velocity.

The mass flow is remarkably reduced by the decreased performance and hence reduced suction of the LPC. Even a steady inlet distortion is an unsteady phenomenon for the single blade of the first rotor. The blades are exposed to unsteady axial velocity variations and therefore ''off design'' velocity components, which lead to higher losses and lower mass flows. Overall pressure ratio p_{t2l} (total pressure behind LPC) over $p_{t2,\mathrm{cor}}$ (momentum averaged total pressure behind the simulator) is lower, indicating reduced performance of the LPC with both inlet distortions. This causes the characteristic to be shifted somewhat to the lower left. For the CO distortion this occurs for $n_{\theta\mathrm{LPC}}>76$ percent, while for the COUNTER distortion this effect exists over the whole speed range. The explanation of this difference can be found by separating the ''hypersonic'' distortion in a superposition of total pressure and swirl distortion. The larger left-tilted triangle symbols on the equilibrium running line represent measurements with the delta wing with no angle of attack resulting in a pure total pressure distribution. Thus reference points are obtained in order to separate the influence of the superposed swirl distortion. These operation points reside between those of the CO and COUNTER distortion. Since corotating swirl at the LPC inlet causes a lower load on the rotor blades thus increasing the mass flow, due to this dethrottling effect the CO operating points are shifted a little to higher pressure ratios and mass flows. Therefore the CO distortion is reducing the negative effects of the total pressure inhomogeneity, whereas the COUNTER distortion amplifies them.

The slopes of the speed lines below the equilibrium running line are steeper for both distortions. The operating range of the stages is reduced because the total pressure distortion leads to reduced axial velocities and those to higher loads on the blades. Hence the distorted sector blocks earlier with no appreciable difference between the two swirl directions.

One remarkable feature of the clean inlet compressor characteristics is the rather flat progression of the upper speedlines. A reason for this progression might be the unusual trend of the total-to-static pressure rise stage characteristics as shown in [11]. While the gradient is always negative for the rear stage indicating stable compressor flow, it tends to be positive for the front stage for all speedlines and all throttling rates. According to the two-dimensional stability analysis presented in [13], the flow becomes unstable with a gradient equal to zero. Nevertheless, the compressor flow as a whole is stable most probably due to stabilizing effects of the second stage. Furthermore, the efficiency decreases with rising throttling thus limiting the pressure rise. Thus, the influence of the swirl distortions can be best detected in the upper speed range. The CO swirl reduces the unstable tendencies of the first rotor resulting in higher efficiencies leading to pressure rise and hence to steeper speedlines with positive progression. The COUNTER swirl causes the first LPC rotor to intensify this instability. Therefore the speedlines are bent downwards to lower pressure ratios similar to the case of clean inlet flow.

From idle speed up to $n_{\theta\mathrm{LPC}}=53$ percent no significant change of the surge line occurs for the CO distortion. Beside the low intensity of the generated distortions for this speed range, the reason for this phenomenon might be the tolerance of the second stage of the compressor for changed incidence at the first rotor of the LPC, caused by the generated swirl and the axial velocity deficits in the areas of reduced total pressure, up to a certain limit. Within this range the second stage is able to absorb and compensate even severe instabilities of the first stage because the compressor matching favors the second stage in the low speed range.

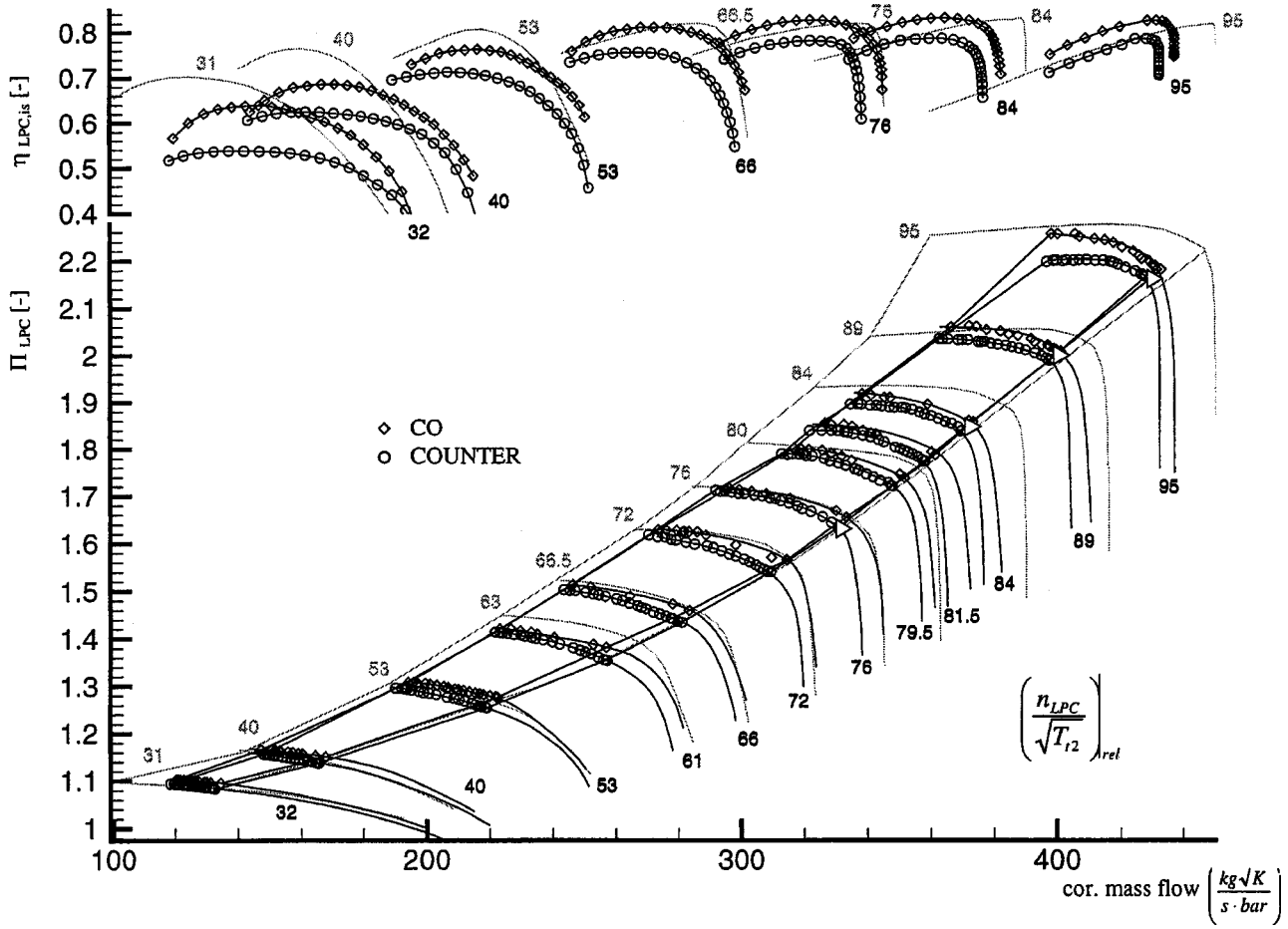

Fig. 7 LPC compressor map

Therefore the LPC runs at the same operating point as for clean inlet flow. For higher speeds the loading of the rear stage increases and reduces its capability of stabilizing the first stage. The ''tolerance'' is exceeded and the higher loads on the first stage blades within the distorted sector lead to significant decrease of the surge margin. Looking at the equilibrium running line where the load on the blades is lower than near the surge line one can see that the ''tolerance'' here is expanded up to $n_{\theta\mathrm{LPC}}=76$ percent. Reduced mass flow and overall pressure ratio at these operating points do not differ from clean inlet. The COUNTER surge line coincides with the CO line up to $n_{\theta\mathrm{LPC}}=84$ percent, indicating similar influence on the stability. Beyond this speed, the counterrotating swirl favors the development of instabilities at the LPC and hence the surge line decreases significantly compared to the CO distortion.

The equilibrium running lines coincide, indicating the equal throttling characteristic of the following components in all cases. Solely at high speeds, mass flows are reduced (see above) shifting the operating points to the left.

Efficiency Over Mass Flow. The efficiency lines prove the above-mentioned observations concerning the influence of the various inlet distortions. The maximum efficiencies of the CO distortion nearly do not vary from the clean inlet for higher speeds while a decrease can be detected below $n_{\theta\mathrm{LPC}}=66$ percent. Compared with the appropriate speed lines, this proves that for higher speeds the corotating swirl reduces the negative effects of the total pressure distortion. Although mass flow and pressure ratio are reduced, the maximum efficiency remains the same. The lines for the COUNTER distortion underline the opposite influence of the counterrotating swirl by reinforcing the negative effects. For all speeds the LPC is running at lower efficiency.

Overall Engine Performance. For in flight operation not only is the compressor behavior of interest, but overall performance losses as a result of inlet distortions are also important. The design of the transport system, its flight envelope and flight performance, strongly depends on the performance of the propulsion system. In order to verify the decrease in engine performance, additional measurements of thrust and specific fuel consumption were performed on the equilibrium running line without throttling. The measured thrust depends not only on engine performance but on inlet and installation conditions. The thrust was first corrected by the drag of the simulator, which is mounted on the same frame as the engine and thus influences the measured thrust. In order to compensate for inlet conditions, thrust performance was obtained by observing the difference of thrust of distorted and clean inlet flow related to the averaged total pressure, related to clean thrust as follows:

$$\Delta F_{s,\mathrm{rel}}=\frac{\dfrac{F_{s,\mathrm{dist}}}{p_{t2,\mathrm{dist}}}-\dfrac{F_{s,\mathrm{clean}}}{p_{t2,\mathrm{clean}}}}{\dfrac{F_{s,\mathrm{clean}}}{p_{t2,\mathrm{clean}}}}$$

Figure 8 depicts increasing losses from 32 to 95 percent LPC-speed up to 8.0 percent. The rising losses reflect the decreasing

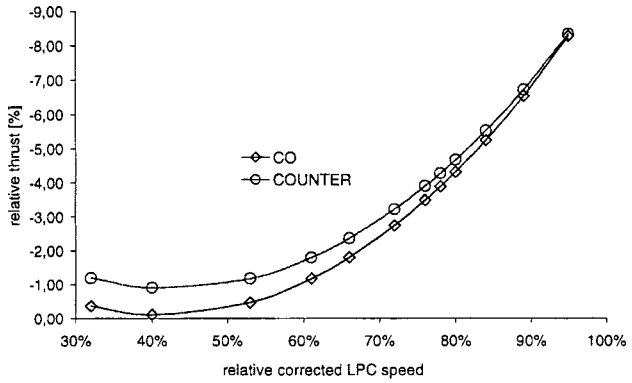

Fig. 8 Relative thrust

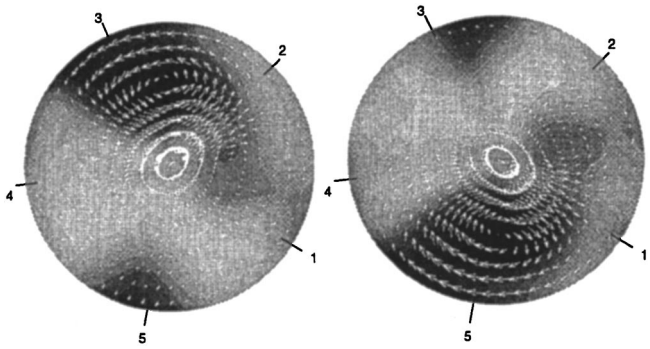

Fig. 10 Position of the high frequency probes relative to the CO and COUNTER distortions

efficiency of the LPC and hence the deterioration of the engine's cycle. At lower speeds, the engine is less sensitive for the distortions while at higher speeds the increasing distortions cause the rising losses. The LPC investigations pointed out a higher influence of the COUNTER distortion. The distribution of thrust loss underlines this more negative influence in the lower and middle speed range whereas the difference between the CO and COUNTER distortion almost vanishes at higher speeds. The total pressure distortion therefore is mainly responsible for the thrust losses.

Figure 9 shows the specific fuel consumption defined as follows. The measured fuel mass flow is related to the drag corrected thrust and the inlet total temperature, respectively:

$$\Delta\dot{m}_{f,\mathrm{rel}}=\frac{\dfrac{\dot{m}_{f,\mathrm{dist}}}{F_{s,\mathrm{dist}}\sqrt{T_{t2,\mathrm{dist}}}}-\dfrac{\dot{m}_{f,\mathrm{clean}}}{F_{s,\mathrm{clean}}\sqrt{T_{t2,\mathrm{clean}}}}}{\dfrac{\dot{m}_{f,\mathrm{clean}}}{F_{s,\mathrm{clean}}\sqrt{T_{t2,\mathrm{clean}}}}}$$

The performance of the turbo engine is reduced in any case. This indicates the lower efficiency of the propulsion system over the whole speed range, with a maximum near $n_{\theta\mathrm{LPC}}=90$ percent but decreasing losses at higher power settings. For the COUNTER distortion, the SFC distribution does not show a tendency to lower at higher speeds. Generally, the reason for the progression of the relative SFC with inlet distortion is the loss of thrust in combination with a decrease of LPC efficiency.

If inlet distortions are considered, a higher fuel amount of about 5 percent has to be carried on board for a certain mission, which can reduce the payload dramatically.

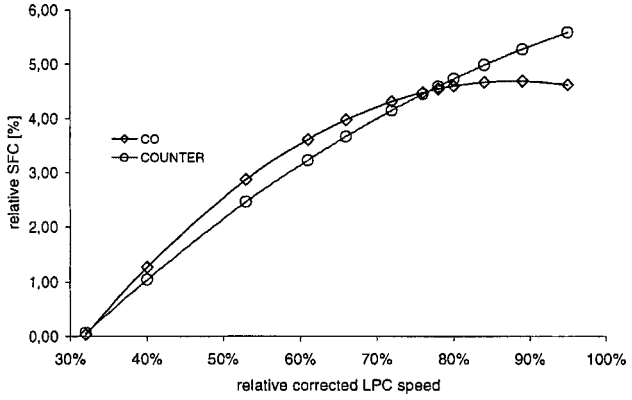

Fig. 9 Relative specific fuel consumption

High-Frequency Measurements. Herein have been presented results of the high-frequency measurements provide a systematic analysis of the data concerning the influence of the swirl direction on LPC rotating stall development. A detailed analysis (temporal and spatial Fourier Transformation, PSD, TWE, and Wavelet Transformation) of the stall inception data is given in [14]. It has been detected that rotating stall develops mainly from so-called spikes. The spikes are precursors of the fully developed stall cells and the elapsed time between the first spike and the rotating stall can be seen as a time of early warning. Depending on the LPC throttling and the distortion intensity, not all spikes lead to rotating stall. Figure 10 shows the position of the high-pressure probes circumferentially installed at the LPC inlet in relation to the distorted flow pattern. The differences of the orientation of the CO and COUNTER distortions are related to the mounting of the simulator in front of the LPC. Therefore the COUNTER flow pattern appears rotated by 180 deg.

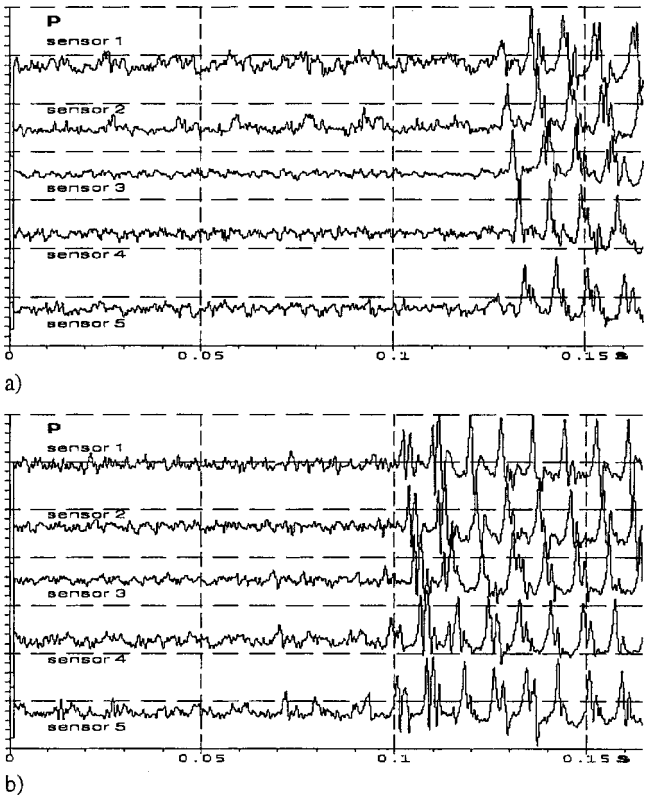

Fig. 11 (*a*) CO and (*b*) COUNTER pressure signals near stall

In the CO case, the spike develops between sensors 5 and 1, where the second total pressure distortion and hence an axial velocity deficit exists, causing higher loads on the first LPC rotor blades due to higher angles of incidence. If the spike gets damped out, this happens only on its way from sensor 2 to sensor 3, where the corotating swirl decreases the incidence angle. This can be seen in Fig. 11(*a*) showing the pressure signals for $n_{\theta\mathrm{LPC}} = 76$ percent with CO distortion, where a spike starts at $t = 0.07$ s at sensor 1 and vanishes between sensors 2 and 3. The damping character of the swirl can be detected in the pressure signal of sensor 3, which is less noisy than the other four signals. If the spike survives the passage through the CO swirl, it grows within one LPC revolution into a rotating stall cell, which is then not damped out anymore. Figure 11(*a*) shows the development of a spike starting at $t = 0.125$ s at sensor 5. One can trace the spike at sensors 1–5 with its intensity growing into rotating stall.

With COUNTER distortion the development of the spikes occurs either between sensors 2 and 3 or sensors 4 and 5, again within a region of low total pressure. Therefore, the mechanism of the spike formation is the same as for the CO distortion. Figure 11(*b*) points out a spike starting at $t = 0.07$ s being amplified by the counterrotating swirl but being damped within the undistorted region near sensor 2 (less noisy signal). If a spike develops near sensor 5 ($t = 0.09$ s) it can get slightly damped on its further way at sensor 2, but the spike is not being damped out and it reappears at sensor 3 reaching the sector of the counterrotating swirl (near sensor 5). The cross-velocity components of the counterrotating swirl then increase the angle of incidence and the spike suddenly grows into a rotating stall cell. Therefore, one can say that rotating stall is triggered by a disturbance passing the counterrotating swirl.

Outlook

The results obtained provide an important database for a gas path analysis modeling the turbo part of the propulsion system. The relationships between intensity and rotating direction of inlet distortion, performance of the compressor and finally thrust performance can then be compared with calculated data. After verifying the calculations, it is possible to simulate the turbo engine and hence the hypersonic propulsion system (intake, turbo and RAM engine, nozzle) over the complete speed range. Then the simulation of the transport system's performance can be calculated, which includes the flight envelopes of design and off-design missions as well as emergency procedures.

Nomenclature

DC = distortion coefficient
SC = swirl coefficient
T_t = total temperature, K
F_s = thrust, N
f = frequency, Hz
$\dot{m}_F$ = fuel mass flow, kg/s
n = rotor speed
p, p_t = static pressure, total pressure, Pa
μ = bypass ratio
ψ = humidity, kg/m^3
ρ = density, kg/m^3
Π = pressure ratio
Δ = difference
$n_{\theta\mathrm{LPC}} = (n_{\mathrm{LPC}}/\sqrt{T}_{t2})_{\mathrm{rel}}$
LPC = low-pressure compressor
HPC = high-pressure compressor
TET = turbine entry temperature
CO = corotating swirl distortion
COUNTER = counterrotating swirl distortion

Subscripts, Superscripts

∞ = free-stream value
mom = momentum-averaged value
max = maximum
loc = local
cross = cross velocities
crit = critical
rel = relative
cor = corrected

References

[1] N.N.: SFB 255, 1998, Transatmosphärische Flugsysteme, *Ergebnisbericht/Finanzierungsantrag 1996–98*, TU-München.
[2] Koelle, D. E., and Kuczera, H., 1990, ''SÄNGER Space Transportation System—Progress Report 1990,'' IAF Paper No. 90–175.
[3] Schwarz, C., Schmid, N. R., and Fottner, L., 1999, ''Model Wind-Tunnel Tests for the Optimisation of the Flow Field Inside the Subsonic Diffuser of an Intake for a Combined Cycle Engine for Hypersonic Flight,'' 7th European Propulsion Forum, Pau, France.
[4] Schwarz, C., 1997, ''Windkanal-Messungen zur Optimierung des Strömungsfeldes im Modell-Einlaufkanal eines Hyperschall-Kombinationstriebwerkes mittels Geometriebeeinflussung im Bereich der Rampen,'' UniBw München, Institut für Strahlantriebe, Diplomarbeit 97/5.2.
[5] Seddon, J., and Goldsmith, E. L., 1985, *Intake Aerodynamics*, Collins Professional Books.
[6] Schmid, N. R., Hildebrandt, Th., and Fottner, L., 1998, ''Numerical Investigations of the Flow Field Inside the Intake Diffuser of a Combined Cycle Engine for Hypersonic Flight,'' *Proc. Fourth European Computational Fluid Dynamics Conference* (ECCOMAS 98), Athens, Greece, Sept.
[7] Wentz, W. H., and Kohlman, D. L., 1969, ''Vortex Breakdown on Slender Sharp-Edged Wings,'' AIAA Paper No. 69–778.
[8] Fischer, F., 1999, ''Erzeugung von für Hyperschallantriebe typischen Eintrittsstörungen mittels geeigneter Simulatoren im Einlaufkanal des Triebwerks LARZAC 04 und Ermittlung des stationären Betriebsverhaltens,'' Diplomarbeit 98/5.8, Institut für Strahlantriebe, UniBw München.
[9] Schmid, N. R., Leinhos, D. C., and Fottner, L., 1999, ''Performance of a Turbofan Engine With Inlet Distortions From the Inlet Diffuser of a Combined Cycle Engine for Hypersonic Flight,'' XIV ISABE, Florence, 5–10 Sept., Italy.
[10] Müller, J.-E., and Fottner, L., 1995, ''Numerical and Experimental Investigation of the Flow Field Inside the Intake Duct of a Combined Cycle Engine for Hypersonic Flight,'' *Symp. on Computational Fluid Dynamics in Aeropropulsion* ASME AD-Vol. 49, pp. 157–168.
[11] Höss, B., Leinhos, D. C., and Fottner, L., 2000, ''Stall Inception in the Compressor System of a Turbofan Engine,'' ASME J. Turbomach., **122**, pp. 32–44.
[12] Herpel, Th., and Fottner, L., 1993, ''A System for Monitoring, Measurement and Analysis of Transient Performance and Stall Phenomena of Gas Turbine Engines,'' IEEE Publication 93CH3199-7.
[13] Stenning, A. H., 1980, ''Rotating Stall and Surge,'' ASME J. Fluids Eng., **102**.
[14] Leinhos, D. C., Schmid, N. R., and Fottner, L., 2001, ''The Influence of Transient Inlet Distortions on the Instability Inception of a Low Pressure Compressor in a Turbofan Engine,'' ASME J. Turbomach., **123**, pp. 1–8.

Implementation of a Compressor Face Boundary Condition Based on Small Disturbances

John W. Slater
John H. Glenn Research Center at Lewis Field,
MS 86-7, 21000 Brookpark Road,
Cleveland, OH 44135
e-mail: john.w.slater@grc.nasa.gov

Gerald C. Paynter
The Boeing Company,
MS 67-LF P.O. Box 3707,
Seattle, WA 98124
e-mail: gerald.c.paynter@boeing.com

A compressor-face boundary condition that models the unsteady interactions of acoustic and convective velocity disturbances with a compressor has been implemented into a three-dimensional computational fluid dynamics code. Locally one-dimensional characteristics along with a small-disturbance model are used to compute the acoustic response as a function of the local stagger angle and the strength and direction of the disturbance. Simulations of the inviscid flow in a straight duct, a duct coupled to a compressor, and a supersonic inlet demonstrate the behavior of the boundary condition in relation to existing boundary conditions. Comparisons with experimental data show a large improvement in accuracy over existing boundary conditions in the ability to predict the reflected disturbance from the interaction of an acoustic disturbance with a compressor.
[DOI: 10.1115/1.1344884]

Introduction

The aerodynamic analysis of the flow in an aircraft inlet for a turbine engine system may involve the analysis of unsteady flow. For example, atmospheric disturbances in pressure or flow angle ingested into a supersonic inlet may interact with the compressor and reflect acoustic waves, which may cause instabilities in the shock system and cause unstart [1].

Acoustic disturbances are changes in pressure that travel at the speed of sound relative to the local fluid velocity. They can travel upstream, as well as downstream. Velocity disturbances are convected at the local fluid velocity, and so, can only travel downstream. Here we are interested in disturbances that travel downstream through the duct, interact with the compressor, and generate an upstream-traveling acoustic disturbance.

The analysis of flows in inlets using computational fluid dynamics generally uses flow domains in which the compressor face is a boundary and some appropriate outflow boundary condition is applied. The alternative is to include the compressor or the entire engine in the flow domain [2]. The latter approach involves considerably more computational resources and is not currently considered practical for design studies.

Several outflow boundary conditions have been used. Since the outflow is subsonic, only one physical quantity needs to be imposed. Most boundary conditions have held a quantity fixed, such as pressure, corrected mass flow [1], Mach number [1,3], or velocity [4]. However, for unsteady flows, such quantities may not be fixed. Experiments have been performed to investigate the unsteady nature of disturbances interacting with compressors [5]. This has led to an analytic study [6]. Paynter has investigated a compressor-face boundary condition that models the unsteady interactions of acoustic [7,8] and convective velocity [4] disturbances with a compressor using locally one-dimensional characteristics along with a small-disturbance model. The reflected acoustic response is computed as a function of the local stagger angle and the strength and direction of the disturbance. Paynter et al. [8] implemented this boundary condition into two one-dimensional codes and demonstrated that it improved the simulation of the response to acoustic disturbances. The current paper addressed the implementation of the Paynter small-disturbance compressor-face boundary condition into the three-dimensional NPARC code [9].

The Paynter small-disturbance compressor-face boundary condition is summarized and an outline is presented of how the boundary condition was implemented. The behavior of the boundary condition is examined in comparison with existing outflow boundary conditions and limited experimental data.

Frames of Reference

The computational fluid dynamic methods operate in a Cartesian (x, y, z) frame of reference. For axial flow compressors, a cylindrical (x, θ, r) frame is useful. At the compressor face, the inlet is assumed to be a constant-area annulus with the axial coordinate denoted as x. The circumferential coordinate θ is coincident with the direction of compressor rotation. The radial coordinate r is perpendicular to the $x-\theta$ surface. A blade-fixed frame has the cylindrical frame rotating with the fan blade.

Summary of the Cascade Computations and the Formulation of a Compressor Model

Paynter and co-workers [7,8] performed two-dimensional, time-accurate Euler flow simulations with step acoustic and convective velocity disturbances interacting with a two-dimensional cascade. The responses were examined with respect to the stagger angle, solidity, axial Mach number, blade loading, blade shape, and disturbance strength. Some of the assumptions and major results are summarized here with respect to the formulation of a model for the compressor face:

1 The compressor face consists of a single row of blades. This is equivalent to saying that all reflected waves are due to interactions with the first stage. Actually, compressors may consists of several stages and waves transmitted through the first stage may reflect from later stages and propagate upstream through the initial stages.

2 The volume of the blade passage is negligible relative to the volume of the annular section of the inlet.

3 The rotational speed of the compressor is constant.

4 The stagger angle Γ of the compressor blade varies linearly in the radial direction,

$$\Gamma(r)=\Gamma_{\text{hub}}+\frac{r-r_{\text{hub}}}{r_{\text{case}}-r_{\text{hub}}}(\Gamma_{\text{case}}-\Gamma_{\text{hub}}). \tag{1}$$

5 $u \gg (v, v_\theta, \tilde{v}_\theta, w, w_r, \tilde{w}_r)$.

Contributed by the International Gas Turbine Institute and presented at the 45th International Gas Turbine and Aeroengine Congress and Exhibition, Munich, Germany, May 8–11, 2000. Manuscript received by the International Gas Turbine Institute February 2000. Paper No. 2000-GT-5. Review Chair: D. Ballal.

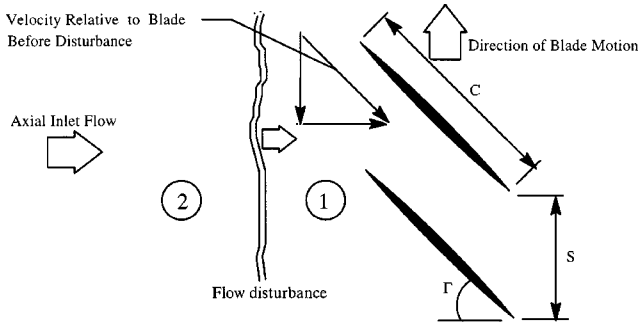

Fig. 1 Flow schematic prior to the disturbance blade passage interaction. The disturbance approaches the blade pair from the left.

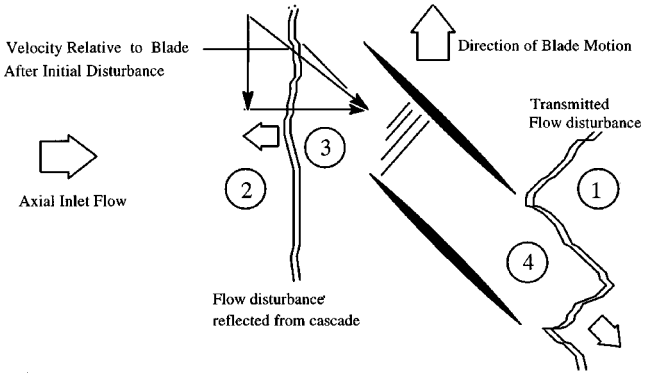

Fig. 2 Flow schematic after the disturbance/blade passage interaction. An acoustic disturbance travels upstream to the left.

6 The flow properties prior to the disturbance are known.

7 Acoustic disturbances propagate axially.

8 Acoustic disturbances yield an acoustic response.

9 Convective axial velocity disturbances are not possible.

10 Convective tangential velocity disturbances are possible and yield an acoustic response. The effect is a local change in the flow angle-of-attack with respect to the compressor blade. The response pressure decreases or increases depending on whether the velocity relative to the blade is increased or decreased, respectively.

11 Convected disturbances are convected axially from the ''adjacent'' to the ''boundary'' grid planes without change.

12 Radial variations in the velocity do not significantly influence the production of the reflected acoustic responses.

13 The response is not a strong function of blade loading; therefore, the compressor blades are assumed to be unloaded. This implies that the flow is attached (unstalled). Further, the compressor blades are assumed to be flat and of zero thickness. Thus, the flow angle is initially aligned with the blades and is equal to the stagger angle. In the blade-fixed frame, the tangential velocity component is then given by

$$\tilde{v}_{\theta cf} = u_{cf} \tan \Gamma \tag{2}$$

This allows the passage Mach number to be determined as

$$\mathrm{M}_{\text{passage}} = \mathrm{M}_{cf} / \cos \Gamma \tag{3}$$

14 The response becomes insensitive to solidity for solidities greater than one. Therefore, the compressor blades are assumed to have a solidity greater than 1.0.

15 If the passage flow is subsonic, the turning of the flow starts at the reflected disturbance and ends well into the blade passage. If the flow is supersonic all of the turning occurs at the reflected disturbance upstream of the blade passage.

16 Four distinct flow regions can be identified and are shown in Figs. 1 and 2. Region 1 is prior to any disturbance. Region 2 is just after the disturbance has passed. Region 3 is between the cascade leading edge and the response. Region 4 is in the blade passage and downstream of the blade passage that is upstream of the transmitted disturbance.

17 A step increase pressure disturbance causes an increase in the axial velocity between regions 1 and 2. The tangential component of velocity is unchanged between regions 1 and 2. For an initially unloaded cascade, this means that the flow in region 2 is no longer aligned with the blade passage. For weak disturbances, the changes in static flow properties between regions 1 and 2 are isentropic. The total properties in a blade frame of reference are different in regions 1 and 2 because the disturbance separates these regions.

18 For a step change in the tangential velocity being convected by the initial axial velocity, the axial velocity and static pressure are unchanged between regions 1 and 2. For an initially unloaded cascade, this means that the flow in region 2 is no longer aligned with the blade passage. Although the static properties are the same in regions 1 and 2, the total properties are different because of the change in velocity.

19 The tangential component of velocity is unchanged across the left running acoustic disturbance. Since only the axial component of velocity is changed, the reflected disturbance is a plane wave. The changes in static properties across the reflected disturbance are isentropic.

Acoustic Response Coefficient

The acoustic response coefficient is defined as

$$\beta \equiv (p_3 - p_2)/(p_2 - p_1). \tag{4}$$

Paynter [4] and Sajben [6] have each developed an expression for the acoustic response coefficient for the response from a compressor face for a small step acoustic disturbance. Both approaches derive the response coefficient by forming a system of linear equations *based on the continuity*, *momentum*, and *energy* equations and using the small-disturbance and isentropic assumptions along with the characteristic relations of the one-dimensional flow.

Paynter's acoustic response coefficient depends on whether the Mach number in the blade passage is subsonic or supersonic. For subsonic passage flow ($\mathrm{M}_{\text{passage}} < 1$),

$$\beta(\mathrm{M}_{cf}, \Gamma) = \tan^2\left(\frac{\Gamma}{2}\right)\left(\frac{1+\mathrm{M}_{cf}}{1-\mathrm{M}_{cf}}\right). \tag{5}$$

For supersonic passage flow ($\mathrm{M}_{\text{passage}} > 1$),

$$\beta(\mathrm{M}_{cf}, \Gamma) = 1.0. \tag{6}$$

Sajben's acoustic response coefficient is

$$\beta(\mathrm{M}_{cf}, \Gamma) = \left(\frac{1+\mathrm{M}_{cf}}{1-\mathrm{M}_{cf}}\right)\left(\frac{\mathrm{M}_{cf} \tan^2 \Gamma}{2(1+\mathrm{M}_{cf}) + \mathrm{M}_{cf} \tan^2 \Gamma}\right) \tag{7}$$

One can obtain a nonreflective condition by imposing $\beta = 0.0$. When $\beta = -1.0$, one recovers the constant-pressure boundary condition. When $\beta = 1.0$, one recovers a constant-velocity boundary condition.

Convective Velocity Response Coefficient

The convective velocity response coefficient is defined as

$$\alpha \equiv \frac{(p_3 - p_2)/p_1}{(v_{\theta 2} - v_{\theta 1})/v_{\theta 1}} \tag{8}$$

Paynter [4] has developed a velocity response coefficient using methods similar to those for the acoustic response coefficient. Since axial velocity disturbances result in axial acoustic distur-

bance, we consider here only step circumferential velocity disturbances, δv_θ. Thus the static pressure, static temperature, and axial velocities all remain unchanged.

The expression for the velocity response coefficient $\alpha(M_{cf},\Gamma)$ is dependent on whether the Mach number of the flow into the blade passage is subsonic or supersonic. For subsonic passage flow ($M_{passage}<1$),

$$\alpha(M_{cf},\Gamma)=\frac{\gamma M_{cf}^2}{1-M_{cf}}\tan\left(\frac{\Gamma}{2}\right)\tan\Gamma \tag{9}$$

For supersonic passage flow ($M_{passage}>1$),

$$\alpha(M_{cf},\Gamma)=\gamma M_{cf} \tag{10}$$

Small Disturbance Boundary Condition

The two central ideas of the Paynter small-disturbance boundary condition are that both acoustic and convective velocity disturbances result in upstream-propagating acoustic responses, and that the acoustic responses are a simple linear combination of the individual responses due to acoustic and convective disturbances. Thus, a simple time difference can be applied to the static pressure at the boundary with respect to the linear combination of responses,

$$p_b^{n+1}=p_b^n+\delta p_{acoustic}+\delta p_{convective}. \tag{11}$$

The response due to an acoustic disturbance is

$$\delta p_{acoustic}=\sigma[1+\beta(M_{cf},\Gamma)](p_a^n-p_b^n). \tag{12}$$

The subscript a denotes the solution point adjacent to the boundary in the direction normal to the boundary. The σ is the local Courant number,

$$\sigma=(u+a)_b\frac{t^{n+1}-t^n}{x_b-x_a}. \tag{13}$$

The time step is chosen such that $\sigma<1.0$ at the boundary.

The response due to a convective velocity disturbance is

$$\delta p_{convective}=-\alpha(M_{cf},\Gamma)\sigma\left(\frac{M_{xb}^n}{M_{xb}^n+1}\right)\frac{p_b^n(v_{\theta a}^n-v_{\theta b}^n)}{U_{cf}\tan\Gamma+v_{\theta b}^n} \tag{14}$$

The M_{xb} is the local axial Mach number at the boundary,

$$M_{xb}=u_b/a_b. \tag{15}$$

Analogous to Eq. (11), the axial velocity can be expressed as,

$$u_b^{n+1}=u_b^n+\delta u_{acoustic}+\delta u_{convective} \tag{16}$$

where

$$\delta u_{acoustic}=\frac{a_b^n[1-\beta(M_{cf},\Gamma)]}{\gamma p_b^n[1+\beta(M_{cf},\Gamma)]}\delta p_{acoustic} \tag{17}$$

and

$$\delta u_{convective}=-\frac{a_b^n}{\gamma p_b^n}\delta p_{convective} \tag{18}$$

Implementation of the Boundary Condition

The implementation of the boundary condition into the NPARC code required that the conservative variables $(\rho,\rho u,\rho v,\rho w,\rho e)$ be computed at each grid point on the boundary at each time step. The computational requirements were no greater than required for other outflow boundary conditions in NPARC. The steps of the implementation include:

1 Properties (p,ρ,u,v,w,a,M) are computed at the ''boundary'' and ''adjacent'' grid points for the nth time level.
2 The stagger angle is computed using Eq. (1).
3 The local Courant number is computed using Eq. (13).
4 The passage Mach number is computed using Eq. (3).
5 The convective velocity response coefficient $\alpha(M_{cf},\Gamma)$ is computed using either Eq. (9) or (10).
6 The Cartesian velocity components are transformed to the fixed cylindrical frame of reference.
7 The $\delta p_{convective}$ is computed using Eq. (14).
8 The acoustic response coefficient β is computed using Eq. (5) or (6).
9 The $\delta p_{acoustic}$ is computed using Eq. (12).
10 The pressure at the new time level is computed using Eq. (11).
11 The density at the new time level is computed as

$$\rho_b^{n+1}=\rho_b^n+\frac{1}{(a_b^n)^2}(p_b^{n+1}-p_b^n)+\left(\frac{\sigma M_{xb}^n}{M_{xb}^n+1}\right)\left[\frac{\rho_b^n}{\gamma p_b^n}(p_b^n-p_a^n)-(\rho_b^n-\rho_a^n)\right]. \tag{19}$$

12 The axial velocity component at the new time level is computed using Eq. (16).
13 The cylindrical velocity components in the fixed frame for the new time level are computed as

$$v_{\theta b}^{n+1}=v_{\theta b}^n+\sigma\left(\frac{M_{xb}^n}{M_{xb}^n+1}\right)(v_{\theta a}^n-v_{\theta b}^n). \tag{20}$$

and

$$w_{rb}^{n+1}=w_{rb}^n+\sigma\left(\frac{M_{xb}^n}{M_{xb}^n+1}\right)(w_{ra}^n-w_{rb}^n). \tag{21}$$

14 The velocity components in the fixed cylindrical frame are transformed back into the fixed Cartesian frame.
15 The total energy for the new time level is computed as

$$(\rho e)_b^{n+1}=(\rho e)_b^n+\frac{(p_b^{n+1}-p_b^n)}{\gamma-1}+\frac{(u_b^n)^2}{2}(\rho_b^{n+1}-\rho_b^n)+(\rho u)_b^n(u_b^{n+1}-u_b^n). \tag{22}$$

16 The procedure is repeated for each boundary grid point.

Results

The following results demonstrate the behavior of the Paynter small-disturbance compressor-face boundary condition in relation to other boundary conditions with comparisons to the limited experimental data for interactions with compressors.

Step Disturbances in a Straight Duct. This case examined the unsteady, inviscid flow in a straight, annular duct created when downstream-traveling step disturbances interact with the outflow boundary modeled with various outflow boundary conditions. The compressor was assumed to have fan blades with stagger angles varying from 45 deg at the hub to 60 deg at the case. The steady-state compressor-face Mach number was 0.2.

The acoustic disturbance was imposed by initializing the flow field in the first quarter of the duct with a +10 percent step pressure perturbation. The step propagated downstream as a pure acoustic wave. Figure 3 shows the response at a sensor located at the three-quarters axial location for the various boundary conditions. At approximately $t=0.62$ ms, the incident wave reached the sensor and the static pressure steped up 10 percent. Some ''ringing'' or ''oscillation'' was noticed, which is due to numerical dispersion. The wave passed by, interacted with the compressor face and the reflected, upstream-traveling wave reached the sensor at approximately $t=1.43$ ms. The different behavior of the various boundary conditions became apparent at that time and agreed quite well with the expected behavior. The constant-pressure boundary condition resulted in an expansion wave that canceled out the incident wave. The nonreflective boundary condition ($\beta=0$) show that the incident wave exited the outflow boundary. The time histories for the Chung–Cole and Mayer–Paynter constant-Mach number boundary conditions show the correct sign for the reflected response with a magnitude approximately equal

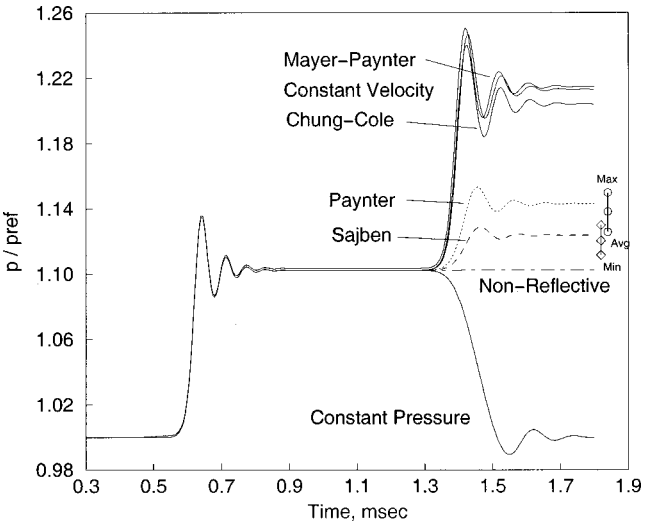

Fig. 3 Time history of the static pressure for a +10 precent step pressure perturbation in a straight annular duct

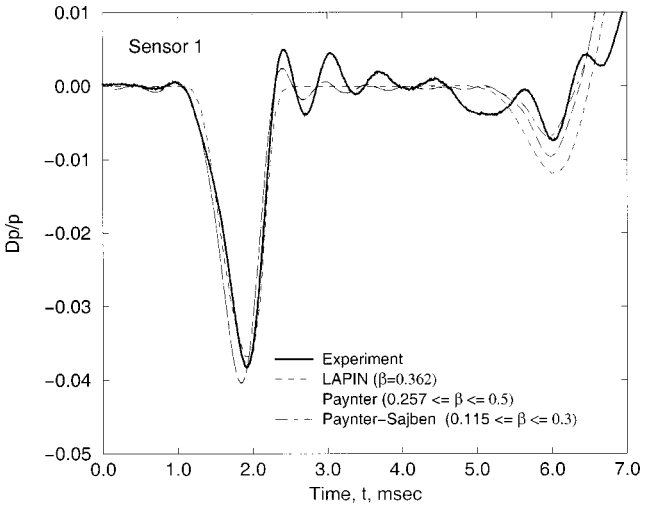

Fig. 5 The time histories of the pressure at sensor 1 for the Paynter small-disturbance boundary condition

to that of the disturbance. Similar results were obtained with the constant-velocity boundary condition ($\beta=1$). The plot shows the Paynter small-disturbance boundary condition predicting a response of about 4 percent of the steady-state pressure. The plot labeled ''Sajben'' is Paynter's small-disturbance boundary condition using Sajben's acoustic response coefficient (Eq. (7)).

The radial variation of the acoustic response coefficient β for a given compressor-face Mach number can be calculated using Eqs. (5) or (7) along with Eq. (1). If one evaluates the response coefficient for the minimum, area-weighted average, and maximum stagger angles, one obtains the vertical lines presented at the right in Fig. 3. The Paynter expression (Eq. (5)) predicts a stronger response than the Sajben expression (Eq. (7)) and its overall response is dominated by the higher stagger angles.

The responses of the boundary conditions to circumferential velocity perturbations of +10 percent and −10 percent of the axial velocity are presented in Fig. 4. The disturbance reached the sensor at a time of $t=3.7$ ms; however, nothing was observed since no acoustic disturbance is created by the velocity disturbance. At a time of $t=6.1$ ms the reflected upstream-traveling acoustic wave reached the sensor. Only the Paynter small-disturbance boundary condition gave a response. The magnitude of the reflected response was quite small at less than 0.4 percent which agreed well with the response predicted by Eq. (9).

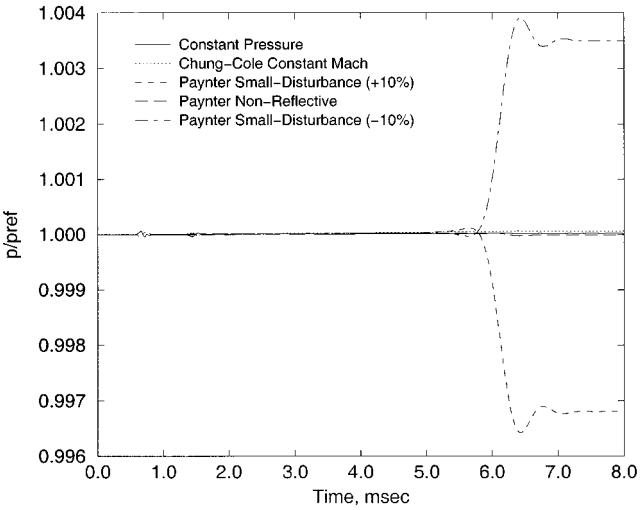

Fig. 4 Time history of the static pressure for ±10 percent step circumferential velocity perturbations

UC Compressor Face Experiment. The experiment by Freund and Sajben [6] provides the limited experimental data for the interaction of an acoustic pulse with a compressor. The configuration consisted of a straight, annular duct connected to a General Electric T58-3 engine by a short convergent section. The blades of the first stage of the compressor had a stagger angle of 45 deg at the hub and 60 deg at the case. The Mach number at the compressor face was 0.2. A planar acoustic pulse was generated by the rapid collapse of a flexible boot located on the hub of the duct. Four sensors along the duct between the boot and the compressor measured the time history of the static pressure. Sensor 1 is located closest to the bump and sensor 4 is closest to the compressor.

The experiment has been simulated by Paynter et al. [8] using the LAPIN unsteady, quasi-one-dimensional flow code along with the Paynter small-disturbance boundary condition. Comparisons were made to other outflow boundary conditions. Suresh et al. [2] simulated the experiment by coupling NPARC with the ADPAC turbomachinery code.

The present work simulated the experiment using NPARC while assuming unsteady, inviscid flow and using dynamic grids to simulate the collapsing bump. The Newton iterative implicit method was used with a constant physical time step of 3.0E-06 seconds, which corresponded to a local Courant number of approximately 0.9.

Figures 5–7 show the time histories of the static pressures at sensors 1, 2, and 3 for the 7.0 ms span beginning when the bump starts to collapse. The lines denoted as ''Paynter'' used Eq. (5) for the acoustic response coefficient, β, while the lines denoted as ''Paynter–Sajben'' used Eq. (7). The ranges of values for β are indicated in Fig. 5. Also plotted are the experimental data and LAPIN results. The LAPIN results were computed using an updated version, which modeled more accurately the bump collapse and used a $\beta=0.362$ based on $\Gamma=52$ deg and $M_{cf}=0.2067$. Figure 8 shows the time histories at sensor 2 for the Chung–Cole, Mayer–Paynter, and the constant-velocity boundary conditions. The time history for the constant-pressure boundary condition is not presented, but gave an incorrect response of opposite sign with a magnitude equal to the incident pulse. The time history for the nonreflective is also not presented, but gave a slight response of the correct sign; however, this response was due to the converging duct at the compressor face.

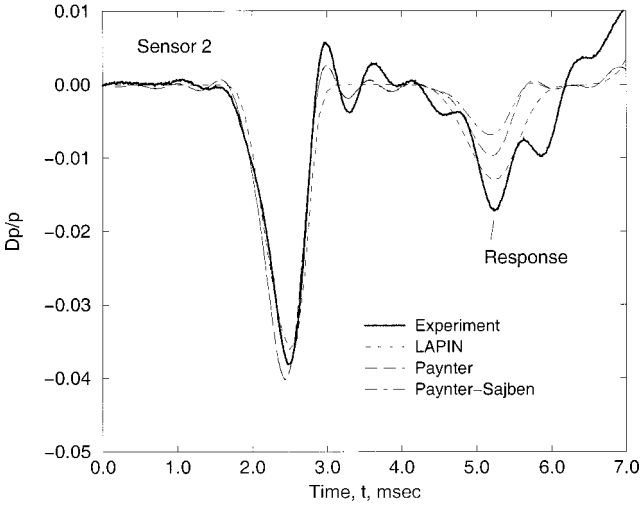

Fig. 6 The time histories of the pressure at sensor 2 for the Paynter small-disturbance boundary condition

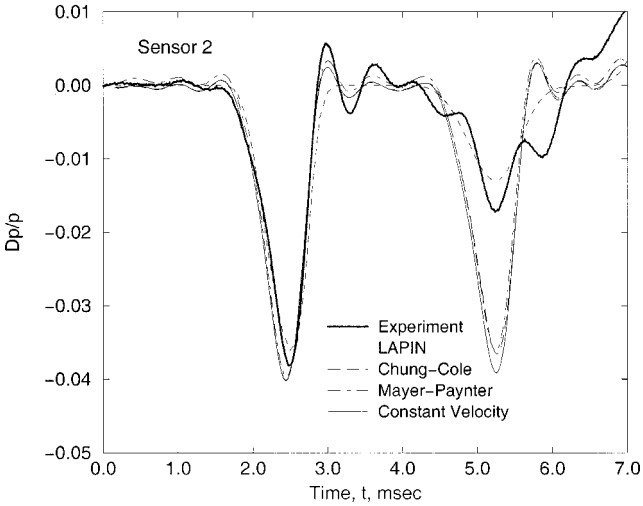

Fig. 8 The time histories of the pressure at sensor 2 for the Chung–Cole, Mayer–Paynter, and constant-velocity boundary conditions

The plots show the acoustic pulse with a magnitude approximately 4 percent of the initial steady-state pressure moving downstream. The initial bump height and collapse time were adjusted in the simulations, so that the acoustic pulse matched the observed pulse. The pulse interacted with the compressor face and a reflected acoustic response was generated with an amplitude of approximately 1.5 percent of the initial steady-state pressure. In Fig. 6, the reflected response is seen at approximately $t=5.3$ ms. If one sequences through the plots from sensor 3 to sensor 1, one can see the reflected response traveling upstream (occurring later in time). The Paynter small-disturbance boundary condition underpredicts the magnitude of the response; however, the reflected response from currently existing boundary conditions, as shown in Fig. 8, grossly overpredicts the magnitude, which is approximately equal to the magnitude of the pulse. The comparisons with the experiment suffer because the simulations do not account for the initial guide vanes or later stages of the compressor, which influence the size and shape of the reflected response.

NASA Variable Diameter Centerbody Inlet. Simulations of the unsteady, inviscid flow in the NASA variable diameter centerbody inlet [10,11] demonstrate the sensitivity of the outflow boundary conditions in predicting terminal shock motion and tolerance to unstart. The inlet is an axisymmetric, mixed-compression inlet designed for Mach 2.5. A normal terminal shock is located aft of the throat. The steady-state flowfield was computed using NPARC with the Chung–Cole boundary condition imposing a compressor-face Mach number of 0.31.

The unsteady flow was initiated by a -4 percent step disturbance in the free-stream pressure. Figure 9 shows the time history of the axial position of the terminal shock. The shock moved forward as the disturbance passed downstream. The disturbance interacted with the compressor face and an upstream-traveling, acoustic wave was created, which then interacted with the shock. The constant-pressure boundary condition created a compression wave, which results in excessive shock motion with eventual unstart. The Paynter small-disturbance and the Chung–Cole constant-Mach number boundary conditions created reflected expansion waves as the response. The constant-Mach boundary condition created the stronger response, which results in less forward motion of the shock. Paynter et al. [8] observed this in the one-dimensional analyses and showed that the behavior became more

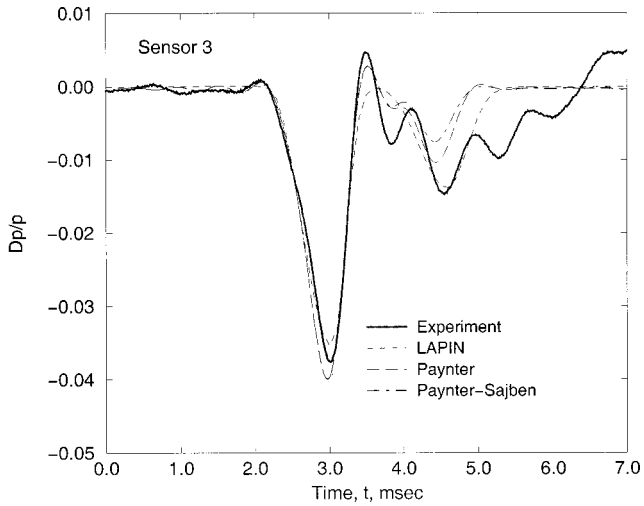

Fig. 7 The time histories of the pressure at sensor 3 for the Paynter small-disturbance boundary condition

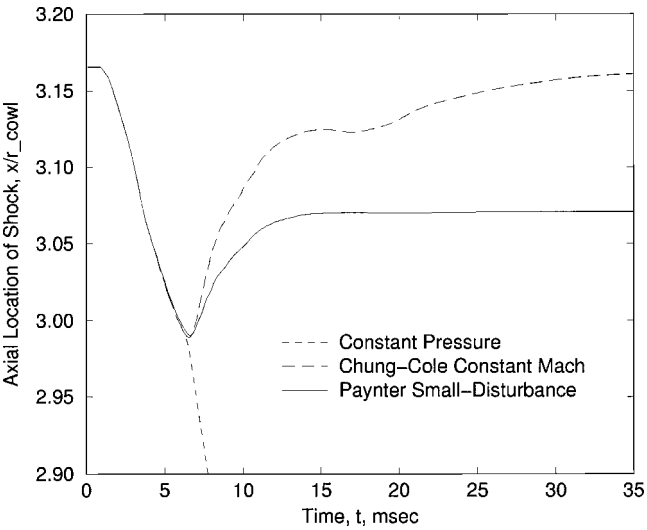

Fig. 9 The time histories of the terminal shock position subject to a free-stream pressure disturbance

apparent with stronger disturbances. The result was that the constant-Mach boundary condition would incorrectly overestimate the unstart tolerance.

Concluding Remarks

The Paynter small-disturbance compressor-face boundary condition was implemented into a three-dimensional computational fluid dynamics code and demonstrated a marked improvement over existing boundary conditions in predicting the response to unsteady acoustic and convective velocity disturbances interacting with a compressor face.

Acknowledgments

The authors would like to thank Mr. Gary L. Cole of the NASA Glenn Research Center and Professor Miklos Sajben of the University of Cincinnati for important insights and corrections to this work. Mr. Cole also provided the LAPIN results.

Nomenclature

C = chord of the compressor fan blade
M = Mach number
S = circumferential spacing of compressor blades
u = desired axial velocity at compressor face
a = acoustic speed
e = specific internal energy
p = static pressure
r = radial coordinate
t = time
u, v, w = cartesian velocity components
u, w_r, v_θ = velocity components in fixed frame
$u, \tilde{w}_r, \tilde{v}_\theta$ = velocity components in blade frame
x, y, z = Cartesian coordinates
α = convective velocity response coefficient
β = acoustic response coefficient
γ = ratio of specific heats; $\gamma = 1.4$ for air
Γ = stagger angle
δ = small discrete difference
θ = circumferential cylindrical coordinate
ρ = density
σ = local Courant number

Subscripts/Superscripts

a = solution point adjacent to boundary
acoustic = component due to acoustic disturbance
b = solution point at boundary
case = location on case
convective = component due to convective disturbance
cf = compressor face
hub = location on hub
n = time level for known state
$n+1$ = time level for new state
passage = conditions within the blade passage
r = radial
x = axial
θ = circumferential

References

[1] Mayer, D. W., and Paynter, G. C., 1994, ''Boundary Conditions for Unsteady Supersonic Inlet Analyses,'' AIAA J., **32**, No. 6, pp. 1200–1206.
[2] Suresh, A., Townsend, S. E., Cole, G. L., Slater, J. W., and Chima, R., 1999, ''Analysis of Inlet-Compressor Acoustic Interactions Using Coupled CFD Codes,'' AIAA Paper No. 99-0749.
[3] Chung, J. K., and Cole, G. L., 1995, ''Comparison of Compressor Face Boundary Conditions for Unsteady CFD Simulations of Supersonic Inlets,'' AIAA Paper No. 95–2627.
[4] Paynter, G. C., 1998, ''Modeling the Response From a Cascade to an Upstream Convective Velocity Disturbance,'' AIAA Paper No. 98–3570.
[5] Freund, D. D. and Sajben, M., 1997, ''Reflection of Large Amplitude Acoustic Pulses from an Axial Flow Compressor,'' AIAA Paper No. 97–2879.
[6] Sajben, M., 1999, ''Prediction of Acoustic, Vorticity, and Entropy Waves Generated by Short-Duration Acoustic Pulses Incident on a Blade Row,'' ASME Paper No. 99-GT-148.
[7] Paynter, G. C., 1997, ''Response of a Two-Dimensional Cascade to an Upstream Disturbance,'' AIAA J., **35**, No. 3, pp. 434–440.
[8] Paynter, G. C., Clark, L. T., and Cole, G. L., 1998, ''Modeling the Response From a Cascade to an Upstream Acoustic Disturbance,'' AIAA J., **38**, No. 8, pp. 1322–1330.
[9] Chung, J., Slater, J. W., Suresh, A., and Townsend, S. E., 1999, ''NPARC v3.1 User's Guide,'' NASA TM-1999-209058.
[10] Wasserbauer, J. F., Shaw, R. J., and Neumann, H. E., 1975, ''Design of a Very-Low-Bleed Mach 2.5 Mixed-Compression Inlet With 45 Percent Internal Contraction,'' NASA TM X-3135.
[11] Shapiro, A. H., 1954, *The Dynamics and Thermodynamics of Compressible Fluid Flow*, Ronald Press Company, New York.

Natural Transition Phenomena on an Axial Compressor Blade

J. D. Hughes[1]

G. J. Walker

School of Engineering,
University of Tasmania,
Hobart, Australia

Data from a surface hot-film array on the outlet stator of a 1.5-stage axial compressor are analyzed to look for direct evidence of natural transition phenomena. An algorithm is developed to identify instability waves within the Tollmien–Schlichting (T–S) frequency range. The algorithm is combined with a turbulent intermittency detection routine to produce space-time diagrams showing the probability of instability wave occurrence prior to regions of turbulent flow. The paper compares these plots for a range of blade loading, with free-stream conditions corresponding to the maximum and minimum inflow disturbance periodicity produced by inlet guide vane clocking. Extensive regions of amplifying instability waves are identified in nearly all cases. The implications for transition prediction in decelerating flow regions on axial turbomachine blades are discussed.
[DOI: 10.1115/1.1351816]

Introduction

It is well known that the boundary layers of blades of an embedded row in a multi-stage axial turbomachine are dominated by the effect of the adjacent upstream stage. The unsteady laminar–turbulent transition behavior under these conditions is largely controlled by periodic transition induced by the relative motion of blade wakes from the row immediately upstream; this is commonly referred to as wake-induced transition. Transition by other modes is observed in regions between wake-induced transitional or turbulent strips. Mayle [1,2] refers to this phenomenon as ''multi-mode'' transition. The overall morphology of unsteady transition behavior for compressors and turbines is well documented by the extensive set of observations reported by Halstead et al. [3].

The three important processes identified by Mayle [1] in his review of laminar–turbulent transition in gas turbines are:

- Natural transition
- Bypass transition
- Separated flow transition

Both Halstead et al. [3] and Mayle [1] provide detailed discussions of these phenomena.

The natural transition process, which occurs under conditions of very low free-stream turbulence level, can be divided into four main regions:

1. A region of instability to small two-dimensional disturbances (T–S waves). The onset of instability and the initial growth of T–S waves are well described by linearized theory.
2. The appearance of three-dimensional instability, which produces periodic spanwise flow distortions. This introduces streamwise vorticity and causes a rapid non-linear amplification of the spanwise waves into vortex loops (hairpin eddies or lambda vortices).
3. The initiation of turbulent spots (or ''breakdowns'') through the appearance of high frequency fluctuations in regions of high shear near the heads of the vortex loops.
4. A transition zone in which adjacent turbulent spots merge to form a continuously turbulent flow.

Bypass transition, as described by Mayle [1], ''...is caused by large disturbances in the external flow (such as free-stream turbulence) and completely bypasses the Tollmien–Schlichting mode of instability.'' Turbulent spots are then ''...directly produced within the boundary layer under the influence of the free-stream disturbances.'' Mayle concluded that linear stability theory would be irrelevant in the case of bypass transition. However, Walker [4] took a contrary view, arguing that stability theory should at least be of relevance in relation to the length of transitional flow in the bypass mode.

Basic experiments on artificially generated turbulent spots such as those of Tso et al. [5], Breuer and Haritonidis [6], Breuer and Landahl [7], and Cohen et al. [8] show that stages 1–2 of natural transition (as defined above) are not necessarily absent from transitional flows generated by external disturbances. Perturbations of the boundary layer by a pulsed jet or surface membrane produce a combination of transient and three-dimensional wave packet disturbances. For weak initial disturbance amplitudes, the transient component decays; turbulent breakdown occurs well downstream of the initial disturbance location after the wave packet has been sufficiently amplified; the initial wave packet growth is well described by linear stability theory. For strong initial disturbance amplitudes, the transient component grows rapidly and turbulent breakdown occurs almost immediately.

The above-mentioned experiments were conducted under zero pressure gradient conditions. Gostelow et al. [9] studied artificially generated turbulent spots under a pressure gradient representative of a controlled diffusion airfoil with low-free-stream turbulence levels. The introduced wave packet showed strong amplification of instabilities in the T–S frequency range prior to the development of a turbulent spot. Wave packets attending the turbulent spot were also observed.

Grek et al. [10] made comparative studies of transition in varying pressure gradient on an isolated airfoil under conditions of high (1.75 percent) and low (0.04 percent) free-stream turbulence with artificial disturbances introduced by a vibrating ribbon. They observed T–S waves with a linear development at the high turbulence level. In this case, the boundary layer eigenoscillations (T–S waves, wave packets, and turbulent spots) were the same as those excited under low free-stream turbulence conditions. However, under the high free-stream turbulence, the boundary layer structures were scattered in time and space with different intensity and phase.

By introducing controlled oscillations with a vibrating ribbon, Boiko et al. [11] were able to demonstrate that T–S waves can exist and develop in a zero pressure gradient boundary layer subjected to a free-stream turbulence intensity of 1.5 percent. Lewalle et al. [12] used wavelet-based techniques to analyze data for a boundary layer subjected to 1.1 percent nominal free-stream turbulence level. They tentatively identified events characteristic of T–S wave frequencies in the neighborhood of turbulent spots.

[1]Present address: Rolls-Royce plc, Derby, England.

Contributed by the International Gas Turbine Institute and presented at the 45th International Gas Turbine and Aeroengine Congress and Exhibition, Munich, Germany, May 8–11, 2000. Manuscript received by the International Gas Turbine Institute February 2000. Paper No. 2000-GT-264. Review Chair: D. Ballal.

Various workers have identified natural transition mechanisms in flows representative of turbomachinery. Dong and Cumpsty [13] investigated unsteady flow transition in a large-scale two-dimensional compressor cascade with moving blade wakes simulated by bar passing. They observed T–S wave activity in the regions between wake-induced turbulent events when the flow returned to a separated laminar state. Similar results for the development of the unsteady suction surface boundary layer of a highly loaded LP turbine airfoil in a rectilinear cascade were presented by Schulte and Hodson [14]. Dring et al. [15] identified T–S waves in the decelerating flow region on the stator suction surface of a single stator/rotor turbine stage. Identification of T–S wave activity in these experiments all occurred when the background turbulence level between passing wakes was below 0.9 percent.

Studies of transition under conditions representative of an embedded axial turbomachine blade row are rare. The definitive investigation of Halstead et al. [3] provided extensive data from surface film arrays on a third-stage compressor stator and second-stage turbine stator. These workers claimed no evidence of T–S waves. Solomon and Walker [16], however, noted some evidence of T–S wave activity from raw surface film traces on the outlet stator of a 1.5-stage axial compressor under essentially similar conditions.

Solomon et al. [17] used the MISES code of Youngren and Drela [18] in a quasi-steady manner to predict transition onset on an axial compressor stator blade over a rotor passing period. Parallel computations for natural transition, with modification for free-stream turbulence level according to the correlation of Mack [19], and bypass transition indicated that the natural transition mode tended to dominate for the compressor blade. The success of these transition onset predictions provided strong circumstantial evidence for the importance of natural transition mechanisms in strongly decelerating flow on an axial compressor blade.

The present paper applies wavelet analysis and filtering techniques to directly identify wave activity characteristic of viscous instability in surface film data from the compressor blade investigated by Solomon et al. [17]. Significant evidence for T–S waves is found, and quantitative data on their probability of occurrence are produced. The results further support the transition prediction method adopted by Solomon et al. [17]; they indicate that linear stability theory remains important for transition in an adverse pressure gradient, even with free-stream turbulence levels as high as 8 percent. This challenges the conventional view that transition at such elevated disturbance levels should occur entirely in a bypass mode.

Experimental Detail

Research Compressor. The compressor is a 1.5-stage axial flow machine with three blade rows: inlet guide vanes (IGV), rotor and stator. Figure 1 shows a cross section of the compressor blading at midpassage. There are 38 blades in each of the stationary rows and 37 blades in the rotor, giving space/chord ratios at midblade height of 0.99 and 1.02, respectively. The blades are all of British C4 section with a constant chord of 76.2 mm and an aspect ratio of 3.0. The blade sections were designed for free vortex flow with 50 percent reaction at midblade height at a flow coefficient ($\phi = V_a / U_{mb}$) of 0.76. The design values of inlet and outlet blade angles from axial at midblade height are, respectively: IGV—0.0 deg, 27.8 deg; rotor and stator—45.0 deg, 14.0 deg. However, for these tests the rotor was restaggered by 2.0 deg to give blade angles of 43.0 and 12.0 deg with a resultant increase in stalling flow coefficient.

The IGV and stator rows are each mounted on rotatable supporting rings to permit circumferential traversing of these blades relative to a stationary probe or clocking of one row relative to the other. The spacing between blade rows is large when compared with modern gas turbine engines, but the increased axial gap allows for detailed measurements of the IGV-rotor wake interaction downstream of the rotor row. The large axial spacing also tends to isolate the stator row from interactions associated with the passing rotor potential field, but similar boundary layer transition results have been obtained for test cases with reduced rotor–stator blade row spacing. Further details of the research compressor can be found in Walker [20], Solomon [21], and Walker et al.[22].

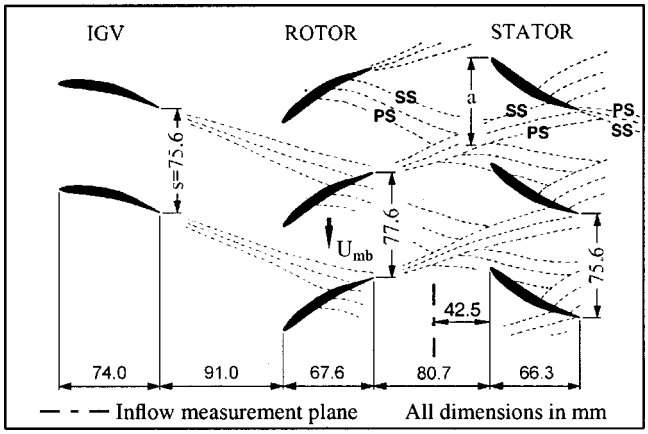

Fig. 1 Cross section of compressor blading at midblade height, showing typical instantaneous wake dispersion: SS =suction side, PS=pressure side, *a*=circumferential offset of stator leading edge from center of IGV wake street.

Range of Investigation. All measurements were conducted at midspan, where radial flows are small. Data were obtained for flow coefficients ($\phi = V_a / U_{mb}$) of 0.600, 0.675, and 0.840. These correspond, respectively, to stator midspan incidence values of 4.1 deg, 1.2 deg, and −6.1 deg, which will be referred to as high, medium, and low loading cases. The medium loading case is close to the Howell [23] nominal incidence value of 0.6 deg.

The corresponding surface velocity distributions obtained from midspan surface pressure tappings are shown in Fig. 2. For the high and medium loading cases, the peak suction surface velocity occurs closer than 5 percent chord from the leading edge, with a roughly linear deceleration over the whole surface. At low loading, the suction surface distribution exhibits a plateau, which peaks much farther rearward near 30 percent chord; a discontinuity in velocity gradient around 70 percent chord clearly indicates the development of a midchord laminar separation bubble.

The range of behavior encompasses the design condition for modern high-pressure compressor airfoils, which typically exhibit a well-rounded suction peak around 20 percent chord. (See the

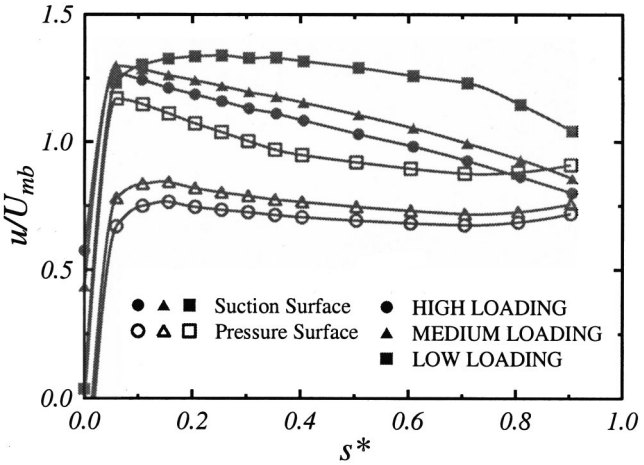

Fig. 2 Variation of stator blade surface velocity distribution with loading at midblade height: Re_{ref}=120,000

Table 1 Stator operating conditions at midblade height

Loading	ϕ (V_a/U_{mb})	i (°)	Re_1	Tu_s (%)	Tu_{D_s} (%)
High	0.600	4.1	110000	3.15	5.39
Medium	0.675	1.2	117000	2.27	3.75
Low	0.840	-6.1	130000	2.03	3.07

baseline compressor case 2B reported by Halstead et al. [3].) The suction surface velocity distribution for the high-loading case of the present investigation is quite similar to that for the near-stall case of Halstead et al. [3]. Hence the present study should also give a useful indication of the importance of unsteady flow effects for modern compressor blade sections operating at off-design conditions.

The stator pressure surface velocity distributions all show a deceleration over the forward part of the blade, followed by an acceleration toward the trailing edge. The deceleration is very mild for the high loading case, but strengthens progressively as incidence is decreased. For the low loading case, the velocity gradient becomes severe enough to cause a leading edge laminar separation bubble.

A constant reference Reynolds number of $Re_{ref}=120{,}000$ was used for all tests. This gives stator inlet Reynolds numbers of $Re_1=110{,}000$, 117,000, and 130,000 for the high, medium, and low loading cases. These values are low compared with inlet Reynolds numbers, $Re_1 \geqslant 600{,}000$, typical of aircraft gas turbine engine operation as reported by Hourmouziadis [24]. They are also lower than the inlet Reynolds number, $Re_1=245{,}000$ (baseline case 2B), for the third-stage stator of the experimental studies of Halstead et al. [3]. The test compressor was nevertheless operating above the critical Reynolds number range where laminar separation starts to cause a significant increase in blade losses (see [25]). As discussed by Solomon [21], the critical Reynolds number for the test machine is lower than that for modern compressors because of the generally milder pressure gradients on the suction surface of C4 blading. Surface hot-film observations on the stator blading reported by Solomon and Walker [16,26] show essentially similar behavior to that in the higher Reynolds number multistage compressor experiments of Halstead et al. [3].

The influence of IGV clocking on the stator boundary layer transition behavior was investigated for $a/S=0.00$ and 0.50. The coordinate a is the circumferential distance of the stator leading edge from the center of the avenue of dispersed IGV wake segments, as shown in Fig. 1. These two clocking positions correspond approximately to the cases of minimum and maximum rotor wake periodicity experienced by the stator blade element at midblade height (as indicated by measurements of the temporal variation of ensemble-averaged stator wake momentum thickness reported by Walker et al. [27]).

Operating conditions for the stator at midblade height are summarized in Table 1. The method used for separating the random disturbance (turbulence), Tu, and periodic unsteadiness, $\widetilde{Tu}$, components from the total disturbance Tu_D is similar to that of Evans [28], and details are given by Walker et al. [22]. The turbulence values in Table 1 are circumferentially averaged values, whereas Fig. 3 provides more detailed information on the variation of ensemble-averaged turbulence level $\langle Tu \rangle$ (percent) on the stator stagnation streamline for the blade loading and clocking cases examined. The peak value of $\langle Tu \rangle$ around 8 percent is always observed within passing rotor wake regions.

Measurement Techniques. The compressor and measurement systems were controlled by two IBM-compatible 486 personal computers. One computer was used to control the compressor and acquire data from slow response instrumentation. The other was used for high-speed data acquisition from the hot-wire and hot-film anemometers. Operating speeds at $Re_{ref}=120{,}000$ were typically 500 rpm, and the compressor speed was continuously adjusted with a speed setting accuracy of ± 0.1 rpm to maintain constant Reynolds number. The throttle setting was left unchanged for an individual flow traverse, after setting the desired flow coefficient prior to the start of measurement.

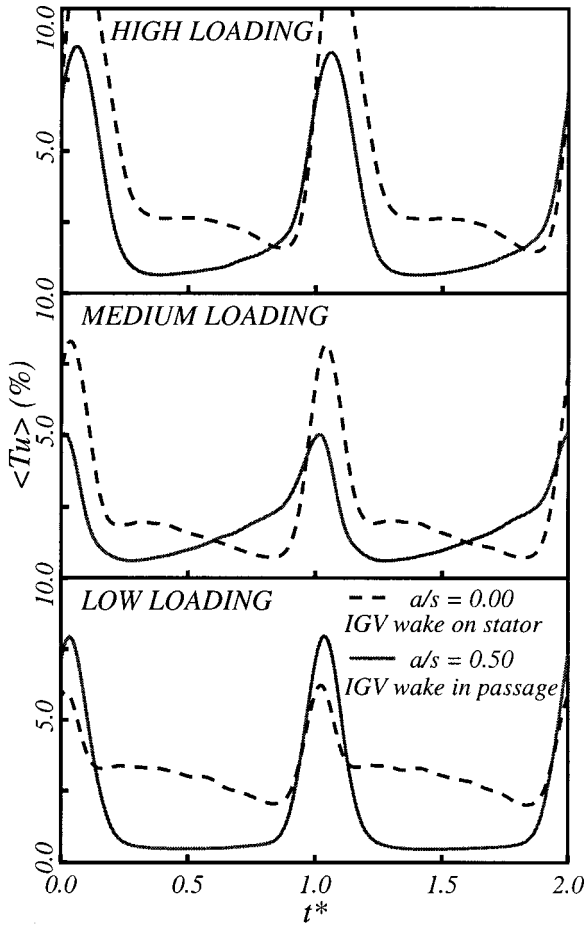

Fig. 3 Temporal variation of ensemble-averaged turbulence level $\langle Tu \rangle$ (percent) on stator stagnation streamline at inflow measurement plane 55.7 percent axial distance upstream of stator leading edge; variation with stator loading and IGV clocking

Hot-wire mesurements with a Dantec 55P03 probe and TSI IFA-100 anemometer were obtained at 55.7 percent c axial distance upstream of the stator to provide information on the inflow disturbance field. Slow response pressure measurements with a United Sensor CA-120 three-hole cobra probe at the same nominal position provided data for *in-situ* anemometer calibrations with pitch-averaged flow angles.

Surface velocity distributions were obtained from static pressure measurements on two adjacent stator blades fitted with pressure tappings opening into the same blade passage. Total pressure values were obtained from a Kiel probe 50 percent c upstream of the stator leading edge. The overall uncertainty of time-averaged pressure data was 0.15 percent.

One of the pressure-tapped stator blades was replaced by a blade instrumented with an array of 61 hot-film sensors at midblade height. The metal sensors, spaced at 2.54 mm intervals, were plated onto a kapton sheet wrapped around the whole blade surface. Data were acquired simultaneously from sets of five film gages using TSI IFA-100 anemometers.

For both hot-wire and hot-film observations, the anemometer output was backed with a DC offset voltage, amplified, and low-pass filtered at 20 kHz before sampling at 50 kHz and data storage. The signal conditioner amplification and DC offset were set automatically for each spatial measurement point to optimize signal to noise ratio. The frequency response of the hot-wire and hot-film measurements was better than 70 kHz and 30 kHz, respectively. The rotor blade passing frequency for these tests was typically 300 Hz.

Ensemble-averaged values of measured quantities were obtained from 512 records, with sampling triggered at the same point on each rotor revolution by an optical encoder mounted on the motor end of the drive shaft so that the wakes of the same rotor blades were observed in each record. Each record consisted of 1024 samples covering about six rotor blade passing periods for a set of wakes previously found by Solomon [21] to exhibit good periodicity. Circumferential traverses upstream of the stator used 32 points per blade spacing, with a greater concentration of points in the IGV wake regions. Time-mean flow data were determined from separate sets of flow observations with continuous sampling at random phase relative to the rotor motion and an averaging time of about 30 seconds.

Hot-film data were processed to give quasi shear stress defined by

$$\tau = \left(\frac{E^2 - E_0^2}{E_0^2} \right)^3 \tag{1}$$

which is proportional to the actual wall shear stress τ_w. This technique was originally developed by Hodson et al. [30] and has also been used by Halstead et al. [3]. Further details on the hot-film data processing can be found in Solomon and Walker [16,26] and Solomon [21]. The latter references provide typical individual gage records, as well as time-mean and envelope curves of quasi-shear stress for some of the test cases reported here.

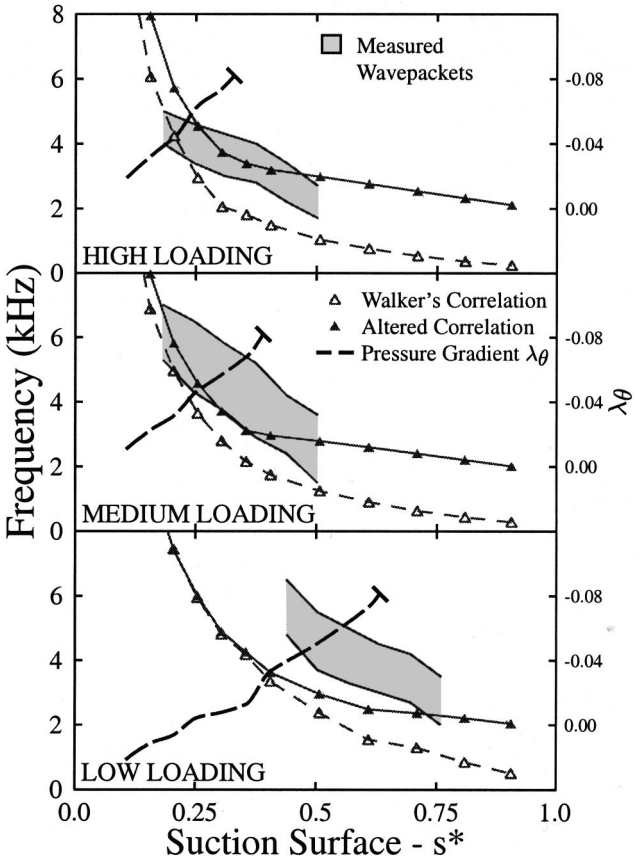

Fig. 4 Comparison of predicted T–S wave frequency and measured instability wave packet frequency

T–S Wave Detection Algorithm

Introduction. The detection algorithm is divided into the following stages and discussed below:

- Estimation of the local T–S wave frequency
- High-pass filtering of the hot-film signal
- Wavelet transform of the filtered signal
- Exclusion of turbulent flow regions
- Identification of instability waves in the laminar flow

More detailed information on the wavelet transform and identification procedure is provided by Hughes et al. [31].

Prediction of T–S Wave Frequency. In order to identify T–S waves it is first necessary to predict the range of frequencies receiving amplification for given local boundary layer conditions. The approximate method of Thwaites [32] is used to predict the streamwise variation in laminar boundary layer properties that would be obtained for the steady flow with the measured time mean surface velocity distributions. Periodic transition and its associated effects mean that it is possible to encounter regions of laminar flow well past the point of separation predicted by a time mean calculation, and it is therefore necessary to continue the calculation artificially past this point. The instability wave frequency in a separated shear layer should be related to the momentum thickness of the layer, which remains basically constant until transition and reattachment commence. In order to achieve this expected consistency of wave frequency, the shape factor $H = \delta^*/\theta$ is assumed to remain constant after separation when calculating a displacement thickness value for application of Eq. (2).

Walker [33] correlated the dimensionless frequency of T–S waves receiving maximum amplification rate against boundary layer displacement thickness Reynolds number by

$$\frac{\omega \nu}{u^2} = 3.2\ \mathrm{Re}_{\delta^*}^{-3/2} \tag{2}$$

In conjunction with the local boundary layer properties computed as described above, Eq. (2) is used to predict the chordwise variation of T–S frequency. The results for different blade loadings are plotted in Fig. 4. Also shown is the measured frequency range of instability wave packet phenomena, as identified by inspecting the wavelet transforms for a number of individual traces. The correlation frequency is less than the measured values. This is to be expected because the correlation returns the frequency of waves with the maximum amplification rate, whose frequency lies close to the center of the neutral stability curve. The observed wave packets are those with maximum amplitude, whose frequency will lie close to the upper branch of the neutral stability curve. In adverse pressure gradients, the frequency range of instability waves receiving amplification is much broader than for zero or favorable pressure gradients. It is therefore likely that as streamwise distance increases, the frequency of wave packets having the maximum amplitude will increasingly differ from that of waves experiencing maximum amplification rate. The maximum amplitude wave packets will be those that have already been amplified upstream, and these will tend to have higher frequencies.

To account for the differences between the maximum amplitude and maximum amplification rate cases, the predicted frequency has been modified according to the value of the Pohlhausen pressure gradient parameter. For zero or favorable pressure gradients, the predicted T–S wave frequency is not altered. As the pressure gradient becomes increasingly adverse, the change in predicted frequency with streamwise distance is simply biased toward the value upstream. There is a linear variation in biasing up to the separation value. Beyond separation, the change in T–S wave

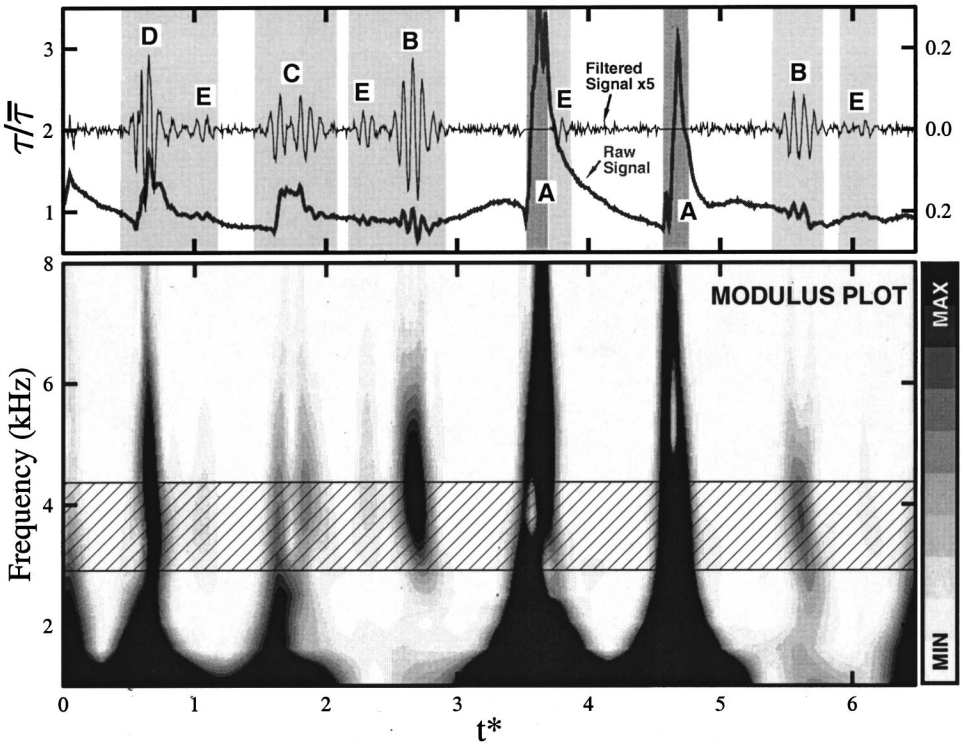

Fig. 5 Top: quasi-wall shear stress record from a hot-film gage located at $s^*=0.3108$ on the stator suction surface for the medium loading case. High-pass filtered signal amplified five times and superimposed. Darker shaded regions indicate turbulent flow; lighter shaded regions indicate instability wave occurrence. Bottom: modulus of the Morlet wavelet transform for the quasi-wall shear stress record. Hatching indicates frequency range under consideration by the detection algorithm.

frequency is limited such that there is almost no change with increasing streamwise distance. The effects on the predicted frequency are clearly illustrated in Fig. 4.

High-Pass Filtering. The upper portion of Fig. 5 shows the signal from a hot-film gage located at $s^*=0.3108$ on the stator suction surface. The signal shows evidence of both wake-induced turbulent strips (labeled ''A'' around $t^*=3.6$ and 4.6) and regions where the passing wake has failed to induce transition. As the regularity of turbulent strips increases, the laminar turbulent switching of the boundary layer tends to dominate the signal output and generally mask the presence of small-amplitude high-frequency fluctuations.

In an attempt to overcome the low-frequency distortion effects associated with blade passing phenomena, the signal was digitally smoothed using a Savitzky–Golay filter. The filter uses a least-squares method to fit a quartic polynomial to a window extending approximately one period of the basic instability wave on either side of the point of interest. Bromba and Ziegler [34] present transfer functions for filters with polynomials of increasing order. The signals were high-pass filtered by subtracting the smoothed signal from the original.

The approach applied here is similar to that applied by Seifert and Wygnanski [35] for identifying attendant wave packets (and consequent breakdowns) for artificially generated turbulent spots in an adverse pressure gradient. Kachanov [36] presents a discussion of the problems involved with filtering of wave packets and the effect on the Fourier spectra produced: High-pass filtering of a signal with a decaying spectrum may introduce an artificial spectral peak; individual events at frequencies close to the cutoff may experience significant phase distortion, but this does not invalidate the use of filtering to reveal the existence of periodic phenomena. The fact that such events are visible in the raw data indicates that the phenomena evident in the high-pass filtered signal of Fig. 5 are essentially genuine and not an artifact of the filtering process.

The high-pass signal is overlaid with the original signal in Fig. 5. It is possible to visually identify regions of instability activity, which will be discussed further in the light of the wavelet transform.

Wavelet Transform. Lewalle [37] provides an introduction to continuous wavelet transforms and illustrates applications to experimental data. The continuous wavelet transform essentially returns a correlation of the analyzing function and the signal at different translations along the signal. Since the wavelet is localized in space, only the local information of the signal is extracted. This process is repeated for different scales (or durations) of the analyzing wavelet and therefore decomposes the original signal into both location and duration scales. The localization of the analyzing function in the wavelet transform makes it ideal for studying transient phenomena.

The bottom portion of Fig. 5 shows the modulus plot for the above raw film signal. The transform is obtained with Morlet wavelet ($\omega_0=5.0$), which closely resembles the signature of typical wave packets on the compressor blade (see Walker and Hughes [29]).

In combination with the filtered signal, it is possible to identify individual events and their associated frequency content. The turbulent nature of the wake-induced strips (A) is evident from the cascade of frequencies present. Events (B) at $t^*=2.6$ and 5.6 are large-amplitude instability waves in the regions where the wake passing has failed to induce earlier transition. There are three other events worthy of attention: event (C), which appears to be a developing turbulent spot with attendant wave packets; event (D), which is a young turbulent spot with evidence of instability wave

frequencies persisting into the new turbulent flow; events (E), which are wave packets developing in the regions between wake-induced transition paths.

Turbulent Flow Detection. Regions of turbulent flow are detected using the intermittency routine of Solomon and Walker [26]. The detection scheme is a combination of probability density function and peak–valley counting methods. Once identified, the turbulent flow regions are not subjected to scrutiny by the T–S wave detection algorithm; therefore, instability waves can only be identified in regions of laminar flow. The results of the intermittency detection are shown as regions of dark shading overlaid on the film signal in Fig. 5. The events previously labeled A are both identified as turbulent, which agrees well with a visual inspection of the wavelet transform results. The results have been processed without manual intervention, apart from setting of universal window time and threshold parameters. The overall uncertainty of the intermittency results is estimated to be of the order of 10 percent.

Identification of Instability Waves. The coefficients of the wavelet transform are weighted by the value of the input signal. Therefore, the gage outputs are normalized by the long-term average value for that particular gage before high-pass filtering and calculation of the wavelet transform. This procedure accounts for the large chordwise variations in shear stress observed over the blade surface. A simple threshold criterion is then used to identify instability waves from the modulus of the wavelet transform for teach individual trace. The results presented are obtained with a constant threshold level. A range of frequencies spanning ± 10 percent of the predicted frequency is searched; this area is highlighted by hatching on the modulus plot in Fig. 5. Light shading on the original signal is used to highlight events that have been identified in the T–S frequency range by the current method.

Results

Simultaneous Raw Surface Film Traces. Figure 6 shows simultaneous traces from five gages on the stator suction surface spanning from $s^*=0.1825$ to 0.4390 for the medium loading case, with minimum inflow periodicity ($a/S=0.00$). Both the raw signal and the high-pass filtered signal are shown for each gage. The middle gage record, at $s^*=0.3108$, is the same as for Fig. 5: The events A, B, and E are again labeled, with their development in the streamwise direction highlighted by the dashed lines. Turbulent regions are identified by the darker shading, while the lighter shading indicates regions of instability wave activity.

Localized instability wave packets are clearly seen to amplify in the streamwise direction, both inside and outside the wake-induced transition paths. The most remarkable feature of Fig. 6 is that all turbulent flow is preceded by regions of wave packet amplification. At the last gage ($s^*=0.4390$) the laminar regions between the wake-induced strips are almost entirely dominated by instability wave activity. This is characteristic of the behavior in a

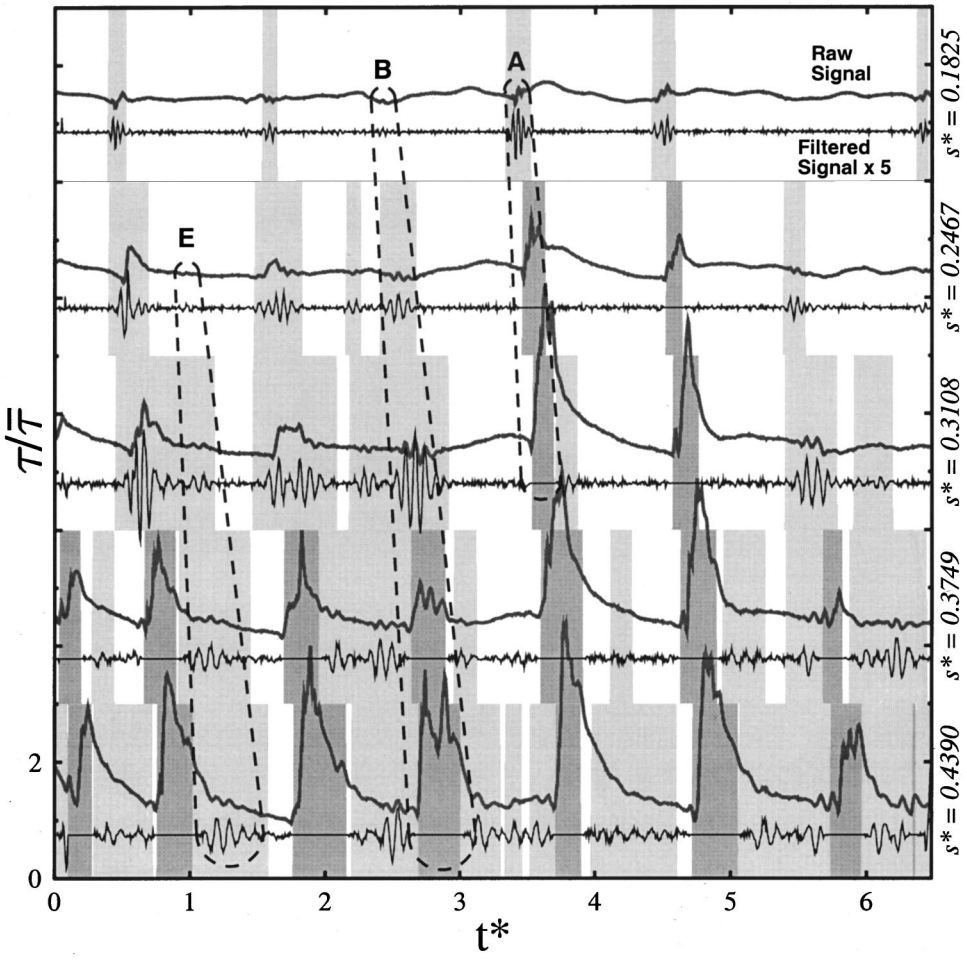

Fig. 6 Simultaneous quasi-wall shear stress records from five gages spanning $s^*=0.1825-0.4390$ on the stator suction surface. High-pass filtered traces amplified five times and overlaid on each raw signal. Darker shaded regions indicate turbulent flow; lighter shaded regions indicated instability wave occurrence. Individual events from Fig. 5 are highlighted by dashed lines.

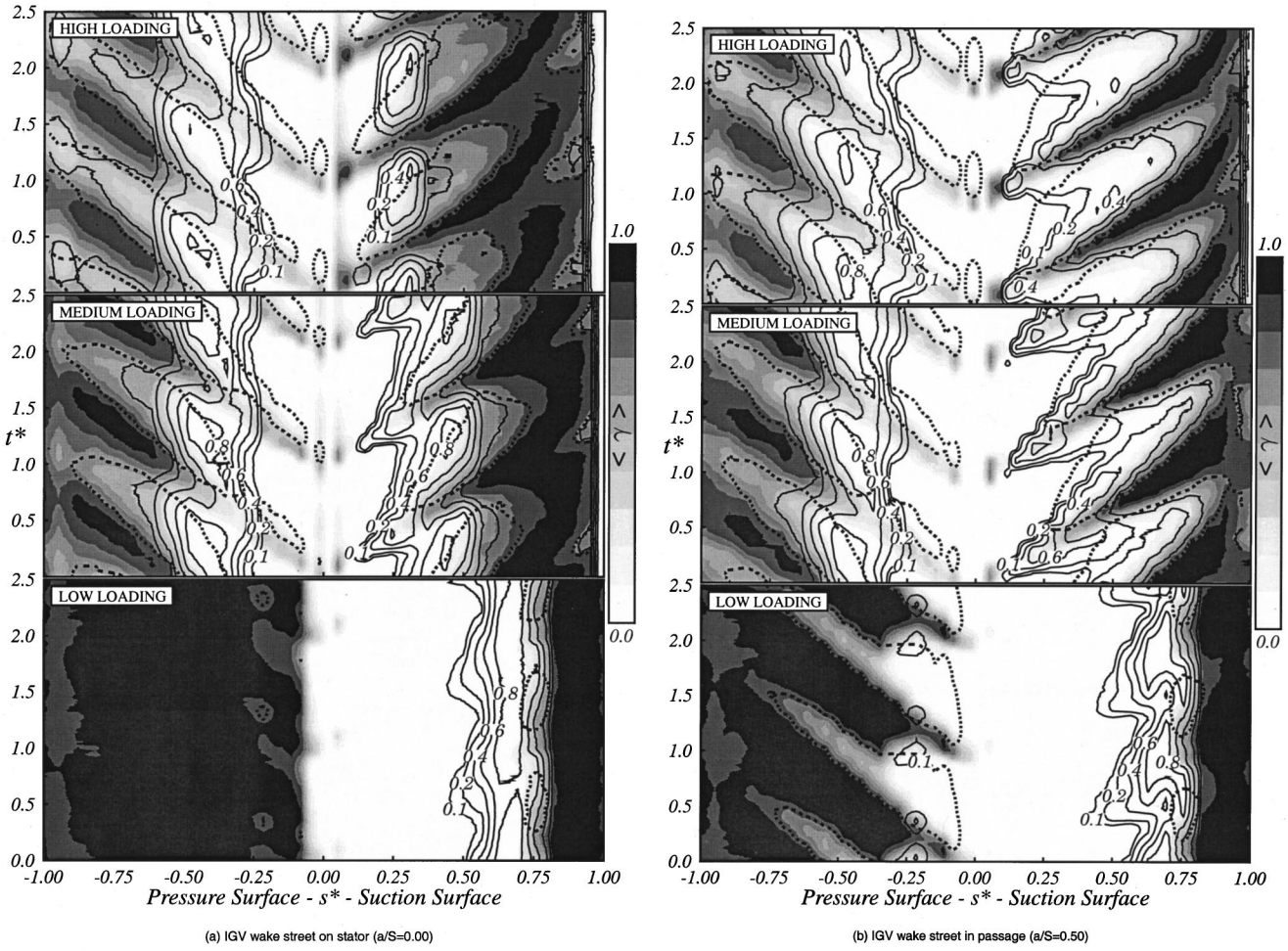

Fig. 7 Ensemble-averaged intermittency (shading) and probability of instability wave occurrence (line contours). Dashed line indicates 10 percent probability contour for relaxing nonturbulent flow: (*a*) IGV wake street on rotor ($a/S=0.00$); (*b*) IGV wake street in passage ($a/S=0.50$)

wide range of similar traces. There is little evidence for the direct production of turbulent spots even in the wake-induced paths where the random free-stream turbulence levels are about ten times larger than the initial pulse amplitudes of the Cohen et al. [8] wave packet experiments.

The event labeled A is characteristic of the above-mentioned behavior. There is instability wave activity at $s^*=0.1825$, which breaks down by $s^*=0.2467$ and is a well-developed turbulent strip in the remaining gage records. Event B, which also lies in the wake-induced path, shows a much longer region of amplification before breakdown. The wave packet is clearly identifiable at $s^*=0.2467$ and continues to be amplified through the next gage position; turbulent flow is not detected until $s^*=0.3749$, 12 percent surface distance farther downstream.

Event E illustrates the transition in the regions between wake-induced paths is also preceded by regions of instability wave activity. The event is first identified at $s^*=0.3108$ and continues to be amplified at the last gage. The above-mentioned events clearly indicate that transition to turbulence in the current situation, either in the wake-induced path (as in events A or B) or in between the wake-induced path (as in event E) is always preceded by instability phenomena. There is no evidence for direct spot production.

It is useful to re-examine the results of Halstead et al.[3] in the light of the present work. Their Fig. 17(*a*), which presents raw shear stress traces for the complete suction surface of a third-stage compressor stator blade, shows strong similarities to Fig. 6 of the present paper. An event similar to that labeled A in Fig. 6 is evident along trajectory *W*4 in Fig. 17(*a*). Activity very similar in nature to event B can be seen along trajectory *W*2. There is also evidence for a number of events of type E (between trajectories *W*1 and *W*2 and area 6). Halstead et al. [3] concluded that T–S waves were not present in their raw data. This is understandable given the difficulties of identifying small-amplitude instability waves in comparison with the large-amplitude fluctuations from laminar–turbulent switching caused by wake-induced transition. The filtering techniques of the present investigation suggest a different conclusion.

Ensemble-Averaged Results. Figure 7 shows line contours of constant ensemble-averaged probability of instability wave occurrence, as determined by the method outlined in the previous section. The contours are spaced at intervals of 0.2, with a contour at 0.1 to indicate the onset of instability wave activity, and overlay the ensemble average values of turbulent intermittency obtained from the surface hot-film measurements. Intermittency is indicated by shading on $t^*\sim s^*$ plots, with grading from white for laminar flow ($\langle\gamma\rangle=0$) to black for fully turbulent flow ($\langle\gamma\rangle=1$).

For each case, the dashed contour indicates the 10 percent probability boundary for the subsequent relaxing nonturbulent flow region. This was identified by $dt/d\tau$ remaining negative immediately following the passage of a turbulent spot. More detailed information on the calming effects for the cases presented is given by Walker et al. [22].

The most notable feature of Fig. 7 is that regions of instability wave amplification exist prior to the appearance of turbulent flow

for nearly all cases. Only when transition occurs through a leading edge bubble (low-loading, pressure-surface) or when the wake-induced transition starts very close to the leading edge (high-loading, suction-surface) is there an absence of detectable instability wave activity. The length of unstable flow is as much as 20 percent of chord in the path between wake-induced transitional strips; regions of wake-induced transition also exhibit lengths of unstable laminar flow, but they are much shorter.

Instability waves are regularly observed in the regions where nonturbulent relaxing flow has been identified. Only when relaxing flow is identified close to the leading edge on the pressure surface is there an absence of instability wave occurrence. In this case, the wake jet effect will impress turbulent fluid into the boundary layer, similar to the suction surface behavior on turbine blading; this may cause either spurious turbulence identification or genuine turbulent flow and associated calming, which cannot be sustained, and undergoes reverse transition. At $s^*=-0.4$, the predicted momentum thickness Reynolds number of $\mathrm{Re}_\theta=140$ from a steady laminar boundary layer calculation is well below the value for self-sustaining turbulence in a steady zero pressure gradient flow. This makes reverse transition a distinct possibility.

With the stator blade inside the IGV wake street ($a/S=0.00$), the suction surface exhibits a high probability of instability wave occurrence in the regions between wake-induced transition events for high and medium loading. In this clocking case the turbulence level between rotor wake passages is generally higher than when the stator blade lies outside the IGV wake street ($a/S=0.50$); this triggers instability events before the calming effect has a chance to delay their development.

With the stator blade outside the IGV wake street ($a/S=0.50$), the suction surface shows reduced probability of instability wave occurrence in the regions between wake-induced transition events for high and medium loading. There is a general trend for the onset of instability waves to occur farther rearward than in the $a/S=0.00$ case. The high levels of instability wave occurrence leading and following wake-induced turbulent strips provide evidence for attendant wake packets similar to those reported by Seifert and Wygnanski [35] for artificially generated turbulent spots in adverse pressure gradients. The wave packets attending the front of the strip are ''overtaken'' by the turbulent strip leading edge due to its greater convection speed. Individual traces also show instability phenomena first identifiable in the regions of strong relaxing flow following the strip. The instability wave packet lags the turbulent strip trailing edge and appears to slide down the relaxing flow tail, thus moving into regions of reduced calming effect. This allows amplification and eventual breakdown to occur. Whether the wave packets are generated by the local perturbation effects of turbulence within the strip or they are packets attending the strip trailing edge remains unclear, but there is strong circumstantial evidence for the wake-induced strip acting as a source of disturbances for the surrounding laminar boundary layer.

There is little change in the pressure surface results with clocking for the high and medium loading cases. Although instability waves are identifiable in the raw traces on the pressure surface, inspection of the results of the T–S wave detection algorithm show that there is a general tendency for the occurrence to be overestimated in this region. The results could possibly be improved by applying a more sophisticated thresholding technique than the one currently employed.

Another striking feature of Fig. 7 is the similarity in shapes of the instability occurrence onset and transition onset contours over a rotor passing period. It should be noted that the method for detecting instability wave occurrence is not related to that of turbulent identification. The two methods are inherently different in nature and the onset detections for both methods are entirely independent. The agreement in shape of the respective onset contours therefore strengthens confidence in both identification techniques.

Differences in instability wave occurrence onset and transition onset are greatest when transition occurs through a midchord separation bubble on the suction surface at low loading. Here the suction peak is much farther rearward (around $s^*=0.3$) than for the other loading cases and there are no detectable instability waves in the accelerating flow region. It is not until $s^*=0.4$, in the adverse pressure gradient region, that the onset of instability waves are identified. In the separated shear layer, the output from the surface-mounted gages will be influenced by the rapid attenuation of small-scale disturbances, and low-frequency high-amplitude shear layer flapping type behavior. These factors make positive identification of turbulent events by the intermittency detection routine difficult. The wavelet transform of these ''missed'' turbulent events almost certainly contains energy at the predicted T–S frequency, and they are wrongly identified as T–S waves. The general effect is that the turbulent intermittency is underestimated and the probability of instability wave occurrence is overestimated in the midchord separation bubble.

Hughes and Walker [38] present results for variations in midchord separation bubble behavior with reduced axial rotor/stator row spacing. As the row spacing is reduced, there is increased periodicity of the free-stream disturbance and increased evidence of wake-induced transition. The transition onset contours then agree more closely with the onset of instability waves shown in Fig. 7.

There is no evidence of instability wave occurrence on the pressure surface for the low loading case. Here transition occurs through a leading edge bubble. The dramatic changes in behavior with blade row clocking (a/S) were shown by Solomon et al. [17] to be the result of changes in random free-stream turbulence level. In the leading edge bubble, the separated shear layer will be thin and therefore the T–S wave frequency will be very high. The predicted T–S wave frequency is well above 10 kHz for the first 10 percent of surface distance from the leading edge. The flow behavior in this region and the greater gage spacing relative to the length of the transition zone make detection difficult and therefore confidence in the results is greatly reduced.

There are general differences in the onset of instability occurrence depending on the location of transition. When transition occurs close to the leading edge, potential flow interactions associated with varying incidence during rotor wake chopping cause large temporal fluctuations of the onset location. As the onset of transition moves rearward, these leading edge effects become less pronounced and the instability wave probability contours in the $t^*\sim s^*$ tend to straighten. This effect is most pronounced on the pressure surface for the high and medium loading cases.

Discussion

The current investigation has produced no evidence for bypass transition resulting in the direct production of turbulent spots within the boundary layer. Under adverse pressure gradient conditions on the compressor, there are identifiable regions of instability wave amplification in practically all cases before the appearance of turbulent spots. This evidence supports the view of Walker [4] that linear stability theory is still relevant to bypass transition in the turbomachinery environment. The passage of free-stream disturbances will excite eigenmodes of the relevant stability equations within the laminar boundary layer, and the scale of these perturbations will ultimately govern the production rate of turbulent spots as described by Walker [33]. Thus, stability theory will also be of significance in relation to the length of transitional flow.

The current results are for a blade design based on the British C4 section, which has a fairly linear deceleration on the suction surface at design conditions. More modern controlled-diffusion airfoils exhibit a suction peak farther rearward than the C4 section, followed by a region of rapid diffusion, which is relaxed as the trailing edge is approached.

This profile shape will generally delay transition onset when compared to C4 blades of similar loading. The increased region of favorable pressure gradient at the front of the blade will reduce the potential interactions associated with rotor wake chopping. The length of unstable laminar flow will be influenced by two counteracting effects: (1) The greater adverse pressure gradient following the suction peak will tend to reduce the length of unstable laminar flow; (2) the more rearward location of the suction peak will increase the boundary layer Reynolds number and tend to increase the length of unstable laminar flow. The instability frequency will scale with the boundary layer thickness and will therefore tend to decrease with a more rearward neutral stability point; this will lower the spot production rate and therefore lengthen the region of transitional flow on the controlled diffusion airfoil. The calming effect following a wake-induced turbulent strip will be weaker on the controlled-diffusion airfoil due to the region of favorable pressure gradient delaying transition onset.

Concluding Remarks

Previous investigations have found little evidence of instability wave activity from visual inspection of the raw data from surface film sensors on turbomachinery blades. Undoubtedly this is due to the small amplitude of instability wave activity being masked by the large amplitude shear stress fluctuations associated with laminar–turbulent switching of wake-induced transition. Removal of the low-frequency high-amplitude fluctuations by suitable filtering techniques makes the wave activity clearly apparent. The additional application of wavelet analysis greatly assists the identification of wave packets that appear randomly in time under the influence of free-stream turbulence.

The present investigation has indicated an almost universal appearance of instability wave amplification prior to turbulent breakdown in deceleration flow regions on an axial compressor blade. There was no evidence for direct production of turbulent spots in the boundary layer despite free-stream turbulence levels up to 8 percent. These observations closely resemble the wave packets and their ultimate breakdown in basic experiments on artificially generated spots arising from weak initial disturbances. It is therefore clear that high free-stream turbulence conditions do not imply the universal occurrence of transition via a bypass mode.

Unstable laminar flow regions up to 20 percent chord in length were observed on the compressor blade in the present investigation, both in the path of the wake-induced transition and in regions between wake-induced paths. The length of transitional flow, which is governed by turbulent spot inception rate, may also reach 20 percent of chord. Thus the total length of blade surface over which the flow is governed by linear stability theory (either directly through wave packet amplification or indirectly through determining the T–S wave frequency that governs the turbulent spot inception rate) may be as much as 40 percent of chord.

Wave activity may both occur in and originate from the calmed region following a wake-induced turbulent strip. This may be either from the attendant wave packets that occur in adverse pressure gradients (as with artificially generated turbulent spots) or from the turbulent perturbations within the wake-induced turbulent strip itself. The more stable flow in the ensuing ''calmed region'' does not guarantee the total absence of instability wave activity.

The present observations of instability wave activity relate entirely to regions of decelerating flow. It is likely that a bypass mode of transition, i.e., a more immediate breakdown, will predominate in accelerating flow regions at high free-stream turbulence levels. However, the authors speculate that the turbulent spot inception rate and length of transitional flow should still be governed by stability theory even under these conditions.

Acknowledgments

Financial support from Rolls-Royce plc and the Australian Research Council is gratefully acknowledged. The authors are indebted to reviewers for their thorough consideration of the manuscript and helpful comments.

Nomenclature

a = circumferential offset of stator blade leading edge from center of IGV wake avenue
c = blade chord
E = anemometer output voltage
E_0 = anemometer voltage at zero flow
H = δ^*/θ = shape factor
i = blade incidence
Re_1 = $w_1 c/\nu$ = chord Reynolds number
$\mathrm{Re}_{\mathrm{ref}}$ = $U_{mb} c/\nu$ = reference Reynolds number
Re_θ = $U\theta/\nu$ = momentum thickness Reynolds number
S = blade pitch
s = surface distance
s^* = $s/s_{\max}$ = dimensionless surface distance from leading edge
T = rotor blade passing period
Tu = random disturbance level (turbulence)
$\widetilde{Tu}$ = periodic disturbance level (unsteadiness)
Tu_D = total disturbance level
t = time
t^* = t/T = dimensionless time
U_{mb} = rotor midspan velocity
U = local free-stream velocity
u = streamwise velocity
w_1 = relative inlet velocity
x = distance along chord line
V_a = mean axial velocity
γ = turbulent intermittency
δ^* = displacement thickness
θ = momentum thickness
λ_θ = $(\theta^2/\nu)(dU/dx)$ = Pohlhausen pressure gradient parameter
ν = kinematic viscosity
τ = quasi-wall shear stress
τ_w = wall shear stress
ϕ = V_a/U_{mb} = flow coefficient
ω = circular frequency
$\langle\ \rangle$ = ensemble (phase-lock) average value
$(\_)_s$ = pitchwise-averaged
$(\bar{\ })$ = time mean

References

[1] Mayle, R. E., 1991, ''The 1991 IGTI Scholar Lecture: The Role of Laminar–Turbulent Transition in Gas Turbine Engines,'' ASME J. Turbomach., **113**, pp. 509–537.
[2] Mayle, R. E., 1992, ''Unsteady Multimode Transition in Gas Turbine Engines,'' AGARD PEP 80.
[3] Halstead, D. E., Wisler, D. C., Okiishi, T. H., Walker, G. J., Hodson, H. P., and Shin, H-W., 1997, ''Boundary Layer Development in Axial Compressors and Turbines: Parts 1–4,'' ASME J. Turbomach., **119**, pp. 114–127; *ibid.*, **119**, pp. 426–444; *ibid.* **119**, pp. 234–246; *ibid.*, **119**, pp. 128–139.
[4] Walker, G. J., 1993, ''The Role of Laminar–Turbulent Transition in Gas Turbine Engines—A Discussion'' ASME J. Turbomach., **117**, pp. 207–217.
[5] Tso, J., Chang, S. I., and Blackwelder, R. F., 1989, ''On the Breakdown of a Localized Disturbance in a Laminar Boundary Layer,'' Arnal, D., and Michel, R., eds. *Laminar–Turbulent Transition*, IUTAM Symposium, Toulouse, France, Springer-Verlag, pp. 199–214.
[6] Breuer, K. S., and Haritonidis, J. H., 1990, ''The Evolution of a Localized Disturbance in a Laminar Boundary Layer. Part 1. Weak Disturbances,'' J. Fluid Mech., **220**, pp. 569–594.
[7] Breuer, K. S., and Landahl, M. T., 1990, ''The Evolution of a Localized Disturbance in a Laminar Boundary Layer. Part 2. Strong Disturbances,'' J. Fluid Mech., **220**, pp. 595–621.
[8] Cohen, J., Breuer, K. S., and Haritonidis, J. H., 1991, ''On the Evolution of a Wave Packet in a Laminar Boundary Layer,'' J. Fluid Mech., **225**, pp. 575–606.

[9] Gostelow, J. P., Hong, G., Melwani, N., and Walker, G. J., 1996, ''Turbulent Spot Development Under a Moderate Adverse Pressure Gradient,'' ASME J. Turbomach., **1189**, pp. 737–743.
[10] Grek, H. R., Kozlov, V. V., and Ramazanov, M. P., 1989, ''Receptivity and Stability of the Boundary Layer at a High Turbulence Level,'' Arnal, D., and Michel, R., eds., *Laminar–Turbulent Transition*, IUTAM Symposium, Toulouse, France, Springer-Verlag, pp. 511–521.
[11] Boiko, A. V., Westin, K. J. A., Klingmann, B. G. B., Kozlov, V. V., and Alfredsson, P. H., 1994, ''Experiments in a Boundary Layer Subjected to Free Stream Turbulence. Part 2. The Role of T–S-Waves in the Transition Process,'' J. Fluid Mech., **281**, pp. 219–245.
[12] Lewalle, J., Ashpis, D. E., and Sohn, K.-H., 1997, ''Demonstration of Wavelet Techniques in the Spectral Analysis of Bypass Transition Data,'' NASA Conf. Publ.
[13] Dong, Y., and Cumpsty, N. A., 1990, ''Compressor Blade Boundary Layers: Part 2—Measurements With Incident Wakes,'' ASME J. Turbomach., **112**, pp. 231–240.
[14] Schulte, V., and Hodson, H. P., 1998, ''Unsteady Wake-Induced Boundary Layer Transition in High Lift LP Turbines,'' ASME J. Turbomach., **120**, pp. 28–35.
[15] Dring, R. P., Joslyn, H. D., Hardin, L. W., and Wagner, J. H., 1982, ''Turbine Rotor–Stator Interaction,'' ASME J. Eng. Power, **104**, pp. 729–742.
[16] Solomon, W. J., and Walker, G. J., 1995, ''Incidence Effects on Wake-Induced Transition on an Axial Compressor Blade,'' *Proc. 12th International Symposium on Air Breathing Engines*, Melbourne, Australia, pp. 954–964.
[17] Solomon, W. J., Walker, G. J., and Hughes, J. D., 1999, ''Periodic Transition on an Axial Compressor Stator—Incidence and Clocking Effects. Part II—Transition Onset Predictions,'' ASME J. Turbomach., **121**, pp. 408–415.
[18] Youngren, H., and Drela, M., 1991, ''Viscous–Inviscid Method for Preliminary Design of Transonic Cascades,'' AIAA Paper No. 91-2364.
[19] Mack, L. M., 1984, ''Boundary-Layer Linear Stability Theory,'' R. Michel, ed., *Special Course on Stability and Transition of Laminar Flow*, AGARD Report No. 709, pp. 3.1–3.81.
[20] Walker, G. J., 1972, ''An Investigation of the Boundary Layer Behavior on the Blading of a Single-Stage Axial-Flow Compressor,'' Ph.D. thesis, University of Tasmania, Australia.
[21] Solomon, W. J., 1996, ''Unsteady Boundary Layer Transition on Axial Compressor Blades,'' Ph.D. thesis, University of Tasmania, Hobart, Australia.
[22] Walker, G. J., Hughes, J. D., and Solomon, W. J., 1999, ''Periodic Transition on an Axial Compressor Stator—Incidence and Clocking Effects. Part I—Experimental Data,'' ASME J. Turbomach., **121**, pp. 398–407.
[23] Howell, A. R., 1945, ''Fluid Dynamics of Axial Compressors,'' Proc. Inst. Mech. Eng., **153**, pp. 441–452.
[24] Hourmouziadis, J., 1989, ''Aerodynamic Design of Low Pressure Turbines,'' Fottner, L., ed., *Blading Design for Axial Turbomachines*, AGARD Lecture Series No. 167, pp. 8.1–8.40.
[25] Walker, G. J., 1975, ''Observations of Separated Laminar Flow on Axial Compressor Blading,'' ASME Paper No. 75-GT-63.
[26] Solomon, W. J., and Walker, G. J., 1995, ''Observations of Wake-Induced Transition on an Axial Compressor Blade,'' ASME Paper No. 95-GT-381.
[27] Walker, G. J., Hughes, J. D., Köhler, I., and Solomon, W. J., 1998, ''The Influence of Wake–Wake Interactions on Loss Fluctuations of a Downstream Axial Compressor Blade Row,'' ASME J. Turbomach., **120**, pp. 695–704.
[28] Evans, R. L., 1975, ''Turbulence and Unsteadiness Measurements Downstream of a Moving Blade Row,'' ASME J. Eng. Power, **97**, pp. 131–139.
[29] Walker, G. J., and Hughes, J. D., 1999, ''The Occurrence of Natural Transition Phenomena in Periodic Transition on Axial Compressor Blades,'' *IUTAM Symposium on Laminar–Turbulent Transition*, Sedona, AZ.
[30] Hodson, H. P., Huntsman, I., and Steele, A. B., 1994, ''An Investigation of Boundary Layer Development in a Multi-stage LP Turbine,'' ASME J. Turbomach., **116**, pp. 375–383.
[31] Hughes, J. D., Walker, G. J., and Gostelow, J. P., 1999, ''Identification of Instability Phenomena in Periodic Transitional Flows on Turbomachine Blades,'' *Proc. 14th Int. Symp. on Air Breathing Engines*, Florence.
[32] Thwaites, B., 1949, ''Approximate Calculation of the Laminar Boundary Layer,'' Aeronaut. Q., **1**, pp. 245–280.
[33] Walker, G. J., 1989, ''Transitional Flow on Axial Turbomachine Blading,'' AIAA J., **27**, No. 5, pp. 595–602.
[34] Bromba, M. U. A., and Ziegler, H., 1981, ''Application Hints for Savitzky–Golay Digital Filters,'' Anal. Chem., **53**, pp. 1583–1586.
[35] Seifert, A., and Wygnanski, I. J., 1995, ''On Turbulent Spots in a Laminar Boundary Layer Subjected to a Self-Similar Adverse Pressure Gradient,'' J. Fluid Mech., **296**, pp. 185–209.
[36] Kachanov, Y. S., 1987, ''On the Resonant Nature of the Breakdown of a Laminar Boundary Layer,'' J. Fluid Mech., **184**, pp. 43–74.
[37] Lewalle, J., 1995, ''Tutorial on Continuous Wavelet Analysis of Experimental Data,'' Mechanical Aerospace and Manufacturing Engineering Dept., Syracuse University, World Wide Web: http://www.mame.syr.edu/faculty/lewalle/tutor/tutor.html.
[38] Hughes, J. D., and Walker, G. J. 1998, ''Unsteady Effects on Separated Flow Transition in an Axial Flow Compressor,'' Thomson, M. C., and Hourigan, K., eds., *Thirteenth Australian Fluid Mechanics Conference*, Melbourne, Australia, pp. 699–702.

Numerical Investigation of Nonlinear Fluid-Structure Interaction in Vibrating Compressor Blades

Volker Carstens
Institute of Aeroelasticity,
DLR,
Göttingen, Germany
e-mail: volker.carstens@dlr.de

Joachim Belz
Institute of Aeroelasticity,
DLR,
Göttingen, Germany
e-mail: joachim.belz@dlr.de

The aeroelastic behavior of vibrating blade assemblies is usually investigated in the frequency domain where the determination of aeroelastic stability boundaries is separated from the computation of linearized unsteady aerodynamic forces. However, nonlinear fluid-structure interaction caused by oscillating shocks or strong flow separation may significantly influence the aerodynamic damping and hence effect a shift of stability boundaries. In order to investigate such aeroelastic phenomena, the governing equations of structural and fluid motion have to be simultaneously integrated in time. In this paper a technique is presented which analyzes the aeroelastic behavior of an oscillating compressor cascade in the time domain. The structural part of the governing aeroelastic equations is time-integrated according to the algorithm of Newmark, while the unsteady airloads are computed at every time step by an Euler upwind code. The link between the two time integrations is an automatic grid generation in which the used mesh is dynamically deformed as such that it conforms with the deflected blades at every time step. The computed time series of the aeroelastic simulation of an assembly of twenty compressor blades performing torsional vibrations in transonic flow are presented. For subsonic flow, the differences between time domain and frequency domain results are of negligible order. For transonic flow, however, where vibrating shocks and a temporarily choked flow in the blade channel dominate the unsteady flow, the energy transfer between fluid and structure is no longer comparable to that of a linear system. It is demonstrated that the application of the time domain method leads to a significantly different aeroelastic behavior of the blade assembly including a shift of the stability boundary.
[DOI: 10.1115/1.1354138]

Introduction

The development of modern aircraft engine compressors with increased pressure ratio and reduced weight has led to highly loaded stages with transonic inflow. As a result, the design engineers of completed engines have often encountered severe aeroelastic problems, the solution of which could be difficult and costly. Therefore, tools are needed which already in the design process are able to correctly predict the aeroelastic behavior of the blading.

In the classical approach the aeroelastic problem is divided into separate steps of aerodynamic and structural computations. The mode shapes of the structural dynamic model are used to generate harmonic motions for the calculation of airloads. The aeroelastic problem is then solved by using these airloads in the structural dynamic problem [1]. Particularly the influence of mass or stiffness variations—the so-called blade frequency mistuning—has attracted the attention of the scientific community over years and has led to numerous publications, *e.g.* Refs. [2–6].

To include nonlinearities in both the structure and/or the aerodynamics, aeroelastic equations have to be solved in the time domain. A principle insight into the numerical stability and accuracy of different coupling techniques is given by Giles [7]. Coupling between structure and fluid for airfoils was demonstrated by Guruswamy [8], Piperno et al. [9], Schulze [10], whereas cascade applications were presented by He [11,12], Vahdati and Imregun [13], Marshall and Imregun [14], Bakhle et al. [15], and Blom [16]. A special treatment of the problem was proposed by Bendiksen [17], who formulated an integration of the fluid-structure interaction in the time domain on a single computational grid.

The main objective of this paper is to present a method for analyzing the aeroelastic stability in the transonic regime where the nonlinearity of the fluid equations requires a time-accurate approach for the interaction between the fluid and the structure. In order to achieve this, the motions of fluid and structure are integrated in time by separate time integration methods while their interaction is realized by a coupling algorithm.

The capability of this method to predict aeroelastic stability is demonstrated for subsonic and transonic flow. In order to concentrate the investigations on the principal physical effects which dominate the fluid-structure interaction in subsonic and transonic flow, a very simple structural model was taken as a basis for the computations.

Aeroelastic Modelling

The structural dynamic model of the cascade is based on a mass-spring-damper system. The motion of each of the N blades is described in a local Cartesian coordinate system with x, y, and z in the axial, circumferential, and radial direction, respectively. Reducing the structural system to an assembly of two-dimensional rigid blade sections, which are suspended by springs, the oscillation of each blade is given by its displacements in the x- and y-direction and its rotation α in the z-direction which are all collected in the displacement vector $\mathbf{w}$. This analysis is restricted to pure pitching motions. Excluding structural stiffness and damping coupling between the blades, the structural properties of each blade are then completely described by its mass moment of inertia Θ_{z_i}, its rotational damping d_{α_i}, and its rotational stiffness k_{α_i}

Contributed by the International Gas Turbine Institute and presented at the 45th International Gas Turbine and Aeroengine Congress and Exhibition, Munich, Germany, May 8–11, 2000. Manuscript received by the International Gas Turbine Institute February 2000. Paper No. 2000-GT-381. Review Chair: D. Ballal.

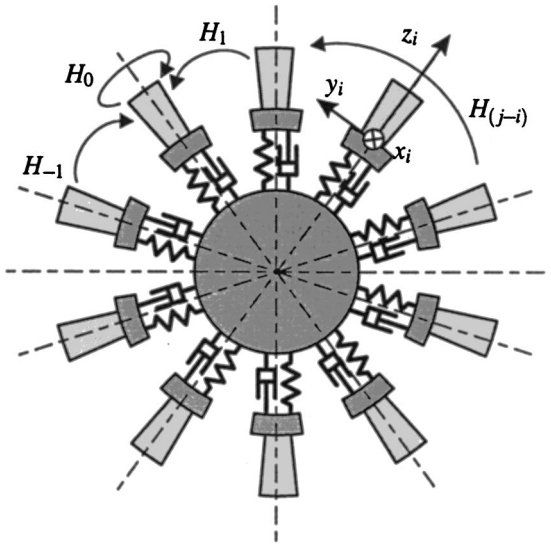

Fig. 1 Structural dynamic cascade model with additional structural damping and aerodynamic coupling

(Fig. 1). Structural stiffness and damping coupling between the blades are possible but are not used in the presented investigation.

When writing the equations of motion for discrete structures in a matrix form, we obtain

$$[M]\ddot{\mathbf{w}}+[D]\dot{\mathbf{w}}+[K]\mathbf{w}=\mathbf{f}, \tag{1}$$

where $[M]$, $[D]$, and $[K]$ denote the mass, damping, and stiffness matrices, respectively. For aeroelastic investigations, the right-hand side vector $\mathbf{f}$ represents the aerodynamic forces and moments acting on the structural system. For fixed flow parameters such as Mach number or reduced frequency these aerodynamic forces are nonlinear functions of the blade's deflection, velocity, and acceleration

$$\mathbf{f}=\mathbf{f}(\mathbf{w},\dot{\mathbf{w}},\ddot{\mathbf{w}}) \tag{2}$$

Classical aeroelastic methods linearize the vector $\mathbf{f}$ with respect to $\mathbf{w}$ and its time derivatives. Additionally assuming a harmonic time dependence of the displacement vector, $\mathbf{f}$ is simplified to

$$\overline{\mathbf{f}}=[A]\overline{\mathbf{w}}, \tag{3}$$

where $\overline{\mathbf{f}}$ and $\overline{\mathbf{w}}$ denote the time-dependent complex vectors

$$\overline{\mathbf{f}}=\overline{\mathbf{f}}_0\cdot e^{j\omega t} \quad \text{and} \quad \overline{\mathbf{w}}=\overline{\mathbf{w}}_0\cdot e^{j\omega t} \tag{4}$$

with the complex amplitudes $\overline{\mathbf{f}}_0$ and $\overline{\mathbf{w}}_0$. $[A]$ is a complex-valued matrix.

Computation of the Aerodynamic Forces

Time-dependent airloads are needed to complete the aeroelastic model of Eq. (1). In the following, the application of linear harmonic and nonlinear airloads for solving Eq. (1) is presented.

Linear Harmonic Airloads. Regarding pure pitching motions, the vectors $\mathbf{f}$ and $\overline{\mathbf{w}}$ represent the aerodynamic moments and pitching angles only, *i.e.* they are given by

$$\overline{\mathbf{f}}=\overline{\mathbf{M}}_0\cdot e^{j\omega t} \quad \text{and} \quad \overline{\mathbf{w}}=\overline{\boldsymbol{\alpha}}_0\cdot e^{j\omega t} \tag{5}$$

The linear dependence of the aerodynamic moments on the angular displacements is expressed in terms of a nondimensional matrix $[H]$ as

$$\overline{\mathbf{M}}_0=[A]\overline{\boldsymbol{\alpha}}_0=(p_0-p_1)L^2b[H]\overline{\boldsymbol{\alpha}}_0, \tag{6}$$

where the element H_{ik} of $[H]$ represents the normalized aerodynamic moment exerted on the ith blade if the kth profile is vibrating. Usually, the generalized aerodynamic forces are not directly available in terms of influence coefficients but are computed by traveling wave modes where all blades vibrate with the same amplitude and a constant interblade phase angle σ. The relationship between $[H]$ and the unsteady aerodynamic moment coefficients computed for traveling wave modes is given by the linear transformation

$$[H]=[E][C][E]^{-1}, \tag{7}$$

where the diagonal matrix $[C]$ is made up of the moment coefficients C_k^{α} which are computed for each of the N traveling wave modes on the basis of forced harmonic vibration. The underlying aerodynamic method usually stems from one of the numerous linearized versions of the Euler or Navier-Stokes equations. The columns of the matrix $[E]$ transforming the C_k^{α} coefficients into influence coefficients are the N traveling wave mode eigenvectors

$$E_{i,k}=\exp\left\{j\,\frac{2\pi ik}{N}\right\}, \quad i,k=1,\ldots,N \tag{8}$$

Nonlinear Airloads. The set of flow equations used here are the two-dimensional unsteady Euler equations in transformed coordinates. The strong conservation law form of these equations can be written as

$$\frac{\partial\hat{Q}}{\partial\tau}+\frac{\partial\hat{F}}{\partial\xi}+\frac{\partial\hat{G}}{\partial\eta}=0. \tag{9}$$

The details of the state vector $\hat{Q}$ and the inviscid fluxes $\hat{F}$ and $\hat{G}$ are explained in Refs. [18] and [19].

The spatial discretization of the inviscid fluxes $\hat{F}$ and $\hat{G}$ is obtained by making use of van Leer's flux vector splitting scheme [20] in combination with a MUSCL extrapolation where the conservative variables of the state vector are extrapolated according to a second-order scheme.

The time integration of the Euler equations (9) for the flow around vibrating blades is performed according to the approximately factored implicit algorithm of Beam and Warming [21]. The time integration interval for the coupled field problem is chosen according to the admissible maximum values of the fluid and the structural solver, *i.e.* according to

$$\Delta t=\min(\Delta t_F,\Delta t_S), \tag{10}$$

where Δt_F and Δt_S are the admissible maximum time steps for the fluid and the structure, respectively.

For turbomachinery flows, the system equation (9) of Euler equations has to be supplied with boundary conditions at the blades' surfaces, at the inflow and outflow boundaries, and at the periodic boundaries of the computational domain which consists of all the twenty blade channels. On the blades' surfaces the normal relative flow velocity is set to zero while the wall pressure is computed from the normal momentum equation. The implementation of the inflow and outflow boundary conditions is accomplished by a method proposed by Chakravarthy [22], where the characteristic formulation of the Euler equations together with the suppression of incoming waves leads to nonreflecting boundary conditions in a quasi-two-dimensional approach. Periodic boundary conditions are applied on the bottom of the first and on the top of the twentieth blade channel. Their implementation is self-evident with the used line-period grid.

The grid generation needed to compute the solution of the Euler algorithm in a boundary-fitted coordinate system is obtained by an elliptic grid generation code based on the solution of Poisson equations [23]. The type of grid used for the cascade flow calculation is a line-periodic H grid where each grid point on the lower channel boundary has its counterpart on the upper channel boundary in the pitchwise direction.

The grid point displacement for oscillating blades must be carefully organized. The meshes of the twenty blade channels have to

be deformed steadily to enable them to conform to the new position of the vibrating blades after each time step. In order to meet this requirement, a special automatic grid generation procedure was applied. A new grid is calculated after each time step, regarding the old grid as the initial solution and the new position of the blades as new boundary condition. This method yields reasonable control of the grid point speed in the interior field and requires only a few iterations of the elliptic grid generation code for each time step.

Flutter Computations

Depending on the aerodynamic method used, the aeroelastic response of the blade assembly is computed either in the frequency or in the time domain. Frequency domain methods make use of the linear dependence of **f** on **w** which permits the removal of the time from Eq. (1) for harmonic motions. In this case, the determination of the flutter boundary is equivalent to the solution of an eigenvalue problem. Time domain methods do not imply any simplification of **f** and require the direct solution of Eq. (1) by an appropriate, but of course more time-consuming integration.

Frequency Domain Method. Inserting

$$\overline{\mathbf{w}}=\overline{\boldsymbol{\alpha}}_0\cdot e^{j\omega t}=\overline{\boldsymbol{\phi}}\cdot e^{j\omega t} \tag{11}$$

and the linear relationship equations (6) into Eq. (1) we obtain

$$\{-\omega^2[M]+j\omega[D]+([K]-[A])\}\overline{\boldsymbol{\phi}}=\mathbf{0} \tag{12}$$

The solution of the quadratic eigenvalue problem equation (12) yields N complex eigenvalues

$$\omega_k=\nu_k+j\,\delta_k \tag{13}$$

with a positive real eigenfrequency ν_k. The eigensolution belonging to ω_k, namely

$$\overline{\mathbf{w}}_k=\overline{\boldsymbol{\phi}}_k e^{j\omega_k t} \tag{14}$$

represents a damped vibration for positive δ_k values and a self-excited oscillation of the blading (flutter) for a negative δ_k. Any arbitrary motion of the cascade can be expressed in terms of a superposition of the N eigensolutions by

$$\overline{\mathbf{w}}=\sum_{k=1}^{N} c_k\overline{\mathbf{w}}_k \tag{15}$$

For tuned cascades, where all blades are assumed to have identical structural eigenfrequencies, the eigenvectors $\overline{\boldsymbol{\phi}}_k$ represent the traveling wave modes mentioned above and are solely dependent on the interblade phase angle

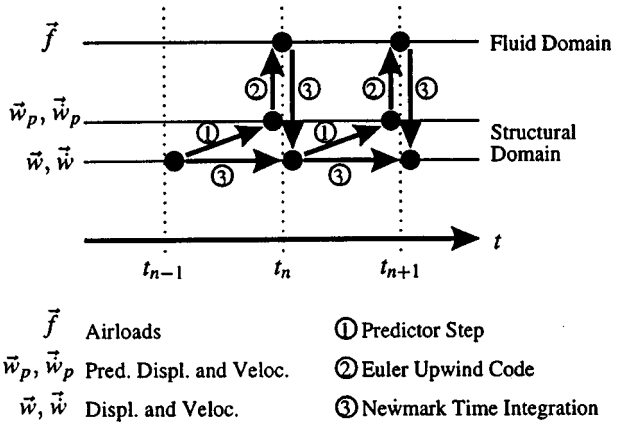

Fig. 2 Coupled time integration of fluid and aeroelastic equations

$$\sigma=\frac{2\pi k}{N},\quad k=1,\ldots,N \tag{16}$$

Time Domain Method. Abandoning the assumption of harmonic unsteady airloads, the aeroelastic equations (1) have to be solved in the time domain. The method of time integration used was the Newmark procedure [24] which is widely used for structural dynamics problems and is well known for its numerical flexibility.

The Newmark time integration calculates the velocities and displacements at t_{n+1} from known values at t_n and the acceleration $\ddot{\mathbf{w}}(t_{n+1})$ using the approximations

$$\begin{aligned}\mathbf{w}(t_{n+1})&=\mathbf{w}(t_n)+\dot{\mathbf{w}}(t_n)\Delta t+((0.5-\gamma)\ddot{\mathbf{w}}(t_n)+\gamma\ddot{\mathbf{w}}(t_{n+1})\Delta t^2\\ \dot{\mathbf{w}}(t_{n+1})&=\dot{\mathbf{w}}(t_n)+((1-\delta)\ddot{\mathbf{w}}(t_n)+\delta\ddot{\mathbf{w}}(t_{n+1})\Delta t\end{aligned} \tag{17}$$

where the yet unknown quantity $\ddot{\mathbf{w}}(t_{n+1})$ is obtained from Eq. (1) according to

$$\ddot{\mathbf{w}}(t_{n+1})=[M]^{-1}\{-[D]\dot{\mathbf{w}}(t_{n+1})-[K]\mathbf{w}(t_{n+1})+\mathbf{f}(t_{n+1})\} \tag{18}$$

The parameters γ and δ are needed to control the stability and accuracy of the Newmark algorithm; the pair used for these investigations was $\gamma=0.25$ and $\delta=0.5$, yielding an implicit time integration.

The algorithm described by Eqs. (17) and (18) requires the unsteady airloads at t_{n+1} which depend on the yet unknown displacements and velocities at this time step. In order to overcome this problem, $\mathbf{w}(t_{n+1})$ and $\dot{\mathbf{w}}(t_{n+1})$ were estimated from the corresponding values at previous time steps. Additionally, a corrector step could be performed to recalculate the airloads with the new displacements and velocities computed by Eq. (17), but it was found that in most of the cases this additional mathematical effort yields negligible improvement of accuracy. A sketch of the integration scheme is depicted in Fig. 2.

In order to judge the aeroelastic stability of the system for different flow conditions the energy transferred to or removed from the structural system was computed. This energy is equivalent to the work performed by the fluid at the system which is given by (the superscript denotes the time level)

$$W^n=W^0+\int_0^{t_n}\dot{\mathbf{w}}(t)\cdot\mathbf{f}(t)dt\approx W^{n-1}+\dot{\mathbf{w}}^n\cdot\mathbf{f}^n\Delta t \tag{19}$$

A decreasing value of Eq. (19) specifies a damped free vibration of the cascade while increasing energy indicates flutter.

Aeroelastic Case Studies

The coupled time domain algorithm presented above was applied to a compressor cascade configuration which is identical to an annular test facility designed for flutter investigations [25]. The blading consists of 20 two-dimensional blade sections (NACA 3506 profiles), the data of which are listed in Table 1.

In order to focus the interest on nonlinear aerodynamic effects and to avoid a mixing with other aeroelastic phenomena such as mode coupling or blade frequency mistuning, the aeroelastic configuration selected for the following investigations was kept as simple as possible. For this reason results for pure pitching oscillations of a perfectly tuned blade assembly were computed. Furthermore, the structural damping of the blades expressed by the damping matrix $[D]$ was set to zero. Time series of the blade displacements were calculated for two steady-state flow conditions, namely for an inflow Mach number of $Ma_1=0.8$ and a transonic flow where the inflow Mach number reaches $Ma_1=0.9$ (Table 2).

In the following, the first test case is called ''subsonic,'' although small areas of supersonic flow originate during the oscillation period on the suction side of the blades.

Table 1 Parameters of test configuration

Chord length	$L = 80.0$	mm
blade span	$b = 40.0$	mm
pitch-chord ratio	$\tau/L = 0.71$	
stagger angle	$\beta_g = 40.0$	°
eigenfrequency	$f_0 = 185$	Hz
rotational stiffness	$k_{\alpha i} = 61.87$	$\mathrm{Nm\,rad^{-1}}$
mass moment of inertia	$\Theta_{zi} = 45.79$	$\mathrm{kg\,mm^2}$
location of pitching axis	$(x_\alpha, y_\alpha) = (40.0, 1.6)$	mm

Table 2 Steady flow parameters

	Subsonic	Transonic
inflow Mach number Ma_1	0.80	0.90
inflow angle β_1	48.3°	48.3°
back pressure ratio p_2/p_0	0.8100	0.7880

The combination of structural parameters (Table 1) and inflow Mach numbers (Table 2) was chosen as such that the cascade was aerodynamically unstable in subsonic as well as in transonic flow.

In contrast to the frequency domain method where the determination of the flutter boundary is self-evident ($\delta_k = 0$), the time domain method provides only the time series which does not automatically allow for an identification of flutter. The reason for this uncertainty is that the development of the time series decisively depends on the selection of the initial blade deflections and velocities. An initial deflection with only one deflected blade, *i.e.* $\alpha_1(0) = 1$ deg, $\alpha_i(0) = 0$ deg, $i = 2, \ldots, 20$ effects an excitation of all modes. When choosing the exact values of an eigenmode as initial conditions, the cascade, on the contrary, will vibrate in this mode for a long time until numerical inaccuracies allow other modes to enter the vibration process.

The influence of different initial conditions is demonstrated in Fig. 3, where the time series of one blade's deflection is depicted for two different initial angular displacements. The figure illustrates the rapid growth of the vibration amplitude when starting with the deflection pattern of the most unstable traveling wave mode ($\sigma = +36$ deg), whereas the initial deflection of only one blade causes a decreasing amplitude of this blade in the first instant followed by a very slow excitation.

Since the unstable aeroelastic modes are not known a priori, the flutter investigations presented in the following were all started with initial conditions where only one blade was deflected. This procedure guarantees the identification of flutter modes.

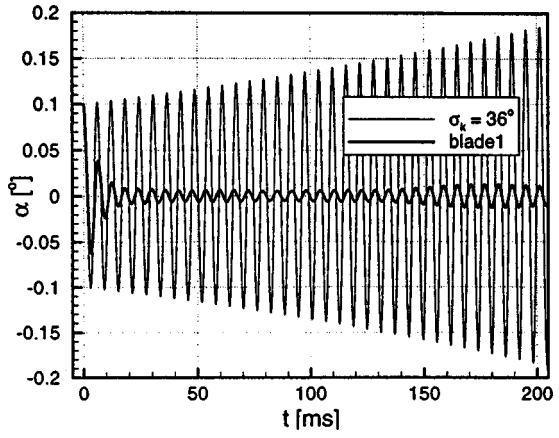

Fig. 3 Influence of the initial conditions: Deflection of blade No. 1 only and initial displacement according to traveling wave mode with $\sigma = 36$ deg

Flutter Investigations for Subsonic Flow Conditions

The flutter behavior of the tuned cascade in subsonic flow is depicted in Fig. 4. It is obvious that the blade assembly becomes aeroelastically unstable which is indicated by the slight increase of the blade deflections, here shown for blade No. 1. The time series illustrates the excitation process which is typical for these flow conditions: First of all, the initial deflection [here $\alpha_1(0) = 0.1$ deg] results in an oscillation with decreasing amplitude within the time interval from 0 to 100 ms. Afterwards, the vibration process is characterized by a few beats due to the superposition of unstable and stable eigenmodes. Approximately 400 ms later, the cascade settles in for a flutter vibration with a monotonously increasing amplitude and an almost constant interblade phase angle between any two blades. This is demonstrated by Fig. 5 where a close-up of the time series of the three adjacent blade Nos. 20, 1, and 2 illustrates the synchronization process of the blade vibrations to a σ value of 36 deg. This is confirmed by comparison of the blade Nos. 1 and 11 (Fig. 5) which vibrate in phase.

It has already been mentioned that the aeroelastic eigenmodes of a perfectly tuned linear system are the traveling wave modes. A computation of the unsteady aerodynamic moment coefficients for

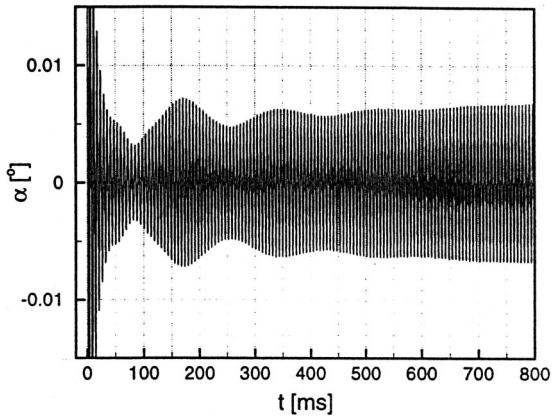

Fig. 4 Free blade vibrations in subsonic flow, $Ma_1 = 0.8$, blade No. 1

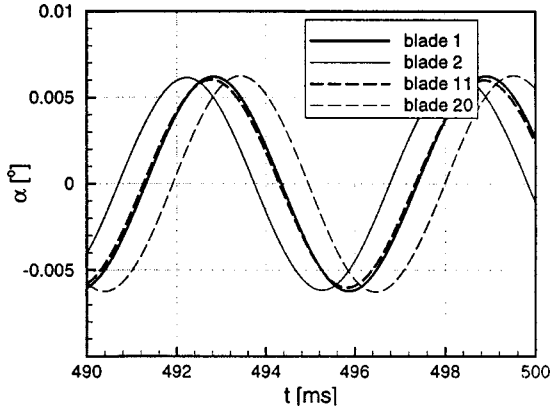

Fig. 5 Free blade vibrations in subsonic flow, $Ma_1 = 0.8$, blade Nos. 20, 1, 2, and 11 after 490 ms

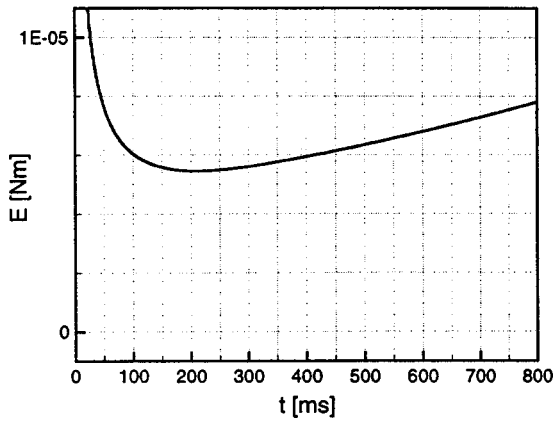

Fig. 6 Total structural energy of the cascade in subsonic flow

these modes with $Ma_1 = 0.8$ showed that among the possible twenty interblade phase angles [Eq. (16)] the only unstable one is the value of $\sigma = 36$ deg. Hence, Figs. 4 and 5 indicate a linear behavior of the aeroelastic system for the given subsonic flow conditions.

The aeroelastic stability of the cascade, though discernible from Fig. 4, is determined by the total structural energy of Eq. (19). Increasing or decreasing values of this quantity indicate unstable or stable vibrations, respectively. Figure 6 confirms the conclusion already drawn from Fig. 4. After a steep decrease at the beginning of the motion where the stable aeroelastic eigenmodes are almost completely disappeared the total structural energy increases monotonously over time.

An important question to be answered is whether the nonlinear method would predict a flutter boundary which differs from the value obtained by a linearized method. In order to clarify this problem, the following numerical experiment was performed: In a first step, linearized airloads were inserted into the Newmark algorithm. These airloads were calculated from the first harmonics of the unsteady aerodynamic moment coefficients computed for traveling wave modes over a certain range of reduced frequencies. In a trial and error process the rotational stiffness k_α was raised until the blades vibrated with a constant amplitude, indicating the boundary of aeroelastic stability. In a second step, the time series were computed with the nonlinear aerodynamic method and the new stiffness parameter $k_\alpha = 66.10\ \mathrm{Nm\ rad^{-1}}$.

The numerical results of both calculations are depicted in Fig. 7. In contrast to the linearized data representing the limit of stability, the application of the Euler method results in a slightly damped vibration. Comparing the phase lags between aerodynamic moment and blade motion, however, the results of both methods differ by no more than 0.5 deg–1.0 deg, *i.e.* by a value corresponding approximately to one step of the time integration algorithm.

It should be stressed that the linearized method used here may not correspond to what is usually done when applying a linearized code to unsteady flow problems. The usual approach is to linearize the unsteady flow with respect to the steady-state flow conditions. Here, the time-dependent flow has been linearized with respect to the average flow values which are identical to the zero Fourier coefficients of the unsteady flow quantities. These coefficients may differ from the steady-state values. Nevertheless, the comparison of the Euler results with the data of the linearized procedure described above yields a valuable insight into the linear or nonlinear flutter behavior of the cascade.

Flutter Investigations for Transonic Flow Conditions

The transonic flow in the vibrating compressor cascade is characterized by the occurrence of strong oscillating shocks and the existence of choked flow conditions. These flow phenomena lead to a completely different aeroelastic behavior of the blade assembly which becomes obvious when looking at Fig. 8, where the time series of blade Nos. 1–4 are depicted for $Ma_1 = 0.9$.

After a time interval of 50 ms in which the blades show a vibrational behavior similar to that under subsonic flow conditions, the blade amplitudes have reached values where choked flow becomes possible in the blade channel. Since the sudden appearance of a moving blade channel shock drastically changes the average aerodynamic moment of the profiles, the deflections of the vibrating blades suddenly skip onto new average values, while the oscillation of the profiles with slightly increasing amplitudes now takes place around this changed balance positions.

The striking fact is that this process happens in an ordered fashion: The odd blades go up and the even down. The physical explanation for this phenomenon is that the front part of the blade channel is either acting as a nozzle or a diffuser as soon as the new balance position is reached. As this cannot happen in adjacent blade channels, the average flow is repeated in every second channel. Figure 9 shows the transonic unsteady flow through the blade row at 70 ms, *i.e.* just after the onset of choked flow. It should be mentioned that the decision whether the odd or the even blades skip up or down depends on the initial deflections and—as demonstrated below—on the total number of blades.

When the blades vibrate with deflections which are large enough to ''unlock'' the choked blade channels, *i.e.* that now the flow is only partly choked during one oscillation period, a severe onset of flutter with rapidly growing amplitudes is observed ($t > 100$ ms). The computations were stopped when the angular blade deflections exceeded a value of 2.5 deg because, beyond these amplitudes the results of an inviscid CFD method seemed to be no longer reliable.

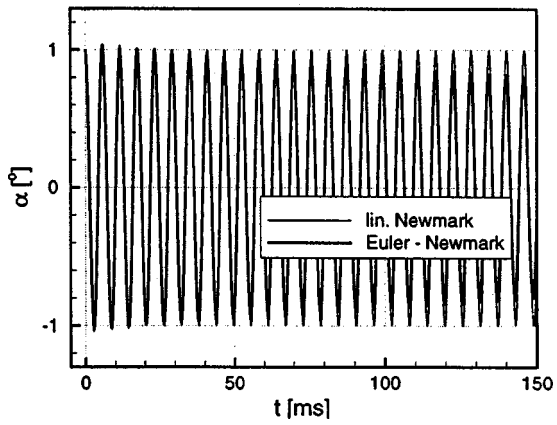

Fig. 7 Flutter boundary in subsonic flow, $Ma_1 = 0.8$

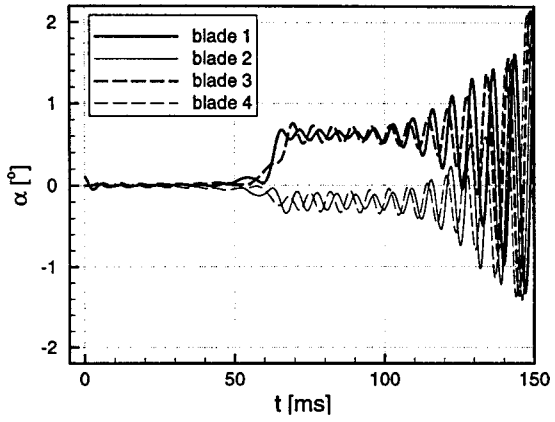

Fig. 8 Free blade vibrations in transonic flow, 20 blades, $Ma_1 = 0.9$

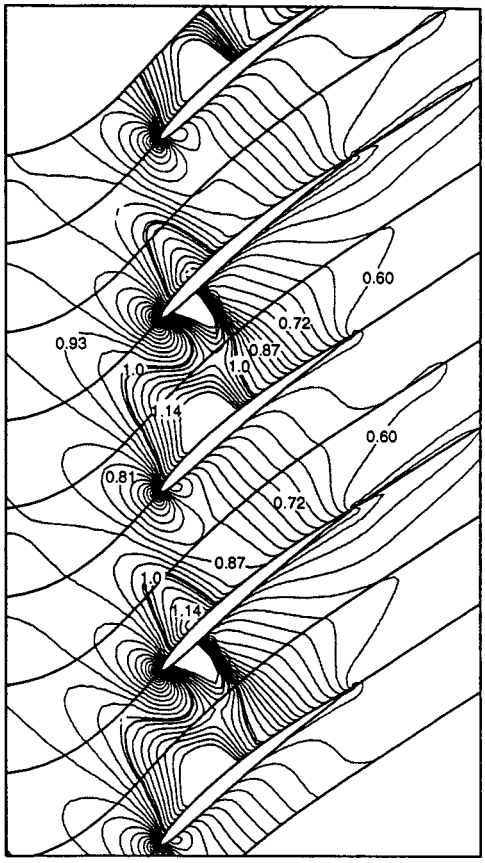

Fig. 9 Iso-Machlines for choked blade channels

A computation of the aerodynamic moment coefficients for the traveling wave modes showed that oscillations with a σ value of 36 deg, 54 deg, and 72 deg become unstable, whereby the most unstable mode among these three is the one with $\sigma=54$ deg. Hence, the flutter vibration of the blade row in transonic flow does not settle in for a clearly discernible traveling wave mode. Although the interblade phase angle between two adjacent blades still remains positive, it varies from blade to blade.

Another interesting phenomenon is the dependence of the flutter scenario on the total number of blades. Figure 10 shows the time series for a cascade of 19 blades for the same structural and aerodynamic parameters. Obviously, the odd and even blades have changed their roles: The odd blades are going down, while the even are going up. Comparing the amplitudes after 150 ms with the previous case, the unsteady angular deflections are significantly smaller than for 20 blades, indicating that a decreased amount of energy is transferred from the fluid to the blade per cycle. Another interesting feature of this nineteen-blade cascade is that the blades jump onto their balance positions with a phase lag from blade to blade. As soon as this process has arrived at blade No. 19, blade No. 1 changes its average position by moving upwards. It should be mentioned that the computation of the time series for a cascade of 18 blades (not shown here) yielded almost the same results as the data for 20 blades.

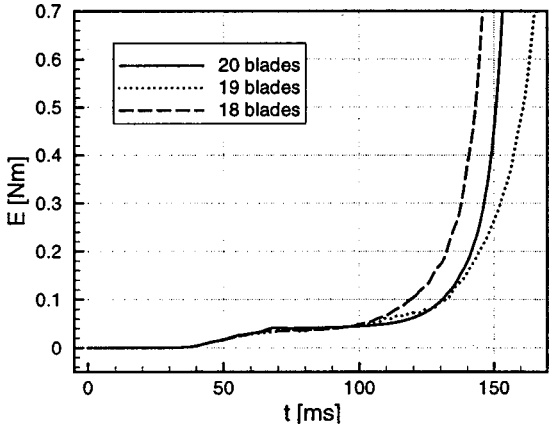

Fig. 11 Total structural energy of the cascade in transonic flow

The development of the total structural energy depicted in Fig. 11 confirms the trend mentioned above. The two cascades with the even total blade numbers run faster into large amplitude vibrations than the blade row with the odd total blade number. Another remarkable feature of this figure is the plateaulike behavior of the energy during the time interval in which the blade channel flow is continuously choked for every second blade channel.

In order to determine the flutter boundary, the same numerical experiment was performed as for subsonic flow. Again, the stiffness parameter k_α was adjusted in the linearized computation to obtain a vibration with neither increasing nor decreasing amplitude. Due to the fact (see above) that in transonic flow the traveling wave modes with $\sigma=36$ deg, 54 deg, and 72 deg become unstable, the time series computed with the linear airloads is a superposition of these three modes in which the 54 deg mode represents the dominating part. The computation of the unsteady blade deflections with the nonlinear aerodynamic method then made use of the new value $k_\alpha=84.17\ \mathrm{Nm\,rad^{-1}}$.

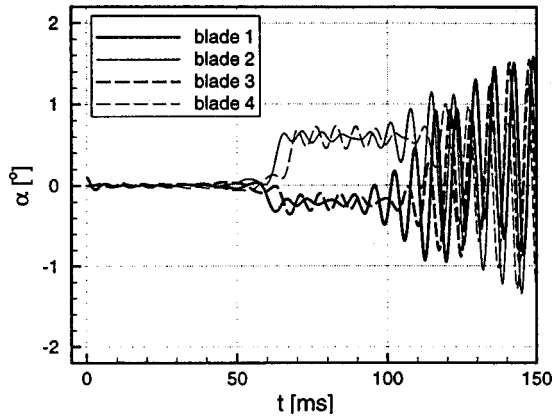

Fig. 10 Free blade vibrations in transonic flow, 19 blades, $Ma_1=0.9$

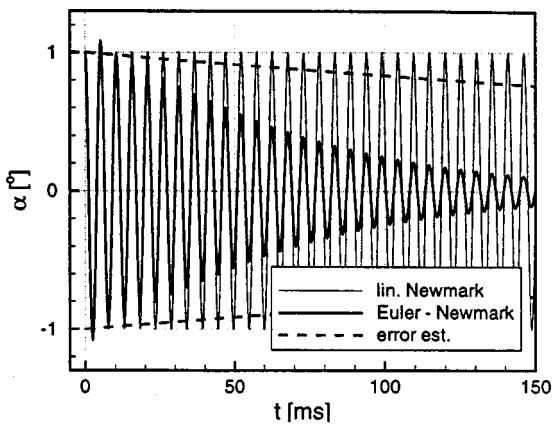

Fig. 12 Flutter boundary in transonic flow

Figure 12 shows the comparison of both calculations together with a dashed curve which denotes the estimated error to determine the phase angle between aerodynamic moment and blade motion with the time integration method used here. The dashed curve was computed by inserting a time lag of one time step into the linearized solution. The important result of Fig. 12 is that the computed time series of the nonlinear method show a distinctly damped behavior in contrast to the blades of the linear system which vibrate at the limit of stability. Since the strong decrease of amplitude is far below the estimated error curve the flutter boundary of the nonlinear system must be different from the corresponding value calculated for linear airloads.

Concluding Remarks

An algorithm investigating the fluid-structure interaction of vibrating compressor blades in the time domain has been presented here. The basic features of this method are the use of a Newmark time integration method for solving the aeroelastic equations and an Euler upwind method for providing the unsteady nonlinear airloads.

In order to focus the interest on the impact of nonlinear aerodynamic phenomena on cascade flutter, a simple structural model originating from an existing test facility was selected. The model consisted of 20 compressor blades performing pure pitching vibrations around mid-chord. The structural parameters of the perfectly tuned blade assembly and the inflow values were adjusted as such that self-excited oscillations could already occur for subsonic flow conditions.

It was found that the cascade shows a linear aeroelastic behavior for subsonic flow conditions. This is confirmed by flutter boundary results where a computation with nonlinear airloads yields an almost identical stability limit in comparison to a value calculated with linear airloads.

A completely different aeroelastic behavior is observed in transonic flow. The occurrence of strong oscillating shocks and choked blade channel flow leads to unstable vibrations which are not comparable with the exponentially increasing deflections of a linear system. Additionally, a dependence of the fluid-structure energy transfer on the total number of blades was identified. The most important result, however, is the shifted flutter boundary when replacing the linearized aerodynamic approach with a nonlinear method. This was clearly demonstrated by determining the stability limit with linear airloads and then computing the time-dependent blade deflections with aerodynamic coefficients from an Euler code for the same structural parameters.

Finally, a remark is necessary concerning the particular CFD method used here. It is believed that the presented results are of importance as long as the shock motion is triggered by the blade vibration and as long as no severe viscous effects occur. Strong shock-boundary layer interaction and massive flow separation may cause an unsteady flow in which the shock oscillation frequency is no longer coupled to the blade motion. This will obviously result in a changed aeroelastic behavior of the cascade.

Nomenclature

$[M]$, $[D]$, $[K]$ = mass, damping, and stiffness matrix
$\mathbf{f}$, $\underline{\mathbf{f}}$ = vector of the (aerodynamic) forces (real and complex notation)
$\mathbf{w}$, $\underline{\mathbf{w}}$ = displacement vector of the blades (real and complex notation)
$[H]$ = influence coefficient matrix
C_k^α = unsteady aerodynamic moment coefficients
$[C]$ = diagonal matrix containing the C_k^α
$\hat{Q}$ = state vector
$\hat{F}$, $\hat{G}$ = inviscid fluxes
Ma = Mach number
N = number of blades
L = blade chord length
b = blade span
p_0 = total pressure
p_1 = upstream pressure
p_2 = downstream pressure
$\underline{\omega_k}$ = eigenvalue of the linear system
$\boldsymbol{\phi}_k$ = eigenvector of the linear system
α_i = unsteady pitching angle of the blade i
β = flow angle
β_g = stagger angle
σ = interblade phase angle
$j=\sqrt{-1}$ = imaginary unit

References

[1] Platzer, M. F., and Carta, F. O., 1987/1988, ''Aeroelasticity in Axial-Flow Turbomachines, Vol. 1: Unsteady Turbomachinery Aerodynamics. Vol. 2: Structural Dynamics and Aeroelasticity AGARD,'' *AGARDograph* 298.
[2] Kaza, K. R. V., and Kielb, R. E., 1982, ''Flutter and Response of a Mistuned Cascade in Incompressible Flow,'' AIAA J., **20**, No. 8, pp. 1120–1127.
[3] Bendiksen, O. O., 1984, ''Flutter of Mistuned Turbomachinery Rotors,'' ASME J. Eng. Gas Turbines Power, **106**, pp. 25–33.
[4] Crawley, E. F., and Hall, K. C., 1985, ''Optimization and Mechanisms of Mistuning in Cascades,'' ASME J. Eng. Gas Turbines Power, **107**, pp. 418–426.
[5] Bloemhof, H., 1988, *Flutter of Blade Rows With Mistuning and Structural Coupling*, Report No. 14, DGM-LTT, EPF-Lausanne.
[6] Pierre, C., and Murthy, D. V., 1992, ''Aeroelastic Modal Characteristics of Mistuned Blade Assemblies: Mode Localization and Loss of Eigenstructure,'' AIAA J., **30**, No. 10, pp. 2483–2496.
[7] Giles, M., 1995, ''Stability and Accuracy of Numerical Boundary Conditions in Aeroelastic Analysis,'' COSMASE (Computation of Sciences, Methods and Algorithms an Supercomputing for Engineering), Short Course on Fluid-Structure-Interaction, May 2–5, KTH, Stockholm, Sweden.
[8] Guruswamy, G. P., 1989, ''Integrated Approach for Active Coupling of Structures and Fluids,'' AIAA J., **27**, pp. 788–793.
[9] Piperno, S., Farhat, C., and Larrouturou, B., 1995, ''Partitioned Procedures for the Transient Solution of Coupled Aeroelastic Problems, Part I: Model Problem, Theory and Two-Dimensional Applications,'' Comput. Methods Appl. Mech. Eng., No. 124, pp. 79–112.
[10] Schulze, S., 1997, ''Transonic Aeroelastic Simulation of a Flexible Wing Section,'' AGARD-R-822, Numerical Unsteady Aerodynamics and Aeroelastic Simulation, AGARD Structures and Materials Panel, Aalborg, Denmark, pp. 10,1–10,20.
[11] He, L., 1996, *Unsteady Flows in Turbomachines, Part 3*, VKI Lectures 1996-05, Mar. 11–15.
[12] Ning, W., and He, L., 1997, ''Computation of Unsteady Flows Around Oscillating Blades Using Linear and Nonlinear Harmonic Euler Methods,'' ASME Paper No. 97-GT-229.
[13] Vahdati, M., and Imregun, M., 1994, ''Non-linear Aeroelasticity Analyses Using Unstructured Dynamic Meshes,'' *Symposium on Unsteady Aerodynamics and Aeroelasticity of Turbomachines*, Sept. 1994, Fukuoka, Japan.
[14] Marshall, J. G., and Imregun, M., 1996, ''An Analysis of the Aeroelastic Behavior of a Typical Fan-Blade With Emphasis on the Flutter Mechanism,'' ASME Paper No. 96-GT-78.
[15] Bakhle, M., Srivastava, R., Stefko, G. L., and Janus, J. M., 1996, ''Development of an Aeroelastic Code Based on an Euler/Navier-Stokes Aerodynamic Solver,'' ASME Paper No. 96-GT-311.
[16] Blom, F. J., 1998, ''Investigations on Computational Fluid-Structure Interaction,'' Thesis, DGM-IMHEF, EPF-Lausanne.
[17] Bendiksen, O. O., 1991, *A New Approach to Computational Aeroelasticity*, AIAA 32nd Structures, Structural Dynamics, and Material Conference, Baltimore, MD, pp. 1712–1727.
[18] Carstens, V., 1991, ''Computation of the Unsteady Transonic 2D Cascade Flow by an Euler Algorithm with Interactive Grid Generation,'' AGARD CP 507, Transonic Unsteady Aerodynamics and Aeroelasticity, Oct. 7–11, San Diego.
[19] Carstens, V., Bölcs, A., and Körbächer, H., 1993, ''Comparison of Experimental and Theoretical Results for Unsteady Transonic Cascade Flow at Design and Off-Design Conditions,'' ASME Paper No. 93-GT-100.
[20] van Leer, B., 1982, *Flux Vector Splitting for the Euler Equations*, ICASE Report no. 82-30.
[21] Beam, A., and Warming, R. F., 1976, ''An Implicit Finite-Difference Algorithm for Hyperbolic Systems in Conservation-Law Form,'' J. Comput. Phys., **22**, pp. 87–110.
[22] Chakravarthy, S. R., 1982, ''Euler Equations—Implicit Schemes and Boundary Conditions,'' AIAA Paper No. 82-0228.
[23] Carstens, V., 1988, ''Two Dimensional Elliptic Grid Generation for Airfoils and Cascades,'' DLR-FB pp. 88–52.
[24] Newmark, N. M., 1959, ''A Method of Computation for Structural Dynamics,'' A.S.C.M., J. Eng. Mech. Div., **85**, pp. 67–94.
[25] Hennings, H., and Belz, J., 1999, ''Experimental Investigation of the Aerodynamic Stability of an Annular Compressor Cascade Performing Tuned Pitching Oscillations in Transonic Flow,'' ASME Paper No. 99-GT-407.

The Impact of Viscous Effects on the Aerodynamic Damping of Vibrating Transonic Compressor Blades—A Numerical Study

Björn Grüber
Daimler Chrysler Aerospace,
MTU Munich,
Munich, Germany
email: bjoern.grueber@muc.mtu.dasa.de

Volker Carstens
Institute of Aeroelasticity,
DLR,
Göttingen, Germany
email: volker.carstens@dlr.de

A parametric study which investigates the influence of viscous effects on the damping behavior of vibrating compressor cascades is presented here. To demonstrate the dependence of unsteady aerodynamic forces on the flow viscosity, a computational study was performed for a transonic compressor cascade of which the blades underwent tuned pitching oscillations while the flow conditions extended from fully subsonic to highly transonic flow. Additionally, the reduced frequency and Reynolds number were varied. In order to check the linear behavior of the aerodynamic forces, all calculations were carried out for three different oscillation amplitudes. Comparisons with inviscid Euler results helped identify the influence of viscous effects. The computations were performed with a Navier-Stokes code, the basic features of which are the use of an AUSM upwind scheme, an implicit time integration, and the implementation of the Baldwin-Lomax turbulence model. In order to demonstrate the possibility of this code to correctly predict the unsteady behavior of strong shock-boundary layer interactions, the experiment of Yamamoto and Tanida on a self-induced shock oscillation due to shock-boundary layer interaction was calculated. A significant improvement in the prediction of the shock amplitude was achieved by a slight modification of the Baldwin Lomax turbulence model. An important result of the presented compressor cascade investigations is that viscous effects may cause a significant change in the aerodynamic damping. This behavior is demonstrated by two cases in which an Euler calculation predicts a damped oscillation whereas a Navier-Stokes computation leads to an excited vibration. It was found that the reason for these contrary results are shock-boundary-layer interactions which dramatically change the aerodynamic damping. [DOI: 10.1115/1.1354139]

Introduction

The development of computational methods for the prediction of unsteady flows through vibrating turbomachinery blade rows is a necessary prerequisite to predict the aeroelastic behavior of the blading. In order to appropriately model the flutter and forced response problem for a given configuration, accurate and efficient aerodynamic methods are required to correctly determine the unsteady airloads that may damp or excite the blade vibrations.

The development of modern aircraft engine compressors with increasing pressure ratio and reduced weight have led to highly loaded stages where the flow in the blade channels often reaches the transonic regime. This type of flow is characterized by the occurrence of shocks, shock-boundary layer interaction, and—at higher incidence angles—by flow separation on the suction side of the blades. A complicated mixture of these phenomena may occur, if the blades vibrate due to self-excitation or inlet flow distortion. Thus, any aerodynamic analysis used to compute the unsteady pressure loads of a blade assembly vibrating in transonic flow should be able to at least partly model the physical flow phenomena mentioned above.

One way to obtain a tool for the purpose of aeroelastic investigations is to linearize the time-dependent flow with respect to the steady flow in the resting blade row. These methods assume the unsteadiness in the flow to be a small disturbance of a known average flow and they approximate the full Euler or Navier-Stokes equations by a set of linear equations for the unsteady flow values. Further simplification of the problem is achieved by assuming the harmonic time-dependency of all unsteady quantities.

Typically representative of these methods are the publications of Hall and Crawley [1], Kahl and Klose [2], Montgomery and Verdon [3] for linearized Euler methods, and Holmes et al. [4], Clark and Hall [5,6] for the corresponding approximation of the Navier-Stokes equations. These simplified analyses meet the requirement of computational efficiency and can be used for routine aeroelastic design studies. Their basic drawback, however, is that their application is restricted to such cases where the blade vibration adds a small disturbance to, e.g., a blade channel shock or a leading edge flow separation and does not produce these nonlinear flow phenomena itself.

Computational resources available today have stimulated the development of numerical methods for solving the full nonlinear equations. Although these methods are far from being a standard tool for routine investigations, they help understand and assess the nonlinear phenomena which occur in an unsteady flow caused by blade vibrations. Nonlinear approaches have been presented for inviscid flows by Gerolymos [7,8], He [9], Carstens [10,11], Peitsch et al. [12] and Chuang and Verdon [13], whereas He [14], Abhari and Giles [15], Ayer and Verdon [16], Grüber and Carstens [17], Weber et al. [18] and Isomura and Giles [19] have published contributions to the solution of the unsteady Reynolds-averaged Navier-Stokes equations. Additionally, Fransson et al. [20] performed an instructive comparison of inviscid/viscous and linear/nonlinear computations of the unsteady flow in an oscillating turbine configuration.

The computation of unsteady flows in oscillating cascades by solving the full Navier-Stokes equations is extremely time consuming. Therefore it is useful to know in which cases viscous

Contributed by the International Gas Turbine Institute and presented at the 45th International Gas Turbine and Aeroengine Congress and Exhibition, Munich, Germany, May 8–11, 2000. Manuscript received by the International Gas Turbine Institute February 2000. Paper No. 2000-GT-383. Review Chair: D. Ballal.

effects dominate the aerodynamic damping and where the assumption of inviscid flow conditions is justified. The basic goal of this paper is to point out where a viscous nonlinear treatment of the unsteady flow problem is mandatory. The highly loaded transonic compressor cascades found in the low-pressure stages of modern aircraft engines are known for their susceptibility to flow separation and shock-boundary layer interaction occurring at small deviations from design flow conditions. If the blades are set to vibrate in such flows, both phenomena mentioned above may significantly change the aerodynamic damping of the blade assembly in comparison to nonseparated shock-free flows. Parametric studies with a transonic compressor cascade performing pitching vibrations at different oscillation amplitudes, reduced frequencies, Mach and Reynolds numbers clearly demonstrate the influence of nonlinear viscous effects on the damping behavior of the blading.

Numerical Method

Basic Equations and Boundary Conditions. The set of flow equations used here are the two-dimensional unsteady compressible Reynolds-averaged Navier-Stokes equations in transformed coordinates. The strong conservation law form of these equations can be written as

$$\partial_\tau \hat{Q} + \partial_\xi \hat{F} + \partial_\eta \hat{G} = \partial_\xi \hat{R} + \partial_\eta \hat{S} \tag{1}$$

where transformed vectors are marked by a $\hat{}$. The dependence of the state vector $\hat{Q}$, the inviscid fluxes $\hat{F}$ and $\hat{G}$ and the viscous fluxes $\hat{R}$ and $\hat{S}$ on the physical quantities density, Cartesian velocity vector, static pressure and temperature are explained in detail by Grüber and Carstens [17].

The numerical approximation of Eq. (1) is written in a finite volume formulation where the spatial discretization of the inviscid fluxes $\hat{F}$ and $\hat{G}$ is obtained by using the AUSM scheme (**A**dvection **U**pstream **S**plitting **M**ethod) of Liou and Steffen [21] in combination with the MUSCL extrapolation of van Leer [22]. The AUSM scheme is characterized by a separate splitting of the convective and pressure terms of $\hat{F}$ and $\hat{G}$ and has the advantage of vanishing numerical dissipation for zero Mach numbers. This property leads to accurate results in the boundary layers where the physical viscosity must not be contaminated by the numerical viscosity. With the MUSCL approach the state vectors at the cell interfaces are obtained by upwind extrapolation between adjacent cell-centered values. The investigations presented here, were carried out with the fully one-sided second-order upwind scheme [17]. Finally, the spatial derivatives of the viscous fluxes $\hat{R}$ and $\hat{S}$ are approximated by central differences.

The time integration of Eq. (1) for the flow around vibrating blades is performed according to the approximately factored implicit algorithm by Beam and Warming [23]. The accuracy of the time integration was restricted to the first order since the very fine resolution of one oscillation period (between 800 and 10000 time steps) was adequate for time-accurate solutions.

The Reynolds-averaged equation (1) are closed with the algebraic turbulence model by Baldwin and Lomax [24]. In the standard model proposed by Baldwin and Lomax the constant C_{wk} which controls the production of eddy viscosity in the outer boundary layer is prescribed by a value of 0.25. It is demonstrated below that modifications of this constant may significantly improve the correct prediction of shock-boundary layer interactions and with that the precise determination of shock vibration amplitudes.

For turbomachinery flows, the system of Navier-Stokes Eq. (1) has to be supplied with boundary conditions at the blade surfaces, the inflow and outflow boundaries and the periodic boundaries of the computational domain. On the blade surfaces the flow velocity is equated with the blade velocity (no slip condition). In order to completely determine the wall fluxes, two further equations are needed which prescribe the thermodynamic variables at the wall. First of all, the wall temperature is calculated by assuming adiabatic walls which require a vanishing normal temperature gradient at the wall. Secondly, the surface pressure is computed from the normal momentum equation which yields the normal pressure gradient as function of the blade acceleration and the derivatives of the velocity.

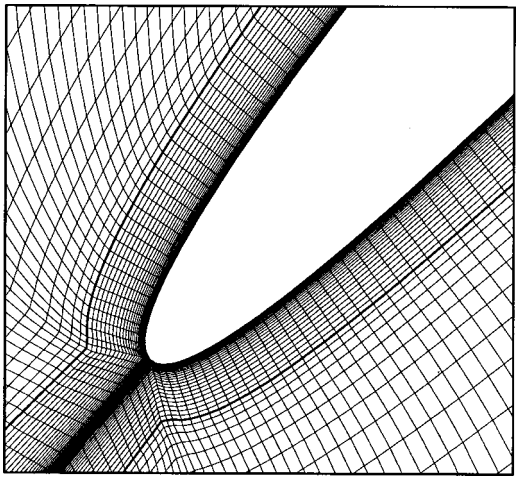

Fig. 1 Composition of grids near the blade's surface

The implementation of inlet and outlet boundary conditions is accomplished by the method of Chakravarthy [25] who proposed a quasi two-dimensional approach. A description of the special application of this technique to steady and unsteady turbomachinery flow was published by Carstens [10]. Assuming that the axial flow component is entirely subsonic at the inlet and outlet planes of the cascade, boundary conditions for steady flow are established by replacing incoming waves with fixed flow values; *i.e.* total pressure, total temperature and flow angle are prescribed at the inlet boundary while the static pressure is kept constant at the outlet boundary. Nonreflecting boundary conditions are used for unsteady flow, *i.e.* incoming waves (three at the inlet, one at the outlet boundary) have to be suppressed which is accomplished by setting their time derivative to zero.

The application of periodic boundary conditions is self-evident with line-period H-grid used here (see below) in combination with the multichannel method.

Grid Generation for Moving Blades. The type of grid used for the cascade flow calculation is a line-periodic H-grid which consists of an inner algebraic mesh (see below) and an outer part generated by an elliptic method [26]. Due to the strong velocity gradient normal to the wall, a viscous flow computation requires a sufficient density of those grid lines which run parallel to solid boundaries. Additionally, the calculation of the outer eddy viscosity coefficient in the Baldwin-Lomax turbulence model is simplified if the grid lines intersecting the wall are orthogonal to the other family of mesh lines. For this reason, a separate ''boundary-layer grid'' which matches the elliptic grid at its outer boundary was generated algebraically (Fig. 1). The grid point displacement must be carefully organized for oscillating blades. As the blades are in motion relative to each other, the total grid has to be deformed to enable it to conform to the new position of the vibrating blades after each time step. For given harmonic blade motions the time-dependent grid generation is achieved by computing the deforming mesh by time-harmonic interpolation from a set of steady-state grids with different blade amplitudes. To avoid unwanted additional numerical diffusion in the boundary layer the algebraic grid moves rigid with the blade.

Validation Example

In order to demonstrate the presented method's capability to predict nonlinear viscous phenomena such as shock-boundary-

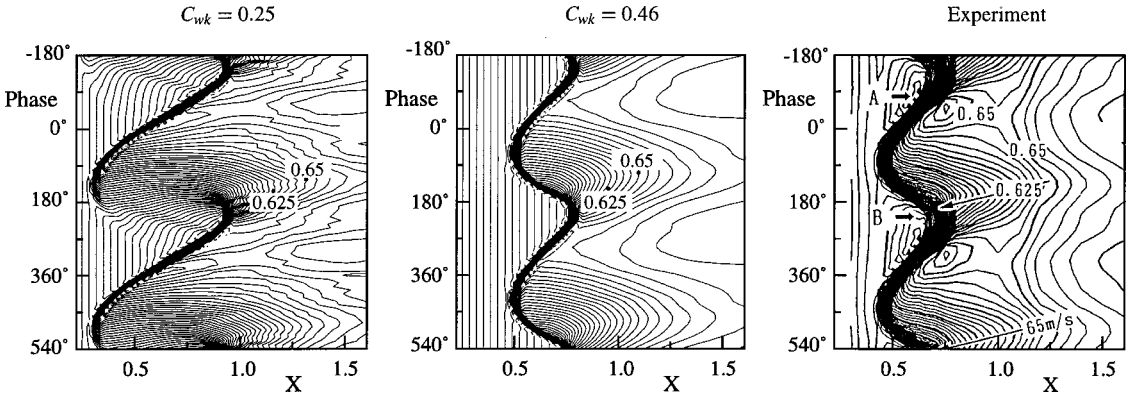

Fig. 2 Computed and measured time history of static pressure in the midplane between profile and wall (the absolute phase is arbitrary)

layer interaction and large-scale shock oscillation, the experiment of Yamamoto and Tanida [27] has been selected for code validation.

In this basic experiment Yamamoto and Tanida investigated the self-induced shock oscillation on a symmetric 10 percent thick circular arc profile in a transonic windtunnel of rectangular cross section. In all experiments the flow was adjusted so that the windtunnel was choked at every instant of the shock vibration while two shocks emanated from the profile's surface to the windtunnel walls. The main motivation for selecting precisely this challenging test case was to investigate the capability of the turbulence model to correctly predict the amplitude and the frequency of the self-induced shock oscillation. Since there is some want of clearness about the correct value of the turbulence model constant C_{wk} (values between $C_{wk}=0.25$ and 1.0 are found in the literature, where higher values lead to a higher turbulent viscosity in the outer boundary layer), special interest was focused on the influence of a varying C_{wk} value on the unsteady flow.

When the back pressure ratio p_2/p_0 is slowly reduced below a value of 0.7 a sudden onset of the self-sustained shock oscillation can be observed in the experiment. The frequency of this vibration is dependent on the average shock position and increases with a shift of the mean shock location towards the trailing edge of the profile.

Among the measured results, the one with a back pressure ratio of 0.667 was chosen since this test case was fully documented and characterized by a smooth, almost harmonic shock motion. The Reynolds number for this case was given as $1\cdot 10^6$ and the transition from laminar to turbulent flow was enforced at 10 percent of the profile chord where a transition strip was mounted on both sides of the profile.

The original C_{wk} value of 0.25 was adopted in a first attempt to compute the unsteady flow for the test case mentioned above. The computational mesh used here consisted of 199×99 grid points with a spacing of $y^+<0.8$ at the blade's surface. The flow along the windtunnel walls was calculated with inviscid boundary conditions since no influence on the shock dynamics was observed.

It was found that the experimental values of the mean shock position and the shock amplitude were not met by the theoretical results. For this reason the back pressure ratio was slightly raised to a value of 0.703 to enforce the agreement of the experimental and theoretical average shock location since this quantity strongly influences the vibration frequency. After this correction, the mean shock position was in agreement with the measured one but the shock amplitude was still too high. The computed and measured shock motions are shown in Fig. 2 where the time histories of the isobars in the midplane between profile and wall are depicted for approximately two oscillation periods ($x=0$ corresponds to midchord of the profile, $x=1$ to the trailing edge). The predicted shock amplitude is approximately twice the measured one and does not show harmonic behavior. The computed shock slowly moves upstream and then suddenly jumps back. The calculated frequency of this process is 647 Hz in contrast to the measured value of 600 Hz.

Similar results for this test case have been reported by other authors who also used the Baldwin-Lomax model for turbulent flow [14,28]. The conclusion which may be drawn from this preliminary result is that the Baldwin-Lomax model in its original version is not able to produce here the required amount of turbulent viscosity μ_t, a failure which causes a much higher shock-boundary layer interaction than that observed in the experiment.

It has already been mentioned that the production of turbulent viscosity can be increased by replacing $C_{wk}=0.25$ with a higher value. For this reason a second attempt was made for $C_{wk}=1.0$. For this value no self-induced shock oscillation was observable and an existing oscillation produced with a lower starting value of C_{wk} was rapidly damped out. Thus C_{wk} was adjusted in a third numerical experiment as such that the experimentally determined shock amplitude was obtained. The value of C_{wk} which yields the desired amplitude was 0.46. The computed time history of the midplane isobars (Fig. 2) are now in much better agreement with the experimental data than in the case before. The gradients of the calculated isobars suggest a smooth vibration of the shock as observed in the experiment. A remarkable fact is the almost unchanged computed frequency of 673 Hz, although the amplitude has been drastically reduced due to the manipulation of C_{wk}. Comparing the iso-Machlines for $C_{wk}=0.25$ and $C_{wk}=0.46$ in Fig. 3, downstream running vortices for the lower value of this constant can be identified. The pattern of vortices completely vanishes at $C_{wk}=0.46$, while the wake of the profile shows an almost steady-state behavior. This is due to the increased turbulent viscosity and—as a consequence of the smaller shock amplitude—significantly reduced flow separation regions on both sides of the profile.

It should be mentioned however, that the shock oscillation does not automatically appear with a choice of $C_{wk}=0.46$ if a fully attached flow is used as an initial solution. In this case, the computation is started with $C_{wk}=0.25$ to obtain the required initial shock-induced flow separation. Afterwards, the calculation is continued with $C_{wk}=0.46$. Another difficulty which complicates the application of the Baldwin-Lomax two layer model consists of finding the boundary between the inner and outer layer in the vicinity of the oscillating shock. Here the boundary layer shows a strong gradient when moving across the shock. If the gridlines are not parallel to the shock the determination of the above-mentioned boundary and, with that, the computation of the turbulent viscosity may be performed with great inaccuracies. Unfortunately, the oscillation amplitude responds very sensitively to small deviations in the turbulent viscosity.

A conclusion of this investigation is that the Baldwin-Lomax

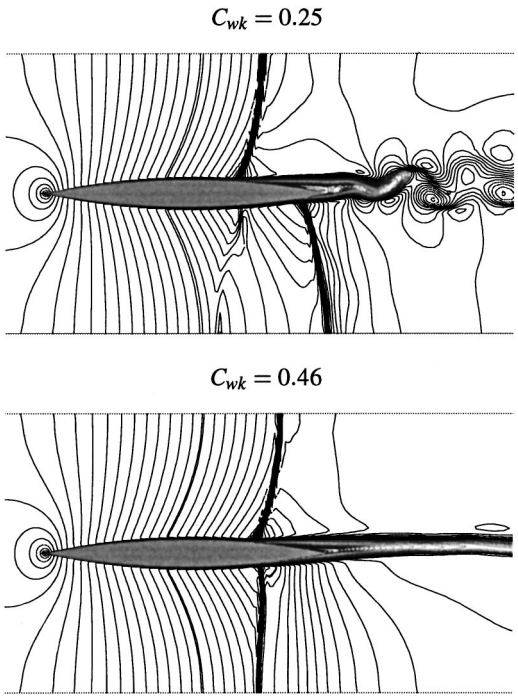

Fig. 3 Mach contours for C_{wk}=0.25 and 0.46, —=sonic line

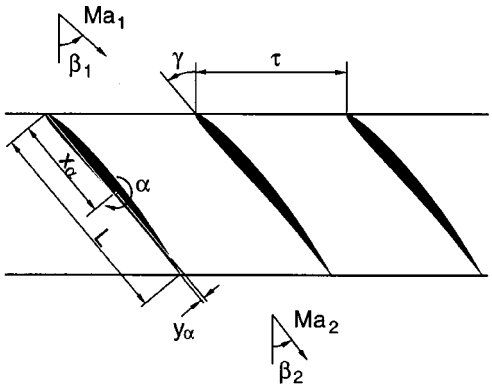

profile	NACA 3506
pitch-chord ratio	$\tau/L = 0.71$
stagger angle	$\gamma = 40°$
pitching axis	$(x_\alpha, y_\alpha) = (0.5, 0.02)$
pitching amplitude	$\alpha = 0.5° - 2.0°$
reduced frequency	$\omega^* = 2\pi fL/V_1 = 0.1 - 0.5$
inflow Mach number	$Ma_1 = 0.60 - 0.85$
inflow angle	$\beta_1 = 48.3°$
outflow Mach number	$Ma_2 = 0.45 - 0.50$
outflow angle	$\beta_2 = 37°$
inflow Reynolds number	$Re_1 = 5 \cdot 10^5 - 3 \cdot 10^6$

Fig. 4 Compressor cascade geometry and operating data

turbulence model is able to predict the amplitude and the frequency of self-induced shock oscillations with sufficient accuracy if one assumes a variable C_{wk} value. A value of $C_{wk}=0.25$ is certainly too low, whereas $C_{wk}=1.0$ is much too high. It is believed that a realistic value lies between 0.4 and 0.5.

Compressor Cascade Results

The preceding example impressively demonstrates the importance of taking into account viscous effects when computing unsteady transonic flows. Regarding the unsteady flow through oscillating blade rows, two basic questions have to be answered:

(1) In which cases do viscous effects significantly influence the vibrational behavior and, with that, the aerodynamic damping of the blades?
(2) What is the physical mechanism controlling these changes?

In order to provide an answer to these questions a numerical study was performed where the most important parameters were systematically varied. The configuration used for calculations is a transonic compressor cascade consisting of NACA 3506 profiles. The geometric and operating data of the cascade are given in Fig. 4. The reason for choosing a compressor instead of a turbine cascade was twofold: The positive pressure gradient in a compressor leads to a formation of thicker boundary layers which are more sensitive to flow separation. The transition from laminar to turbulent flow usually takes place very close the leading edge and can be approximated by fully turbulent flow if no appropriate transition model is available.

It is well known from numerical and experimental studies that blade rows performing pitching oscillations show a much more unstable behavior than cascades vibrating in bending motion. For this reason only pitching vibrations were investigated here. The remaining parameters to be varied were then the Mach number, the Reynolds number, the reduced frequency, the interblade phase angle and—most importantly—the oscillation amplitude. The computational meshes used here consisted of 119×27 grid points for Euler and 205×91 grid points for Navier-Stokes solutions. The latter mesh fineness guarantees a resolution of the boundary layer with 15 to 30 grid lines ($y^+<2.0$).

The following results for steady-state and unsteady flow were all computed with the original Baldwin-Lomax constant, *i.e.* with $C_{wk}=0.25$, since it had to be guaranteed that a possible occurrence of shock-boundary-layer interactions was not missed by taking a too high value of this constant. In the appearance of strong interactions additional calculations with higher C_{wk} values were done to prove that the results are realistic.

Steady-State Results. The two parameters to be varied in steady-state flow are the Mach and the Reynolds number. A computation with inflow Mach numbers increasing from 0.60 to 0.85 shows that the flow at $Ma_1=0.60$ is completely subsonic (even a large-amplitude oscillation does not lead to transonic flow), while the higher value of $Ma_1=0.85$ calls forth a pronounced region of supersonic flow terminated by a shock on the suction side of the blades. The isentropic Mach number distribution over the chord is depicted in Fig. 5, where Euler and Navier-Stokes results are presented for the lowest and highest inflow Mach number. The Reynolds number for the viscous flow computations is $Re_1=5\cdot10^5$. In the rear part of the blade the Navier-Stokes solutions yield higher Mach numbers than the Euler calculations. The reason for these different results is the blockage effect of the increasing boundary layer thickness leading to higher flow velocities in this region.

A second diagram showing the wall friction coefficient (Fig. 6) illustrates the occurrence of flow separation on the suction side of the blades. The flow separation at the trailing edge moves upstream with an increasing inflow Mach number ($Ma_1=0.60$: $x/L(\text{sep})=0.95$, $Ma_1=0.85$:$x/L(\text{sep})=0.90$). Significant differences are noticeable in the vicinity of the shock where a small separation bubble appears in transonic flow.

Higher Reynolds numbers (e.g., $Re_1=1.5\cdot10^6$ and $3.0\cdot10^6$, not shown here) effect a shift of the flow separation to the trailing edge combined with the disappearance of the separation bubble at the shock location.

Results for Oscillating Blade Rows. The results for unsteady flow through vibrating blade rows were all computed for tuned

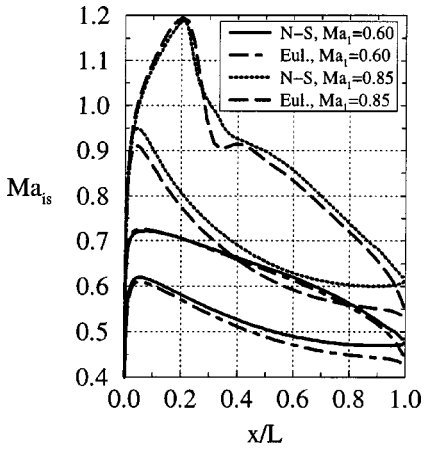

Fig. 5 Isentropic Mach number distribution for subsonic and transonic steady-state flow ($Re_1=5\cdot10^5$)

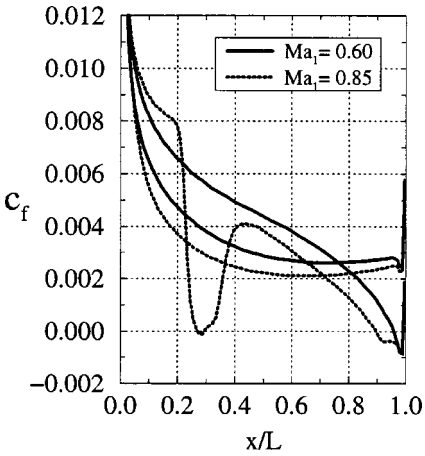

Fig. 6 Wall friction coefficient for subsonic and transonic steady-state flow ($Re_1=5\cdot10^5$)

pitching oscillations, i.e., for torsional vibrations with the same frequency and amplitude, but with a constant interblade phase angle (IBPA) σ.

In order to obtain a general view of the interesting domain of parameters, Euler calculations of the unsteady flow were performed first where Mach number, reduced frequency, and IBPA were systematically varied. An example is presented in Fig. 7 depicting the aerodynamic damping as function of the IBPA for increasing reduced frequencies $\omega^*=0.1$, 0.3, 0.5. The damping coefficient is defined as the out of phase part of the unsteady moment per unit torsional amplitude. Inflow Mach number and pitching amplitude were kept fixed at $Ma_1=0.85$ and $\alpha=0.5$ deg, respectively. The key result in this figure is that the lowest reduced frequency $\omega^*=0.1$ yields unstable oscillations in the IBPA range between 0 deg and +90 deg, whereas the vibration at $\omega^*=0.5$ is damped for all IBPA's. The aerodynamic damping computed at lower values of Ma_1 shows almost the same behavior. Since it is desirable to investigate the influence of viscous effects for stable as well as for unstable oscillations, the reduced frequency in the subsequent computations was varied in the range from 0.1 to 0.5. The computations were carried out with the so-called multichannel method, where the number of blade channels to be calculated depends on the IBPA [17]. Due to the extreme computational effort that would be necessary if every IBPA is taken into account the viscous computations were restricted to σ values of 0 deg, 180 deg, −90 deg, and +90 deg. In the following, the presentation of Euler and Navier-Stokes solutions is restricted to results for $\sigma=+90$ deg, since this IBPA is very close to the predicted range of unstable interblade phase angles and proved to be the most interesting case. Moreover, the computed results for $\sigma=0$ deg, −90 deg, 180 deg do not show any additional viscous phenomena of interest. For $\sigma=0$ deg no viscous effects are observable. Although the greatest differences between Euler and Navier-Stokes calculations occurred for $\sigma=180$ deg, the cascade is damped for the entire investigated parameter range.

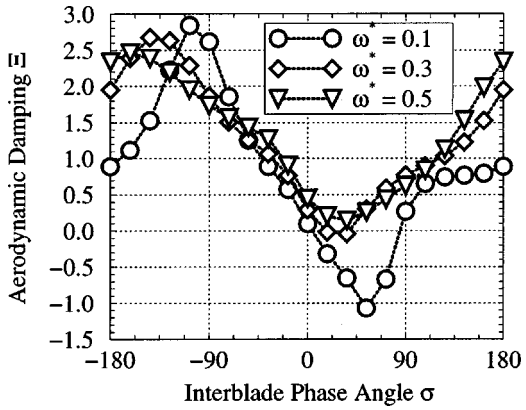

Fig. 7 Aerodynamic damping as function of IBPA, Euler results, $Ma_1=0.85$, $\alpha=0.5$ deg

To investigate the different behavior of inviscid and viscous flow at a varying inflow Mach number, Ma_1 was increased from 0.60 to 0.85 (with values of 0.75 and 0.80 in between), while the reduced frequency and Reynolds number were kept fixed at $\omega^*=0.3$ and $Re_1=5\cdot10^5$, respectively. In Fig. 8 Euler and Navier-Stokes results are presented showing the aerodynamic damping over the inflow Mach number for the three vibration amplitudes $\alpha=0.5$ deg, 1.0 deg, 2.0 deg. The damping predicted by the *N-S* solutions are, without exception, lower than the corresponding value of the Euler results which is due to slightly different initial steady-state solutions. The inviscid as well as the viscous solutions yield an increasing damping with increasing inflow Mach number. The only exception from this trend is the result for the highest oscillation amplitude and highest Mach number where both CFD methods produce decreasing damping in comparison to the preceding value.

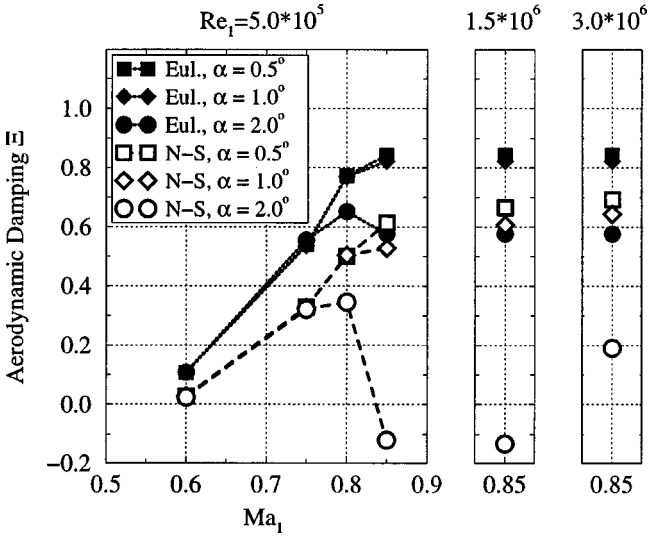

Fig. 8 Aerodynamic damping as function of inflow Mach number, $\omega^*=0.3$, $\sigma=+90$ deg

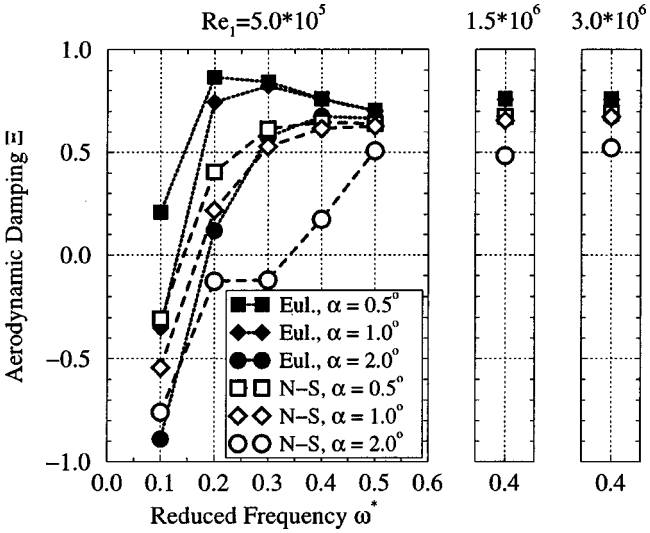

Fig. 9 Aerodynamic damping as function of reduced frequency, $Ma_1=0.85$, $\sigma=+90$ deg

The most striking result following from Fig. 8, however, is the amplitude nonlinearity of the aerodynamic damping for higher Mach numbers. Whereas the lower Mach numbers 0.60 and 0.75 are characterized by constant damping coefficients for all amplitudes, the higher Ma_1 values 0.80 and 0.85 give rise to pronounced nonlinearities for $\alpha=2.0$ deg. Here a decreasing damping value is observed if the vibration amplitude for a fixed Mach number is raised from 1 deg to 2 deg. For $Ma_1=0.80$ the magnitude of decrease is of the same order for both the Euler and the N-S results, thus it is assumed that this lowered damping is due more to compressibility than to viscous effects.

In contrast, a significantly different change in damping occurs at $Ma_1=0.85$. Here, the decrease in damping predicted by the viscous solution is much higher and yields a negative value indicating an unstable oscillation, whereas the Euler result shows a moderate reduction with a still positive damping. This different behavior is obviously due to a viscous effect for which the physical interpretation will be given in the next section.

Additionally, Fig. 8 shows the influence of the Reynolds number on the aerodynamic damping for the highest inflow Mach number. A small influence is observable only for $\alpha=2.0$ deg when increasing the Reynolds number to $Re_1=3\cdot10^6$ (which is a very high value for compressor blades).

Another important issue is the dependence of the aerodynamic damping on the reduced frequency. The influence of this quantity was investigated at $Ma_1=0.85$ since this inflow Mach number yielded the strongest effects with respect to amplitude nonlinearity and differences between inviscid and viscous computational results. As in the parametric study with varying Mach numbers the Reynolds number was kept fixed at $5\cdot10^5$. The aerodynamic damping as function of the reduced frequency, which was varied between 0.1 and 0.5, is depicted in Fig. 9. This diagram confirms the previously shown Euler results of Fig. 7, namely that all vibrations become stable above a certain frequency limit. The general trend as observed in Fig. 9 is that the damping increases with rising reduced frequency. Exceptions from this behavior are the Euler results for $\alpha=0.5$ deg and 1.0 deg which show a maximum between $\omega^*=0.2$ and 0.3 followed by a slight decrease in damping.

Another important result which again demonstrates the dominance of nonlinear and viscous effects is that the calculated damping may change its sign depending on vibration amplitude and/or computation with an inviscid or viscous method. Strong amplitude nonlinearities were predicted by both CFD methods for $\omega^*=0.1$ where the Euler code yielded a damped vibration for $\alpha=0.5$ deg in contrast to all other results for this ω^* value. It is noticeable that for this reduced frequency the nonlinearity concerning the damping is clearly weaker for the N-S results than for the Euler results. A further remarkable example is the unstable oscillation computed with the viscous code for $\omega^*=0.2$ and 0.3 with an amplitude $\alpha=2.0$ deg, while the Euler solutions for all amplitudes and the N-S calculations with $\alpha=0.5$ deg and 1.0 deg show a positive damping.

The complex behavior of the aerodynamic damping for lower reduced frequencies (0.1–0.3) is no longer observed for higher ω^* values, where the amplitude dependence of the damping almost disappears ($\omega^*=0.5$) and the difference between inviscid and viscous flow is much smaller than for lower ω^* values.

Also, a growing influence of the Reynolds number for increasing reduced frequencies is observable. An example of this is shown in Fig. 9 for $\omega^*=0.4$. In contrast to the previous case, ($\omega^*=0.3$, Fig. 8) the strong nonlinearity already disappears for $Re_1=1.5\cdot10^6$.

Detailed Investigation of the Aerodynamic Damping Behavior. The great discrepancies between Euler and *N-S* results for $Ma_1=0.85$ are obviously due to viscous effects. In this section an attempt is made to interpret these differences from a more physical point of view.

As an example, the unsteady flow for $Ma_1=0.85$ and $\omega^*=0.3$ is investigated here in detail. This test case is characterized by the occurrence of a permanent supersonic flow region on the blade's suction surface close to the leading edge and a supersonic zone on the pressure side appearing and disappearing during one period of vibration. A particular scenario is observed for the largest amplitude $\alpha=2.0$ deg where the unsteady flow through the blade channel is choked for a certain space of time. During this choking period, the flow is accelerated to supersonic values in the entire cross section of the blade channel creating a strong oscillating channel shock which produces pronounced shock-boundary layer interactions on both the blade's suction and pressure sides. On the contrary, no choked flow occurs for the two smaller vibration amplitudes $\alpha=0.5$ deg and $\alpha=1.0$ deg.

Figure 10 shows the iso-Machlines of the viscous solution at four specific times in the course of one oscillation period ($\alpha=2.0$ deg). Here, the nondimensional time $\hat{t}$ is referred to the vibration period of the blade. When the blade channel shock has been formed it causes a strong boundary layer separation accompanied by a forward shift of the shock and a reduction of the supersonic flow region to a small pocket ($\hat{t}=0.5$). Later on, the separation bubble on the pressure side breaks down while the flow reattaches ($\hat{t}=0.6$). The time interval between the onset of the shock-induced flow separation and the reattachment is rather short ($\hat{t}=0.4-0.6$). In contrast, the Euler solution (not shown here) is characterized by a choking period that is twice the corresponding time interval of the N-S result.

The local aerodynamic work coefficients depicted in Fig. 11 (Euler) and Fig. 12 (Navier-Stokes) illustrate the zones of the blade's surface where energy is subtracted from the flow (excitation) and the other zones where energy is submitted to the flow (damping). Primarily, the remarkable damping computed by both CFD methods at the mean position of the oscillating front shock is noticeable. Assessing the viscous effects pointed out by both figures, the following two statements are appropriate:

(1) Since no other viscous effects are observable here, the good agreement of the Euler with the N-S results for the amplitudes $\alpha=0.5$ deg and $\alpha=1.0$ deg indicates that the small flow separation at the trailing edge does not influence the aerodynamic damping.

(2) The application of the viscous CFD method to the test case with the largest amplitude ($\alpha=2.0$ deg) obviously leads to a completely different influence of the vibrating blade channel shock on the work coefficient and hence on the aerodynamic damping.

With regard to the latter statement, the Euler code yields a distinct instability at the shock's average position on the suction

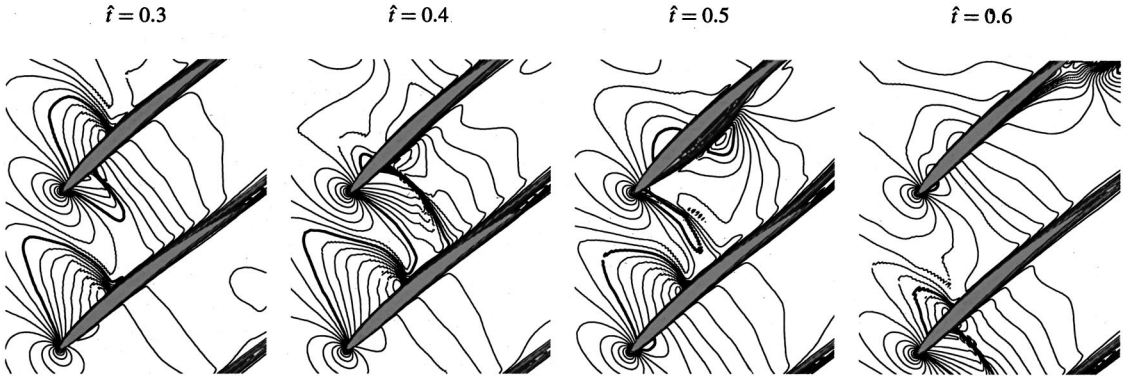

Fig. 10 Mach contours for different timesteps, Navier-Stokes results, α=2.0 deg, ω^*=0.3, Ma_1=0.85, Re_1=5·10^5, σ=+90 deg, —=sonic line

side ($x/L=0.65$) and a damping influence at the corresponding location on the pressure side ($x/L\leqslant 0.2$). The viscous result for α=2.0 deg shows no pronounced response to the channel shock vibrating on the suction side, a behavior that may be explained by the reduced choking period of the flow. In contrast to the inviscid results, the N-S method predicts a reception of energy in the front part of the pressure side. This must be due the strong shock-boundary layer interaction followed by the downstream flow separation.

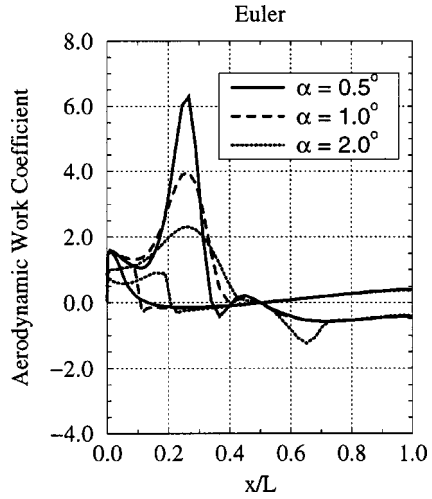

Fig. 11 Aerodynamic work coefficient, Euler results, ω^*=0.3, Ma_1=0.85, σ=+90 deg

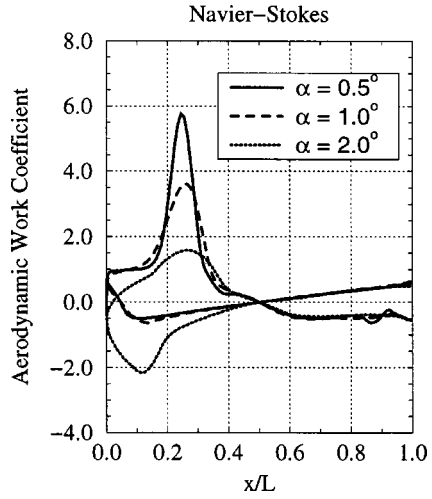

Fig. 12 Aerodynamic work coefficient, Navier-Stokes results, ω^*=0.3, Ma_1=0.85, Re_1=5·10^5, σ=+90 deg

Another interesting test case demonstrating the importance of taking into account viscous effects is the unsteady flow for $Ma_1=0.85$ and $\omega^*=0.1$.

An important feature of the viscous flow computed for this test case is that a self-induced shock oscillation of the channel shock appears during a blade oscillation period. It is caused by a shock-induced flow separation occurring alternately on the suction and pressure side of neighboring blades. The amplitude of this oscillation is so large that the shock disappears completely while moving upstream but as soon as the flow has reattached the shock appears again. The frequency of the shock oscillation is much higher than the blade vibration frequency; the shock moves upstream and downstream three times in the time interval $\hat{t}=0.3-0.6$. In contrast to this, the Euler code yields a continuously choked blade channel in this time interval; here the shock movement is controlled by the blade motion only. The local aerodynamic work coefficients depicted in Fig. 13 (Euler) and Fig. 14 (Navier-Stokes) illustrate the agreements and discrepancies between the inviscid and the viscous computation of this test case:

(1) Although the flow features in the blade channel during one oscillation period are completely different, both codes yield a similar distribution of aerodynamic work loading on the pressure side which produces the governing contribution to an unstable blade vibration.

(2) Amplitude nonlinearities, *i.e.* amplitude-dependent values of the local work coefficient are mainly observable on the suction side, but here are significantly higher for inviscid than for viscous flow. Again, the viscous results show no pronounced response to the channel shock vibrating on the suction side ($x/L=0.6-0.8$).

As mentioned before, all calculations have been performed with the turbulence model constant $C_{wk}=0.25$ to circumvent the uncertainty that the Baldwin-Lomax model may not start self-induced shock oscillations. This procedure guarantees that all possible shock-induced boundary layer separations are found. In order to prove that the results are realistic, all calculations where strong shock-induced flow separation occurred are recalculated with $C_{wk}=0.5$. Unfortunately, no strong flow separation occurs for σ=90 deg, thus it is not quite clear if this behavior is due to the real flow physics or to the inability of the used method to initiate the shock oscillation. Starting the calculation with $C_{wk}=0.25$ and then switching to higher C_{wk} values—as was done for the circular arc profile—would make no sense because the oscillation appears only for a short time during the blade oscillation period and hence has to be restarted for each period, a technique which is impossible. In contrast to this, the strong shock-

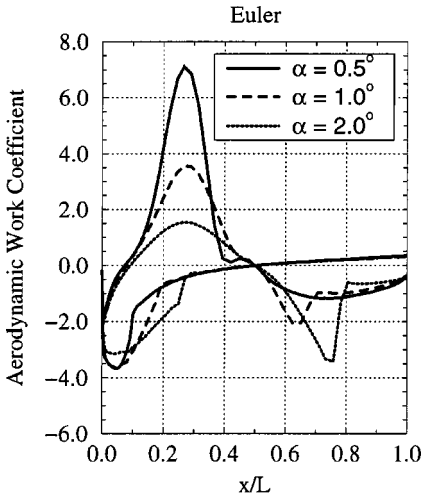

Fig. 13 Aerodynamic work coefficient, Euler results, $\omega^*=0.1$, $Ma_1=0.85$, $\sigma=+90$ deg

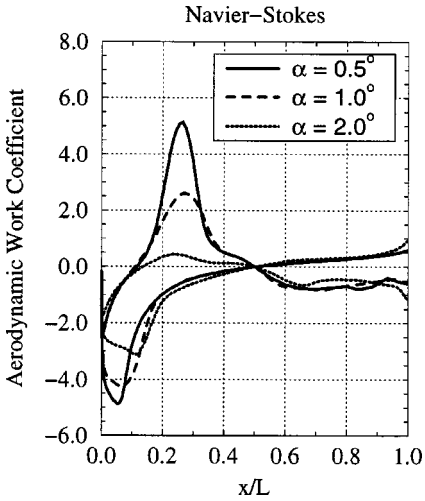

Fig. 14 Aerodynamic work coefficient, Navier-Stokes results, $\omega^*=0.1$, $Ma_1=0.85$, $Re_1=5.0\cdot10^5$, $\sigma=+90$ deg

boundary-layer interaction still exists for $\sigma=180$ deg, where the unsteady pressure amplitude is much higher due to the greater channel cross section variation during a blade oscillation period. From this it can be concluded that even if the presented results may not be realistic for specific flow conditions, the viscous effects mentioned above will appear for flow conditions which produce stronger shocks, *e.g.* flows with higher inflow Mach numbers, larger oscillation amplitudes, and/or lower pitch-chord ratios.

Concluding Remarks

The aim of this work was to investigate the influence of viscous effects on the aerodynamic damping of vibrating compressor blades.

In a first step, the ability of the Baldwin-Lomax turbulence model to predict the self-induced shock oscillations due to shock-boundary-layer interaction was investigated. It was demonstrated that the frequency of the shock oscillation was calculated with sufficient accuracy, but that the amplitude significantly depends on the value of the turbulence model constant C_{wk}. The commonly accepted values of $C_{wk}=0.25$ and 1.0 published in the literature are obviously too low and too high, respectively. Furthermore, a great dependence of the shock's vibration amplitude on the implementation of the turbulence model and on the grid-line orientation was observed, thus an exact value of C_{wk} could not be provided. An appropriate value was found between $C_{wk}=0.4$ and 0.5. Hence, the Baldwin-Lomax turbulence model cannot be used as a ''black-box'' and the results obtained with this model have to be interpreted very carefully.

In a second step, a parametric study for a transonic compressor cascade consisting of NACA 3506 profiles was performed. The Mach number, Reynolds number, reduced frequency, oscillation amplitude and interblade phase angle were varied. To identify viscous effects, all results were compared to inviscid Euler data. It was found that viscous effects could severely affect the aerodynamic damping in such cases where the unsteady pressure distribution of inviscid flow is significantly changed due to a growing boundary layer displacement thickness, *e.g.*, if strong shock-boundary interactions occur. The influence of viscous effects become more important with increasing Mach number and oscillation amplitude and with decreasing reduced frequency and Reynolds number. The impact on the aerodynamic damping is multifarious. It was found that viscous effects can effect both a distinct increase or decrease of the damping. Additionally, the amplitude nonlinearities can be both enlarged and reduced. In some cases the discrepancies between the viscous and inviscid solution are so great that the aerodynamic damping changes its sign. Finally, it was found that the small boundary layer separation observed in the steady solutions at the trailing edge of the blade has only a negligible influence on the unsteady pressure distribution and hence on the aerodynamic damping.

References

[1] Hall, K. C., and Crawley, E. F., 1989, ''Calculation of Unsteady Flows in Turbomachinery Using the Linearized Euler Equations,'' AIAA J., **27**, pp. 777–787.

[2] Kahl, G., and Klose, A., 1993, ''Computation of the Linearized Transonic Flow in Oscillating Cascades,'' ASME Paper No. 93-GT-269.

[3] Montgomery, M. D., and Verdon, J. M., 1997, ''A 3D Linearized Unsteady Euler Analysis for Turbomachinery Blade Rows, Part 1: Aerodynamic and Numerical Formulations, Part 2: Unsteady Aerodynamic Response Predictions,'' *Proceedings of the 8th International Symposium on Unsteady Arodynamics and Aeroelasticity of Turbomachines*, Stockholm, Sweden, Sept. 14–18.

[4] Holmes, D. G., Mitchell, B. E., and Lorence, C. A., 1997, ''Three Dimensional Linearized Navier-Stokes Calculations for Flutter and Forced Response,'' *Proceedings of the 8th International Symposium on Unsteady Arodynamics and Aeroelasticity of Turbomachines*, Stockholm, Sweden, Sept. 14–18.

[5] Clark, W. S., and Hall, K. C., 1995, ''A Numerical Model of the Onset of Stall Flutter in Cascades,'' ASME Paper No. 95-GT-377.

[6] Clark, W. S., and Hall, K. C., 1999, ''A Time-Linearized Navier-Stokes Analysis of Stall Flutter,'' ASME Paper No. 99-GT-383.

[7] Gerolymos, G. A., 1988, ''Numerical Integration of the Blade-to-Blade Surface Euler Equations in Vibrating Cascades,'' AIAA J., **26**, pp. 1483–1492.

[8] Gerolymos, G. A., and Vallet, I., 1994, ''Validation of 3D Euler Methods for Vibrating Cascade Aerodynamics,'' ASME Paper No. 94-GT-294.

[9] He, L., 1989, ''An Euler Solution for Unsteady Flows Around Oscillating Blades,'' ASME Paper No. 89-GT-279.

[10] Carstens, V., 1991, ''Computation of the Unsteady Transonic 2D Cascade Flow by an Euler Algorithm with Interactive Grid Generation,'' AGARD CP 507, Transonic Unsteady Aerodynamics and Aeroelasticity, San Diego, USA, October 7–11.

[11] Carstens, V., Bölcs, A., and Körbächer, H., 1993, ''Comparison of Experimental and Theoretical Results for Unsteady Transonic Cascade Flow at Design and Off-Design Conditions,'' ASME Paper No. 93-GT-100.

[12] Peitsch, D., Gallus, H. E., and Weber, S., 1994, ''Computation of Unsteady Transonic 3D-Flow in Turbomachine Bladings,'' *Proceedings of the 7th International Symposium on Unsteady Arodynamics and Aeroelasticity of Turbomachines*, Fukuoka, Japan, Sept. 25–29.

[13] Chuang, H. A., and Verdon, J. M., 1998, ''A Nonlinear Numerical Simulator for Three Dimensional Flows through Vibrating Blade Rows,'' ASME Paper No. 98-GT-18.

[14] He, L., 1993, ''New Two-Grid Acceleration Method for Unsteady Navier-Stokes Calculations,'' J. Propul. Power, **9**, No. 2, March–April, pp. 272–280.

[15] Abhari, R. S., and Giles, M., 1995, ''A Navier-Stokes Analysis of Airfoils in Oscillating Transonic Cascades for the Prediction of Aerodynamic Damping,'' ASME Paper No. 95-GT-182.

[16] Ayer, T. C., and Verdon, J. M., 1998, ''Validation of a Nonlinear Unsteady Aerodynamic Simulator for Vibrating Blade Rows,'' ASME J. Turbomach., **120**, No. 1, pp. 112–121.

[17] Grüber, B., and Carstens, V., 1998, ''Computation of the Unsteady Transonic Flow in Harmonically Oscillating Turbine Cascades Taking Into Account Vis-

cous Effects,'' ASME J. Turbomach., **120**, No. 1, pp. 104–111.
[18] Weber, S., Benetschik, H., Peitsch, D., and Gallus, H. E., 1997, ''A Numerical Approach to Unstalled and Stalled Flutter Phenomena in Turbomachinery Cascades,'' ASME Paper No. 97-GT-102.
[19] Isomura, K., and Giles, M.B., 1997, ''A Numerical Study of Flutter in a Transonic Fan,'' ASME Paper No. 97-GT-235.
[20] Fransson, T.H., Jöcker, M., Bölcs, A., and Ott, P., 1998, ''Viscous and Inviscid Linear/Nonlinear Calculations Versus Quasi 3D Experimental Cascade Data for a New Aeroelastic Turbine Standard Configuration,'' ASME Paper No. 98-GT-490.
[21] Liou, M. S., and Steffen, Jr., C. J., 1993, ''A New Flux Splitting Scheme,'' J. Comput. Phys., **107**, pp. 23–39.
[22] van Leer, B., 1979, ''Towards the Ultimate Conservative Difference Scheme, V. A Second Order Sequel to Godunov's Method,'' J. Comput. Phys., **32**, pp. 101–136.
[23] Beam, R. M., and Warming, R. F., 1976, ''An Implicit Finite-Difference Algorithm for Hyperbolic Systems in Conservation-Law Form,'' J. Comput. Phys., **22**, pp. 87–110.
[24] Baldwin, B. S., and Lomax, H., 1978, ''Thin Layer Approximation and Algebraic Model for Separated Turbulent Flows,'' AIAA-78-257.
[25] Chakravarthy, S. R., 1982, ''Euler Equations—Implicit Schemes and Boundary Conditions,'' AIAA Paper No. 82-0228.
[26] Carstens, V., 1988, ''Two-Dimensional Elliptic Grid Generation for Airfoils and Cascades,'' DLR-FB, pp. 88–52.
[27] Yamamoto, K., and Tanida, T., 1987, ''Self-Exited Oscillation of Shock Waves on an Airfoil in Two-Dimensional Transonic Channel Flow,'' *Proceeding of Fourth Symposium on Unsteady Aerodynamics and Aeroelasticity of Turbomachines and Propellers*, Aachen, pp. 769–783.
[28] Yamamoto, K., and Tanida, T., 1989, ''Self-Excited Oscillation of Transonic Flow Around an Airfoil in a Two-Dimensional Channel,'' ASME Paper No. 89-GT-58.

An Investigation of Surge in a High-Speed Centrifugal Compressor Using Digital PIV

Mark P. Wernet

Michelle M. Bright

National Aeronautics and Space Administration,
Glenn Research Center,
Cleveland, OH 44135

Gary J. Skoch

Army Research Laboratory,
Vehicle Technology Directorate,
Glenn Research Center,
Cleveland, OH 44135

Compressor stall is a catastrophic breakdown of the flow in a compressor, which can lead to a loss of engine power, large pressure transients in the inlet/nacelle, and engine flameout. The implementation of active or passive strategies for controlling rotating stall and surge can significantly extend the stable operating range of a compressor without substantially sacrificing performance. It is crucial to identify the dynamic changes occurring in the flow field prior to rotating stall and surge in order to control these events successfully. Generally, pressure transducer measurements are made to capture the transient response of a compressor prior to rotating stall. In this investigation, Digital Particle Imaging Velocimetry (DPIV) is used in conjunction with dynamic pressure transducers to capture transient velocity and pressure measurements simultaneously in the nonstationary flow field during compressor surge. DPIV is an instantaneous, planar measurement technique that is ideally suited for studying transient flow phenomena in high-speed turbomachinery and has been used previously to map the stable operating point flow field in the diffuser of a high-speed centrifugal compressor. Through the acquisition of both DPIV images and transient pressure data, the time evolution of the unsteady flow during surge is revealed. [DOI: 10.1115/1.1343465]

1.0 Introduction

Turbomachines are used in a wide variety of engineering applications for power generation, pumping, and aeropropulsion. The need to reduce acquisition and operating costs of aeropropulsion systems drives the effort to improve propulsion system performance. Improving the efficiency in turbomachines requires understanding the flow phenomena occurring within rotating machinery. In addition to improving efficiency at design conditions, work is also in progress to investigate compressor stall. Compressor stall is a catastrophic breakdown of the flow in a compressor, which can lead to a loss of engine power, large pressure transients in the inlet/nacelle, and engine flameout. The distance on a performance map between the operating point of a compressor and its stall point is referred to as the ''stall margin.'' Stall margin is required to offset a loss of stability within the compressor caused by throttle transients and component deterioration with age. Optimal engine designs tend toward minimal stall margins since modifications to increase the stall margin typically result in heavier, less efficient, and less loaded compressors. However, if active or passive stall control is employed, stable operation over a wider range of flow conditions (improved stall margin) can be obtained with a minimal loss in performance, as demonstrated by Weigl et al. [1]. The instantaneous flow field capture capability of DPIV is well suited to the task of studying the change in flow conditions surrounding the development of stall precursors, stall cell propagation, and eventually compressor surge.

Digital Particle Imaging Velocimetry (DPIV) provides near real-time flow field measurements through the use of refined data processing techniques combined with advances in Charge Coupled Device (CCD) sensor technology. DPIV is a planar measurement technique wherein a pulsed laser light sheet is used to illuminate a flow field seeded with tracer particles small enough to accurately follow the flow. The positions of the particles are recorded on a digital CCD camera at each instant the light sheet is pulsed. In high-speed flows, pulsed Neodymium:Yttrium–Aluminum–Garnet (Nd:YAG) lasers are required to provide sufficient light energy ($\sim$100 mJ/pulse) in a short time interval ($<$10 ns) to record an unblurred image of the particles entrained in the flow. The data processing consists of determining either the average displacement of the particles over a small interrogation region in the image or the individual particle displacements between pulses of the light sheet. Knowledge of the time interval between light sheet pulses then permits computation of the flow velocity. While each processing technique has some inherent benefits, the appropriate choice depends on the characteristics of the flow and the recorded image quality.

Numerous researchers have employed various PIV techniques to study the unsteady flows in rotating machines. Paone et al. [2] used PIV to make blade-to-blade plane velocity measurements in a centrifugal compressor. Although this is not a rotating machine application, Bryanston-Cross et al. [3] described photographic PIV measurements obtained in a transonic turbine cascade rig. The light sheet illumination was introduced via an 8.0-mm-dia hollow turbulence generating bar, which was already part of the experimental rig. Rothlübbers et al. [4] used digital PIV to study the flow in a radial pump. Low seed particle concentrations were identified as not suitable for rotating machine studies, where high spatial resolution measurements are required. Oldenburg and Pap [5] used a digital PIV setup to investigate the flow field in the impeller and volute of a centrifugal pump. The lab scale facility used water as the working fluid and a transparent impeller. Gogineni and Goss [6] have described a two-color DPIV technique, which should be applicable to turbomachinery. A high-resolution (3000×2000 pixel) single CCD sensor color camera was employed to record the particle images at two instances in time on a single CCD image frame using red and green illumination pulses. Day-Treml and Lawless [7] used a high-resolution (2000×2000 pixel) digital camera to obtain DPIV measurements of rotor-stator interactions in a low-speed turbine facility. Again a light sheet probe was used to introduce the light sheet into the flow and the measured velocities were on the order of 30 m/s. Bryanston-Cross et al. [8] performed particle tracking measurements of the high-speed flow in the stator trailing edge region of a transonic axial compressor blowdown facility. Wernet [9] obtained high spatial resolution DPIV measurements in the rotor blade passage of a transonic axial compressor. Wernet [10] also employed DPIV to

Contributed by the International Gas Turbine Institute for publication in the ASME JOURNAL OF TURBOMACHINERY. Manuscript received by the International Gas Turbine Institute January 2000. Associate Editor: T. H. Okiishi.

obtain both time-averaged and instantaneous velocity maps in the diffuser region of a high-speed centrifugal compressor at a stable operating point.

A complete two-dimensional DPIV velocity mapping campaign in the diffuser region of a 431 mm diameter, 4:1 pressure ratio centrifugal compressor operating at stable conditions has recently been completed. The results will be used to augment previous surveys obtained using Laser Doppler Velocimetry (LDV) in both the diffuser and impeller regions [11]. The DPIV measurements have been obtained from 6 to 95 percent span, which is closer to the diffuser hub than was possible using LDV. Both the DPIV and LDV data are being used to assist in computational fluid dynamics code validation. These DPIV measurements of the stable operating point of the compressor were used to generate time-averaged, phase-stepped velocity vector maps of the periodic unsteady flow field due to the impeller–diffuser interaction. In this paper we present results from the simultaneous capture of instantaneous flow field data along with dynamic pressure measurements to diagnose the range of flow conditions experienced during surge.

Many researchers have investigated the area of active stall control in axial compressors. Paduano et al. [12] demonstrated the first use of active stall control to increase the operating range of compressors by oscillating the inlet guide vanes in a low-speed axial compressor. Day [13] used pulsed air injection to extend the operating range successfully on a low-speed axial compressor. Weigl et al. [1] demonstrated the use of controlled air injection in a transonic axial compressor resulting in an extension of the surge margin by over 17 percent. The work of Oakes et al. [14] on a low-speed centrifugal compressor equipped with air injection for active stall control showed that rotating stall precursors occurring in the impeller region were largely responsible for initiating the stall and surge cycle. Unsteady air injection was used to squelch the rotating stall events and lower the stalling mass flow of the compressor with minimal injection. Since active control strategies used at low speed may not be directly applicable in high-speed compressors, due to compressible modes and the influence of the diffuser on surge and stall, it is not clear whether the approach used by Oakes et al. [14] would be successful in a high-speed centrifugal compressor as well.

In all of these compressor stall and active stall control investigations, dynamic pressure data were primarily used to document the changes occurring in the compressor flow. Without detailed measurements of the flow, the use of dynamic pressure data restricts the researchers to a cause and effect analysis. The pressure characteristics are used to document the compressor behavior with and without stall control, and can be used only to infer what is actually happening in the flow and why one stall control approach has only a minimal effect while another has a more dramatic effect. In this work we demonstrate that DPIV is an invaluable tool for diagnosing the kinematic changes in the flow field during stall/surge events. Application of DPIV to active stall control studies should offer a wealth of insight into the actual mechanisms leading to stall and in the evaluation of the different stall control algorithms, and should therefore significantly reduce the time required to understand and implement an active stall control system. The next phase of this research investigation will utilize the information gained from the DPIV measurements to optimize the air injection locations for active stall control in the high-speed centrifugal compressor.

2.0 Compressor Facility, Optical Access, and Light Sheet Delivery

The centrifugal compressor is a Rolls Royce-Allison design that was scaled to a flow size of 4.54 kg/s from the original size of 1.66 kg/s. The impeller and vaned diffuser were designed to produce a pressure ratio of 4:1 at the design mass flow. The standard day corrected speed for the design flow condition is 21,789 rpm with an exit tip speed of 492 m/s. The inlet relative Mach numbers on the suction surface range from 0.9 at the tip to 0.45 at the hub. The absolute Mach number at the impeller exit is 0.87. The impeller contains 15 main blades with 15 splitter blades and has 50 deg of backsweep from radial at the discharge. The splitter blade leading edge, located at 30 percent of the main blade chord, is offset slightly toward the main blade suction surface to provide an even flow split. The inlet tip diameter is 210 mm and the inlet blade height is 64 mm. The exit diameter is 431 mm and the exit blade height is 17 mm. The vaned diffuser consists of 24 two-dimensional wedge vanes with the leading edges located at a radius ratio of 108 percent relative to the impeller exit. The diffuser has an overall area ratio of 2.75 with a total divergence angle of 7.8 deg. The diffuser exit radius is 363 mm and discharges directly into a 90 deg annular bend. The nominal operating impeller exit clearance is 0.4 mm, or 2.4 percent of the passage height at the exit. The static temperature at the diffuser throat is 108°C based on the total temperature of 198°C, measured using thermocouples in the hub wall, and the DPIV measured absolute flow velocity of 300 m/s. The compressor flow is subsonic under stable operating conditions, where the absolute local speed of sound at the diffuser throat is 357 m/s based the estimated static temperature. The compressor can be driven into stall by backpressuring the compressor via the collector valve. The compressor enters stall at a mass flow rate just below 4.26 kg/s.

A test-rig cross section showing the flow path through the impeller and diffuser can be seen in Fig. 1, while Fig. 2 shows a frontal view of the impeller and diffuser. The rig casing is designed to accept four separate window frame inserts, each containing a different set of windows with interspersed locations to provide access all along the flow path from the impeller entrance to the diffuser. Figure 1 shows two small-diameter LDV optical access ports in the forward insert. The port located farthest upstream, which is shown in Fig. 1, was used to obtain DPIV measurements of the flow entering the impeller. The port is 25 mm in diameter and has a centerline location 25 mm upstream of the impeller leading edge. Most of the DPIV data were obtained using the large window port (70×70 mm) located over the impeller exit/diffuser section of the compressor, as shown in Figs. 1 and 2. There is insufficient space near the compressor rig for the DPIV CCD camera to view the illuminated flow passage directly. A mirror mounted at 45 deg to the illumination plane is therefore used to provide the CCD recording camera with a view of the illuminated diffuser flow passages.

A compact light sheet delivery system was constructed using a periscope-type configuration, as discussed by Wernet [9]. The pulsed Nd:YAG laser beam is directed down the bore of the tube, which contains light sheet forming optics and a 45 deg turning

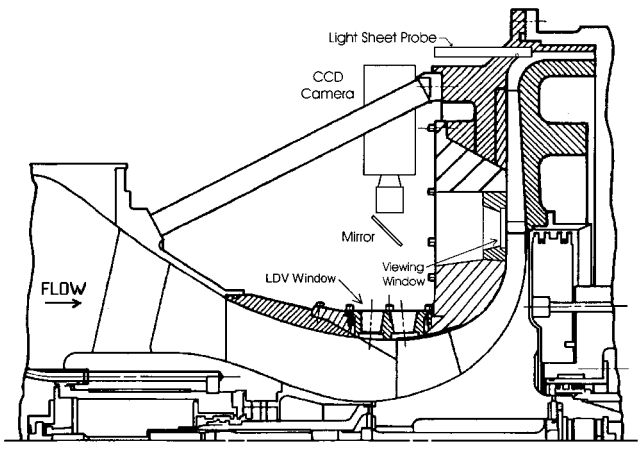

Fig. 1 Schematic cross section of centrifugal compressor facility. Optical access port and CCD camera mounting configuration are shown. Light sheet insertion and recession into compressor casing are also illustrated.

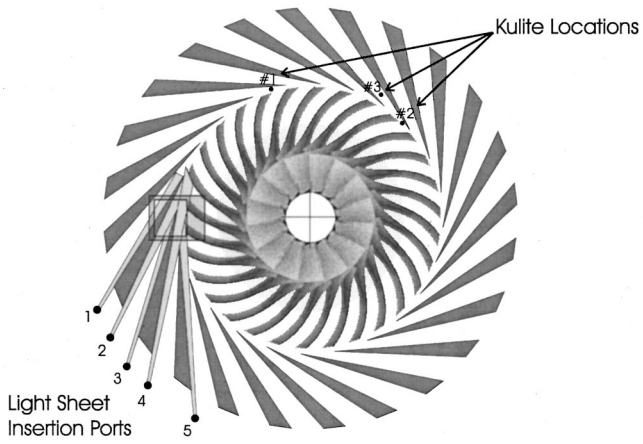

Fig. 2 Schematic drawing of vaned diffuser and impeller showing the optical viewing port, light sheet probe insertion locations, light sheet extents, and Kulite locations

mirror. The periscope probe has an outside diameter of 12.7 mm and utilizes 8-mm-dia optics (256 mm focal length spherical and −102 mm focal length cylindrical lenses) to form the laser beam into a laser sheet of approximately 13×1 mm. The distance from the probe to the measurement location is approximately 240 mm. An articulated light arm with mirror joints was used to couple the beam from the Nd:YAG laser to the probe. Use of the light arm simplifies the coupling of the laser beam to the periscope and also adds an increased level of safety to the installation since the beam is entirely enclosed when outside of the compressor casing. There is a tendency for the laser beam path to wander depending on the orientation of the light arm. Some care must be taken to ensure that the laser beam travels down the center of the light arm to couple light into the probe properly. The light sheet delivery probe has been used successfully to deliver 125 mJ pulsed illumination into the compressor passages. The light sheet exits the probe through a sealed window, which keeps the optics inside the probe protected from contamination by seed material.

The small-diameter periscope probe is inserted through the compressor casing downstream of the diffuser vanes at the 90 deg bend in the collector, as shown in Fig. 1. Five insertion holes were machined into the collector housing to permit illumination of four different diffuser vane passages. The four illuminated diffuser vane passages are successively higher in the optical viewport window, providing access to both the pressure and suction sides of the diffuser passages and the space between the exit of the impeller and the diffuser; see Fig. 2. Moving the probe in and out through the collector housing changes the spanwise location of the illumination plane. The insertion holes were machined so that approximately half of the probe diameter was recessed in the housing wall. These insertion locations ensure that the light sheet probe does not disturb the flow at the actual measurement location.

The compressor casing was fitted with dynamic pressure transducers (three 340 kPa and one 100 kPa Kulite transducers) at four locations. The transducer circumferential locations are referenced in degrees from top-dead-center, proceeding in a clockwise direction. The center of the optical access viewing port is located at 270 deg. The locations of the three 340 kPa Kulite transducers are indicated in Fig. 2. Two transducers were located in the vaneless space between the impeller and the vaned diffuser (from 100 to 108 percent of the impeller radius). Transducer #1 was located at 343 deg and #2 was located at 35 deg. Transducer #3 was located in the diffuser throat at 43 deg from top-dead-center. Transducer #4, a 100 kPa Kulite that is not shown in Fig. 2, was located 25 mm upstream of the impeller at 338 deg from top-dead-center, at the same axial location as the centerline of the forward most LDV optical access port shown in Fig. 1. Only four transducers were used during these initial measurements, due to the concern over seed particle contamination. However, no degradation of the dynamic pressure transducers resulting from the flow seeding has been observed in the course of this work.

In order to measure the incipient stalling mechanisms, dynamic pressure measurements of the stall precursors were collected in the centrifugal compressor facility before the DPIV measurements were obtained. Dynamic pressure data were collected over a matrix of mass flows and rotational speed combinations. The measurements were obtained around the circumference of the compressor from transducers mounted in the compressor casing ahead of the impeller, in the vaneless passage, and in the diffuser throat. These measurements illustrated that rotating stall cells travel at approximately 25 percent to 33 percent of the impeller rotational speed. Measurements also indicate that at 70 percent speed and below stall begins in the impeller region, whereas at design speed stall originates in the diffuser.

3.0 Seeding

Seeding the high-temperature and high-speed flow encountered in the diffuser is a challenging task. In a previous LDV velocity mapping program conducted in this centrifugal compressor facility, a seeding system was specifically designed to enable measurements in the high-temperature flows encountered in the diffuser region [11]. Attempts to use PolyStyrene Latex spheres (PSL) failed due to the seed material collecting and then melting on the optical access ports. A technique employing pH stabilized dispersions of alumina in ethanol was therefore used [15]. The dispersions of alumina were injected into the facility via two commercial spray nozzles mounted in the plenum tank, approximately 10 m upstream of the impeller. The specific gravity of the alumina powder is 3.96 and the particle size distribution has a mean of 0.7 μm and a standard deviation of 0.2 μm. The concentration of alumina powder used in the dispersions was approximately 25 g/l. A side benefit of the alumina seeding is that it does not have a tendency to adhere to the optical access ports, permitting long rig run times without contamination of the view ports.

The frequency response and particle lag distance behind an oblique shock for various seed materials has been reported by Melling [16]. Using Melling's results, the seed particles used here would have a frequency response on the order of 3 kHz. The alumina particles have adequate flow following attributes for the flow field characteristics to be encountered in the centrifugal compressor under stable operating conditions.

4.0 Image Acquisition and Data Processing

Electronic image acquisition based DPIV has been demonstrated to provide adequate spatial resolution velocity measurements in the narrow flow passages encountered in turbomachinery. Another advantage of electronic image acquisition is near real-time feedback of the experimental parameters such as: laser pulse energy; seed particle concentration; assessment of flare light from blade surfaces; and camera inter-exposure time. Use of a 1008×1016 pixel, ''frame-straddling'' CCD camera enables acquisition of single exposure image pairs, which can be processed using the cross-correlation technique. Cross-correlation data reduction is the optimal data reduction technique for DPIV since it offers directionally resolved velocity vectors and the maximum dynamic range in the velocity measurements. The accuracy of the velocity estimates is inversely proportional to the particle displacement between exposures. The maximum displacement is restricted to 1/4 of the correlation subregion size; hence using a correlation subregion size of 32×32 pixels yields a maximum measurable displacement of 8 pixels. The correlation peak location can nominally be estimated to within 0.1 pixels, yielding measurement errors on the order of 1 percent of full scale for 32 ×32 pixel subregion processing. For more details of the DPIV technique, hardware and data reduction strategies, see Raffel et al. [17].

An electronic shaft angle encoder triggered from a once-per-rev signal on the impeller drive shaft was used to trigger image acquisition and laser firing, permitting DPIV data to be reliably recorded from a selected blade passage of the impeller under stable operating conditions. Increasing or decreasing the trigger delay time enabled collecting velocity vector maps at different impeller phasing positions relative to the diffuser vanes. The camera image acquisition and laser firing were all software controlled via a commercial synchronizer. The DPIV control and data acquisition computer was located next to the compressor rig. Remote operation was accomplished through the use of a commercial remote computer control box, which enables a remotely located monitor, keyboard, and mouse to control the DPIV computer from the facility control room.

The image acquisition software used in the DPIV system enables acquisition of a single-image frame pair or alternatively, a sequence of image frames. Efficient data acquisition was achieved by acquiring 100 frame sequences (50 frame pairs) into the computer's memory and saving them directly to the hard disk. Correlation processing of the images was performed off-line after the experiment was completed. Using the once-per-rev signal to trigger the DPIV system resulted in an image acquisition rate of approximately 8 frame pairs/s. Images were written to the hard drive at the rate of 1 per second.

The onset of compressor stall is a random event, which cannot be precisely predicted. Therefore, the DPIV sequence acquisition was initiated before the compressor went into surge, capturing images of the flow field during the evolution of stall precursors, rotating stall, and surge. DPIV image data were asynchronously acquired throughout the full range of the stall/surge process. A separate computer was used to digitize the signals from the dynamic pressure transducers and the Nd:YAG laser Q-switch trigger signals. Triggering the Nd:YAG laser Q-switch produces the pulsed output. The Q-switches are only fired when image data are being acquired from the cross-correlation CCD camera. The digitized laser Q-switch trigger and dynamic pressure signals were examined to determine when a DPIV image pair acquisition coincided with the passage of a stall precursor or a surge event. This data acquisition strategy therefore enabled *a posteriori* synchronization of the DPIV data with the compressor stall events. An ancillary benefit of the pulsed laser illumination (5 ns) and high-speed image acquisition was the recording of the precise impeller position for each image frame pair acquired, which was used to determine the impeller orientation relative to the diffuser vanes for each instantaneous flow field measurement.

The commercial DPIV system used to collect the data offers on-line data visualization capabilities that are extremely useful for optimizing the experiment parameters. However, the commercial system lacked some features necessary to expedite processing the large volumes (gigabytes) of data acquired in this measurement program. A custom Windows 95/NT application interface-based cross-correlation data processing program was written to process the large volumes of data in batch mode, automating many steps that would otherwise have to be done manually. The FORTRAN-based data reduction software incorporated left/right image reversal correction, image gain scaling, region of interest processing, fuzzy logic data validation, and on-line graphical display of the velocity vector maps as they were processed [18].

5.0 Results and Discussion

5.1 Light Sheet Probe and Flow Seeding. The light sheet probe worked very well for providing the requisite 13×1 mm light sheet with minimal scattering from the diffuser vanes and impeller. The light sheet probe was located in insertion port #3 for all of the raw and processed DPIV image data shown in this work. The normal seed particle concentration obtained in the diffuser region was approximately 8 particles/mm^3. During compressor surge, the seed particle concentration in the diffuser increased by nearly an order of magnitude over the stable operating point seed concentration. A sample single exposure DPIV image illustrating the very high concentration of seeding obtained during compressor surge is shown in Fig. 3. The diffuser vanes have been overdrawn to highlight their locations in the image and the pressure and suction surfaces of the vanes are marked in the figure. The impeller is faintly visible on the right side of the figure. The alumina powder did not adhere to the glass surfaces, as was observed by the lack of seed material buildup on the optical access port window and light sheet probe exit window. The optical access port and probe exit window only remained clean if the seeder was turned on after the compressor was operated at its design speed long enough for the casing temperature to reach thermal equilibrium. At design conditions the tip clearance gap is 0.4 mm and the compressor casing temperature near the diffuser reaches 175°C. If the seeder was turned on at less than design speed, then the optical access ports became coated with seed material in a matter of seconds.

5.2 Anatomy of Compressor Surge. The compressor was operated just above stall at approximately 4.26 kg/s mass flow and 21,750 rpm. The camera field of view for the DPIV measurements was approximately 61×61 mm, yielding a spatial resolution of 61 μm/pixel. Image frame pairs were acquired with an intraframe time (time between laser pulses) of 1.8 μs. The data were processed using 64×64 pixel subregions, subregion image shifting, and with 75 percent overlap to ensure that high-quality velocity vector maps with minimal data dropout were obtained (see Raffel et al. [17] for more details of DPIV processing techniques). Particle image displacements ranged from 0 to over 16 pixels for the data presented here. Velocity measurements were obtained at 12, 30, 50, 90, and 95 percent span (0 percent span is at the hub, while 100 percent span is at the casing) on both the suction and pressure sides of the diffuser channel.

The compressor was driven into stall by restricting the flow in the compressor via the downstream collector valve. After the compressor entered stall the collector valve was then reopened to allow the compressor to recover. Approximately 3–5 surge cycles occurred between entering and exiting surge. As described above,

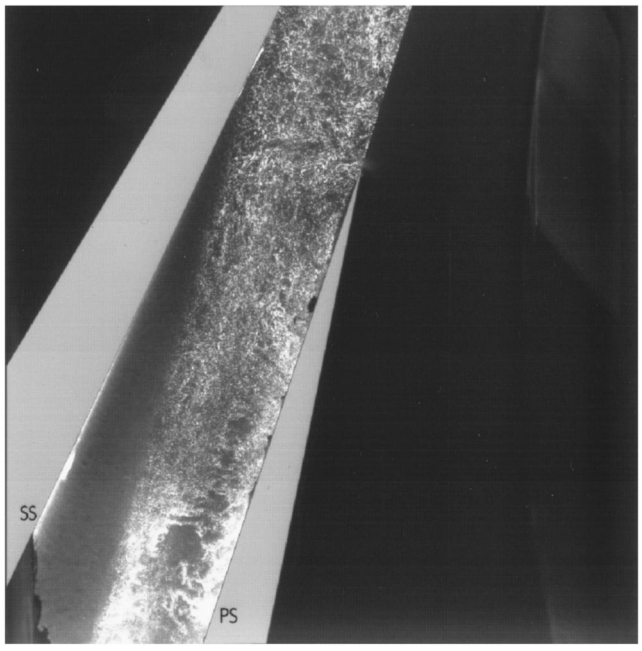

Fig. 3 Sample single exposure DPIV image obtained from the centrifugal compressor rig. The diffuser vanes have been overdrawn on the image to accentuate their extents and the pressure (PS) and suction surfaces (SS) have been labeled.

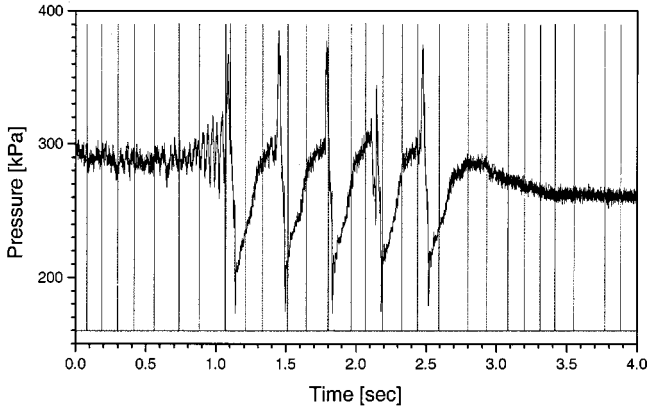

Fig. 4 Sample of the digitized Kulite #3 signal along with the laser Q-switch trigger signals (narrow spikes) showing a complete surge event

the dynamic pressure transducer measurements were used to reconcile the acquired DPIV image data with the time evolution of the rotating stall and surge events. Both the laser Q-switch trigger signals and pressure transducer signals were digitized at a 3 kHz sampling rate for a period of 15 seconds. The DPIV image sequence acquisition lasted about 10 seconds. The data were acquired by first starting the pressure signal digitization. Then the DPIV image sequence acquisition was initiated (this ensured that the DPIV data was contained within the 15 second pressure data record). While these measurements were being acquired, the collector valve was closed down, driving the compressor into surge.

A section of the digitized signals from the laser Q-switch trigger and the #3 pressure transducer signal (located in the diffuser throat region) are shown in Fig. 4. DPIV image acquisition and Kulite signal digitization both preceded and followed the surge events. The spiked signals represent the laser Q-switch trigger pulses, and hence pulsed laser output. The observed spacing between laser firings is slightly irregular, since the once-per-rev signal from the compressor was used to initiate the laser firing. The compressor surge events are illustrated by the large high to low pressure fluctuations observed in the data. Surge events were differentiated from rotating stall by the simultaneous occurrence of large high to low pressure fluctuations on all three dynamic pressure transducers located in the diffuser. The stable operating point pressure in the diffuser throat was approximately 280 kPa and the observed surge fluctuations contained peak pressure levels of 540 kPa and minimum pressure readings of 170 kPa. Each surge cycle consists of an initial large spike in pressure in the diffuser. The increasing back pressure caused by closing down the collector valve decreases the mass flow, which results in flow separation on both the pressure and suction sides of the diffuser passage. As will be discussed below, low-momentum fluid on the pressure side of the passage is observed downstream of the diffuser throat prior to surge. Other velocity vector data obtained using the light sheet probe at insertion port #2 (not shown here) revealed an even larger low-momentum region on the suction side of the diffuser passage. The low-momentum flow on both sides of the passage reduces the effective flow area in the diffuser. The impeller pumps against the blockage that develops in the diffuser, which we believe leads to the large rise in pressure at the start of the surge event. The pressure in the diffuser increases until the impeller can no longer work against the developed head. At this point the high-pressure fluid in the diffuser rushes back upstream into the vaneless space, resulting in a sharp drop in pressure in the diffuser. The pressure then slowly recovers from the minimum value back to the stable operating point pressure level before the next surge cycle begins. The frequency of the surge cycles is approximately 3 Hz. The impeller makes roughly 100 revolutions during each surge cycle. The stable operating pressure level before the surge event is higher than the pressure level following surge since the collector valve has been opened up wider than the pre-stall position to allow quick recovery. An indication of rotating stall in the pressure trace shown in Fig. 4 is observed in the steadily increasing amplitude of the sinusoidal variation of the pressure readings just prior to the first surge cycle. The lifetime of the rotating stall cells is directly influenced by the rate at which the collector valve is closed. Our goal was to capture both rotating stall and surge events within the 10 second DPIV system data acquisition window. As a result, not much rotating stall information is contained in the pressure data prior to the onset of surge.

The dynamic pressure transducer data enabled the DPIV measurements to be reconciled with the surge events passing through the DPIV measurement location. Our collection of DPIV measurements over hundreds of surge cycles indicates that the flow features measured during the surge cycles are repeatable with respect to the time of occurrence within the surge cycle. Figure 5 shows a surge cycle pressure fluctuation measured by Kulite #3 and four processed DPIV velocity vector maps. The four velocity vector maps in Fig. 5 are from different surge cycles. A representative dynamic pressure trace is shown at the top of Fig. 5 where four laser Q-switch trigger pulses are also displayed. The four spikes (labeled A, B, C, and D) mark the relative location of the DPIV image acquisitions during the surge event. The independent DPIV velocity fields have been referenced onto this representative pressure trace using the pressure minima of the individual pressure trace data for the independent surge cycles as a common timing reference point. In the velocity vector plots, the x direction corresponds primarily to the compressor radial coordinate, while the y direction corresponds primarily to the circumferential compressor coordinate. The black velocity vectors are overlaid on a color contour plot of the velocity vector magnitudes, which enhances the changes in flow magnitude. Only half of the velocity vectors computed are shown. Every other horizontal row of velocity vectors has been omitted to improve the legibility of the plot. The impeller wheel and blades are shown on the right side of the plots, along with a reference vector near the top of the plots. The image synchronization technique breaks down during the surge event since the radical changes in compressor loading cause deviations in the rotational speed of the impeller, which also affects the triggering of the DPIV system. The loss of synchronization is manifested in the impeller blades being captured at random positions relative to the diffuser vanes. Figure 5(A) shows the velocity field at a stable operating mass flow just above surge at 90 percent span. At this stable operating condition just above surge, the high-speed flow upstream of the diffuser is observed to slow significantly as it enters the diffuser, indicating that diffuser stall is imminent. At the bottom of Fig. 5(A) we observe that the low-momentum flow that develops from both the suction and pressure sides of the diffuser passage has grown large enough to span the full passage width. As mentioned above, we believe that this low-momentum fluid provides the blockage that results in the sharp pressure rise at the start of the surge cycle.

The impeller builds pressure against the blockage in the diffuser until the impeller can no longer pump against the developed head. At this point in the surge cycle, the high-pressure fluid built up in the diffuser flows back upstream into the vaneless space. Two main factors influence the characteristics of the reversing flow: the time-dependent pressure gradient and the circumferential orientation of the impeller relative to the diffuser. During backflow, the diffuser vane passage acts as a convergent one-dimensional nozzle. In the absence of the impeller and with a steady-state pressure drop from diffuser exit to the diffuser throat, we would expect to see an accelerating backflow in the diffuser vane passage with the maximum velocity occurring at the throat of the diffuser. However, the pressure gradient along the diffuser passage is changing with time (or where we are in the surge cycle); therefore, the magnitude of the reversing flow is a function

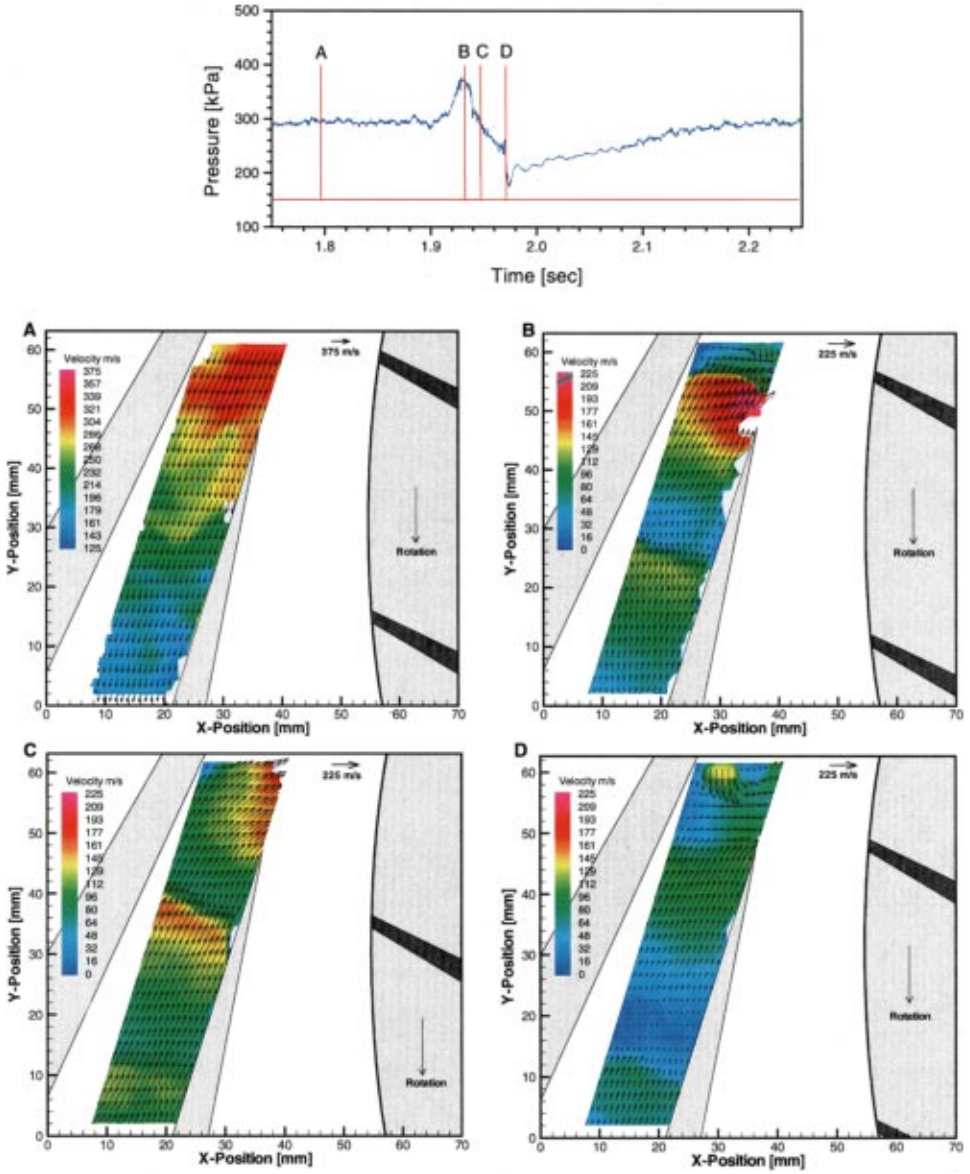

Fig. 5 Pressure time history measured using Kulite #3 during a surge event is shown across top, where the labeled laser Q-switch trigger signals indicate time location in surge cycle of each respective velocity vector plot (velocity scale in plot A is not the same as the scales in plots B–D). (A) normal flow before the onset of surge; (B) reverse flow field at peak of high-pressure surge cycle; (C) reverse flow field on the falling edge of the high-pressure surge cycle; (D) reverse flow at the transition between the high-pressure and low-pressure portion of the surge cycle.

of the driving pressure gradient in the diffuser. In addition to the time-dependent nature of the reversing flow, we also observed spatial variations within the reverse flow. The backflowing fluid in the diffuser appears to contain streamwise velocity gradients. These spatial velocity gradients manifest themselves as isolated waves of high to low-velocity fluid within the diffuser. The high-velocity wave fronts appear to be phase locked with the passing impeller blade positions. Potential pressure fields emanate from the impeller blades. They also can be generated at the diffuser vane leading edge due to the high incidence angles that occur during surge. The strength of these potential pressure fields (which will be referred to here as pressure waves) drops off exponentially away from the blades. These pressure waves appear to interact with the backflowing fluid in the diffuser. The character of the reversing flow exiting the diffuser is influenced by the relative orientation of the impeller blades and hence the pressure waves relative to the diffuser vane leading edge. In the data shown below, we are able to identify the time of the DPIV image acquisitions with respect to the time-dependent pressure gradient along the diffuser; however, the impeller is still captured at random orientations relative to the diffuser vane leading edge.

The velocity data shown in Figs. 5(B–D) was obtained at 95 percent span. In order to enhance the details of the lower dynamic range flow, the color scale and vector magnitudes in Figs. 5(B–D) are different from the data in Fig. 5(A). Figure 5(B) shows the flow field corresponding to the highest pressure condition in the diffuser, where the entire flow field is backflowing and the velocities range from 50 to 225 m/s. There appear to be streamwise velocity gradients within the backflowing fluid that are phase-locked to the impeller blade locations, as evidenced by the high-velocity fluid fronts. The highest velocity backflow (denoted by red/pink region) is observed just at the diffuser throat. Flare light

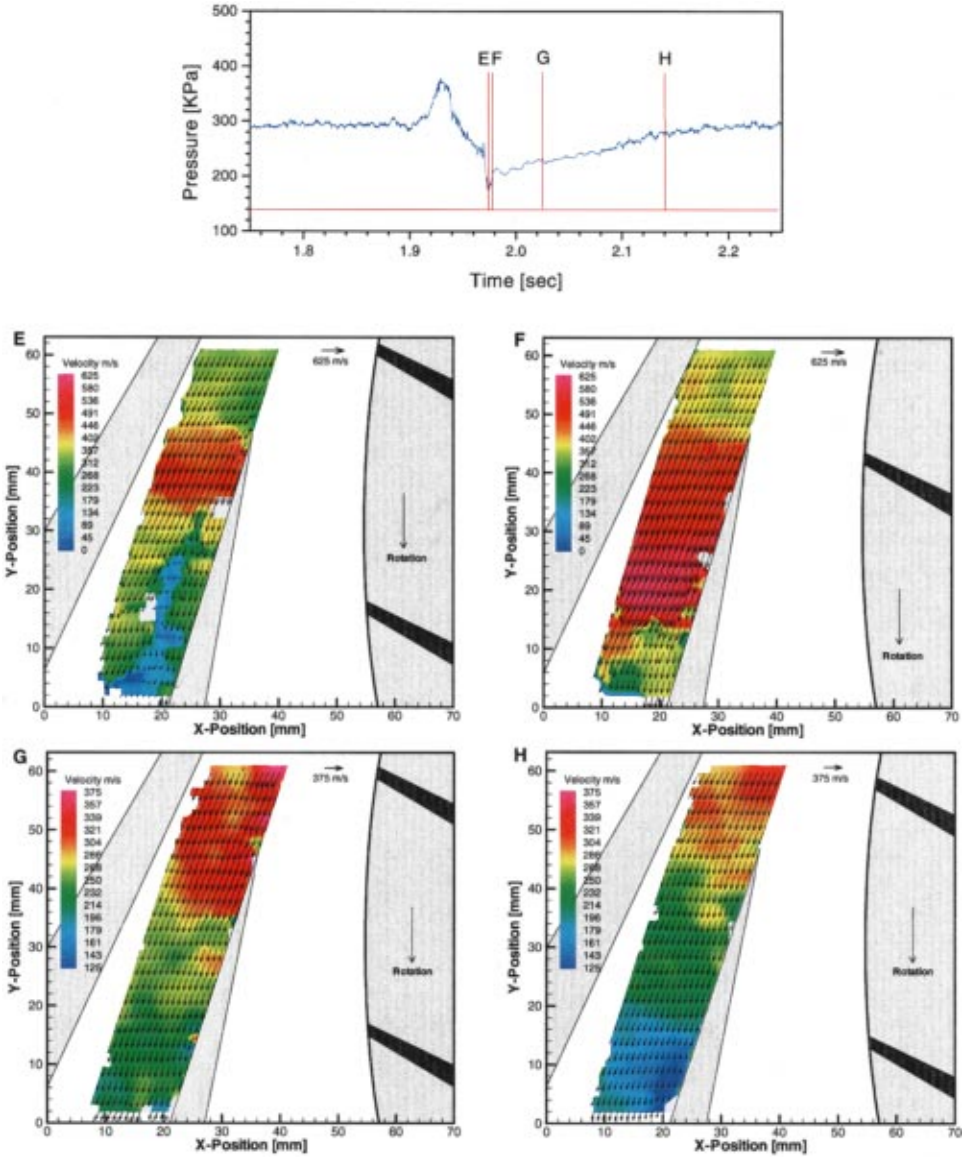

Fig. 6 Pressure–time history during a surge event is shown across top, where the labeled laser Q-switch trigger signals indicate time location in surge cycle of each respective velocity vector plot (velocity scales in plots E and F are the same, scales in plots G and H are the same). (E) initiation of forward flow in the diffuser; (F) minimum pressure and peak velocity in diffuser; (G) pressure recovery and flow deceleration in the diffuser; (H) end of surge cycle and return to presurge conditions observed in Fig. 5(A).

around the diffuser vane leading edge is the source of the data dropout in the leading edge region. The backflow is observed to turn sharply as it clears the diffuser vane leading edge and flows up into the vaneless space. Two impeller blades are observed in this figure. The pressure wave from the upper blade is seen to be encroaching on the high-velocity fluid exiting the diffuser throat and a complete flow reversal is observed just behind the upper blade's pressure wave. The lower blade is also observed to have an effect on the flow deep into the diffuser. The high-velocity fluid front deep in the diffuser appears to be phase locked with the lower impeller blade position.

In Fig. 5(C), the pressure trace data indicates that the DPIV image data were acquired on the falling edge of the high-pressure spike, at a point roughly equal to the stable operating point pressure level. The pressure gradient driving the backflow is smaller than in the case of the flow shown in Fig. 5(B). The processed velocity vector map shows moderate velocity gradients (ranging from 30 to 150 m/s) within the reversing flow and the phase fronts of these flow gradients (orange/yellow region) are still phase-locked to the impeller blade positions. In this image, the impeller blade is below the vane tip and the flow is leisurely turning into the vaneless space. Recall that the characteristics of the instantaneous flow field are influenced by the relative strength of the pressure gradient along the diffuser and the impeller circumferential orientation at the time of the DPIV image acquisition. Therefore, each instantaneous velocity vector map will be unique unless the instantaneous pressure gradient along the diffuser and impeller orientation are identical, which is not the case for any of the data presented here.

Figure 5(D) shows the backflowing condition near the end of the high-pressure spike, just before the pressure in the diffuser makes the sharp drop to its lowest point. At this point in the surge event it appears that the pressure gradient driving the reverse flow has reached equilibrium with the head developed by the impeller.

Here we observe streamwise velocity gradients in the backflowing fluid that range from 0 up to 70 m/s. The high-velocity phase front in the fluid is aligned with the pressure surface of the upper impeller blade. The fluid exiting the diffuser throat turns sharply to the right and flows into the constricted region of the vaneless space defined by the pressure wave from the upper blade and the vane leading edge. The fluid phase front in the diffuser corresponding to the lower impeller blade is lagging slightly behind the blade. These reverse flow vector plots represent the general character of the over 100 DPIV image frames that were acquired depicting backflow in the diffuser passage. Additional DPIV measurements at 12, 30, and 50 percent span during compressor surge verified that the backflow condition shown here spans the entire diffuser vane passage from hub to tip. Therefore, the 90 and 95 percent span data shown here in Figs. 5 and 6 are considered to be representative of the full passage reversing flow field during compressor surge.

Figure 6 shows the surge cycle pressure fluctuation measured by Kulite #3 and four processed DPIV velocity vector maps acquired at 90 percent span that illustrate the start of the process which re-establishes forward flow and pressure recovery within the diffuser prior to the next surge cycle. The four velocity vector maps are again from different data sets, combined here to illustrate the evolution of the flow during the low-pressure portion of the surge cycle. The four spikes (labeled E, F, G, and H) in the pressure data plot mark the relative location of the image acquisitions during recovery from the surge event. The velocity scales in Figs. 6(E–F) are different from those in Figs. 6(G–H) again to better accentuate the flow features. In addition, half of the velocity vectors have been omitted to improve the legibility of the velocity vectors. As shown by the results in Fig. 5, the backflow condition appears to last in the diffuser until the pressure reaches the point marked by laser pulse E in Fig. 6. Prior to this point, the pressure has been gradually falling in the diffuser. However, at laser pulse E we observe an almost instantaneous 70 kPa drop in pressure. At this point in the surge cycle forward flow begins to be re-established in the diffuser.

Figure 6(E) shows the velocity field at laser firing pulse E, corresponding to the point just prior to the minimum in pressure in the diffuser. The sharp drop in pressure causes a rush of air to flow into the diffuser. As shown in the velocity vector map, the diffuser throat acts as a convergent/divergent nozzle and supersonic flow with velocities on the order of 550 m/s (corresponding to an absolute Mach number of 1.5) is obtained within the diffuser. Although this Mach number is based on the stable operating point temperature in the diffuser throat, any temperature variations during surge would have minimal impact on the local Mach number. Just below the supersonic shock front, a region of nearly stagnated flow is observed (indicated by the blue/green region). This stagnated region is the last remnant of the reversed flow shown in Fig. 5(D), which occurs near the end of the high-pressure portion of the surge cycle. The existence of the low-momentum flow (region of irregular seeding) is readily observed on the pressure side of the diffuser passage in the raw DPIV image shown in Fig. 3. The apparent lack of seed in this stagnated region lends further evidence that this is low-pressure air (hence low-density and low seed particle concentration) left over from the reverse flow state.

Figure 6(F) shows the highest velocity flow that was observed during the low-pressure condition in the diffuser. The DPIV image acquisition corresponds to the laser Q-switch trigger pulse F indicated in the pressure trace plot at the top of Fig. 6. The location of the laser Q-switch trigger pulse relative to the Kulite #3 signal shows that the DPIV image pair has been acquired a short time after the lowest pressure was recorded at the diffuser throat. The maximum velocity achieved at this condition was 625 m/s, corresponding to an absolute flow Mach number of 1.7. The relatively uniform flow outside of the diffuser steadily accelerates as it enters the diffuser throat. The propagation of the shock front (pink colored region) is readily observed just above the low-velocity flow region (green/yellow region). Figure 6(F) shows the last remnants of the low-velocity region in the diffuser (near the bottom of the image). This region is smaller and further down in the diffuser than in the velocity field shown in Fig. 6(E).

Figures 6(G,H) show the velocity field in the diffuser as the pressure continues to recover from the minimum level. This gradual pressure rise is the longest portion of the surge cycle. Figure 6(G) corresponds to the point where the pressure has recovered from the pressure minimum to approximately 80 percent of the stable operating point value and shows a region of high-speed flow still down inside the diffuser. The flow in the diffuser is no longer supersonic, but is relaxing back to the stable operating point conditions as the pressure recovers. Figure 6(H) shows the flow field when the pressure has recovered to nearly the stable operation level. In this vector plot the flow closely resembles the stable operating point flow shown in Fig. 5(A), where the high-speed flow is mostly outside of the diffuser. The collection of velocity vector plots in Figs. 5 and 6 describe the changes in the flow occurring within a single surge cycle in the diffuser of this centrifugal compressor. The plots in Fig. 6 were obtained at 90 percent span, and in general depict the flow features occurring during the last half of the surge cycle. Future efforts will be devoted to examining the re-establishing flow in the diffuser at more span locations in order to identify any other spanwise time-dependent variations in the flow.

We have no definitive evidence that the flow reversing in the diffuser flows all the way out through the front of the impeller. The data shown here on the pressure side of the diffuser passage do not actually show the reversed flow going up through the impeller. Other DPIV data collected on the suction side of the diffuser passage using the light sheet probe at insertion port #4 (which is not shown here) showed that during surge, the reverse flow propagates into the vaneless space toward the impeller, but not actually into the impeller. The lack of conclusive evidence of the flow reversing through the impeller may only be the result of not capturing the surge flow at the right instant in time.

We have several pieces of evidence that lead us to believe that the fluid from the diffuser may actually reverse all the way up and out of the impeller. Evidence of flow reversal at the front of the impeller is given in Fig. 7. Here we have plotted static pressure data from Kulites #3 (in the diffuser throat) and #4 (25 mm upstream of the impeller leading edge) during several surge cycles. The pressure traces show that a pressure disturbance is detected at the impeller inlet a short time (10 ms) after the pressure spike is observed in the diffuser. The inlet total pressure into the impeller is atmospheric (100 kPa). The unsteady static pressure at the inlet (peaking at approximately 120 kPa) is higher than the stable operating point plenum static pressure of 83 kPa. If the flow exiting

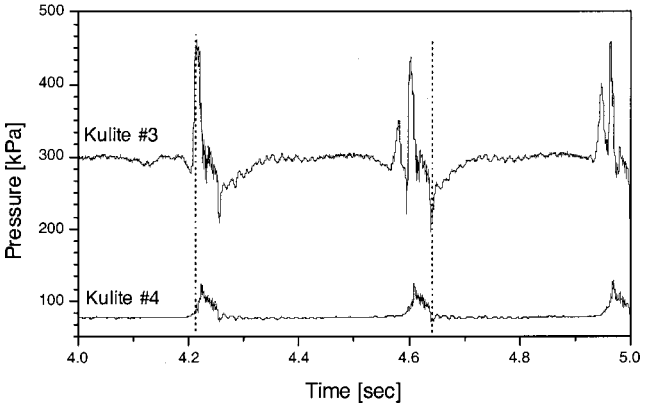

Fig. 7 Pressure traces for Kulites #3 (diffuser throat) and #4 (25 mm upstream of the impeller) during a surge event

the impeller were to be suddenly stopped (as in the case of the blockage that occurs during surge) then the pressure at the inlet would not be expected to exceed 100 kPa. However, the measured peak static pressure of 120 kPa at the inlet during surge indicates that the high-pressure fluid that built up in the diffuser must have expanded back out through the impeller. Note that the pressure disturbance at the inlet terminates, indicating a return to stable operating point flow conditions, when the pressure in the diffuser reaches a minimum.

A second compelling indication of flow reversal through the impeller was obtained by taking additional DPIV measurements upstream of the impeller. A small LDV optical access port in the casing, which can be seen in Fig. 1, enabled DPIV image data to be obtained 25 mm upstream of the impeller at 10 percent span. The light sheet was introduced via a removable casing plug located 180 deg from top dead center. The stable operating point seed particle concentration upstream of the impeller is very low (6 particles/mm^3) compared to the concentration in the high-pressure diffuser region, but still sufficient to obtain correlation results. The DPIV measurement results are shown in Fig. 8, where the measured flow region is small (28×28 mm) due to the 25 mm diameter optical access port. The blade profiles and spacings at the measurement plane are shown on the left side of the plots and the velocity data are shown in the absolute reference frame. The circumferential orientation of the impeller blades for these measurements is not known, the blades are shown for qualitative reference only. The horizontal axis corresponds to the axial position upstream of the impeller and the vertical axis corresponds to the circumferential position relative to the impeller centerline. The flow is from right to left and the impeller is rotating from top to bottom. A reference vector is shown in the plots along with the axial location of Kulite #4. The DPIV data in Fig. 8(*a*) show a uniform 105 m/s flow entering the impeller under stable operating conditions. The region of missing velocity vectors is due to flare light from the impeller centerbody. During a surge event, as the pressure starts to rise in the impeller inlet, the low seed concentration flow slows and starts to turn in the direction of rotation of the impeller. As the pressure peaks in the inlet, the flow reverses out of the impeller and moves tangentially with the impeller, as depicted in Fig. 8(*b*). The magnitude of the reversing flow at this condition is approximately 50 m/s. The fluid reversing out of the impeller contains a factor of five more seed particles (33 particles/mm^3) than the stable operating point flow entering the impeller, which compares favorably with the high seed concentration observed in the diffuser region during the reverse flow condition. This suggests that the fluid coming out of the impeller originates in the diffuser, not in the impeller. After the flow reversal, there appears to be a brief period where the flow moves in a direction opposite the impeller rotation direction. At this point we cannot offer an explanation for this phenomenon, but it has been measured on several occasions. After this counterrotating flow is observed, the flow quickly resumes the uniform stable operating point flow profile.

The 3 kHz sampling rate used to digitize the signals from the Kulites is insufficient to prove that the pressure waves from the impeller blades are correlated with the fluid phase fronts in the backflowing fluid observed in the diffuser. The highest sampling rate at which the Kulite signals could be digitized with the computer-based analog-to-digital converter board was 10 kHz. The minimum sampling rate to correctly resolve unaliased pressure disturbances phase locked to the impeller blade passing frequency of 10,875 Hz would be at least 22 kHz. A high-speed digital storage oscilloscope was therefore used to record a pressure surge cycle from Kulite #3 at a sampling rate of 25 kHz. The recorded Kulite signal showed a high-frequency oscillation (on the order of 10.8 kHz) on top of the low-frequency (3 Hz) surge waveform.

The computer-based analog-to-digital converter system was then used to digitize the signals from Kulite #3 at 10 kHz. The

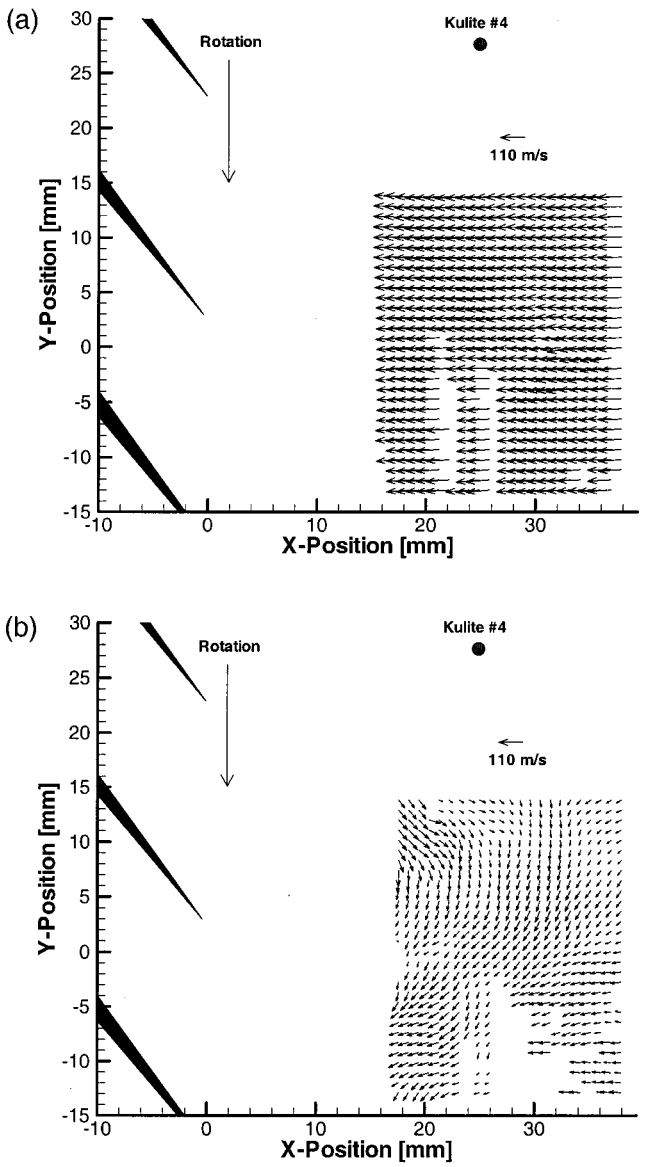

Fig. 8 PIV measurements (absolute reference frame) of the flow upstream of the impeller obtained at 10 percent span: (*a*) steady flow field prior to surge; (*b*) reversing flow at the instant of peak static pressure observed at Kulite #4

data are obviously aliased, but we have the information from the digital oscilloscope to confirm the actual frequency of the blade wakes. The 10 kHz sampled Kulite signal is shown in Fig. 9. Figure 9(*a*) shows a series of surge cycles. Figure 9(*b*) shows an expanded region of the pressure measurements (region outlined by dashed box) from $T=3.8$ to 3.9 seconds, or one surge cycle. The data clearly show the presence of the pressure waves on the rising and falling edges of the high-pressure portion of the surge cycle. The influence of the pressure waves only appears to be significant during the period of reverse flow in the diffuser. Although no valid frequency information can be gleaned from these measurements, the amplitude of the pressure fluctuations is observed to be roughly ± 35 kPa during the high to low-pressure transition of the surge cycle. These high-frequency oscillations confirm that the pressure waves from the blades are strong enough to significantly impact the character of the reversing flow during the high to low-pressure transition portion of the surge cycle. We therefore believe that the observed fluid phase fronts within the reversing flow originate from the interaction of the pressure waves and the re-

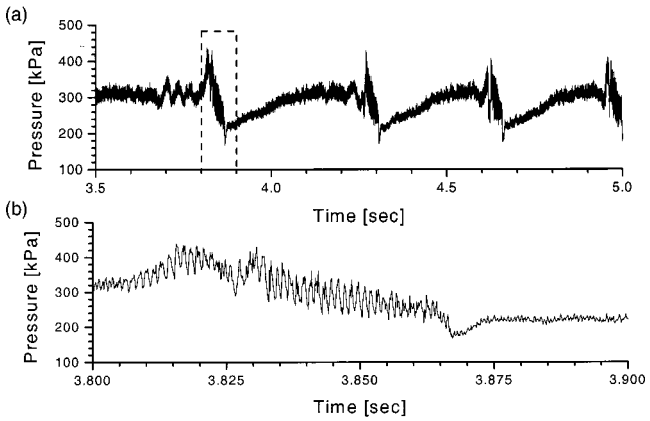

Fig. 9 Kulite #3 signal digitized at 10 kHz, yielding an aliased dynamic pressure signal: (*a*) time record of several surge cycles; (*b*) expanded time record of the dashed box region from Fig. 9(*a*)

versing flow. These pressure fluctuations essentially disappear at the pressure minimum of the surge cycle, which appears to be the point where forward flow is re-established in the diffuser.

6.0 Conclusions

Successful DPIV measurements have been obtained in a high-speed centrifugal compressor yielding instantaneous snapshots of the complex flow fields occurring during compressor surge. High-frequency response pressure transducer signals were used to reconcile the DPIV image data with the evolution of the compressor surge event. Light sheet illumination was obtained by inserting a light sheet generating probe through the collector housing downstream of the measurement location. Global seeding of the flow with alumina yielded sufficiently high seed particle concentrations to support correlation data reduction. Seed material contamination of the optical access port and light sheet generating probe was not significant.

Previous investigations of surge in compressors have relied only on dynamic pressure data as an indicator of the flow conditions within the compressor. DPIV has been shown to be a remarkably powerful technique for capturing instantaneous flow field phenomena, enabling a study of the time evolution of flow variations occurring during the compressor surge cycle. The dynamic pressure data illustrate that a typical surge event consists of high-pressure spike followed by a sharp drop in pressure and then a slow recovery back to the stable operating point pressure. DPIV measurements indicate that a significant low-momentum fluid blockage develops in the diffuser at a stable operating point just above the stalling mass flow. With a further constriction of the mass flow, the blockage in the diffuser appears to cause the large pressure spike observed at the start of the surge cycle. Furthermore, the DPIV measurements show that at the peak of the high-pressure spike, the flow in the diffuser completely reverses and flows up into the vaneless space, indicating a failure of the impeller to maintain the developed head. At the point of minimum pressure in the diffuser, forward flow is re-established in the form of a supersonic shock front that propagates back down through the diffuser. The supersonic shock front forces the remnants of the reversing flow out of the diffuser. As the pressure slowly recovers in the diffuser, the high-speed flow subsides and the flow field approaches the stable operating point conditions of high-speed flow entering the diffuser and low-speed flow within the diffuser. High seed particle concentration flow was noted to occur in the diffuser during the period of reverse flow. High seed particle concentration fluid is also observed to exit the front of the impeller during surge. DPIV measurements also showed reverse flow exiting the impeller inlet. We cannot conclusively say that full flow reversal occurs throughout the diffuser/impeller, but the evidence compels us to believe that it may be possible. The DPIV image data also indicate that the reverse flow occurring during compressor surge is influenced by the pressure waves emanating from the passing impeller blades. After the DPIV data alerted us to the existence of the pressure waves influencing the reversing flow, high-frequency dynamic pressure data were collected that confirmed that ± 34 kPa pressure fluctuations are caused by pressure waves emanating from the impeller blades. These pressure waves in turn cause streamwise velocity gradients in the reversing flow within the diffuser.

Combined DPIV and transient pressure measurements are helping us to understand pre-stall and pre-surge phenomena occurring in the compressor. In the data presented here, the compressor was quickly transitioned into surge within the DPIV image acquisition window, which did not allow for significant data acquisition during stall inception processes. Our future work will concentrate on operating the compressor in a sustained rotating stall condition during which DPIV data will be obtained. These measurements will concentrate on the precursive events that grow into large amplitude rotating stall and surge. Flow measurements of the stall precursors should contribute significantly to our understanding of the mechanisms leading up to compressor surge. Both the stable operating and unstable operating flow field data obtained in this work will be used to optimize the location of air injection ports for active control of rotating stall and surge. The ultimate goal of this work is the successful stabilization of the compressor for operation beyond its normal surge limit. Active stall control allows the compressor to achieve peak performance while maintaining adequate surge margin. Successful measurement and analysis of the stalling flow is the first step toward achieving this goal.

Acknowledgments

The authors would like to thank Tony Zaldana, Angela Surgenor, Stephen Helland, and Tom Jett for their support in the operation of the centrifugal compressor facility. We would also like to thank Mr. W. T. John for his assistance in the setup and installation of the DPIV system. A special thanks to Tony Strazisar and Jerry Wood for their many helpful comments and suggestions throughout this research program.

References

[1] Weigl, H. J., Paduano, J. D., Fréchette, L. G., Epstein, A. H., Greitzer, E. M., Bright, M. M., and Strazisar, A. J., 1997, ''Active Stabilization of Rotating Stall and Surge in a Transonic Single Stage Axial Compressor,'' ASME J. Turbomach., **120**, No. 4, pp. 625–636.

[2] Paone, N., Riethmuller, M. L., and Van den Braembussche, R. A., 1988, ''Application of Particle Image Displacement Velocimetry to a Centrifugal Pump,'' *Proc. Fourth International Symposium on Applications of Laser Techniques to Fluid Mechanics*, Lisbon, Portugal, July 11–14.

[3] Bryanston-Cross, P. J., Towers, C. E., Judge, T. R., Towers, D. P., Harasgama, S. P., and Hopwood, S. T., 1992, ''The Application of Particle Image Velocimetry (PIV) in a Short-Duration Transonic Annular Turbine Cascade,'' ASME J. Turbomach., **114**, pp. 504–509.

[4] Rothlübbers, C., Scheffler, T., Orglmeister, R., and Siekmann, H., 1996, ''Particle Tracking Velocimetry Measurements in a Radial Pump With Particle Pair Detection Using the Hough Transform,'' *Proc. Eighth International Symposium on Applications of Laser Techniques to Fluid Mechanics*, Lisbon, Portugal, July 8–11, pp. 8.6.1–8.6.6.

[5] Oldenburg, M., and Pap, E., 1996, ''Velocity Measurement in the Impeller and in the Volute of a Centrifugal Pump by Particle Image Displacement Velocimetry,'' *Proc. Eighth International Symposium on Applications of Laser Techniques to Fluid Mechanics*, Lisbon, Portugal, July 8–11, pp. 8.2.1–8.2.5.

[6] Gogineni, S., Goss, L., Copenhaver, W., and Gorrell, S., 1998, ''Development of Digital Two-Color PIV for Turbomachinery Applications,'' Paper No. AIAA-97-0494.

[7] Day Treml, K., and Lawless, P. B., 1998, ''Particle Image Velocimetry of Vane–Rotor Interaction in a Turbine Stage,'' Paper No. AIAA-98-3599.

[8] Bryanston-Cross, P. J., Burnett, M., Lee, W. K., Udrea, D. D., Chana, K., and Anderson, S. J., 1997, ''Transonic PIV (Particle Image Velocimetry) Measurements Made in the Stator Trailing Edge and Rotor Region of the ILPF (Isentropic Light Piston Facility) at Pyestock Farnborough,'' *Proc. SPIE Conference on Optical Diagnostics in Fluid and Thermal Flow*, Vol. 3172, pp. 561–574.

[9] Wernet, M. P., 1997, ''Demonstration of PIV in a Transonic Compressor,''

Proc. AGARD 90th Symposium on Nonintrusive Measurement Techniques for Propulsion Engines, Brussels, Belgium, Oct. 20–24.
[10] Wernet, M. P., 1998, ''Digital PIV Measurements in the Diffuser of a High Speed Centrifugal Compressor,'' Paper No. AIAA-98-2777.
[11] Skoch, G. J., Prahst, P. S., Wernet, M. P., Wood, J. R., and Strazisar, A. J., 1997 ''Laser Anemometer Measurements of the Flow Field in a 4:1 Pressure Ratio Centrifugal Impeller,'' ASME Paper No. 97-GT-342.
[12] Paduano, J. D., Epstein, A. H., Valavani, L., Longley, J. P., Greitzer, E. M., and Guenette, G. R., 1993, ''Active Control of Rotating Stall in a Low-Speed Axial Compressor,'' ASME J. Turbomach., **115**, pp. 48–56.
[13] Day, I. J., 1993, ''Stall Inception in Axial Flow Compressors,'' ASME J. Turbomach., **115**, pp. 1–9.
[14] Oakes, W. C., Lawless, P. B., and Fleeter, S., 1999, ''Characterization of the Behavior of a Centrifugal Compressor With Active Stall Control,'' J. Propul. Power, in press.
[15] Wernet, J. H., and Wernet, M. P., 1994, ''Stabilized Alumina/Ethanol Colloidal Dispersion for Seeding High Temperature Air Flows,'' *Proc. ASME Symposium on Laser Anemometry: Advances and Applications*, Lake Tahoe, NV, June 19–23.
[16] Melling, A., 1997, ''Tracer Particles and Seeding for Particle Image Velocimetry,'' Meas. Sci. Technol., **8**, pp. 1406–1416.
[17] Raffel, M., Willert, C., and Kompenhans, J., 1998, *Particle Image Velocimetry, A Practical Guide*, Springer, New York.
[18] Wernet, M. P., 1999, ''Fuzzy Logic Enhanced Digital PIV Processing Software,'' *Proc. 18th International Congress on Instrumentation for Aerospace Simulation Facilities (ICIASF)*, Toulouse, France, June 14–17, pp. 2.1–2.10.